

Jordan Journal of Mechanical and Industrial Engineering (JJMIE)

JJMIE is a high-quality scientific journal devoted to fields of Mechanical and Industrial Engineering. It is published by Hashemite University in cooperation with the Jordanian Scientific Research and Innovation Support Fund, Ministry of Higher Education and Scientific Research.

EDITORIAL BOARD

Editor-in-Chief

Prof. Ali M. Jawarneh

Assistant Editors

Dr. Ahmad AlMigdady

Dr. Mohannad Jreissat

Editorial Board

Prof. Tariq A. ALAzab

Al Balqa Applied University

Prof. Adnan A. Bashir

The Hashemite University

Prof. Ibrahim Abu-Alshaikh

Jordan University

Prof. Mohammed Ali Almomani

Jordan University of Science and Technology

Prof. Nabil Beithou

Tafila technical University

Prof. Hitham M. Tlilan

The Hashemite University

THE INTERNATIONAL ADVISORY BOARD

Khaled Abou-El-Hossein

Nelson Mandela University, South Africa

Hosni Abu-Mulaweh

Purdue University, USA

Habil. Salman Ajib

Hochschule Ostwestfalen-Lippe, Germany

Abdelsalam Al-Sarkhi

King Fahd University, Saudi Arabia

Mohammad Khasawneh

Binghamton University, U.S.A

Afzal Khan

University of Engineering and Technology, Pakistan

Mohd Sapuan Salit

University Putra, Malaysia

Shyh-Chour Huang

National Kaohsiung University of Science and Technology, Taiwan

Suhil Kiwan

Jordan University of Science and Technology, Jordan

Amer Ababneh

Hashemite University, Jordan

Naseem Sawaqed

Mutah University, Jordan

Rebhi Damsch

Al-Balqa Applied University, Jordan

Safwan Al-Qawabah

Al-Zaytoonah University, Jordan

Mohammed Al-Nawafleh

Al-Hussein Bin Talal University, Jordan

Hubert Roth

Siegen University, German

Eiyad Abu-Nada

Khalifa University, UAE

Petr A. Nikrityuk

University of Alberta, CANADA

Editorial Board Support Team

Language Editor

Dr. Baker M. Bani-khair

Publishing Layout

Eng. Ali Abu Salimeh

SUBMISSION ADDRESS

Prof. Ali M. Jawarneh, Editor-in-Chief

Jordan Journal of Mechanical & Industrial Engineering,

Hashemite University,

PO Box 330127, Zarqa, 13133, Jordan

E-mail: jjmie@hu.edu.jo



Hashemite Kingdom of Jordan



Hashemite University

Jordan Journal of
Mechanical and Industrial Engineering

JJMIIE

An International Peer-Reviewed Scientific Journal

Financed by Scientific Research Support Fund

Volume 16 Number 5, December 2022

<http://jjmie.hu.edu.jo/>

ISSN 1995-6665

Jordan Journal of Mechanical and Industrial Engineering (JJMIE)

JJMIE is a high-quality scientific journal devoted to fields of Mechanical and Industrial Engineering. It is published by Hashemite University in cooperation with the Jordanian Scientific Research and Innovation Support Fund, Ministry of Higher Education and Scientific Research.

Introduction: The Editorial Board is very committed to build the Journal as one of the leading international journals in mechanical and industrial engineering sciences in the next few years. With the support of the Ministry of Higher Education and Scientific Research and Jordanian Universities, it is expected that a heavy resource to be channeled into the Journal to establish its international reputation. The Journal's reputation will be enhanced from arrangements with several organizers of international conferences in publishing selected best papers of the conference proceedings.

Aims and Scope: *Jordan Journal of Mechanical and Industrial Engineering* (JJMIE) is a refereed international journal to be of interest and use to all those concerned with research in various fields of, or closely related to, mechanical and industrial engineering disciplines. *Jordan Journal of Mechanical and Industrial Engineering* aims to provide a highly readable and valuable addition to the literature which will serve as an indispensable reference tool for years to come. The coverage of the journal includes all new theoretical and experimental findings in the fields of mechanical and industrial engineering or any closely related fields (Materials, Manufacturing, Management, Design, Thermal, Fluid, Energy, Control, Mechatronics, and Biomedical). The journal also encourages the submission of critical review articles covering advances in recent research of such fields as well as technical notes.

Guide for Authors

Manuscript Submission:

High-quality submissions to this new journal are welcome now and manuscripts may be either submitted online or email.

Online: For online and email submission upload one copy of the full paper including graphics and all figures at the online, submission site, accessed via <http://jjmie.hu.edu.jo>. The manuscript must be written in MS Word Format. All correspondence including notification of the Editor's decision and requests for revision, takes place by e-mail and via the Author's homepage, removing the need for a hard-copy paper trail

Submission address and contact :

Prof. Ali M. Jawarneh

Editor-in-Chief

Jordan Journal of Mechanical & Industrial

Engineering, Hashemite University

PO Box 330127, Zarqa, 13115, Jordan

E-mail: jjmie@hu.edu.jo

Types of contributions: Original research papers and Technical reports

Corresponding author: Clearly indicate who is responsible for correspondence at all stages of refereeing and publication, including post-publication. Ensure that telephone and fax numbers (with country and area code) are provided in addition to the e-mail address and the complete postal address. Full postal addresses must be given for all co-authors.

Original material: Submission of an article implies that the work described has not been published previously (except in the form of itstan abstract or as part of a published lecture or academic thesis), that it is not under consideration for publication elsewhere, the publication is approved by all authors and that, if accepted, it will not be published elsewhere in the same form, in English or in any other language, without the written consent of the Publisher. Authors found to be deliberately contravening the submission guidelines on originality and exclusivity shall not be considered for future publication in this journal.

Withdrawing: If the author chooses to withdraw his article after it has been assessed, he shall reimburse JJMIE with the cost of reviewing the paper.

Manuscript Preparation:

General: Editors reserve the right to adjust style to certain standards of uniformity. Original manuscripts are discarded after publication unless the Publisher is asked to return original material after use. Please use MS Word for the text of your manuscript

Structure: Follow this order when typing manuscripts: Title, Authors, Authors title, Affiliations, Abstract, Keywords, Introduction, Main text, Conclusions, Acknowledgements, Appendix, References, Figure Captions, Figures and then Tables. Please supply figures imported into the text AND also separately as original graphics files. Collate acknowledgements in a separate section at the end of the article and do not include them on the title page, as a footnote to the title or otherwise.

Text Layout: Use 1.5 line spacing and wide (3 cm) margins. Ensure that each new paragraph is clearly indicated. Present tables and figure legends on separate pages at the end of the manuscript. If possible, consult a recent issue of the journal to become familiar with layout and conventions. All footnotes (except for table and corresponding author footnotes) should be identified with superscript Arabic numbers. To conserve space, authors are requested to mark the less important parts of the paper (such as records of experimental results) for printing in smaller type. For long papers (more than 4000 words) sections which could be deleted without destroying either the sense or the continuity of the paper should be indicated as a guide for the editor. Nomenclature should conform to that most frequently used in the scientific field concerned. Number all pages consecutively; use 12 or 10 pt font size and standard fonts.

Corresponding author: Clearly indicate who is responsible for correspondence at all stages of refereeing and publication, including post-publication. The corresponding author should be identified with an asterisk and footnote. Ensure that telephone and fax numbers (with country and area code) are provided in addition to the e-mail address and the complete postal address. Full postal addresses must be given for all co-authors. Please consult a recent journal paper for style if possible.

Abstract: A self-contained abstract outlining in a single paragraph the aims, scope and conclusions of the paper must be supplied.

Keywords: Immediately after the abstract, provide a maximum of six keywords (avoid, for example, 'and', 'of'). Be sparing with abbreviations: only abbreviations firmly established in the field may be eligible.

Symbols: All Greek letters and unusual symbols should be identified by name in the margin, the first time they are used.

Units: Follow internationally accepted rules and conventions: use the international system of units (SI). If other quantities are mentioned, give their equivalent quantities in SI

Maths: Number consecutively any equations that have to be displayed separately from the text (if referred to explicitly in the text).

References: All publications cited in the text should be presented in a list of references following the text of the manuscript.

Text: Indicate references by number(s) in square brackets in line with the text. The actual authors can be referred to, but the reference number(s) must always be given.

List: Number the references (numbers in square brackets) in the list in the order in which they appear in the text.

Examples:

Reference to a journal publication:

[1] M.S. Mohsen, B.A. Akash, "Evaluation of domestic solar water heating system in Jordan using analytic hierarchy process". Energy Conversion & Management, Vol. 38 (1997) No. 9, 1815-1822.

Reference to a book:

[2] Strunk Jr W, White EB. The elements of style. 3rd ed. New York: Macmillan; 1979.

Reference to a conference proceeding:

[3] B. Akash, S. Odeh, S. Nijmeh, "Modeling of solar-assisted double-tube evaporator heat pump system under local climate conditions". 5th Jordanian International Mechanical Engineering Conference, Amman, Jordan, 2004.

Reference to a chapter in an edited book:

[4] Mettam GR, Adams LB. How to prepare an electronic version of your article. In: Jones BS, Smith RZ, editors. Introduction to the electronic age, New York: E-Publishing Inc; 1999, p. 281-304

Free Online Color : If, together with your accepted article, you submit usable color and black/white figures then the journal will ensure that these figures will appear in color on the journal website electronic version.

Tables: Tables should be numbered consecutively and given suitable captions and each table should begin on a new page. No vertical rules should be used. Tables should not unnecessarily duplicate results presented elsewhere in the manuscript (for example, in graphs). Footnotes to tables should be typed below the table and should be referred to by superscript lowercase letters.

Notification: Authors will be notified of the acceptance of their paper by the editor. The Publisher will also send a notification of receipt of the paper in production.

Copyright: All authors must sign the Transfer of Copyright agreement before the article can be published. This transfer agreement enables Jordan Journal of Mechanical and Industrial Engineering to protect the copyrighted material for the authors, but does not relinquish the authors' proprietary rights. The copyright transfer covers the exclusive rights to reproduce and distribute the article, including reprints, photographic reproductions, microfilm or any other reproductions of similar nature and translations.

Proof Reading: One set of page proofs in MS Word format will be sent by e-mail to the corresponding author, to be checked for typesetting/editing. The corrections should be returned within 48 hours. No changes in, or additions to, the accepted (and subsequently edited) manuscript will be allowed at this stage. Proofreading is solely the author's responsibility. Any queries should be answered in full. Please correct factual errors only, or errors introduced by typesetting. Please note that once your paper has been proofed we publish the identical paper online as in print.

PAGES**PAPERS**

-
- | | |
|----------|---|
| 653– 662 | Numerical Analysis of Crack Initiation Life on Tunnel Boring Machine Cutter Seat
<i>LI Jie, ZHANG Xin, HUANG Yuanjun, SUKang, HU Bo, GUO Jingbo</i> |
| 663– 676 | Parametric Optimization of Pulse TIG Welding Process during Joining of Dissimilar Tensile Steels Used in Automotive Industries
<i>A.Sahoo, S. Tripathy, D.K. Tripathy</i> |
| 677– 688 | Performance Enhancement of Multi-Modal Piezoelectric Energy Harvesting Through Parameter Optimization
<i>Ossama Mokhiamar, David Omooria Masara, Hassan El Gamal</i> |
| 689– 700 | A Lubricating Oil-Based Maintenance for Diesel Engines at the End-user: An Effective Predictive Approach
<i>Mokhtar Ali Amrani, Yara Haddad, Mohammed Abdulhameed, Omar S. Hyder, Amin Saif, Atef M. Ghaleb, Sobhi Mejjiaoui</i> |
| 701– 715 | Copula Approach to Performance Evaluation of Manufacturing System
<i>Ibrahim Yusuf, Abdullahi Sanusi, Nafisatu Muhammad Usman, Mus'abu Musa</i> |
| 717– 728 | Effects of Using a Special Car Cover on the Temperatures and Cooling Load Inside a Parked Car Under Severe Summer Conditions; Iraq Case of Study
<i>Hasan Abbas Hussein, Issam M. Ali Aljubury</i> |
| 729– 742 | Modelling and Prediction of Micro-hardness of Electroless Ni-P coatings Using Response Surface Methodology and Fuzzy Logic
<i>Subhasish Sarkar, Rupam Mandal, Nitesh Mondal, Shouvik Chaudhuri, Tapendu Mandal, Gautam Majumdar</i> |
| 743– 752 | Numerical Simulation Study on Steel Pipe Row Pile Support of Temporary Road Slope
<i>Jian-guang BAI, Hai-jun LI</i> |
| 753– 763 | Study of Repairing a Corroded Cryogenic Tank by Composite Wrap Subjected to Thermal and Mechanical Loadings
<i>Leila BELKADDOUR, Mohamed BERRAHO</i> |
| 765– 775 | Study the Effect of the Shape of the Laser's Path on the Mechanical Properties of Acrylic Layer
<i>Raed Naeem Hwayyin, Azhar Sabah Ameen, Ahmed Salman Hamood</i> |
| 777– 785 | A New Trajectory Planning Method of 6-DOF Apple Picking Manipulator
<i>Junying Li</i> |
| 787– 792 | Experimental Research and Mathematical Modeling of Parameters Affecting Cutting Tool Wear in Turning Process of Inconel 625
<i>Fitim Zeqiri, Burim Fejzaj</i> |
| 793– 809 | An Optimization Approach for Predictive-Reactive Job Shop Scheduling of Reconfigurable Manufacturing Systems
<i>A.A. Abdul Rahman, O.J. Adeboye, J.Y. Tan, M.R. Salleh, M.A. A.Rahman</i> |
-

PAGES**PAPERS**

811– 819

An Integrated Systematic Approach for Reconfiguration of Facilities Layout in a Stochastic Product Demand*A.A. Abdul Rahman, R.N.H. Leong, O.J. Adeboye, E. Mohamad, T.J. Yee, M.H. Md Saad*

821– 833

A Conceptual Framework for Cyber-Physical Quality Monitoring System using Machine Learning*Mathew Chacko , Atul , Satish Babu Boddapati*

835– 863

Design Optimization of Selected Mechanical Engineering Components using Variants of Rao Algorithms*Ravipudi Venkata Rao, Niket Zinzuvadia*

865– 878

Study on the Impact of Sawtooth Roof Inclination Angles and Asymmetrical Opening Positions for An Isolated Building in Cross Ventilation*Osamah Hashem Al-Aghbari , Lip Kean Moey , Vin Cent Tai , Tze Fong Go, Mohammad Hossein Yazdi*

Numerical Analysis of Crack Initiation Life on Tunnel Boring Machine Cutter Seat

LI Jie^{*}, ZHANG Xin, HUANG Yuanjun, SU Kang, HU Bo, GUO Jingbo

¹ School of mechanical engineering, Shijiazhuang Tiedao University, Shijiazhuang 050043, Hebei, China

Received 7 Apr 2022

Accepted 5 Sep 2022

Abstract

Aiming at the fatigue failure of TBM cutter seat under alternating load, the theoretical calculation and numerical simulation analysis method of cutter seat crack initiation life are investigated. According to the rock breaking process of disc cutter, the stress spectrum of cutter seat is obtained. Through the finite element analysis of cutter seat, the dangerous point position of cutter seat is determined. Combined with Q345D material S-N curve and fatigue damage accumulation theory, the prediction model of cutter seat crack initiation life is established, and the prediction of cutter seat crack initiation life is realized. Finally, the crack initiation life of cutter seat is analyzed numerically. The results show that the dangerous part of the cutter seat is at the "L" shape corner, which is consistent with the actual situation. The crack initiation life of the cutter seat is 9.46×10^8 times, 3.00×10^8 times, 2.13×10^8 times and 1.25×10^8 times with the survival rate of 50%, 90%, 95% and 99%. The errors between the theoretical analysis and simulation analysis results are 4.6%, 4.3%, 2.0% and 8.4% respectively. The feasibility of the numerical analysis method and the correctness of the crack initiation life prediction mode of the cutter seat is verified.

© 2022 Jordan Journal of Mechanical and Industrial Engineering. All rights reserved

Keywords: Tunnel boring machine (TBM); Cutter seat; Crack initiation; Load Spectrum; Life prediction.

1. Introduction

Tunnel Boring Machine (TBM) is a highly mechanized and automated large-scale tunnelling equipment for excavation and lining, which has been widely used in tunnel construction projects in railway, municipal, highway, water conservancy and other fields[1-3]. The TBM breaks rock through cutters installed on the cutter head. The cutter shaft of cutter is fixed on the cutter seat through C-shaped blocks and bolts, and the box-type cutter seat is welded on the cutter head. The structure of cutter head and cutter seat is shown in Figure 1[4]. In the process of tunnelling, the cutter is driven by the thrust and torque provided by the cutter head to rotate around the cutter shaft while making the circular motion with the cutter head, and the cutter directly contacts with the rock. The cutter is acted by vertical force, tangential force and lateral force at the cutter ring when it is breaking the rock, as shown in Figure 2. Due to the uncertainty and step of geological rock in tunnelling, the load of cutter is complex in rock breaking, and the cutter seat bears the rock breaking load and strong impact from cutter, so the cutter seat is prone to crack, deformation and other failure problems under alternating load [5-6]. The fatigue crack propagation of the cutter seat structure will be caused once the cutter head cracks appear, which may delay the construction period and lead to major safety accidents.

Therefore, it is very important to study the fatigue failure of the cutter seat and predict the crack initiation life of the cutter seat in the design stage.

In recent years, many scholars have done a lot of research on fatigue crack failure of cutter head and cutter seat cracks of tunnel boring machine. Yang [7] based on the rock breaking mechanism of the central cutter seat, combined with the fatigue life curve of Q345D material and fatigue damage criterion, established a prediction model of crack initiation life of the central cutter seat, and predicted the fatigue life of the central cutter seat under full load. Liu [8] et al. established a calculation model of crack initiation life at dangerous points of TBM cutter head, and studied the influence of geological factors on crack initiation life at dangerous points and the influence of failure regional factors on residual crack initiation life at dangerous points. Ouyang[9] et al. used multi-body dynamics and finite element method, combined with statistical counting method to obtain the stress spectrum of cutter head, and established the crack initiation life model of cutter head according to the stress-life curve of materials. Huo [10] et al. proposed an improved quasi-static method to calculate the dynamic stress of the cutter head, and introduced the plastic constraint factor α to change the yield stress value of the material, and proposed a small time scale fatigue crack growth model of the cutter head with plane stress-strain transition. Zhang [11] et al. modified the short-time scale crack propagation model considering the influence of residual stress, and predicted the crack propagation life of the weld of the cutter head in

* Corresponding author e-mail: tbmlijie@126.com.

view of the fatigue crack problem at the weld of the split cutter head. Kheder, A. [12] et al. Studied the fatigue characteristics of as-cast acicular ductile iron (ASGI) produced by alloying and controlled cooling and as-rolled 42CrMo4 steel. Under the condition of alternating load, the fatigue failure of the structure mainly occurs, and the causes of fatigue failure of the cutter seat are summarized as the material of the cutter seat, working environment and load. Therefore, it is necessary to study the crack initiation life of the cutter seat based on the actual geological conditions of the project.

The tunnel boring machine in this paper is based on a tunnel construction bid section, whose diameter is 6470mm, and the cutter head contains 40 disc cutters. In the process of changing the cutters, 23 cracks were found in the cutter seat, which led to the shutdown to repair the cracks and reduced the construction efficiency greatly. The cracks in the cutter seat are shown in Figure 3. However, if the maintenance of the cutter seat is not carried out in time, the cutter head may crack and increase the construction

safety risk. Especially under complex geological conditions, the alternating load condition of the cutter seat is more severe, and the reliability decline of the cutter seat is more prominent [13].

To sum up, the stress spectrum of the cutter seat obtained through the simulation analysis of rock breaking of cutter, determines the dangerous position of the cutter seat on the basis of establishing the finite element model of the cutter seat, and the prediction model of the crack initiation life of the cutter seat was established based on the modified nominal stress legislation by combining the S-N curve of Q355 material and the fatigue damage accumulation theory, so as to realize the prediction of the crack life of the cutter seat. At the same time, nCode fatigue analysis software is used to verify the correctness of the prediction model of crack initiation life of cutter seat, which provides an effective method for studying crack initiation life of cutter seat.

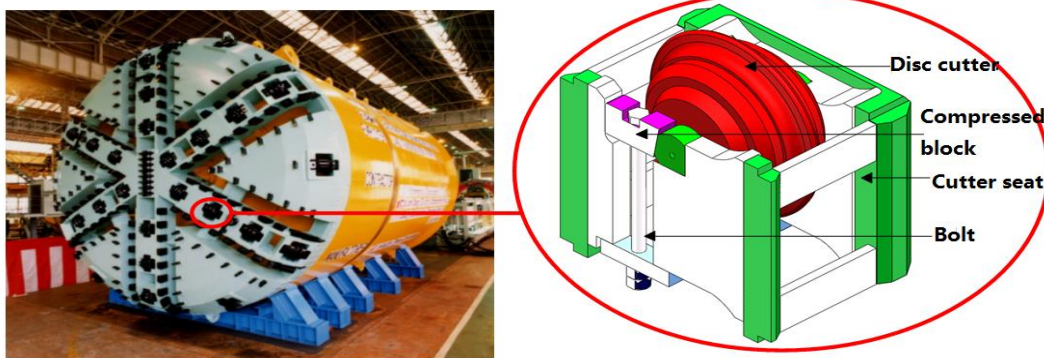
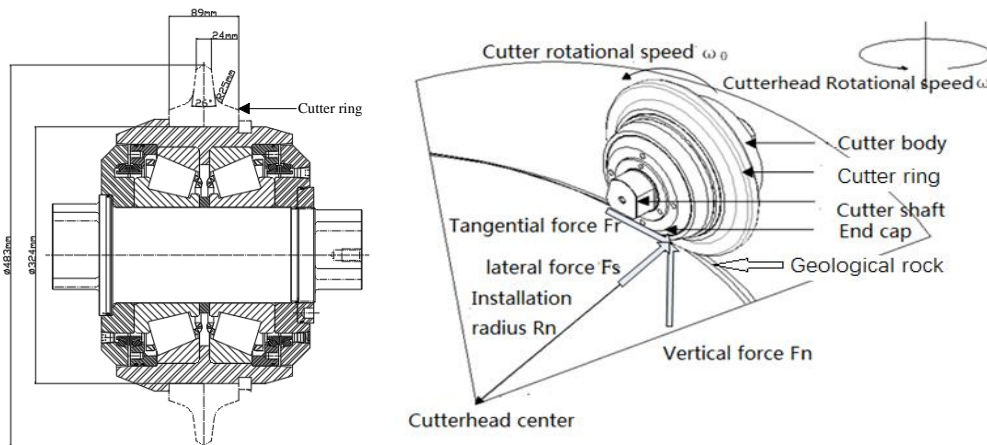


Figure 1. Cutter head and cutter seat



(a) Disc cutter structure and parameters (b) Rock breaking process and force of disc cutter

Figure 2. Disc cutter structure and rock breaking process

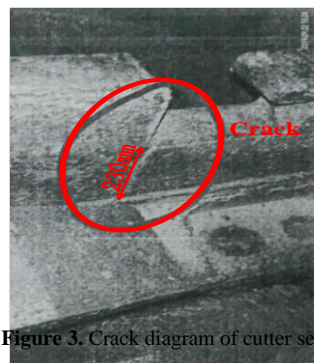


Figure 3. Crack diagram of cutter seat

2. Acquisition of stress spectrum of cutter seat of TBM

Aiming at the fatigue crack failure problem of TBM cutter seat under alternating load, the stress of cutter seat is obtained by simulation analysis of cutter rock breaking, and the load spectrum of cutter seat is obtained by statistical and counting methods. On the basis of determining the dangerous point position of cutter seat, the stress spectrum of dangerous point is obtained by loading the load spectrum of cutter seat, which provides theoretical basis for predicting the crack initiation life of cutter seat.

2.1. Acquisition of load spectrum of cutter seat

Many scholars have done a lot of research on the stress analysis of disc cutter. At present, the CSM disc cutter stress prediction model proposed by Colorado Institute of Mining and Technology is widely used, which comes from the summary of a large number of tunnel construction experiences and has strong practicability[14-15]. See the following formula for the force of disc cutter when it's breaking rock.

$$\left\{ \begin{array}{l} F_t = \frac{P^0 \phi RT}{l + \psi} \\ \phi = \arccos\left(\frac{R-h}{R}\right) \\ P^0 = C_3 \sqrt{\frac{S}{\phi \sqrt{RT}}} \sigma_c^2 \sigma_t \end{array} \right. \quad (1)$$

In the formula (1), F_t is the resultant force (kN) of the disc cutter; R is the radius (mm) of the disc cutter; T is the blade width (mm) of disc cutter; ψ is the pressure distribution coefficient of the cutter tip, which decreases with the increase of the blade width, and the pressure distribution coefficient of the cutter tip is 0.2 ~-0.2; ϕ is the contact angle (rad) between disc cutter blade and rock; h is the penetration of disc cutter (mm); P^0 is the pressure of rock fracture zone, which is related to rock strength, disc cutter geometry, penetration and cutter spacing ($P^0 = f(\sigma_t, \sigma_c, T, R, \phi, S)$); C is a constant similar to rock contact angle ϕ , and its value is 2.12; S is the cutter spacing (mm) of disc cutter; σ_c is the uniaxial compressive strength of rock; σ_t is the tensile strength of rock.

Because the simulation analysis method has better accuracy and economy, Abaqus software is used to simulate the rock breaking process of disc cutter. According to the actual disc cutter used in TBM, the 19-inch disc cutter model is adopted. Considering that only the cutter ring contacts with rock in the process of rock breaking, only the rock breaking simulation model of disc cutter ring is established. The rock breaking model of disc cutter is shown in Figure 4. The structural parameters of cutter ring are shown in Table 1.

Table 1. Structure parameters of cutter ring

Outer diameter of cutter ring	Inner diameter of cutter ring	Width of cutter ring	Blade width	Cutting edge angle	Fillet radius
483mm	324mm	89mm	24mm	26 °	25mm

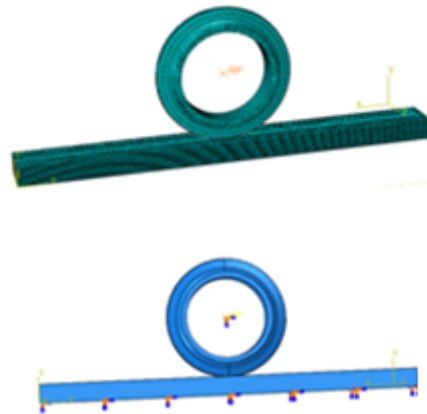


Figure 4. rock breaking model with disc cutter

The mesh type of disc cutter ring is hexahedral element, and the number of meshes is 2269. The mesh type of rock is hexahedral element, and the number of meshes is 43200. According to the field tunneling parameter data, the cutter head diameter is 6470mm, of the TBM is 7800mm, the cutter installation radius is 0.9 m, the cutter head rotation speed is 6.5 r/min, and the penetration is taken as the actual penetration average value of 5mm. The loads and constraints are set as follows: the translation speed of the cutter is 613mm/s, the rotation speed is 2.536 rad/s, and 5mm is pressed into the rock surface; the degrees of freedom at the bottom and both sides of the rock are all constrained.

The geological parameters are concluded that the geology traversed by the bid section of the project. It can be divided into four typical geology, and the compressive strength of rocks is 150 MPa, 120 MPa, 80 MPa and 40 MPa respectively. When the rock compressive strength is 150MPa, the physical parameters are: elastic modulus is 47.6 GPa, Poisson's ratio is 0.18, compressive strength is 150MPa, tensile strength is 4.2 MPa. Drucker-Prager strength criterion is selected as the failure criterion. The rock-breaking model of disc cutter is simulated by control variable method. After the rock-breaking simulation of disc cutter is completed, the stress of disc cutter is derived in the data post-processing module. Then, when the rock compressive strength is 120MPa, 80MPa and 40MPa, the stress of disc cutter breaking rock is obtained in turn, and then the load value of vertical force of disc cutter is derived and its average value is calculated. Then the vertical force is calculated according to CSM model, and the results of comparing them are shown in Table 2.

Table 2. Simulation and CSM model calculation results

Working condition	Rock compressive strength/MPa	Vertical Force Simulation Average/kN	CSM model calculation results/kN	Error value/%
Condition 1	150	231.129	247.456	6.5
Condition 2	120	191.029	203.251	6.0
Condition 3	80	157.832	162.741	3.0
Condition 4	40	98.412	102.52	4.0

It can be seen from Table 2 that with the increase of rock compressive strength, the vertical force on disc cutter also increases, and the average value of vertical force obtained by simulation is consistent with the calculation result of CSM model, and the relative error between them

is between 3% and 6.5%. The reason for the error is that the CSM model is fitted based on a large number of experimental data, and the geological parameters in the actual tunnelling are not a certain value, and the changes of the geological parameters will cause certain errors. In the Abaqus simulation model, the geological parameters are set to a certain value, and the mesh size and shape of the finite element model have a certain impact on the results.

Under the working condition 1, the cutter seat bears the maximum force, which is a dangerous working condition compared with others, and the characteristics of fatigue crack initiation life of the cutter seat are more obvious. Therefore, the rain flow counting method [16] is used to analyze the cutter seat load during rock breaking under the working condition 1, and the load amplitude is tested for normal distribution, and the function normplot is executed. If a straight line is obtained, it obeys normal distribution, and the test result is shown in Figure 5. Jarque-Bera test is used to test the goodness of fit of the amplitude of normal distribution, and the results show that the amplitude of the resultant force of working condition one accords with the normal distribution. Same as above, the load amplitude of working condition 2, working condition 3 and working condition 4 is also tested by normal distribution, and the results show that it also conforms to normal distribution.

Based on the normal distribution, the load data is expanded first and then synthesized to compile the 8-level load spectrum of the cutter seat [17], and the finally obtained 8-level load spectrum of the cutter seat is shown in Table 3.

2.2. Acquisition of stress spectrum of cutter seat

The cutter seat model is introduced into ANSYS Workbench software [18-19]. The cutter seat material is

Q355, the limit load is 320kN, the boundary conditions and the meshes are divided by tetrahedral and hexahedral elements. The number of meshes is 24771 and the number of nodes is 45007. Static analysis is carried out on the cutter seat, and its stress and displacement nephogram is shown in Figure 6.

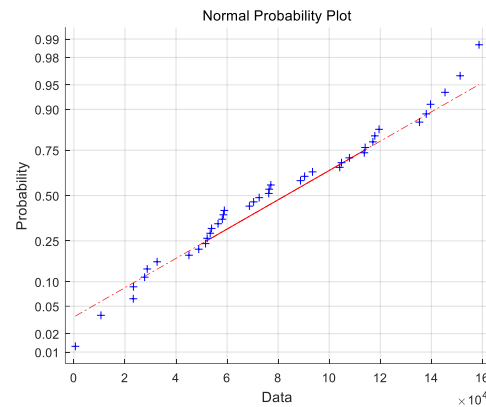


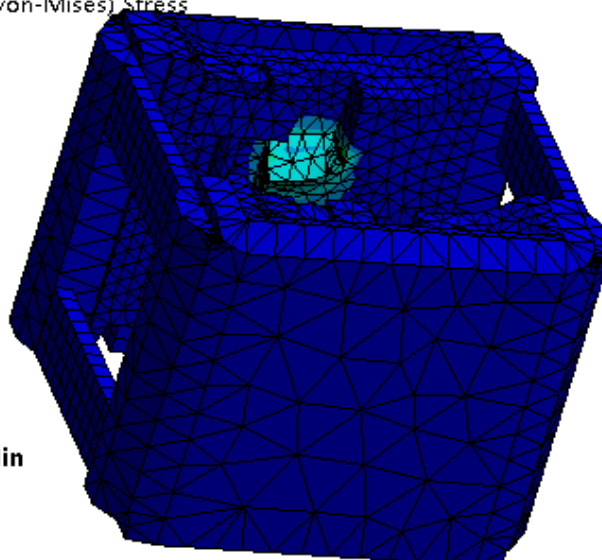
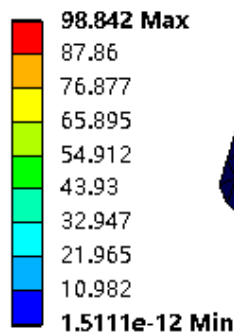
Figure 5. Normal distribution probability diagram of work condition 1

Table 3. The eight-level load spectrum

Load level	Load ratio coefficient	Load value/kN X_i	Number of load frequencies per stage	Cumulative frequency
1	1	300.31	1	1
2	0.95	290.758	1	2
3	0.85	271.656	7	9
4	0.725	247.776	45	54
5	0.575	219.121	363	417
6	0.425	190.466	2267	2684
7	0.275	161.812	10678	13362
8	0.125	133.157	36972	50334

A: Static Structural

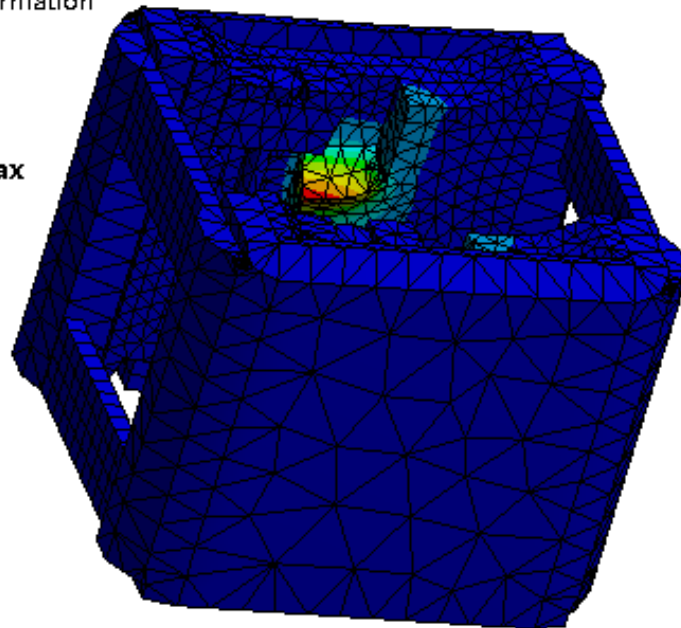
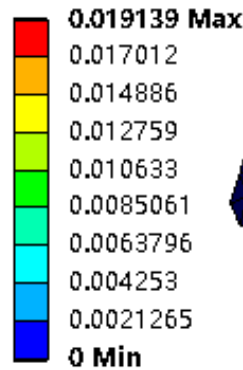
Figure
Type: Equivalent (von-Mises) Stress
Unit: MPa
Time: 1
2020/9/14 15:44



(a) The stress nephogram of cutter seat

A: Static Structural

Total Deformation
 Type: Total Deformation
 Unit: mm
 Time: 1
 2020/9/14 15:46



(b) The displacement nephogram of cutter seat

Figure 6. Stress and displacement nephogram

It can be seen from Figure 6, when the cutter seat bears the limit load, that the dangerous part is the corner of the "L" shape of the cutter seat, with the maximum stress of 98.842 MPa and the maximum displacement of 0.019 mm. The maximum stress of the cutter seat after loading does not exceed the strength of the cutter seat, which indicates that the structural part will not undergo plastic deformation. In this paper, it is assumed that there is no initial defect in the cutter seat structure, the crack initiation occurs at the stress concentration on the surface of the cutter seat, the plastic deformation does not occur when the cutter seat is loaded, and the fatigue type is high cycle fatigue, so the nominal stress method is used to calculate the crack initiation life of the cutter seat.

Load spectrum is the time history of load borne by parts. The load cycle type of cutter seat is asymmetric cycle. Considering the influence of average stress, Goodman formula is used to correct the stress amplitude [20], and the modified eight-level stress amplitude of cutter seat is shown in Table 4.

Table 4. Modified eight-level stress amplitude

Load level	1	2	3	4	5	6	7	8
Load value/kN	300.3 1	290.7 58	271.6 56	247.7 76	219.1 21	190.4 66	161.8 12	133.1 57
Stress amplitude/MPa	92.68 4	89.73 7	83.83 9	76.47	67.93 1	59.04 7	50.16 5	41.28
Modified stress amplitude/MPa	99.87 5	94.54 4	90.34 4	82.40 3	73.20 2	63.62 8	54.05 7	44.48 3

3. Prediction of crack initiation life of cutter seat

In order to predict the crack initiation life of the cutter seat, according to the stress spectrum of the dangerous

point of the cutter seat, combined with the S-N curve of the material Q345D and the fatigue damage theory, the traditional nominal stress method was modified considering the influence of stress concentration, geometric structure of the cutter seat and machining technology, and a prediction model of the crack initiation life of the cutter seat based on the modified nominal stress method was established to predict the cutter seat crack initiation life.

3.1. Establishment of crack initiation life model of cutter seat

Considering that it takes a lot of energy and financial resources to obtain the S-N curve of the cutter seat directly through experiments, this paper modifies the nominal stress method based on the S-N curve of materials. Also, considering the influence factors, such as stress concentration, size and surface machining, a prediction model of crack initiation life of the cutter seat is established based on the nominal stress method forming a prediction method of crack initiation life of the cutter seat, and realizing the crack initiation life prediction of cutter seat.

3.1.1. Modification of nominal stress method

The nominal stress method is often used to calculate the life of parts under high cycle fatigue. It is known that the fatigue life of the cutter seat is a high cycle fatigue generally, so the nominal stress method is selected to analyze the crack initiation life of the cutter seat [21]. The mathematical model of nominal stress method is

$$S^m N = C \tag{2}$$

Where, S is the stress value, N is the number of cycles, and m and C are the parameters related to the material of the structural part.

The nominal stress method is modified by using the correction coefficient, and the modified model is as follows

$$K_\sigma S^m N = \frac{C}{(K_\sigma)^m} \tag{3}$$

The correction coefficient K_σ takes into account the comprehensive influence of stress concentration coefficient K_t , size coefficient ϵ and surface machining coefficient β , and the expression of the correction coefficient K_σ is as follows:

$$K_\sigma = \frac{1+q(K_t-1)\beta}{\epsilon\beta} \tag{4}$$

Where: q is the sensitivity coefficient, which q is 0.6289 according to the situation of the cutter seat; the surface machining coefficient β is 0.75.

The stress concentration factor and size factor can be solved by finite element calculation method [22]. By obtaining the best integration path of the cutter seat dangerous part, the nominal stress can be solved according to the stress field function on the integration path as follows:

$$\sigma_n = \frac{\int_0^L \sigma(L) dL}{L} \tag{5}$$

Where: σ_n is nominal stress, MPa; L is the path length, mm.

The stress concentration factor of structural parts K_t is:

$$K_t = \frac{\sigma_{max}}{\sigma_n} \tag{6}$$

Where: σ_{max} is the maximum stress, MPa.

Dimension coefficients ϵ is:

$$\epsilon = \frac{\sigma_f}{\sigma'_f} \tag{7}$$

Where: σ_f is the fatigue limit of large specimen, MPa;

σ'_f is the fatigue limit of small specimens, MPa.

Combined with the stress field strength method [23-24], it can be seen that the relationship between structural parts and fatigue limits of materials is as follows:

$$\sigma_{0r} = \frac{\sigma_r}{K_t} [f(x_1, x_2)]^{-1} \tag{8}$$

Where: σ_r is the fatigue limit of the material, MPa; σ_{0r} is the fatigue limit of structural parts, MPa; $f(x_1, x_2)$ is the stress field function near the local maximum stress, x_1 and x_2 are the coordinate parameter of the plane field. $f(x_1, x_2)$ can be expressed by the distance L between the node and the maximum stress point under the integral path, that is,

$$f(x_1, x_2) = \omega_1 + \omega_2 L(i) + \omega_3 L^2(i) + \omega_4 L^3(i) \tag{9}$$

The above formula is solved simultaneously, and the calculation formula of size coefficient is:

$$\epsilon = \frac{\int_0^L (\omega_1 + \omega_2 L + \omega_3 L^2 + \omega_4 L^3) dL}{\int_0^L (\delta_1 + \delta_2 L + \delta_3 L^2 + \delta_4 L^3) dL} \tag{10}$$

Where: ω_i and δ_i are the coefficients of the stress field function.

3.1.2. S-N curve of cutter seat material

According to reference [23], the fatigue parameters of Q345D under different survival rates can be found out. By fitting the fatigue parameter data, the mathematical expression of P-S-N curve of Q345D under different survival rates is as follows. The fatigue fitting curves of Q345D under different survival rates are shown in Figure 7.

The expression of survival rate is 50% expression: $S=1202 \times N^{-0.1276}$

The expression of survival rate is 90% expression: $S=1435 \times N^{-0.145}$

The expression of survival rate is 95% expression: $S=1524 \times N^{-0.1509}$

The expression of survival rate is 99% expression: $S=1726 \times N^{-0.1631}$

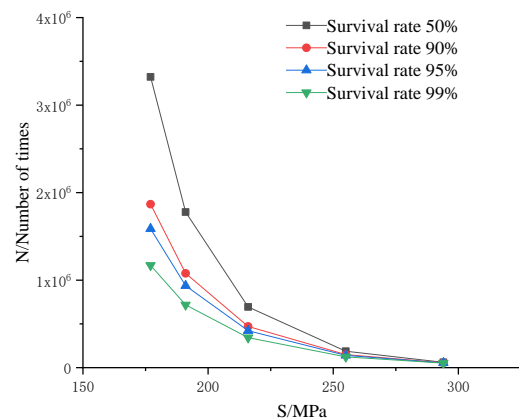


Figure 7. P-S-N Curve of Q345D

3.1.3. S-N curve of cutter seat

The S-N curve of the cutter seat is $S^m N = \frac{C}{(K_\sigma)^m}$,

where the correction coefficient is K_σ . Based on the finite element analysis results of the cutter seat, the best integration path is selected at the maximum stress point, as shown in Figure 8. The stress values corresponding to different path lengths on the integration path are shown in Table 5.

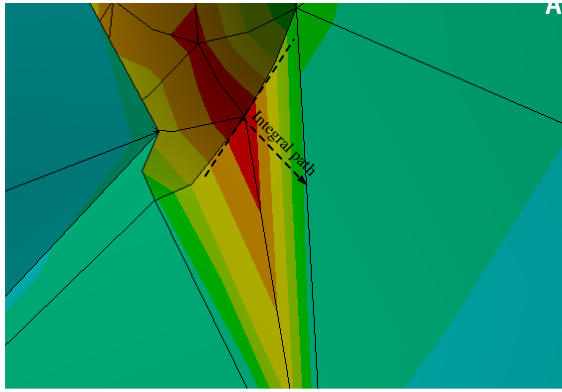


Figure 8. Cutter seat integrated path

Table 5. Integrated path stress values

L/mm	S/MPa
0	98.842
2.275	93.41
5.6875	87.588
...	...
40.95	68.103
50.05	43.55
54.6	20.717

The stress field function obtained by fitting the data in Table 5 is:

$$S = -0.002186x^3 + 0.1753x^2 - 4.522x + 103.333 \quad (11)$$

According to Equations (6), (10) and (11), the stress concentration factor and dimension factor of the cutter seat are calculated to be 1.43 and 0.9546 respectively.

The stress concentration factor K_t , dimension factor ϵ and surface machining factor β are substituted into equation (4), and the result K_σ is 1.68.

After correction, the P-S-N curve of the cutter seat is shown in Figure 9, and the mathematical expression is:

Survival rate 50% expression: $S^{7.837} N = 2.351 \times 10^{22}$

Survival rate 90% expression: $S^{6.897} N = 1.651 \times 10^{20}$

Survival rate 95% expression: $S^{6.627} N = 3.983 \times 10^{19}$

Survival rate 99% expression: $S^{6.131} N = 2.917 \times 10^{18}$

The fatigue life curves of the cutter seat under different survival rates can be obtained from Figure 9. It can be seen from Figure 9 that when the survival rate increases, the fatigue strength of the cutter seat decreases and the fatigue life will be shortened. The fatigue life curve of cutter seat provides a theoretical basis for crack life prediction of cutter seat.

3.2. Prediction of cutter seat crack initiation life

According to Miner's fatigue damage accumulation theory [22], when the structural member r is under the action of different stresses S_i , the fatigue failure life corresponding to each stress level is N_i , and the damage

$$D = \sum_{i=1}^r \frac{n_i}{N_i}$$

level is n_i . At that time $D = 1$, the structural member is damaged.

The number of cycles that can bear the load spectrum when fatigue failure occurs at the dangerous part of the cutter seat is δ , and its mathematical expression is:

$$\delta = \frac{1}{D} \quad (12)$$

The expression of fatigue life of cutter seat is:

$$N = \delta \sum_{i=1}^8 n_i \quad (13)$$

Therefore, the fatigue crack initiation life of the cutter seat under different survival rates can be obtained as shown in Figure 10.

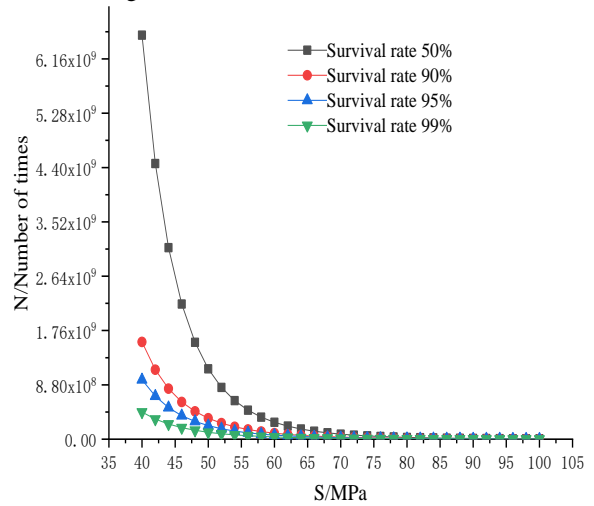


Figure 9. P-S-N curve of cutter seat

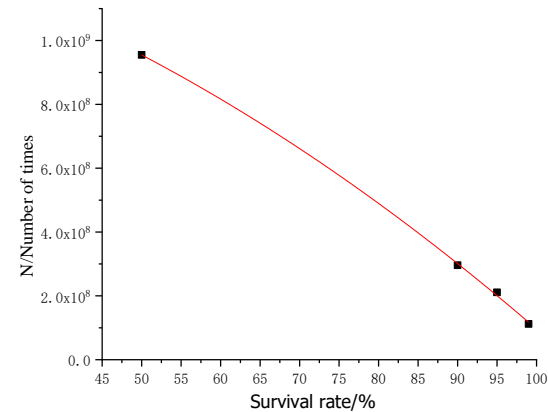


Figure 10. Fatigue crack initiation life of Cutter seat

Fitting from the data in the above figure, the fitting formula is as follows:

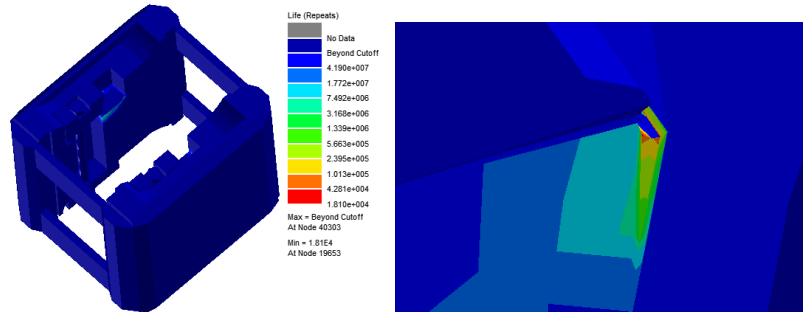
$$N = -8.3 \times 10^4 x^2 - 4.66 \times 10^6 x + 1.40 \times 10^9 \quad (14)$$

Where x is the survival rate. The crack initiation life of the cutter seat decreases with the increase of the survival rate, and the function relationship presents an inverse convex function relationship. When the survival rate increases from 50% to 90%, the crack initiation life decreases, and when the survival rate increases from 90% to 99%, the crack initiation life continues to decrease and the change rate increases.

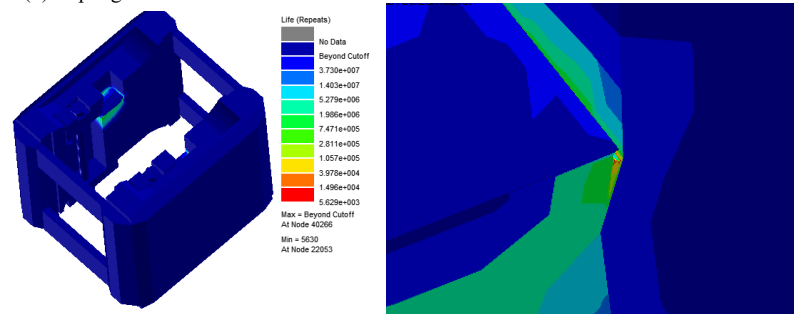
4. Simulation analysis of crack initiation life of cutter seat based on nCode

The finite element model of the cutter seat, S-N curve and load spectrum of the cutter seat are introduced into nCode software, and the fatigue analysis process is

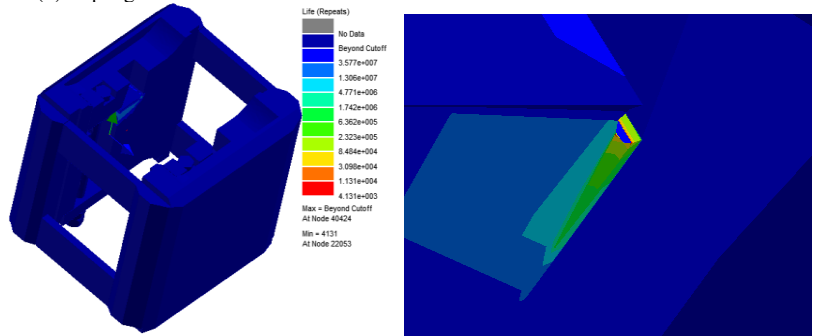
established. When the survival rate is set to 50%, 90%, 95% and 99%, the crack initiation life of the cutter seat is solved respectively, and the distribution nephogram of the crack initiation life of the cutter seat is obtained as shown in Figure 11.



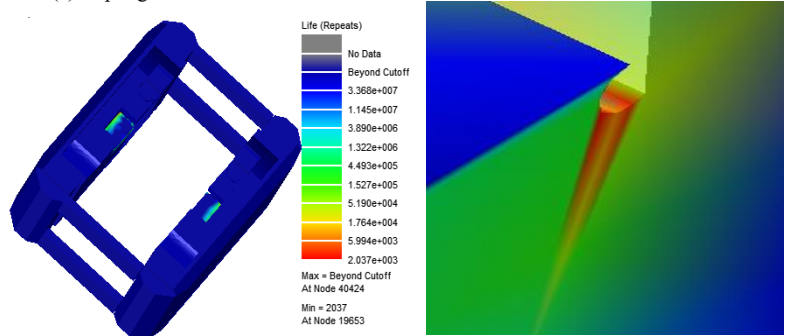
(b) Nephogram of crack initiation life distribution of cutter seat with 50% survival rate



(b) Nephogram of crack initiation life distribution of cutter seat with 90% survival rate



(c) Nephogram of crack initiation life distribution of cutter seat with 95% survival rate



(d) Nephogram of crack initiation life distribution of cutter seat with 99% survival rate

Figure 11. Fatigue analysis results of cutter seat under different survivor rates

As can be seen from Figure 11, the first crack initiation position is the corner of the "L" shape of the cutter seat. When the survival rate is 50%, 90%, 95% and 99%, the crack initiation life of the cutter seat simulated by nCode is 9.11×10^8 , 2.83×10^8 , 2.07×10^8 and 1.03×10^8 times respectively.

The fatigue crack initiation life of the cutter seat obtained by fatigue life simulation analysis of the cutter seat is compared with the fatigue crack initiation life of the cutter seat calculated based on the modified nominal stress method, as shown in Figure 12.

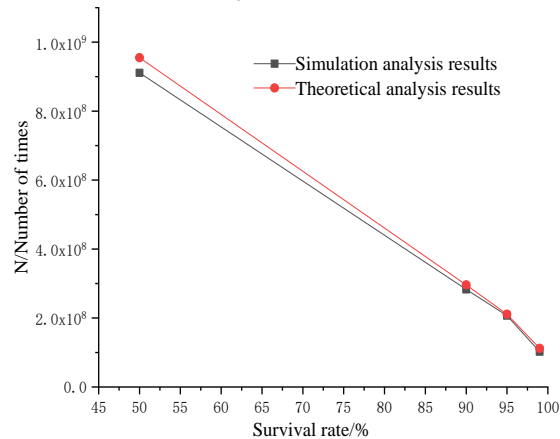


Figure 12. Comparison of fatigue life results of cutter seat under different survival rates

As can be seen from Figure 12, with the increase of survival rate, the crack initiation life of the cutter seat decreases. The simulation results have the same trend with the calculation results. The error between the simulation results and the theoretical analysis results is 4.6%, 4.3%, 2.0% and 8.4% when the survival rate is 50%, 90%, 95% and 99%, respectively. The error between the theoretical calculation results and the simulation results is small, which verifies the correctness of the prediction model of cutter seat crack initiation life. The causes of errors are mainly caused by the following points: Firstly, the correction coefficient mainly considers stress concentration coefficient, size coefficient and surface machining coefficient, but does not fully consider other influencing factors; Secondly, the meshing accuracy of the cutter seat has a certain influence on the fatigue crack initiation life of the cutter seat by using simulation method.

5. Conclusion

Aiming at the crack failure problem of TBM cutter seat under alternating load, the theoretical calculation and numerical simulation analysis of crack initiation life of TBM cutter seat are carried out in this paper, and the main conclusions are as follows:

1. The statics analysis of the cutter seat is carried out, and the crack initiation position is determined at the corner "L" shape of the cutter seat. The maximum stress under the ultimate load is 98.842 MPa, and the maximum deformation is 0.019 mm.
2. Considering the influence of stress concentration, geometrical dimension and surface machining, the prediction model of cutter seat crack initiation life based on modified nominal stress method is established, and

the crack initiation life of cutter seat with survival rate of 50%, 90%, 95% and 99% is calculated as 9.46×10^8 , 3.00×10^8 , 2.13×10^8 and 1.25×10^8 times respectively.

3. Based on the results of statics analysis, the numerical simulation of crack initiation life of cutter seat is analyzed using ANSYS nCode software. When the survival rate is 50%, 90%, 95% and 99% of the cutter seat, the crack initiation life of the cutter seat is 9.11×10^8 , 2.83×10^8 , 2.07×10^8 and 1.03×10^8 times. The error between the results and the theoretical analysis is 4.6%, 4.3%, 2.0% and 8.4%, respectively. The error is small, which verifies the correctness of the prediction model of the crack initiation life of the cutter seat.

Conflicts of interest

There are no conflicts of interest.

Acknowledgments

This work is financially supported by the Research & Development project of Hebei Province (22351901D), the Major National Research & Development project of china (2020YFB1709502), the Hebei Natural Science Foundation Project (E2019210275 and E2019210104) and the Science Research Project of the Education Department of Hebei Province (Grant No. ZD2021093)

References

- [1] Zhang K . The Study on Feasibility and Welding Characteristics of GMAW Surfacing Remanufacturing of H13 Steel Cutter Ring of TBM Hob[J]. Coatings, 2021, 11.
- [2] Mifkovic M ,Swidinsky A , Mooney M . Imaging ahead of a tunnel boring machine with DC resistivity: A laboratory and numerical study[J]. Tunnelling and Underground Space Technology, 2021, 108:103703.
- [3] J Huo, Zhang Z ,Meng Z , et al. Dynamic Analysis and Experimental Study of a Tunnel Boring Machine Testbed under Multiple Conditions[J]. Engineering Failure Analysis, 2021, 127(5):105557.
- [4] ZHANG Wei, YUAN Chao-wei, CHENG Yong-feng, et al. Weld Performance Analysis and Structural Design of TBM Cutter head[J]. Modular Machine Tool & Automatic Manufacturing Technique, 2021(05): 153-156+160.
- [5] LI Hongliang. Troubleshooting for disc cutter cracking of model TB880E rock tunneler[J]. Construction Machinery, 2010, 41(03): 62-67+4. (in chinese)
- [6] Jingxiu Ling, Wei Sun, Junzhou Huo, Li Guo. Study of TBM cutter head fatigue crack propagation life based on multi-degree of freedom coupling system dynamics[J]. Computers & Industrial Engineering, 2015, 83: 1-14.
- [7] Yang Yun. Prediction of crack initiation life of shield machine center cutter seat[J]. Modern Manufacturing Engineering, 2020(10): 143-147. (in chinese)
- [8] Liu Jianqin, Ji Xuanbin, Guo Wei, et al. Study on geological matching and failure of TBM cutter head based on crack initiation [J]. Journal of Tianjin University (Natural Science and Engineering Technology Edition), 2017, 50 (11): 1148-1153. (in chinese)
- [9] Ouyang Xiangyu, Sun Wei, Huo Junzhou. Crack initiation life prediction of TBM cutter head under multi-point distributed load [J]. Mechanical Science and Technology for Aerospace Engineering, 2016, 35 (10): 1484-1488.
- [10] Huo J Z, Zhu D, Hou N, et al. Application of a small-timescale fatigue, crack-growth model to the plane

- stress/strain transition in predicting the lifetime of a tunnel-boring-machine cutter head[J]. *Engineering Failure Analysis*, 2016, 71: 11-30
- [11] Shuli Zhang, Jianfu Zhang, ZhongGuo, Peng Gao, Tianyu Du. Welding Residual Stress Characteristics of Boltwelding Joint in TBM Split Cutter head[C]//Proceedings of 2019 International Conference on Electronical, Mechanical and Materials Engineering(ICE2ME 2019). 2019:118-121.
- [12] Kheder, A., R., I., Jubeh, N., M., Tahah, E., M. Fatigue Properties under Constant Stress/Variable Stress Amplitude and Coaxing Effect of Acicular Ductile Iron and 42 CrMo4 Steel.[J]. *Jordan Journal of Mechanical and Industrial Engineering*, 2011, 5(4):301-306.
- [13] Cai Zheng. Study on safety risk management of subway tunnel shield construction[D]. China University of mining and technology, 2016. (in chinese)
- [14] Rostami J, Ozdemir L, Nilsen B. Comparison between CSM and NTH Hard Rock TBM Performance Prediction Models[C]//Proceedings of Annual Technical Meeting of the Institute of Shaft Drilling Technology. Las Vegas, 1996:1-10.
- [15] J Li, Nie YF, Fu K, et al. Experiment and analysis of the rock breaking characteristics of disc cutter ring with small edge angle in high abrasive grounds[J]. *Journal of the Brazilian Society of Mechanical Sciences & Engineering*, 2018, 40(10).
- [16] Ouyang Xiangyu. Life prediction of TBM cutter head crack initiation propagation under multi-point impact [D]. Dalian University of technology, 2015. (in chinese)
- [17] Bian Ye. Compilation of load spectrum of disc cutter of Full Face Rock Roadheader[D]. Northeastern University, 2009. (in chinese)
- [18] Emad A M, Ibrahim R. An Application of Finite Element Method and Design of Experiments in the Optimization of Sheet Metal Blanking Process[J]. *Jordan Journal of Mechanical and Industrial Engineering*, 2008, 2(1): 53-63.
- [19] Zhenqi Yu, Huifang Jia, Xingyuan Huang. Vibration Fatigue Analysis and Optimization Design of a Lighttruck Ur a Box Bracket[J]. *Jordan Journal of Mechanical and Industrial Engineering*, 2020, 14(1):167-173.
- [20] YANG Long, YANG Bing, YANG Guangwu, et al. Analysis on fatigue characteristics of spot welded joints of stainless steel car body[J]. *Transactions of the china Welding Institution*, 2020, 41(07):18-24+52+97-98. (in chinese)
- [21] CHEN Zhuo-yi, LI Chuan-xi, KE Lu, et al. Fatigue Crack Repair and Optimization of Cope Holes in Orthotropic Steel Decks[J]. *China Journal of Highway and Transport*, 2021, 34(07):301-312. (in chinese)
- [22] JIANG Yong. Three dimensional stress concentration and crack analysis of aviation connecting structure[D]. Nanjing University of Aeronautics and Astronautics, 2009. (in chinese)
- [23] Editorial board of mechanical engineering material performance data manual. *Mechanical engineering material performance data manual*[M]. Machinery Industry Press, 1995. (in chinese)
- [24] HUANG Jian, LI Chao-yang, CHEN Bing-kui. Mechanical behaviors of cross roller bearings with raceway roundness error[J]. *Journal of Central South University*, 2021, 28(07):2091-2104.

Parametric Optimization of Pulse TIG Welding Process during Joining of Dissimilar Tensile Steels Used in Automotive Industries

A.Sahoo^{1, a}, S. Tripathy^{2, b*}, D.K. Tripathy^{3, c}

¹Department of Mechanical Engineering, Institute of Technical Education and Research, Siksha 'O' Anusandhan (Deemed to be University), Bhubaneswar, India

²Department of Mechanical Engineering, Institute of Technical Education and Research, Siksha 'O' Anusandhan (Deemed to be University), Bhubaneswar, India

³Ex-Professor Emeritus, IIT Kharagpur, India

Received 8 Apr 2022

Accepted 23 Oct 2022

Abstract

The present study focuses on multi-criteria optimization of pulse current tungsten inert gas (TIG) welding process parameters using technique for order of preference by similarity to ideal solution (TOPSIS) based Taguchi approach to enhance quality and productivity characteristics. The tig welding process is controlled by the input parameters, and optimization of process parameters is, therefore, useful for metallurgical advancements, which improve weld quality and enhance weld life. The work material used for the investigation are SAILMA 450 and EN 14B which find huge application in manufacture of rear axle in high-tech automobile industries. These materials have not been given much attention in the past but find a range of applications and hence need to be investigated. Taguchi's L₂₅ experimental design is used to investigate the influence of process parameters like peak current (I_p), base current (I_b), pulse frequency (F) and shielding gas flow rate (Q) on properties like yield strength (YS), ultimate tensile strength (UTS), flexural strength (FS) and microhardness (H) of the welded joints. The tensile property testing and characterization of welded sub-surface has been done to improve the weld quality and investigate the effect of welding phenomena on tensile steels. To understand the impact of pulse tig welding process parameters, analysis of variance has been used. Confirmatory tests show an improvement of 0.5457 in the preference values. The recommended settings of process parameters is found to be $I_p=220A$, $I_b =120A$, $F=5Hz$ and $Q=17l/min$. Microstructure analysis of optimal sample shows absence of welding defects and crack formation in the fusion zone.

© 2022 Jordan Journal of Mechanical and Industrial Engineering. All rights reserved

Keywords: SAILMA 450, EN 14B, rear axle, pulse tig, Taguchi, TOPSIS.

1. Introduction

The modern manufacturing market is driven by performance quality and customer satisfaction. To obtain permanent joints and for repairing of metal components in various industries, such as manufacturing, aviation, automobile, shipbuilding, construction, power, petroleum etc., arc welding has found enormous application. Arc welding possesses advantages, such as low set up cost, ease of operation, and adaptability which make them the most sought after operations. The structural integrity and weld quality are the key measures for welding process analysis. The weld life is governed by the critical structural and material phase properties. TIG welding is among the most preferable arc welding processes because of its high precision, suitability for joining of active alloys like aluminium, magnesium, titanium and other high strength steels in different combinations due to low sensitivity to hot cracking [1,2]. The process has certain limitations like

constant heat input and wider arc formation which reduces the efficiency of the process. These drawbacks may be mitigated by gaining control over heat input which is possible with pulse current tig welding, a modified version of the traditional constant current TIG welding. In pulse current tig welding, coalescence is produced after the job gets heated by an electric arc generated between the tungsten electrode and the base metal. There is no involvement of flux and the molten metal and arc are shielded by an inert gas of either argon, helium or mixture of argon and helium. Welding current is supplied to the base material in pulses as on-time which avoids the overheating of the weld metal. Two forms of current are used as peak current and base current. Peak current is given as input to the weld metal with some time interval for melting of the base metal. The base current helps to maintain the arc ionization and allows the weld metal to cool. SAILMA 450 and EN 14B steels are commonly used for rear axle automotive parts. SAILMA 450 is widely used for machine building, lifting equipment, architectural

* Corresponding author e-mail: sasmeetatripathy@soa.ac.in.

structures, containers, transport vehicle equipment, frame work structures, and bridge construction, and EN 14B steel is used for manufacturing machine tools, parts of the ship industry, vehicles, turbine fasteners, boiler support rods, gear shafts, valve and connecting rods, rotator blades, and excavator bucket teeth, among other applications. The joints of SAILMA 450 and EN 14B are used to make rear axles in automobile industries. The joining of dissimilar metals has always gained the attention of researchers due to the application oriented performance characteristics. Joining of dissimilar materials still remains a challenge due to property variations, and defective joining may lead to catastrophic consequences. Several researchers have reported studies for improvement of weld characteristics resulting from grain refinement occurring from grain size and grain structure. Controlling the input process parameters through optimization techniques to obtain good quality joints has thus attracted researchers to a greater extent. Design of experiments has been the most efficient, less time consuming and cost-effective way to predict the behaviour of the process parameters with minimum number of experiments. The multi-objective optimization techniques like TOPSIS and grey relational analysis are used to simultaneously optimize the process parameters and help acquire the desirable quality characteristics. The investigations on pulse current TIG welding has gained much concentration from researchers. Optimization of process parameters using TOPSIS has also been focused in the past where materials like Al6061 and Cu101 have been welded by micro friction stir welding for maximization of UTS, microhardness and minimization of surface roughness [3]. Hybrid optimization has been performed using NSGA-II and TOPSIS for friction stir welding of aluminium alloy 6061 series [4]. Welding of Inconel 625 was done by activated TIG welding process and optimum hardness and aspect ratio were determined by TOPSIS [5]. TOPSIS has also been used to optimize input process parameters during friction vibration welding of polypropylene glass composites [6]. Inconel 625 was welded by A-TIG process and optimization was performed using TOPSIS to obtain maximum depth of penetration, with increased microhardness, weld bead width and height in weld current [7]. The optimum condition for 316 Stainless Steel is welding current of 150 A, shielding gas flow rate of 15 l/min and weld speed of 190 mm/min that produce maximum UTS, impact strength and hardness obtained using Taguchi and GRA [8]. Ti-6Al-4V was welded by laser welding process and optimized by TOPSIS approach in order to maximize the hardness, depth of penetration and minimize the weld bead width [9]. Welding speed and shielding gas flow rate are two important weld parameters after laser power which influence the hardness and depth of penetration for joining hastelloy C-276 by laser welding and TOPSIS method is used to optimize the weld parameter [10]. Genetic Algorithm and PSO have been used to compare the predicted values obtained using design of experiments

[11]. Taguchi method has been employed for design and analysis of experimental results in pulse current tig welding process. Further, grey relational analysis has been performed to optimize multiple response factors simultaneously [12]. Authors have performed studies on optimization of process parameters to obtain sound weld characteristics and minimizing hardness in the weld zone in steels. During arc welding, continuous current flow produces high amount of heat leading to development of hot cracks, new phase formation, segregation of alloying elements [13-15]. Taguchi and TOPSIS have been combined in many recently conducted studies using electro-discharge machining [16], powder mixed electro discharge machining [17-19] and turning of steels where the input parameters have significant influence on the response factors [20-22]. The hybrid optimization techniques improve the performance characteristics and surface quality of the processes while establishing the optimal conditions for machining.

In the present work a five level four factor design technique has been used on experimental data for modeling of pulse current tig welding process. Process parameters selected for the test are peak current, base current, pulse frequency and shielding gas flow rate, considered in five different ranges, based upon the pilot experiment for the present investigation. Considering the number of input parameters and their levels, L₂₅ orthogonal array has been used for the experiments. TOPSIS has been used to perform the optimization of process parameters and obtain the most suitable set of parametric combination to achieve maximized values of yield strength, ultimate tensile strength, flexural strength and microhardness. Microstructure analysis has been done for the optimal sample to evaluate the quality of the weld joint.

2. 2. Materials and Methods

2.1. Experimental Set up

The pulse tig welding set up used for the experiment is shown in Figure.1. The experiments were carried out with ER70S series filler wire. The chemical compositions of the base material, parent material and filler wire were measured using an X-Ray Fluorescence (XRF) analyser and is presented in Table 1. For shielding and back purging, commercial argon gas was employed. In welding equipment, automatic voltage regulation was offered. The influence of fixture variation has not been taken into account at the time of the trial. Both base plates were cleaned with acetone and a free cloth, and the grooved part was cleaned using a rotating stainless steel tool. Figure.2 shows the graphical illustration of the work process flow. For tensile testing, Instron UTM machine was used as shown in Figure.4 and Vickers's microhardness test was carried out for evaluating the hardness of the welded samples.



Figure 1. Pulse TIG Set up

2.2. Materials

SAILMA 450 and EN 14B steel were employed in this study, which are both commonly used for rear axle auto motive parts. SAILMA 450 is widely used for machine building, lifting equipment, architectural structures, containers, transport vehicle equipment, frame work structures, and bridge construction, and EN 14B steel is used for manufacturing machine tools, parts of the ship industry, vehicles, turbine fasteners, boiler support rods, gear shafts, valve and connecting rods, rotator blades, and excavator bucket teeth, among other applications. The joints of SAILMA 450 and EN 14B are used to make rear axles in automobile industries. Two foundation plates of

SAILMA 450 and EN 14B steel, with dimensions 60x60x5mm, were welded using pulse tig welding set up shown in Figure.1 with a square butt joint and a single 60v groove with suitable angle edge preparation. The samples prepared for tensile testing are shown in Figure.3. The mechanical properties of base and filler materials have been presented in Table 2. Figure.5 shows the tensile test samples after the test is performed.

Table 1. Chemical composition of base and filler material

Base metals/ Filler metals	C%	Mn%	S%	P%	Al%	Si%	Ni%	NB+Ti+V%
SAILMA 450	0.16	1.38	0.045	0.045	0.02	0.45	-	0.25
EN14 B	0.20	1.40	0.06	0.06	-	0.35	0.40	-
ER70S-6	0.15	1.40	0.035	0.02	-	0.80	0.15	0.03

Table 2 Mechanical properties of base and filler material

Base metals/ Filler metals	Yield strength (MPa)	UTS (MPa)	Hardness (Hv)	% Elongation
SAILMA 450	453	577	184	18
EN14 B	357	512	176	22
ER70S-6	452	538	167	22

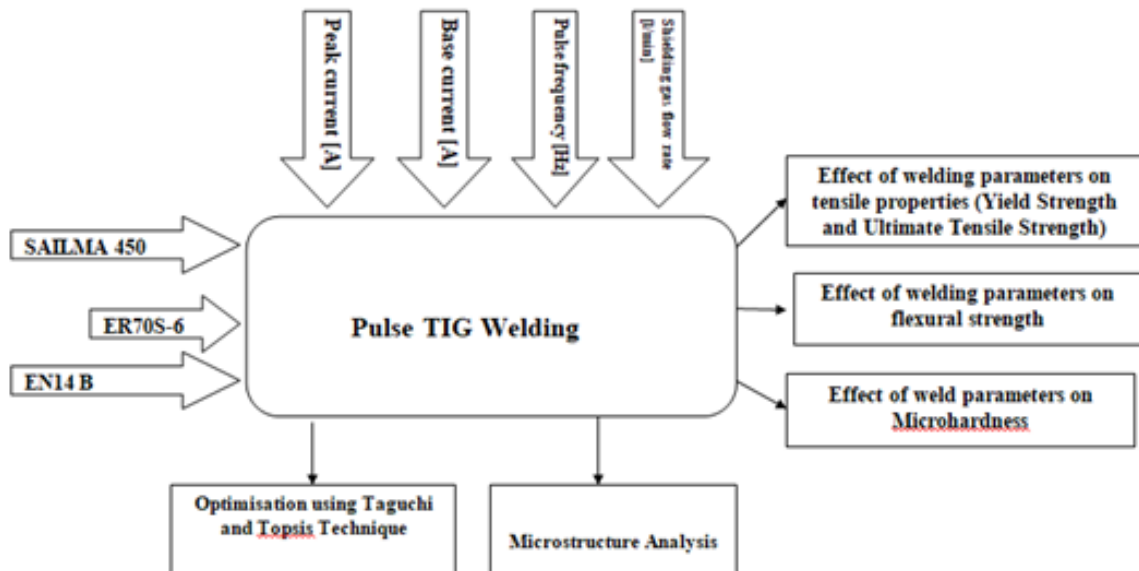


Figure 2. Graphical illustration of the work process of pulse current TIG welding of SAILMA 450 and EN-14B



Figure 3. Specimen preparation for tensile test



Figure 4. Instron UTM machine used for tensile test



Figure 5. Tensile specimen after testing

2.3. Design of experiments

Taguchi’s Technique is used to identify the influence of process parameters on the welding performance. The technique is simple and effective for quality optimization of processes and products. In the present study, the effect of pulse current tig welding process parameters has been investigated using Taguchi’s technique. Process parameters selected for the test are peak current, base current, pulse frequency and shielding gas flow rate in five different ranges, based upon the pilot experiment for the present investigation. Considering the number of input parameters and their levels, L₂₅ orthogonal array is used for the experiments as presented in Table 3. Taguchi’s process uses means to normalize the functions. Signal to noise (S/N) ratio reduces the variation in the output responses obtained from the experimental data by identifying the characteristic as “higher the better” (HB), Lower the better (LB) and nominal the best” (NB). The following equations are used to evaluate the type of performance characteristic using S/N ratio [23-24]. Table 4 shows the Taguchi’s L₂₅ orthogonal array used for the experiments along with the response values obtained in different runs.

Equation (1) and (2) represent the expressions for higher the better and lower the better used in Taguchi’s approach:

$$HB: S/N \text{ ratio} = -10 \log_{10} \left[\frac{1}{n} \sum_{i=1}^n y_i^{-2} \right] \quad (1)$$

$$LB: S/N \text{ ratio} = -10 \log_{10} \left[\frac{1}{n} \sum_{i=1}^n y_i^2 \right] \quad (2)$$

Table 3. Factors and their levels

Factors (Units)	Levels				
	Level 1	Level 2	Level 3	Level 4	Level 5
Peak current [A]	100	140	180	220	260
Base current [A]	60	80	100	120	140
Pulse frequency [Hz]	2	5	8	11	14
Shielding gas flow rate [l/min]	9	11	13	15	17

Table 4. L₂₅ experimental design with response variables

Run	I _p	I _b	F	Q	YS	UTS	FS	H
1	100	60	2	9	417	520	1163	174
2	100	80	5	11	420	529	1167	179
3	100	100	8	13	426	539	1170	182
4	100	120	11	15	429	540	1172	184
5	100	140	14	17	427	537	1171	181
6	140	60	5	13	423	532	1174	178
7	140	80	8	15	431	538	1182	183
8	140	100	11	17	434	541	1185	185
9	140	120	14	9	433	533	1177	182
10	140	140	2	11	430	531	1178	177
11	180	60	8	17	436	549	1188	189
12	180	80	11	9	440	548	1179	187
13	180	100	14	11	438	550	1176	191
14	180	120	2	13	435	547	1179	188
15	180	140	5	15	443	549	1186	194
16	220	60	11	11	439	556	1189	213
17	220	80	14	13	441	554	1191	211
18	220	100	2	15	442	550	1187	208
19	220	120	5	17	449	560	1199	218
20	220	140	8	9	452	557	1193	216
21	260	60	14	15	424	529	1166	177
22	260	80	2	17	426	531	1164	176
23	260	100	5	9	430	534	1159	178
24	260	120	8	11	432	536	1165	181
25	260	140	11	13	428	535	1167	180

2.4. Multi-objective optimization using Technique for order of preference by similarity to ideal solution (TOPSIS)

TOPSIS is a multi-criteria decision making technique which is used to find the best option from a set of alternatives. This approach is useful to convert multi-objective performance into a single objective performance as per desired condition by arranging all in ranking order. TOPSIS technique is widely used for decision making in manufacturing industries and among practitioners in cases where more number of alternatives and their interactions have significant impact on output responses. The approach is more efficient and easy to use. The chosen criteria must be close to the positive best solution and far away from the negative best solution, making the relative closer to the ideal solution as the best solution. The steps followed are expressed as:

Step-1: In first step of TOPSIS method, decision matrix is formed which having ‘r’ attributes and ‘c’ alternatives which can be expressed as:

$$D_m = \begin{bmatrix} k_{11} & k_{12} & k_{13} & \dots & \dots & k_{1r} \\ k_{21} & k_{22} & k_{23} & \dots & \dots & k_{2r} \\ k_{31} & k_{32} & k_{33} & \dots & \dots & k_{3r} \\ \vdots & \vdots & \vdots & \ddots & \ddots & \vdots \\ \vdots & \vdots & \vdots & \ddots & \ddots & \vdots \\ k_{c1} & k_{c2} & k_{c3} & \dots & \dots & k_{cr} \end{bmatrix} \quad (3)$$

Where, K_{lm} is represented as performance of lth alternative for mth attribute.

Step 2: Now normalized matrix has to be obtained by using the given formula:

$$J_{lm} = \frac{k_{lm}}{\sqrt{\sum_{i=1}^c k_{im}^2}} \quad \text{where } m=1, 2, 3, \dots, r \quad (4)$$

Step-3: Each attributes weight was assumed as W_m (m=1,2,3,...r). The weighted normalized decision matrix F= [v_{lm}] can be obtained by using:

$$F = W_m J_{lm} \quad (5)$$

Where $\sum_{m=1}^r W_m = 1$

Step 4: The positive and negative ideal solutions can be calculated by using the expressions given by:

$$F^+ = \left\{ \left(\sum_l^{\max} f_{lm} \mid m \in M \right), \left(\sum_l^{\min} m \mid m \mid l = 1, 2, \dots, c \right) \right\} \\ = \{f^+_1, f^+_2, f^+_3, \dots, f^+_r\} \quad (6)$$

$$F^- = \left\{ \left(\sum_l^{\min} f_{lm} \mid m \in M \right), \left(\sum_l^{\max} m \mid m \mid l = 1, 2, \dots, c \right) \right\} \\ = \{f^-_1, f^-_2, f^-_3, \dots, f^-_r\} \quad (7)$$

Step 5: Separation between alternatives was calculated. Separation of each alternative from ideal solution is expressed as:

$$S_i^+ = \sqrt{\sum_{m=1}^r (f_{lm} - f_m^+)^2}, \quad l=1, 2, \dots, c \quad (8)$$

And separation of each alternative from negative ideal solution is given as:

$$S_i^- = \sqrt{\sum_{m=1}^r (f_{lm} - f_m^-)^2}, \quad l=1, 2, \dots, c \quad (9)$$

Step 6: The relative closeness of an alternative to the ideal solution can be expressed as:

$$P_i = \frac{S_i^-}{S_i^+ + S_i^-} \quad \text{where } l=1, 2, 3, \dots, c \quad (10)$$

Step 7: The P_i value is ranked in descending order to get the alternatives with best and worst solutions.

3. Results and discussion

3.1. Effect of welding parameters on tensile properties

Weld quality and weld life depend upon the weldability of base materials. The weld life is dependent on the mechanical behaviour of the welded joint which is governed by the microstructural changes taking place within the work material. For any arc welding process, welding current plays a vital role for melting of base material. Choosing the appropriate range of welding current depends on the base material thermal properties and material thickness [11]. Determining the proper range of welding current particularly for pulse TIG welding is a challenging task as it involves the action of two currents viz. peak current and base current. Generally, base current is chosen in such a way that roots mean square of current value becomes 70% of peak current value. Peak current helps to melt the base material, so heat input and depth of penetration are mainly influenced by the value of peak current which has direct impact on mechanical properties and in microstructural changes. It has been observed by the experimental results that as the peak current range increases, the yield strength and ultimate tensile strength

also increase. This is due to the increase in heat input in the weld zone which improves the weld depth of penetration. The maximum yield strength and UTS are achieved at a peak current of 220 A as shown in Figure.6 (a) and (b). Beyond 220A of peak current with combination of other input parameters, the mechanical strength gets reduced due to the high current input which produces defects like undercut and coarser grain in weld zone. For a peak current of 100 A, the yield strength is about 422 MPa and UTS achieved is 536 MPa which is lower than other peak current values due to lack of fusion. Thus low peak current value is not sufficient to melt the base metal completely but with rise in peak current from 100 A to 220 A, yield strength and ultimate tensile strength increase with suitable combination of other welding process parameters like base current, pulse frequency and shielding gas flow rate as shown in

Figure.6(c), (d), (e), (f), (g), (h). At a peak current of 180 A, low pulse frequency and high shielding gas flow rate, the yield strength gets reduced. It may be due to less pulse frequency which is not able to produce stable arc and is associated with defects like porosity caused by high shielding gas flow rate. At a peak current of 140 A, with very low base current and low pulse frequency, tensile strength gets reduced as the welding current is not sufficient to melt the base material as well as for maintaining the weld arc. Hence, optimized welding parameters are preferable for achieving better mechanical properties for welded joints and suitable joint strength. Maximum YS is achieved at an I_b of 140 A and maximum UTS is observed at an I_b of 110A. The variation of yield strength and UTS with the chosen input parameters is shown in Figure. 6(a)-Figure. 6(h).

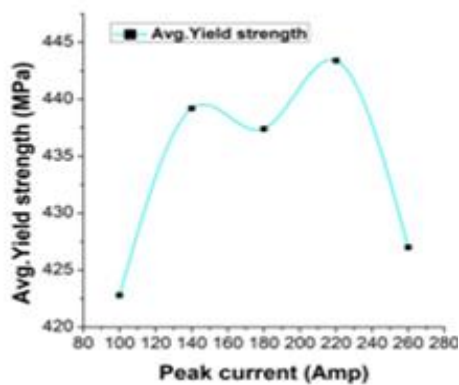


Figure 6. (a) Variation of Yield Strength with I_p

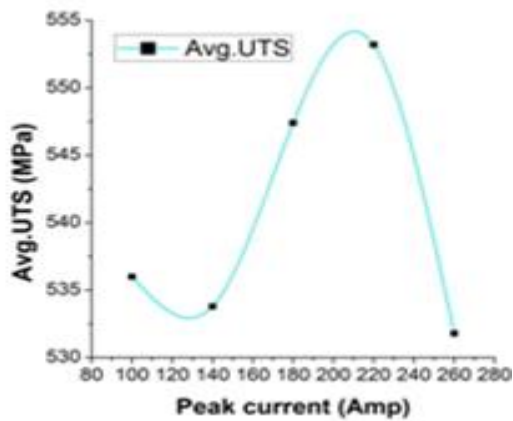


Figure 6. (b) Variation of UTS with I_p

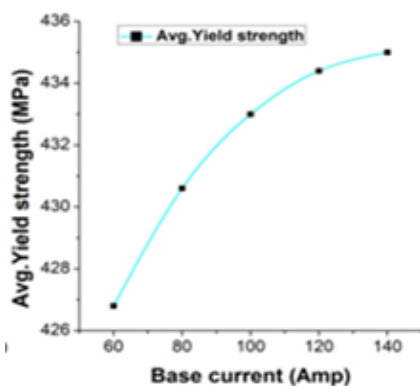


Figure 6. Variation of Yield Strength with I_b

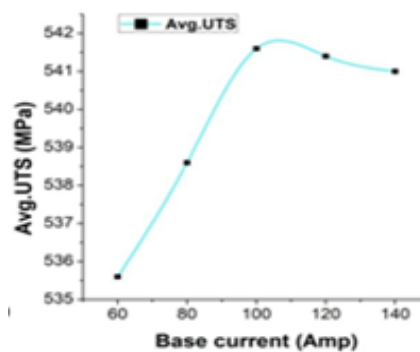


Figure 6. (d) Variation of UTS with I_b

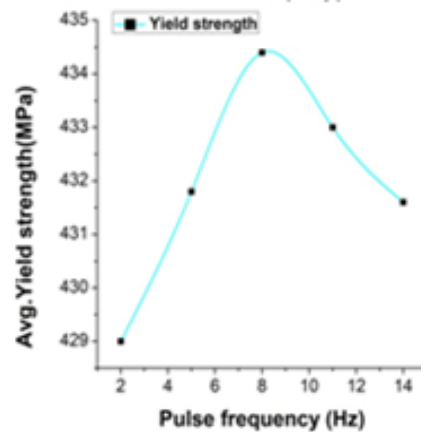


Figure 6. (e) Variation of Yield Strength with PF

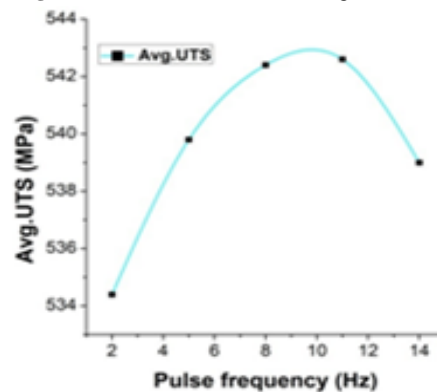


Figure 6. (f) Variation of UTS with PF

3.2. Effect of welding parameters on flexural strength

To predict formation of a sound weld joint and susceptibility to crack formation in the weld zone, flexural strength test is performed. To find out the flexural strength, a three point bending test is done for all the welded samples. Maximum flexural strength of around 1190 MPa is found for a peak current of 220 A with high shielding gas flow rate. Flexural strength is mainly influenced by high temperature produced by increased welding current range along with high shielding gas flow rate. Base current and pulse frequency have less significance on bonding strength than comparatively peak current and shielding gas flow rate. By using the argon shielding gas and high peak current, the bonding strength in fusion zone gets increased due to high heat input which causes rise in welding temperature, leading to more solidification time and change in microstructure. In fusion zone microstructure change takes place by grain refinement which forms smaller nuclei and improves the bonding strength. It is observed that for a base current of 100 A with lowest and highest range value of peak current flexural strength drastically decrease which may be attributed to the low depth of penetration which involves more solidification time in weld pool and produces coarser grains and result in formation of welding defects like undercut and shrinkage. Lower value of argon shielding gas flow rate with lowest pulse frequency range chosen also minimizes the flexural strength due to low temperature in weld pool. Figure. 7 (a), (b), (c), (d) show the variation of flexural strength with the selected input parameters.

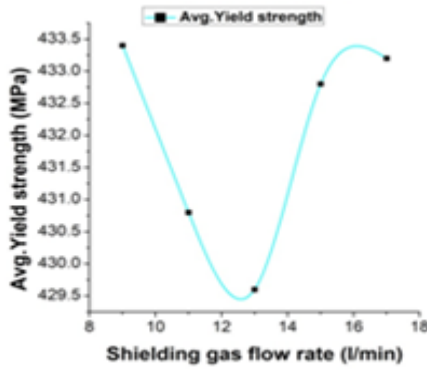


Figure 6. (g) Variation of YS with Q

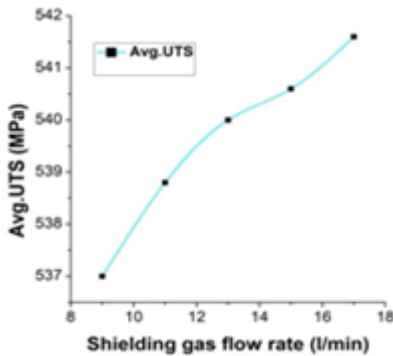


Figure 6. (h) Variation of UTS with Q

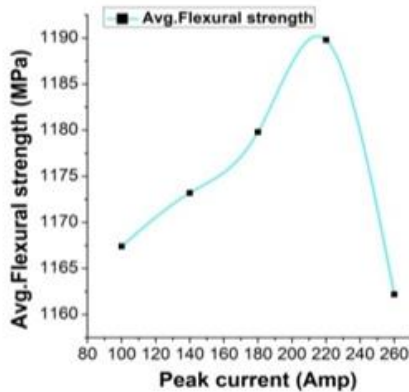


Figure 7. (a) Variation of FS with I_p

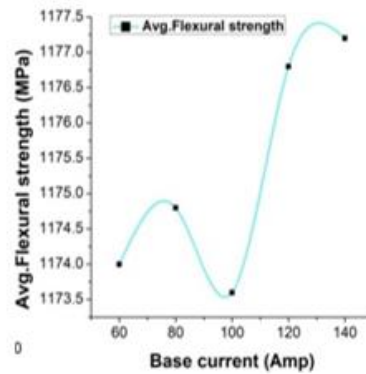


Figure 7. (b) Variation of FS with I_b

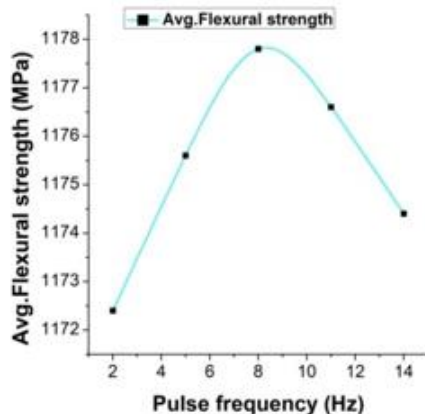


Figure 7. (c) Variation of FS with PF

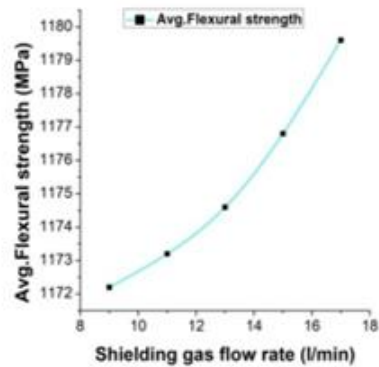


Figure 7. (d) Variation of FS with Q

3.3. Effect of weld parameters on microhardness

To predict the resistance to deformation in the welded joints, microhardness test is performed at different points in the welded zone and nearby heat affected regions with a diamond indenter. The resultant indentation is measured with the help of an optical microscope. The microhardness value increases with the increase in peak current and pulse frequency. In fusion zone, grain refinement is mostly influenced by pulse frequency. Optimum pulse frequency produces finer grain and choosing higher pulse frequency with high input or high peak current results in formation of coarser grains. This is due to the requirement of sufficient and longer cooling times in the absence of which coarser grains are formed which consequently result in lower hardness values. Increase in peak current upto 220 A with optimum range of other weld input parameters leads to increase in hardness value. Beyond 220 A current, the microhardness value decreases with any combination of

input process parameters. Lowest hardness value is recorded for shielding gas flow rate 13 l/min with low base current and lowest and highest value of pulse frequency. This decrease in microhardness is due to welding defects like porosity, unstable arc formation and wider weld bead width. Apart from these factors microhardness value gets varied with respect to temperature generated by interpass weld and thickness of plate. Figure.8 (a), (b), (c) (d) show the variation of microhardness with other input parameters.

3.4. ANOVA analysis

3.4.1. ANOVA for Yield Strength

The significant process parameters affecting yield strength can be determined using analysis of variance (ANOVA) [25]. ANOVA result for means of YS is given in Table 5 which indicates that the I_p , I_b and F are parameters which have significant contribution towards improvement in YS while the role of Q is insignificant.

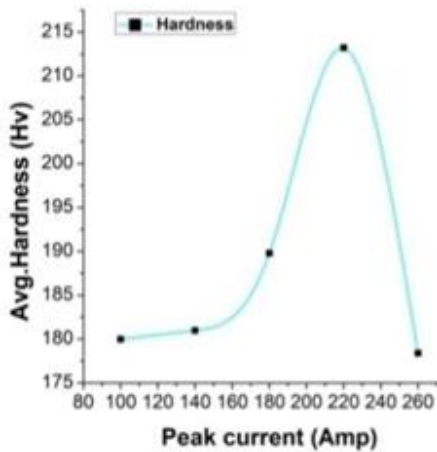


Figure 8. (a) Variation of microhardness with I_p

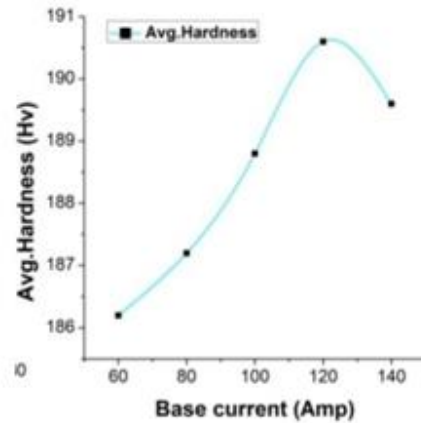


Figure 8. (b) Variation of microhardness with I_b

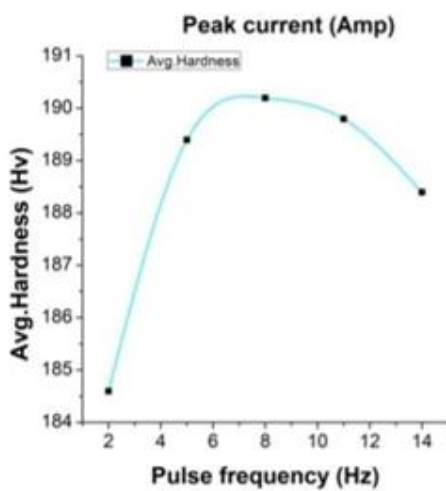


Figure 8. (c) Variation of microhardness with PF

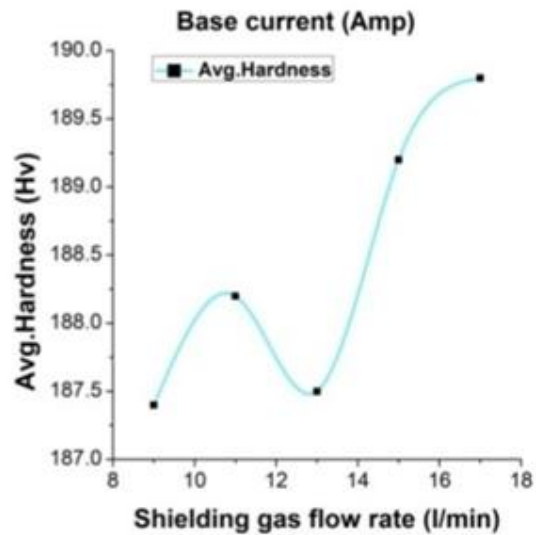


Figure 8. (d) Variation of microhardness with Q

Table 5. ANOVA table for means of YS

Source	DF	Adj SS	Adj MS	F	P
I _p	4	1990.16	497.54	89.81	0.000
I _b	4	130.96	32.74	5.91	0.016
F	4	221.36	55.34	9.99	0.003
Q	4	66.96	16.74	3.02	0.086
Residual Error	8	44.32	5.54		
Total	24	2453.76			
S= 2.35372	R- Sq=98.19%	R- Sq(adj)=94.58%			

3.4.2. ANOVA for Flexural Strength

The significant process parameters affecting flexural strength using ANOVA analysis has been presented in Table 7 which indicates that the I_p and Q are parameters which have significant contribution towards improvement in FS while the role of I_b and F is insignificant.

Table 7. ANOVA table for means of FS

Source	DF	Adj SS	Adj MS	F	P
I _p	4	2340.64	585.16	95.77	0.000
I _b	4	53.44	13.36	2.19	0.161
F	4	85.84	21.46	3.51	0.061
Q	4	176.24	44.060	7.21	0.009
Residual Error	8	48.88	6.110		
Total	24	2705.04			
S= 1.4282	R- Sq=99.19%	R- Sq(adj)=94.58%			

3.4.3. ANOVA for microhardness

The significant process parameters affecting yield strength can be determined using analysis of variance (ANOVA). ANOVA result for means of YS is given in Table 8 which indicates that the I_p, I_b and F are parameters which have significant contribution towards improvement in YS while the role of Q is insignificant.

Table 8. ANOVA table for means of YS

Source	DF	Adj SS	Adj MS	F	P
I _p	4	4211.44	1052.86	295.75	0.000
I _b	4	63.44	15.86	4.46	0.035
F	4	103.04	27.76	7.24	0.009
Q	4	19.84	4.96	1.39	0.319
Residual Error	8	28.48	3.56		
Total	24	4426.24			
S= 1.8868	R- Sq=99.36%	R- Sq(adj)=98.07%			

3.5. TOPSIS

Optimum range of welding process parameters are found out for output responses like Yield strength, Ultimate tensile strength, flexural strength and

microhardness using TOPSIS. The preference value for each experimental combination can be achieved using equation (4-9) considering that the preference value has comparative nearness to the best solution. The normalized matrix is shown in Table 9. The ratio of negative ideal separation measure divided by the sum of negative ideal separation measure and the positive ideal separation measure gives the best solution and is calculated using equation (10). Equal weightage is assigned considering the performance parameters equally important while welded under ideal conditions. The weighted normalized matrix is shown in Table 10. A multi-attribute optimization problem is transformed into single objective optimization problem using a Taguchi based TOPSIS approach. Table 11 shows the preference values of TOPSIS for each run. The experimental run with maximum preference value and highest rank has relative closeness to the ideal solution and is considered as best value. It is apparent that run 19 achieves highest preference order with multiple performance characteristics and is thus the optimal set of process parameters followed by run 20 and run 16. The optimal setting obtained is I_p4I_b4F₂Q₅.

Table 9. Normalized Matrix

Run	YS	UTS	FS	H
1	0.193	0.1923	0.1975	0.1841
2	0.194	0.1956	0.1984	0.1894
3	0.197	0.1993	0.1989	0.1926
4	0.198	0.1997	0.1992	0.1947
5	0.197	0.1986	0.199	0.1915
6	0.195	0.1967	0.1994	0.1884
7	0.199	0.1989	0.2007	0.1937
8	0.2004	0.2001	0.2013	0.195
9	0.1999	0.1971	0.1999	0.1926
10	0.1985	0.196	0.2001	0.1873
11	0.201	0.2026	0.2018	0.20005
12	0.2032	0.2023	0.2002	0.1979
13	0.2022	0.2030	0.1997	0.2021
14	0.2009	0.2019	0.2004	0.1989
15	0.204	0.2041	0.2014	0.2053
16	0.2027	0.2052	0.2019	0.2254
17	0.2036	0.2045	0.2023	0.2233
18	0.2041	0.2034	0.2016	0.2201
19	0.2069	0.206	0.2036	0.2307
20	0.2087	0.2056	0.2026	0.2286
21	0.1958	0.1952	0.198	0.1873
22	0.1967	0.1963	0.1977	0.1862
23	0.1985	0.1975	0.1968	0.1884
24	0.1995	0.1982	0.1979	0.1915
25	0.197666	0.1978	0.1982	0.1905

3.5.1. Confirmatory experiment for TOPSIS

After getting optimized parameter setting, for improving the quality characteristic, prediction and confirmation test is carried out for optimal set of process parameters. An increase in yield strength, UTS, flexural strength and microhardness values are obtained for optimized parameter setting and are presented in Table 12. The improvement in preference value for ideal solution is 0.5457.

Table 10. Weighted normalized matrix with positive and negative ideal solutions

Run	WYS	WUTS	WFS	WH	S_i^+	S_i^-
1	0.04814	0.048	0.0493	0.046044	0.012887	0.000171
2	0.04849	0.0489	0.0496	0.047367	0.011345	0.001647
3	0.04918	0.049	0.0497	0.048161	0.010199	0.002987
4	0.04953	0.0499	0.0498	0.04869	0.009578	0.003566
5	0.0493	0.0496	0.0497	0.047897	0.01044	0.002749
6	0.04883	0.0491	0.0498	0.047103	0.011393	0.001801
7	0.04976	0.0497	0.0501	0.048426	0.009763	0.003469
8	0.05011	0.05002	0.05032	0.048955	0.009119	0.004165
9	0.04999	0.0492	0.049986	0.048161	0.01007	0.003154
10	0.04964	0.049	0.050029	0.046838	0.011457	0.002099
11	0.05034	0.0506	0.050454	0.050013	0.007952	0.00537
12	0.0508	0.0505	0.050071	0.049484	0.008415	0.005089
13	0.05057	0.0507	0.049944	0.050543	0.007429	0.005821
14	0.05022	0.0504	0.050114	0.049749	0.008282	0.004966
15	0.05115	0.051	0.050369	0.051337	0.006477	0.006868
16	0.0506	0.0513	0.050497	0.056364	0.002057	0.011186
17	0.05092	0.0511	0.050582	0.055835	0.002304	0.010713
18	0.05103	0.0508	0.050412	0.055041	0.003004	0.009923
19	0.05173	0.0515	0.050922	0.057688	0.000463	0.01277
20	0.05219	0.0514	0.050667	0.057158	0.000595	0.012375
21	0.04895	0.0488	0.049518	0.046838	0.011722	0.001387
22	0.04918	0.04909	0.049433	0.046573	0.011858	0.001564
23	0.04964	0.04937	0.04922	0.047103	0.011223	0.00225
24	0.04987	0.04956	0.049476	0.047897	0.010349	0.00295
25	0.049417	0.04946	0.049561	0.047632	0.010717	0.002487

Table 11 Preference values with rank order

Run	Preference value	Rank
1	0.013062	25
2	0.126773	22
3	0.226548	15
4	0.2713	12
5	0.208409	17
6	0.136519	21
7	0.262164	13
8	0.313552	11
9	0.238477	14
10	0.154813	20
11	0.403088	8
12	0.376845	9
13	0.43932	7
14	0.374851	10
15	0.514665	6
16	0.844689	3
17	0.823034	4
18	0.767603	5
19	0.965024	1
20	0.954109	2
21	0.105796	24
22	0.116547	23
23	0.167011	19
24	0.221839	16
25	0.188375	18

Table 12. Results of confirmatory experiment

Initial factor setting	Optimal set	
	Initial	Experimental
Level	$I_{p3}I_{b3}F_3Q_3$	$I_{p4}I_{b4}F_2Q_5$
Peak current	180	220
Base current	100	120
Pulse frequency	8	5
Shielding gas flow rate	13	17
Value of preferred solution	0.4193	0.965024

3.5.2. ANOVA for TOPSIS

ANOVA is useful to determine the effect of input process parameters on output responses. Table.13 shows the ANOVA results for preference solution. Using MINITAB software, the result of factor responses were considered following “higher the better” criterion. From the response table of means shown in Table 14, it is clear that peak current, pulse frequency and base current have more contribution for improvement in the value of preference solution than the shielding gas flow rate. Figure.9 shows the variation of S/N ratio for the preference value. From the S/N ratio it can be observed that the trend of variation of all the process parameters is initially increasing followed by a decrease. This shows that as the current and pulse frequency increase, the weld quality shows deterioration. The most optimum setting is at the moderate values of all parameters [17-18].

Table 13. ANOVA table for TOPSIS

Source	DF	Adj SS	Adj MS	F-value	P-value
Peak current	4	1.80079	0.450198	352.45	0.000
Base current	4	0.04466	0.011166	8.74	0.005
Pulse frequency	4	0.05039	0.012598	9.86	0.003
Shielding gas flow rate	4	0.01069	0.002674	2.09	0.174
Error	8	0.01022	0.001277		
Total	24	1.91676			

Table 14. Response table for means of preference value

Factor	Response for means of preference value						
	Level-1	Level-2	Level-3	Level-4	Level-5	Delta	Rank
Peak current	0.1692	0.2211	0.4217	0.8708	0.1599	0.7109	1
Base current	0.3006	0.3410	0.3828	0.4142	0.4040	0.1136	3
Pulse frequency	0.2853	0.3819	0.4135	0.3989	0.3630	0.1281	2
Shielding gas flow rate	0.3499	0.3574	0.3498	0.3843	0.4013	0.0514	4

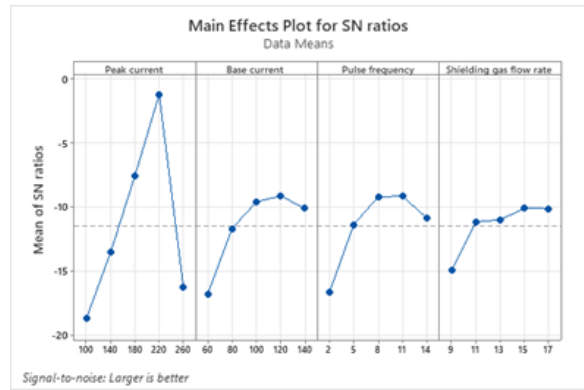


Figure 9. S/N ratio plot for preference value

4. Microstructure analysis

Microstructure analysis has been carried out for the base material, heat affected zone and fusion zone for optimized weld samples at 500x magnification. Figure.10 (a),(b),(c) and Figure.11(a),(b),(c) represent the base material microstructure, microstructures at HAZ and fusion zone for SAILMA 450 and EN 14B respectively. From the microstructure shown in Figure. 10(a), it can be observed that for SAILMA 450, the base structure is mostly ferrite and pearlite is present in banded form. Fine equiaxed grains are observed which are mixture of ferrite and pearlite. The presence of pearlite helps to retain the strength of the material. Since the material possess more strength, it is used in power plants and finds application as a construction material. Figure. 10(b) shows the microstructure at the heat affected zone (HAZ) at SAILMA450 side. The HAZ involves the presence of EN-14B due to fusion, hence demonstrates change in structure and properties. Pearlite transforms into bainitic structure. The microstructure thus contains bainite, pearlite and ferrite. Figure. 10(c) shows a fused structure combining bainite, pearlite and ferrite. In EN 14B, the base material consists of lower pearlite with some ferrite present in it. The grains are equiaxed and finer in nature as observed in Figure. 11(a).The microstructure at heat affected zone of EN-14B shown in Figure. 11(b)consists of bainite.The grains appear to be coarser which improve the creep properties of the material. In the fusion zone, transformation occurs from bainite to lower martensite with reduced grain size as shown in Figure 11(c). The microstructure contains pearlite, ferrite, tempered martensite and the weld zone shows good compatibility.

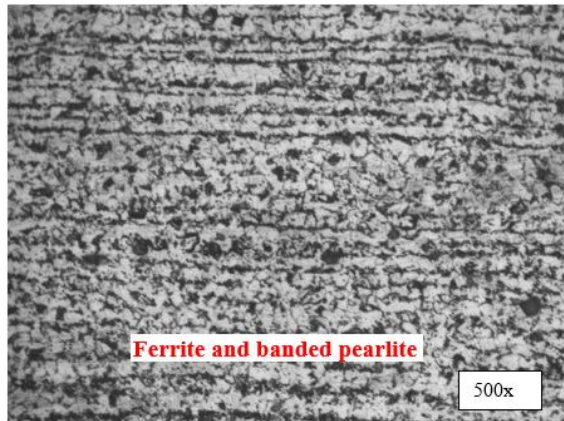


Figure 10. (a) Base Material microstructure of SAILMA 450 captured at 500x

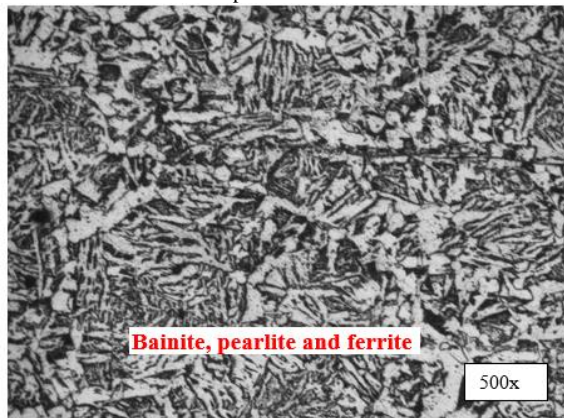


Figure 10. (b) Grain orientation at HAZ captured at 500x

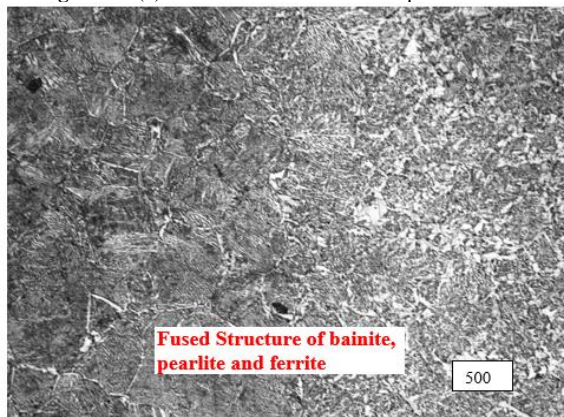


Figure 10. (c) Microstructure at fusion zone for SAILMA 450 captured at 500x

5. Conclusion

The present study involves pulse current tig welding of SAILMA 450 with EN 14B steel. The process parameters have been optimized using Taguchi technique and multi-objective optimization has been performed using TOPSIS to maximize yield strength, ultimate tensile strength, flexural strength and microhardness simultaneously. The major conclusions drawn are as follows:

1. Pulse current TIG welding process is considered to be among the most difficult welding processes used in industries. The process is slower, involves complexity and is difficult to master. It requires high skill of

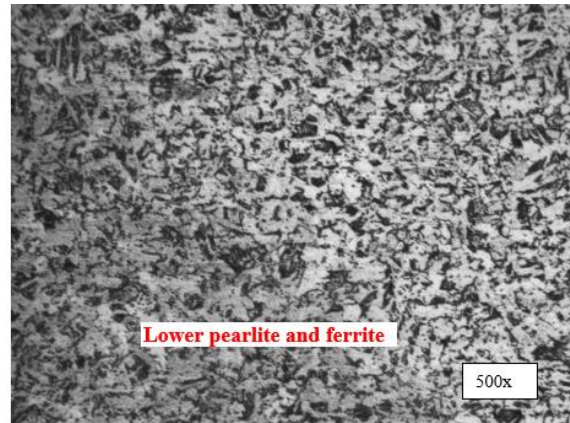


Figure 11. (a) Base Material microstructure captured at 500x

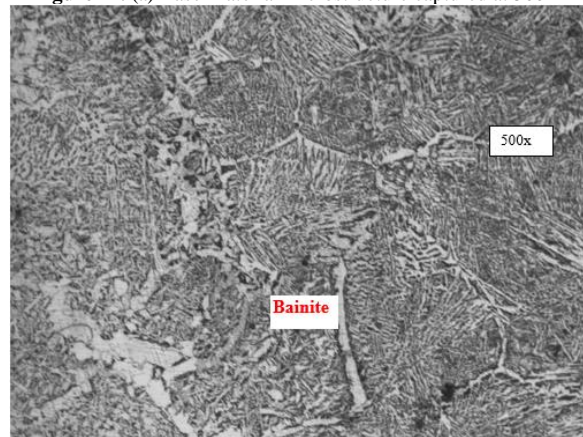


Figure 11. (b) Grain orientation at HAZ captured at 500x

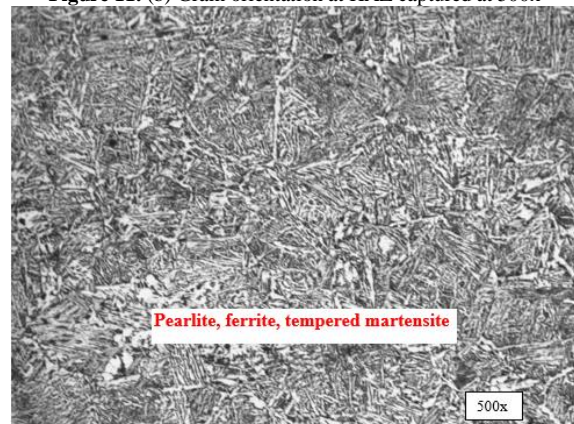


Figure 11. (c) Microstructure at fusion zone for EN 14B captured at 500x

operation, greater care and the welder must maintain a short arc length to prevent contact between electrode and workpiece.

2. Design of experiments has been used to establish the relationship between process variables. TOPSIS has been used to optimize the process parameters simultaneously to achieve maximized output in terms of mechanical strength and hardness of the weld joint.
3. The optimum set of process parameters for achieving maximized mechanical strength and microhardness is peak current of 220 A, base current of 120 A, pulse frequency of 5 Hz and shielding gas flow rate 17 l/min.
4. Yield strength and ultimate tensile strength increase with increase of current but when pulse frequency is

- beyond 8Hz then the mechanical strength gets reduced due to arc instability produced by high pulse frequency.
5. For flexural strength, peak current and shielding gas flow rate are more dominant parameters than base current and pulse frequency.
 6. Microhardness value increases up to a peak current of 220 A with pulse frequency of 5Hz and after that the microhardness value gets reduced due to grain coarsening.
 7. The tensile specimen usually fails at the base metal side of EN 14B steel due to less tensile strength than SAILMA 450 steel side.
 8. No crack has been found up to 120° of three point bending test which proves that welded joints are more ductile in nature.
 9. Microstructure of weld zone consists of martensitic structure which leads to increase in the hardness. Finer grains are observed in SAILMA 450 fusion zone side than fusion zone side of EN 14B.
 10. TOPSIS acts as a powerful tool for optimization of the process. Confirmatory tests show an improvement of 0.5457 in the preference values which is acceptable. The achieved results show that the optimized set of process parameters may be used in the industries to achieve good quality welded structures during welding of SAILMA 450 and EN14B. These steels have been combined together for various applications and have been welded by advanced welding processes like friction stir welding.
 11. The suggested work can be extended further and brought to application in automotive industries. Also, the optimization methods may be used to solve problems in other manufacturing processes like conventional and non-conventional machining, forming etc.

References

- [1] L. Liu, X. Xu, G. Xu, G., Z. Zhang, "Effect of laser on double-arc physical characteristics in pulsed laser induced double-TIG welding". *International Journal of Advanced Manufacturing Technology*, Vol.119 (2021), 1515-1529.
- [2] T.S. Balasubramanian, M. Balakrishnan, V. Balasubramanian, M.M. Manickam, "Influence of welding processes on microstructure, tensile and impact properties of Ti-6Al-4V alloy joints". *Transactions of Nonferrous Metals Society of China*, Vol. 21 (2011) No. 6, 1253-1262.
- [3] M.S. Manohar, K. Mahadevan, "Multi-response optimization of weld-process variables for micro-friction stir welding of Al6061 (T6) and Cu101 sheets using Topsis Method". *IOP Conf. Series: Materials Science and Engineering*, Vol. 1168 (2021) No. 012002.
- [4] T. Medhi, S.A.I. Hussain, B.S. Roy, S.C. Saha, "An Intelligent Multi-Objective framework for optimizing friction-stir welding process parameters". *Applied Soft Computing*, Vol.104 (2021) No.107190.
- [5] J. Sivakumar, N.N. Korra, "Optimization of welding process parameters for activated tungsten inert welding of Inconel 625 using the technique for order preference by similarity to ideal solution methodology." *Arabian Journal for Science and Engineering*, Vol.46 (2021), 7399-7409.
- [6] D.J. Daniel, K. Panneerselvam, "Process parameters optimization for friction vibration joining of polypropylene/spherical glass composites using Topsis." *Surface Review and letters*, Vol. 27 (2020) No.06, 1950167.
- [7] J. Sivakumar, M. Vasudevan, M., N.N. Korra, "Systematic welding process parameter optimization in activated tungsten inert gas (A-Tig) welding of Inconel 625." *Transactions of the Indian Institute of Metals*, Vol. 73(2020) No.3, 555-569.
- [8] V. Chodha, R. Dubey, R. Kumar, S. Singh, S. Kaur, "Selection Of Industrial Arc Welding Robot With Topsis And Entropy Mcdm Techniques." *Material Today Proceedings*, Vol. 50 (2022) No. 5, 709-715.
- [9] K. R. Sampreet, V. Mahidhar, R. Kannan, T. D. B. Kannan, "Optimization of Parameters In Nd: Yag Laser Welding of Ti-6Al-4V using Topsis." *Material Today Proceedings*, Vol. 21 (2020), 244-247.
- [10] V. Mahidhar, K.R. Sampreet, R. Kannan, T. D. B. Kannan, "Parameter optimization in laser welding of hastelloy C-276 using Topsis." *Material Today Proceeding*, Vol.21 (2020) 595-600.
- [11] P.K. Baghel, T. Gupta, "Optimization of parameters of pulse current gas tungsten arc welding using non conventional techniques". *Journal of advanced joining processes*, Vol.6 (2022) No. 100124.
- [12] S. Avinash, Y. Balram, B. S. Babu, G. Venkatramana, "Multi-response optimization of pulse TIG welding process parameters of welds AISI 304 and Monel 400 using grey relational analysis". *Material Today Proceedings*, Vol. 19 (2019) No.2, 296-301.
- [13] A.K.Srirangan, P. Sathiyar, "Optimisation of Process Parameters for Gas Tungsten Arc Welding of Incoloy 800HT Using TOPSIS". *Materials Today: Proceedings*, Vol. 4 (2017) No.2, 2031-2039.
- [14] J. Joseph, S. Muthukumar, "Optimization of activated TIG welding parameters for improving weld joint strength of AISI 4135 PM steel by genetic algorithm and simulated annealing." *International Journal of Advanced Manufacturing Technology*, Vol.93 (2017), 23-34
- [15] G. Magudeeswaran, S.R. Nair, L. Sundar, N. Harikannan, "Optimization of process parameters of the activated tungsten inert gas welding for aspect ratio of UNS S32205 duplex stainless steel welds." *Defence Technology*, Vol. 10 (2014) 251-260.
- [16] H.P. Nyugen, V.D. Phm, N.V. Ngo. "Application of TOPSIS to Taguchi method for multi-characteristic optimization of electrical discharge machining with titanium powder mixed into dielectric fluid." *International Journal of advanced manufacturing Technology*, Vol. 98 (2018), 1179-1198.
- [17] Tripathy, S., Tripathy, D.K.: Multi-attribute optimization of machining process parameters in Powder Mixed Electro-Discharge Machining using TOPSIS and Grey Relational Analysis. *Engineering Science and Technology: An International Journal*, 19(1), 62-70 (2016).
- [18] Tripathy, S. and Tripathy, D.K. 'Multi-response optimization of machining process parameters for powder mixed electro-discharge machining using grey relational analysis and topsis.' *Machining Science and Technology*, Vol. 21(3), (2017); p.362-384.
- [19] G.Talla, D. K. Sahoo, S. Gangopadhyay, C.K. Biswas, "Modeling and multi-objective optimization of powder mixed electric discharge machining process of aluminium /alumina metal matrix composite." *Engineering Science and Technology: an International Journal*, pp. 1-5, (2015).
- [20] S. Balasubramanian, T. Selvaraj, "Application of integrated Taguchi and TOPSIS method for optimization of process parameters for dimensional accuracy in turning of EN25 steel." *Journal of the Chinese Institute of Engineers*, Vol.40 (2017) No. 4, 267-274.
- [21] A.Singh, S.Datta, S.S.Mahapatra, "Application of TOPSIS in the Taguchi Method for optimal machining parameter

- selection. "Journal for Manufacturing Science and production, Vol.11(2011) No. 1-3, 49-60.
- [22] B.Singaravel, T.Selvaraj, " Application of Taguchi method for optimization of parameters in turning operation." Journal for Manufacturing Science and production, Vol.16(2016) No.3, 183-187.
- [23] M. Soori , M. Asmael, "A Review of the Recent Development in Machining Parameter Optimization."Jordan Journal of Mechanical and Industrial Engineering, Vol.16 (2022) No.2, 205-223.
- [24] H. Q. Ayun, J. Triyono, E. Pujiyanto, "Optimization of Injection Molding Simulation of Bioabsorbable Bone Screw Using Taguchi Method and Particle Swarm Optimization." Jordan Journal of Mechanical and Industrial Engineering, Vol.16 (2022) No.2, 319-325.
- [25] G.V.S.S.Sharma, P. Srinivasa Rao , B. Surendra Babu, "Establishing Process Capability Indices in a Sugar Manufacturing Industry – an Industrial Engineering Perspective." Jordan Journal of Mechanical and Industrial Engineering, Vol.15 (2021) No.4, 319-325.

Performance Enhancement of Multi-Modal Piezoelectric Energy Harvesting Through Parameter Optimization

Ossama Mokhiamar^{1, *}, David Omooria Masara^{1,2}, Hassan El Gamal¹

¹ Alexandria University, Faculty of Engineering, Mechanical Engineering Department, El-Chatby, Alexandria 21544, Egypt

² University of Eldoret, School of Engineering, Department of Mechanical and Production Engineering, 1125-30100, Eldoret, Kenya

Received 19 Apr 2022

Accepted 13 Sep 2022

Abstract

This study presents an optimized multi-resonant piezoelectric energy harvester to scavenge broadband energy over a frequency range between 11 Hz -17 Hz. The harvester encompasses a rectangular beam with two parallel splits to form three branches. The branches are of unequal length and width. End masses of dissimilar sizes were affixed at the ends of each branch to tailor the resonant frequencies. A piezoelectric material was laid on both sides of the driving beam to form a bimorph. The initial parameters of the harvester were obtained from a parametric study using the Finite Element Method. COMSOL Multiphysics software was used to apply boundary conditions to the design and to perform the optimization. The Bound Optimization by Quadratic Approximation (BOBYQA) algorithm was deployed in optimization because of its versatility in derivative-free, bound-constrained optimization problems. In comparison to its unoptimized form, a 31.67% average power increment was realized from the design. The optimal impedance was reduced from 5.62 k Ω to 1.778 k Ω , which enhances the efficiency of the harvester by reducing electrical damping. The proposed optimized harvester was compared to a Multi-Resonant Piezoelectric Energy Harvester for verification. It was shown to be more effective by harvesting sufficiently higher broadband energy.

© 2022 Jordan Journal of Mechanical and Industrial Engineering. All rights reserved

Keywords: piezoelectric energy harvesting; optimization; low-frequency; multimodal.

Nomenclature		$\ddot{x}, \ddot{y}, \ddot{z}$	Harvester acceleration, Base acceleration, Relative acceleration
C	Damping coefficient matrix	\dot{z}, z	Relative velocity and displacement vector tensors respectively.
C_p	Capacitance of the piezoelectric material	$\{D\}$	Electrical Displacement Tensor
k	Stiffness matrix	$\{E\}$	Electric Field Tensor
m	Mass matrix of the harvester	$\{T\}$	Mechanical Stress Tensor
m_1	Mass on Branch 1	$\{s\}$	Mechanical Strain Tensor
m_2	Mass on Branch 2	$[d]$	Direct Piezoelectric Matrix
m_3	Mass on Branch 3		
R	Load resistance		
v	Induced voltage		
x	Harvester displacement	$[s^E]$	Electric compliance matrix
y	Base displacement	α	Effective electromechanical coupling coefficient
w_1	Width of Branch 1	ω	Vibration frequency in rad/s
w_2	Width of Branch 2	$[\epsilon]$	Permittivity Matrix
w_3	Width of Branch 3		
d_{31}, d_{33}, d_{15}	Piezoelectric Constants		
T_1, T_2 and T_3	Normal Stresses in x, y, and z Axes	Abbreviations	
T_4, T_5 and T_6	Shear Stresses	CPEH	Conventional Piezoelectric Energy Harvester
E (superscript)	Zero or Constant Electric Field	DOF	Degrees of Freedom
T (superscript)	Zero or Constant Stress Field	FEM	Finite Element Method
t (superscript)	Transpose of a Matrix	MRPEH	Multi-Resonant Piezoelectric Energy Harvester

* Corresponding author e-mail: usamam@alexu.edu.eg.

PEH	Piezoelectric Energy Harvester
PZT	Lead zirconate Titanate
SCMEH	Split Cantilever Multi-Resonant Energy Harvester

1. Introduction

The advancement in technology, especially in automation, structural health monitoring (SHM), predictive maintenance [1] and the Internet of Things (IoT), has triggered the need for self-powered microelectronic devices. Previously, such devices primarily drew their power from depletable chemical batteries that required periodic replenishment. Such batteries are hazardous to the environment at the end of their useful life, as noted by Lange et al [2], that the sharp rise in energy usage has posed serious environmental consequences. The mechanical-to-electrical transduction mechanisms used include electromagnetic transduction, electrostatic transduction, and mainly piezoelectric transduction. Piezoelectric transduction involves the use of piezoelectric materials laid on one or both sides of a mechanical beam. When the composite is subjected to vibrations, the elastic substrate beam deforms and strains the piezoelectric material. Piezoelectricity is thus induced under strain to generate electrical energy. The harvesters possess different configurations spanning from narrow bandwidth harvesters that operate on a sole resonant frequency to multimodal harvesters with more than one operational resonant frequency. The essence of energy harvesting is to complement replaceable batteries and provide a sustained energy supply for microelectronic devices. Energy harvesters, therefore, offer a theoretically perpetual power source to enhance autonomy and prognostics. As a result, vibration, an otherwise unsolicited phenomenon, can be put to valuable use like charging mobile devices [3].

A harvester must discharge vital power to a specified electrical load (appliance) for extended periods to be efficient. For this motive, the energy from a harvester should be maximized with diminutive alteration to the existing constraints such as space and vibration source frequencies. One primary method of accomplishing power maximization is through optimization. Optimization is a technique that has been widely deployed in many forms, such as: stochastic and deterministic optimization, shape optimization, geometry optimization, and topology optimization. Hybridization is a technique whereby more than a single transduction method is deployed in attempts to optimize harvesters, although Ahmad et al. highlighted the benefits of using a standalone device [4]. Besides these techniques, optimization has been capacitated through increasing the electromechanical coupling. For instance, Cho et al. [5] highlighted the impact of piezoelectric residual stress and coverage of the electrode on the electrical coupling coefficient. It was concluded that the optimum coupling was achieved at an electrode coverage of 60%. Wang and Wu further investigated the impact of piezoelectric patch positioning and measurements on the performance of a cantilever harvester. It was inferred that the efficiency decreases as the position of the piezoelectric patch moves away from the fixed end of the beam. In an attempt to maximize the power output, beams with initial curvature were also exploited by Yoon et al. [7]. Elahi [8], on the other hand, inferred that the piezoelectric material

and substrate length ratio had a significant impact on the performance of the harvester. Elahi et al. [9] proved that a rectangular patch is more efficient than a circular patch, and the length of the patch in relation to the driving beam length affects the harvester's performance. For instance, equal lengths of aluminum substrate combined with a PZT-5A piezoelectric material were reported to have the maximum voltage induced at the utmost tip displacement.

Topology optimization entails material removal and/or material orientation such that the material is deposited at a location where its maximum performance can be achieved. Acciani et al. [10] realized a 16% increase in harvested energy efficiency from a multimodal device. The increment was achieved by varied material removal from the said structure. A differential configuration is used to achieve maximum efficiency. Kim and Shin [11] reported a topologically optimized harvester. A method to optimize material layout was developed using a semi-empirical equation for electromechanical coupling. Various piezoelectric materials were tested, and enhanced efficiency was realized for all of them. Lee and Tovar [12] optimized an energy harvesting skin using a Hybrid Cellular Automata. The domain is discretized to form Cellular Automata, and the output power is maximized by finding optimum densities and polarizing directions in every Automata. Later, Thein and Liu [13] performed a two-stage optimization process, where the shape of the cantilever and intrinsic topology features were adopted to enhance power. In the first stage, the notable increment doubled, while in the second stage, the increment was 11% higher, compared to a traditional rectangular cantilever. Wein et al. [14] incorporated stress constraints to optimize a harvester topologically. Their design has higher flexibility due to its varying shapes. High power capacity is achieved for structures at their resonance.

In shape and geometry optimization, optimum design shapes and geometric configurations are determined to maximize output power. Dietl and Garcia [15] sought to optimize the shape of a non-uniform width harvester. They intended to localize the strain in zones where it could yield the utmost power. A heuristic code was developed and utilized to obtain optimum shapes. Harvested power was found to increase in devices constrained by mass, and the mass was found to decrease in devices constrained by power. Similarly, Park et al. [16] optimized a rotary motion energy harvesting device. Well tapered and rectangular cantilevers were analyzed. The setup was simulated using Sequential Quadratic Programming, and a 37% energy increase was realized. On the other hand, Mohamed et al. [17] validated a new shape optimization technique. A range of shapes from rectangular to triangular, T-shaped, L-shaped, and variable-width shapes were optimized. It was inferred that the T-shape produced the highest power. Wang et al. [18] attempted to improve output from a harvester by the use of a double cantilever. A substantial improvement was realized.

Many optimization techniques have been developed and deployed. Shape and topology optimization are the most common, and they are well suited for single-mode harvesters. It is also challenging to envisage locations of high stress for piezoelectric material placement. Similarly, the use of prestressed beams or beams with an initial curvature reduces the amount of force under which the

harvesters can operate effectively, as they encourage failure. If implemented in the multi-mode harvesters, these techniques affect the distribution of the fundamental frequencies, resulting in a large separation between them. This study aims to enhance the power output of a multimodal energy harvester through the selection of optimal geometrical parameters using the COMSOL Multiphysics optimization module. On the other hand, the end masses have been used for frequency tuning in the literature with no consideration of their effect on the power output. Therefore, this study attempts to determine the optimum magnitude of the end masses for maximum power output.

Finite Element Method (FEM) has been extensively used to accurately study vibration energy harvesters. Validation of the finite element method results has been achieved through either analytical methods [19, 20], or experimentally [21, 22]. Both these methods have shown that FEM can accurately and effectively study energy harvesting methods, and as a result, COMSOL FEM has been chosen for this study.

2. Harvester design

The harvester's design features a split cantilever multi-resonant energy harvester (SCMEH), as shown in Fig.1. The design presented by the authors in the un-optimized form [23] will be subject to optimization in this study.

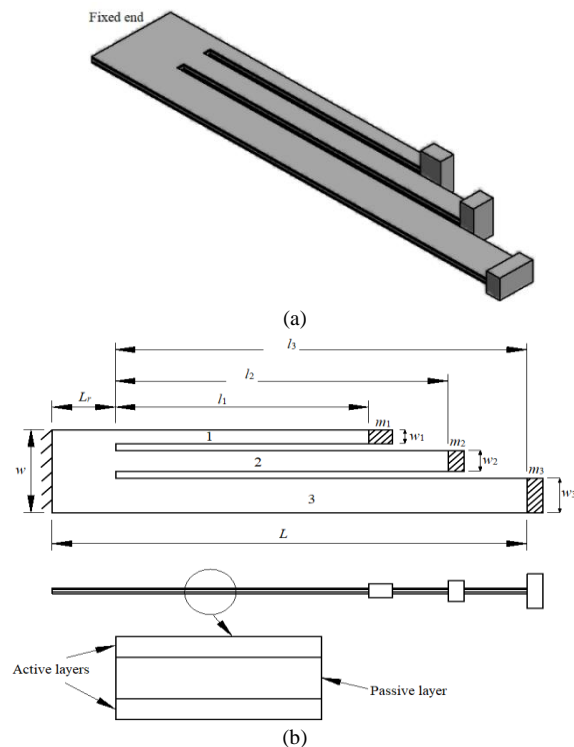


Figure 1. Schematic view of the proposed harvester:(a) Design of the SCMEH; and (b) detailed view.

The design constitutes a beam with two parallel splits to form branches of unequal length and width. The difference in width serves to lessen out-of-phase vibration of the branches, which may lead to voltage cancellation. On the other hand, the effect of the difference in length of the branches, on the other hand, aids in providing an appropriate distribution of natural frequencies. The piezoelectric layer is deposited on both sides of the substrate to form a bimorph. Each branch has a tip mass for tuning the fundamental frequencies of the harvester. The harvester's design is versatile since it can effortlessly be modified to suit target vibration sources, and thus it can be used in a wide range of applications. Furthermore, it requires low excitation forces as it is free of linkages, which makes it suitable for ambient environmental vibrations. The design minimizes phase differences and thereby achieves higher peak energy when compared to other designs explored in the literature, as well as produces high power density. The materials used for both the substrate and piezoelectric material of the harvester are shown in Table 1.

Table 1. Material properties of the harvester

Parameter	Substrate	Piezoelectric
Material	Brass	PZT-5H
Elastic modulus (GPa)	110	127
Poisson's ratio	0.33	0.31
Density(kg/m ³)	9000	7500

Brass is the preferred substrate material due to its high modulus, which supports a substantial magnitude of the tip masses without deflection. In addition, it can be applied in several vibration environments. Similarly, PZT-5H is the preferred piezoelectric material because of its higher piezoelectric constant.

3. Harvester parametric study

The parameters chosen for the harvester's optimization are the tip masses' magnitudes, the harvester's length, and the thicknesses of the substrate and piezoelectric materials. The effect of mass and length on natural frequencies was found and demonstrated in the previous work by the authors [23]. It was inferred that increasing beam length reduces the fundamental frequencies while increasing beam thickness increases the natural frequency. However, the effect of width on the natural frequency is relatively small[24], but the branch width significantly affects the phase variation in the vibration, as previously confirmed by the authors [23]. Therefore, proper selection of beam size parameters is essential to achieve a suitable design for a specified application. The initial parameters of the harvester, as obtained from the parametric study by the authors [23], are presented in Table 2.

Table 2. Parameters of the proposed SCMEH [23]

Parameter Symbol	Description	Substrate	PZT	Mass
$L(\text{mm})$	Length	60	60	
$L_r(\text{mm})$	Length of root	18	18	
$w(\text{mm})$	Width	12	12	
$w_1(\text{mm})$	Width of branch 1	2	2	
$w_2(\text{mm})$	Width of branch 2	3	3	
$w_3(\text{mm})$	Width of branch 3	5	5	
$l_1(\text{mm})$	Length of branch 1	32	32	
$l_2(\text{mm})$	Length of branch 2	42	42	
$l_3(\text{mm})$	Length of branch 3	52	52	
$t(\text{mm})$	Depth	0.4	0.2	
$m_1(\text{g})$	Mass on branch 1			49
$m_2(\text{g})$	Mass on branch 2			41
$m_3(\text{g})$	Mass on branch 3			51

4. Modeling of the harvester

The harvester, being a mechanical system, is represented as a spring mass and damper system with the applied acceleration as a forcing function. Modeling the system as an inertial mass component under a base acceleration, its internal resistance analogizes the stiffness element. A damper is incorporated to analogize the energy dissipation.

For simplicity, the system is assumed to be a lumped mass model, and its coupled governing equations are written as:

$$m\ddot{z} + c\dot{z} + kz + \alpha v = m\ddot{y} \quad (1)$$

$$\frac{v}{R} + c_p \frac{dv}{dt} = \alpha \frac{dz}{dt} \quad (2)$$

$$\text{where; } \ddot{z} = \ddot{x} - \ddot{y}$$

α and c_p in Eq. (2) are defined as;

$$\alpha = \frac{eA}{L}$$

$$c_p = \varepsilon^s \frac{A}{L} \quad (3)$$

where \dot{z} and z are the relative velocity and displacement vector tensors respectively. Eq. (3) depicts the influence of harvester parameters on piezoelectric constants.

Eq. (1) represents the mechanical part of the system, while Eq. (2) represents the electrical part. A combination of the two is known as electromechanical coupling [26]. On the other hand, the following equations govern the piezoelectric effect:

$$\{S\} = [s^E] \{T\} + [d^t] \{E\} \quad (4)$$

$$\{D\} = [d] \{T\} + [\varepsilon^T] \{E\} \quad (5)$$

Equations (4) and (5) express the inverse and direct piezoelectric effects, respectively. Since the system is under the direct piezoelectric effect, Eq. (5) is used to describe it, whereby the induction of stress in the beam leads to the production of charge.

The constants in Eq. (4) show the influence of individual harvester parameters on the harvester's performance. The above model is solved as a distributed model using the Finite Element Method (FEM) in COMSOL Multiphysics to determine its response.

4.1. Optimization formulation

The finite element model of the design described above is modeled in COMSOL Multiphysics. Through a grid-independent test, a range of element sizes ranging from coarse to extremely fine were tested and their effects analyzed. The element size is selected such that the accuracy of the solution is not dependent on it while maintaining a reasonable computational time. Hence, a fine size was used in this study and skewness was used to test for the element quality. A natural frequency study was conducted to determine its eigen frequencies. In the frequency domain study, the optimization module is applied. BOBYQA (Bound Optimization BY Quadratic Approximation) is chosen as the optimization solver due to its robustness and numerous advantages as described by Powell [27]. BOBYQA is an iterative algorithm to optimize any function, with each iteration employing a quadratic approximation. The medians of the bounds are selected as the initial values to reduce the computational effort when seeking the optimal values. Since BOBYQA is bound-constrained, no derivatives are provided by the user, and for this reason, extreme geometric parameter values related to the objective can be executed.

The output power (P) of the harvester is selected as the design objective function and it is defined as:

$$P = I_0 V_0 = I_0^2 R \quad (6)$$

Where I_0 and V_0 are the output current of the harvester and the voltage drop, respectively, at the initial load resistance ($R = 10k\Omega$). The relationship between the harvester output power and the device parameters is illustrated by α and c_p in Eq. (3), whereas the relationship between the mechanical strain and piezoelectricity is shown in Eqs. (4) and (5).

By incorporating the terms in Eq. (3) the objective function as derived by Lefeuvre et al.[28] becomes:

$$P = V_{rec} \left(\frac{2\alpha}{\frac{\pi}{2} + Rc_p \omega} + c_v \frac{\frac{\pi}{2} + Rc_p \omega}{\alpha R} \right) \quad (7)$$

To illustrate the effect of the respective harvester parameters on the power output, the constituent terms of Eq. (3) are substituted in Eq. (7) yields the following equation:

$$P = V_{rec} \left(\frac{2eA}{\frac{\pi L}{R} + R\omega A\varepsilon^s} + c_v \frac{\frac{\pi L}{2} + R\omega A\varepsilon^s}{2eAR} \right) \quad (8)$$

In Eq. (8), the length L represents all the aspects of length l_1 , l_2 , and l_3 . On the other hand, all the mass elements m_1 , m_2 , and m_3 are illustrated since the natural frequency depends on the inertial component of mass.

$$\text{Since } V_{rec} = \frac{V_0}{\sqrt{2}},$$

Therefore, the objective function is

$$P = \frac{(V_0)^2}{2R} \quad (9)$$

With the objective function now set as Eq. (9), the control variables can be expressed as the lower and upper bounds of the design parameters shown in Table 3, while the constraint, which is the natural frequency of the vibration, is expressed as:

$$g_1 \leq 17 \text{ Hz} \quad (10)$$

The 17 Hz constraint is chosen to accommodate any deviation that may ensue due to the changes in dimensions and mass magnitudes after the optimization process, as the structure, in its unoptimized form, was initially designed to perform at a frequency below 15 Hz.

Table 3. control variables

parameter	Lower bound	Upper bound
$l_1(\text{mm})$	10	60
$l_2(\text{mm})$	10	60
$l_3(\text{mm})$	10	60
$t_1(\text{mm})$	0.1	0.5
$t_2(\text{mm})$	0.1	0.5
$m_1(\text{g})$	5	60
$m_2(\text{g})$	5	60
$m_3(\text{g})$	5	60

The objective function in Eq. 9 and the control variables in Table 3 are applied in the optimization module, and the BOBYQA algorithm generates optimal parameters for the harvester. The fixed values of the design parameters represent the bounds around which the algorithm attempts to find the values that yield the maximum power. The upper bound was selected as the longest permissible length under which the structure could operate without initial curvature occurring, while the lower bound was chosen arbitrary to a length under which no notable deflection could happen with the available loading. The optimization procedure is shown in Fig. 2. A COMSOL FE model is used to compute the performance required for optimization. Power and mechanical stress are two examples. The optimal values obtained are shown in Table 4.

Table 4. Optimum parameters of the harvester

parameter	Optimal value
$l_1(\text{mm})$	27.704
$l_2(\text{mm})$	36.886
$l_3(\text{mm})$	51.224
$t_1(\text{mm})$	0.44015
$t_2(\text{mm})$	0.20402
$m_1(\text{g})$	49.0846
$m_2(\text{g})$	41.5765
$m_3(\text{g})$	51.975

The parameters for the optimal harvester presented in Table 4 are used to simulate the optimized SCMEH, and to

determine its performance which will be discussed in the coming section.

5. Simulation of the optimized harvester

The optimized harvester is modeled in COMSOL Multiphysics using the optimal parameters obtained from optimization shown in Table 4. Boundary conditions are applied to the harvester to simulate its response. The boundary conditions include a base acceleration of 0.2 g and a load resistance of 10 k Ω . The resistance is chosen to emulate an open circuit state. The condition that must be satisfied by the resistance is that it must be greater than the internal resistance of the piezoelectric material. However, later in this work, an optimum resistance for maximum power output will be evaluated. A damping loss factor of 0.001 is selected for damping. The loss factor is selected according to the material properties, as provided in the COMSOL material library. The initial displacement is zero, and the ground and terminals are configured to assume a parallel connection. An eigenfrequency study was first conducted to obtain the mode shapes and the fundamental frequencies that need to be matched to the source frequency for the harvester to operate at its resonant frequencies.

5.1. Eigenfrequency study

The optimized harvester's mode shapes are shown in Figure 3. The first, second, and third fundamental frequencies are 11.729 Hz, 13.951 Hz, and 15.36 Hz. In the harvester's unoptimized form, the first, second, and third natural frequencies are 10.702 Hz, 12.702 Hz, and 14.007 Hz, respectively. This signifies a slight variation in the natural frequency. However, the variation is within the targeted value of ≤ 17 Hz. The variation in the magnitude of the natural frequencies is due to the change in harvester dimensions brought about by optimization. In the first mode shape, Fig. 3(a), all the branches deflect in the same direction, with branch 3 having the maximum deflection. No phase difference is experienced; hence maximum strain is induced on the piezoelectric element, since torsional vibration is minimal. During this mode, the highest peak power is expected since no voltage cancellation effect exists. Branches 1 and 2 deflect in the same direction in the second mode, while branch 3 deflects slightly in the opposite direction resulting in a slight out-of-phase vibration as illustrated in Fig. 3 (b). For this reason, the expected voltage and power peaks will be somewhat lower than the voltage and power in the first mode. During the third mode, shown in Fig. 3 (c), branches 1 and 2 deflect in opposite directions, while branch 3 remains undeflected. Such deflection results in a large out-of-phase vibration, and the lowest power peak is expected in this mode. This is due to the cancellation effect of the power and voltage peaks in the bending modes. The cancellation arises because part of the beam is under tension while the other part is under compression to produce a torsional effect. The energy from the torsional modes is not considered in this study.

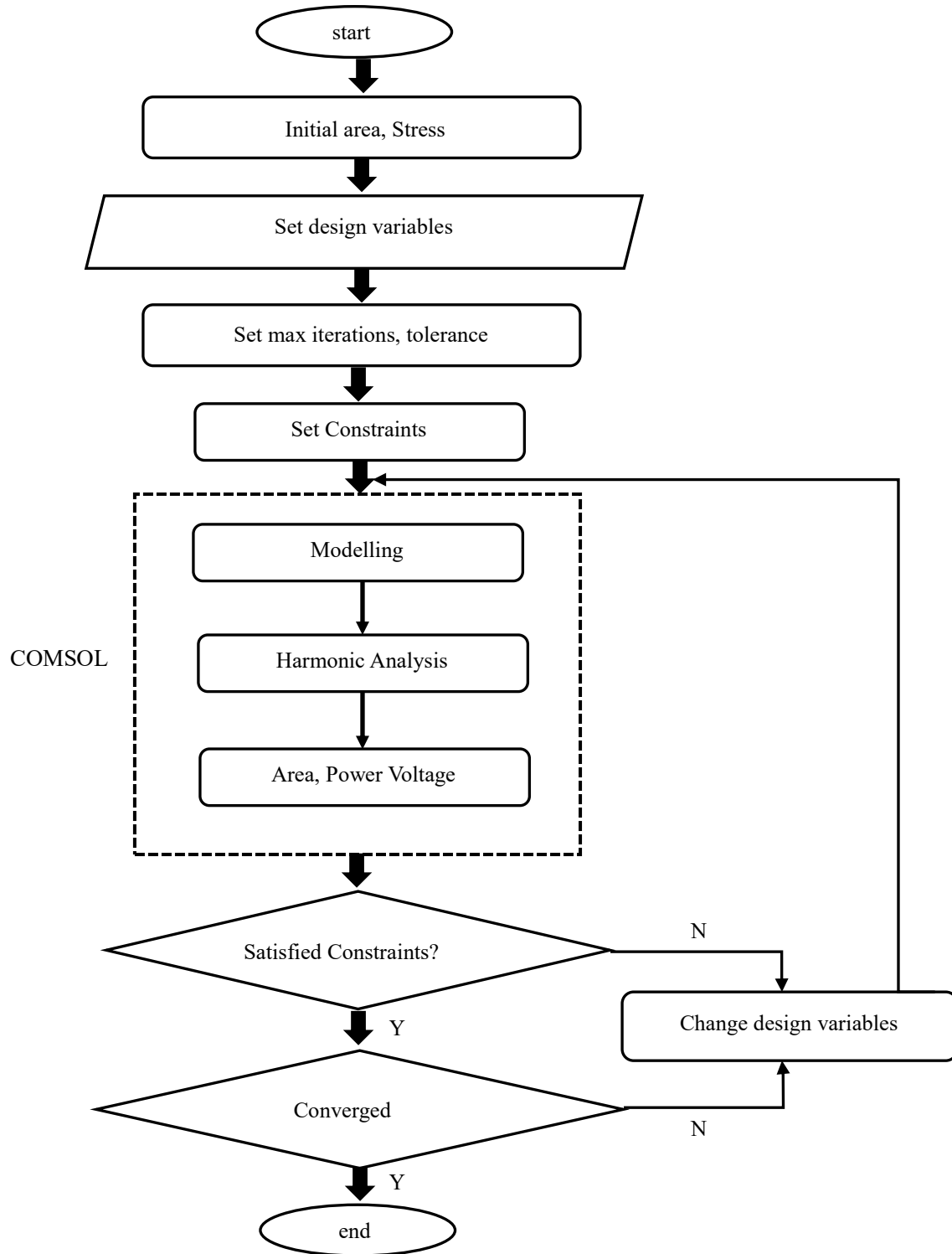


Figure 2. Procedure for COMSOL Optimization process

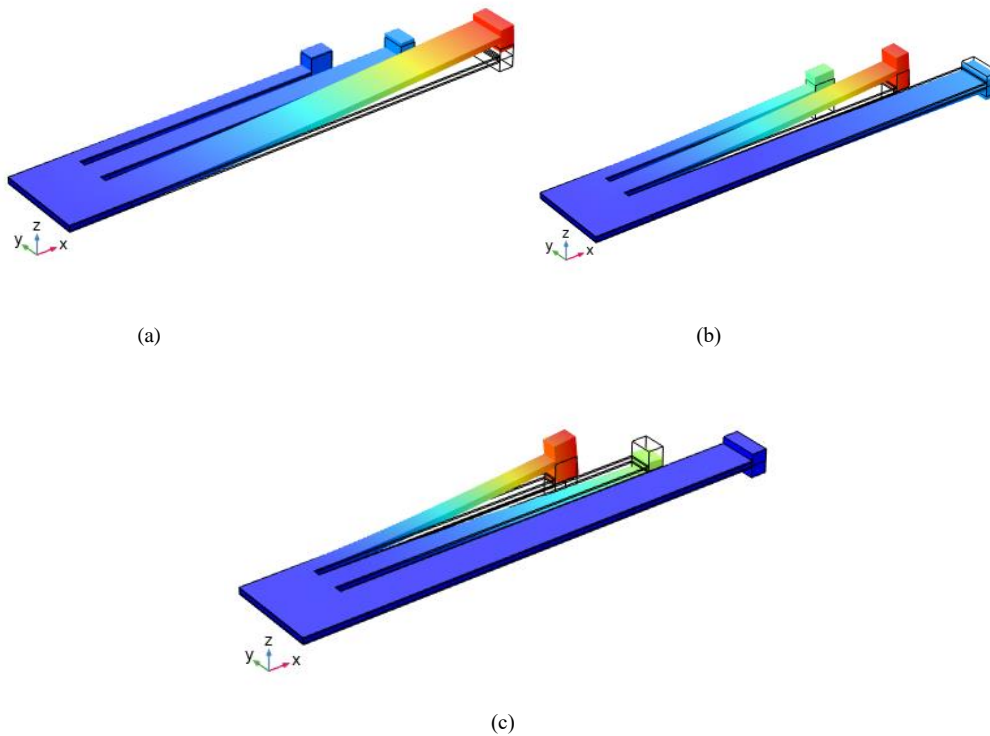


Figure 3. Eigen frequencies and mode shapes of the harvester: (a) 1st mode shape, (b) 2nd mode shape and (c) 3rd mode shape

5.2. Frequency response of the harvester

A harmonic analysis is conducted to determine the response of the harvester in the frequency domain and to verify the natural frequencies obtained from the modal analysis. The boundary conditions under which the study is carried out include a base acceleration of 0.2g, a resistance of 10 k Ω , initial displacement of zero, and a damping loss factor of 0.001. The criteria for selecting the resistance and the damping factor are stated in the previous section. A frequency sweep is carried out at a frequency range between 9.5Hz and 16.5Hz, and the response of the harvester is observed.

Figure 4 illustrates the frequency response of the harvester in both the unoptimized and optimized states. The dashed line represents the response of the unoptimized state, while the solid line represents the optimized state. The response is highlighted in terms of voltage and power. Fig. 4 (a) shows the voltage drop across the piezoelectric element due to the vibration-induced piezoelectric effect. For the unoptimized state, the voltage values obtained are 65.11 V, 37.41 V, and 15.32V at the first, second, and third resonant frequencies, respectively. The natural frequencies corresponding to the voltage peaks are 10.25 Hz, 12.60 Hz, and 14.01 Hz.

On the other hand, the optimized harvester has three voltage peaks corresponding to the open circuit resonant frequencies. The first, second, and third resonant frequencies are 11.2 Hz, 13.8 Hz, and 15.4 Hz. The voltage magnitude values corresponding to these frequencies are 68.55 V, 53.33 V, and 14.24 V, respectively. It is worth noting that there is a slight variation between the natural frequencies obtained from modal analysis and harmonic analysis. The alteration of the harvester stiffness due to induced electrical damping brings about this variation in

frequency. A comparison between the optimized and unoptimized states of the harvester shows a sufficient improvement through optimization. A notable increment of 15.41% in average voltage was realized compared to the prior unoptimized harvester. The maximum increment of 42.55% is observed in the second mode due to the reduced phase difference, which in turn reduces the voltage cancellation effect. The cancellation is prominent in the unoptimized harvester. However, the cancellation is high in the third mode due to a large out of phase variation. The variation leads to a slight reduction in the peak voltage. The reduction in voltage does not affect the overall improvement of the harvester's performance since the third peak is generally lower than the first two peaks. A notable drop in voltage and power is seen between the first and second resonant peaks of the unoptimized harvester at 12Hz. The decline is caused by the antiresonance phenomenon [25]. The 12Hz frequency is the antiresonance frequency, whereby the vibration amplitude drops to almost zero. Even though the performance is improved after optimization, the antiresonance effect is still visible at 13.1 Hz, which is a prevalent occurrence in multi-degree of freedom systems, particularly those under direct excitation [29]. Fig.4(b) shows the power generated across the 10k Ω resistor. As shown by the dashed line, the power peak values of the unoptimized harvester are 212.8 mW, 69.95 mW, and 11.73 mW, corresponding to the first, second, and third resonant frequencies, respectively. For the optimized harvester, the three power peaks conforming to the first three resonant frequencies are 235.02 mW, 142.2 mW, and 10.15 mW, respectively, illustrated by the solid line. The utmost peak power increase is obtained in the second mode, with a rise of 74.52%. The average power increase across all the modes is 31.67%. The harvested power shows similar behavior to the voltage drop, except that the power is mainly dependent on the impedance. The relationship between the

harvested power and the voltage is $\frac{v^2}{2R}$. The dependence

of the harvested power on the impedance indicates that there exists a critical value of impedance upon which the harvested power is maximum and will be determined in the next section.

5.3. Performance at optimal resistance

A load dependence analysis in the frequency domain was undertaken to select the optimal resistance to generate maximum power. Theoretically, the tip deflection is

minimum at a load resistance of $R = \frac{1}{2\omega c_p}$ where ω is

the vibration frequency in rad/s. This propounds that for improved performance, the resistance should be set at a critical value. It is noted that very high or very low impedance has a detrimental impact on the harvester's power or voltage magnitude [31, 32].

Fig.5 illustrates the response of the optimized and unoptimized states of the SCMEH at their respective optimal load resistances. The response of the optimized harvester is plotted by the dashed line, while the solid line plots that of the unoptimized harvester. It is worth noting that each mode has its own load value where maximum power can be harvested. Therefore, the optimum load is considered to be at the first peak, where the output power of the harvester is generally higher and can compensate for the subsequent modes. For the optimized harvester, the optimal load resistance obtained from the load dependence study is 1.778 k Ω , whereby a peak power of 416.8 mW is realized in the first mode, as shown in Fig.5(a).

On the other hand, the optimal resistance of the unoptimized harvester is 5.62 k Ω , with a peak power of 220.1 mW in the first mode. When comparing the performance of the SCMEH in both the optimized and unoptimized states, an 89% power increase is achieved in the first mode. On average, a power increase of 56% is realized across all resonant peaks of the optimized harvester compared to the unoptimized one. The optimized harvester is thus more efficient since the optimum load is lower than that of the unoptimized state. The capability of the harvester to operate at a low impedance eliminates the need to use infinitely large loads as previously employed in the literature. The advantage of lowering optimal loads is that sufficiently high power values can be obtained without sacrificing the voltage magnitudes, which yields relatively high voltages while minimizing the power output. Fig.5(b) shows the relationship between load magnitudes and the voltage drop in the two states of the harvester. In both states, the voltage increases to an asymptotic value with an increase in load resistance. However, at a specific value of the load, the effect of the load diminishes. This further explains the need for an optimal resistance value since any further increase in load will adversely affect the power output. The voltage values in the optimized state are generally higher than those in the unoptimized states.

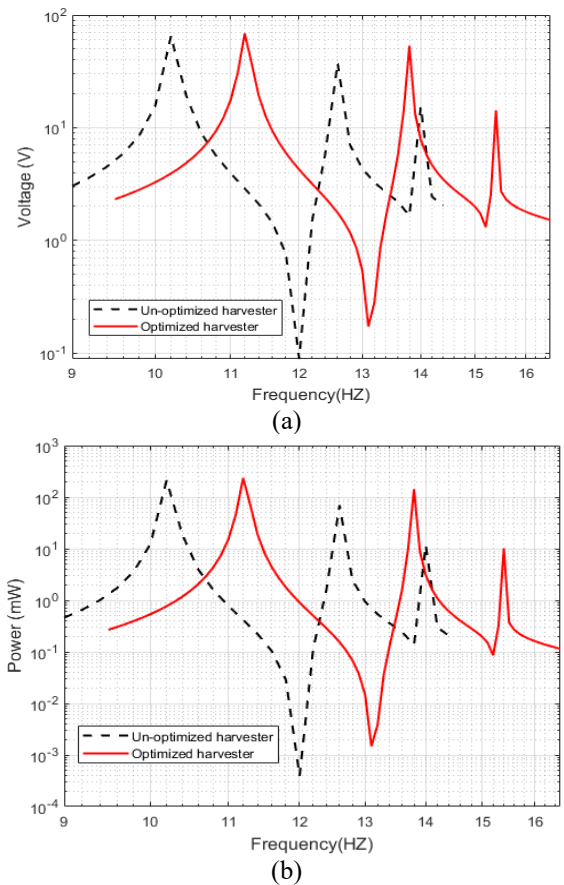


Figure 4. Frequency response of the harvester : (a)voltage and (b) power

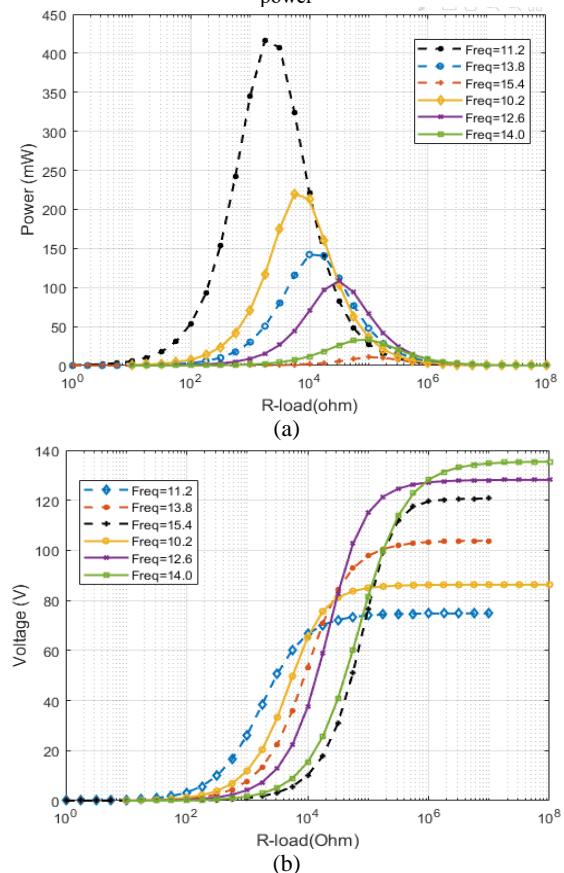


Figure 5. Performance under varying load resistance: (a) power and; (b) voltage

5.4. Performance under varying acceleration

It is logical to predict that as acceleration values increase, so will the performance of both harvesters. However, the proportion of the increase is unknown, and therefore, this analysis seeks to understand the relationship between acceleration and harvester performance.

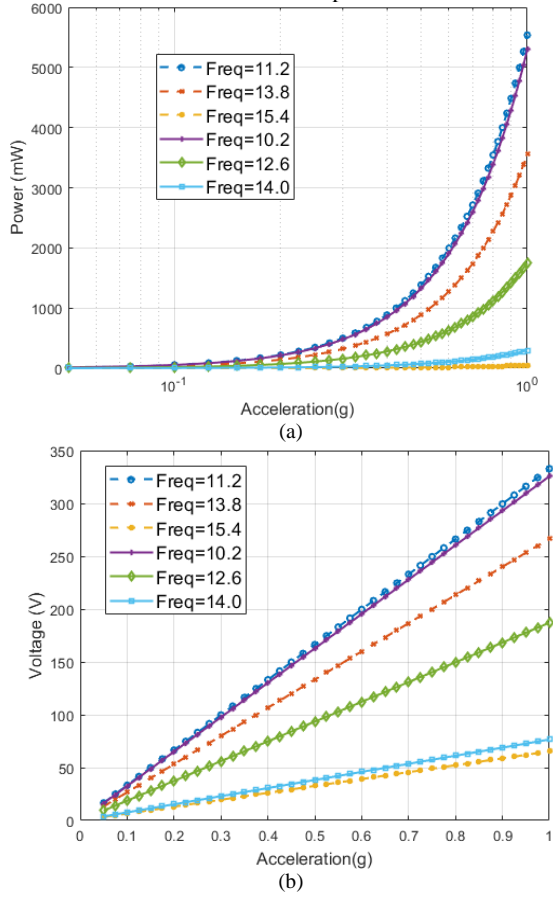


Figure 6. Performance under varying acceleration: (a) power and; (b) voltage

Figure 6 illustrates the influence of acceleration on both the optimized and unoptimized states of the SCMEH. The dashed line shows the performance of the optimized state, while the solid line shows the performance of the unoptimized state. Usually, the performance of any given harvester largely depends on the magnitude of force applied through acceleration. This force, however, should be limited to the factor of safety of the harvester’s materials to avoid damage or singularity [33]. The harvested power for optimized and unoptimized states varies exponentially with the applied base acceleration, as shown in Fig. 6 (a). On the other hand, the voltage varies linearly with the base acceleration, as shown in Fig. 6 (b). Under the same acceleration values, the average power and voltage trend indicate that the optimized state has higher magnitudes, unlike the unoptimized one. This shows that more energy levels can be harvested with the optimized state even when lower excitation forces are used. However, acceleration may give a false impression if solely used as the only factor to enhance the harvester’s performance. This is because, beyond critical strain values, no more strain can be induced in the material, provided yield stress is not exceeded.

6. Influence of individual material proportions on the performance of the harvester

The proportions of both the piezoelectric and substrate materials tend to affect the frequency and performance of the harvester [9]. This has been brought to light by the volume difference between the optimized and unoptimized harvesters. The un-optimized harvester has a 50% proportion of the substrate and piezoelectric materials, whereas the optimized one has 48% of the piezoelectric material and 52% of the substrate material. Therefore, a study was carried out on the optimized harvester to empirically determine the effect of material proportions on the harvester’s performance. Since the length and breadth of both materials are identical, a sweep of the material depths will be used to study this variation. However, during the study of this variation, the volume of the harvester was kept constant. This is achieved by varying the material thickness and not limiting the variation to the piezoelectric material.

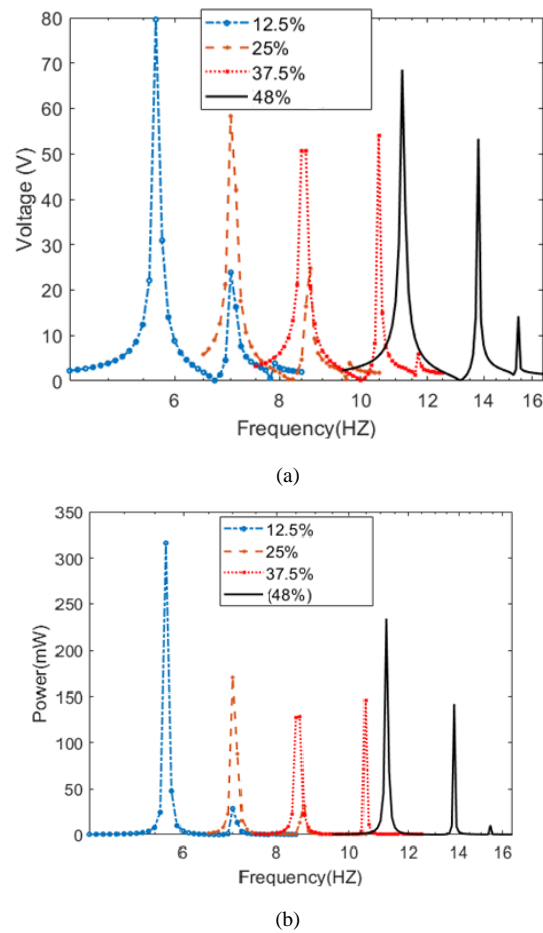


Figure 7. Effect of varying piezoelectric proportion percentage below the optimum: (a) voltage and; (b) power

Figure 7 shows the harvester’s performance with various values of the piezoelectric material depth below the optimum depth. The material is varied from 0.05mm to 2mm at an interval of 0.05 mm, which translates to a proportion of 12.5% to 37.5% at a 12.5% interval of the total volume of the harvester. At 12.5%, the first mode peak is the highest, at 79V, but with a little noise as its value rises towards the peak. The second and third modes are relatively lower compared to the corresponding modes of other proportions. At the 25% piezoelectric proportion, the voltage is somewhat higher at the first peak, at 59V, while

the subsequent modes' peaks diminish significantly with some noise as the vibration transitions from the first peak to the second peak. At a 37.5% piezoelectric proportion, the first and second mode voltage peaks tend to have the same magnitude of about 54V. Their distribution is reasonably good, but the first mode terminates at the beating frequency before resonance is reached. In addition, in the first mode, the vibration changes direction before fully equalling the natural frequency of the harvester. Therefore, it does not have a distinct peak, and for this reason, this piezoelectric proportion is not appropriate for use in the SCMEH. At the optimal design, where the piezoelectric proportion is 48%, improved performance is realized. Sufficiently higher voltages of 69.95 V, 53.3 V, and 11.73V are obtained in the first, second, and third modes.

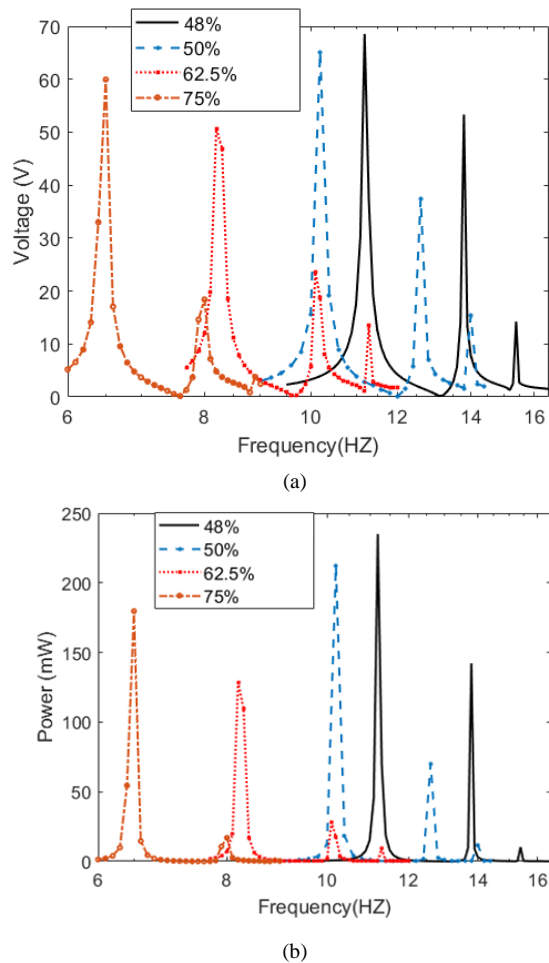


Figure 8. Effect of varying piezoelectric proportion percentage above the optimum: (a) voltage and; (b) power

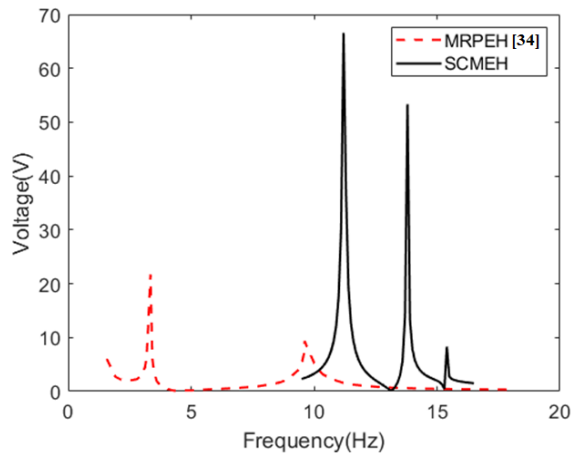
Figure 8 illustrates the harvester's performance under varied substrate material depths. Since the substrate thickness is varied, the piezoelectric depth is above the optimum value. When the piezoelectric proportion is above the optimum, it has a significant effect on the harvester's performances well as the overall strength and integrity of

the device. This, in turn, translates into the service life of the harvester. Therefore, it is not recommended to design the harvester with the 87.5% and 75% piezoelectric proportions because the depth of the substrate is significantly reduced, and initial curvature may occur before excitation. However, the 75% piezoelectric proportion has been included in this study to examine the behavioral response but not for operational purposes. As shown in Fig. 8 (a), the peak voltages are 59.95 V and 18.4 V for the 75% proportion. On the other hand, the 62.5% piezoelectric material proportion has a voltage of 50V in the first mode, with some noise immediately after the peak. The voltages in the second and third modes are 23.56 V and 13.48 V, respectively. At the 50% piezoelectric proportion, a fair distribution of voltage peaks is shown, with 65.1 V, 36.2 V, and 13.6 V in the first, second, and third modes, making it a reasonably good design for this harvester. Nevertheless, compared to the optimized form, all the other proportions have a relatively lower output power, rendering the optimal design efficient. Moreover, the power generated is proportional to the voltage when the load resistance is maintained at a constant relationship as presented in Eq. (9). Therefore, a considerable improvement is experienced in the optimal design in terms of power and noise elimination. It is inferred that high performance is achieved when the piezoelectric material is slightly lower at 46% to 48% of the harvester's total volume. The changing piezoelectric coupling coefficient brings about differences in the harvester's performance with various piezoelectric proportions in the piezoelectric material. Furthermore, the mass element affects performance because performance is heavily dependent on the inertial component. However, with large thickness values of the substrate, the performance tends to decrease since high excitation forces are required to induce reasonable strain, as the internal resistance of the substrate resists deformation. The power values in both figures 7 and 8 are proportional to the voltage. The proportionality is similar to that illustrated in section 5.2.

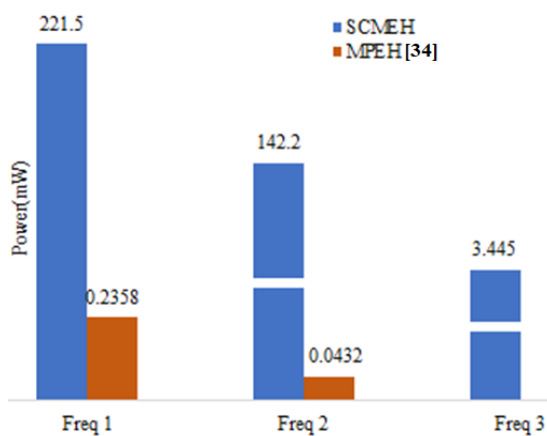
7. Comparison to a Multi-Resonant Energy Harvester (MRPEH)

The performance of an optimized SCMEH is compared to that of an experimentally validated Multi-Resonant Piezoelectric Energy Harvester (MRPEH) [34]. The MRPEH features two triangular branches on the main beam and a Macro-Fiber Carbon (MFC), a piezoelectric element. The MPEH's base is excited with a 0.2 g base acceleration and a 1 M Ω load connected across its terminals. Two resonant peaks are obtained at the frequencies of 3.89 Hz and 7.81 Hz, at which a voltage of 21.69 V and 9.3 V, respectively, is shown in Fig. 9(a).

The power comparison, on the other hand, shows a greater disparity. Because it can perform efficiently at low impedance values, the SCMEH achieves superior peak values as shown in Fig. 9(b). For this reason, at its optimal impedance of 1.778 k Ω , the maximum peak obtained is 416.8 mW.



(a)



(b)

Figure 9. Performance comparison between SCMEH and MRPEH [34]: (a) voltage and (b) power

Conclusion

The optimized multimodal harvester in this study provides an insight into an optimization technique to optimize a multimodal harvester without using sensors or complex algorithms. In the literature, the magnitudes of the end masses and harvester lengths have been used to tune the resonant frequencies but not to enhance performance and output. However, in this work, masses and lengths have been used to influence the output power. The efficiency of the optimized harvester is reflected by high output power and superior power density (power per unit volume) compared to the unoptimized harvester. The proposed dimensional optimization technique showed that using 48% of the piezoelectric proportion for this harvester and 52% substrate proportion yields the maximum power. Also, the load resistance was reduced from 5.62k Ω in the unoptimized harvester to 1.778k Ω , and this is an advantage since unmatched impedance leads to power loss. It is also realized that the effective mass of the harvester was reduced, which increases its applicability, as it can be retrofitted in many additional different areas. By increasing the acceleration values, the output of the optimized harvester increases. However, acceleration cannot indicate better performance since, at practically higher values, the harvester materials may yield. Generally, through

optimization, the average power output increased by 31.67% at 0.2g acceleration and 10k Ω load resistance. With the high rate of adoption of IoT and wireless sensor networks in structures, the development of highly efficient energy harvesters will aid in the continuity of their operation. Therefore, the harvester proposed in this study is deemed to offer a solution to the intermittency experienced in the operations of microelectronic devices during battery replacements. Further incorporation of active frequency tuning mechanisms can be explored for the proposed multimodal harvester in the future.

Conflict of interest

The authors declare that there is no conflict of interest regarding this submission.

References

- [1] V. S. Gaikwad and S. S. Chinchankar, "Adaptive Neuro Fuzzy Inference System to Predict the Mechanical Properties of Friction Stir Welded AA7075-T651 Joints," *Jordan Journal of Mechanical and Industrial Engineering*, vol. 16, no. 3, pp. 381–393, 2022.
- [2] J. Lange, J. Hilgedieck, and M. Kaltschmitt, "Renewable resources of energy for electricity generation-development trends and necessities within the overall energy system," *Jordan Journal of Mechanical and Industrial Engineering*, vol. 13, no. 3, pp. 207–220, 2019.
- [3] E. J. Majeed and A. J. Majeed, "Harvesting Human Being Energy to Charge Smartphone," *Jordan Journal of Mechanical and Industrial Engineering*, vol. 16, no. 3, pp. 439–448, 2022.
- [4] M. M. Ahmad, N. M. Khan, and F. U. Khan, "Multi-degrees of freedom energy harvesting for broad-band vibration frequency range: A review," *Sensors Actuators A Phys.*, vol. 344, no. June, 2022, doi: 10.1016/j.sna.2022.113690.
- [5] J. Cho, M. Anderson, R. Richards, D. Bahr, and C. Richards, "Optimization of electromechanical coupling for a thin-film PZT membrane: II. Experiment," *J. Micromechanics Microengineering*, vol. 15, no. 10, pp. 1804–1809, 2005, doi: 10.1088/0960-1317/15/10/003.
- [6] Q. Wang and N. Wu, "Optimal design of a piezoelectric coupled beam for power harvesting," *Smart Mater. Struct.*, vol. 21, no. 8, 2012, doi: 10.1088/0964-1726/21/8/085013.
- [7] H. S. Yoon, G. Washington, and A. Danak, "Modeling, optimization, and design of efficient initially curved piezoceramic unimorphs for energy harvesting applications," *J. Intell. Mater. Syst. Struct.*, vol. 16, no. 10, pp. 877–888, 2005, doi: 10.1177/1045389X05055759.
- [8] H. Elahi, "The investigation on structural health monitoring of aerospace structures via piezoelectric aeroelastic energy harvesting," *Microsyst. Technol.*, vol. 27, no. 7, pp. 2605–2613, 2021, doi: 10.1007/s00542-020-05017-y.
- [9] Elahi, H.; Rizwan Mughal, M.; Eugeni, M.; Qayyum, F.; Israr, A.; Ali, A.; Munir, K.; Praks, J.; Gaudenzi, P. Characterization and Implementation of a Piezoelectric Energy Harvester Configuration: Analytical, Numerical and Experimental Approach. In-tegr. Ferroelectr. 2020, 212, 39–60.10.1080/10584587.2020.1819034.
- [10] G. Acciani, A. Dimucci, and L. Lorusso, "Multimodal piezoelectric devices optimization for energy harvesting," *Int. J. Multiphys.*, vol. 7, no. 3, pp. 227–243, 2013, doi: 10.1260/1750-9548.7.3.167.
- [11] C. Kim and J. W. Shin, "Topology optimization of piezoelectric materials and application to the cantilever beams for vibration energy harvesting," *Int. J. Precis. Eng. Manuf.*,

- vol. 14, no. 11, pp. 1925–1931, 2013, doi: 10.1007/s12541-013-0261-1.
- [12] S. Lee and A. Tovar, “Topology optimization of piezoelectric energy harvesting skin using hybrid cellular automata,” *J. Mech. Des. Trans. ASME*, vol. 135, no. 3, pp. 1–11, 2013, doi: 10.1115/1.4023322.
- [13] C. K. Thein and J. S. Liu, “Numerical modeling of shape and topology optimisation of a piezoelectric cantilever beam in an energy-harvesting sensor,” *Eng. Comput.*, vol. 33, no. 1, pp. 137–148, 2017, doi: 10.1007/s00366-016-0460-3.
- [14] F. Wein, M. Kaltenbacher, and M. Stingl, “Topology optimization of a cantilevered piezoelectric energy harvester using stress norm constraints,” *Struct. Multidiscip. Optim.*, vol. 48, no. 1, pp. 173–185, 2013, doi: 10.1007/s00158-013-0889-6.
- [15] J. M. Dietl and E. Garcia, “Beam shape optimization for power harvesting,” *J. Intell. Mater. Syst. Struct.*, vol. 21, no. 6, pp. 633–646, 2010, doi: 10.1177/1045389X10365094.
- [16] J. Park, S. Lee, and B. M. Kwak, “Design optimization of piezoelectric energy harvester subject to tip excitation,” *J. Mech. Sci. Technol.*, vol. 26, no. 1, pp. 137–143, 2012, doi: 10.1007/s12206-011-0910-1.
- [17] K. Mohamed, H. Elgamal, and S. A. Kouritem, “An experimental validation of a new shape optimization technique for piezoelectric harvesting cantilever beams,” *Alexandria Eng. J.*, vol. 60, no. 1, pp. 1751–1766, 2021, doi: 10.1016/j.aej.2020.11.024.
- [18] J. Wang, B. Fan, J. Fang, J. Zhao, and C. Li, “A Piezoelectric Energy Harvester Based on Multi-Cantilevers and Magnetic Force,” *SSRN Electron. J.*, pp. 1–11, 2022, doi: 10.2139/ssrn.4153197.
- [19] Z. Q. Lu, J. Chen, H. Ding, and L. Q. Chen, “Two-span piezoelectric beam energy harvesting,” *Int. J. Mech. Sci.*, vol. 175, no. February, 2020, doi: 10.1016/j.ijmecsci.2020.105532.
- [20] L. Tang and Y. Yang, “A multiple-degree-of-freedom piezoelectric energy harvesting model,” *J. Intell. Mater. Syst. Struct.*, vol. 23, no. 14, pp. 1631–1647, 2012, doi: 10.1177/1045389X12449920.
- [21] P. Panthongsy, D. Isarakorn, T. Sudhawiyangkul, and S. Nundrakwang, “Piezoelectric energy harvesting from machine vibrations for wireless sensor system,” *ECTI-CON 2015 - 2015 12th Int. Conf. Electr. Eng. Comput. Telecommun. Inf. Technol.*, 2015, doi: 10.1109/ECTICon.2015.7207051.
- [22] O. Rubes, M. Brablc, and Z. Hadas, “Nonlinear vibration energy harvester: Design and oscillating stability analyses,” *Mech. Syst. Signal Process.*, vol. 125, pp. 170–184, 2019, doi: 10.1016/j.ymsp.2018.07.016.
- [23] D. O. Masara, H. El Gamal, and O. Mokhiamar, “Split Cantilever Multi-Resonant Piezoelectric Energy Harvester for Low-Frequency Application,” *Energies*, vol. 14, no. 16, p. 5077, Aug. 2021, doi: 10.3390/en14165077.
- [24] K. Mohamed, H. Elgamal, and S. A. Kouritem, “An experimental validation of a new shape optimization technique for piezoelectric harvesting cantilever beams,” *Alexandria Eng. J.*, vol. 60, no. 1, pp. 1751–1766, 2021, doi: 10.1016/j.aej.2020.11.024.
- [25] D. Upadrashta and Y. Yang, “Trident-Shaped Multimodal Piezoelectric Energy Harvester,” *J. Aerosp. Eng.*, vol. 31, no. 5, p. 04018070, 2018, doi: 10.1061/(asce)as.1943-5525.0000899.
- [26] Q. Wang, W. Dai, S. Li, J. A. S. Oh, and T. Wu, “Modelling and analysis of a piezoelectric unimorph cantilever for energy harvesting application,” *Mater. Technol.*, vol. 35, no. 9–10, pp. 675–681, 2020, doi: 10.1080/10667857.2020.1751470.
- [27] M. Powell, “The BOBYQA algorithm for bound constrained optimization without derivatives,” *NA Rep. NA2009/06*, p. 39, 2009, [Online]. Available: <http://www6.cityu.edu.hk/rcms/publications/preprint26.pdf>.
- [28] E. Lefeuvre, D. Audigier, C. Richard, and D. Guyomar, “Buck-boost converter for sensorless power optimization of piezoelectric energy harvester,” *IEEE Trans. Power Electron.*, vol. 22, no. 5, pp. 2018–2025, 2007, doi: 10.1109/TPEL.2007.904230.
- [29] J. Welte, T. J. Kniffka, and H. Ecker, “Parametric excitation in a two degree of freedom MEMS system,” *Shock Vib.*, vol. 20, no. 6, pp. 1113–1124, 2013, doi: 10.3233/SAV-130826.
- [30] E. L. B. Van De Vorst, D. H. Van Campen, A. De Kraker, and R. H. B. Fey, “Periodic solutions of a multi-DOF beam system with impact,” *J. Sound Vib.*, vol. 192, no. 5, pp. 913–925, 1996, doi: 10.1006/jsvi.1996.0225.
- [31] J. Liang and W.-H. Liao, “Impedance matching for improving piezoelectric energy harvesting systems,” *Act. Passiv. Smart Struct. Integr. Syst. 2010*, vol. 7643, no. 852, p. 76430K, 2010, doi: 10.1117/12.847524.
- [32] A. Koszewnik, P. Grześ, and W. Walendziuk, “Mechanical and electrical impedance matching in a piezoelectric beam for Energy Harvesting,” *Eur. Phys. J. Spec. Top.*, vol. 224, no. 14–15, pp. 2719–2731, 2015, doi: 10.1140/epjst/e2015-02585-5.
- [33] X. D. Xie, A. Carpinteri, and Q. Wang, “A theoretical model for a piezoelectric energy harvester with a tapered shape,” *Eng. Struct.*, vol. 144, pp. 19–25, 2017, doi: 10.1016/j.engstruct.2017.04.050.
- [34] I. Izadgoshasb, Y. Y. Lim, R. V. Padilla, M. Sedighi, and J. P. Novak, “Performance enhancement of a multiresonant piezoelectric energy harvester for low frequency vibrations,” *Energies*, vol. 12, no. 14, 2019, doi: 10.3390/en12142770.

A Lubricating Oil-Based Maintenance for Diesel Engines at the End-user: An Effective Predictive Approach

Mokhtar Ali Amrani^{1,2*}, Yara Haddad¹, Mohammed Abdulhameed²

Omar S. Hyder², Amin Saif², Atef M. Ghaleb³, Sobhi Mejjaouli³

¹Department of Alternative Energy Technology, Faculty of Engineering & Technology, Philadelphia University, 19392, Amman, Jordan

²Faculty of Engineering and Information Technology, Taiz University, 6803 Taiz, Yemen,

³Department of Industrial Engineering, College of Engineering, Alfaisal University, 11533, Riyadh, Saudi Arabia

Received 21 Apr 2022

Accepted 12 Sep 2022

Abstract

This study aims to analyze the used lubricating oil of small Diesel engines under different conditions in order to monitor their instant health condition, indicate their useful life, and provide early warnings of failure progress. It is an attempt to monitor different oil properties together with oil contaminants to diagnose the possible failures before occurring and identify their root causes. It is an effective tool in the case where there are no historical data records for the engines. Specifically, used lubricating oil samples from eight Diesel-powered engines are analyzed as an important information source for early failure detection and decision support. Oil properties; kinematic viscosity, density, and total acidic number (TAN) were analyzed. Also, oil contaminants; wear debris particles, soot, and water content were also elucidated in attempting to predict engine health conditions, wear mechanisms, and useful life. Scanning Electron Microscope (SEM) was used to analyze the wear debris particles. The root causes of engine failure were specified using the 5 Why's method, and interviews with specialists, while the results were schematically presented using the Fishbone diagram. The analysis of oil viscosity showed that engines of high capacities performed better at high operating temperatures than small engines. Besides, the large oil imperfections are not directly related to the oil viscosity reduction but to the high oil TAN and the type and concentration of the oil impurities. This work analysis could assist in robust decision-making on the engine health condition, service life, and maintenance activity that should be applied.

© 2022 Jordan Journal of Mechanical and Industrial Engineering. All rights reserved

Keywords: Condition-Based Maintenance; Wear debris particles; Viscosity measurement; Industrial Engine; Wear mechanism; Proactive maintenance; Tribology science.

1. Introduction

The effective maintenance management of mechanical systems is of utmost importance in current industrial systems [1]. It plays a vital role in the final product costs, machinery service life, and the quality of the final product [2,3]. This warrants the rapid growth of new technologies and effective maintenance service strategies for controlling maintenance costs, reducing the frequency of failures, and enhancing the quality of operations. Current maintenance management systems have been extensively implemented for large and medium-sized industrial systems where real-time data are available [4-7]. However, small systems at the end-user, such as electrical generators and small engine units, are rarely investigated despite their frequent failures [8-10]. In general, small-size systems involve low-level or no historical records and maintenance facilities. Besides, end-user machines commonly employ no maintenance management systems and often rely on a run-to-failure approach as a maintenance strategy, which is the most primitive, unmanageable, and expensive approach [2,11].

The selection of maintenance approach depends on the nature of operations, equipment complexity, equipment reliability, and critical conditions. To this, it is impracticable to measure the performance of small systems at the end-user using common approaches without historical data records, such as overall equipment effectiveness (OEE), total productive maintenance (TPM), artificial intelligence, or reliability-centered maintenance (RCM) [12-15].

Condition-Based Maintenance (CBM) is at the heart of predictive maintenance, where the failure can be detected early and manipulated [5]. Recently, equipment manufacturers have embedded CBM tools, such as sensors, probes, and cameras to continuously monitor the conditions of equipment, especially those subjected to the continuous deterioration [5-7]. Although these tools instead of additional costs to the initial investment, they provide valuable data to reveal the system's health state, predict the system remaining useful life, and decrease the overall maintenance cost. Therefore, it is the most cost-effective maintenance strategy based on detecting root

* Corresponding author e-mail: mokh_ali2007@yahoo.com.

causes through the operational conditions of the assets [11].

CBM has different tools for identifying failure at an early stage [16,17]. Oil-Based Maintenance (OBM) and vibration-based maintenance (VBM) are the most widely applicable techniques in use nowadays [6,7,18]. Although the analysis results of VBM (the process of measuring the vibration of moving parts as an indication of the wear rate [19] and OBM are conforming for continuous monitoring of engines. OBM has several merits over VBM when applied to monitor complicated types of machinery such as internal combustion engines. It provides accurate information on the wear condition, service life, and the severity of failures for entire engine components [5]. Interestingly, it has been inferred that OBM gives approximately 10 times earlier warnings than VBM for predicting machine breakdown [20]. Besides, VBM systems are susceptible to rotational speed, and sensor failures, and need to be built to the engine at the design step [19], making them improper tools for engines at the end-user.

Elemental analysis of used lubricating oil using atomic emission spectrometry has been widely investigated in the literature [16,17,21,22]. It provides accurate elemental analysis of the contaminants of wear debris in the oil. However, such analysis requires accurate data about the manufactured materials for the machine parts that are in contact with oil circulation. That is a compulsory requirement to identify the most stressed engine part.

OBM can be performed based on online and offline systems. In online monitoring mode, the online sensor is carefully installed on the oil passage on a machine during operation [6,7,23]. Many studies in the literature have investigated online monitoring approaches for lubricating oil using online sensors for measuring viscosity [24], dilution [25], oxidation [26], moisture, [27], wear debris [27,6,7], soot [28], and other contaminations [29]. The aforementioned studies dealt with these conditions separately to study their interaction with engine components. In contrast, the offline monitoring mode requires a physical mass of lubricating oil to be analyzed against its properties and contamination in the laboratory far away from the machine [5-7,30]. Frequent offline oil inspection avoids the difficulties associated with dismantling inspection technologies and provides accurate information about the wear condition of oil-lubricated machines, especially those systems that do not have historical maintenance records [18].

Till now, offline methods remain the most predictive tool commonly used for diagnosing oil and machinery conditions [6,7]. It is a proper method for studying different oil parameters altogether since a single parameter analysis provides a meaningless diagnosis [3,5]. A limited number of studies on single-unit systems at the end-user with continuous monitoring have been reported [5,11]. To the best of the researcher's knowledge, no study has monitored various oil properties and contaminants altogether that could assist in robust decision-making on the engine health condition, service life, and maintenance activity that should be applied. The present work aims to analyze the used lubricating oil of 8 Diesel engines of different conditions in order to monitor their instant health condition, indicate their useful life, and provide early warnings of failure progressing. It is an attempt to monitor different oil properties together with oil contaminants to diagnose the possible failures before occurring and identify their root causes.

2. Methods and Experiments

2.1. Oil Properties

Lubrication oil is a viscous fluid in nature that can be considered the life-blood circulation of machinery. When introduced to the engine components, it creates a separating layer between mating surfaces and moving parts to inhibit direct contact between surfaces, decrease wear, and impede the generating of excessive heat [5-7]. Additives are different classes of chemicals used mainly to improve their functionalities, based on the working condition [5]. By comparing the oil analysis results of base and used oils, a maintenance technician can identify the health condition of oil and engine components.

2.2. Data and Samples Collection Procedure

A base lubricating oil of high grade (50w TITAN SAE engine lubricating oil) was used for all engines and then analyzed along with the used oil samples to make the results comparable. Discrete data were collected from different measurement tools and compared with the reading of the base lubricating oil. ASTM standards for each property measurement were carefully followed. Used lubricating oil samples (operated for ~ 150 hours) were collected in 2019 from eight electrical Diesel engines from different customers, with different capacities, and different design considerations. The oil samples were properly agitated for getting homogenous fluid and then a total of one liter of used oil samples was collected from the eight engines and kept for further analysis. **Table 1** shows the engine's name, model, output power, number of cylinders, cooling system, and operating conditions. The oil samples were tabulated in **Table 1** with the following codes; S1, S2... to S8, while the base oil is S0.

Table 1. Characteristics of the selected Diesel operated generators. The used lubricant oil samples were collected from engines after 150 operating hours for each.

Sample Code	Output (KVA)	No. of cylinders	Cooling System	Purchase Date
S1	10	1	water	1991
S2	15	4	water	2016
S3	20	3	air	2013
S4	25	1	water	2018
S5	35	4	water	2013
S6	100	4	air	2017
S7	120	6	water	2014
S8	200	6	Air	2008

2.3. Measurement Devices

Measurements were officially conducted at Yemen Lubricant Manufacturing Co. Ltd., Taiz. All measurement devices were calibrated based on the manufacturer's recommendations and all experiments and measurements for each variable were done by the same person. A basic magnetic stirrer with a heater (IKA IKAMAG RCT) was used for experiments. A portable digital gram lab balance scale (Ohaus Scout Pro SP401) with a capacity of 0.1 – 400 g was used for measurements. A thermometer ($\pm 0.02^\circ\text{C}$) to measure the temperature of oil samples in the

range from 0 to 100°C. The measurements were carried out at room temperature (31°C) and device correcting equations were used to make the results in line with the device readings. Kinematic viscosity was measured using Seta Vis kinematic viscometer (PMT THOMSON), while a glass capillary thermometer (± 0.01 °C) was used to determine the temperature within the worm bath. The density of oil samples was measured using a Density meter DMA 35 (Paar Scientific Ltd.) working in the range of 0 – 1955 kg.m⁻³ for density measurements and 0 – 40 °C for temperature measurements. Scanning Electron Microscope (SEM, JCM 6000Plus, Jeol, Japan) was used to investigate the debris particle's size, shape, and concentration. MATLAB software was used for image processing and acquisition to calculate the particle features such as size, shape, and wear nature.

2.4. Wear debris measurements

In the first step, 500 ml of an oil sample was diluted with ethanol to enhance the collection procedure of wear debris. A permanent magnet was used to collect the ferric wear debris particles from the sample. In the subsequent step, the magnet was removed from the oil sample, washed several times, and then dried at 60 °C for 2 hours. Finally, the wear particles were then separated from the magnet, weighed, packed, and sent for further characterizations (SEM tool). The above mentioned procedure was repeated for all other samples.

2.5. Water content Measurements

A sensitive measuring tool was used to control the mass of the oil samples to be only 10 ± 0.02 g for each sample. Water content is determined by removing moisture (dehydration up to 250 °C for 2 h.) and then by measuring weight loss. The difference in mass measurements before and after dehydration can be considered the amount of water content, neglecting any other evaporated particulates. A crackle test was also implemented to monitor bubbles in the oil samples.

2.6. Density measurements

The standards of ASTM D1298-12b and API (American Petroleum Institute) for measuring density and relative density are performed at a standard temperature of 60 °F (15 °C) [31]. The procedure could be explained briefly in the following steps: the injection was carefully cleaned and 10 g of oil sample was pumped into the density meter through the entrance slot. As the oil moves from its orifice slot, the density value will be exhibited on the device screen. The same procedure was repeated for all other samples and the results were recorded in turn. A device factor was considered because the device was calibrated at 15 °C [31]. Therefore, the actual density of oil samples will be calculated based on the following equation:

$$\rho_{oil} = (T_{amb} - 15^{\circ}\text{C}) \times 0.00061 + \rho_{device} \quad (1)$$

Where 0.00061 is a device factor, T_{amb} is the ambient temperature at which the experiments were performed, and ρ_{device} is the density measured by the device.

2.7. Kinematic Viscosity measurements

The test is simple and follows the basic standard procedure of ASTM D445-06 standard test of kinematic viscosity [32], while the standard of ASTM D2270 at 40 and 100°C was used to calculate the viscosity index [33]. In brief, the viscometer was first cleaned thoroughly by several rinsing solvents and dried by passing multi-stage filtered air through the instrument to remove the final traces of solvents. 10 mL of oil sample was directly charged from the pipette through the tube into the lower reservoir of a calibrated tube in the viscometer. The oil sample was then allowed to settle instantaneously in a warm bath at 40 °C. In the subsequent step, the oil was poured slowly to the tube until it reached the highest line on the right side of the tube. During the process, a stopwatch was used to measure the efflux time, which was then carefully recorded, converted into seconds, and multiplied by a device constant (different for different working temperatures) that is specific for the glass viscosity tube. This simple calculation leads to depict the kinematic viscosity of the oil samples. Furthermore, the whole procedure was then repeated at 100 °C, while other parameters were kept unchanged. For more reliable results, the measurements were repeated twice for each sample and only the average was considered.

2.8. Total Acid Number (TAN) measurements

ASTM D974 is a standard method that is widely used to determine the TAN of an oil [34]. It is a colorimetric method that uses p-naphtholbenzein as a color change pointer to identify the neutralized end-point. For OBM purposes, this test is accurate enough, simple and cost-effective, and exhibited rapid response. In brief, the test was starting with filling the test tube with $20\text{g} \pm 0.2$ of the oil sample. This process was followed by adding 0.098 mol/L of KOH reagent solution slowly to the above solution until the color of the sample was changed. The titrant test tube was precisely marked with graduated regular increments. The difference between the initial states of the oil to the end-point (the point where the oil color was changed) was then measured and converted to TAN units (mg KOH/g of oil) based on the following equation:

$$TAN = \frac{[(V_a - V_b) \times M_c \times M_w]}{w} \quad (2)$$

Where: V_a and V_b are the volume of KOH in ml at the end and start points on the test tube, respectively; M_c = concentration of KOH solution (0.0980 mole/L); M_w = Molecular weight of KOH (56.1 g/mole); and w = sample mass (g). The measurement process was conducted for all oil samples twice and the average was recorded accordingly. A control sample of base lubricating oil was also tested in order to make the results comparable.

3. Results and Discussion

3.1. Water Content in lubricating oil

Table 2 shows the quantitative results of water content in oil samples, which were compared with the results of the base oil sample (**S0**). As a matter of fact, less than 0.25 % of water impurities in the lubricating oil indicates the good condition the engine is [27,35]. To this, the results from all oil samples are at abnormal conditions except **S4**

(the engine operated only a few months). Oil samples **S1**, **S6**, and **S8** have the highest percentage of water contents at 2.2, 2.61, and 3.1 %, respectively. The results of oil samples **S2**, **S3**, **S5**, and **S7** showed a moisture ratio in the range of 1.0 – 1.5 %, which indicates that these engines are also at abnormal conditions. Finally, oil sample **S4** exhibited the lowest water content (0.06%), which is in the safe region of normal operation.

Water emulsified in engine oil is annoying contamination even at low concentrations [36]. There are different plausible processes where water can leak into the crankcase oil. Cooling circulation system, rain, condensed humid air from the surrounding, and fuel combustion reactions through piston rings are the most important sources of water in the lubricating oil [27,36]. Once water impurities are emulsified in oil engine, their hazards depend mainly upon oil composition and additives, working conditions and its physiochemical characteristics; leading to a vast change to oil properties and accelerating abrasive wear rate of engine components [27]. Experimental studies indicated that the presence of 1% of the water in engine oil can reduce the life span of journal bearing by 90% [36,37].

During moisture experiments, the observations of oil bubbles at the laboratory level were captured and analyzed. The bubbles' concentration, size, and period of appearance are good indications of the amount of water in the oil samples [38]. By studying the size of the bubbles, a quantitative conclusion was made regarding the water concentration in the oil sample. The results of observation were recorded in which some samples showed negligible or no bubbles and crackles, which mean no free/emulsified water in the oil samples, such as that observed in base oil sample (**S0**) and relatively in **S4**. However, very small bubbles (~0.5 mm) were produced but quickly disappeared like what noticed in **S5**. Another promising finding was that bubbles of ~ 2 mm were initiated, gathered at the center of the oil spot, and then disappear, that exactly what happened in **S3**, **S6**, and **S7**. In the same way, the results of **S1**, **S2**, and **S8** showed further novel findings in which higher moisture levels, violent bubbling, and audible crackling were observed. Bubbles start out about 2 - 3 mm and then grew to 4 mm. As we had expected, the bubbles' size and the time until they disappear match well with the water content results.

Table 2. The results of measuring the water content, mass of wear debris particles, soot mass, and density changes of used oil samples and base oil.

Sample Names	Water Content (%)	Net mass of debris particles (g)	mass of soot (g/0.5litre -oil)	Density change %
S0	0.00	--	--	----
S1	2.2	0.17	1.04	1.33
S2	1.13	0.57	0.17	0.00
S3	1.29	0.08	0.97	0.33
S4	0.06	0.13	0.00	0.00
S5	0.984	0.15	0.09	0.44
S6	2.61	0.90	0.93	1.00
S7	1.45	0.85	1.15	0.22
S8	3.101	0.12	0.84	1.22

3.2. Wear Debris Analysis

Table 2 records the results of the mass of debris particles excluding the mass of permanent magnet mass of each magnet. The results showed that **S2**, **S6**, and **S7** samples held bulk quantities of ferrous wear debris particles indicating that these samples need more investigation using microscopic techniques. Furthermore, the results of sludge and soot contents are also reported in **Table 2**, which are good indication to the condition of engines [8]. The results of samples **S1**, **S3**, **S6**, **S7**, and **S8** showed a large yield of soot, indicating imperfect engine combustion and probably frequent and intermittent operation. The poor air/fuel premixing charge and high compression ratios of Diesel engines lead to an increase in the concentration of blow-by gases and then more soot in the lubricant oil. Soot in lubricating oil behaves as an adsorbent to anti-wear additives (ZDDP) and therefore increases the wear rate [28,8].

Figure 1 depicts high and low magnification SEM micrographs of **S2**, **S6**, and **S7** samples. In fact, SEM measurements are useful for identifying the wear mechanism and can avoid the drawbacks of spectroscopy (no detection less than 10 microns) [39] or vibration monitoring (no control at low rotating speeds)[39,40]. The obtained SEM images showed a wide-range variety of different sizes and features. A common feature of all particles is their very small thickness, mainly less than 20 μm . Initial analysis of the images showed that the available sizes of particles increase as the engine deteriorated. In addition, the particle edges also seem to become more irregular rather than smooth. In fact, a new engine being in normal operation could show wear debris size typically between 1–20 μm and almost constant concentration. As the engine wears-out, larger debris particles vary between 20–100 μm could be observed and the engine diagnosed to be at abnormal operation[41]. Obviously, the presence of debris particles larger than 100 μm (comparable to the human hair) is a good indication that the engine at catastrophic conditions and requires immediate maintenance action (repair or replacement) [3,6,7,42]. This offline investigation gives an early warning of the machine conditions and helps in decision making.

The features of particles of **S2** shows particles of varied shapes and sizes. Particle range from few microns to about 80 μm was observed. The shape of the particles is irregular with relatively thin dimensions. However, the shape of flake-like debris particles is the dominance morphology as shown in **Fig. 1 (S2)**. The number of generated wear particles with size $\geq 50 \mu\text{m}$ are less compared to smaller particles. Accordingly, the majority of the particles have a size range of 20 - 40 μm . The mean value and standard deviation of particle size from **S2** images were calculated to be 52.60 μm , and 26.77, respectively. This indicated that the state of the engine started to be in critical condition and requires continuous monitoring. Furthermore, fine particles with the length range from 1 μm to several microns are seen. They were produced during the rolling fatigue of mating surfaces within oil passage with random outlines of shape boundary [34,41,42]. Another wear debris in the form of a long chip with a length of ~ 50 μm and width of ~ 5 μm were also observed through the cutting wear process [3,43].

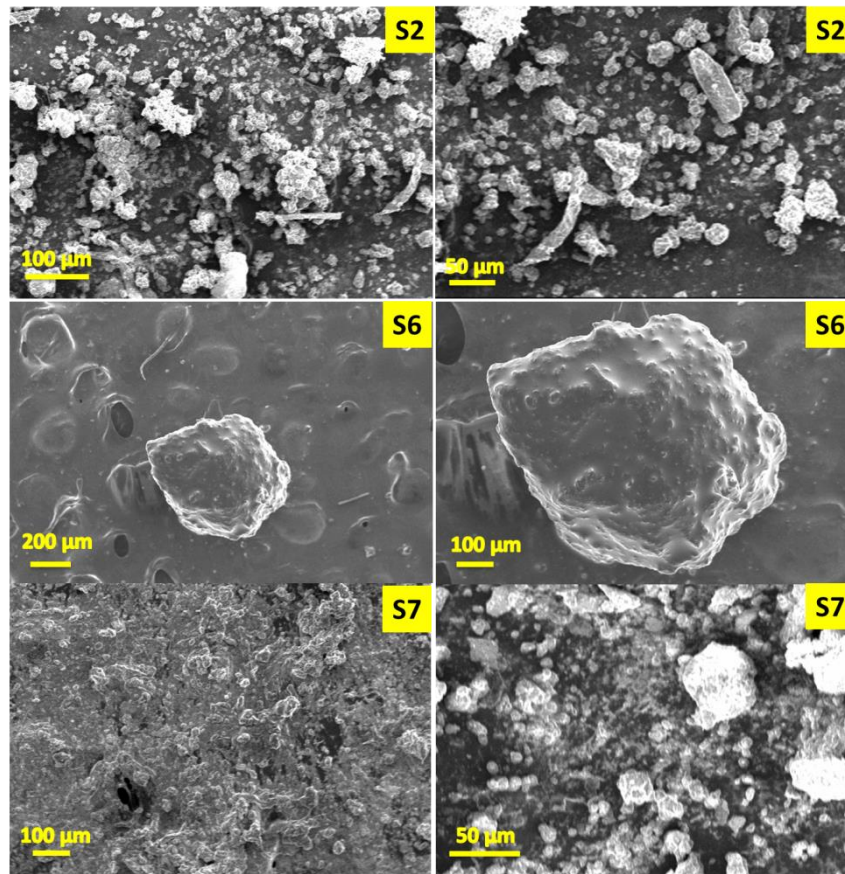


Figure 1. Low and high magnification SEM micrographs and size distribution diagrams of wear debris particles extracted from samples **S2**, **S6**, and **S7**.

Similarly, the information from SEM images of the debris particles of **S6** sample is the largest among other samples. This could be attributed to the bad condition of used oil and perhaps engine design-related problems. The probability of particles with a size of larger than $100\ \mu\text{m}$ is almost high with irregular morphologies and wide size distribution generated plausibly by severe sliding for the internal surfaces. The particle size analysis indicated that the mean value and standard deviation of debris were determined to be $281.25\ \mu\text{m}$, 45.8 , respectively. This quantitative analysis indicated that the debris particles from the **S6** image are greater than the other two samples. However, there is a single particle as shown in the image (**Fig. 1 (S6)**), which is too large. Close observation of this particle inferred that it contains various other small debris particles and other residues in the oil that were agglomerated. Generally, the presence of millimeter size particles is an indication of rapid failure zone often arises from surface fatigue [41]. Large quantities of severe sliding wear particles were also found in **S6**, which can create excessive wear of mating surfaces [43]. Finally, particles from the **S7** sample are shown in **Fig. 1 (S7)** and had features similar to that of **S2** in terms of sizes, shapes, and surface. The particles are of large dimensions and narrowed size distribution. Particles of less than $30\ \mu\text{m}$ sizes are rarely seen in the images but most of the particles are within $10 - 60\ \mu\text{m}$ range but denser and more aggregated.

All in all, the results depicted from the above analysis of **S2**, **S6**, and **S7** samples provide valuable information

about engines' deterioration. They indicate that these engines are working in abnormal conditions. Close observation to **Fig. 2S2**, **S6** and **S7** indicated the presence of rolled like (rod-like) particles, which are plausibly initiated as flat platelets subjected to rolling process due to the high operating temperatures [3,41]. Similarly, the presence of small spheres ($< 20\ \mu\text{m}$) is clearly shown in the three samples. These spheres are of normal nature, generated often in bearing fatigue cracks due to one or a combination of cavitation, rolling, grinding, welding processes under high operating temperatures [3,41-43]. As a conclusion, the engines corresponding to **S2** and **S7** are in abnormal condition and require focused maintenance. However, the condition of engine matching with oil sample **S6** is at catastrophic failure and needs immediate action either for replacing or overhaul maintenance.

3.3. Density measurements and Interpretations

Table 2 shows the results depicted from density measurements at ambient temperature ($31 \pm 0.1^\circ\text{C}$) for all samples, and a device factor was implemented as per **Equation 1**. The results of the reduction of oil density indicated that all samples exhibited a reduction of oil density from that of base oil except samples **S2**, and **S4**, which showed almost zero change of oil density. Furthermore, oil samples **S1**, **S6**, and **S8** are the most oil samples with a percentage reduction in density $\geq 1.00\%$, which are identical results with moisture content in the same oil samples.

3.4. Kinematics Viscosity

Table 3 depicts the results of Kinematic viscosities at 40 °C and 100 °C in centistoke units and viscosity index (VI). In fact, VI is essential to determine oil shear forces or resistance to motion between oil layers and mating parts [44]. An increase of VI value is an indication of the stability of oil viscosity under temperature change [44,45]. The large increase of VI suggests that the engine is able to operate at higher temperatures effectively[45]. The VI of the base oil (**S0**) was measured to be 96.41 and kept as a reference for other oil samples. Besides, the results of VI of used oil samples fluctuates above and below the VI of base oil. Samples **S2** and **S4** showed a negligible change to the VI, indicating, and not necessarily, the good conditions of the corresponding engines. Besides, Oil samples **S1**, and **S3** are the only samples that exhibit a dramatic decrease of VI at 54.88, and 71.28, respectively. A decrease in VI indicates a dramatic change in the viscosity as temperature increases and may cause excessive wear to the engine components and rapid oil deterioration rates [46]. The reduction of oil VI could be attributed to the high level of fuel dilution and invalidity of the base oil used as per the manufacturers' recommendations [45]. In contrast, oil samples **S5**, **S6**, **S7**, and **S8** showed an increase in VI. Interestingly, the results of VI from oil samples showed that as engine output power increases the values of VI also increase, plausibly due to design considerations.

Table 3 shows also the percentage change of viscosity of the used oil samples and interesting results were elucidated. It is worth mentioning that a reduction of 20% of oil viscosity is a critical baseline for predictive maintenance [44]. The reduction of oil viscosity of **S1** and **S8** is the most worsening sample with a reduction of 64.36%, and 62.2%, respectively. Similarly, their reductions at high operating temperatures are also alarming. The viscosity result of **S1** is in coordination with the results of VI of the same sample. Samples **S2** and **S4** showed the smallest change of oil viscosity among all other samples, indicating the good working condition of those engines and the results are in-line with the results of VI. Similarly, oil samples **S5** and **S7** showed that the viscosity reduction is slightly around the 20% baseline with improved performance at high operating temperatures (100 °C). Finally, Samples **S3** and **S6** showed also

relatively alarming reduction of oil viscosity with better performance for **S6** at high operating temperatures.

All in all, keep in mind that viscosity is the most important physiochemical property of a lubricant and the analysis of the kinematic viscosity change (%) and VI of oil samples provides precious investigation to the deterioration of engine components. The results of the VI are more specific. All the calculated VI of used oil samples (**Table 3**) are below the recommended VI value (above 150) for good operations[45]. We found that the rate of increase of VI is correlated well to the engine's output. This suggests that larger engines perform better at higher operating temperatures than small engines, as the science of the rmdynamics also claimed.

3.5. Total Acid Number (TAN)

Table 3 shows the results of the Total Acid Number (TAN) measured based on ASTM 974 standard test [34]. TAN results are given as the number of milligrams of KOH required to neutralize 1 g of oil. The higher the TAN value is, the higher the acidity of the oil [46]. The results showed that all used oil samples are at acidic medium, which means that these oil samples more susceptible to physiochemical reactions than those at neutral mediums. Therefore, the oil samples with large TAN numbers (≥ 1.0) are plausibly exposed to higher oxidation and wear reactions.

The results showed that the base oil sample (**S0**) gives the minimum value at 0.244 mg-KOH/g-Oil. In fact, ideal fresh oil is assumed to give zero TAN (pH = 7). All samples of used lubricating oil showed TAN numbers above 1 mg-KOH/g-Oil, indicating plausible oil degradation and excessive wear[34,41,42]. Samples **S3**, **S6**, and **S7** exhibited the highest TAN values at 3.29, 3.19, and 3.24 mg-KOH/g-Oil, respectively. These high values imply high oxidation rate and the high degradation level of corresponding engines. In contrast, sample **S4** demonstrated the lowest TAN values at 1.11mg-KOH/g-Oil. The remaining samples have high TAN numbers in the range of 1.5 – 2.2. These results need to be interpreted with the results of other parameters, such as viscosity, water content, and density to support robust decision making on the engine's deterioration rates.

Table 3. K. Viscosity, Viscosity index (VI), and TAN measurement results of the used oil samples and base oil sample (S0).

Parameter/Sample code	S0	S1	S2	S3	S4	S5	S6	S7	S8
K. Viscosity @ 40°C	268.5	95.69	263.71	175.98	268.23	215.9	151.5	203.14	101.46
K. Viscosity @ 100°C	21.58	9.06	21.17	14.2	21.12	19.34	16.71	19.15	12.00
Viscosity index (VI)	96.41	54.88	95.42	71.28	94.734	101.25	117.97	106.43	108.33
Vis. Change (%) @ 40 °C	0.00	64.36	1.784	34.45	0.1	19.6	43.57	24.34	62.2
Vis. Change (%) @ 100 °C	0.00	58.0	1.9	34.29	2.13	10.38	22.54	9.82	44.39
TAN (mg of KOH/g of oil)	0.25	1.53	1.80	3.29	1.11	2.2	3.19	3.24	1.83

4. Failure modes Analysis

In this section, the failure mode analysis is performed for all engines under study. It employs visiting the place of engines, meeting with maintenance technicians, reading manuals, and asking the questions that possibly indicates the root causes of the dramatic changes in oil properties. Analysis tools such as 5 Why technique and fishbone diagram were implemented whenever they required. This section aims to interpret the results for each engine, investigate the root causes of failure and their effects. Also, its goal is to elucidate technical and managerial recommendations to the owners of those engines.

4.1. Low Capacity Engines (< 50 KVA)

Table 4 summarizes the test results of used lubricant oil samples of low capacity engines. The engine related to **S1** is a Diesel engine (Single cylinder, 10KVA, in service since 1991) belongs to a small business shop in the city. The engine shows the worst results in terms of reduction of kinematic viscosity and VI, plausibly due to the high water and fuel dilution. This was supported by the high water content in the oil at 2.2%, presumably due to the aging of the water circulation system and low combustion efficiency. The high reduction of density (1.33%) also supports that high fuel dilution (low density and viscosity than oil). The high contents of the solid residual in oil (1.04 g/0.5 liter-oil) is another confirmation of the low combustion efficiency. There is excessive wear in engine rings and bearing that assist in fuel dilution. The investigation from the owner of the engine indicated that it works at short periods (4 hours daily) and irregularly, indicating that the engine exposed to large start-up and end-up frequency as another indication to fuel dilution and incomplete combustion[28]. The high frequency of failure in this engine can be explained due to its long-period in service. As a conclusion, this engine is at a catastrophic condition, and over-aged. Our recommendation goes to immediate replacement with a new engine for reliable performance and cost saving.

The engine related to **S2** is a Diesel engine (4 cylinders, 15 KVA, in service since 2012) belongs to a small business shop in the city. The engine operates with short and irregular periods and light loads; hence the time span to change the oil is long. The results of oil properties and contamination (**Table 4**) showed that the engine is currently operated at abnormal conditions. The analysis of wear debris particles shows that almost all particle sizes are below 70 μm indicating that the engine is in the abnormal working area[41]. The analysis of kinematic viscosity showed that almost no change to the oil

viscosities even at high temperature working conditions while VI results showed that it has a value close to that of base oil as shown in **Table 4**. The good results of oil viscosity and contamination after 150 working hours are good signs of the health condition of this engine. The above results could be supported by the zero change in oil density. The high value of TAN number (1.802) indicates that the oil is at acidic conditions, which presumably the reason behind yielding bulk quantity of debris particles (0.57 g). The low soot residue in the oil (0.17 g) indicated that the engine combustion efficiency is relatively good and our suggestions to follow strict guidance offered by the manufacturer to enhance its performance and lengthen its service life.

The engine related to sample **S3** is a Diesel engine (3 cylinders, 20 KVA, in service since 2013) belongs to a small enterprise in the city. The analysis of viscosity reduction (34%) and VI (71.73) indicated the abnormal condition of the engine, especially at high operating temperatures (**Table 4**). The high reduction in viscosity could be understood with the high water content (1.33%) and possibly high oxidation arises from extremely high TAN number. The results of high acidity of oil (TAN = 3.29) are alarming since acidic mediums excite the physiochemical reactions of oil constituents. The low reduction of oil density (0.33%) could possibly be explained as the balance between water and fuel dilution, high oxidation reaction, and soot. This engine requires immediate extensive maintenance and follows strict instructions made by the maker.

The engine related to **S4** is a Diesel engine (4 cylinders, 25 KVA, in service since 2018) belongs to a workshop in the city. This engine is like a new engine and only a few months since it was brought to the service. All measurements are close to the new one (**Table 4**). It was inserted in this work for more reliability measurements.

The engine related to **S5** is a Diesel engine (4 cylinders, 37 KVA, in service since 2013) belongs to a cancer center, a public authority in Taiz city. The oil viscosity reduction was recorded in the range (< 20%) with improved properties at high temperatures. This could be supported with the increase of VI (101.25) than that of base oil (96.42). Its water content (0.984 %), soot concentration (0.09 g/0.5 liter-oil), and density reduction (0.44%) are relatively low as compared to other samples, plausibly due to its low service. The only alarming parameter is TAN number at 2.2, indicating the acidic medium of oil and then the oil constituents and engine components in contact with the oil will be prone to high oxidation. This parameter should be monitored continuously by following instructions from the maker to ensure its proper operating.

Table 4. A summarization of the measured oil properties of low capacity engines (< 50 KVA).

S. No.	Debris particles (μm)	Vis. Red. (%@40 °C)	Vis. Red. (%@100 °C)	Vis. Index (VI)	Water in oil %	Density Red. %	TAN	Soot (g)	Engine Condition
S0	-----	0.0	0.0	96.41	0.0	0.0	0.25	-----	-----
S1	-----	64.36	58.0	54.88	2.2	1.33	1.527	1.04	catastrophic
S2	20-70	1.784	1.9	95.42	1.13	0.00	1.8	0.17	average
S3	-----	34.45	34.2	71.73	1.29	0.33	3.29	0.97	very critical
S4	-----	0.1	2.13	94.73	0.06	0.00	1.109	0.00	very good
S5	-----	19.6	10.38	101.25	0.984	0.44	2.2	0.09	Need more monitoring

4.2. Large Capacity Engines (100-200 KVA)

The engine related to **S6** is a Diesel engine (4 cylinders, 100 KVA, in service since 2017) belongs to an internet shop in the city. Although this engine worked for almost one year only, it is working under heavy loads and continuous work for about 18 hours daily. Microscopic analysis of wear debris particles showed alarming results with particle sizes $> 150 \mu\text{m}$. This finding could be the first indication of the catastrophic condition of the engine.

The results of viscosity reduction (**Table 5**) showed an ultimately high reduction (43.57%) as compared to about 20 % of normal reduction [44]. The measurement of viscosity reduction at high temperature (100 °C) showed an average reduction (22.54%), which indicates that the engine is designed to sustain high-temperature conditions. This finding could be supported by the results of VI (117.97), which is the highest VI for all studied oil samples. The result of water content (2.6% as compared to ~0.25% permitted percentage) in the oil is also alarming [35,36]. During visiting this engine, our observation indicated that the engine was not protected against rains and humid air and was installed in free space and even beside the rain channels to assist the air cooling system.

The density of oil was also reduced by ~ 1.0% due to the high water content and plausibly fuel dilution (lighter contaminants). The high yield of soot (0.93 g/0.5 liter-oil) is an indication of the incomplete combustion, high oxidation reactions, and wear rate. The above investigation could be verified using the result of TAN value (3.19) (**Table 5**), which is extremely alarming, indicating that the oil is at highly acidic and then excessive oxidation reactions and wear rates are plausibly the case. What is more, the engine follows a careless maintenance management system, despite its short-period in service. The engine useful life was shortened promptly due to the bad maintenance and overload. The fishbone diagram (**Figure 2**) summarizes the root causes of deterioration and their effects. The analysis classifies the base problems to the bad working environments, unskilled technicians, bad management, and old maintenance techniques. Our investigation has proved that the frequency of engine main time to failure is high. The long hours operating (> 16 hours daily), heavy loading, incorrect place, and the bad maintenance are the main causes of rapid deterioration of this engine. Our recommendation to purchase another unit with the same characterization to allow each unit to work short time and apply strict maintenance schedules.

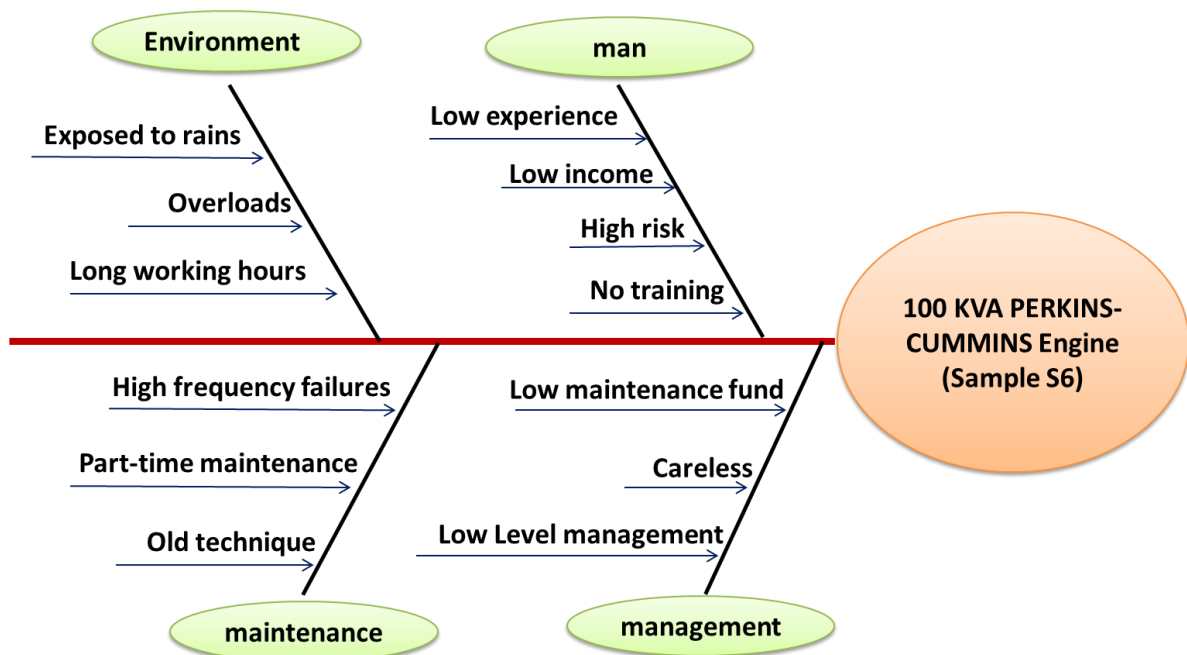


Figure 2. Fishbone diagram Cause-Effect analysis of the engine matching with oil sample S6.

The engine related to **S7** is a Diesel engine (6 cylinders, 120 KVA, in service since 2014) belongs to a public Health Authority in the city. The microscopic analysis of wear debris particles of this engine showed a variety of particle sizes and shapes in the range of 10 -600 μm , which are in abnormal operation [41]. The analysis of kinematic viscosity showed a pronounced reduction (24.34%), which is close to the world standard of 20% reduction [44]. The reduction of viscosity at high temperature showed in-range reduction (9.82%), which indicated that the engine performance at high-temperature condition is good. These findings are in-line with the results of VI which showed an increase than that of base oil. The results of density reduction showed only 0.22%, which could be understood as a balance between high and low-density contaminants and degradation products. The high value of TAN (3.24) (**Table 7**) is another approve of excessive oxidation and abrasive wear reactions. The results of water content tests are relatively high at 1.45%, but not as high as other engines.

5 Whys' technique was implemented to investigate the failure mode for this engine. Our inspection depicts that this engine follows a quit good routine maintenance. It works 11 hours a day and the lubricating oil changed as per routine schedule. What is more, the engine was installed at the right place where it protected from rains and exposed to open air. However, there are some management problems such as slow response to failure signs and they attribute that to the lack of maintenance funds. We observed that the oil quantity slightly decreases with time, plausibly due to evaporating at high operating temperatures close to the combustion chamber and high oil degradation raised from excessive acidic medium (high measured TAN value).The research team observation and inquiry from maintenance technicians have detected a water leakage to the engine combustion case through engine head plausibly due to fitting problems and aged engine. Although the engine viscosity and VI are not bad, the large debris particles could be attributed to the ultimately high TAN (3.24 mg of KOH/g oil). The low reduction of viscosity could be explained as a balance between high wear products, high soot and other residue (1.15 g/0.5 liter-oil), and water and fuel dilution. There fore,this engine is at catastrophic condition due to the presence of large impurities on its oil. The maintenance management is bad and the engine requires overhaul maintenance to retain its efficiency.

The engine matching with the **S8** oil sample is a Diesel engine (6 cylinders, 200 KVA/160 W, in service since 2008) belongs to a public Engineering college in the city. Fishbone diagram is selected to investigate the failure causes and effects of this engine with the help of staff interviews. The research team observation and inquiry from maintenance technician depict that his engine follows bad routine maintenance and management. Different technicians dealt with this engine for a short time without any training and experience. The team has also observed that the engine was installed in an open atmosphere and exposed to rains and humid air. This engine is operated only 4 hours for only two days weekly (a total of 8 hours in the week) with irregular nature. Therefore, the time span to change the oil takes long months, considering it the longest duration among all other engines.

The results showed the second-worst kinematic viscosity reduction among all other engines at low and high-temperature tests at 62.2% and 44.39%, respectively. This ultimate reduction in kinematic viscosity is questionable. We can explain it in terms of the high-frequency starting and shutdown of this engine, which derives the condensed water and fuel dilution processes [27] and then the excessive reduction in oil viscosity. From a scientific view, a rich fuel/air ratio takes place at starting and shutdown leading to incomplete combustion and then fuel dilution [28]. The above scenario could be supported by the high reduction of oil density (1.22%) of this engine [47]. What is more, the high water contamination (3.1%), high TAN (1.83), and large soot (0.84 g) offer a proper environment to the corrosion and oxidation reactions to propagate and accelerate with more than five folds [48], resulting in dramatic changes to the oil properties and engine deteriorations.

To this, in spite of engine low useful life (10 years since the installation), light loads, and low-frequency operations, the aforementioned catastrophic conditions of this engine and the analysis of Fishbone Diagram (**Fig. 3**) drive an immediate decision to make an urgent action towards overhaul maintenance followed by building a strict regulation to follow the manufacturer routine maintenance, relocate the current place of the engine to be in a safe mode against all unwanted environmental conditions, apply a suitable maintenance management system, train the operation and maintenance staff, and change filters and oils as scheduled.

Table 5. A summarization of the measured oil properties and impurities of large capacity engines (> 50 KVA).

S. No.	Debris particles (μm)	Vis. Red. (%)@40 °C	Vis. Red. (%)@100 °C	Vis. Index (VI)	Water in oil %	Density Red. %	TAN	Soot (g)	Engine Condition
S0	-----	0.0	0.0	96.41	0.0	0.0	0.25	-----	-----
S6	> 150	43.57	22.54	117.97	2.6	1.00	3.19	0.93	catastrophic
S7	40-130	24.34	9.82	106.43	1.45	0.22	3.24	1.15	very critical
S8	-----	62.2	44.39	108.33	3.101	1.22	1.83	0.84	catastrophic

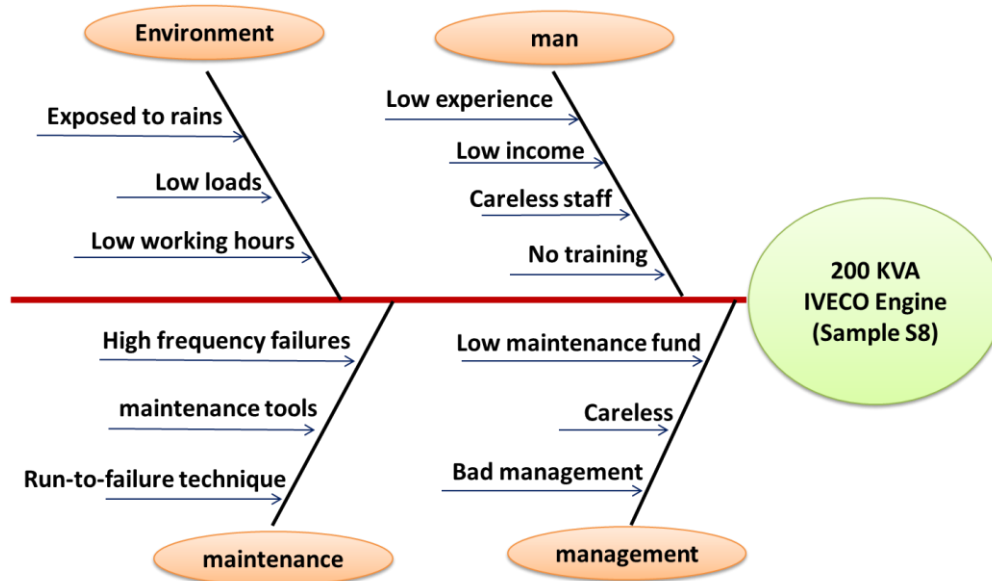


Figure 3. Fishbone diagram failure (causes-effect) analysis of the engine related to sample S8.

5. Conclusions and Recommendations

This study investigated the health conditions of small unit engines at the end-user, which are rarely reviewed in the literature. The absence of failure records, clear maintenance plans, and maintenance funds for small-unit engines are the major dominating causes of the rapid degradation of engine. Therefore, the analysis of used oil properties and contaminants is an optimum option for predicting health conditions. Failure analysis investigated the root causes of engine failure could be traced to (1) Wear debris particle features are the most reliable offline diagnosed technology for small unit engines, (2) irregular and frequent startup of the engines are one cause of rapid degradation of engines, (3) bad working conditions and incorrect installation are plausible causes of early deterioration of engines, (4) Continuous monitoring of oil viscosity is an effective tool for early detection of failures in small-unit engines, (5) more contaminants in the engine oil are an indication of deteriorating engines, (6) large capacity engines performs better than small engines in term of viscosity degradation and wear rate propagation, and (7) the type of oil, and oil working hours before replacing influence the quality of lubricating oil and engines.

This study recommends including oil lubricant analysis as a major source of the maintenance routines. The management should implement CBM systems regularly to monitor operating conditions and invest sufficient funds to extend the useful life of engines. Also, the technical work should be assigned to skilled and experienced technicians for performing maintenance duties effectively. The engine technicians should monitor lubricating oil levels, oil filters, oil working hours, and oil type as per the manufacturer's recommendations. Furthermore, the engine should be placed in suitable environments; far away from the rain with a suitable ventilation system. Finally, an offline oil analysis needs to be taken frequently for maintenance.

6. Acknowledgments

This work is supported by Alfaisal University, Saudi Arabia. Authors thank Yemen Lubricant Manufacturing Co. Ltd., Taiz, for conducting oil analysis measurements. Special thanks to Hamza Mothana, Reyadh Abdullah, Shoib A. Amrani, and Randa M. Haza'a for their help and support during collecting data.

References

- [1] K. K. Tahboub, "An Assessment of Maintenance Practices and problems in Jordanian Industries", *Jordan Journal Mechanical and Industrial Engineering*, Vol. 5, pp. 315-323, 2011.
- [2] Maillart, L. M. a. P. M., "Cost-optimal condition-monitoring for predictive maintenance of 2-phase systems". *IEEE Transactions on Reliability*, Vol. 51, pp. 322-330, 2002.
- [3] Amrani, M.A., Alhomdi, M., Aswaidy M, B., Ghaleb, A.M., Al-Qubati, M. and Shameeri, M., "Implementing an integrated maintenance management system for monitoring production lines: a case study for biscuit industry", *Journal of Quality in Maintenance Engineering*, Vol. 28, pp. 180-196, 2020.
- [4] Garg, A. and Deshmukh, S.G., "Maintenance management: literature review and directions", *Journal of Quality in Maintenance Engineering*, Vol. 12, pp. 205-238, 2006.
- [5] Wakiru, J. M., Pintelon, L., Muchiri, P. N. and Chemweno, P. K., "A review on lubricant condition monitoring information analysis for maintenance decision support", *Mechanical Systems and Signal Processing*, Vol. 118, pp. 108-132, 2019.
- [6] Zhu, X., Li Du and Zhe, J., "A 3x3 wear debris sensor array for real time lubricant oil conditioning monitoring using synchronized sampling", *Mech. Sys. Signal Proc.*, Vol. 8315, pp. 296-304, 2017.
- [7] Zhu, X., Zhong, C. and Zhe, J., "Lubricating oil conditioning sensors for online machine health monitoring – A review", *Tribol. Int.*, Vol. 109, pp. 473-484, 2017.
- [8] R. Al-Hasanat, M. Qawasmi, "Control of Soot Emission from Diesel Engines", *Jordan Journal Mechanical and Industrial Engineering*, Vol. 5, pp. 77-82, 2011.

- [9] S. H. Gawande, L. G. Navale, M. R. Nandgaonkar, D. S. Butala, S. Kunamalla, "Identification and Analysis of Engine Speed and Noise in In-line Diesel Engine", *Jordan Journal Mechanical and Industrial Engineering*, Vol. 6, pp. 71-74, 2012.
- [10] S. Nada, A. M. Attia, M. S. Gad, "Effect of Castor Biodiesel on Diesel Engine Performance, Emissions, and Combustion Characteristics", *Jordan Journal Mechanical and Industrial Engineering*, Vol. 12, pp. 261-268, 2018.
- [11] Gugaliya, A. and Naikan, V.N.A., "A model for financial viability of implementation of condition based maintenance for induction motors", *Journal of Quality in Maintenance Engineering*, Vol. 26, pp. 213-230, 2019.
- [12] O. T. R. Almeanazel, "Total Productive Maintenance Review and Overall Equipment Effectiveness Measurement", *Jordan Journal Mechanical and Industrial Engineering*, Vol. 4, pp. 517-522, 2010.
- [13] H. Afefy, A. Mohib, A. M. El-kamash, M. A. Mahmoud, "A New Framework of Reliability Centered Maintenance", *Jordan Journal of Mechanical and Industrial Engineering*, Vol. 13, pp. 175-190, 2019.
- [14] A. Mukattash, R. H. Fouad, H. Kitan, M. Samhour, "Computer-Aided Maintenance Planning System for Industrial Companies", *Jordan Journal Mechanical and Industrial Engineering*, Vol. 5, pp. 227-234, 2011.
- [15] M. Samhour, A. Al-Ghandoor, S. Alhaj Ali, I. Hinti, W. Massad, "An Intelligent Machine Condition Monitoring System Using Time-Based Analysis: Neuro-Fuzzy Versus Neural Network", *Jordan Journal Mechanical and Industrial Engineering*, Vol. 3, pp. 294-305, 2009.
- [16] Kang, J., Sobral, J., Soares, C. G., "Review of condition-based maintenance strategies for offshore wind energy", *Journal of Marine Science and Application*, Vol. 18, pp. 1-16, 2019.
- [17] Guo, D., Chen, X., Ma, H., Sun, Z., & Jiang, Z., "State Evaluation Method of Robot Lubricating Oil Based on Support Vector Regression, Computational intelligence and neuroscience, ID 9441649, 2021.
- [18] Yan S, Ma B, Wang X, Chen J, Zheng C., "Maintenance policy for oil-lubricated systems with oil analysis data", *Maintenance and Reliability* Vol. 22, pp. 455-464, 2020.
- [19] Prajapati, A., Bechtel, J. and Ganesan, S., "Condition based maintenance: a survey", *Journal of Quality in Maintenance Engineering*, Vol. 18 pp. 384-400, 2012.
- [20] Poley, J., "The metamorphosis of oil analysis, Machinery Failure Prevention Technology (MFPT) Conference, Condition Based Maintenance", Sec. 1, Conference Proceedings, Ohio, p. 24 - 26, 2012.
- [21] C. Zheng, P. Liu, Y. Liu, Z. Zhang, "Oil-based maintenance interval optimization for power-shift steering transmission", *Advances in Mechanical Engineering*, Vol. 10, pp. 1-8, 2018.
- [22] R. Q. Aucélio, R. M. de Souza, R. C. de Campos, N. Miekeley, L. P. da Silveira, "The determination of trace metals in lubricating oils by atomic spectrometry", *Spectrochimica Acta Part B: Atomic Spectroscopy*, Vol. 62, pp. 952-961, 2007.
- [23] W. Cao, M. Xu, R. Niu, Q. Wu, R. Xie, "Online Monitoring and Early Warning Technology of Repeated Multiple Blackouts in Distribution Network Based on Multi-source Information Fusion and Delphi Method", *Jordan Journal Mechanical and Industrial Engineering*, Vol. 14, pp. 7-14, 2020.
- [24] Markova, L. V., Myshkin, N. K., Kong, H. and Han, H. G., "On-line acoustic viscometry in oil condition monitoring". *Tribol. Int.*, Vol. 44, pp. 963-970, 2011.
- [25] Delvigne, T., Deconninck, B., Obiols, J., China, P. and Carlier, P., "A new methodology for on line lubricant consumption measurement". *SAE Int. J. Fuels Lubricants*, Vol. 114, pp. 1028-1033, 2005.
- [26] Ozogan, M., Khalil, A. and Katsoulakos, P., "Tribological failure detection and condition monitoring for diesel engines", *Wear*, Vol. 130, pp. 189-201, 1989.
- [27] Yang, K., Sun, X., Zeng, X. and Wu, T., "Research on influence of water content to the measurement of wear particle concentration in turbine oil online monitoring simulation", *Wear*, Vol. 376-377, pp. 1222-1226, 2017.
- [28] George, S., Balla, S. and Gautam, M., "Effect of diesel soot contaminated oil on engine wear", *Wear*, Vol. 262, pp. 1113-1122, 2007.
- [29] Shi, H., Zhang, H., Ma, L. and Zeng, L., "A multi-function sensor for online detection of contaminants in hydraulic oil", *Tribol. Int.*, Vol. 138, pp. 196-203, 2019.
- [30] S. Ghosh, B. Sarkar, S. Sanyal, J. Saha, "Automated Maintenance Approach for Industrial Machineries by Soft Computing Techniques at Offline Monitoring Process", *Jordan Journal Mechanical and Industrial Engineering*, Vol. 3, pp. 59-68, 2009.
- [31] ASTM D1298 - 12b, "Standard Test Method for Density, Relative Density, or API Gravity of Crude Petroleum and Liquid Petroleum Products by Hydrometer Method", West Conshohocken, PA, USA, 2017.
- [32] ASTM D445 - 06, "Standard Test Method for Kinematic Viscosity of Transparent and Opaque Liquids (And Calculation of Dynamic Viscosity)", West Conshohocken, PA, 2018.
- [33] ASTM D2270 - 10, "Standard Practice for Calculating Viscosity Index from Kinematic Viscosity at 40 and 100 8C", West Conshohocken, PA, 2016.
- [34] ASTM Standard D664, "ASTM International. Standard Test Method for Acid Number of Petroleum Products by Potentiometric Titration", West Conshohocken, PA, USA, 2004.
- [35] Smiechowski, M.F. and Lvovich, V.F., "Electrochemical monitoring of water/surfactant interactions in industrial lubricants", *J. Electroanalytical Chemistry*, Vol. 534, pp. 171-180, 2002.
- [36] Parsaeian, P., Ghanbarzadeh, A. and Wilson, M., "An experimental and analytical study of the effect of water and its tribochemistry on the tribocorrosive wear of boundary lubricated systems with ZDDP-containing oil", *Wear*, Vol. 358, pp. 23-31, 2016.
- [37] Richard, C.E., "The Effect of Water in Lubricating Oil on Bearing Fatigue Life", *ASLE Trans.*, Vol. 20, pp. 244-248, 1976.
- [38] Juliastuti, E., Tanogono, E. W. and Kurniadi, D., "Detection of Water Content in Lubricating Oil using Ultrasonics", 2017 5th International Conference on Instrumentation, Control, and Automation (ICA), Indonesia, s.n., pp. 188-192, 2017.
- [39] Morley, G. R., "Comparison of spectrographic and ferrographic analysis of crankcase oils from the High Speed Train", *Tribology International*, Vol. 14, pp. 159-165, 1981.
- [40] Johnson, J. H. and Hubert, C. J., "An overview of recent advances in quantitative ferrography as applied to diesel engines", *Wear*, Vol. 90, pp. 199-219, 1983.
- [41] Dan, R., "Multi-view and three-dimensional (3D) images in Wear debris analysis (WDA)", A ph. D thesis submitted to the University of Manchester", 2013.
- [42] Kumar, A., and Ghosh, S. K., "Size distribution analysis of wear debris generated in HEMM engine oil for reliability assessment: A statistical approach", *Measurement*, Vol. 131, pp. 412-418, 2019.
- [43] Cao, W., Zhang, H., Wang, N., Wang, H. W. and Peng, Z. X., "The gearbox wears state monitoring and evaluation based on on-line wear debris features", *Wear*, Vol. 426-427, pp. 1719-1728, 2019.
- [44] Totten, G. E., Shah, R. J. and Westbrook, S. R., "Fuels and lubricants handbook: technology, properties, performance, and testing", 2nd ed. s.l.: PA: ASTM international, 2019.

- [45] Yunus, S., Abd Rashid, A., Abdul Latip, S., Abdullah, N., Ahmad, M. and Abdullah, A., "Comparative study of used and unused engine oil based on Property Analysis Basis", *Procedia Eng.*, Vol. 68, pp. 326 – 330, 2013.
- [46] Mohamed, M., El-Naga, H. and El Meneir, M., "The effect of viscosity index improvers on the determination of metal content in new and used multi-grade oils", *Lubric. Sci.*, Vol. 11, pp. 389-406, 2006.
- [47] Agarwal, A., "Experimental investigations of the effect of biodiesel utilization on lubricating oil tribology in diesel engines", *Proceed. Instit. Mech. Eng.*, Vol. 219, pp. 703-713, 2005.
- [48] Wolak, A. , "Changes in Lubricant Properties of Used Synthetic Oils Based on the Total Acid Number", *Measurement and Control*, Vol. 51, pp. 65– 72, 2018.

Copula Approach to Performance Evaluation of Manufacturing System

Ibrahim Yusuf^{1*}, Abdullahi Sanusi², Nafisatu Muhammad Usman³, Mus'abu Musa⁴

¹Department of Mathematical Sciences, Bayero University, Kano, Nigeria

²Department of Science, School of Continuing Education (SCE), Bayero University, Kano, Nigeria

³Department of Arts and Humanities, School of General Studies, Kano State Polytechnic, Kano, Nigeria

⁴Department of Mathematics, Faculty of Physical Sciences, Kebbi State University of Science and Technology, Aliero, Kebbi State, Nigeria

Received 17 May 2022

Accepted 24 Sep 2022

Abstract

The present paper aimed at examining the performance of multi-station manufacturing system consisting of processors, conveyors and units arranged in series in terms of availability, reliability, Mean Time To failure (MTTF), sensitivity and expected profit under general and copula repairs for rectifying partial and complete failure. Supplementary variable technique and Laplace transforms are used to establish and resolve the differential equations associated with transition diagram, which are essential to this research. The numerical validation of explicit expressions for system availability, reliability, MTTF, MTTF sensitivity, and profit function is performed and presented in the form of tables and graphs. From the tables and graphs, it is clear that copula repair is a better repair policy for system's performance enhancement. The findings of this research are thought to be valuable for analyzing performance and determining the best system design and feasible maintenance strategies that may be used in the future to improve system performance, production output as well as revenue mobilization.

© 2022 Jordan Journal of Mechanical and Industrial Engineering. All rights reserved

Keywords: Availability, Copula, Evaluation, Operation, Performance, Priority, Profit, Reliability.

1. Introduction

Manufacturing systems today are highly automated and comprise a number of interconnected machines. These interconnected machines are prone to failure, which has an impact on the system's reliability and availability, as well as on the revenue generated. Consumers nowadays demand complete assurance that the goods produced by the manufacturing systems are of high qualities and will continue to function. The design and manufacturing stages are critical in ensuring the reliability of goods produced.

The tendency that a system will work satisfactorily under specified working conditions for a given period of time is known as reliability. Reliability is one of the most crucial performance indices. If the system is unreliable, it will not be able to complete all of the manufacturing tasks or meet the production targets. Several research articles on reliability analysis of various systems have been studied. Similarly, the reliability of manufacturing systems is being researched, with several studies being presented.

Aggarwal et al. [1] investigated the profitability of a system with two units in cold standby. Preventive maintenance is performed on the system on a regular basis. In the event of a failure, repair facilities are set aside. The revenue, maintenance costs, and server costs are used to calculate profit using a stochastic process. Alazzam and Tashtoush [2] developed models for reliability modelling

and analysis of lead-free solder due to aging time and temperature using adaptive neuro fuzzy inference system. Aly et al. [3] looked into the use of reliability, availability and maintainability to improve the operational performance of oil and gas industry system. Batra and Malhotra[4] analyzed the availability and reliability for two identical unit cold standby PCB manufacturing system with failure due arrival of faults. Models of availability and reliability are evaluated using the semi Markov and regenerative methods. Chang et al. [5] investigated the dependability of a network with multi-state manufacturing and multiple production lines (MSMN-MPL) when taking into account a joint buffer station.

Chen et al. [6] suggested a mission reliability evaluation for multistate manufacturing systems based on operational data. Chopra and Ram[7] conducted a study of the system's availability and reliability in a parallel network with two distinct units under copula. The availability of crank-case production systems in the automobile industry is described by Garg et al. [8]. The units under investigation can fail in either a regular working or partial failure state. Gulati et al. [9] investigated the reliability of a complex system with three subsystems in series when they failed completely or partially. Gahlot et al. [10] examined the dependability of a complex system made up of two subsystems, subsystem-1 and subsystem-2, in a series configuration under the policies of 2-out-of-3: F and 1-out-of-2: G; copula and

general repair policies; and full and partial failure types. Gahlot et al. [11] investigated the performance of a complex system with two subsystems in sequence under the 2-out-of-3: G and 1-out-of-2: G policies. A human operator is attached to the system to keep it up and running, and the system fails completely due to human error.

He et al. [12] developed mission reliability models for multi-station production systems. He [13] proposed cost-oriented predictive maintenance models for mission reliability. Kadyan and Kumar [14] analyzed the availability and profit of feeding system consisting of six subsystems using supplementary variable technique. [15] investigated the reliability measures of a system comprised of two non-identical warm standby units attended by a single server under a first come, first served maintenance policy. The profit of the system is investigated using a semi-Markov process and regenerative methods. Kumar et al. [16] explore the profit of a system made up of two non-identical warm standby units under a first come, first served maintenance policy with preventive maintenance before failure. For manufacturing systems with serial arrangement, Lu and Zhou [17] suggest condition-based maintenance for dependability and quality. Lado and Singh [18] looked at the cost of a serial system with a human operator. Mehta et al. [19] developed models for availability analysis and enhancement of butter oil production system.

Failure is unavoidable in any man-made system. As a result, it can happen at any time during system operations. It can be a partial/minor failure or a total/complete failure. When a system experiences partial failure, its performance is reduced, and when it experiences complete failure, the system's operations are halted. When a system fails partially, it is repaired using general repair, while when it fails completely, it is repaired using the Copula approach Nelson [20]. Niwas and Garg [21] investigated the performance of an industrial system under a free warranty policy. A mathematical model for optimizing system efficiency and failure rate is proposed using the Markov process, resulting in high system profit and availability. Ram and Goyal [22] developed a stochastic model that included repair impact, failure modes, time trend variation, and coverage factor. Sha [23] investigated the working unit dependency using Clayton copula functions and Farlie-Gumbel-Morgenstern established models for parallel-series and series-parallel. Sanusi and Yusuf [24] studied the resilience of a dispersed data center network topology with three components. Singh and Ayagi [25] investigate a complicated system with a serial arrangement that includes two subsystems that are vulnerable to human failure and are monitored by a human operator.

Singh and Ayagi [26] investigated the dependability of complex systems controlled by a human operator, with three units operating under the super-priority, priority, and ordinary policies, as well as a preemptive resume repair policy. Tyagi et al. [27] developed stochastic model for behavioral analysis of a multi-state system consisting of two non-identical units by incorporating the concept of coverage factor and two types of repair facilities. Temraz [28] created models for analyzing availability and reliability in a parallel system with independent and identical units. The cost of component repair is reduced by using the Lagrange multiplier. Ye et al. [29] looked examined the reliability of a repairable machine while it was subjected to shocks and degradation from low-quality

feedstock. In order to investigate the relationships between the inspection process, product quality, and machine failures, Ye et al. [30] developed a new model for competing failure. The dependability characteristics of a computer network system comprised of load balancers, distributed database servers, and a centralized server arranged as a series parallel system with three subsystems are discussed in Yusuf et al. [31]. Yusuf and Ismail [32] created availability models for parallel systems involving group and individual unit replacement in the event of partial or complete failure. The effect of replacing individual and groups of units with new and similar ones on system availability is investigated. Models development and evaluation of performance manufacturing system with serial arrangement that takes into account rework and product polymorphism is captured by Zhang et al. [33].

The aforementioned researchers provided excellent work on reliability, availability and profit analysis of complicated repairable systems using a copula technique, claiming that their operations improved the performance of the repairable systems. Still, a new sort of model with a justified and satisfactory evaluation is required. In addition, a few research articles on performance analysis of manufacturing systems using the copula approach have been published based on the literature study. Also, it is erroneous to judge the performance of production systems based on their components. Keeping the above facts in view, this paper dealt with performance analysis of manufacturing system producing two types of product; A and B. The system has two units, conveyors and processors as shown in Figure 1.

This paper is structured as follows: Section 1 contains the introduction as well as a brief review of the literature. Notations, assumptions, and system description are found in Section 2, whereas model formulation and solutions are found in Section 3. Section 4 discusses system analysis for specific scenarios, while the results were discussed in Section 5 and Section 6 brought the work to a close with references.

2. Notations, Assumptions, and Model description

2.1. Notations

t: variable representing time.

s: representing variable of Laplace transform

η_1 : stand for rate of failure of processor 1 and 2

η_2 : stand for rate of failure of conveyor 1

η_3 : stand for rate of failure of unit 1 and 2

η_4 : stand for rate of failure of conveyor 2

η_5 : stand for rate of failure of unit 3 and 4

$h(y_1)$: stand for rate of repair by general repair of processor 1 and 2

$h(y_2)$: stand for rate of repair by general repair of conveyor 2

$h(y_3)$: stand for rate of repair by general repair of unit 1 and 2

$h(y_4)$: stand for rate of repair by general repair of conveyor 2

$h(y_5)$: stand for rate of repair by general repair of unit 3 and 4

$m_0(y_1)$: stand for rate of repair by copula of processor 1 and 2

$m_0(y_2)$: stand for rate of repair by copula of conveyor 2

$m_0(y_3)$: stand for rate of repair by copula of unit 1 and 2

$m_0(y_4)$: stand for rate of repair by copula of conveyor 2

$m_0(y_5)$: stand for rate of repair by copula of unit 3 and 4

$P_i(t)$: stand for chance of the system sojourning in S_i state at instants for $i = 0, 1, 2, 3, \dots, 15$.

$\bar{P}(s)$: stand for Laplace transformation of state transition probability $P(t)$.

$P_i(y_1, t)$: stand for chance of the system sojourning in S_i with y_1 variable of repair and variable time t .

$P_i(y_2, t)$: stand for chance of the system sojourning in S_i with y_2 variable of repair and variable time t .

$P_i(y_3, t)$: stand for chance of the system sojourning in S_i with y_3 variable of repair and variable time t .

$P_i(y_4, t)$: stand for chance of the system sojourning in S_i with y_4 variable of repair and variable time t .

$P_i(y_5, t)$: stand for chance of the system sojourning in S_i with y_5 variable of repair and variable time t .

$E_p(t)$: Expected profit during the time interval $[0, t]$

Z_1, Z_2 : Revenue and service cost per unit time, respectively.

$m_0(x)$: The expression of joint probability according to Gumbel-Hougaard family Copula definition is given as:

$$c_\theta(\mu_1(x), \mu_2(x)) = \exp\left(x^\theta + \{\log \phi(x)\}^{\frac{1}{\theta}}\right)$$

, $1 \leq \theta \leq \infty$. Where $\mu_1 = \phi(x)$ and $\mu_2 = e^x$.

2.2. Assumptions

1. Units are presumed to be up and running the start.
2. Any unit failure results in sufficient system performance.
3. Any unit of any subsystem that fails while in operation or in the failure state can be restored.

$$\left(\frac{\delta}{\delta t} + 2\eta_1 + \eta_2 + 2\eta_3 + \eta_4 + 2\eta_5\right)P_0(t) = \int_0^\infty h(y_1)P_1(y_1, t)dy_1 + \int_0^\infty h(y_5)P_2(y_5, t)dy_5 + \int_0^\infty m_0(y_5)P_3(y_5, t)dy_5$$

$$+ \int_0^\infty h(y_3)P_5(y_3, t)dy_3 + \int_0^\infty m_0(y_1)P_{12}(y_1, t)dy_1 + \int_0^\infty m_0(y_3)P_{13}(y_3, t)dy_3 + \int_0^\infty m_0(y_2)P_{14}(y_2, t)dy_2 +$$

$$\int_0^\infty m_0(y_4)P_{15}(y_4, t)dy_4 \tag{1}$$

4. Failure rates are taken to be constant and distributed exponentially.

5. Fully failed states can be restored using the Gumbel-Hougaard Family Copula, whereas partially failed states can be restored using universal/general distribution.

2.3. Model description

The system under consideration in this paper is a manufacturing system producing two types of product; A and B. The system consists of two units, conveyors and processors as depicted in Figure 1 below. The processors received items to be processed, and then channel them to the conveyor 1 for the process in either unit 1 and 2 or to the conveyor 2 for onward process in unit 3 and for usage. It is assumed that product A is of higher priority over product B. It is also assumed that unit 3 and 4 can manufacture product B only while unit 1 and 2 can manufacture product A, and product B only at the failure of unit 3 and 4. When the processors received items meant for making product A, the items will be processed in processor 1 and 2 and channeled to conveyor1, which will be forwarded to unit 1 and 2 to manufacture product A, while items meant for product B are processed by processor 1 and 2 and channeled to unit 3 and 4 through conveyor 2.

3. Model formulation and Solutions

3.1. Model formulation

For system modeling and analysis, reliability models were created using the supplementary variable technique and Laplace transforms. The differential equations were generated from the transition diagram using a probabilistic approach. These equations were then solved using initial and boundary conditions to obtain the steady state probabilities that serve as the foundation for the formulation of performance models.

The steps in getting the solutions of the state probabilities $P_k(s)$ for the formulation of the models involve

1. Derivation of the partial differential equations from Figure 1
2. Derivation of the boundary conditions of the states other than initial state
3. Taking the Laplace transformation of (a) and (b) above
4. Solving (c) to obtain the state probabilities $P_k(s)$

The following partial differential equations are obtained via Figure 1:

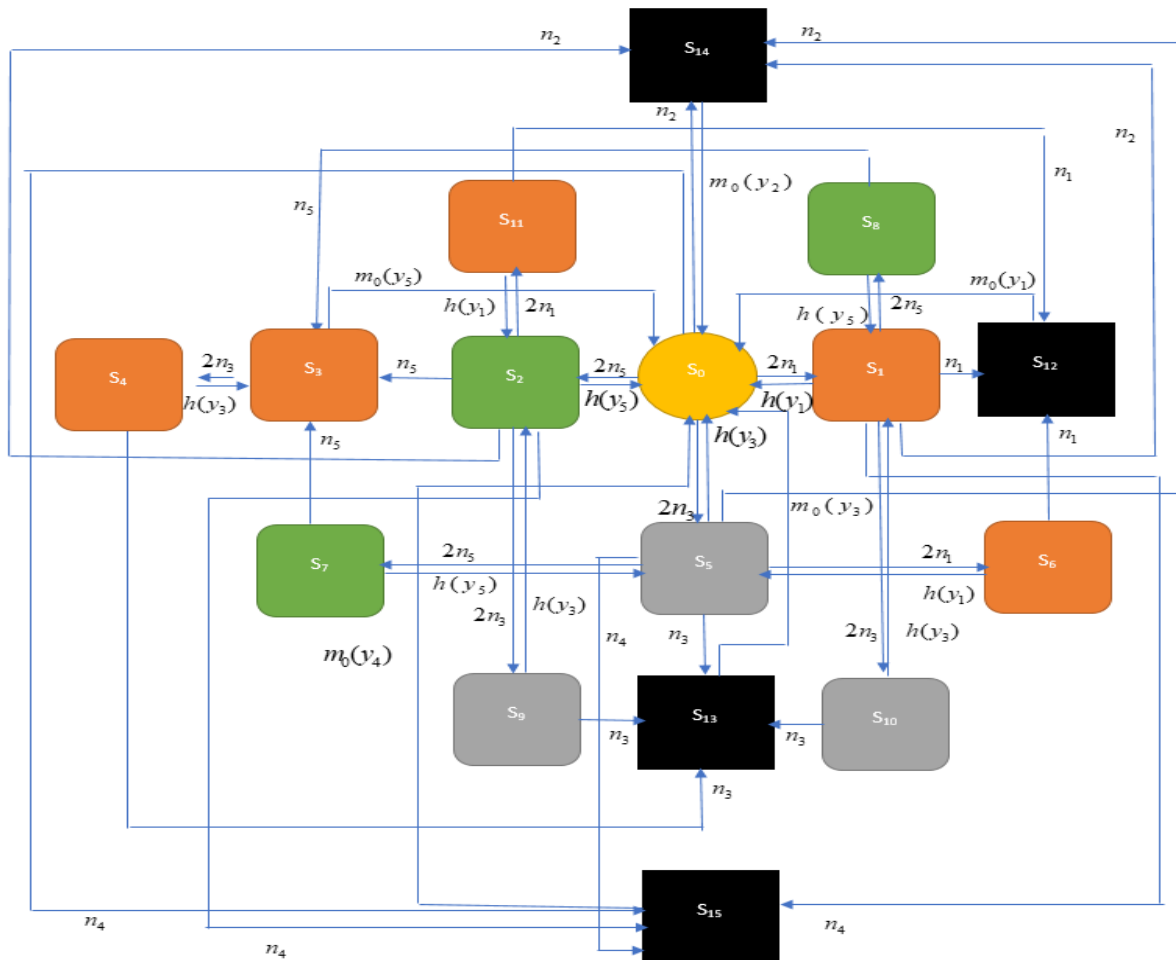


Figure 1. Diagram of transition of the model

S_0 : Initial state. The subsystems and the system are in perfect state. The system is up and running.

S_1 : Processor 1 has failed; processor 2 is up. The system is up and running.

S_2 : Unit 3 has failed on the course of manufacturing product B; unit 4 has continued with manufacture of product B. The system is up and running.

S_3 : Unit 3 and 4 have both failed on the course of manufacturing product B; unit 1 continue with manufacture of product B. The system is up and running.

S_4 : Previously Unit 3 and 4 have both failed on the course of manufacturing product B; unit 1 has failed on the course of manufacturing product B, unit 2 has continue with manufacture of product B. The system is up and running.

S_5 : Unit 1 has failed on the course of manufacturing product A; unit 2 continue with manufacture of product A. The system is up and running.

S_6 : Previously unit 1 has failed on the course of manufacturing product A and is followed by the failure of processor I, processor 2 and unit 2 continue with manufacture of product A. The system is up and running.

S_7 : Unit 3 has failed on the course of manufacturing product B and unit 4 has continued with manufacture of product B; unit 1 has failed on the course of manufacturing product A and unit 2 continue with manufacture of product A. The system is up and running.

S_8 : Processor 1 has failed previously and is followed by failure of unit 3 on the course of manufacturing product B, processor 2 and unit 4 are up. The system is up and running.

S_9 : Unit 3 has failed on the course of manufacturing product B, and unit 4 has continued with manufacture of product B; unit 1 has failed on the course of manufacturing product A; unit 2 continue with manufacture of product A. The system is up and running.

S_{10} : Processor 1 has failed; processor 2 is up, unit 1 has failed on the course of manufacturing product A; unit 2 has continued with manufacture of product A. The system is up and running.

S_{11} : Unit 3 has failed on the course of manufacturing product B previously and is followed by failure of processor I; unit 4 has continued with manufacture of product B, processor 2 is up. The system is up and running.

S_{12} : Processor 1 and 2 have both failed. The system is down.

S_{13} : Unit 1 and 2 have both failed. The system is down.

S_{14} : Conveyor1 has failed. The system is down.

S_{15} : Conveyor 2 has failed. The system is down.

$$\left(\frac{\delta}{\delta t} + \frac{\delta}{\delta y_1} + \eta_1 + \eta_2 + 2\eta_3 + \eta_4 + 2\eta_5 + h(y_1)\right)P_1(y_1, t) = 0 \quad (2)$$

$$\left(\frac{\delta}{\delta t} + \frac{\delta}{\delta y_5} + 2\eta_1 + \eta_2 + 2\eta_3 + \eta_4 + 2\eta_5 + h(y_5)\right)P_2(y_5, t) = 0 \quad (3)$$

$$\left(\frac{\delta}{\delta t} + \frac{\delta}{\delta y_5} + 2\eta_5 + m_0(y_5)\right)P_3(y_5, t) = 0 \quad (4) \quad \left(\frac{\delta}{\delta t} + \frac{\delta}{\delta y_2} + m_0(y_2)\right)P_{14}(y_2, t) = 0 \quad (15)$$

$$\left(\frac{\delta}{\delta t} + \frac{\delta}{\delta y_3} + \eta_3 + h(y_3)\right)P_4(y_3, t) = 0 \quad (5) \quad \left(\frac{\delta}{\delta t} + \frac{\delta}{\delta y_4} + m_0(y_4)\right)P_{15}(y_4, t) = 0 \quad (16)$$

$$\left(\frac{\delta}{\delta t} + \frac{\delta}{\delta y_3} + 2\eta_1 + \eta_2 + \eta_3 + \eta_4 + 2\eta_5 + h(y_3)\right)P_5(y_3, t) = 0 \quad (6) \quad \text{Conditions of boundary}$$

$$\left(\frac{\delta}{\delta t} + \frac{\delta}{\delta y_1} + \eta_1 + h(y_1)\right)P_6(y_1, t) = 0 \quad (7) \quad P_1(0, t) = 2\eta_1 P_0(t) \quad (17)$$

$$P_2(0, t) = 2\eta_5 P_0(t) \quad (18)$$

$$\left(\frac{\delta}{\delta t} + \frac{\delta}{\delta y_5} + \eta_5 + h(y_5)\right)P_7(y_5, t) = 0 \quad (8) \quad P_3(0, t) = 2\eta_5^2(1 + 2\eta_1 + 2\eta_2)P_0(t) \quad (19)$$

$$P_4(0, t) = 4\eta_3\eta_5^2(1 + 2\eta_1 + 2\eta_2)P_0(t) \quad (20)$$

$$\left(\frac{\delta}{\delta t} + \frac{\delta}{\delta y_5} + \eta_5 + h(y_5)\right)P_8(y_5, t) = 0 \quad (9) \quad P_5(0, t) = 2\eta_3 P_0(t) \quad (21)$$

$$\left(\frac{\delta}{\delta t} + \frac{\delta}{\delta y_3} + \eta_3 + h(y_3)\right)P_9(y_3, t) = 0 \quad (10) \quad P_6(0, t) = 4\eta_1\eta_3 P_0(t) \quad (22)$$

$$P_7(0, t) = 4\eta_3\eta_5 P_0(t) \quad (23)$$

$$\left(\frac{\delta}{\delta t} + \frac{\delta}{\delta y_3} + \eta_3 + h(y_3)\right)P_{10}(y_3, t) = 0 \quad (11) \quad P_8(0, t) = 4\eta_1\eta_3 P_0(t) \quad (24)$$

$$P_9(0, t) = 4\eta_3\eta_5 P_0(t) \quad (25)$$

$$\left(\frac{\delta}{\delta t} + \frac{\delta}{\delta y_1} + \eta_1 + h(y_1)\right)P_{11}(y_1, t) = 0 \quad (12) \quad P_{10}(0, t) = 4\eta_1\eta_3 P_0(t) \quad (26)$$

$$P_{11}(0, t) = 4\eta_1\eta_5 P_0(t) \quad (27)$$

$$\left(\frac{\delta}{\delta t} + \frac{\delta}{\delta y_1} + m_0(y_1)\right)P_{12}(y_1, t) = 0 \quad (13) \quad P_{12}(0, t) = 2\eta_1^2(1 + 2\eta_3)P_0(t) \quad (28)$$

$$\left(\frac{\delta}{\delta t} + \frac{\delta}{\delta y_3} + m_0(y_3)\right)P_{13}(y_3, t) = 0 \quad (14)$$

$$P_{13}(0, t) = 2\eta_3^2 \{1 + 2\eta_1 + 2\eta_5 + 2\eta_5^2 (1 + 2\eta_1 + 2\eta_3)\} P_0(t) \quad (29)$$

$$P_{14}(0, t) = \eta_2 (1 + 2\eta_1 + 2\eta_3 + 2\eta_5) P_0(t) \quad (30)$$

$$P_{15}(0, t) = \eta_4 (1 + 2\eta_1 + 2\eta_3 + 2\eta_5) P_0(t) \quad (31)$$

Applying (b) to (d) to equations (1) to (31) to derive the state probabilities below:

$$\bar{P}_0(s) = \frac{1}{\Delta(s)} \quad (32)$$

$$\bar{P}_1(s) = \frac{2\eta_1}{\Delta(s)} \left[\frac{1 - \bar{s}_h(s + \eta_1 + \eta_2 + 2\eta_3 + \eta_4 + 2\eta_5)}{(s + \eta_1 + \eta_2 + 2\eta_3 + \eta_4 + 2\eta_5)} \right] \quad (33)$$

$$\bar{P}_2(s) = \frac{2\eta_5}{\Delta(s)} \left[\frac{1 - \bar{s}_h(s + 2\eta_1 + \eta_2 + 2\eta_3 + \eta_4 + 2\eta_5)}{(s + 2\eta_1 + \eta_2 + 2\eta_3 + \eta_4 + 2\eta_5)} \right] \quad (34)$$

$$\bar{P}_3(s) = \frac{2\eta_5^2 (1 + 2\eta_1 + 2\eta_5)}{\Delta(s)} \left[\frac{1 - \bar{s}_{m_0}(s + 2\eta_3)}{(s + 2\eta_3)} \right] \quad (35)$$

$$\bar{P}_4(s) = \frac{4\eta_3\eta_5^2 (1 + 2\eta_1 + 2\eta_2)}{\Delta(s)} \left[\frac{1 - \bar{s}_h(s + \eta_3)}{(s + \eta_3)} \right] \quad (36)$$

$$\bar{P}_5(s) = \frac{2\eta_3}{\Delta(s)} \left[\frac{1 - \bar{s}_h(s + 2\eta_1 + \eta_2 + 2\eta_3 + \eta_4 + \eta_5)}{(s + 2\eta_1 + \eta_2 + 2\eta_3 + \eta_4 + \eta_5)} \right] \quad (37)$$

$$\bar{P}_6(s) = \frac{4\eta_1\eta_3}{\Delta(s)} \left[\frac{1 - \bar{s}_h(s + \eta_1)}{(s + \eta_1)} \right] \quad (38)$$

$$\bar{P}_7(s) = \frac{4\eta_3\eta_5}{\Delta(s)} \left[\frac{1 - \bar{s}_h(s + \eta_5)}{(s + \eta_5)} \right] \quad (39)$$

$$\bar{P}_8(s) = \frac{4\eta_1\eta_5}{\Delta(s)} \left[\frac{1 - \bar{s}_h(s + \eta_5)}{(s + \eta_5)} \right] \quad (40)$$

$$\bar{P}_9(s) = \frac{4\eta_3\eta_5}{\Delta(s)} \left[\frac{1 - \bar{s}_h(s + \eta_3)}{(s + \eta_3)} \right] \quad (41)$$

$$\bar{P}_{10}(s) = \frac{4\eta_1\eta_3}{\Delta(s)} \left[\frac{1 - \bar{s}_h(s + \eta_3)}{(s + \eta_3)} \right] \quad (42)$$

$$\bar{P}_{11}(s) = \frac{4\eta_1\eta_5}{\Delta(s)} \left[\frac{1 - \bar{s}_h(s + \eta_1)}{(s + \eta_1)} \right] \quad (43)$$

$$\bar{P}_{12}(s) = \frac{2\eta_1^2 (1 + 2\eta_3)}{\Delta(s)} \left[\frac{1 - \bar{s}_{m_0}(s)}{(s)} \right] \quad (44)$$

$$\bar{P}_{13}(s) = \frac{2\eta_3 \{1 + 2\eta_5 + 2\eta_5^2 (1 + 2\eta_1 + 2\eta_3)\}}{\Delta(s)} \left[\frac{1 - \bar{s}_{m_0}(s)}{s} \right] \quad (45)$$

$$\bar{P}_{14}(s) = \frac{\eta_2(1+2\eta_1+2\eta_3+2\eta_5)}{\Delta(s)} \left[\frac{1-\bar{s}_{m_0}(s)}{s} \right] \tag{46}$$

$$\bar{P}_{15}(s) = \frac{\eta_4(1+2\eta_1+2\eta_3+2\eta_5)}{\Delta(s)} \left[\frac{1-\bar{s}_{m_0}(s)}{s} \right] \tag{47}$$

Where,

$$\Delta(s) = \left\{ \begin{aligned} &(s + \eta_1 + \eta_2 + 2\eta_3 + \eta_4 + 2\eta_5) - 2\eta_1 \bar{s}_h(s + \eta_1 + \eta_2 + 2\eta_3 + \eta_4 + 2\eta_5) \\ &- 2\eta_5 \bar{s}_h(s + 2\eta_1 + \eta_2 + 2\eta_3 + \eta_4 + \eta_5) - 2\eta_3 \bar{s}_h(s + \eta_1 + \eta_2 + 2\eta_3 + \eta_4 + 2\eta_5) \\ &2\eta_5^2(1+2\eta_1+2\eta_3)\bar{s}_{m_0}(s+2\eta_3) - \eta_2(1+2\eta_1+2\eta_3+2\eta_5)\bar{s}_{m_0}(s) - \\ &2\eta_1^2(1+2\eta_3)\bar{s}_{m_0}(s) - 2\eta_3^2\{1+2\eta_1+2\eta_5+2\eta_5^2(1+2\eta_1+2\eta_3)\}\bar{s}_{m_0}(s) - \\ &\eta_2(1+2\eta_1+2\eta_3+2\eta_5)\bar{s}_{m_0}(s) \end{aligned} \right\}$$

Using the state probabilities of operation states in Figure 1, the chance that the system is up and running is,

$$\bar{P}_{up}(s) = \sum_{j=0}^{11} \bar{P}_j(s) \left\{ \begin{aligned} &1 + 2\eta_1 \frac{1-\bar{s}_h(s+\eta_1+\eta_2+2\eta_3+\eta_4+2\eta_5)}{(s+\eta_1+\eta_2+2\eta_3+\eta_4+2\eta_5)} + 2\eta_5 \frac{1-\bar{s}_h(s+2\eta_1+\eta_2+2\eta_3+\eta_4+\eta_5)}{(s+2\eta_1+\eta_2+2\eta_3+\eta_4+\eta_5)} \\ &2\eta_5^2(1+2\eta_1+2\eta_3) \frac{1-\bar{s}_{m_0}(s+2\eta_3)}{(s+2\eta_3)} + 4\eta_3\eta_5^2(1+2\eta_1+2\eta_2) \frac{1-\bar{s}_h(s+\eta_3)}{(s+\eta_3)} + \\ &2\eta_3 \frac{1-\bar{s}_h(s+2\eta_1+\eta_2+2\eta_3+\eta_4+\eta_5)}{(s+2\eta_1+\eta_2+2\eta_3+\eta_4+\eta_5)} + 4\eta_5(\eta_1+\eta_3) \frac{1-\bar{s}_h(s+\eta_5)}{(s+\eta_5)} + 4\eta_1\eta_5 \frac{1-\bar{s}_h(s+\eta_5)}{(s+\eta_5)} \\ &+ 4\eta_3\eta_5 \frac{1-\bar{s}_h(s+\eta_3)}{(s+\eta_3)} + 4\eta_1\eta_3 \frac{1-\bar{s}_h(s+\eta_3)}{(s+\eta_3)} + 4\eta_1\eta_5 \frac{1-\bar{s}_h(s+\eta_1)}{(s+\eta_1)} \end{aligned} \right\} \tag{48}$$

4. Model analysis for specific cases

In order to gain a comprehensive understanding of this study. This section shows numerical simulations of the models.

4.1. System Availability

In the availability model for both copula and general repairs, the following scenarios are taken into account for consistency.

$$\text{Fixed } s_{m_0}(s) = \bar{s}_{\exp} \left[x^\theta + \{\log \varphi(x)\}^\theta \right]^{1/\theta} \quad (s) = \frac{\exp \left[x^\theta + \{\log \varphi(x)\}^\theta \right]^{1/\theta}}{s + \exp \left[x^\theta + \{\log \varphi(x)\}^\theta \right]^{1/\theta}}, \quad \bar{s}_{m_0}(s) = \frac{h}{s+h} \quad \text{and taking failure rates at}$$

various values, such as:

Case 1: $\eta_5 = 0.05, \eta_1 = 0.01, \eta_3 = 0.03, \eta_2 = 0.02$ and $\eta_4 = 0.04, m_0 = h = x = y = 1, h(y_1) =$

$$h(y_2) = h(y_3) = h(y_4) = h(y_5) = m_0(y_1) = m_0(y_2) = m_0(y_3) = m_0(y_4) = 1$$

Case 2: $\eta_5 = 0, \eta_1 = 0.01, \eta_3 = 0.03, \eta_2 = 0.02$ and $\eta_4 = 0.04, m_0 = h = x = y = 1, h(y_1) = h(y_2) =$

$$h(y_3) = h(y_4) = h(y_5) = m_0(y_1) = m_0(y_2) = m_0(y_3) = m_0(y_4) = 1$$

Case 3: $\eta_5 = 0, \eta_1 = 0.01, \eta_3 = 0.03, \eta_2 = 0.02$ and $\eta_4 = 0, m_0 = h = x = y = 1, h(y_1) = h(y_2) = h(y_3) = h(y_4) = h(y_5) = m_0(y_1) = m_0(y_2) = m_0(y_3) = m_0(y_4) = 1$

Case 4: $\eta_5 = 0, \eta_1 = 0.01, \eta_3 = 0, \eta_2 = 0.02$ and $\eta_4 = 0, m_0 = h = x = y = 1, h(y_1) = h(y_2) = h(y_3) = h(y_4) = h(y_5) = m_0(y_1) = m_0(y_2) = m_0(y_3) = m_0(y_4) = 1$

4.1.1. System Availability via Copula repair

We derive the following explicit equations for copula repair by substituting each of the scenarios considered in equation (48) and using inverse Laplace transformation as:

Case 1

$$P_{up}(t) = \left\{ \begin{array}{l} -0.002996924489e^{-1.05t} - 0.001648902716e^{-1.01t} - \\ 0.003506172167e^{-1.03t} - 0.02804402347e^{-2.799541089t} - \\ 0.03219732828e^{-1.348312856t} - 0.0001279546981e^{-1.201426001t} \\ -0.0009275277378e^{-1.062398069t} + 1.013486002e^{-0.01035423720t} \end{array} \right\} \quad (49)$$

Case 2

$$P_{up}(t) = \left\{ \begin{array}{l} -0.0006884534335e^{-1.01t} - 0.0006161332316e^{-1.03t} + \\ 0.02486438232e^{-2.788179765t} - 0.009705610644e^{-1.18500683t} - \\ 0.0001441966181e^{-1.123828940t} + 0.9862900113e^{-0.001284464747t} \end{array} \right\} \quad (50)$$

Case 3

$$P_{up}(t) = \left\{ \begin{array}{l} -0.0005460429236e^{-1.01t} + 0.008985774245e^{2.743070575t} - \\ 0.006754225850e^{-1.149523258t} - 0.00007252051143e^{-1.083917205t} + \\ 0.9988153713e^{-0.001788962241t} - 0.0004283559453e^{-1.03t} \end{array} \right\} \quad (51)$$

Case 4

$$P_{up}(t) = \left\{ \begin{array}{l} 0.0007603256047e^{-2.739136591t} - 0.0007715044997e^{-1.049180434t} + \\ 0.9931682484e^{-0.00001702574081t} \end{array} \right\} \quad (52)$$

For $t \in [0, 20]$ in the above equations i.e., equation (49)-(52), the result is given below when the repair is done by copula distribution.

Table 1. Availability with passage of time in various scenarios via copula repair

Time	Case 1	Case 2	Case 3	Case 4
0	1.00000	1.00000	1.00000	1.00000
2	0.98948	0.98276	0.99447	0.99314
4	0.97208	0.98113	0.99161	0.99322
6	0.95241	0.97871	0.98814	0.99327
8	0.93291	0.97621	0.98462	0.99330
10	0.91380	0.97370	0.98111	0.99334
12	0.89507	0.97120	0.97760	0.99337
14	0.87672	0.96871	0.97411	0.99341
16	0.85875	0.96623	0.97063	0.99344
18	0.84115	0.96375	0.96716	0.99347
20	0.82391	0.96128	0.96371	0.99351

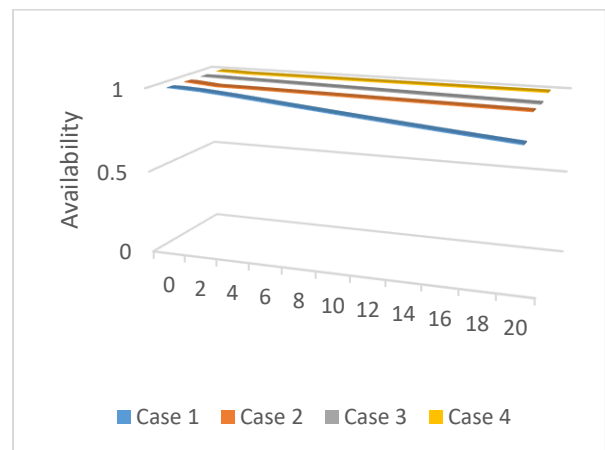


Figure 2. Availability with respect to time in various scenarios via copula repair

4.1.2. System availability via General repair

In a similar way, we obtain expressions for system availability for General repair by substituting each of the

cases considered in equation (48) and using Laplace transformation as:

Case 1

$$P_{up}(t) = \left\{ \begin{aligned} & -0.007341858038e^{-1.05t} + 0.0005840154227e^{-1.01t} - \\ & 0.002741497978e^{-1.391811163t} + 0.0001221344453e^{-1.226515584} \\ & + 0.0001758949705e^{-1.201730597t} + 0.002167622614e^{-1.065184534t} \\ & 0.01485750988e^{-1.034805818t} + 0.9736558977e^{-0.009952303992t} + \\ & 0.01852028107e^{-1.03t} \end{aligned} \right\} \tag{53}$$

Case 2

$$P_{up}(t) = \left\{ \begin{aligned} & 0.0002377116294e^{-1.01t} + 0.003090659341e^{-1.03t} + \\ & 0.02149851512e^{-1.219142592t} + 0.0005490604380e^{-1.124556391t} \\ & + 0.02528881487e^{-1.035064605t} + 0.9493352385e^{-0.001236412652t} \end{aligned} \right\} \tag{54}$$

Case 3

$$P_{up}(t) = \left\{ \begin{aligned} & 0.005180660394e^{-1.163096569t} + 0.0002835218455e^{-1.084281633t} + \\ & 0.004191164857e^{-1.010857358t} + 0.9850928524e^{-0.001764439983t} + \\ & 0.005858375000e^{-1.01t} + 0.0006075744279e^{-1.03t} \end{aligned} \right\} \tag{55}$$

Case 4

$$P_{up}(t) = \left\{ \begin{aligned} & 0.01102912438e^{-1.059657927t} + 0.008243990789e^{-1.010358885t} + \\ & 0.9807268847e^{-0.00001681245554t} \end{aligned} \right\} \tag{56}$$

When the general distribution is used, the system’s availability is shown in table 2 and figure 4 using varying numbers of time t as:0,2,4,6,8,10,12,14,15,16,18,20 in equation (53)-(56).

Table 2. Availability with respect to time in various scenarios via general repair

Time	Case 1	Case 2	Case 3	Case 4
0	1.00000	1.00000	1.00000	1.00000
2	0.95800	0.95254	0.98342	0.98318
4	0.93612	0.94528	0.97838	0.98111
6	0.91728	0.94239	0.97475	0.98086
8	0.89915	0.93910	0.97129	0.98086
10	0.88142	0.93767	0.96786	0.98089
12	0.86405	0.93535	0.96445	0.98092
14	0.84702	0.93304	0.96106	0.98096
16	0.83033	0.93074	0.95767	0.98099
18	0.81396	0.92844	0.95430	0.98102
20	0.79792	0.92615	0.95094	0.98106

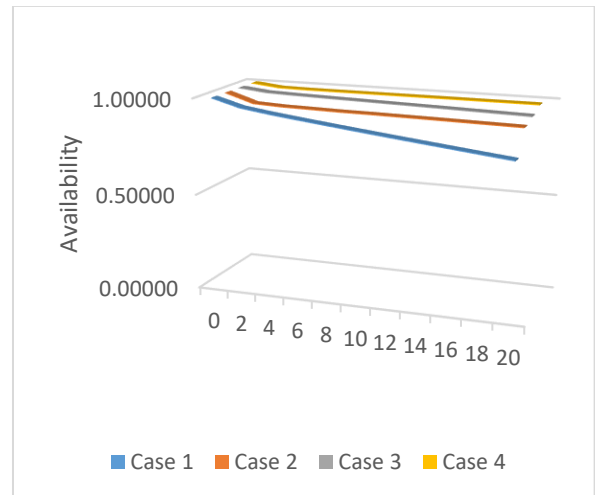


Figure 3. Availability with respect to passage of time in various scenarios via general repair

4.2. Reliability analysis

In reliability analysis, vanishing repairs to zero and considering $\eta_5 = 0.05, \eta_1 = 0.01, \eta_3 = 0.03,$

$\eta_2 = 0.02$ and $\eta_4 = 0.04,$ in (48) and applying Laplace transformation, we obtain reliability equation as:

$$R(t) = \left\{ \begin{aligned} & -5.121846878e^{-0.2400000000t} + 2e^{-0.2400000000t} + 0.1391304348e^{-0.1000000000t} \\ & 2e^{-0.2300000000t} + 0.4210526316e^{-0.5000000000t} + 2e^{-0.1900000000t} + \\ & 0.3000000000e^{-0.6000000000t} + 0.3582857143e^{-0.3000000000t} \end{aligned} \right\} \quad (57)$$

Table 3 and the corresponding figure 5 represent system reliability when $t \in [0, 20]$ are used in equation (89).

Table 3. System reliability with respect to time

Time	0	2	4	6	8	10	12	14	16	18	20
$R(t)$	1.00000	0.88716	0.73789	0.59175	0.46472	0.36106	0.27960	0.21713	0.16993	0.13460	0.10826

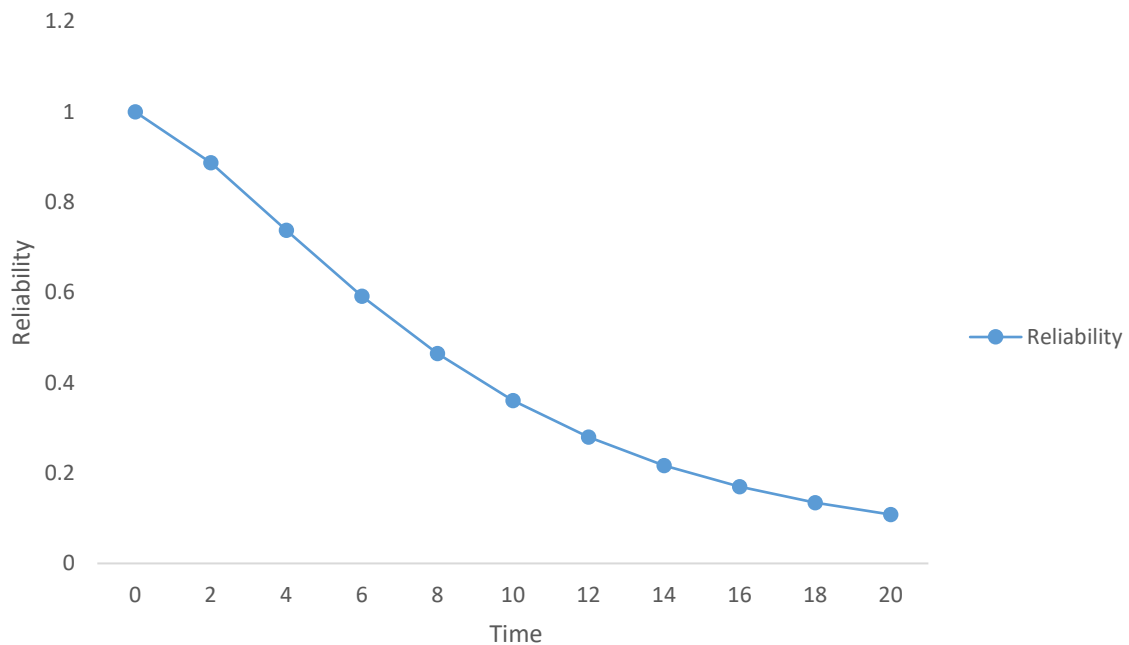


Figure 4. System reliability with respect to passage of time

4.3. Mean Time To Failure (MTTF) analysis

Supposing all repairs vanished to zero. When s tends to zero, the MTTF can be evaluated using limit as follows:

$$MTTF = \lim_{s \rightarrow 0} \bar{P}_{up}(s) = \frac{1}{\Delta(s)} \left\{ \begin{aligned} & 1 + \frac{2\eta_1}{\eta_1 + \eta_2 + 2\eta_3 + \eta_4 + 2\eta_5} + \frac{2\eta_5}{2\eta_1 + \eta_2 + 2\eta_3 + \eta_4 + 2\eta_5} + \\ & \frac{2\eta_3}{2\eta_1 + \eta_2 + 2\eta_3 + \eta_4 + \eta_5} + \frac{\eta_5^2 (1 + 2\eta_1 + 2\eta_3)}{\eta_3} + \\ & \frac{4\eta_5^2 (1 + 2\eta_1 + 2\eta_2) + 2(6\eta_1 + 2\eta_3 + 5\eta_5)}{\eta_3} \end{aligned} \right\} \quad (58)$$

Table 4 and the associated figure 6 display the MTTF when the values of failure rates are fixed at $\eta_5 = 0.05, \eta_1 = 0.01, \eta_3 = 0.03, \eta_2 = 0.02$ and $\eta_4 = 0.04,$ and each $\eta_j \in [0.01, 0.10]$

Table 4.MTTF variation with respect to failure rate

η_j	$j=1$	$j=2$	$j=3$	$j=4$	$j=5$
0.01	11.33244	12.03159	13.53796	13.71016	13.32648
0.02	10.79382	11.33244	12.12079	12.81847	12.57653
0.03	10.35470	10.70744	11.33244	12.03159	12.03717
0.04	9.98772	10.14562	10.76760	11.33244	11.63629
0.05	9.67470	9.63803	10.32443	10.70744	11.33244
0.06	9.16433	9.17735	9.95955	10.14562	11.10008
0.07	9.40318	8.75746	9.64973	9.63803	10.92253
0.08	8.95173	8.37329	9.38086	9.17735	10.78836
0.09	8.76064	8.02054	9.14368	8.75746	10.68942
0.10	8.58742	8.69557	8.93176	8.37329	10.61967

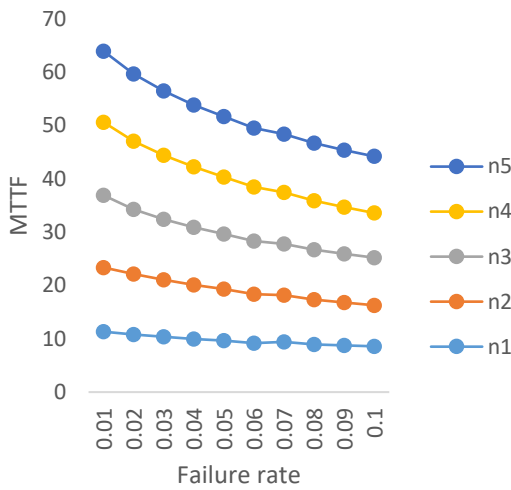


Figure 5. MTTF variation against η_j

4.4. Sensitivity analysis

To calculate system sensitivity when the values of failure rates are fixed at $\eta_5 = 0.05$, $\eta_1 = 0.01$, $\eta_3 = 0.03$, $\eta_2 = 0.02$ and $\eta_4 = 0.04$, each $\eta_j \in [0.01, 0.10]$, the result is

$$E_p(t) = Z_1 \left\{ \begin{aligned} &-0.003404050648e^{-1.003000000t} - 0.001001736448e^{-2.799541089t} + \\ &0.02387971615e^{-1.3488312856t} + 0.0001021107079e^{-1.226267748t} \\ &+ 0.0001065023547e^{-1.201426001t} + 0.0008730510388e^{1.062398069t} \\ &- 97.88128110e^{-0.01035423720t} + 0.002854213799e^{-1.05000000t} + \\ &0.001632576947e^{-1.01000000t} + 97.85844624 \end{aligned} \right\} - Z_2 t \quad (60)$$

Table 5.System sensitivity against failure rate

η_j	$\delta(MTTF)$ $\delta\eta_1$	$\delta(MTTF)$ $\delta\eta_2$	$\delta(MTTF)$ $\delta\eta_3$	$\delta(MTTF)$ $\delta\eta_4$	$\delta(MTTF)$ $\delta\eta_5$
0.01	-60.09123	-74.04882	-222.90246	-95.08696	-89.25306
0.02	-48.32948	-66.00476	-97.38191	-83.61018	-62.88985
0.03	-39.94090	-59.17734	-65.04694	-74.04882	-46.13418
0.04	-33.75326	-53.33617	-49.40803	-66.00476	-34.70971
0.05	-29.05445	-48.30249	-39.90348	-59.17734	-26.47453
0.06	-25.39490	-43.93590	-33.44354	-53.33617	-20.26999
0.07	-22.48115	-40.12500	-28.74873	-48.30249	-15.42769
0.08	-20.11592	-36.78050	-25.17691	-43.93590	-11.54038
0.09	-18.16312	-33.83019	-22.36553	-40.12500	-8.34792
0.10	-16.52660	-31.21521	-20.09321	-36.78050	-5.67717

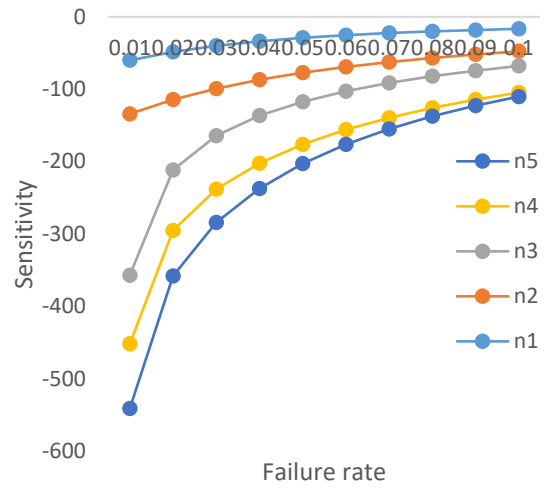


Figure 6.Sensitivity versus η_j

4.5. Profit analysis

The expected profit for $t \geq 0$ is

$$E_p(t) = Z_1 \int_0^t P_{up}(t) dt - Z_2 t \quad (59)$$

4.5.1. Expected profit when the repair policy is obeyed by copula distribution

Assuming $\eta_5 = 0.05$, $\eta_1 = 0.01$, $\eta_3 = 0.03$, $\eta_2 = 0.02$ and $\eta_4 = 0.04$, one can obtain equation (92) by combining equation (79) and equation (91) as:

Table 6 and figure 8 are when $t \in [0, 20]$ and by applying the inverse Laplace transform to equation (92) with $Z_2 \in [0.01, 0.06]$ and $Z_1 = 1$ respectively.

Table 6.Expected profit for repair policy obeyed by copula distribution

Time	$E_p(t)$ $Z_2 = 0.06$	$E_p(t)$ $Z_2 = 0.05$	$E_p(t)$ $Z_2 = 0.04$	$E_p(t)$ $Z_2 = 0.03$	$E_p(t)$ $Z_2 = 0.02$	$E_p(t)$ $Z_2 = 0.01$
0	0	0	0	0	0	0
2	1.86599	1.88599	1.90599	1.92599	1.94599	1.96599
4	3.70855	3.74855	3.78855	3.82855	3.86855	3.90855
6	5.51307	5.57307	5.63307	5.69307	5.75307	5.81307
8	7.27834	7.35834	7.43834	7.51834	7.59834	7.67834
10	9.00498	9.10498	9.20498	9.30498	9.40498	9.50498
12	10.69378	10.81378	10.93378	11.05378	11.17378	11.29378
14	12.34551	12.48551	12.62551	12.76551	12.90551	13.04551
16	13.96093	14.12093	14.28093	14.44093	14.60093	14.76093
18	15.54078	15.72078	15.90078	16.08078	16.26078	16.44078
20	17.08578	17.28578	17.48578	17.68578	17.88578	18.08578

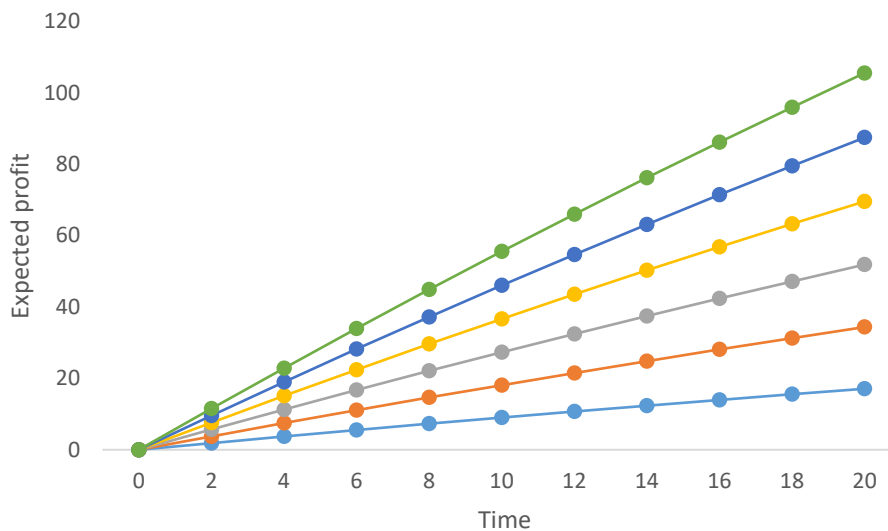


Figure 7.Expected profit for repair policy obeyed by copula distribution versus time t

4.5.2. Expression for Expected profit when the repair policy is obeyed by general distribution

Assuming $\eta_5 = 0.05$, $\eta_1 = 0.01$, $\eta_3 = 0.03$, $\eta_2 = 0.02$ and $\eta_4 = 0.04$, one can get profit function for general repair by using equation (79) in equation (91) as:

$$E_p(t) = Z_1 \left\{ \begin{array}{l} -0.01798085541e^{-1.003000000t} + 0.001969734150e^{-1.391811163t} - \\ 0.00009957838848e^{-1.226515584t} - 0.0001463680553e^{-1.201730597t} \\ -0.002034973795e^{-1.065184534t} - 0.0143577575e^{-1.034805818t} \\ -97.832221036e^{-0.009952303992t} + 0.00692245750e^{-1.05000000t} + \\ 0.0005782330918e^{-1.01000000t} + 97.85844624 \end{array} \right\} - Z_2 t \quad (61)$$

Table 6 and figure 8 are when $t \in [0, 20]$ and by applying the inverse Laplace transform to equation (93) with $Z_2 \in [0.01, 0.06]$ and $Z_1 = 1$ respectively.

Table 7.Expected profit for repair policy obeyed by general distribution versus time t

Time	$E_p(t)$ $Z_2 = 0.06$	$E_p(t)$ $Z_2 = 0.05$	$E_p(t)$ $Z_2 = 0.04$	$E_p(t)$ $Z_2 = 0.03$	$E_p(t)$ $Z_2 = 0.02$	$E_p(t)$ $Z_2 = 0.01$
0	0	0	0	0	0	0
2	1.83083	1.85083	1.87083	1.89083	1.91083	1.93083
4	3.60391	3.64391	3.68391	3.72391	3.76391	3.80391
6	5.33711	5.39711	5.45711	5.51711	5.57711	5.63711
8	7.03346	7.11346	7.19346	7.27346	7.35346	7.43346
10	8.69397	8.79397	8.89397	8.99397	9.09397	9.19397
12	10.31938	10.43938	10.55938	10.67938	10.79938	10.91938
14	11.91040	12.05040	12.19040	12.33040	12.47040	12.61040
16	13.46769	13.62769	13.78769	13.94769	14.10769	14.26769
18	14.99193	15.17193	15.35193	15.53193	15.71193	15.89193
20	16.48376	16.68376	16.88376	17.08376	17.28376	17.48376

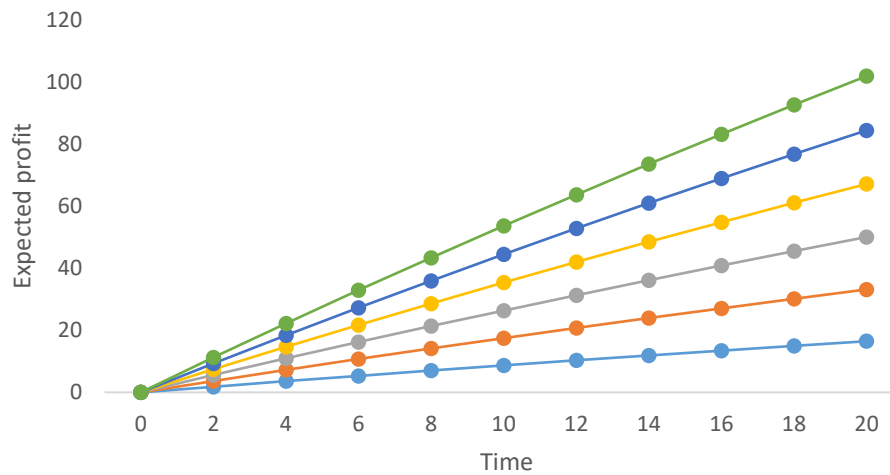


Figure 8.Expected profit for repair policy obeyed by general distribution versus time t

5. Results discussion

The decision-making process for performance evaluation of the model under consideration is carried out based on Tables 1-7 and Figures 2-8. First and foremost, failure rates must be determined, preferably ones with the lowest risk of error.

Figure 2 and Table 1 show the system’s availability when repair policy is followed by copula which reduces and eventually stabilizes as time passes in all the scenarios studied. This analysis demonstrates that the system’s performance can be simply deduced at any point in time. Table 1 and figure 2 also revealed that the failure rates with the highest availability are the failure rates of processor 1 and 2 and conveyor 1, respectively. So, it is required to start enhancing the performance of the system from these subsystems. Similar trend is observed in Figure 3 and table 2 when the repair is done via general distribution. The system’s availability for copula repair appears to be greater than its availability for general repair, implying that copula repair is preferable to general repair. For the system under copula and general repair, four different cases (1 to 4) are considered to see the impact of change in failure rate of unit in some subsystems on system effectiveness and performance optimization. As

can be seen in tables and figures where case 4 has the highest availability due to nonfailure of unit 1 and 2, conveyor 1 and 2, unit 3 and 4. This will allow the plant management to lay emphasis on regular inspection, condition base maintenance, both online and offline preventive maintenance to avoid sudden system failure that can be detrimental to the system, costly, low production output, inadequate product quality as well as less revenue mobilization.

When the repairs vanished to zero, and the failure rates are set as: $\eta_5 = 0.05$, $\eta_1 = 0.01$, $\eta_3 = 0.03$, $\eta_2 = 0.02$ and $\eta_4 = 0.04$, Figure 4 and Table 3 for system reliability. The reliability of various failure rates degrades drastically over time, as shown in this table 3 and figure 4. This analysis illustrates the consequences of failing to restore the system. It is widely believed that the higher the maintenance, the greater the reliability is. The table and figure show that system reliability decreases dramatically with time, from maximum level 1.0000 to 0.10826. This enables the plant management to choose the best time to perform PM. According to the table and figure, it is worthwhile to perform preventive maintenance on the system at regular intervals [4, 6].

Table 4 and figure 5 show the diversity of critical reliability measures viz, mean time to failure. With rising

values of $\eta_j, j = 1, 2, 3, 4, 5$, it is discovered that the MTTF decreases. This implies that the system MTTF can be enhanced on decreasing the values of $\eta_j, j = 1, 2, 3, 4, 5$. According to table 4 and figure 5, the MTTF is higher at the start of system operation and gradually decreases as the system's life span begins to deteriorate with increasing unit/subsystem failure rates. However, when compared to the MTTF of other units/subsystems, the conveyor 2 has the lowest value of 8.37329 because the failure rate is 0.10. This clearly demonstrates the disparity in MTTF values. The problem can be avoided by implementing various maintenance strategies such as the use of fault tolerant units, applying the k-out-of-n: G policy to the system's units, regular inspection, and preventive maintenance prior to system failure.

The information on sensitivity analysis explored in this study is presented in table 5 and figure 6. It is a way of telling the outcome of a choice based on a set of variables. The negative signs in this table and figure suggest that when the value of the system parameters (failure rates) increases, the performance indices decrease.

The change in the profit with passage of time t for $Z_2 \in [0.01, 0.06]$ when Z_1 is fixed at 1 for repair policy of copula as shown in Figure 7 and Table 6. Figure 7 and Table 6 show that increasing the duration (time) and decreasing the service rate/cost will likely raise the estimated profit. Table 7 and Figure 8 show the same outcome with the repair policy of general distribution. When comparing the two procedures: repair policy of general and copula distributions, it appears that the predicted profit is larger when the repair policy follows copula distribution, and becomes lower when the repair follows general distribution. In both circumstances, the predicted profit is highest when the service cost is lowest, and lowest when the service cost is highest. This analysis will assist the analysts to set the budget for the system's smooth operation in advance based on the system's usability.

6. Conclusion

The availability, reliability, maintenance strategy/technique, and revenue generated are some of the factors that influence the development of any process sector. So, in order to get the most out of operating production systems, they must be meticulously maintained so that the rate of failure and repair is kept to a minimum. In this manner, various maintenance policies or tactics can be planned to improve system strength and performance. As a result of the preceding, this paper presents evaluation of performance of a series-parallel manufacturing system through copula characteristics. The inclusion of copula characteristics has increased the application of the developed model to a wider range of performance analysis of repairable systems operating under repair policy of copula and general repair. System MTTF, availability, cost function, sensitivity, and reliability explicit expressions are established and statistically validated. Based on the availability analysis, the failure rates priority for each subsystem are identified. Through the cost function analysis, it has been discovered that higher cost of services entailed lower system profit and vice versa. On the basis of

availability and cost analysis, repair policy of copula distribution enhanced system profit and availability than repair policy of general distribution. These are the contributions of this study. This work can be extended by incorporating offline and online preventive maintenance.

Conflicts of interests

The authors declare that there is no conflicts of interest with regard to this manuscript

References

- [1] Aggarwal, C., Ahlawat, N., & Malik, S. C. Profit analysis of a standby repairable system with priority to preventive maintenance and rest of server between repairs. *Journal of Reliability and Statistical Studies*, 14(1), 57–80, (2021). <https://doi.org/10.13052/jrss0974-8024.1414>
- [2] Alazzam, A and Tashtoush, T. Lead-free solder reliability modeling using adaptive neuro fuzzy inference system (ANFIS), *Jordan Journal of Mechanical and Industrial Engineering*, 15(2), 181-189, (2021).
- [3] Aly, M.F., Afefy, I.H., Abdel-Magied, R.K and Abd Elhalim, E.K. A Comprehensive model of reliability, availability, and maintainability (RAM) for industrial systems evaluations, *Jordan Journal of Mechanical and Industrial Engineering*, 12(1), 59 – 67, (2018).
- [4] Batra, S., Malhotra, R. (2021). Reliability and Availability Analysis of a Standby System of PCB Manufacturing Unit. In: Panchal, D., Chatterjee, P., Pamucar, D., Tyagi, M. (eds) *Reliability and Risk Modeling of Engineering Systems*. EAI/Springer Innovations in Communication and Computing. Springer, Cham. https://doi.org/10.1007/978-3-030-70151-2_6
- [5] Chang, P.C., Lin, Y.K and Chen, J.C. System reliability for a multi-state manufacturing network with joint buffer stations, *J Manuf Syst*; 42: 170–178, (2017).
- [6] Chen Z., He Y., Zhao Y., Han X., He Z., Xu Y and Zhang A. Mission reliability evaluation based on operational quality data for multistate manufacturing systems, *International Journal of Production Research*, 57:6, 1840-1856, (2019). DOI: 10.1080/00207543.2018.1508906.
- [7] Chopra, G and Ram, M. Reliability measures of two dissimilar units' parallel system using Gumbel-Hougaard family copula, *International Journal of Mathematical, Engineering and Management Sciences* Vol. 4, No. 1, 116–130, (2019). DOI: 10.33889/IJMEMS.2019.4.1-011.
- [8] Garg, S., Singh, J and Singh, D. V. Availability analysis of crank-case manufacturing in a two-wheeler automobile industry. *Applied Mathematical Modelling*, 34, 1672–1683, (2010).
- [9] Gulati, J., Singh, V.V., Rawal, D.K. and Goel, C.K. Performance analysis of complex system in series configuration under different failure and repair discipline using copula', *International Journal of Reliability, Quality and Safety Engineering*, Vol. 23, No. 2, pp.812–832, (2016).
- [10] Gahlot, M., Singh, V. V., Ayagi, H.I., and Goel, C.K. Performance assessment of repairable system in series configuration under different types of failure and repair policies using copula linguistics. *International Journal of Reliability and Safety*. 12(4), pp. 367-374, (2018).
- [11] Gahlot, G., Singh, V. V., Ayagi, H. I., Abdullahi, I. Stochastic Analysis of a two units' complex repairable system with Switch and Human failure using Copula Approach, *Life Cycle Reliability and Safety Engineering*. Vol. 9(1), pp. 1-11.

- [12] He, Y., Gu, C., Han, X., Cui, J and Chen, Z. Mission reliability modeling for multi-station manufacturing system based on Quality State Task Network. *Proc. Inst. Mech. Eng. Part O J. Risk Reliab.* ;231: 701–715, (2020). doi: 10.1177/1748006X17728599.
- [13] He, Y., Han, X., Gu, C and Chen, Z. Cost-oriented predictive maintenance based on mission reliability state for cyber manufacturing systems. *Adv Mech Eng*; 10(1),1–15, (2018).
- [14] Kadyan, M. S., & Kumar, R. Availability and profit analysis of a feeding system in sugar industry. *International Journal of System Assurance Engineering and Management*, 8(1), 301-316, (2015).
- [15] Kumar, A., Pawar, D. & Malik, S.C. Profit analysis of a warm standby non-identical unit system with single server performing in normal/abnormal environment. *Life Cycle Reliab Saf Eng* 8, 219–226 (2019). <https://doi.org/10.1007/s41872-019-00083-2>
- [16] Kumar Ashok, Malik SC, Pawar Dheeraj. Profit analysis of a warm standby non-identical units system with single server subject to priority. *Int J Future Revolut Comput Sci Commun Eng* 4(10):108–112, (2018).
- [17] Lu., B and Zhou., X. Quality and reliability-oriented maintenance for multistage manufacturing systems subject to condition monitoring. *J. Manuf. Syst.*; 52:76–85. doi: 10.1016/j.jmsy.2019.04.003.
- [18] Lado A., and Singh, V. V. Cost assessment of complex repairable systems in series configuration using Gumbel Hougaard family copula. *International Journal of Quality and Reliability Management*. 36(10), pp. 1683-1698, (2019).
- [19] Mehta, M., Singh, J and Sharma, S. (2018). Availability analysis of an industrial system using supplementary variable technique, *Jordan Journal of Mechanical and Industrial Engineering*, 12(4), 245-251.
- [20] Nelson, R.B. (2006) *An Introduction to Copulas*, 2nd ed., Springer Publisher, New York.
- [21] Niwas R and Garg, H. An approach for analyzing the reliability and profit of an industrial system based on the cost free warranty policy. *J Braz Soc Mech Sci Eng* 40:265, (2018). <https://doi.org/10.1007/s40430-018-1167-8>
- [22] Ram, M and Goyal, N. Bi-directional system analysis under copula-coverage approach. *Communications in Statistics-Simulation and Computation*, 47(6), 1831-1844, (2018).
- [23] Sha, N. A Copula Approach of Reliability Analysis for Hybrid Systems. *Reliability: Theory & Applications*, 16(1), 231-242, (2021).
- [24] Sanusi, A., Yusuf, I. Reliability assessment and profit analysis of distributed data center network topology. *Life Cycle Reliab and Saf Eng* (2022). <https://doi:10.1007/s41872-022-00186-3>.
- [25] Singh, V. V., Ayagi, H. I. Study of reliability measures of system consisting of two subsystems in series configuration using copula. *Palest J Math*, 6(1), 1-10, (2017).
- [26] Singh, V. V., and Ayagi, H.I. Stochastic analysis of a complex system under preemptive resume repair policy using Gumbel Hougaard family copula. *International Journal of Mathematics in Operational Research*. 12(2), pp. 273-292, (2018).
- [27] Tyagi, V., Arora, R., Ram, M., Triantafyllou, I. S. Copula based Measures of Repairable Parallel System with Fault Coverage. *International Journal of Mathematical, Engineering and Management Sciences*. (2021). DOI:10.33889/IJMEMS.2021.6.1.021.
- [28] Temraz, N. S. Y. Availability and reliability of a parallel system under imperfect repair and replacement: analysis and cost optimization. *Int J Syst Assur Eng Manag* 10:1002–1009, (2019). <https://doi.org/10.1007/s13198-019-00829-2>
- [29] Ye, Z., Cai, Z., Si, S., Zhang, S and Yang, H. Competing Failure Modeling for Performance Analysis of Automated Manufacturing Systems with Serial Structures and Imperfect Quality Inspection, *IEEE Transactions on Industrial Informatics*, vol. 16, no. 10, 6476-6486, (2020). doi: 10.1109/TII.2020.2967030.
- [30] Ye, Z., Cai, Z and Yang, H. Reliability Analysis of Manufacturing Machine with Degradation and Low-quality Feedstocks," *2020 Asia-Pacific International Symposium on Advanced Reliability and Maintenance Modeling (APARM)*, 2020, pp. 1-5, doi: 10.1109/APARM49247.2020.9209452.
- [31] Yusuf, I., Ismail, A. L., Singh, V. V., Ali, U. A., Sufi, N. A. (2020). Performance Analysis of Multi-Computer System Consisting of Three Subsystems in Series Configuration Using Copula Repair Policy. *SN Computer Science*, Vol. 1(5), pp. 1-11.
- [32] Yusuf, I and Ismail, M. M. (2021) Availability analysis of a complex system consisting of two subsystems in parallel configuration with replacement at failure. *Int J Math Operational Res* 19:1–21
- [33] Zhang, H, Li., A.P and Liu., X.M. Modeling and performance evaluation of a multistage serial manufacturing system considering rework and product polymorphism. *Chin J Mech Eng*; 53: 191–201, (2017).

Effects of Using a Special Car Cover on the Temperatures and Cooling Load Inside a Parked Car Under Severe Summer Conditions; Iraq Case of Study

Hasan Abbas Hussein^{1*}, Issam M. Ali Aljubury²

MSc Student Assistant Professor

^{1,2}Mechanical Engineering Department, College of Engineering, University of Baghdad, Baghdad, Iraq

Received 29 May 2022

Accepted 5 Sep 2022

Abstract

Summer in Iraq is extremely hot and dry, with temperatures reaching around 50 °C with extremely dry conditions. Due to a shortage of shaded parking spots, many drivers park their automobiles in the sunlight. Many of those drivers complain about the heated interior temperature of their vehicles after a few hours of parking. This issue is not only harmful to the driver and passengers, but it also causes damage to the vehicle's components. Furthermore, the high temperature inside the compartment implies a large cooling load in order to keep the cabin at thermal comfort limits. In the present study, a special car cover was suggested to reduce the high temperature inside the car cabin. Different arrangements of the suggested cover with window openings have been examined. The results revealed that in the unshaded situation, the temperature of the air inside the cabin could reach 74.8 °C, and the dashboard temperature could reach up to 93 °C. The optimum solution was found by covering all windows, with opening the windows by 15 mm. This solution reduced the average inside air temperature to 53.3 °C, representing 20.8 % lower than the unshaded case and 7.4 °C higher than the average ambient temperature. It also led to about 32.3 % reduction in the average cooling load compared to the unshaded case.

© 2022 Jordan Journal of Mechanical and Industrial Engineering. All rights reserved

Keywords: Parked Car, External Car Cover, Cabin Temperature, Thermal Comfort, Cooling Load, Dashboard Temperature, Vehicle Cabin.

Nomenclature

$c_{p,a}$	Air specific heat at constant pressure (J/kg.K)
\dot{m}	Mass flow rate of the AC (air conditioning) ventilation air (kg/s)
Q_{sens}	Sensible cooling load (W)
$T_{a,avg}$	Average temperature of the inside air (°C)
T_{amb}	Ambient temperature (°C)
T_{case}	Temperature of measuring points in each case (°C)
T_{comf}	Air temperature at thermal comfort level (°C)

1. INTRODUCTION

In hot weather conditions such as in Iraq, when the temperature in summer reaches 50 °C, the temperature inside a parked car during summer could rise to 70 °C [1], [2], [3]. One of the solutions that the drivers do is to use internal sunshades, due to the lack of shaded parking areas. That temperature rise could be harmful to both the driver and passengers since the solar radiation during summer in Iraq and near countries that penetrates the cabin is at high levels, around 1000 W/m² [4], [5], [6]. According to a study

by [7], among 23 incidents, about 40 fatalities were reported due to hyperthermia between 2011-2020 in India. These incidents involved children between 4 to 6 years old who got locked inside the car accidentally. In addition, the high temperature inside the cabin could cause damage to the components of the cabin. Also, the heating, ventilation, and air conditioning (HVAC) system will require more energy to reach thermal comfort. Consequently, this increase in energy leads to more fuel consumption.

To reduce the high temperature inside the cabin, the researchers have studied the effects of some passive methods, such as sunshades, ventilation systems, solar reflecting cover and films, window gaps, etc. on the cabin soak temperature. Figure 1 shows some of these passive methods.

Some researchers have conducted some experiments to study the soak temperature of a car's cabin when parked under the direct sun. The results indicated that the maximum temperatures inside the cabin were at the dashboard, the steering wheel, and the inside air by 87.5 °C, 60 °C, and 59 °C respectively. The application of the sunshades reduced the dashboard's temperature by about 21.7% and the steering wheel by 7%; however, it was not effective with the air temperature [8]. Another study showed the effect of a ventilation system consisting of a PV panel and a set of DC fans to extract the hot air from

* Corresponding author e-mail: h.hussien1303@coeng.uobaghdad.edu.iq.

the cabin and supply fresh air. Without the ventilation system, the air temperature inside the cabin was about 66 °C, representing 22 °C above the ambient temperature, while installing the ventilation system reduced the temperature difference between the cabin and the ambient to 10 °C [9]. Another study used solar panels to run a mini air cooler installed on the dashboard to reduce the high temperature resulting from parked under the sunlight. They used two cars, and only one car was equipped with mini air cooler. Before using the mini air cooler, both cars reached same cabin temperature of 56 °C after being soaked in the sun. The results showed that the car with the mini air cooler experienced about 6°C reduction in the cabin temperature without adding fresh air [10]. Other researchers used the mini air cooler and exhaust fans with the PV panels to extract the hot air and replace it with fresh air. The mini air cooler is an evaporative cooler with a wet foam so that the water evaporates when the hot air passes through it. Without the proposed device, the cabin temperature reached about 57 °C after 7 hours of soaking in the sun. With the help of the suggested system, the cabin temperature was reduced by about 10 °C. Furthermore, the amount of heat rejected by this system was about 0.356 kW [11]. Other researchers investigated the effect of solar reflective cover and the solar reflective film on the air temperature inside the cabin. They found that the highest air temperature in the car with the solar reflective cover was about 45.6 °C, while the maximum air temperature in the car with the solar reflective film was about 60.1 °C, indicating a 14.5 °C difference between the two approaches [12]. Others studied the effects of solar radiation on the soak temperature, and they found that the air temperature inside the cabin could reach 70 °C and about 100 °C at the dashboard. To reduce this increase in temperature, they suggested a cover on the windows with lowering the side windows by 1 cm. They found that using the cardboard inside the cabin did not reduce the cabin air temperature, but it reduced the dashboard's temperature by 40% from the unshaded case. In addition, the cardboard from outside the windscreen, with lowering the side windows by 1 cm, reduced the average maximum temperature in different locations inside the car cabin. [1]. Another study on heat accumulation and temperature variations was done by [13], which involved different methods to reduce the high temperature inside the compartment such as sunshades and window openings. The findings showed that opening the front windows by 20 mm resulted in a 10 °C drop in front air temperature compared to the case of the closed windows. While utilizing a sunshade beneath the front windscreen reduced the dashboard by 25 °C. The effect of solar reflectance on the soak temperature has been studied by [14]. They used two identical cars, one was black and the other was silver. For the black car, it was found that the maximum temperature was located on the roof. On the other hand,

the maximum temperature in the silver car was found on the black dashboard. That was due to the reflectance of the silver car being higher than the black one, so it reflects more solar radiation. The maximum temperature difference between the black and silver cars was 25 °C at the roof. Also, the difference between the ceiling temperature in the two cars was 11 °C, and it was less than 5°C and 2 °C, in the dashboard and the windshield, respectively. Table 1 provides a summary of prior experimental research, as well as the technique employed and the reduction in air temperature attained. The summary focused solely on the air temperature because it is the most essential parameter in estimating the cooling load needed to maintain thermal comfort within the automobile cabin. The present paper research will investigate experimentally the temperature patterns inside a parked automobile, and the effects of various arrangements of a suggested automobile cover on temperature and cooling loads. Seven distinct parking setups were tested, with and without externally and internally sunshades, and in various cover and window gap combinations have been studied. Also, the research focuses on the difference between the internal and external shading on the temperatures inside the cabin.

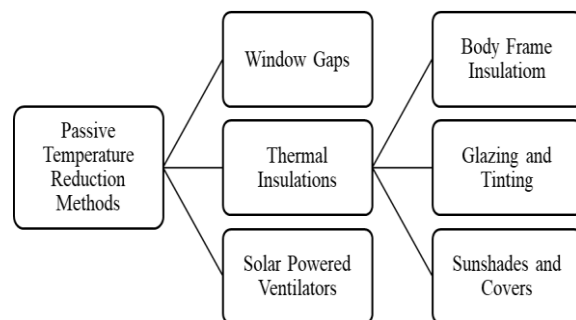


Figure 1. Passive temperature reduction methods.

2. METHODOLOGY

2.1. Materials

The test vehicle for this study was a yellow SAIPA 131. The vehicle was oriented South, as shown in Figure 2 to ensure full sun exposure for the whole period of the test. The car was parked in an open area in Amarah, Iraq (31.8 N, 47.1 E) and it was ensured that there was no shading on the car during the tests. Before each test, the doors and the windows were opened for 30 minutes to let the temperature of the cabin reach a steady-state temperature with the ambient.

Table 1. Summary of the previous experimental research on the air temperature inside the car cabin

Approach	Setup	Maximum Reduction(°C)	Maximum Ambient Temperature(°C)	Reference
Sunshades	All windows	19	n/a	[8]
	Under the front windshield	0	44	[1]
	Front windshield only	6.2	34	[16]
Cover	Cover on all vehicle	30.5	23.1	[17]
	On the roof and all windows	13.4	36	[12]
Tinted Glass	All windows	5.3	n/a	[8]
Solar Reflective Glass	SRF on all glazing	4.6	46.1	[18]
	SRF all glazing except the windshield	0	36	[12]
	Increasing the reflectivity from 0.05 to 0.58	6	36	[14]
Window Gap	All windows 4 cm	12.4	34	[16]
	front windows by 2 cm	10	n/a	[13]
	Driver's window by 2.5 cm	3	45	[19]
	Driver's window by 5 cm	6-7		
PV powered ventilators	On all windows	3.3	n/a	[8]
	Two fans to exhaust hot air and one fan to supply fresh air	10	44	[9]
	Using blower evaporator with a mass flow rate of 0.0114 kg/s	9.5	35	[20]
Solar Chimney		20.5	36	[21]
PCM Insulation	Inserting PCM materials under the roof	15	23	[22]

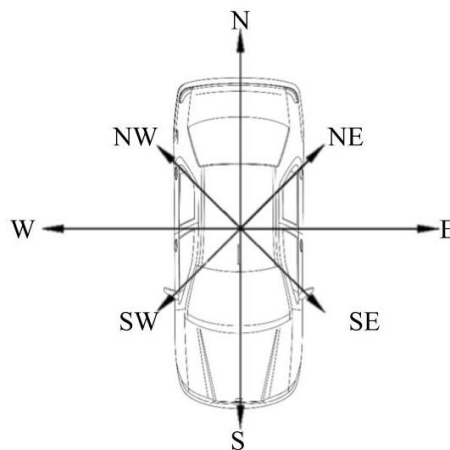


Figure 2. Direction of the test vehicle.

2.2. Measurements and Instruments

In order to take measurements for the temperature, six thermocouples of type K were placed inside the car. The accuracy of the thermocouples is within ± 0.75 °C and the range of measurement within $-50 \sim 204$ °C. Only one of them was set to measure the air temperature, and it was hung in the middle of the cabin at 5 cm below the ceiling. The other thermocouples were set to measure the temperature of the internal components such as the dashboard, steering wheel, windshield, and front seats. The locations of the thermocouples are shown in **Figure 3**. and Table 2. The thermocouples attached to the surfaces were covered with opaque adhesive tape to prevent the influence of solar radiation. To collect data, the thermocouples were connected to a 12-channel data logger (BTM-4208SD). The data logger has a measuring range of $-100 \sim 1300$ °C with a resolution of 0.1 °C and an accuracy of ± 0.5 °C. The temperature was recorded at an interval of 10 minutes from the start to the end of each test. Figure 4. shows a type-K thermocouple and the data logger. The measurements were taken from 8 A.M to 5 P.M.

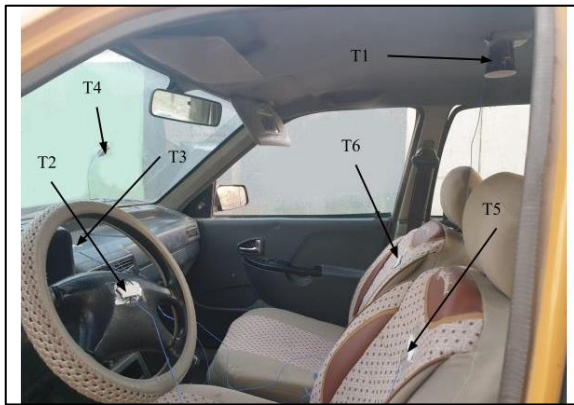


Figure 3. Locations of the thermocouples inside the cabin.

Table 2. Location of the thermocouples inside the cabin.

Thermocouple	Measuring type	Location
T1	Air	Middle of the cabin, 5 cm below the ceiling.
T2	Surface	Steering Wheel
T3	Surface	Dashboard
T4	Surface	Front Windshield
T5	Surface	Passenger Seat
T6	Surface	Driver Seat

2.3. Special Car Cover

A special car cover was suggested to reduce the temperature inside the cabin. The cover is available commercially and it is made of polyethylene foam of 5 mm thickness with a thin aluminum foil on the top side, then another layer of cloth was added to the bottom side of the cover. The cover was cut into the shape of the windows and the windshields only since a high percentage of the solar radiation that falls on the vehicle passes through the glass into the cabin. The cover consists of 4 pieces, 2 for the side windows and 2 for the windshields. Figure 5. (a & b) shows two sides of the cover.

The advantages of this cover compared to the traditional car cover are [1]:

- Lighter and smaller.
- Relatively cheap and easy to assemble.
- Reflect solar radiation.
- Provide thermal insulation.



Figure 4. Measuring instruments: (a) data logger, (b) type-K thermocouple.

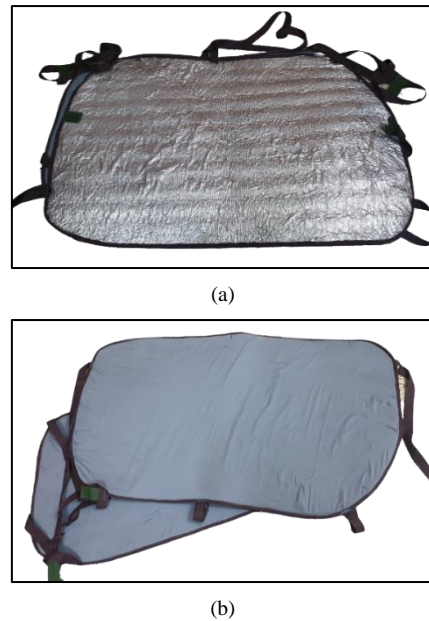


Figure 5. The suggested car cover: (a) front side, (b) back side

2.4. Climate Conditions

Iraq weather is known for the high temperatures and dryness in summer, especially the south region (Amarah city), where the temperature hit 50 °C. Figure 6. and Figure 7. show the ambient temperature and relative humidity for each day of the experiments, respectively. The average wind speed during test days was around 2.6 m/s. For all cases, the meteorological data was taken from the Iraqi Meteorological Organization & Seismology, and it included ambient temperature, relative humidity, and wind speed. The solar radiation intensity was obtained from Metonorm software and it is shown in Figure 8.

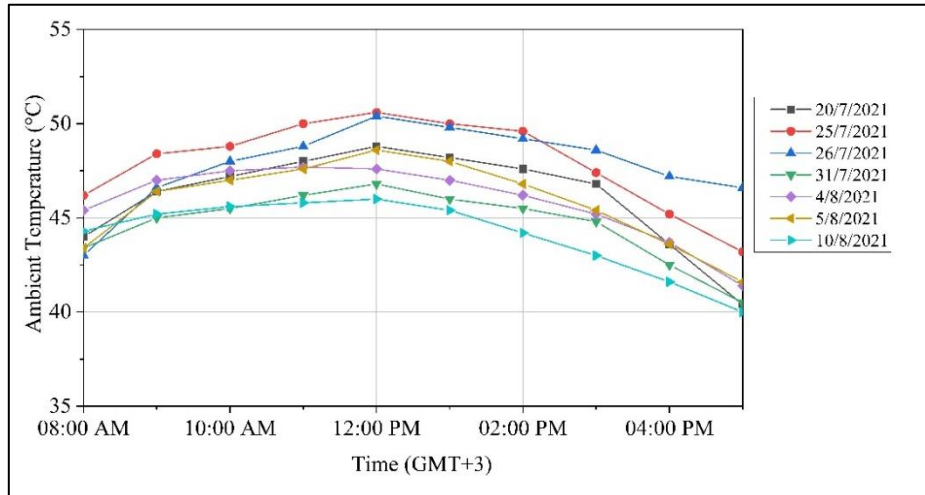


Figure 6. Ambient temperature during the test days.

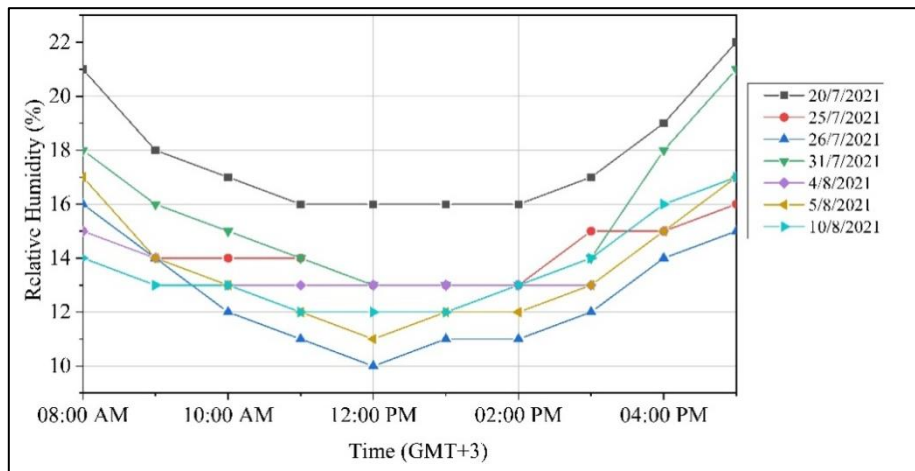


Figure 7. Relative humidity during the test days.

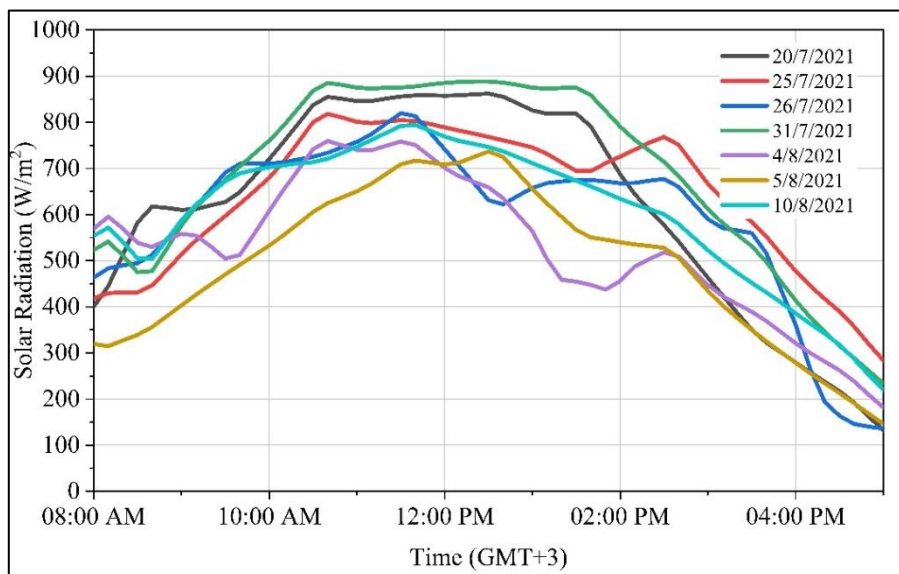


Figure 8. Global horizontal radiation during the test days.

2.5. Experimental Procedure

Seven different parking cases under direct exposure to sunlight were conducted between July and August of 2021, in which the effects of different arrangements of special car cover with window openings were studied.

The cases can be summarized as follows, see Table 3:

Case #1: In this case, no shading and windows opening were employed and it was considered as the base case.

Case #2: The second case was conducted with windows opened 15 mm only, without any shading.

Case #3: only shades were used and the cover was externally placed above the front and rear windshields (partially shaded).

Case #4: Windows were opened 15 mm and the cover was externally placed above the front and rear windshields (partially shaded). The vehicle with the cover used for cases #3 and case #4 is shown in Figure 9.

Case #5: All windows and the windshields were covered (totally shaded) and the windows were 15 mm open.

Case #6: All windows and the windshields were covered (totally shaded) and the windows were closed.

The vehicle with the cover used for case #5 and case #6 is shown in Figure 10.

Case #7: In the last case, the cover was internally placed beneath the front and rear windshields. The vehicle with the cover used for case #7 is shown in Figure 11.

Table 3. Summary of the studied cases.

Case	Parking setup			
	All windows open 15 mm	Shading above the windshields	Shading beneath the windshields	Shading on all the glass
Case #1				
Case #2	✓			
Case #3		✓		
Case #4	✓	✓		
Case #5				✓
Case #6	✓			✓
Case #7			✓	



Figure 9. The external cover above the windshields.



Figure 10. The external cover on all glass.



Figure 11. The internal cover beneath the windshields.

3. Results and Discussion

The cases were carried out on the hottest days of the summer in Iraq during July and August during the period from the 20th of July to the 10th of August. Each test was carried out for 9 hours of soaking in the sun from 8 A.M. to 5 P.M. The results of these cases are presented below.

3.1. Temperature Variations

The temperature of each measuring point was plotted for different cases to indicate the temperature reduction obtained from each case. Figure 12. shows a summary of the average temperature reductions of the measuring points compared to the base case.

3.1.1. Inside Air Temperature:

Figure 13 shows the inside air temperature of all cases. It is clear that the temperature was the highest in the cases with no covers; case #1 and case #2. The temperature in

case #1 reached about 75 °C, while in case #2 it was about 73 °C. The temperature curves in these two cases are rising steeply until reaching the maximum temperature, then they start to decrease in the afternoon. Also, the cases with a car cover on the windshields only (case #3, case #4, and case #7) all have similar behavior with a maximum temperature less than the first two cases. The last two curves represent case #5 and case #6, where full coverage on all windows was used, but only in case #5, the windows were opened. The temperature in these two cases (#5 and #6) has the minimum peak temperature (60.9 °C in case #5 and 58.2 °C in case #6). It can be seen that in the cases without the car cover (#1 and #2), solar radiation has a significant effect on the temperature inside the car cabin. The high intensity of solar radiation that penetrates the walls and windows of the cabin warms up the surfaces and components inside thus increasing the temperature of these surfaces. While using the car cover, a large percentage of solar radiation is being blocked and is not transmitted through the windows.

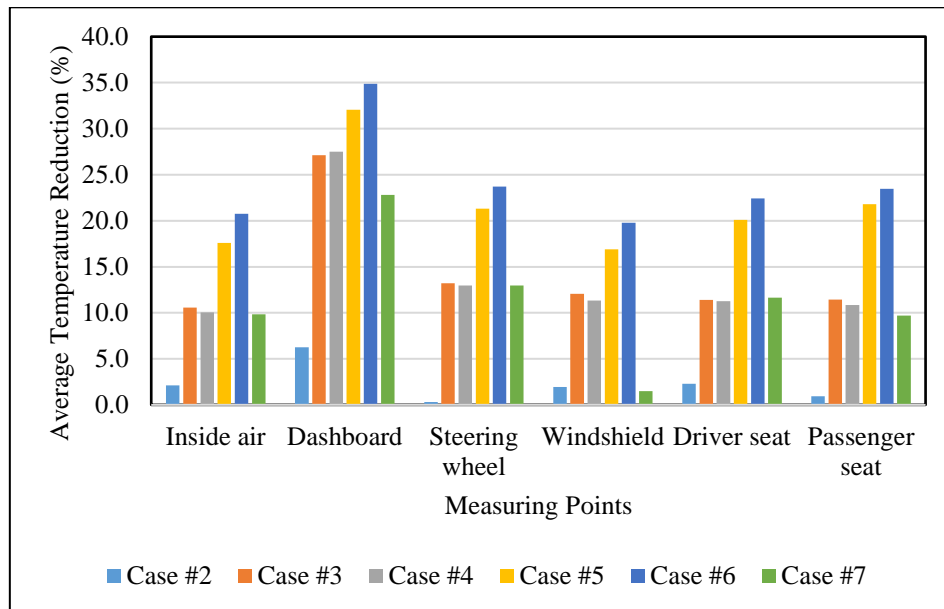


Figure 12. Average temperature reductions of the measuring points compared to the base case.

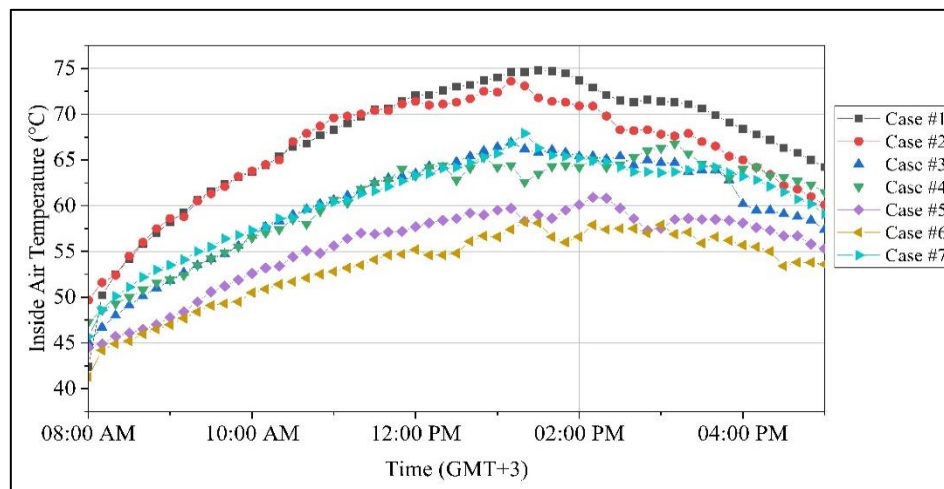


Figure 13. Car cabin inside air temperature.

3.1.2. Dashboard Temperature:

As the dashboard is located beneath the front windshield, it receives the most solar radiation transmitted through it, consequently, having a higher temperature than other components inside the cabin. As shown in **Figure 14**, the maximum temperature of the dashboard in case #1 is about 92.8 °C, while in case #2 when the windows were opened, the air was allowed to exchange with surrounding air due to air movement, and the temperature dropped to a maximum of 86.1 °C. The temperature curves in these two cases are rising steeply until reaching the maximum temperature, then they start to decrease in the afternoon. The effect of using the car cover from the outside is more obvious in the temperature of the dashboard. The temperature dropped from 86.1 °C in case #2 to 66.3 °C in case #3 due to the usage of the external car cover on the windshields which blocked the solar radiation that enters the cabin through them. In case #4, in addition to the cover on the windshields, the side windows were also opened, and the average temperature drop was about 25 % compared to case #1. Further decrease in temperature was achieved by using full cover in case #5, which reached a maximum of 59.4 °C since more solar radiation has been blocked from penetrating the glass, while with the opening of the windows in case #6 it dropped further to 56.5 °C due to the air circulation between the cabin and the ambient. Using the cover internally beneath the windshields in case #7 resulted in a slightly higher temperature in most measuring points compared with using a car cover on the external side of windshields. As

the cover is beneath, the windshield still absorbs some solar radiation that causes the temperature inside the cabin to rise.

The cover on all windows (case #5) reduced the average temperature of the dashboard by about 32% from the base case, while [8] achieved only a 21% reduction.

3.1.3. Steering Wheel Temperature:

As in the dashboard, the steering wheel is also subjected to a large amount of solar radiation that is transmitted through the windshield. As shown in **Figure 15** the temperature in case #2 was higher than in case #1 before the afternoon, but after the afternoon, it starts to decrease more rapidly in case #1. The maximum temperatures in case #1 and case #2 were 77.3 °C and 78.5 °C, respectively. The external sunshades on the windshields in case #3 led to a significant drop in the average temperature, about 13.2% relative to case #1 as shown in **Figure 15**. The temperature curves with the external and internal sunshades have similar patterns and have maximum temperatures lower than in the first two cases, about 65.5 °C and 65.4 in case #3 and case #7, respectively. The average temperature drops while using the external sunshades on the windshields with opening the windows by 15 mm (case #4) was about 12.9 % relative to case #1. In cases 5 and 6, a further reduction in temperature was achieved by using the sunshades on all windows. In case #5, the average temperature decrease was about 21.3 % and about 23.7 % in case #6, compared to case #1.

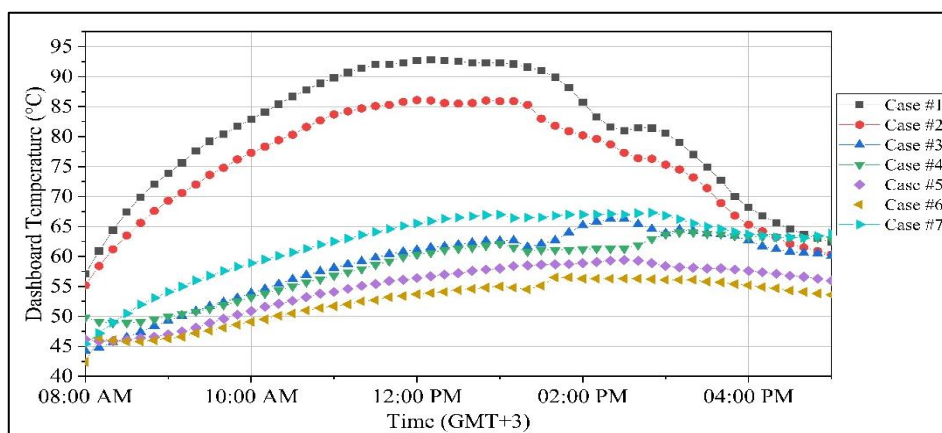


Figure 14. Dashboard temperature.

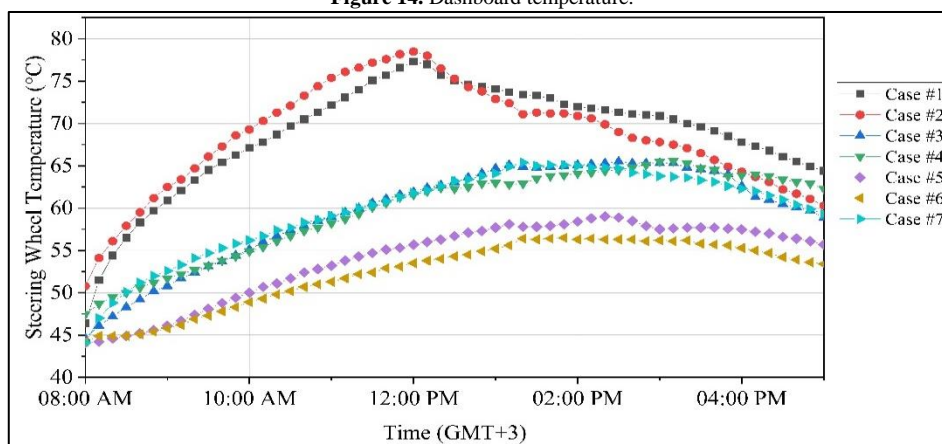


Figure 15. Steering wheel temperature.

3.1.4. Windshield Temperature:

The windshield represents the largest glazed area in the car which through the solar radiation enters the cabin. In addition to the ability of the glass to transmit solar radiation, it also absorbs some of that radiation, which leads to an increase in the temperature of the windshield. From **Figure 16** it can be seen that the windshield temperature could reach 74.6 °C in case #1. The curve of case #2 with windows openings looks almost similar to case #1 curve with an average temperature difference of 2% less than case #1. It can be seen that the temperature reaches its peak between 12:00 and 1:00 PM and it drops more rapidly after the afternoon. In case #3, the temperature peak dropped to 63.6 °C. However, with the window gap in case #4, the temperature did not drop further, since the windshield is more affected by the external parameters (ambient temperature and solar radiation). Further reduction in the average temperature was achieved in case #5 and case #6, about 17 %, and 19.8 %, respectively. In these cases where the full cover was used, almost no solar radiation entered the cabin which led to an average temperature for the windshield; being about 53.5°C in case #6. Case #7 with the cover on the inside of the windshield looks similar to the first two cases, and

with a maximum temperature of 72.8 °C. That's because the cover on the inside does block the solar radiation from entering the cabin, but it does not cover the windshield, so it gets hot by absorbing a portion of solar radiation.

3.1.5. Driver Seat Temperature:

Figure 17 shows the temperature of the driver's seat. It is clear that the temperature is highest in case #1 with a maximum temperature of 71.5 °C followed by 69.6 °C in case #2, so the ventilation without covering the windows did not achieve a significant reduction in the seat temperature. In case #3, the temperature was dropped to a maximum of 64.7 °C by using the cover on the windshields. While in case #4, no considerable reduction in the temperature was obtained where the average temperature was 59.1°C which is 11.2 % lower than the average base case. A similar result was achieved in case #7 since only 11 % drop in the average temperature was achieved. The highest temperature drop compared to the base case was recorded in cases 5 and 6. In case #5, the average temperature was 53.2°C representing a 22.4 % drop in the average seat temperature. The average temperature drops in case #6 was about 22.4 %.

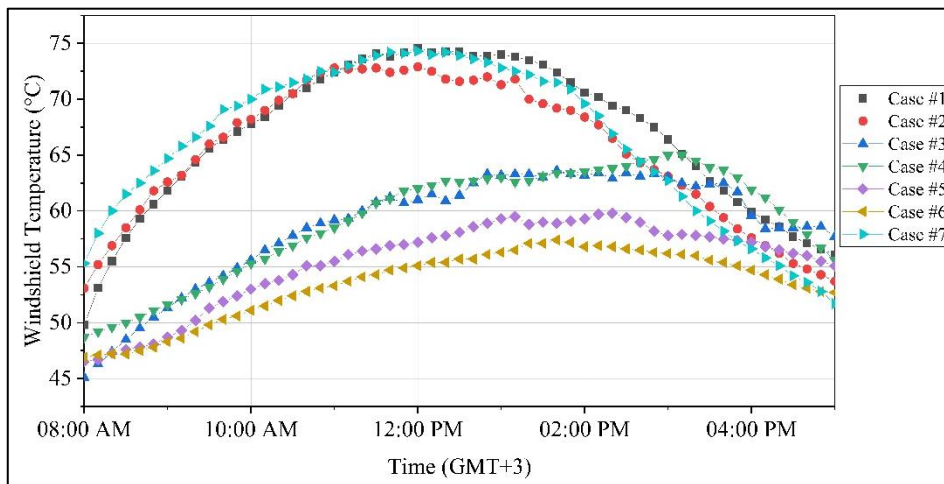


Figure 16. Windshield temperature.

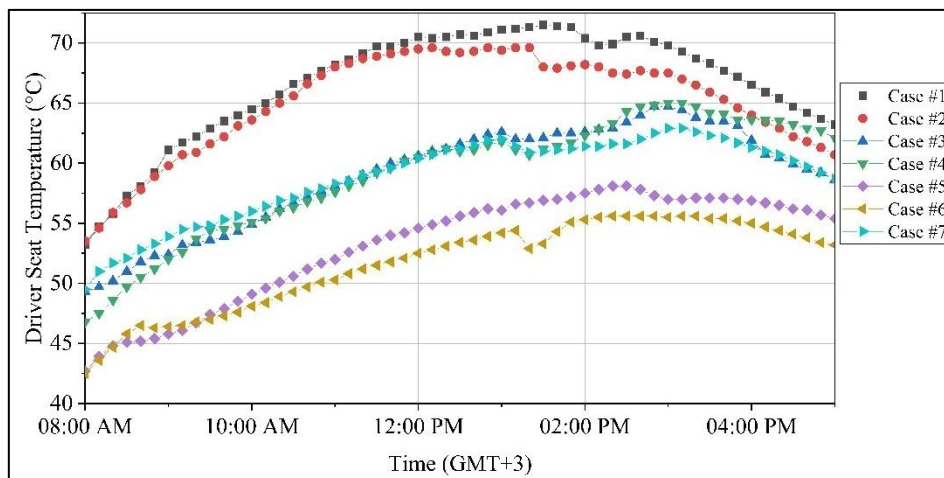


Figure 17. Driver seat temperature.

3.1.6. Passenger Seat Temperature:

The patterns of temperature in the passenger seat are comparable to those in the driver's seat. Case #1 had a maximum temperature of 73.7 °C at 1:30 PM, whereas Case #2 had a maximum temperature of 72.9 °C at 1:10 PM. As a result, opening the windows by 15 mm did not result in a significant drop in passenger seat temperature. The highest temperature in case #3 was around 67.3 °C, whereas adding ventilation air in case #4 did not result in a substantial drop in passenger seat temperature. Cases #5 and #6 exhibited much more reduction since covering all windows and windshields resulted in more sunlight being blocked. In case #5, the temperature reached a peak of 58 °C, whereas in case #6, it was 57 °C after adding ventilation air. The use of internal shading had no effect on lowering the temperature of the passenger seat. Temperatures reached greater levels than in the external shading (case #3), as indicated in Figure 18, with a maximum of 68.7 °C.

3.2. Temperature Reductions from the Ambient

Since the tests were conducted on different days, showing the obtained temperature measurements compared to the ambient would give a clear idea about the reductions achieved by the suggested solutions (the sunshades and window openings). Figure 19 shows the average temperature reduction of measuring points minus ambient temperature for all cases. For the inside air, the average temperature difference was 21.2°C in case #1, since there was no method used to reduce the inside air temperature. In case #2, the difference was also high, about 17.9 °C, since the sunlight is still entering the cabin through the unshaded glass. Using the suggested cover with opening the windows in case #6, achieved a minimum difference relative to the ambient of 7.4°C. On the dashboard, it reached the highest temperature difference between the measuring points and the ambient, since it recorded 34.4°C. Only about 27.5°C drop was achieved in case #2, thus the ventilation alone could not decrease the temperature to levels near the ambient temperature. While the lowest recorded temperature relative to the ambient was in case #6 with only 6.6°C.

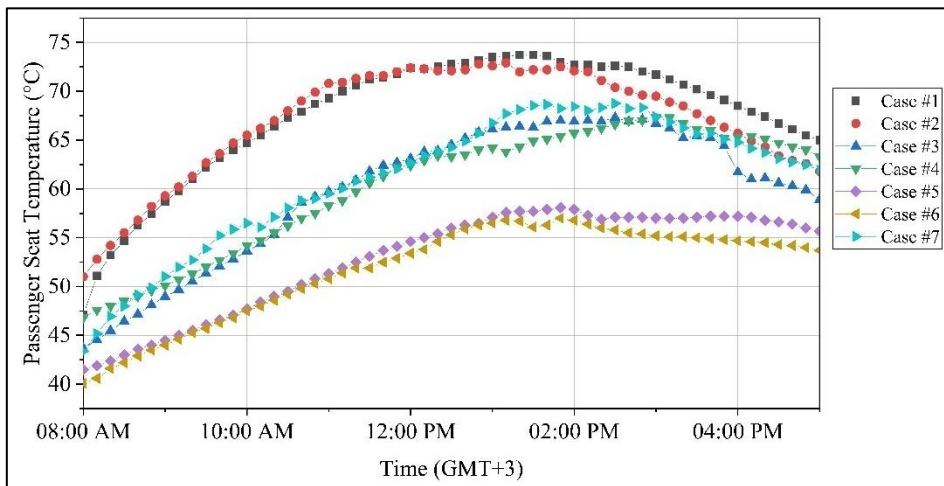


Figure 18. Passenger seat temperature.

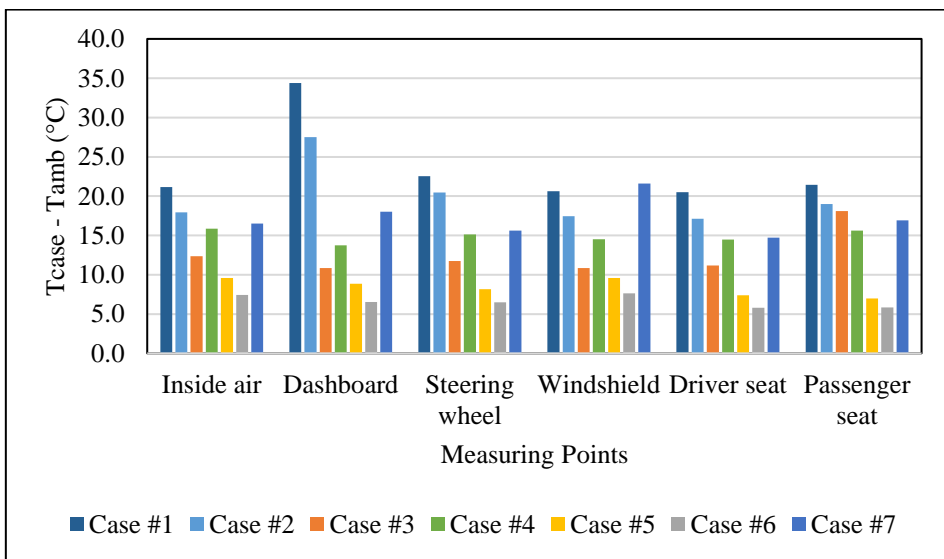


Figure 19. Reductions in average temperature of measuring points minus the ambient temperature.

The steering wheel temperature recorded a temperature difference of 22.5 °C in case #1. Cases #2, #3, and #4 had high temperatures with a difference of 20.5 °C, 11.8 °C, and 15.1 °C, respectively. On the other hand, cases #5 and #6 had the lowest temperature difference about 8.2 °C and 6.5 °C respectively. On the windshield, the high temperatures were recorded in cases #1, #2, and #4, and the recorded difference was about 20.6 °C, 17.5 °C, and 14.5 °C, respectively. However, the lowest difference was in cases #3, #5, and #6, since the temperature difference was 10.8 °C, 9.6 °C, and 7.6 °C, respectively. The front seats (driver's seat and passenger's seat) also had the highest temperature in the first 4 cases, and the lowest in cases #5, and #6. For the driver's seat, the highest temperature difference was in case #1 with about 20.5 °C, while the minimum difference was in case #6 with about 5.8 °C. The same was for the passenger's seat since the highest temperature difference in case #1 was about 21.5 °C, and the lowest was in case #6 with about 5.8 °C. It can be noticed that in all measuring points, using the internal shading (case #7) resulted in a high-temperature difference, and it was higher than the cases with external shading and window openings (cases #3, and #4). For the inside air, the difference was about 16.5 °C, and for the dashboard, it was 18 °C, while for the steering wheel and the windshield it was 15.6 °C, and 21.6 °C, respectively. For the driver's seat, it was about 14.7 °C, and for the passenger's seat, it reached 16.9 °C. Comparing the cases #3 and #4, it can be noticed that in case #3 with using the external cover on the windshields only, the maximum difference was lower than the case #4, even with opening the windows in addition to the cover on the windshields, that's due to the ambient temperature in case #3 (day 4/8/2021 in Figure 6) is lower in case #4 (day 26/7/2021 in Figure 6).

3.3. Reductions in Cooling Load

The comparison of internally (case #7), partially external (case #4), and totally external (case #6) shading relative to the baseline scenario is shown below as the research's point. Table 4 shows the average drop in interior air temperature as a result of utilizing the proposed cover, as well as the situation of using the cover inside the cabin. It also illustrates the theoretical average reduction in the cooling load that may be gained by employing this cover.

The sensible cooling load that required to bring the cabin temperature to a comfort level can be estimated from the air temperature based on Equation (1)

$$Q_{sens} = \dot{m}c_{p,a}(T_{a,avg} - T_{comf}) \quad (1)$$

Where: \dot{m} is the mass flow rate of the AC (air conditioning) ventilation air, assumed 0.055 kg/s,

$c_{p,a}$ is the specific heat of the air, computed at the average temperature (J/kg°C),

$T_{a,avg}$ is the average temperature of the inside air (°C),

T_{comf} is the air temperature at thermal comfort level, assumed to 24 °C [15]

Table 4. Average reduction in air temperature and cooling load.

Case	Average Temperature (°C)	Average Temperature Reduction (%)	Average Cooling Load (kW)	Average Cooling Load Reduction (%)
Case #1	67.3	0	2.397	0
Case #2	65.8	2.1	2.318	3.3
Case #3	60.2	10.4	2.01	16.3
Case #4	60.5	10.1	2.024	15.6
Case #5	55.4	17.5	1.742	27.3
Case #6	53.3	20.8	1.624	32.3
Case #7	60.6	9.9	2.031	15.3

As seen in the Table 4, the average temperature in the baseline case reached around 67.3 °C, resulting in a considerable average cooling load of approximately 2.4 kW. The average temperature in case #4 was around 60.5 °C, which was 10.1 % lower than in case #1. In addition, the average cooling load was roughly 2.024 kW, which represented a 15.6 % reduction over the basic case. Case #6 saw a significant fall in average air temperature, reaching 53.3 °C, reflecting a 20.8 % reduction from the base case. The average cooling load was also significantly reduced. Case #6 had an average cooling load of roughly 1.624 kW, showing a 32.3% decrease over the base case. Case #7 had an average temperature of 60.6 °C, which was 9.9 % lower than the unshaded case. Furthermore, the cooling load was 2.031 kW, which is 15.3 % less than the base scenario. As can be seen above, the greatest reductions obtained in the air temperature and cooling load were in case #6 (totally external shading with opening the windows by 15 mm). While the internal shading (case #7) could not provide a considerable reduction in both air temperature, and cooling load.

4. Conclusions

These points can be drawn from the current research:

1. The air temperature inside the cabin in the unshaded situation (case #1) could reach a level of 74.8 °C, while the dashboard temperature reached a maximum of 92.8 °C.
2. Using the suggested cover externally and on all windows while opening the windows by 15 mm (case #6) resulted in the greatest temperature drop across all measuring points.
3. In case #6, the average temperature of the inside air was reduced to 53.3 °C, representing 20.8 % lower than the unshaded case and 7.4 °C higher than the average ambient temperature, while the average temperature of the dashboard was reduced to 52.4 representing nearly 35 % lower than the unshaded case, and approximately 6.6 °C higher than the average ambient temperature.
4. Using the cover inside the cabin (case #7) did not achieve any significant reduction in the average temperature of the measuring points. The average temperature of the inside air was decreased by only 9.9 %, however, the average temperature of the dashboard was lowered by 22.8 %.
5. The temperature reductions resulted from using the suggested cover (case #6) led to significant reductions

in the cooling load required to keep the cabin thermally comfort, where the average cooling load dropped by 32.3 % from the unshaded case. However, the internal shading (case #7) resulted in only 15.3 %.

Future Work:

As for future work, the temperature reduction inside the cabin can be enhanced by combining the suggested cover with other passive techniques. Also, the cooling load estimation can be enhanced by considering the latent part as well, and validate the results with CFD softwares.

Acknowledgment:

The authors are grateful to the Department of Mechanical Engineering, College of Engineering, University of Baghdad, Iraq, for the assistance provided to achieve this research.

References

- [1] I. M. A. Aljubury, A. A. Farhan, and A. Mussa, "Experimental Study of Interior Temperature Distribution Inside Parked Automobile Cabin," *J. Eng.*, vol. 21, no. 3, 2015.
- [2] A. H. M. Alhosainy and I. M. A. Aljubury, "Two Stage Evaporative Cooling of Residential Building Using Geothermal Energy," *J. Eng.*, vol. 25, no. 4 SE-Articles, pp. 29–44, Apr. 2019.
- [3] L. J. Habeeb, D. G. Mutasher, and F. A. M. A. Ali, "Solar panel cooling and water heating with an economical model using thermosyphon," *Jordan Journal of Mechanical and Industrial Engineering*, vol. 12, no. 3, pp. 189–196, 2019.
- [4] A. M. Kadhim and I. M. A. Aljubury, "Experimental Evaluation of Evaporative Cooling for Enhancing Photovoltaic Panels Efficiency Using Underground Water," *J. Eng.*, vol. 26, no. 8, pp. 14–33, 2020.
- [5] S. Jaber and A. A. Hawa, "Optimal design of PV system in passive residential building in Mediterranean climate," *Jordan Journal of Mechanical and Industrial Engineering*, vol. 10, no. 1, pp. 39–49, 2016.
- [6] M. R. Abdelkader, A. Al-Salaymeh, Z. Al-Hamamre, and F. Sharaf, "A comparative Analysis of the Performance of Monocrystalline and Multicrystalline PV Cells in Semi Arid Climate Conditions: the Case of Jordan., *Jordan Journal of Mechanical and Industrial Engineering*, vol. 4, no. 5, 2010.
- [7] G. Fatima Siddiqui, M. Vir Singh, A. Shrivastava, M. Maurya, A. Tripathi, and S. Akhtar Siddiqui, "Children Left Unattended in Parked Vehicles in India: An Analysis of 40 Fatalities from 2011 to 2020," *J. Trop. Pediatr.*, vol. 67, no. 3, p. fmaa075, Jun. 2021.
- [8] M. A. Jasni and F. M. Nasir, "Experimental Comparison Study of the Passive Methods in Reducing Car Cabin Interior Temperature," *Int. J. Automob. Eng.*, vol. 3, no. 1, pp. 229–233, 2012.
- [9] S. C. Vishweshwara, J. Marhoon, and A. L. Dhali, "Study of Excessive Cabin Temperatures of the Car Parked in Oman and its Mitigation," *Int. J. Multidiscip. Sci. Eng.*, vol. 4, no. 9, pp. 18–22, 2013.
- [10] M. Setiyo, B. Waluyo, N. Widodo, M. L. Rochman, and I. B. Raharja, "Performance of mini air cooler on parked car under direct sunlight," in *Journal of Physics: Conference Series*, 2020, vol. 1517, no. 1.
- [11] B. C. Purnomo, I. C. Setiawan, and H. A. Nugroho, "Study on Cooling System for Parked Cars using Mini Air Cooler and Exhaust Fan," *Automot. Exp.*, vol. 3, no. 2, pp. 81–88, 2020.
- [12] A. A. Lahimer, M. A. Alghoul, K. Sopian, and N. G. Khrit, "Potential of solar reflective cover on regulating the car cabin conditions and fuel consumption," *Appl. Therm. Eng.*, vol. 143, pp. 59–71, 2018.
- [13] H. H. Al-Kayiem, M. F. B. M. Sidik, and Y. R. A. L. Munusamy, "Study on the thermal accumulation and distribution inside a parked car cabin," *Am. J. Appl. Sci.*, vol. 7, no. 6, pp. 784–789, 2010.
- [14] R. Levinson, H. Pan, G. Ban-weiss, P. Rosado, R. Paolini, and H. Akbari, "Potential benefits of solar reflective car shells : Cooler cabins , fuel savings and emission reductions," *Appl. Energy*, vol. 88, no. 12, pp. 4343–4357, 2011.
- [15] ANSI/ASHRAE, *ANSI/ASHRAE Standard 55-2013: Thermal Environmental Conditions for Human Occupancy*. 2013.
- [16] S. N. David Chua, B. K. Chan, and S. F. Lim, "Experimental and simulation study of thermal accumulation in an enclosed vehicle," *Proc. Inst. Mech. Eng. Part D J. Automob. Eng.*, vol. 233, no. 14, pp. 3621–3629, 2019.
- [17] Y. Lv, A. Huang, J. Yang, J. Xu, and R. Yang, "Improving cabin thermal environment of parked vehicles under direct sunlight using a daytime radiative cooling cover," *Appl. Therm. Eng.*, vol. 190, no. February, p. 116776, 2021.
- [18] J. P. Rugh, T. J. Hendricks, and K. Koram, "Effect of solar reflective glazing on ford explorer climate control, fuel economy, and emissions," in *SAE Technical Papers*, 2001, no. x.
- [19] I. R. Dadour, I. Almanjahie, N. D. Fowkes, G. Keady, and K. Vijayan, "Temperature variations in a parked vehicle," *Forensic Sci. Int.*, vol. 207, no. 1–3, pp. 205–211, 2011.
- [20] M. Setiyo, B. Waluyo, N. Widodo, M. L. Rochman, S. Munahar, and S. D. Fatmaryanti, "Cooling effect and heat index (HI) assessment on car cabin cooler powered by solar panel in parked car," *Case Stud. Therm. Eng.*, vol. 28, no. June, p. 101386, 2021.
- [21] A. A. Lahimer, K. Sopian, A. A. Razakb, M. H. Ruslan, and M. A. Alghoul, "Experimental investigation on the performance of solar chimney for reduction of vehicle cabin soak temperature," *Appl. Therm. Eng.*, vol. 152, no. November 2018, pp. 247–260, 2019.
- [22] C. A. Saleel, M. A. Mujeebu, and S. Algarni, "Coconut oil as phase change material to maintain thermal comfort in passenger vehicles An experimental analysis," *J. Therm. Anal. Calorim.*, vol. 0123456789, 2018.

Modelling and Prediction of Micro-hardness of Electroless Ni-P coatings Using Response Surface Methodology and Fuzzy Logic

Subhasish Sarkar^a, Rupam Mandal^a, Nitesh Mondal^{b*}, Shouvik Chaudhuri^c,
Tapendu Mandal^d, Gautam Majumdar^a

^aDepartment of Mechanical Engineering, Jadavpur University, Kolkata, India, 700032

^bDepartment of Mechanical Engineering, Ghani Khan Choudhury Institute of Engineering & Technology, Malda, India, 732141

^cCentre for Industrial Mechanics, South Denmark University, Sønderborg, Denmark, 6400

^dDepartment of Metallurgy and Materials Engineering, Indian Institute of Engineering Science & Technology, Shibpur, India, 711103

Received 8 Jun 2022

Accepted 20 Sep 2022

Abstract

The current study has focused on the electroless deposition of Ni-P alloy over the copper substrate to improve the microhardness of the substrate. Central Composite Design (CCD) has been performed using Design-Expert software for maximizing the microhardness of the coating. Along with that, CCD is also utilized to analyze the influence of various process parameters viz. concentration of Nickel Sulphate, the concentration of Sodium Hypophosphite, and bath temperature. Due to the congruity of the indenter with the coating, the Vickers Hardness Test has been executed for determining the microhardness of each coated sample. 33.8223g/L of Nickel Sulphate, 19.6602g/L of Sodium Hypophosphite and 87.6331°C of bath temperature are the optimum conditions for the deposition of coating to achieve a hardness value of 1129.7867 HV_{10g} as obtained from the model analysis of CCD and the same optimum point prediction data of microhardness results to 1070 HV_{10g}. Applying Fuzzy logic, the effect of various parameter on microhardness for electroless Ni-P coating has been studied. Further, Analysis of Variance (ANOVA) has been implemented which corroborated that the parameter Nickel Sulphate along with the interaction between Sodium Hypophosphite and bath temperature are the significant ones in determining the microhardness of the coating deposited in optimized conditions. Optical Microscopy, Scanning Electron Microscopy (SEM), and Energy Dispersive X-ray analysis (EDX) are conducted to study the surface morphology and the elemental composition of the coated substrate respectively.

© 2022 Jordan Journal of Mechanical and Industrial Engineering. All rights reserved

Keywords: Electroless Coating; Microhardness; Central Composite Design; ANOVA; Fuzzy Logic; SEM; EDX.

1. Introduction

Since the discovery of Electroless Coating by Brenner and Riddell in 1947[1], there has been a colossal amount of development in this field of research. As the name indicates, the electrons for the deposition of coating are furnished by the reducing agent instead of the electric current. The process comprises of a substrate dipped in an electroless bath comprising of a source of metal ions, reducing agent, complexing agent, bath stabilizer, accelerator, buffering agent, and surfactants[2]. The metallic ions present in the solution are reduced by the reducing agent and get deposited over the substrate as an initial film which further acts as a catalyst for the rest of the process, thus summarizing the entire autocatalytic technique. Owing to the uniformity and evenness of the deposition, electroless coatings have gained ample significance as compared to other surface coating methodologies[3]. In a drive of development during the past few decades, industries thrive for materials with

improved mechanical, tribological, aesthetic, and chemical properties. Electroless Nickel (EN) deposits fulfill the above criterion perfectly and hence they have achieved immense usage in aerospace, automobile, marine, mining, electronics, textile industries, etc[4–6].

EN coatings can be classified into pure nickel, alloy and composite coatings[7]. Alloy coatings can be further classified into binary, ternary and quaternary alloy coatings[8]. Phosphorous and Boron are by far the two most extensively used elements along with Nickel to form electroless Ni-P and Ni-B deposits[9]. Ni-B coatings are known for their high hardness along with the competence to retain lubricants attributable to their cauliflower-shaped surface morphology[10]. On the other hand, Ni-P coatings have a smoother surface with a wavy surface texture[11]. Due to its excellent wear, abrasion, and corrosion resistance along with significant hardness, electroless Ni-P coating is one of the most popular binary alloys accompanied by well-executed research and widespread development. The phosphorous content in the nickel lattice is a significant criterion that controls the properties and

* Corresponding author e-mail: niteshju@yahoo.com.

microstructures of the electroless Ni-P deposits. Low phosphorous (1-4% P) EN deposits are microcrystalline in nature with high hardness and wear resistance. Medium phosphorous (5-10% P) EN deposits have combined crystalline and amorphous structure and high phosphorous (>10% P) EN deposits have amorphous structure with excellent corrosion resistance and ductility[12]. Inclusion of W, Cu, Co, Mo, Zn, Fe, etc. is done to meet the exigency of the research and development sectors which would impart a high hardness, tensile strength, wear, abrasion, and corrosion resistance along with improved thermal stability[13–16]. EN composite coatings, on the other hand, are formed by the implementation of an inert phase component (PTFE, SiC, Al₂O₃, WC, TiO₂, ZrO₂, etc.) into the metal matrix thereby improving the tribological properties to a greater extent[17–20].

The property that resists localized plastic deformation, abrasion, or scratching is defined as the hardness of a material and it is referred to as microhardness when there is the involvement of hardness testing using a small indenter or when the load is quite less[21,22]. Hardness is one of the most important mechanical properties which requires to be improved to meet the demand of industries syncing with the environment. The salient reason behind this is that this property and the property of wear and abrasion resistance bear a direct relationship. When the crystallization of the amorphous state takes place during heat treatment in an attempt to improve the hardness of the deposits, deposition of the intermetallic Ni₃P phase occurs which is the sole reason for the increase in hardness of the electroless Ni-P deposits[23]. Although, heat treatment of electroless Ni-P deposits [24] is not the solution in every situation whatsoever. In industries, precision instruments, internal surfaces, and other delicate gadgets have to be handled carefully and there is a chance that they might get damaged over severe heat treatment processes due to a lack of precautions.

A lot of work has been done in the past relating to the hardness of electroless Ni-P deposits. Keong *et al.*[25] found that the Vickers hardness of the as-deposited electroless substrates increased with the decrease in phosphorous content. They achieved the highest hardness value of 1011 ± 9 HV_{0.1} after heat-treating the substrates at 400-450°C. They also performed Knoop micro indentation testing on the cross-section of the samples to find the variation of hardness in relation to the depth of the coating. Yan *et al.* [26] prepared electroless Ni-P substrates with varying phosphorus content by varying the ratio of lactic acid to acetic acid in the electroless bath. They further observed a transition of phase from nanocrystalline to a mixture of nanocrystalline and amorphous and finally to a fully amorphous phase with the increase in phosphorous content of the coating. At a 7.97 at. % Of P, they obtained the highest hardness value of 910 HV_{0.1} for the electroless Ni-P deposits. Zangeneh-Madar and MonirVaghefi[27] studied the effect of thermochemical

treatment on the structure and hardness of electroless Ni-P coated low alloy steel. Hardness, roughness tests, phases present, and surface characterization are further performed. They proved that the hardness of the coating increases when complete crystallization occurs. Sivarao *et al.*[28] compared Taguchi Method and Response Surface Methodology (RSM), to predict the near values of average error, the RSM technique is more promising in predicting the response via mathematical modelling than Taguchi technique. A Mukhopadhyay *et al.*[29] studied the effect of fuzzy logic on Ni-P coating to predict the wear depth after using taguchi method. It has been shown that the accuracy of prediction by fuzzy logic is better than the Taguchi method. R. Vinayagamoorthy *et al.* [30] have built the central composite design (CCD) model and the model is validated by comparing it with the fuzzy model and confirmatory runs. It has been shown that the error is minimum for both central composite design and fuzzy logic. Balaji M *et al.*[31] observed that Fuzzy TOPSIS prioritization of ASCA of ISM acknowledged driver enablers, emphasized that the priority should start from End to end connectivity had the minimum ranking score and training programme on time management concepts had the maximum ranking score. Azmi Alazzam *et al.*[32] utilizes adaptive NeuroFuzzy Inference System (ANFIS) which is based on the BPN-ANN structure with two inputs and one output using Matlab software to predict the components' reliability of Lead-free solder process. Qingyong Zhang *et al.*[33] used Multi-hierarchical Fuzzy system to determine the driving cycle of a Hybrid Electric Vehicles based on four different driving patterns.

In our current research, we have employed Central Composite Design (CCD)[34] intending to maximize the micro-hardness by analyzing the impact of the process parameters for the deposition of the coating. Although optimization using CCD analysis has been already performed on a similar experiment[35] and fuzzy logic is also applied to the data evaluated by CCD model, results at the optimization point from both fuzzy and CCD have been compared with the experimental result. Further, to study the surface morphology and the elemental compositions, Optical Microscopy, Scanning Electron Microscopy (SEM), and Energy Dispersive X-ray analysis (EDX) have been performed respectively.

2. Details of Experiment

In this work, at first, the synthesis part has been done with the help of central composite design (CCD) in Minitab software and the effect of input parameters on the output parameter is found. From the output of CCD, the optimization of maximum microhardness has been done and simultaneously the Fuzzy logic is also applied for data prediction and comparison. The process is completed with the validation test. Figure 1 shows the complete flow chart of this work.

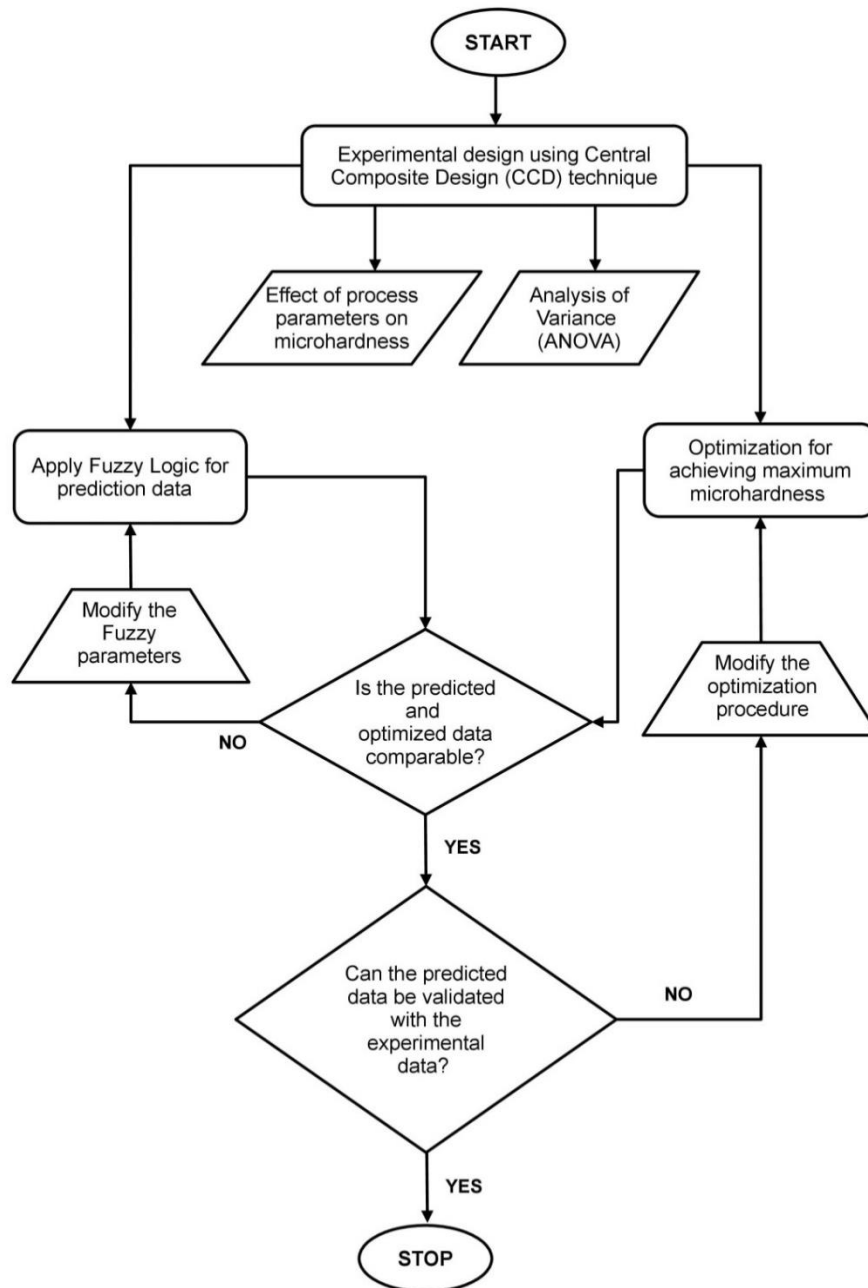


Figure 1. Experimental Flow Chart

2.1. Preparation of substrate and coating deposition

Copper substrates have been cut into pieces of size 20 x 15 x 1mm³ from a copper foil (99% pure, LobaChemie) in rolled form. In the first place, the copper substrates have been rinsed in distilled water for a couple of minutes. Then, they have been dipped in 25% dilute HCl solution for some time to remove impurities and oxide layers. Then henceforth, the cleaned substrates are subjected to activation using an adsorbing reagent, Palladium Chloride (PdCl₂) solution pre-heated at 55°C. Being adsorbing in nature, it forms a fine layer over the substrate thereby initiating the reaction. Great adhesion along with deposition rates are obtained with the help of this activation process.

Nickel Sulphate (NiSO₄) is used as the source of nickel ions along with Sodium Hypophosphite (NaH₂PO₄) as the reducing agent for the reduction of nickel ions as obtained from the Nickel Sulphate solution. To slow down the reaction rate to a suitable one by forming metastable nickel complexes, we have used Trisodium Citrate Dihydrate (TCD) as the complexing reagent. Furthermore, we have used Sodium Acetate (CH₃COONa) as the buffering agent to maintain the pH level of the bath to a constant value of 5. The chemical compositions along with the parameters of this electroless bath are displayed in Table 1. In one beaker, the nickel ions source is mixed with the reducing agent, and in another, the remaining chemicals are mixed with 250ml of deionized water distributed proportionately amongst them. The two solutions are separately heated up to 60°C before they are mixed to form the electroless bath.

The activated substrates are now dipped in the bath which is in turn heated to a temperature ranging from 85-90°C. After 1hr of electroless deposition, we would observe a bright greyish coating deposited onto the substrate with the solution turning black gradually. It would then be the perfect moment to take out the coated substrates from the bath and clean them by rinsing them in deionized water for a few minutes.

Now, the electroless Ni-P deposited copper substrates are mounted with the aid of epoxy resin because the handling of coatings of such a minute thickness is neither easy nor safe. Finally, they are ready for the hardness measurement procedure.

Table 1. Chemical composition along with process parameters of electroless bath for Ni-P coating deposition over the copper substrate

Factors	Values
Nickel Sulphate	21.59-38.41 g/L
Sodium Hypophosphite	13.27-26.72 g/L
Temperature	76.6-93.41°C
Trisodium Citrate Dihydrate	15 g/L
Sodium Acetate	5 g/L
pH of solution	5

2.2. Hardness Measurement

The mounted electroless Ni-P deposited copper substrates are subjected to the Vickers Hardness Test (VHT) (as displayed in Figure 2) to obtain their microhardness number (HV). The VHT method is carried out as per ASTM standard E384-16 with the help of a right pyramidal-shaped diamond indenter with an apex angle of 136°. The substrate is subjected to a load of 10g with a total time of 15s for loading and unloading. An indentation is left by the indenter whose depth is measured. The lower the indentation depth left by the applied force on the surface of the coated substrate, the harder the tested sample. The microhardness tester provides us with an average of six hardness values. The hardness value (HV) is measured using equation (1) where 'F' is the applied load in grams and 'd' is the average of the two diagonals in mm left by the pyramidal indenter during the impact.

$$HV = \frac{1.8655F}{d^2} \quad (1)$$

VHT is the preferred hardness test because high accuracy is the first priority in our present study. Other hardness tests such as Brinell Hardness Test (BHT) and Rockwell Hardness Test (RHT) are not as accurate enough as VHT since the surface area in contact with the indenter is very small in the case of VHT. Non-destructive hardness tests can be carried out in VHT which is not possible in the other cases. Furthermore, the microstructural constituents can be targeted using VHT after magnifying the surface of the coating and the post-heat treatment options can also be obtained using this technique.

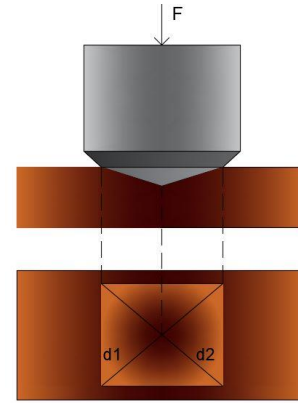


Figure 2. Vickers Hardness Test

2.3. Central Composite Design (CCD)

Central Composite Design (CCD) is a method of response surface analysis based on a two-tiered factorial design. This analysis helps to model and optimize the output response. The behavior of CCD depends on multiple independent variables. It gives three-dimensional surface plots and contour plots through which, the relationship between output and input factors can be effectively analyzed. It also provides regression equations through which feedback for any input value can be effectively predicted. The generalised form of the regression equation has been given in equation 2.

$$x = a_0 + a_1v_1 + a_2v_2 + a_3v_3 + a_{12}v_1v_2 + a_{13}v_1v_3 + a_{23}v_2v_3 + a_{11}v_1^2 + a_{22}v_2^2 + a_{33}v_3^2 \quad (2)$$

where x denotes the output response, all y terms represent the input variables, all a terms represent the constants.

2.4. Fuzzy Logic

Fuzzy Logic is a mathematical theory of the irrational reasoning process that allows the modeling of the human reasoning process in linguistic terms. It does not need any mathematical model to build up. The fuzzy Logic system (madami system) consists of a fuzzyfier, membership function, a fuzzy rule base, an interference engine, and a defuzzifier[36]. Fuzzifier is used to convert crisp values to values. The membership function is a graphical representation of the level of participation of each input. Fuzzy rules use input membership values as weight factors to determine their effect on obscure output values of the final output conclusion[37]. Once the functions are assumed, scaled, and assembled, they are defuzzified to a crisp output that drives the system. Then the Mamdani fuzzy interference system performs obscure arguments in Fuzzy rules to create fuzzy value. Finally, the defuzzifier converts the fuzzy predicted value.

3. Results and Discussions

3.1. Optimization of process parameters using Central Composite Design (CCD)

For several projects working in the field of process parametric optimization, a highly beneficial approach is to go through one of the basic designed optimization

processes. These designs are fully based on mathematical modeling. Based on requirements, one such design is chosen. In this paper, the Central Composite Design (CCD) of the experiment has been employed.

The basic design behind the response surface is CCD. Basically, like other designs for optimization, it also shows the interactions amongst the experimental variables. Keeping this into consideration, it increases the replications of central points (keeping all the parameters in their mean values) to check the error of the experiments. The most vital entity of CCD is the increase in the range between two axial points. Thus, it makes a sphere (where a number of parameters are 3) with a radius α (the distance between the central point and any of the corner points). This depicts how the accuracy has been obtained while analyzing the parametric optimization using CCD.

Nickel Sulphate (NiSO_4), Sodium Hypophosphite (NaH_2PO_4), and Temperature are the significant factors for optimization. The main constituents of the electroless coating are Nickel and Phosphorous. The quantity of Nickel deposited depends upon the concentration of Nickel

Sulphate in the electroless bath which in turn affects the microhardness of the coating to a great extent. Similarly, the concentration of Sodium Hypophosphite decides the amount of Phosphorous deposited over the copper substrate. Temperature, on the other hand, controls the rate of reaction occurring along with the deposition. Thus, they are the most important factors deciding the value of the response, microhardness. The regression equation is the reaction between the response and the process parameters. To obtain a full-factorial regression equation, six central points have been considered and their coded values are displayed in Table 2.

Further, to analyze the problem statistically as well as mathematically, Response Surface Methodology (RSM) have been adopted. The Central Composite Design (CCD) of the experiment is chosen to be the tool based on which response surfaces has been developed. This design encloses 6 central points, 6 axial points, and 8 factorial points. On all of the 20 sets of the experiment, microhardness testing using VHT have been carried out and the obtained results have been provided in Table 3.

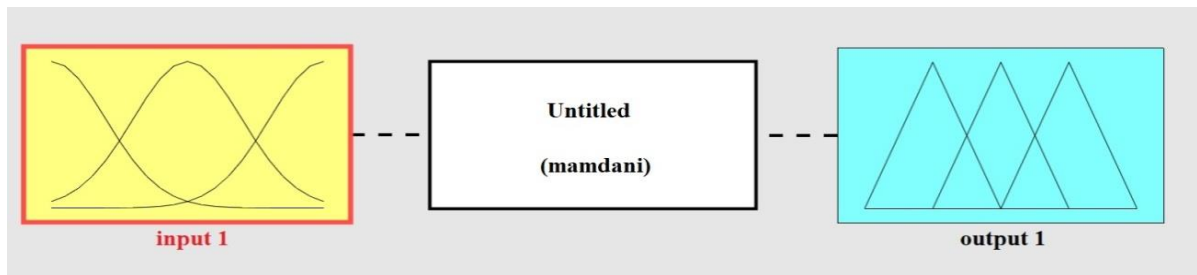


Figure 3. Fuzzy logic controller

Table 2. Coded values of process parameters

Actual Values			Coded Values		
Nickel Sulphate (g/L)	Sodium Hypophosphite (g/L)	Temperature (°C)	Nickel Sulphate (g/L)	Sodium Hypophosphite (g/L)	Temperature (°C)
X1	X2	X3	Z1	Z2	Z3
21.59	13.27	76.6	- α	- α	- α
25	16	80	-1	-1	-1
30	20	85	0	0	0
35	24	90	+1	+1	+1
38.41	26.72	93.41	+ α	+ α	+ α

Table 3. 20 sets of Experimental Data for Central Composite Design (CCD) of the experiment for electroless Ni-P deposits

Set of Expt.	Nickel Sulphate (g/L)	Sodium Hypophosphite (g/L)	Temperature (°C)	Micro hardness (HV _{10g})
1	35	16	90	1007
2	35	24	90	1056
3	30	20	85	1107
4	30	20	85	1110
5	30	20	85	1107
6	25	16	80	910
7	25	24	90	920
8	30	20	76.6	895
9	30	20	85	1108
10	30	20	93.41	1015
11	30	20	85	1109
12	35	16	80	980
13	30	20	85	1107
14	25	16	90	840
15	38.41	20	85	1100
16	30	26.72	85	981
17	30	13.27	85	960
18	21.59	20	85	880
19	25	24	80	1023
20	35	24	80	810

The analysis by Design Expert Software suggested the Central Composite Design (CCD) of the experiment evaluated for microhardness with substantial factors to be quadratic in the actual and coded equation which are as follows:

Final Equation in Terms of Coded Factors-

$$\begin{aligned} \text{Micro Hardness} = & 1108.65 + 38.81A + 7.80B \\ & + 22.15C - 39.25AB + 55.75AC + 23.35BC \\ & - 45.98A^2 - 52.92B^2 - 58.42C^2 \end{aligned} \quad (3)$$

Final Equation in Terms of Actual Factors-

$$\begin{aligned} \text{Micro Hardness} = & -12916.43746 - 32.19199 \times \text{NS} \\ & + 94.30347 \times \text{SH} + 311.54621 \times \text{T} - 1.96250 \\ & \times \text{NS} \times \text{SH} + 2.23000 \times \text{NS} \times \text{T} + 1.16250 \\ & \times \text{SH} \times \text{T} - 1.83911 \times \text{NS}^2 - 3.30726 \times \text{SH}^2 - 2.33686 \times \text{T}^2 \end{aligned} \quad (4)$$

Where NS, SH and T stands for Nickel Sulphate, Sodium Hypophosphite and Temperature respectively.

Using the CCD-RSM method for parametric optimization, the optimized value of micro-hardness is 1129.7867 HV_{10g} and the corresponding input parameters are 33.8223g/lit of NiSO₄, 19.6602g/lit of NaH₂PO₂, and 87.6331°C of temperature.

3.2. Fuzzy Modelling

The basis of a fuzzy model is a linguistic variable, which aims to use fuzzy sets instead of crisp sets. In this study, the fuzzy model uses type-1 fuzzy sets with Mamdani Fuzzy Inference System (FIS) [28, 29] and the centroid defuzzification technique. In the input step, the parameters, viz. the concentration of Nickel Sulphate, Sodium Hypophosphate, and Temperature are fuzzified with triangular membership functions for sake of simplicity. The input space is divided into three obscure subsets, i.e., low (L), medium (M), and high (H). On the

other hand, the defuzzifier also employs three subsets viz. low (L), medium (M), and high (H), of triangular membership functions to determine the output value of Microhardness. These membership functions of Nickel sulphate, sodium Hypophosphite, Temperature, and Microhardness are illustrated in Figure 5. The choice of the range of these parameters and their subsets are determined based on the experimental data for CCD design as provided in Table 3. For the concentration of Nickel Sulphate and Temperature, the input range is equally divided into the three subsets. For the concentration of Sodium Hypophosphite, the mid-values of three subsets are equally placed at 16, 20 and 24, respectively. On the other hand, for the output variable, microhardness, the membership function is so designed that the mid-values for the three subsets are equally placed at 900, 1000 and 1100. However, due to constraints on the maximum value, i.e., 1150, the 'High' subset is asymmetric.

The rule base for relating microhardness to the process parameters through the Mamdani Inference system is designed based on the qualitative nature of the experimental data for CCD design presented in Table 3. For instance, in table 3, the 6th experimental set depicts that the values for all the three process parameters are in the LOW subset, and the subsequent microhardness takes a value in the MEDIUM subset. Based on this observation, 20 such rules are designed directly from the combination of parameters in CCD-RSM given in Table 3. The IF-THEN rulebase with output is listed in Table 4. When a set of input assumptions is adopted by the FIS, it introduces a certain number of rules, and a fuzzy output is obtained using Mamdani's max-min implication. This fuzzy output is defined using the centroid defuzzification method. A three-input single-output fuzzy model is illustrated in Figure 6. In the present study, the fuzzy modeling has been done using the Fuzzy Logic Toolbox in MATLAB R2018a.

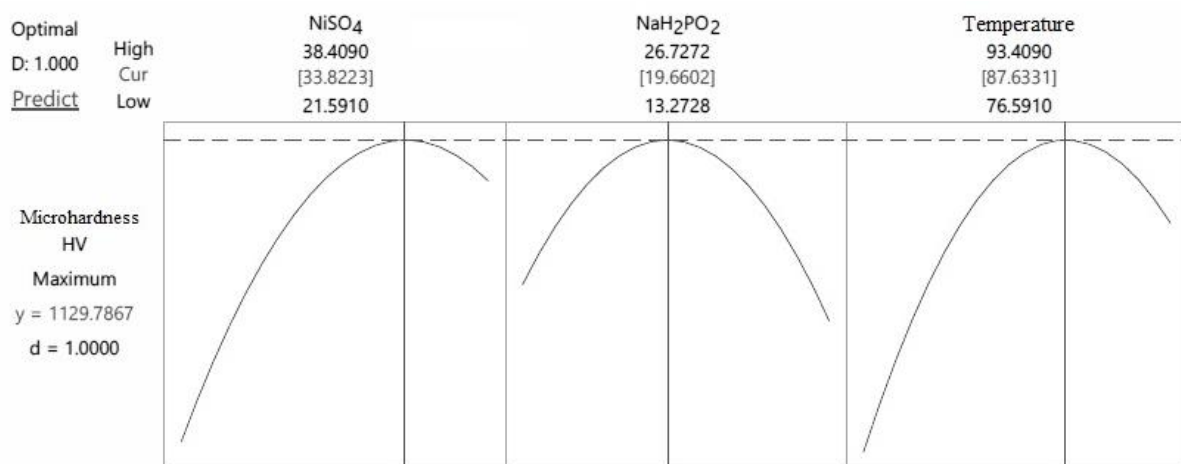


Figure 4. CCD optimized input parameters and output value

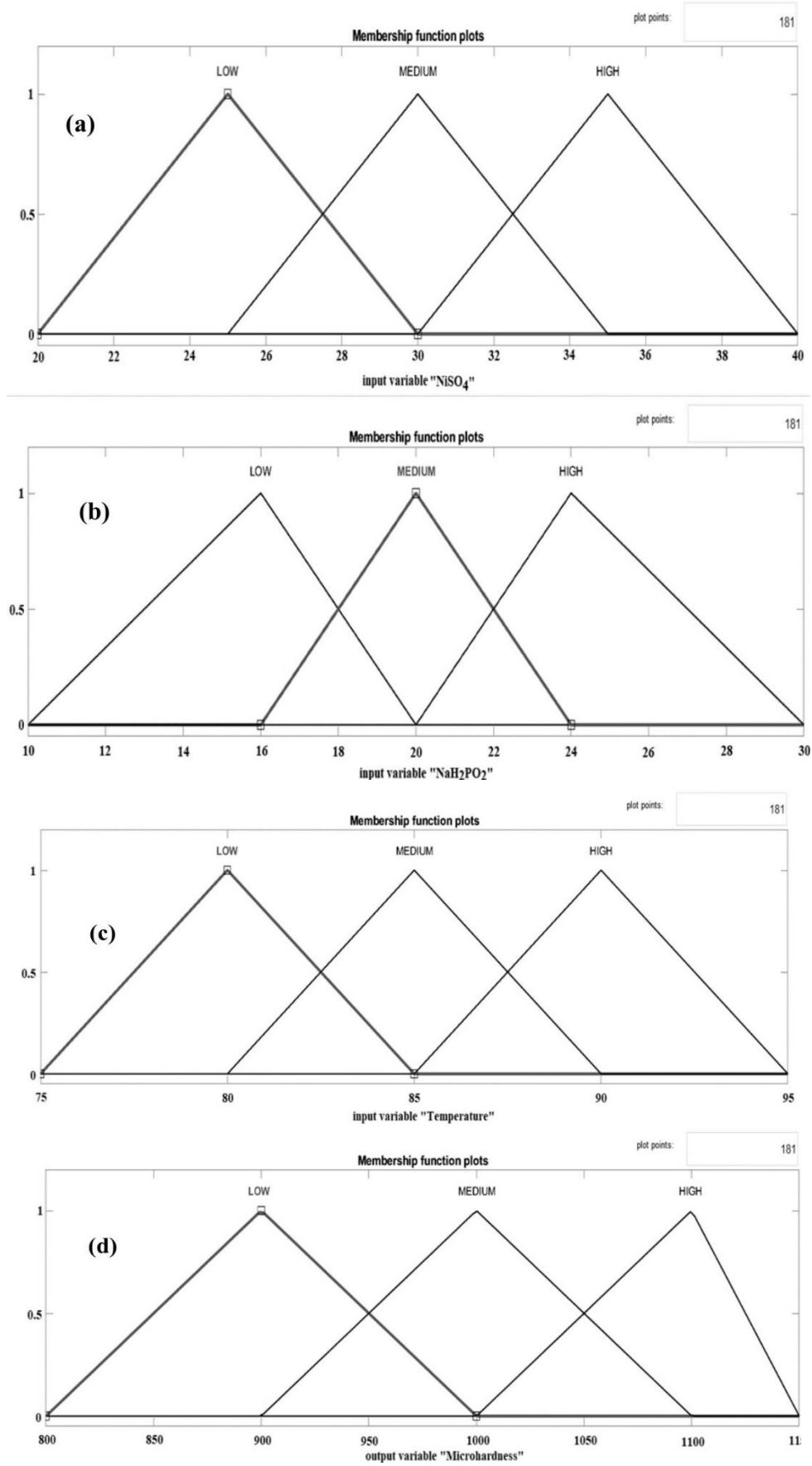


Figure 5. Membership functions: (a) input membership function for Nickel Sulphate (NiSO₄) (b) input membership function for Sodium Hypophosphite (NaH₂PO₂) (c) input membership function for Temperature (d) output membership function for Micro Hardness (HV)

Using Fuzzy logic, the prediction value of micro-hardness is 1070 HV_{10g} in input parameters 33.8223 g/lit

of NiSO₄, 19.6602g/lit of NaH₂PO₂, and 87.6331°C of temperature which is shown in the fig. 7.

Table 4. Fuzzy rules

Rule No.	IF				THEN
	Nickel Sulphate		Sodium Hypophosphate		Microhardness
1	H		L		H
2	H		H		H
3	M		M		H
4	M		M		H
5	M		M		H
6	L		L		M
7	L		H		M
8	M		M		L
9	M		M		H
10	M		M		H
11	M	AND	M	AND	H
12	H		L		M
13	M		M		H
14	L		L		L
15	H		M		H
16	M		H		M
17	M		L		M
18	L		M		L
19	L		H		H
20	H		H		L

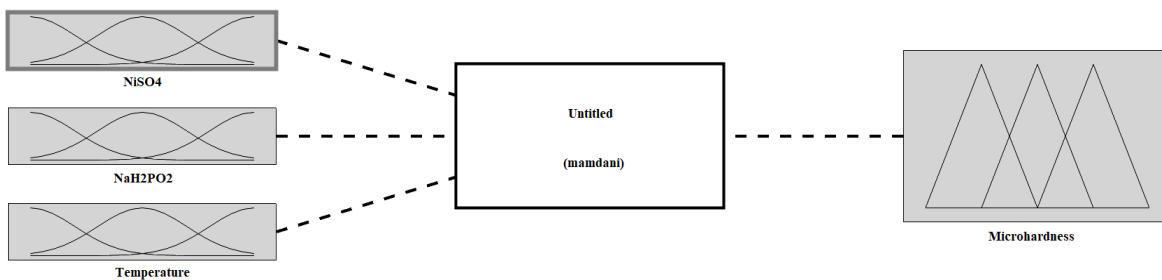


Figure 6. Three input single output fuzzy inference system

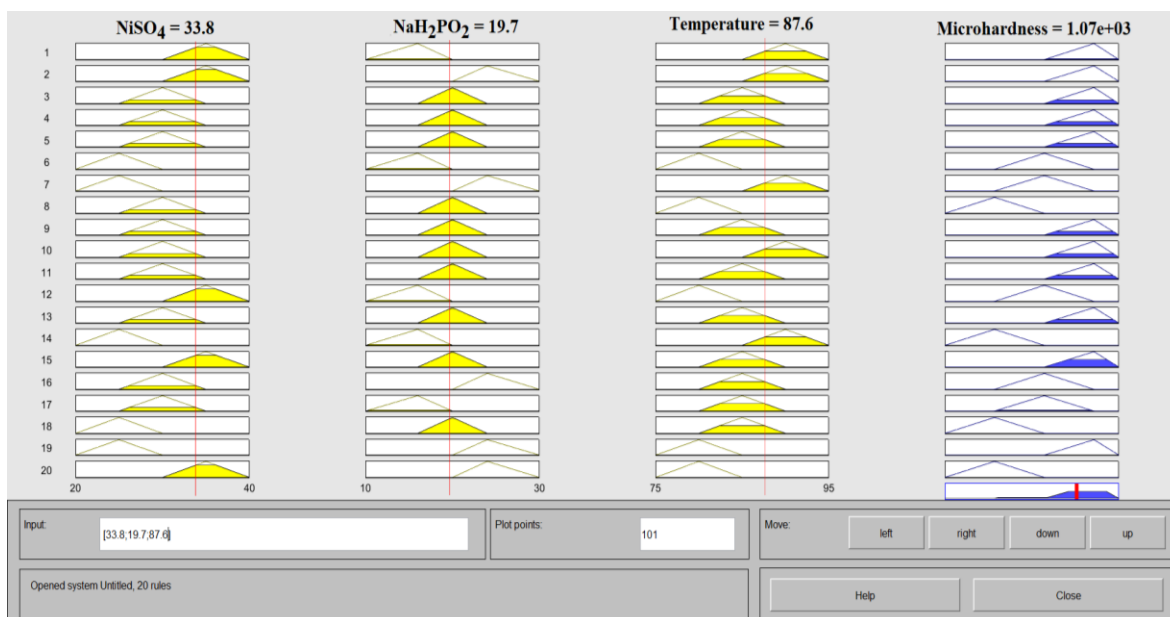


Figure 7. Fuzzy prediction data

3.3. Response Surface Plot Analysis From CCD

Microhardness in this case; the response has been predicted using the response surface plots. 3D surface plots have been analyzed to optimize the response and to interpret the interaction between every single significant process parameter. The surface plots have been obtained by plotting the response, microhardness as the z-axis against two of the three process parameters on the x and y-axes. Thus, on a 2-D plane, we have successfully achieved a 3-D response surface plot.

Figure 8 shows the three-dimensional graphical representation for the variation of microhardness (response) by varying the concentration of NiSO₄ and concentration of NaH₂PO₂ keeping the temperature constant. By Figure 8 it can be said that microhardness increased by increasing the concentration of NiSO₄ and concentration of NaH₂PO₂. This plot has a more or less symmetric surface with its peak at the center.

Figure 9 shows the three-dimensional graphical representation for the variation of microhardness (response) by varying the concentration of NiSO₄ and

temperature keeping the concentration of NaH₂PO₂ constant. By Figure 9 it can be said that microhardness increased by increasing the concentration of NiSO₄ and temperature. This surface plot also has a nearly symmetric surface with its peak at the center.

Figure 10 clearly shows the three-dimensional graphical representation of microhardness (response) as a function of the concentration of NaH₂PO₂ and temperature keeping the concentration of NiSO₄ constant. From Figure 10, it can be said that microhardness increased by increasing the concentration of NaH₂PO₂ and temperature. This surface plot has a perfectly symmetric surface with its peak at the center.

Though from all three RS plots, the huge effect of all three parameters over the response has been observed. The interaction between the bath temperature and sodium hypophosphite for increasing the microhardness is the most significant one by comparing the symmetry of the curvature. It is also concluded from the three surface plots that for obtaining the best-optimized result, NiSO₄ should be valued at 30 g/L.

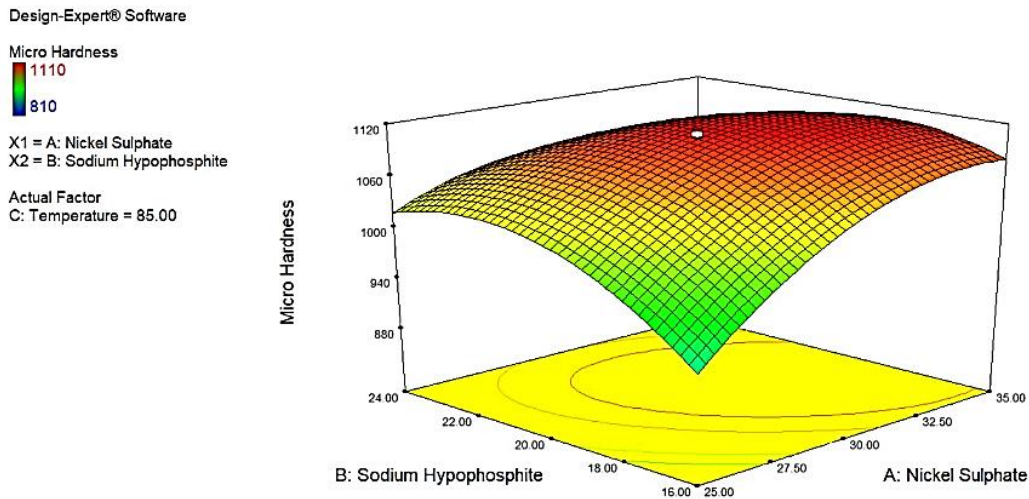


Figure 8. 3D-Response surface plot showing the effect of Nickel Sulphate and Sodium Hypophosphite

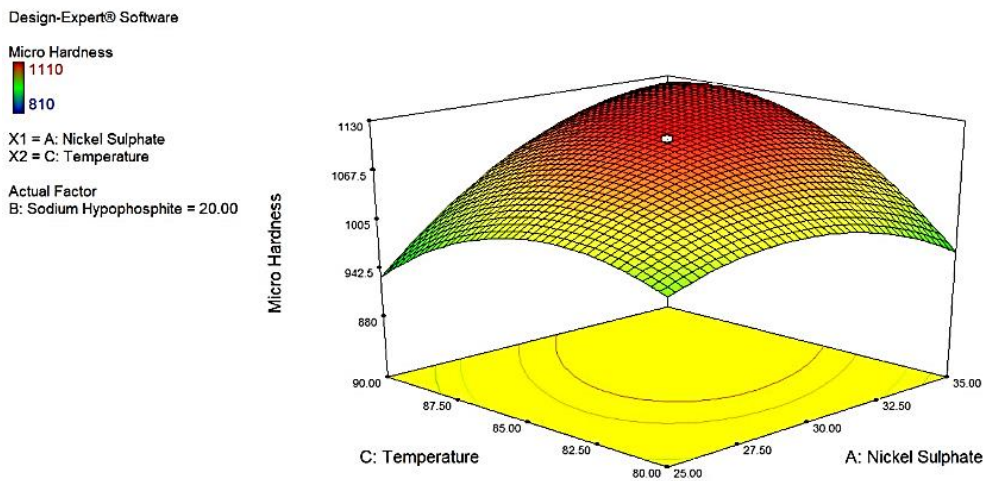


Figure 9. 3D-Response surface plot showing the effect of Nickel Sulphate and Temperature

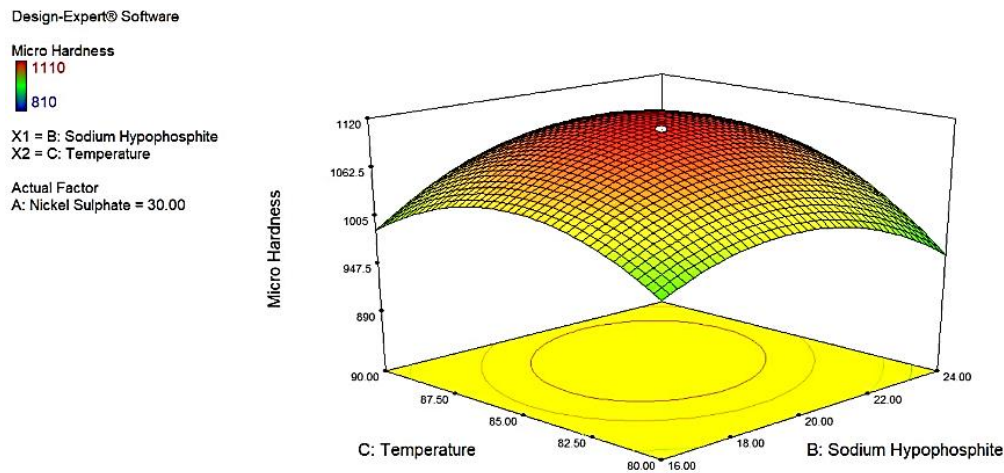


Figure 10. 3D-Response surface plot showing the effect of Temperature and Sodium Hypophosphite

Table 5. ANOVA table for Response Surface Quadratic Model

Source	Sum of Squares	df	Mean Square	F-value	p-value Prob > F	Remarks
Model	169973.56	9	18885.95	10.54	0.0005	
A-Nickel Sulphate	20569.43	1	20569.43	11.48	0.0069	significant
B-Sodium Hypophosphite	831.20	1	831.2027	0.46	0.5112	
C-Temperature	6698.70	1	6698.709	3.73	0.0819	
AB	12324.5	1	12324.5	6.88	0.0255	
AC	24864.5	1	24864.5	13.88	0.0039	
BC	4324.5	1	4324.5	2.41	0.1513	
A ²	30478.64	1	30478.64	17.01	0.0021	
B ²	40313.45	1	40313.45	22.50	0.0008	
C ²	49114.43	1	49114.43	27.41	0.0004	
Residual	17912.18	10	1791.218			
Lack of Fit	17904.18	5	3580.84	2238.02	<0.0001	significant
Pure Error	8	5	1.6			
Cor Total	187885.75	19				

3.4. Analysis of Variance (ANOVA)

From Table 3, it has been found that the maximum microhardness occurs in Experiment 4 with a combination of Nickel Sulphate concentration of 30 g/L, Sodium Hypophosphite concentration of 20g/L, and a bath temperature of 85°C whereas the minimum microhardness has been obtained in Experiment 20 with a combination of Nickel Sulphate concentration of 35 g/L, Sodium Hypophosphite concentration of 24g/L and a bath temperature of 80°C. Hence, to find the perfect combination of these three process parameters for obtaining the maximum microhardness, we have employed a powerful and effective mathematical tool named Analysis of Variance (ANOVA).

The significant combination of factors taking place in an experiment has been determined using this tool. It works on the methodology of the F-value and p-value. The decision about whether we can reject the null hypothesis has been provided by the p-value. When the amount of this p-value is less than 0.05, we can conclude with the

affirmation of rejecting the null hypothesis thereby stating that the factor is significant. The ratio of summation of the factors, each raised to the power of two to the variance of errors has been referred to as the F-value. Thus, the amount of F-value is directly proportional to the relative significance of the concerned factor with respect to others. Table 5. displays the CCD analysis results.

From the Model F-value data of 10.54in Table 5, we can conclude that the model is significant. The chance that such a high model F-value would generate is 0.05%. If the values of Prob>F have been found less than 0.05, then we can arrive at the fact that those corresponding factors are significant. Thus, in this case, A, AB, AC, A², B², and C² are the substantial model terms.

From the above facts, it is concluded that the input parameter i.e. the concentration of Nickel Sulphate is significant. Now, the p values have been considered for determining the level of significance of linear main effects and linear interactions of the process parameters Nickel Sulphate, Sodium Hypophosphite, and bath temperature. Therefore, the squared terms have not been considered.

3.5. Surface analysis from fuzzy model

Surface plot is one of the graphical representations to predict the relationship between dependent and independent parameters. Here, the surface plots illustrate the trends in the variation of microhardness for electroless NI-P coating through Fuzzy logic considering the effect of various parameters. The relationship or variation of microhardness, temperature and concentration of NiSO_4 have been shown in fig. 11a. It is interesting that microhardness has no such influence in temperature and NiSO_4 concentration. Microhardness has maintained a flat surface for any region of the surface plot. An interesting

trend has been observed from fig. 11b, when there is a correlation build up among microhardness, temperature and concentration of NaH_2PO_2 . The variation of microhardness is very high at high temperature and moderate concentration of NaH_2PO_2 . The role of temperature and concentration of NaH_2PO_2 is very prominent to determine the microhardness. Figure 11c. explore the effect of NaH_2PO_2 concentration and NiSO_4 concentration together on micro hardness. The hardness is increasing when the concentration of NaH_2PO_2 is between 17 to 22 and the concentration of NiSO_4 is near about 35. After increasing the concentration of NiSO_4 , hardness maintains a constant value for the same concentration of NaH_2PO_2 .

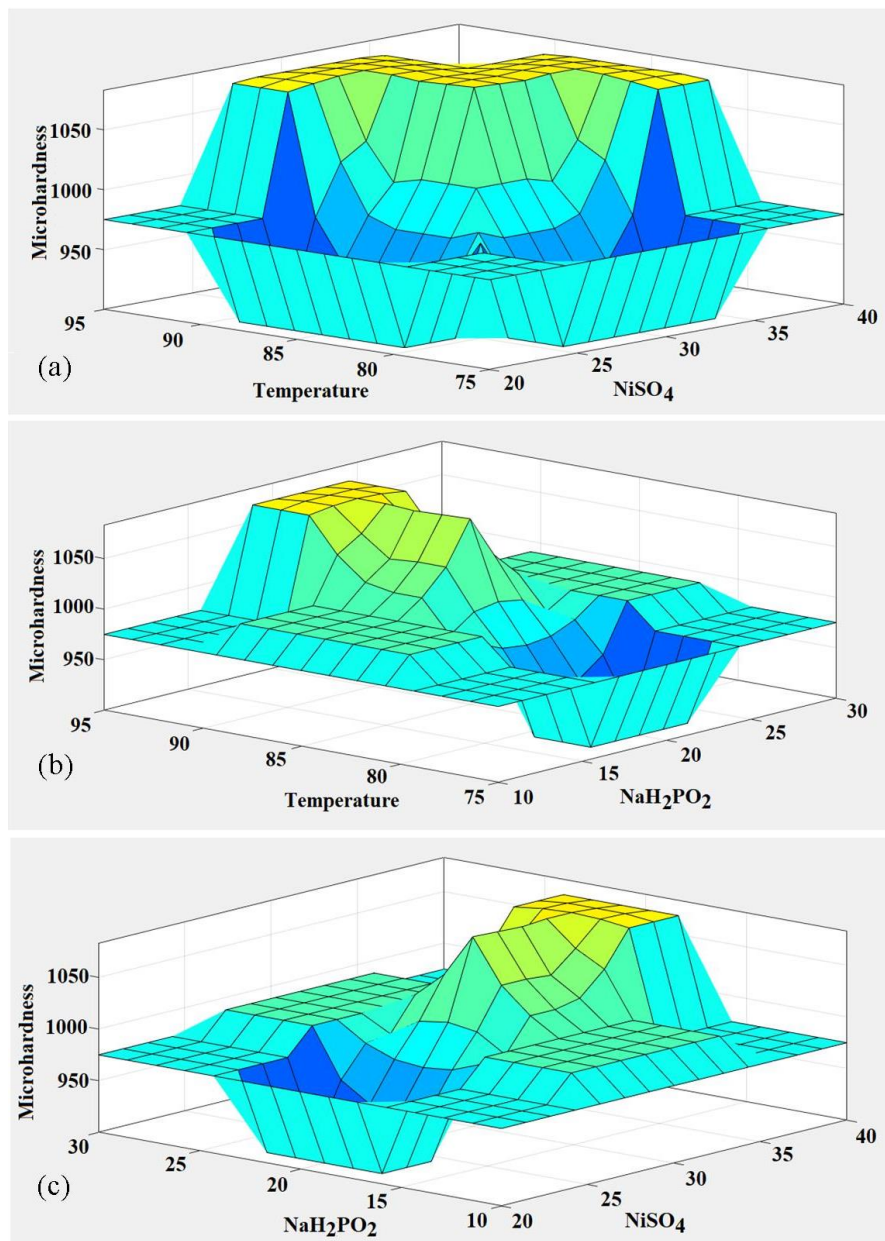


Figure 11. Surface plot showing the variation of Microhardness with (a) Temperature and concentration of NiSO_4 (b) Temperature and concentration of NaH_2PO_2 (c) concentration of NaH_2PO_2 and concentration of NiSO_4

4. Comparison and validation test

Based on the advanced CCD model and the Fuzzy model, the validity of the model has been tested. They have been carried out with different input values of concentration of Nickel Sulphate. The concentration of sodium hypophosphate, and temperature, and the experimental, CCD optimized result, and fuzzy predicted results have been compared. The value of the concentration of Nickel Sulphate, concentration of sodium hypophosphate, and temperature considered for the validation tests have been selected from within the range of the parameters considered ($\text{NiSO}_4 = 33.8 \text{ g/L}$, $\text{NaH}_2\text{PO}_2 = 19.7 \text{ g/L}$, Temperature = 87.6331°C).

Figure 12 shows the results of verification tests, and it is observed that both models can predict microhardness values with high accuracy. However, the accuracy obtained from the fuzzy model is about 2.02% compared to -3.46% of the CCD model, where the negative sign is an indication of overprediction. Therefore, we conclude that the fuzzy model is more accurate and can be used effectively to predict the microhardness of the electroless Ni-P coating. This observation regarding the fuzzy model is corroborated by other studies as well [28].

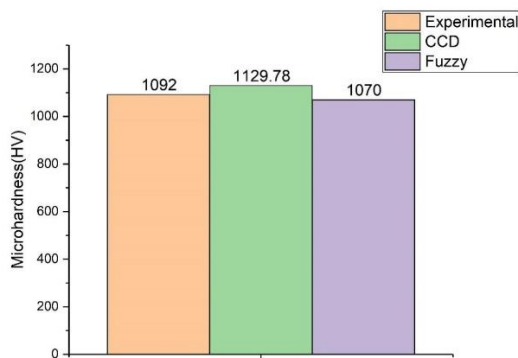


Figure 12. Validation test result

5. Characterization of the electroless coated Ni-P substrate deposited in optimized condition

5.1. Surface Morphology using Optical and Scanning Electron Microscopy

Round nodules of non-uniform sizes but uniform shapes have been observed throughout the Optical micrograph of the electroless Ni-P coating deposited in optimal condition (Figure 13). The particles have been scattered throughout the micrograph but in some portions, clusters of Ni-P have been observed.

Coarse globular uniform microstructures of varying sizes ranging from 5-30 μm have been spread throughout the scanning electron micrograph (Figure 14) of the as-deposited optimized electroless Ni-P substrates. The few white spots present in the micrograph depict that the porosity of the deposition is very less, thus signifying higher hardness of the as-deposited substrate. No cracks or holes are observed throughout the micrograph suggesting that the coating is dense with negligible defects. The grain boundaries are well-defined.

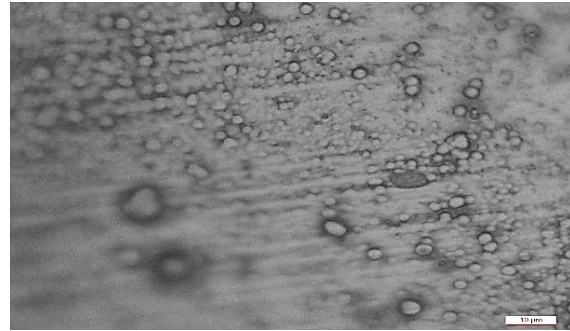


Figure 13. Optical Microstructure of electroless Ni-P coating deposited in optimal conditions

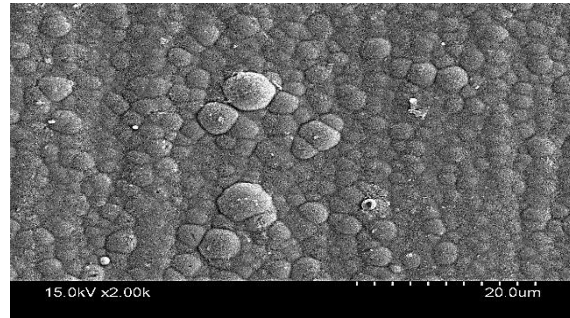


Figure 14. Scanning Electron Micrograph of the as-deposited optimized Ni-P coating

5.2. EDX study of the as-deposited optimized sample

Figure 15 depicts the EDX spectra of the as-deposited optimized coating. The peaks of Ni and P are observed, and thus arrive at the conclusion of the confirmed presence of Nickel and Phosphorous in the coating. From the EDX analysis, the elemental compositions are obtained as Ni - 90.39% and P - 9.61%. This data signifies that the coating is a medium Phosphorous content and thus it has a high hardness value.

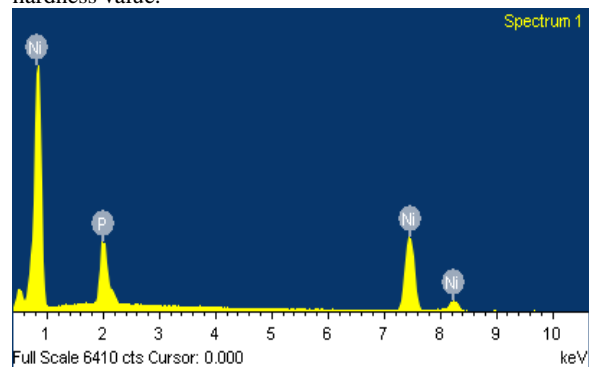


Figure 15. EDX spectra of the as-deposited optimized coating

6. Conclusion

Electroless Ni-P coating has been successfully deposited over the copper substrate with a 9.61 wt. % of Phosphorous as determined from EDX analysis. From the Response Surface Methodology Based on CCD design and the ANOVA analysis, it is prominent that Nickel Sulphate along with the interaction between Sodium Hypophosphate and Bath Temperature are the most significant factors in maximizing the microhardness of the coating. The

optimized conditions for obtaining the maximum hardness are 33.8 g/L of Nickel Sulphate, 19.7 g/L of Sodium Hypophosphite, and 87.6 °C of bath temperature under these conditions, the microhardness of the coating is found to be 1129.78 HV_{10g} from CCD model and for fuzzy and experimental results are respectively 1070 HV_{10g} and 1092 HV_{10g} whereas the microhardness of the copper substrate is originally 651 HV_{10g}. Thus there is an increase in the microhardness of the coating SEM micrograph of the as-deposited optimized coating revealed the presence of globular structures and the lower porosity of the coating which is a vital reason for its high hardness.

References

- [1] Brenner A, Riddell G. Deposition of nickel and cobalt by chemical reduction. *J Res Natl Bur Stand.* 1947 Nov;39(5):385.
- [2] Sudagar, Jothi, Jianshe Lian, and Wei Sha, "Electroless nickel, alloy, composite and nano coatings—A critical review". *Journal of alloys and compounds*, Vol. 571, 2013, 183-204.
- [3] Wang, Sheng-Chang, and Wen-Cheng J. Wei. "Kinetics of electroplating process of nano-sized ceramic particle/Ni composite". *Materials Chemistry and Physics*, Vol. 78.3, 2003, 574-580.
- [4] Xu, Yong, et al. "Flexible shear-stress sensor skin and its application to unmanned aerial vehicles". *Sensors and Actuators A: Physical*, Vol. 105.3, 2003, 321-329.
- [5] Trudgeon, M. A., and J. R. Griffiths. "Corrosion resistance of electroless nickel coatings in mining environments". *British Corrosion Journal*, Vol. 21.2, 1986, 113-118.
- [6] Liu, Xi, Jia-Qiang Gao, and Wen-Bin Hu. "Application of electroless Ni-P alloys in electronics industry". *Diandu yu Jingshi(Plating & Finishing)*, Vol. 28.1, 2006, 30-34.
- [7] Agarwala, R. C., and Vijaya Agarwala. "Electroless alloy/composite coatings: A review". *Sadhana*, Vol. 28.3, 2003, 475-493.
- [8] Sharma, S. B. "Characterization of carbon fabric coated with Ni-P and Ni-P-ZrO₂-Al₂O₃ by electroless technique". *Journal of materials science*, Vol. 37.24, 2002, 5247-5254.
- [9] Oraon, B., G. Majumdar, and B. Ghosh. "Improving hardness of electroless Ni-B coatings using optimized deposition conditions and annealing". *Materials & design*, Vol. 29.7, 2008, 1412-1418.
- [10] Oraon, B., G. Majumdar, and B. Ghosh. "Parametric optimization and prediction of electroless Ni-B deposition". *Materials & design*, Vol. 28.7, 2007, 2138-2147.
- [11] Krishnan, K. Hari, et al. "An overall aspect of electroless Ni-P depositions—A review article". *Metallurgical and materials transactions*, Vol. A 37.6, 2006, 1917-1926.
- [12] Narayanan, TSN Sankara. "Deposition of electroless Ni-P graded coatings and evaluation of their corrosion resistance". *Surface and Coatings Technology*, Vol. 200.11, 2006, 3438-3445.
- [13] Bangwei, Zhang. "Preparation, formation and corrosion for Ni-WP amorphous alloys by electroless plating". *Transactions of the IMF*, Vol. 74.2, 1996, 69-71.
- [14] Kumar, Anuj. "Study on thermal stability of electroless deposited Ni-Co-P alloy thin film". *Journal of Materials Science: Materials in Electronics*, Vol. 22.9, 2011, 1495-1500.
- [15] Armyanov, S. "Electroless deposition of Ni-Cu-P alloys in acidic solutions". *Electrochemical and solid-state letters*, Vol. 2.7, 1999, 323.
- [16] Chou, Yu Hsien. "Studies on Ni-Mo-P coatings by electroless deposition". *Key Engineering Materials*, Vol. 364. Trans Tech Publications Ltd, 2008.
- [17] Ger, Ming-Der, and Bing Joe Hwang. "Effect of surfactants on codeposition of PTFE particles with electroless Ni-P coating". *Materials chemistry and physics*, Vol. 76.1, 2002, 38-45.
- [18] Song, Y. W., D. Y. Shan, and E. H. Han. "Comparative study on corrosion protection properties of electroless Ni-P-ZrO₂ and Ni-P coatings on AZ91D magnesium alloy". *Materials and Corrosion*, Vol. 58.7, 2007, 506-510.
- [19] Szczygieł, B., A. Turkiewicz, and J. Serafińczuk. "Surface morphology and structure of Ni-P, Ni-P-ZrO₂, Ni-W-P, Ni-W-P-ZrO₂ coatings deposited by electroless method". *Surface and Coatings Technology*, Vol. 202.9, 2008, 1904-1910.
- [20] Ma, Chunyang. "Effect of heat treatment on structures and corrosion characteristics of electroless Ni-P-SiC nanocomposite coatings". *Ceramics International*, Vol. 40.7, 2014, 9279-9284.
- [21] Gadhari, Prasanna, and Prasanta Sahoo. "Effect of process parameters on microhardness of Ni-P-Al₂O₃ composite coatings". *Procedia Materials Science*, Vol. 6, 2014, 623-632.
- [22] Mejias, A. "Hardness evaluation from a bilayer coating system of Ni-P deposited on carbon steel plates by multicycle indentation tests". *Surface and coatings technology*, Vol. 334, 2018, 410-419.
- [23] Kumar, P. Sampath, and P. Kesavan Nair. "Studies on crystallization of electroless Ni-P deposits". *Journal of Materials Processing Technology*, Vol. 56.1-4, 1996, 511-520.
- [24] Sarkar, Subhasish. "Optimization of process parameters for electroless Ni-Co-P coating deposition to maximize microhardness". *Materials Research Express*, Vol. 6.4, 2019, 046415.
- [25] Keong, K. G., Wei Sha, and Savko Malinov. "Hardness evolution of electroless nickel-phosphorus deposits with thermal processing". *Surface and Coatings Technology*, Vol. 168.2-3, 2003, 263-274.
- [26] Yan, M., H. G. Ying, and T. Y. Ma. "Improved microhardness and wear resistance of the as-deposited electroless Ni-P coating". *Surface and Coatings Technology*, Vol. 202.24, 2008, 5909-5913.
- [27] Zangeneh-Madar, K., and SM Monir Vaghefi. "The effect of thermochemical treatment on the structure and hardness of electroless Ni-P coated low alloy steel". *Surface and Coatings technology*, Vol. 182.1, 2004, 65-71.
- [28] Milkey, K. R., et al. "Comparison between Taguchi Method and Response Surface Methodology (RSM) in Modelling CO₂ Laser Machining." *Jordan Journal of Mechanical and Industrial Engineering*, Vol. 8.1, 2014.
- [29] Mukhopadhyay, Arkadeb, et al. "Wear analysis of electroless Ni-P coating under lubricated condition using fuzzy logic". *Portugaliae Electrochimica Acta*, Vol. 34.1, 2016, 63-83.
- [30] Vinayagamorthy, R. "A central composite design based fuzzy logic for optimization of drilling parameters on natural fiber reinforced composite". *Journal of Mechanical Science and Technology*, Vol. 32.5, 2018, 2011-2020.
- [31] Balaji, M. "A fuzzy approach for modeling and design of agile supply chains using interpretive structural modeling". *JJMIE*, Vol. 10.1, 2016, 67-74.
- [32] Alazzam, Azmi, and Tariq Tashtoush. "Lead-Free Solder Reliability Modeling Using Adaptive Neuro-Fuzzy Inference System (ANFIS)." *Jordan Journal of Mechanical and Industrial Engineering*, Vol. 15.2, 2021.
- [33] Zhang, Qingyong, et al. "Driving Pattern Recognition of Hybrid Electric Vehicles Based on Multi-hierarchical Fuzzy

- Comprehensive Evaluation." Jordan Journal of Mechanical and Industrial Engineering, Vol. 14.1, 2020.
- [34] Manousi, Natalia. "Determination of rare earth elements by inductively coupled plasma-mass spectrometry after dispersive solid phase extraction with novel oxidized graphene oxide and optimization with response surface methodology and central composite design". Microchemical Journal, Vol. 152, 2020, 104428.
- [35] Sarkar, Subhasish. "Parametric optimization of process parameters on the response of microhardness of electroless Ni-P coating". Journal of Molecular and Engineering Materials, Vol. 6.01, No. 02, 2018, 1850003.
- [36] Daws, Kasim M., Zouhair I. Al-Dawood, and Sadiq H. Al-Kabi. "Selection of metal casting processes: a fuzzy approach". JJMIE, Vol. 2.1, 2008.
- [37] Moneim, Ahmed Farouk Abdul. "Fuzzy genetic prioritization in multi-criteria decision problems". Jordan Journal of Mechanical and Industrial Engineering, Vol. 2.4, 2008, 175-182.

Numerical Simulation Study on Steel Pipe Row Pile Support of Temporary Road Slope

Jian-guang BAI , Hai-jun LI*

College of Energy and Transportation Engineering, Inner Mongolia Agricultural University, Hohhot 010018, China

Received 11 Jun 2022

Accepted 26 Oct 2022

Abstract

The slope stability analysis and support structure design of temporary roads are particularly important for the normal traffic of roads and the safe construction of underground structures. In this paper, FLAC^{3D} software is used to study the numerical simulation of steel pipe piles support structure of the slope of temporary road by using the equivalent stiffness method. It is shown that under the action of road load, the normal stress of steel pipe pile has a peak value at 1.0m above the bottom of foundation pit, and the shear stress has two peaks at 1.0m above the bottom of foundation pit and 0.5m above the pile tip, which decrease at the pile tip. The horizontal displacement of the pile occurs at different depth, the displacement of the pile top is the largest, and the displacement from the pile top to the bottom of foundation pit decreases nonlinearly, and the horizontal displacement of the pile below the bottom of foundation pit is very small and remains unchanged. The vertical displacement of the pile increases gradually from the pile top to the pile tip, which results in tensile deformation of the pile. Stress concentration occurs at the temporary road position in the slope, and obvious horizontal displacement and vertical displacement which have obvious differences in different positions appear in the slope. The arrangement of piles can ensure the stability of the slope and there will be no overall shear failure surface.

© 2022 Jordan Journal of Mechanical and Industrial Engineering. All rights reserved

Keywords: Temporary road; Steel pipe row pile; Slope support; FLAC^{3D} ; Numerical simulation.

1. Introduction

With the rapid development of social economy, urban population density increases sharply, and the demand for urban space is increasing while the utilization space is gradually shrinking. The space environment under urban roads becomes the main site for laying urban infrastructure such as water supply and drainage, telecommunications, power supply and heat supply. In order not to affect the normal operation of traffic, temporary roads should be built during the construction of underground works. The side of the temporary road close to the construction of underground works will form a slope due to the excavation of foundation pit, and its stability will directly affect the safety of the temporary road. Therefore, the slope stability analysis and slope support design of temporary roads are particularly important and become an important subject of geotechnical engineering.

Steel pipe row piles (hereinafter referred to as steel pipe piles) are mainly filled with concrete in seamless steel pipes. The surface between piles is woven with reinforcing mesh and sprayed with concrete to form an integral structure, which can not only ensure the stability of soil at the pile position, but also prevent the extrusion of soil between piles. Steel pipe piles have the characteristics of high strength and fast construction speed [1], and are widely used in engineering [2-5]. The construction site of underground works under urban roads is narrow and there

is not enough sloping space, so the temporary road on one side of the underground works will form a vertical slope. In view of the characteristics of steel pipe piles, steel pipe piles have become one of the preferred methods for slope support of temporary roads. Liu Aihuan etc. applied micro steel pipe piles in the protection of soft rock high slope and studied the stability of slope with steel pipe pile support structure [6]. Steel pipe piles are used for the expressway reconstruction project in soft soil areas, which can quickly construct and restore traffic in a short time. Therefore, steel pipe pile support structure has obvious advantages [7]. Slope protection pile and steel pipe pile are used to support the slope of deep foundation pit, which can ensure that the slope displacement is less than the safety alarm value given in the specification [8]. Park, No-Won etc. [9] studied the bending capacity of steel pipe piles through transverse pile load test and showed that steel pipe piles have higher bending capacity. Wang, XQ etc. [10] analyzed the influence of different cross-section parameters on the bending capacity of steel pipe piles. Moonkyung, Chung etc. [11] adopted 3D numerical simulation to analyze the yield behavior of pile material and the elastic-plastic behavior of soil, indicating that the horizontal bearing capacity of steel pipe pile is large.

Xiaoshuang Li, et al. used Midas GTS to simulate the three-dimensional static stability of the slope, and the slope's own frequency, damping characteristics, and dynamic response acceleration distribution after detonation were studied [12]. In order to reveal the deformation and

* Corresponding author e-mail: 326833988@qq.com.

failure process and evolution laws of fractured rock masses, semi-quantitative indicators such as the shape, quantity, density, size, distribution range, spatial position, and rock mass movement angle of the developed fissures were analyzed[13].Fadi Alfaqs used finite element method to study the fiber orientation effect on mid-plane transverse deflection and inter laminar shear stress[14].Louay S. Yousuf used ANSYS software to check and verify normal stresses[15].Benamar Balegh,et al.used finite element method to model the crevice corrosion effect on sheet pile steel,the results show that while a tensile strain enhances stress uniformly through sheet pile steel, an increasing depth of crevice corrosion results in a concentrated stress at localized corrosion[16].Therefore, numerical simulation is an effective method to study slope stability and structural mechanical properties [17].In this paper, FLAC^{3D} software is used to study the regularities of stress and deformation of steel pipe pile support structure and the effect of temporary road slope, so as to provide reference for rational use of steel pipe piles.

2. Introduction to FLAC^{3D} software

FLAC^{3D} is a 3D continuous fast Lagrange analysis software for numerical analysis of geotechnical engineering [18]. It adopts the mixed discrete element model [19] and the finite difference method to simulate the failure process of all kinds of rock and soil, so as to calculate the deformation and stress of rock and soil under various external loads. It has a relatively perfect post-processing function, and it is easy to realize data and results processing[20].It has been widely used in the fields of slope [21-24], stope[25, 26], roadway[27], foundation pit[28, 29] and tunnel[30, 31].

3. Modeling

3.1. Zones

In this paper, it is assumed that the soil under temporary road is homogeneous and isotropic, and the

Mohr-Coulomb model is adopted in the constitutive model.

The length of slope model is 30m in horizontal direction (X) , 5m in temporary road extension direction (Y) , and 18m in vertical direction(Z). Grid cells are divided every 1m in three directions. Eight-node hexahedron elements are adopted. The whole model includes 43,200 zones and 47,901 nodes. In the calculation of the model, the soil has been consolidated under the action of gravity.The acceleration of gravity is set at 10kN/m³, the temporary road load is strip and is set at 20kPa, and the range of action is one time of the depth of the foundation pit and 1.0m away from the top line of the foundation pit. Vertical excavation was carried out on one side of temporary road, and the excavation depth(D) was 6.0m. In order to facilitate pile modeling, the soil was divided into three groups of soil1, soil2 and soil3 through two planes X =27 and Z =6. The soil type and the parameters of each group are the same. The specific parameters were shown in Table 1, and the 3D entity model established is shown in Fig. 1.

Table 1. Basic parameters

Density (kg/m ³)	Cohesive force (kPa)	Internal friction angle (°)	Modulus of compression E_s (MPa)	Poisson's ratio μ
1860	16	24	6.8	0.25

The bulk modulus (K) and shear modulus (G) are calculated by equations (1) and (2) [32, 33] respectively, $K=13.6\text{MPa}$, $G=8.16\text{MPa}$.

$$K = \frac{E}{3(1-2\mu)} \quad (1)$$

$$G = \frac{E}{2(1+\mu)} \quad (2)$$

Where: E is the elastic modulus, $E= 3E_s$.

As the influence of temporary road load on the ground is mainly considered,the free constraint is adopted at $z=18$, lateral displacement constraint is adopted at the vertical side of the outer boundary $X=0$, $X=30$, $Y =0$ and $Y =5$, and fixed constraint condition is adopted at the bottom.

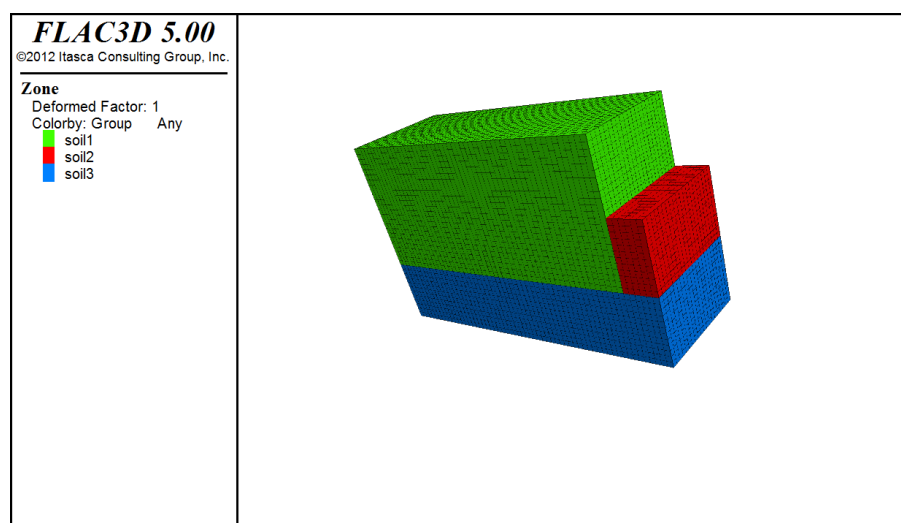


Figure 1. Zones model

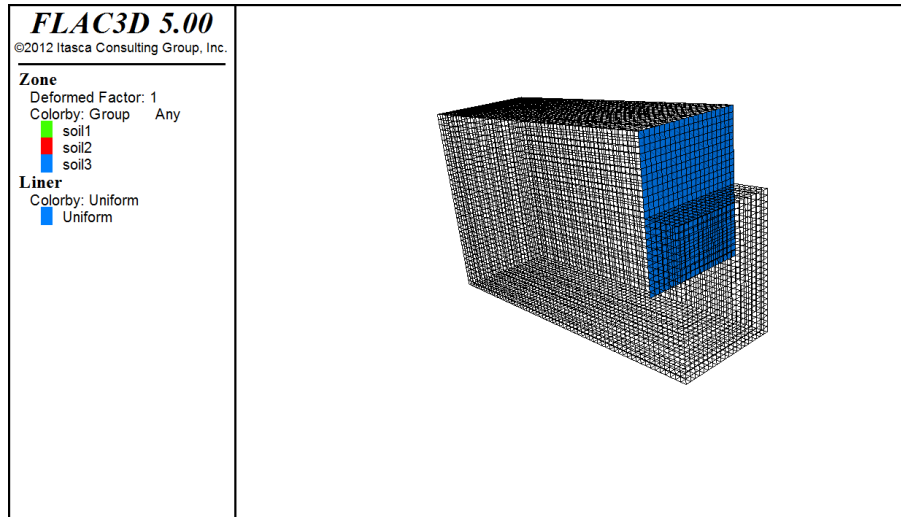


Figure 2. Structural element model

3.2. Structural elements

1. Element type

Steel mesh is laid between piles and concrete is sprayed on the surface of steel pipe pile support structure. The overall strength of support structure is provided by pile and concrete between piles. Liner element not only has certain bending resistance, but also can produce friction resistance with solid grid in shear direction. Taking the integrity of support structure and liner element attributes into consideration, liner structural element is used to simulate steel pipe piles, and discontinuous steel pipe piles are converted into continuous liner element. The established structural element model is shown in Fig.2. A total of 10 piles are arranged along the y axis direction, the pile length is 12m, the pile spacing is L=0.5m, the steel pipe material is seamless steel pipe, the yield strength is 235MPa, the type is 168mm×8mm, and the steel pipe is filled with C30 concrete. The equivalent stiffness method is adopted to convert the steel pipe piles into liner element and determine the liner element thickness, as shown in Fig. 3.

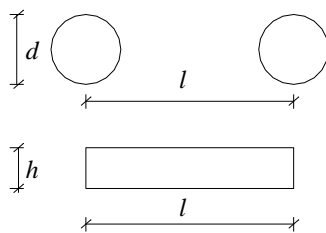


FIG.3 Diagram of equivalent stiffness

The steel pipe pile type is 168mm×8mm, the pile spacing is l=0.5m, so the moment of inertia $I_{x1} = \frac{\pi d^4}{64} = 3.098 \times 10^{-5} \text{ m}^4$. According to the equivalent stiffness method, the equivalent thickness of liner structural element is calculated according to equation 3, and the result is 0.098m.

$$I_{x1} = \frac{\pi d^4}{64} = I_{x2} = \frac{lh^3}{12} \tag{3}$$

2. Parameters Elastic modulus

The elastic modulus of steel pipe pile is calculated by weighted average of elastic modulus of steel pipe and concrete according to area. The elastic modulus of seamless steel pipe is 192GPa, and the elastic modulus of

C30 concrete is 30GPa, so the weighted elastic modulus of concrete-filled steel pipe pile is 59.39GPa.

3. Stiffness and strength

The stiffness kn and ks per unit area of normal and tangential coupling spring of the pile are taken as 10 times of the stiffness of the adjacent zones, and the normal surface stiffness of zones is calculated according to Formula (4). The result of kn and ks is $4.9 \times 10^5 \text{ KN/m}$. The tensile stiffness of pile-soil interface is 0, and the residual strength of pile-soil interface after failure is 0.

$$\max \left[\frac{K+4/3G}{\Delta z_{\min}} \right] \tag{4}$$

4. Other parameters

The cohesion between pile and soil is 0.8 times that of soil, so the cohesion is 12.8kPa and the internal friction angle is 19.2°. The density of steel pipe pile is 2500kg/m³.

4. Discussion

4.1. Numerical simulation analysis of steel pipe piles

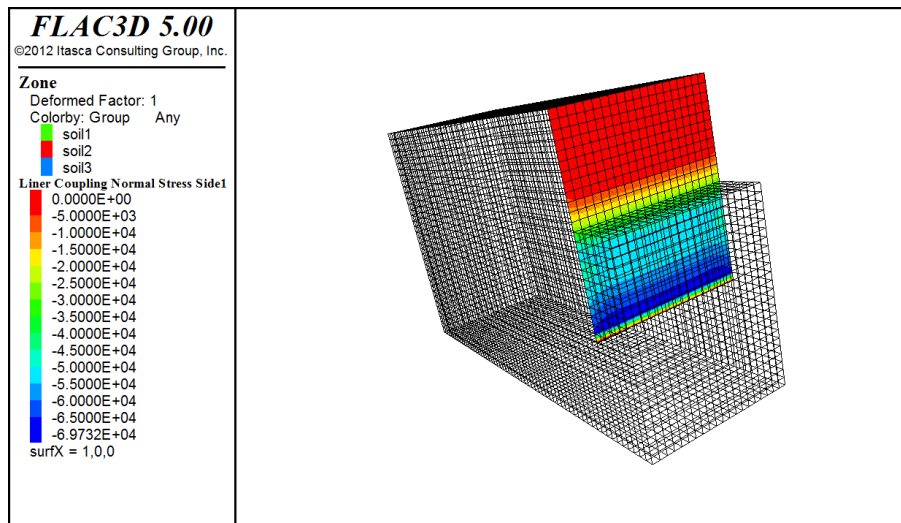
1. Stress of steel pipe piles

Figure 4(a) and Figure 4(b) respectively show the contour of normal stress and shear stress of steel pipe piles. As shown in Fig. 4(a), the normal stress of piles is zero between the pile top and 1.0m above the bottom of foundation pit. It increases first and then decreases from the position 1.0m above the bottom of foundation pit to the pile tip, and reaches its maximum at the position 0.5m above the pile tip. Pile tip effect occurs at the pile tip, and the normal stress decreases locally, which direction is the same as x negative direction. As shown in Fig. 4(b), the shear stress of piles has two peak values, which are located at 1.0m above the bottom of foundation pit and 0.5m above the pile tip. Pile tip effect occurs at the pile tip, and the normal stress decreases locally, which direction is the same as x negative direction. As shown in Fig. 4(b), the shear stress of piles has two peak values, which are located at 1.0m above the bottom of foundation pit and 0.5m above the pile tip. Pile tip effect occurs at the pile tip, and the normal stress decreases locally, which direction is the same as x negative direction. The shear stress on both sides of the first peak decreases gradually, and the range of action is from the pile top to the position half the depth below the bottom of foundation pit. The shear stress on both sides of the second peak decreases gradually, and the range of action is from the pile tip to the position half the depth below the bottom of foundation pit, which direction is the same as z negative direction.

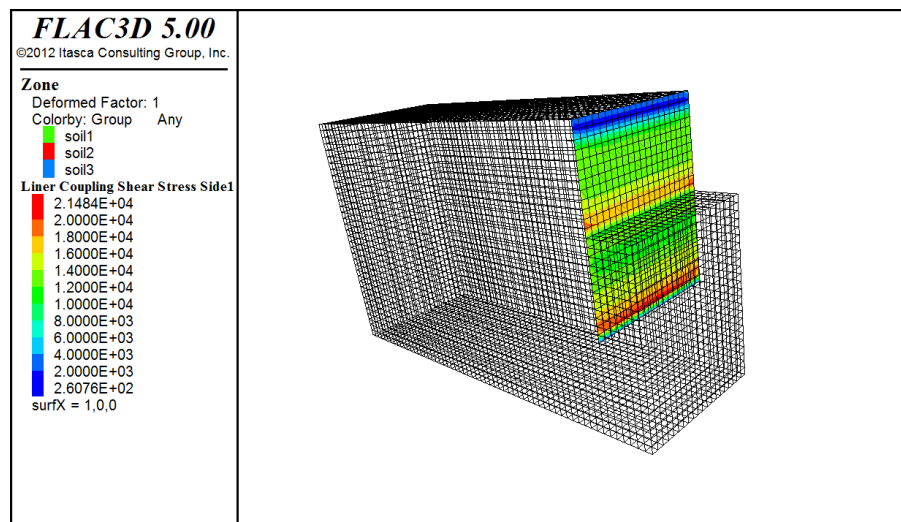
2. Displacement of steel pipe piles

The monitoring data show that the steel pipe pile will produce horizontal and vertical displacement under the action of earth pressure[35].Figure 5(a) and Figure 5 (b) respectively show the contour of Horizontal displacement and Vertical displacement of steel pipe piles.As shown in Fig. 5(a), different from the steel pipe pile with support [36], the cantilever steel pipe pile is subject to horizontal displacement under the action of earth pressure, and the displacement of the pile top is the largest[37], reaching 4.2cm. From the top of the pile to the bottom of the foundation, the displacement gradually decreases, and the reduction rate continuously decreases, showing a nonlinear decreasing trend in general, rather than increasing first and then decreasing [38]. The main reason is that the latter

adopts the combination of steel pipe pile and concrete row pile, which has strong stiffness and good bending resistance.From the bottom of the foundation pit to the pile tip, the displacement is consistent under the reverse extrusion of the soil under the bottom of the foundation pit, and the bending moment at the bottom of the foundation pit is the largest.As shown in Fig. 5(b), the steel pipe pile has vertical displacement.From pile top to pile tip, the displacement changes from 7.29mm to 7.35mm , and the relative displacement change rate of pile top is only 9.1%.The difference of vertical displacement between pile top and pile tip indicates that the pile has vertical tensile deformation.



(a)



(b)

Figure 4. Contour of stress of steel pipe piles
(a) Contour of Normal stress (b) Contour of Shear stress

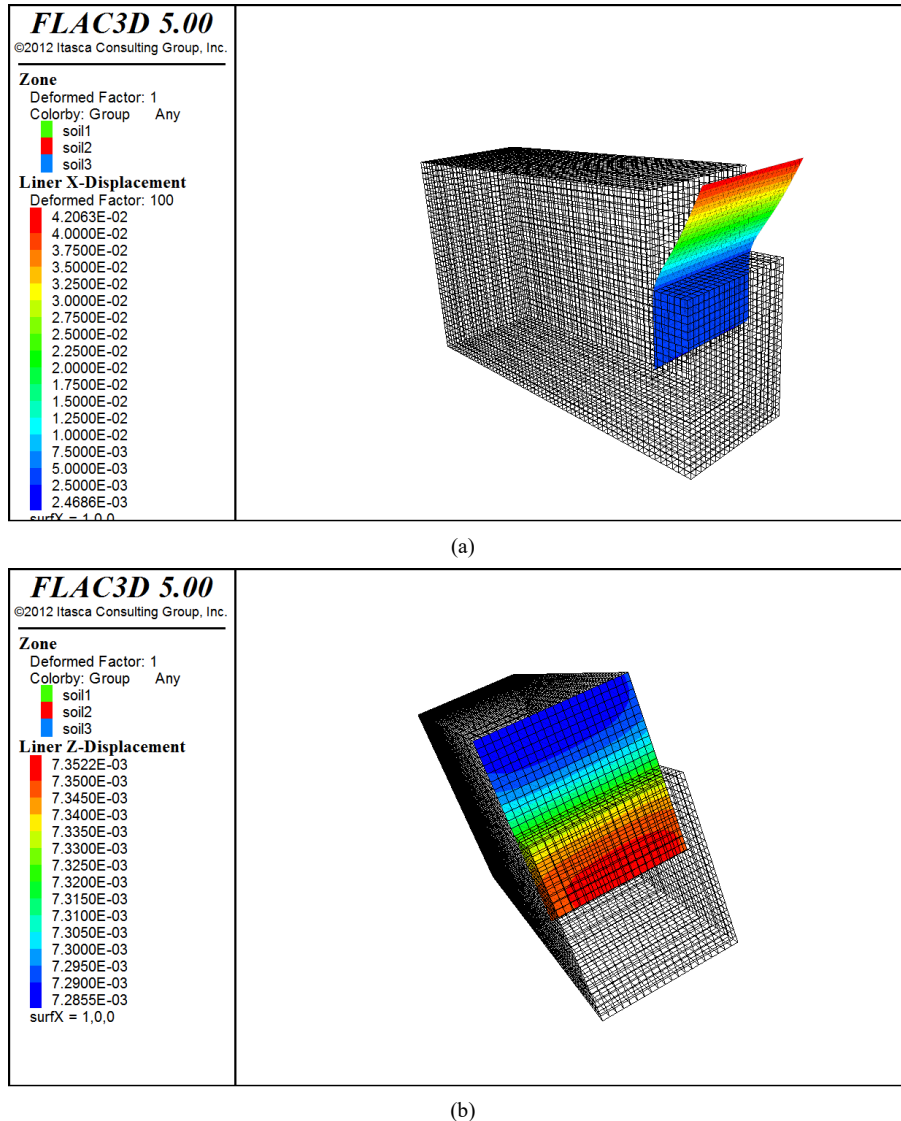


Figure 5. Contour of displacement of steel pipe piles
 (a) Contour of Horizontal displacement (b) Contour of Vertical displacement

4.2. Numerical simulation analysis of slope

1. Displacement of slope

As shown in Fig. 6(a), the horizontal displacement of the slope increases first and then decreases from the position far away from the foundation pit to the position of the foundation pit. The displacement at the start point (0,5,18) is 0, and increases approximately linearly in the range of 0-15m. After 15m, the displacement increases gradually at a faster rate and reaches the maximum at 24.7m. Therefore, it is affected in the range of 4.5D away from the top line of the foundation pit, and begins to have a strong influence in the position of 2.0D (15m) away from the top line of the foundation pit. The displacement is the largest at the position 1/4 of the road width away from the road center towards the direction of the foundation pit. Limited by the piles, the displacement decreases towards the pile. The results indicate that centered on the position 1/4 of the road width away from the road center towards the direction of the foundation pit, the soil at the side far away from the center has a relative tensile effect, and the soil near the center has a relative compaction effect.

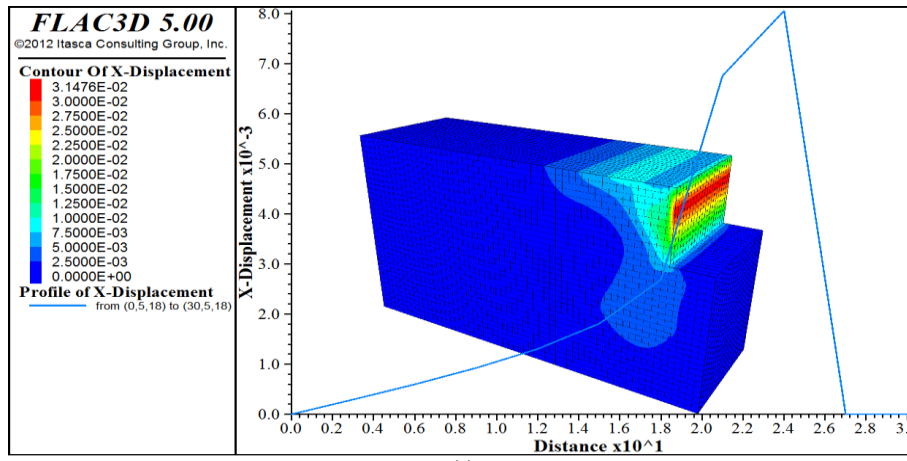
As shown in Fig. 6(b), affected by the temporary road load, the soil under the road has significant settlement, the displacement at the center of the road reaches 1.01cm. With the increase of the horizontal distance from the road, the vertical displacement of the slope on both sides of the road decreases gradually. Affected by the lateral limit of the pile, the vertical displacement near the piles increases, and the soil beside the pile rises upward. Along the depth direction, the vertical displacement is zero in the range of (1/3~2/3) D beside the pile above the bottom of foundation pit, and the displacement outside the range is positive. The soil beside the pile and at the bottom of the foundation pit rises upward. The vertical displacement of the slope away from the pile decreases gradually from the surface to the underground.

2. Slope sliding analysis

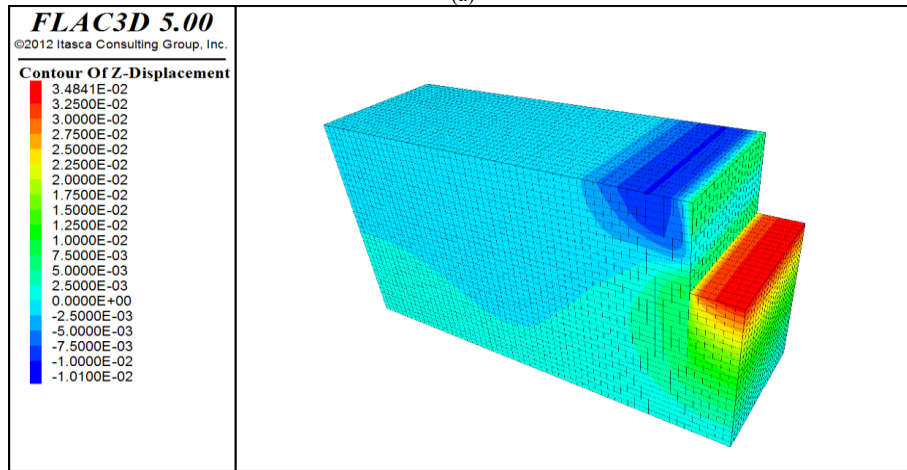
As shown in Fig. 7, the shear deformation mainly occurs in the soil at the pile position and the bottom of the foundation pit. In the 1/2D section downward from the ground surface, the shear deformation is mainly distributed between the top line of the foundation pit and the boundary line of the temporary road. From the surface downward, the

shear deformation tends to increase with the increase of depth, and the maximum shear deformation occurs in the range of $(1/4 \sim 1/2) d$ depth. In the section from $1/2D$ to the bottom of the foundation pit, the shear deformation decreases gradually from top to bottom, and it is not only distributed between the top line of the foundation pit and the boundary line of the temporary road, but also extends to the inside of the slope. The horizontal extension range is mainly distributed in the temporary road range, and does not extend to the surface. The shear strain increment gradually decreases from the piles to the inside, and no

through sliding surface is formed. In the section below the bottom of foundation pit, the shear deformation outside the pile row gradually decreases with the increase of the depth. The shear deformation of slope from the pile position along the horizontal direction to the inside of the foundation pit also decreases gradually, and it is the largest at the pile position at the bottom of the foundation pit. At the inner side of the piles, the shear deformation of the slope is obvious only at the depth of 1.5m below the bottom of the foundation pit, and the shear deformation below 1.5m is very small.



(a)



(b)

Figure 6. Contour of displacement of slope
(a) Contour of Horizontal displacement (b) Contour of Vertical displacement

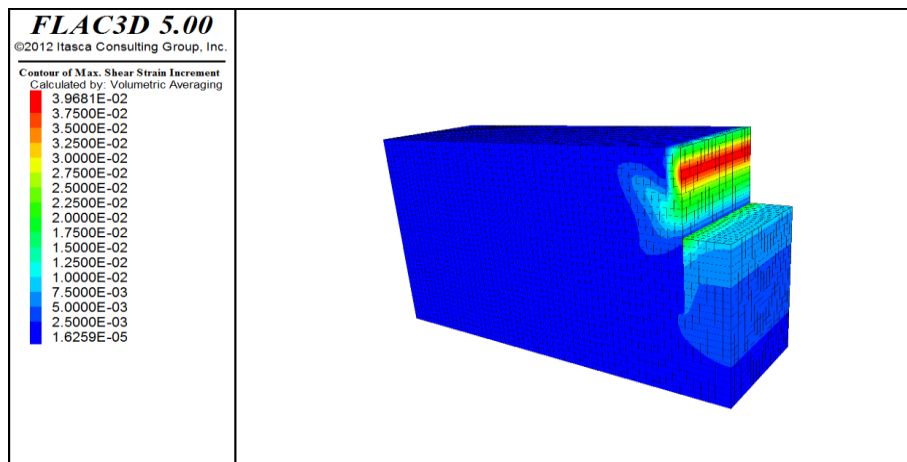


Figure 7. Contour of Max. shear strain increment

3. Slope stress analysis

Fig. 8 shows the contour slice of vertical stress determined with y as normal direction. According to the figure, the vertical stress in the slope gradually increases from the surface downward, and the stress is more concentrated at the position of temporary road. Therefore, the construction of temporary roads has an adverse impact on slope stability. At the same depth below the ground, the vertical stress of the pile position is lower than that of the ground without load. Therefore, the piles can not only bear the shear action in the horizontal direction, but also produce upward friction on the soil, which can reduce the vertical deformation of the soil. It indicates that the soil and pile have relative deformation. Below the bottom of the foundation pit, the stress changes on both sides of pile. The stress of soil in the excavation area increases locally in the range of 1/2 embedment depth, and decreases locally below the range of 1/2 embedment depth, and the stress of pile tip tends to be stable.

5. Validation analysis

Lizheng is the main software for the stability analysis of foundation pit slope, which is widely used in the actual slope support engineering design. The support design of the slope is calculated through Lizheng in the paper. The cohesion and internal friction angle of the soil layer used

in the calculation are shown in Table 1, some parameters are shown in Table 2, and the values of other parameters are the same as those used in the numerical simulation.

Table 2. Design parameters

Weight (kN/m ³)	Importance coefficient	Tensile, compressive and bending strength (MPa)	Shear strength (MPa)	Section plastic development coefficient
18.6	1.0	215	215	1.05

5.1. Stability analysis

The most unfavorable sliding surface is determined through the calculation of Lizheng. The Swedish slice method is adopted in the calculation, and the soil strip width of 1.0m is selected. The results show that the center coordinates of the most unfavorable sliding arc are (-1.947, 1.923) and the radius is 8.201 (as shown in Fig. 9). The integral stability safety coefficient of the slope is 2.490, greater than 1.30, meeting the specification requirements.

It can be seen from Fig. 7 that the slope with steel pipe pile support does not form a through sliding surface, the integral stability of the slope is good, and no sliding failure will occur. The numerical simulation is consistent with the calculation results of Lizheng design.

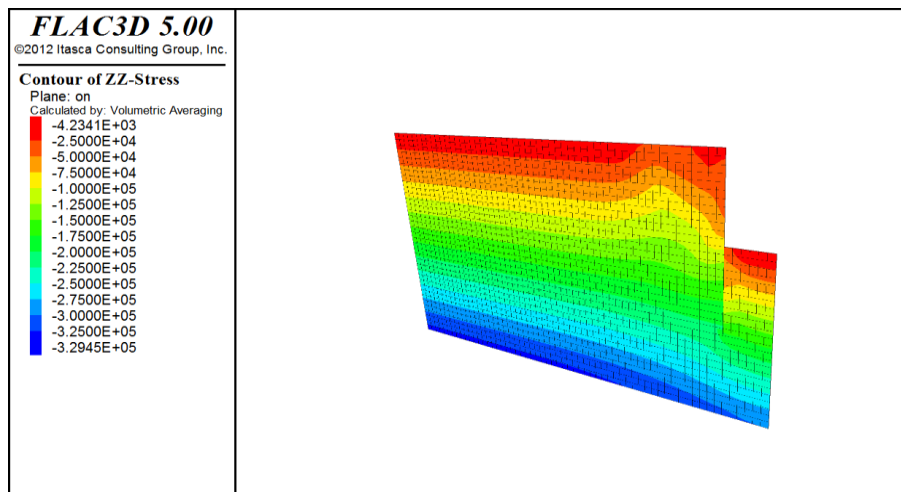


Figure 8. Contour slice of Vertical stress

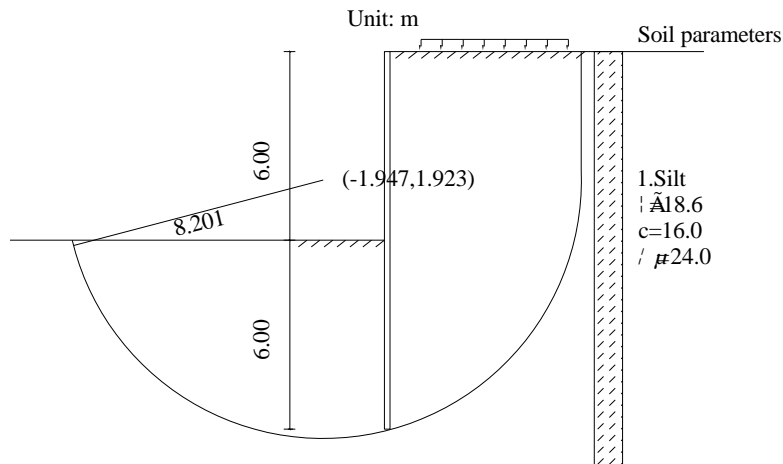


Figure 9. Integral stability (LiZheng software)

5.2. Displacement analysis

According to the comparison between Fig. 5 (b) and Fig. 6 (b), the vertical displacement of piles and soil at the same depth is different. It indicates that the piles and soil move relatively, resulting in friction on the contact surface. Because the vertical displacement of pile and soil is nonlinear, the friction is different at different depths. At the same depth, there is a difference in the horizontal displacement between the piles and the soil. The horizontal displacement of the row piles is greater than that of the soil, resulting in a certain degree of void between the piles and the soil, which is mainly caused by the bending deformation of the steel pipe piles due to the large bending moment near the bottom of the foundation [39]. The conclusion of slope stability shows that there is a certain degree of void between the piles and the slope, which will not affect the integral stability of the slope to a certain extent. Therefore, void phenomenon can be allowed to a certain extent in the actual design, which can save materials.

In the numerical simulation, the pile spacing is 500mm and the pile diameter is 168mm, so the distance diameter ratio is 2.98. As shown in Fig. 5 and Fig. 6, the maximum horizontal displacement of the slope is 3.1cm, and its maximum vertical displacement is 1.0cm. The maximum horizontal displacement of the pile is 4.2cm, and its maximum vertical displacement is 0.7cm. As the support structure is of class II, the monitoring alarm value specified in the specification is not exceeded [40]. Therefore, the arrangement of steel pipe piles with a distance diameter ratio of 2 [41] is not suitable for all situations. The reason is that the appropriate distance diameter ratio is related to the soil type of the slope, groundwater, ground load, crown beam setting and other factors, which need to be determined through comprehensive analysis.

As shown in Fig. 10, the maximum horizontal displacement of piles calculated by LiZheng is -466.39mm - -0.95mm, which is close to the maximum horizontal displacement of 420mm obtained by numerical simulation, and the error is only 9.9%, so the numerical simulation results are relatively reliable.

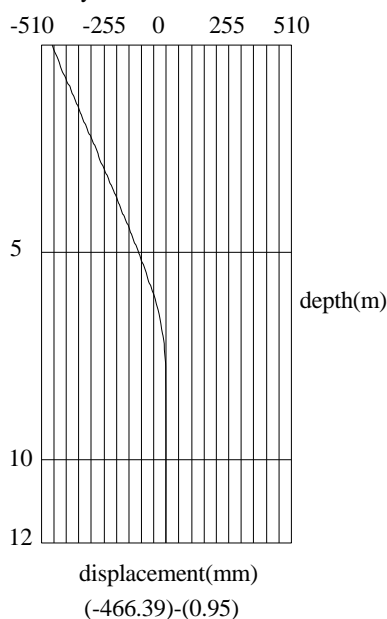


Figure 10. Displacement (LiZheng design)

6. Conclusions

1. The position 1.0m above the bottom of the foundation pit is the boundary point of pile stress. The normal stress increases from this point downward, and the shear stress peaks. The maximum normal stress occurs at 0.5m above the pile tip, and the shear stress peaks again. The normal stress and shear stress at pile tip decrease.
2. Due to the deformation of slope soil, the steel pipe pile has horizontal and vertical displacement under the action of soil. The bottom of the foundation pit is the boundary point of horizontal displacement. The horizontal displacement above the bottom of the foundation pit is large and changes obviously. The horizontal displacement at the pile top is the largest, and the displacement below the bottom of the foundation pit is very small. The vertical displacement of pile increases gradually from pile top to pile tip, and the relative displacement between pile and soil leads to friction, resulting in tensile deformation of pile.
3. The horizontal displacement of slope is the largest at the position 1/4 of the road width away from the road center towards the direction of the foundation pit. It gradually decreases to both sides, and the influence range mainly concentrates on the range of 4.5D away from the top line of the foundation pit. The vertical displacement of slope is the largest under the temporary road, and gradually decreases from the surface downwards. The vertical displacement near the pile increases upward and downward with $(1/3 \sim 2/3) D$ as the center. The influence of the vertical displacement in the horizontal direction exceeds the range of 4.5D from the excavation top line.
4. Small shear deformation occurs in the slope near pile, and the shear deformation is not obvious in the slope. It does not form a through sliding surface in the slope, and steel pipe piles can ensure the stability of the slope.
5. Affected by the load of the temporary road, the slope at the temporary road location produces stress concentration and causes displacement of the slope. The displacement of slope is different from that of pile, resulting in friction between slope and pile.

Expectation

Only a single type of soil is considered in the paper, the ground has no load other than that of the temporary road, and there is no groundwater. In practice, the stress and displacement of pile and slope are affected by a variety of factors, which should be comprehensively analyzed.

Void phenomenon between piles and the soil can be allowed to a certain extent in the actual design. Under the condition of ensuring the integral stability of the slope, the degree of voids allowed to occur needs to be further studied.

Acknowledgements

The authors would like to thank "the 13th five year plan" for educational science research in Inner Mongolia Autonomous Region (NGJGH2019402) for this study.

Reference

- [1]W. LI, K. Zhang, C.Y. Guo, Q. Cui, C.Q. Zhang, H.H. Ma, "Mechanical Properties and Microstructure an Pile-soil interface of Post-grouting Steel Pipe Pile". *Science and Technology*, Vol. 21, No. 19, 2021, 8159-8165.
- [2]M.Y. Zhang, J.X. Ma, S.J. Yang, Y.H. Wang, X.Y. Bai, S.X. Sun, "Experimental Study on Bending Moment of Double-Row Steel Pipe Piles in Foundation Excavation". *Advances in Civil Engineering*, 2020, 1-8.
- [3]H.W. Jin, "Design of Retaining and Protecting for a Deep Foundation Excavation". *Advanced Construction Technologies*, 2014, 1416-1420.
- [4]Y. Ishihama, J. Takemura, V. Kunasegaram, "Analytical evaluation of deformation behavior of cantilever type retaining wall using large diameter steel tubular piles into stiff ground". *Geotechnics For Sustainable Infrastructure Development*, No. 62, 2020, 91-98.
- [5]S.F. Zhang, C. Xia, H.C. Qin, T.F. Wang, Q.G. Chai, "Study on the Application of the Combined Retaining Structure of Anchor and Steel Pipe Pile in Reinforcement of High Fill Subgrade". *Construction Technology(Chinese and English)*, Vol. 50, No. 19, 2021, 88-91+96.
- [6]A.H. Liu, Y.W. Zhao, K. Huang, H.L. Tang, "Application of Mini-Steel Pipe Piles in Soft Rock High Slope". *Water Conservancy Science and Technology and Economy*, Vol. 28, No. 04, 2022, 115-121.
- [7]J.L. Yan, "Application Analysis of Steel Pipe Pile Supporting Structure in Soft Soil Area". *China Municipal Engineering*, No. 01, 2022, 85-88+127.
- [8]J. Sun, M.H. Fan, X. Li, "Combined Supporting system of the Slope Protection Pile and the Compound Soil Nail Wall with Micro Steel Pipe Piles". *Drilling Engineering*, Vol. 48, No. 10, 2021, 116-124.
- [9]N.W. Park, K.H. Paik, "Lateral Behavior of Hybrid Composite Piles Using Prestressed Concrete Filled Steel Tube Piles". *Journal of the Korean Geotechnical Society*, Vol. 34, No. 12, 2018, 133-143.
- [10]X.Q. Wang, S.M. Zhang, Y.S. Huang, "Influences of Cross Section Parameters on Bending Resistance of TSC Pile". *Advances in Civil and Industrial Engineering*, 2014, 464-468.
- [11]C. Moonkyung, S.H. Lee, S.R. Kim, "Reinforcement Effect of Steel-Concrete Composite Group Piles by Numerical Analysis". *Journal of the Korean Geotechnical Society*, Vol. 26, No. 11, 2010, 29-38.
- [12]X. S. Li, Q. H. Li, Y. J. Hu, et al, "Study on Three Dimensional Dynamic Stability of Open-Pit High Slope under Blasting Vibration ". *Lithosphere*, Vol.2022,2022, 1-1731.
- [13]X. S. Li, Q. H. Li, Y. J. Hu, et al, " Evolution Characteristics of Mining Fissures in Overlying Strata of Stope after Converting from Open-Pit to Underground". *Arabian Journal of Geosciences*, Vol. 14, No.24, 2021, 1-18.
- [14]F.Alfaqs, " Dynamic Behavior of Thin Graphite/Epoxy FRP Simply Supported Beam Under Thermal Load Using 3-D Finite Element Modeling". *Jordan Journal of Mechanical and Industrial Engineering*, Vol. 15, No. 3, 2021, 301-308.
- [15]L.S. Yousuf, " The Effect of Temperature on the Stresses Analysis of Composites Laminate Plate". *Jordan Journal of Mechanical and Industrial Engineering*, Vol. 13, No. 4, 2019, 265-269.
- [16]B.Balegh, H. Trouzine, Y. Houmadi, "Finite Element Simulation and Prediction of Mechanical and Electrochemical Behavior on Crevice Corrosion in Sheet Pile Steel". *Jordan Journal of Mechanical and Industrial Engineering*, Vol. 12, No. 1, 2018, 23-31.
- [17]A.S. Alshyyab, F.H. Darwish, "Three-Dimensional Stress Analysis around Rivet Holes in a Plate Subjected to Biaxial Loading". *Jordan Journal of Mechanical and Industrial Engineering*, Vol. 12, No. 4, 2018, 323-330.
- [18]C. Sun, G.G. Yue, M.X. Li, "Study on the Influence of Pile Displacement of Foundation Pit Retaining Pile Based on Flac3D Numerical Simulation". *Journal of Jilin Jianzhu University*, Vol. 37, No. 02, 2020, 28-32.
- [19]Q.P. Xiao, Y.R. Zhong, X. Chen, X.L. Wang, "Analysis of Mechanical effect of Roadway Excavation and Support Based on Flac3D". *Shandong Chemical Industry*, Vol. 50, No. 22, 2021, 162-165+168.
- [20]J. Zhao, J.C. Sheng, B.Y. Su, Z.T. Zhang, "Method of Section -node Control for Mesh Auto-generation in 3D FEM Analysis". *Journal of Yangtze River Scientific Research Institute*, Vol. 17, No. 04, 2000, 34-37.
- [21]B. Hou, H.J. Jiang, "Stability Analysis of Maowu Slope Based on Flac3D Numerical Simulation Method". *Jiangxi Building Materials*, No. 07, 2021, 76-78.
- [22]H. Zhang, Z.G. Fan, "Treatment engineering and numerical simulation of a highway accumulation landslide based on FLAC3D". *China Water Transport*, Vol. 22, No. 02, 2022, 35-37.
- [23]Y. Tang, X. Yu, Z.H. Sun, "Study on Seismic Reinforcement Mechanism and Model of Anti-slide Piles based on FLAC3D". *Hydropower Generation*, Vol. 45, No. 07, 2019, 33-37.
- [24]Z.Y. Zou, H. Chen, Z.X. Wang, X.M. Long, L.Y. Chen, "Improvement of the strength reduction method on the basis of FLAC3D in slope stability". *International Journal of Earth Sciences and Engineering*, Vol. 9, No. 02, 2016, 486-491.
- [25]Q.H. Li, X.S. Li, J.B. Gen, L. Luo, "FLAC3D Numerical Simulation of Open-pit Transformation to Underground Slope and Stope Stability". *Nonferrous Metals (mine part)*, Vol. 73, No. 02, 2021, 5-10.
- [26]Y.Q. Gong, G.L. Guo, "A data-intensive FLAC3D computation model: Application of geospatial big data to predict mining induced subsidence". *Computer Modeling in Engineering and Sciences*, Vol. 119, No. 02, 2019, 395-408.
- [27]J. Zhou, "Optimization Analysis of Wall Rock Support Parameters of Mining Roadway based on FLAC3D". *China Mine Engineering*, Vol. 50, No. 05, 2021, 49-52.
- [28]B. Qiu, "Impact of Foundation Pit Construction Process load on Surrounding Environment based on FLAC3D Simulation". *Foundation & Structure Engineering*, Vol. 37, No. 06, 2019, 245-247+251.
- [29]Y.F. Liu, S.G. Liu, "FLAC3D simulation analysis of excavation and supporting structure of deep foundation pit". *International Journal of Earth Sciences and Engineering*, Vol. 9, No. 05, 2016, 2321-2326.
- [30]S. Tang, J.X. He, X.L. Lin, "Study on the Pre-reinforcement Measures of Tunnel Shed with Soft Surrounding Rock based on FLAC3D". *Subgrade Engineering*, No. 05, 2021, 226-230.
- [31]Z.S. Shao, B.X. Li, "Study on Deformation and Secular Stability of Argillaceous Siltstoue Tunnel". *Chinese Journal of Underground Space and Engineering*, Vol. 17, No. 03, 2021, 883-896.
- [32]D.W. Song, F.M. Zhang, X.J. Han, Z.Q. Liu, "Analysis of the Deformation of the Soft and Hard Rock Interaction Slope based on FLAC3D". *Journal of Hebei University of Engineering(Natural Science Edition)*, Vol. 33, No. 02, 2016, 86-90.
- [33]Q.Y. Meng, "Deformation and Stability Analysis of Excavated Slope by FEM". *Journal of Hebei University of Engineering(Natural Science Edition)*, Vol. 27, No. 03, 2010, 32-34.
- [34]General Administration of Quality Supervision, Inspection and Quarantine of the People's Republic of China & Standardization Administration, Carbon Structural steels(GB/T700-2006). Peking: China Standards Press, 2006.

- [35]Y.W. Mao, J. Zhang, "Analysis on Monitoring the Supporting Effect of Micro Steel Pipe Pile Under the Condition of Miscellaneous Fill". *Urbanism and Architecture*, Vol. 17, No. 29, 2020, 113-114+117.
- [36]J. Rao, "Analysis on Application of Prefabricated Steel Pipe Pile Retaining Structure". *Urban Roads Bridges & Flood Control*, No. 11, 2021, 134-137+141+18.
- [37]B.Dong,Y.T. Zi,Y.W. Yang, "Miniature Steel Tube Pile Using in a Deep Foundation Pit in Coastal Area". *Shanxi Architecture*, Vol. 46, No. 13, 2020, 48-50.
- [38]J.Sun, "Combined Supporting System of the Slope Protection Pile and the Compound Soil Nail Wall with Micro Steel Pipe Piles". *Drilling Engineering*, Vol. 48, No. 10, 2021, 116-124.
- [39]F.G Hu, W.L. Chao, L.J. Feng, "Study on bearing failure mode of slope strengthened by micro single pile based on ultimate resistance". *Highway*, Vol. 65, No. 04, 2020, 12-18.
- [40]Construction Department of Shandong Province. *Technical Code for Monitoring of Building Excavation Engineering(GB50497-2009)*.Peking:China Planning Press;2009.
- [41]B.J. Yang,C.H. Zhu, "Numerical simulation of foundation pit based on steel pipe pile supporting system". *Water Conservancy Science and technology and Economy*, Vol. 26, No. 11, 2020, 65-69.

Study of Repairing a Corroded Cryogenic Tank by Composite Wrap Subjected to Thermal and Mechanical Loadings

Leila BELKADDOUR*, Mohamed BERRAHOU

University of Ahmed Zabana, GIDD Industrial Engineering and Sustainable Development Laboratory, Relizane, Algeria

Received 11 Jul 2022

Accepted 5 Sep 2022

Abstract

Cryogenic tanks are still considered the most efficient method of storing fluids. This is due to its resistance to much damage caused by corrosion induced by low temperature and internal pressure. In this study, the finite element method is used to analyze the repair performance by a composite wrap in a corroded tank. A parametric analysis was carried out in order to highlight the effects of low temperature and pressure on the thermo-mechanical behavior of the corroded structure and to predict the evolution of stresses in the vicinity of corrosion. An approach to this problem based on the notion of material strength was necessary since it was essential to take both the size of the pre-existing defect and the amount of mechanical stresses. The results obtained show the effect of thermal and mechanical loading to examine their impact on the strength of the structure on the one hand, and on the other hand, the influence of the composite wrap repair in the different corrosion lengths (Path 1, 2, 3) on the reinforcement of the tank. Finally, repairing damage (corrosion) using FRP composites increases the durability of cryogenic tanks, which increases their efficiency their performance and increases their life, although the rate of improvement depends largely on operating conditions, such as pressure and temperature.

© 2022 Jordan Journal of Mechanical and Industrial Engineering. All rights reserved

Keywords: Cryogenic ; tanks; Temperature; Internal Pressure; Corrosion; Finite Element Method (FEM); thermo-mechanical behavior; Von Mises Stress; Fiber Orientation, Composite; wrap..

Nomenclature

R_{ext}	internal radius [mm]
R_{int}	internal radius [mm]
t	thickness of tank [mm]
L	tank length [mm]
A	corrosion depth [mm]
C	half-corrosion length [mm]
t_p	Composite wrap thickness [mm]
L_p	Composite wrap length [mm]
t_a	thickness of adhesive [mm]
s	stacking sequences [mm]
E_1	Young's Modulus in X direction [GPa]
E_2	Young's Modulus in y direction [GPa]
E_3	Young's Modulus in z direction [GPa]
ν_{12}	Poisson Ratio in X-Y plan
ν_{13}	Poisson Ratio in X-Z plan
ν_{23}	Poisson Ratio in Y-Z plan
G_{12}	Shear Modulus in X-Y plan [GPa]
G_{13}	Shear Modulus in X-Z plan [GPa]
G_{23}	Shear Modulus in Y-Z plan [GPa]
CTE	coefficient of thermal expansion [°C]
P_i	internal pressure [MPa]
T_{int}	internal temperature [°C]
T_{ext}	external temperature [°C]

1. Introduction

Storage tanks have long been used in the industrial sector as the most cost-effective and safest method for storing and transporting gas. However, the incidence of accidents has increased significantly as the number of people using them has increased [1-3]. Reinforcement of composite wrap on damaged surfaces is a common local repair approach in the industry [4], to reduce stresses at the corrosion tips and improve the life of the damaged structure [5].

On the basis of bibliographic research, Xugang Wang et al studied the fracture characterization of a 6061 aluminum alloy tube to analyze the mechanism of improvement of the cryogenic forming limit. However, their study was limited to numerical analysis [6]. A study of the effects of surface corrosion damage on the fatigue behavior of 6061 aluminum alloy extrusions was analyzed by Matthew Weber et al [7]. In addition, a numerical study to analyze the transient temperature field and the residual stress distribution caused by the thermal effect in a 6061 aluminum alloy sheet was evaluated by Jianing Wang et al [8]. Sohail et al investigated the behavior of a damaged aluminum aircraft structure repaired with a composite plate under traction using experimental tests and numerical modeling. A parametric study was also conducted for such a repaired cracked plate in order to observe the effect of

* Corresponding author e-mail: laibelkaddour@gmail.com.

the orientation of the fibers and the influence of stress intensity factor lengthening the life of the structure [9, 11]. M. Salem and Faycal Benyahia used numerical modeling to study the behavior of a cracked aluminum plate. The stress intensity factor was calculated for a plate with a horizontal crack under thermo-mechanical loading. The cracked plate was eventually repaired using a composite material, and the effect of this material on fatigue life stress was observed using the finite element method [12]. Mohamed Berrahou et al developed an extensive finite element method to study the thermo-mechanical behavior of a corroded aluminum plate that is repaired with a composite wrap. The effects of patch repair use with different corrosion lengths on stress intensity factor reduction and distribution of damaged areas are also investigated [13, 14]. A number of researchers have evaluated the effectiveness of repair of a tube corroded with a composite material. The uniformity of stress transfer across the enclosed area is the main benefit of the composite repair process, which increases the fatigue life of the repaired structure [15, 17]. Jin-Ho Hong et al conducted a numerical analysis to study corrosion repair from a damaged hydrogen storage tank, determining the effect of variation in winding angle on thermal and mechanical properties [18]. hashin, Zhengyun Hu et al studied the effect of patch type on stress reduction using numerical analysis. They also sought to obtain the best patch shape in a carbon fiber composite polymer when it was glued to a damaged hydrogen storage tank at the center. It has been found that this type of patch is more effective in reducing stress concentration [19]. In his study on a corroded cylindrical tank S.H. Dehghan Manshadi and Mahmoud R. Maheri observed the behavior of fatigue corrosion of a tank through experimental experiments. The storage tank was finally repaired using a composite glass/epoxy polymer patch as a repair procedure using the finite element method [20]. Furthermore, Xiaohang Zhao et al studied the mechanical and thermal behavior of a hydrogen storage tank to determine the influence of the stress distribution and displacement of the stacking sequence [21]. D. Ouinas et al performed a three-dimensional finite element analysis to compare the performance of a carbon/epoxy patch and boron/epoxy patch on a cracked aircraft structure. They demonstrated that the mechanics of the two repair methods are completely different and concluded that the boron/epoxy patch is more efficient [22]. Benyahia et al analyzed the effect of patch shape on stress intensity factor reduction by three-dimensional finite element analysis. The patch shapes considered were rectangular, trapezoidal, circular and elliptical. It was observed that the elliptical shape is more optimal and effective in reducing SIF[23]. Several researchers have performed three-dimensional numerical finite element analysis to determine the best composite patch shape for structural repair [24, 26]. M.Berrahou et al studied the mechanical behavior of a structure damaged by a crack and repaired by different types and forms of patches in order to analyze the effectiveness of the repair. The boron/epoxy patch is the best type used for successful repair by experimental tests and extended finite element method [27]. While doing the library search, we found many researchers who studied domestic hot water tanks, and among these researchers are N. Beithou and M. Abu

Hilal [28-30], who research in this field for multiple goals, such as studying the experimental energy of hot water tanks and thermal analysis of discrete water supply in domestic hot water storage tank. In addition to Ammar Alkhalidi et al., who studied Improving Mixing in Water Aeration Tanks Using Innovative Self-Powered Mixer and Power Reclamation from Aeration Tank [31].

The purpose of this article is a method for strengthening a hydrogen tank with a composite wrap to reduce structural damage in the corroded part. The effect of corrosion length on the variance of Von Mises stresses, in addition to the effect of temperature and pressure on the distribution Von Mises Stress, and finally the effect of fiber orientations on the presence of oval corrosion in a thermo-mechanical loading tank were all examined. This paper is based on modeling and simulation methods to address the risks and failures of a hydrogen storage tank.

2. Geometrical and FE models

2.1. Description of the model

The geometry of the corroded structure considered in this study is shown in Figure 1. Consider the following dimensions for a 6061-T6 aluminum tank see Figure 2: the external radius $R_{ext} = 376$ mm, the internal radius $R_{int} = 364$ mm, the thickness of the tank is $t = 12$ mm, tank length is $L = 1800$ mm.

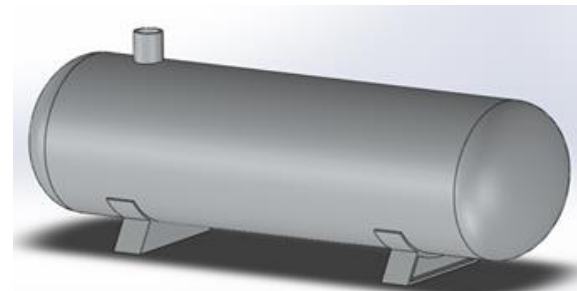


Figure 1. hydrogen tank

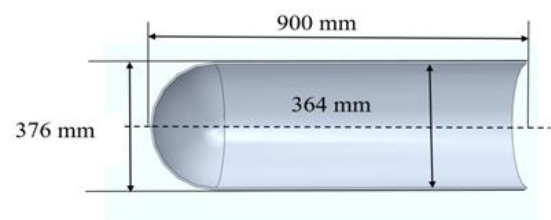


Figure 2. Dimensions of the structure

The longitudinal plan of the tank is used to model corrosion of an ellipsoidal shape. These are defined by their depth -corrosion depth- (a), and their length -half-corrosion length- (c). In this repair, Composite wrap fiber reinforced polymers FRPC has a length L_p of 200mm and a thickness t_{pf} of 6mm. The collage is assured by a thickness of adhesive $t_a=0.2$, in the Figure 3.

For this study, the corroded tank repaired by composite wrap whose ply orientation is of the form $[\mp 45/90/0]$, the plies in the wrap have unidirectional stacking where the fibers are oriented along the length direction, parallel to the load direction as shown in the following table 1

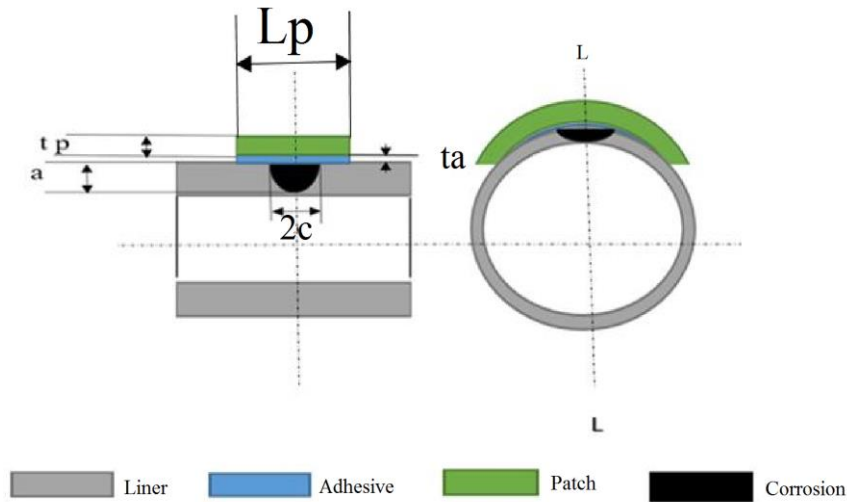


Figure 3. composite wrap repair of ellipsoidal corrosion in a tank

Table 1. Different stacking sequences employed for the composite

	S1	S2	S3	S4	S5
Laminatesequences	[0] _s	[90] _s	[0/45] _s	[0/90] _s	[±45/90/0] _s

The physical properties of the model (wrap, adhesive and liner) are shown in Table 2.

Table 2. Material properties of the tank repair [32-34]

	Type	E ₁ [GPa]	E ₂ [GPa]	E ₃ [GPa]	v ₁₂	v ₁₃	v ₂₃	G ₁₂ [GPa]	G ₂₃ [GPa]	G ₁₃ [GPa]
Liner	Al 6061-T6	68			0.33					
Composite	FRPC	13,94	62.25	94.5	0.2	0.2	0.33	5.415	10.71	4.286
Adhesive	FM73	2,55			0,3					

The thermal properties of the materials are shown in Table 3

Table 3. Thermal properties of the tank materials [33]

	Density (kg.m ⁻³)	CTE (°C ⁻¹)	Thermal conductivity (w.m ⁻¹ .°C ⁻¹)
Liner	2700	2.3×10 ⁻⁵	150
Composite	1560	3.5×10 ⁻⁵	0.2

Table4. The elastic properties of tanks as a function of temperature

Temperature(°C)	-200	-100	25	100	150	200
Young's modulus (MPa)	76500	72700	68900	65800	62700	57700

3. Numerical modeling

The analysis involves a three-dimensional finite element method using the ABAQUS finite element code [35]. Due to the symmetry of the geometry and the applied loads, only a 1/4 model was used. As illustrated in Figure 4, first of all, to analyze the mechanical behavior of the tank at internal pressure and temperature, solid elements with higher order version of the hexahedral linear displacement type were used coupled to temperature C3D8RT, while the element used in the mesh of the corroded part of the cylinder is the tetrahedral linear type C3D4RT. Because this element tolerates irregular shapes without loss of precision, plus the total number of elements generated for this structure is 300888, see Figure 4, the type of element used in the wrap and adhesive is quadratic tetrahedral C3D10. So we kept the same type of element to maintain the precision of the numerical calculation between the thicknesses of the structure. The generation of the wrap band mesh is shown in Figure 5.

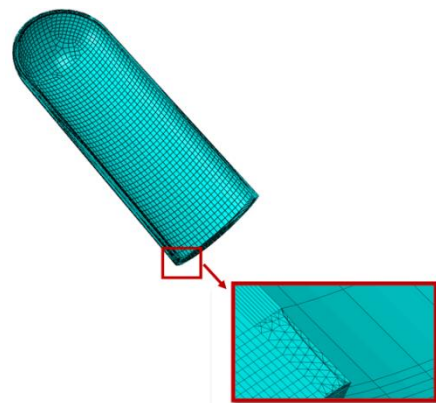


Figure 4. Mesh of the structure and in the vicinity of the corrosion zone

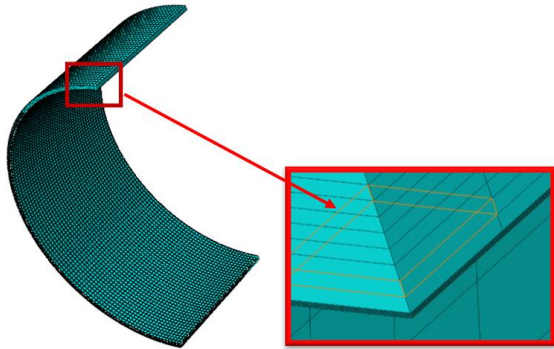


Figure 5. Mesh of the wrap and adhesive

4. Boundary conditions

As a result of the geometric symmetry of the tank, loading internal pressure and temperature and boundary conditions; the model could be reduced to one quarter (1/4) of the structure of symmetry, the longitudinal half and the transverse half.

The reflective symmetry conditions are applied in the longitudinal direction ($U_x = \theta_y = \theta_z = 0$) and in the transverse direction ($U_y = \theta_x = \theta_z = 0$) of one quarter of the structure, see Figure 6.

Figure 7 shows the internal surface of the tank is subjected to mechanical loading of the transported gases under a variant internal pressure $P_i = 35, 30, 25$ and 20 MPa.

The existence of a thermal gradient due to the difference in temperature of the internal surface in contact with the stored gases T_{int} varying between 0 and -250°C and the external surface exposed to the ambient environment $T_{ext} = 20^\circ\text{C}$, In Figure 8.

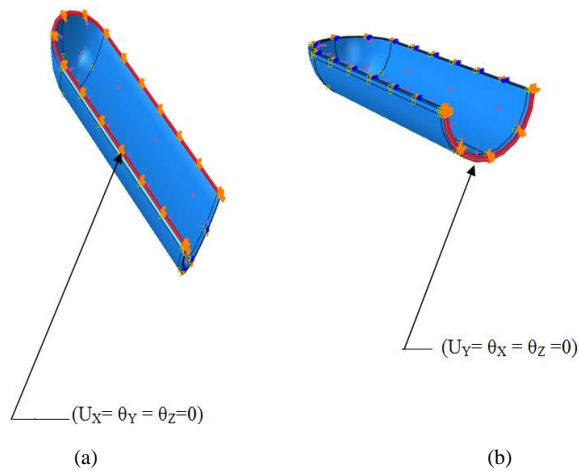


Figure 6. Reflective symmetry conditions, (a) longitudinal direction, (b) transverse direction

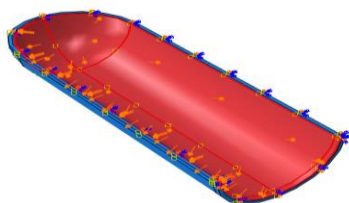
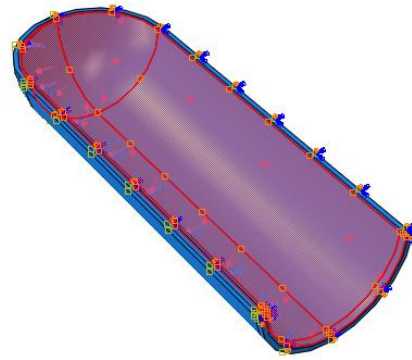
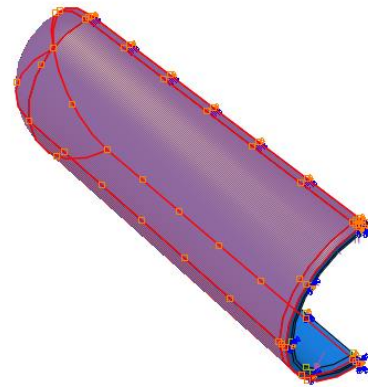


Figure 7. The tank under the internal pressure



(a)



(b)

Figure 8. The tank under thermal loading, (a) internal temperature, (b) external temperature

5. Results and discussion

In this paper, the quality and durability of carbon/epoxy patches with different fiber orientations are examined as shown in Figure 9. The objective of this numerical study is to show the evolution of the Von Mises stress distribution as a function of corrosion length for the three paths and the variation of the maximum Von Mises stresses compared with pressure and temperature.

Yu-Qi Qin et al [33] analyze the failure of the aluminum alloy lining of the vehicle's hydrogen storage tank, which causes cracking during oil circulation, and conduct experimental tests to discover the causes of failure. Maxime Bertin et al [36] evaluated the influence of temperature on the multi layer polymer/composite fatigue behavior and showed the different stresses applied to a hydrogen tank through experimental experiments.

The novelty in our work is the composite patch repair of a corroded cryogenic tank under thermo-mechanical loading to see the effect of temperature and pressure on the distribution of Von stresses and the influence of fiber orientations. All the papers that talk about cryogenic tanks have studied fatigue or structural cracking, but in our research the corrosion behavior has been studied.

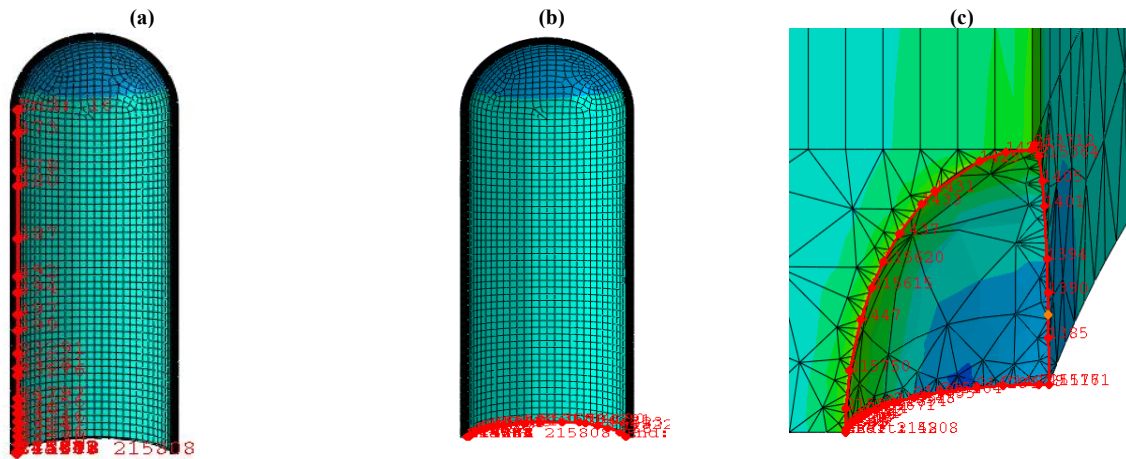


Figure 9. Corrosion length for different directions: (1) path1, (2) path2 and (3) path3

5.1. Effect of corrosion length on the variation of Von Mises stresses for different pressures

Figure 10 shows the variation of Von Mises stress as a function of the longitudinal length (path1) of corrosion for different internal pressures. The presence of pressures, as seen in this figure, minimizes the VonMises stresses exerted on the corrosion point. It can be stated that the increase in longitudinal length generates a considerable decrease in Von Mises stresses. Indeed, an increase in the longitudinal length of the corrosion in the interval [0-13] mm leads to an 80% reduction of the Von Mises stress. This impact is less pronounced for lengths between 13 mm and 55 mm. The values of the Von Mises stress recorded along the tip of the corrosion, for the 20 MPa pressure, are the most inferior to those of the other pressures. The highest value for von Mises stress is recorded when the pressure value is high. In the longitudinal plane, it is also interesting to note that the repair technique used reduces the stress values around the damaged area.

Figure 11 illustrates the influence of the transverse length (Path 2) of corrosion on Von Mises stresses. The increase in this length leads to a decrease in Von Mises stress, until a minimum value of 122 MPa is reached, which corresponds to a transverse length value of 13 mm. We observed that the longitudinal length is influenced more than the transverse length, with stresses being higher than the other direction.

Figure 12 represents the evolution of the Von Mises stresses for different transported gas pressures $P_i = 20; 25; 30$ and 35 MPa. The variation of Von Mises stresses throughout circumferential corrosion reveals that the highest stresses are located in the two corrosion peaks $\theta = 0^\circ$ and 180° . Then, according to this figure, it can be seen that the Von Mises stresses away from the corrosion are stable, while the stresses between the two corrosion peaks are significantly reduced.

Therefore, it can be concluded that the length of the corrosion is strongly affected by the pressure and much more by the temperature at the damaged area.

5.2. Effect of corrosion length on the variation of Von Mises stresses for different temperatures

Figure 13 illustrates the evolution of the Von Mises stress for different temperatures. It shows that the maximum value is recorded at the bottom of the corrosion. It can be seen from this figure that the Von Mises stresses decrease as the longitudinal length (path1) of the corrosion increases. The same behavior was observed for all lengths. Moreover, this variation in stress decreases by increasing the length of the damaged surface. Indeed, the stress evolution for a temperature of 23 k is significantly more important than for a temperature of 173 k, since the temperature of the corroded zone affects the stress distribution.

The temperature effect is shown in Figure 14. The same phenomenon is observed for the variation of VonMises stresses at different temperatures in the longitudinal corrosion direction. VonMises stresses are more highly concentrated at the bottom of the corroded zone, and these stresses decrease as the transverse length (Path 2) of the corrosion tip increases. In addition, the stresses reach minimum values for different temperatures. Beyond this threshold, the distribution tends to produce more or less constant stress levels. It should also be noted that a reduction in temperature reduces the resistance of the liner to mechanical stress, which implies a high risk of structural failure. Longitudinal length is more affected than transverse length because the stresses are greater in one direction than the other.

Figure 15 shows the effect of temperature on the repair of Von Mises stresses as a function of the circumferential length (Path3) of the repaired corrosion. It is noted that the distribution of the opening stress in the vicinity of the corrosion point always has a maximum, after which it gradually slows down to a stable value.

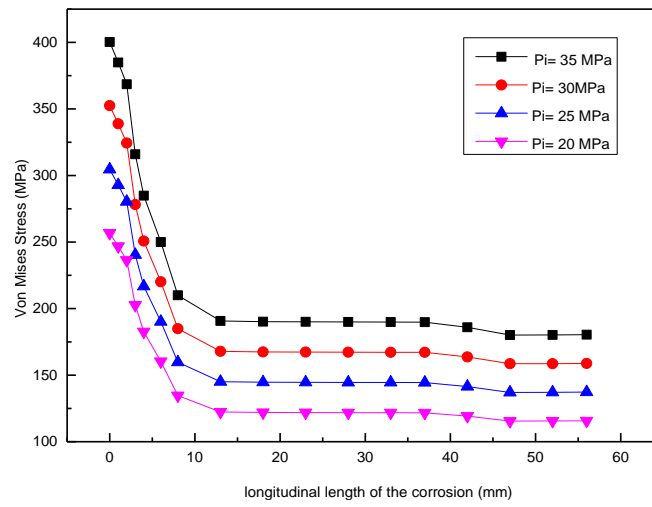


Figure 10. Variation of Von Mises stresses compared to longitudinal corrosion length for different pressures in the case ($a/t=0.5$, $a/c=0.7$)

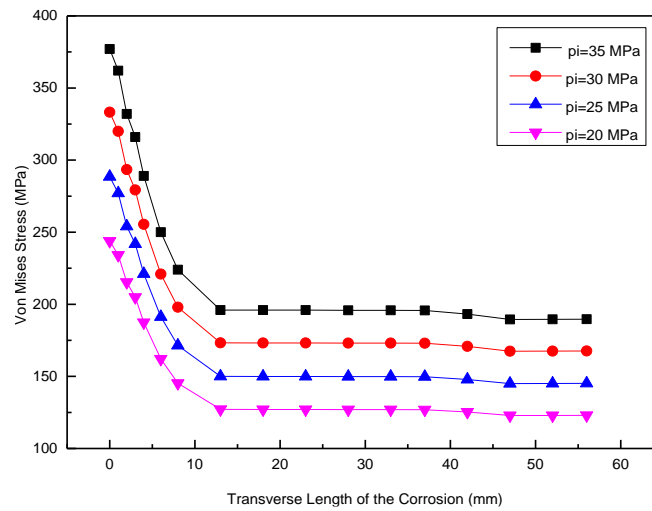


Figure 11. Variation of VonMises stresses compared to the transverse length of the corrosion for different pressures in the case ($a/t=0.5$, $a/c=0.7$)

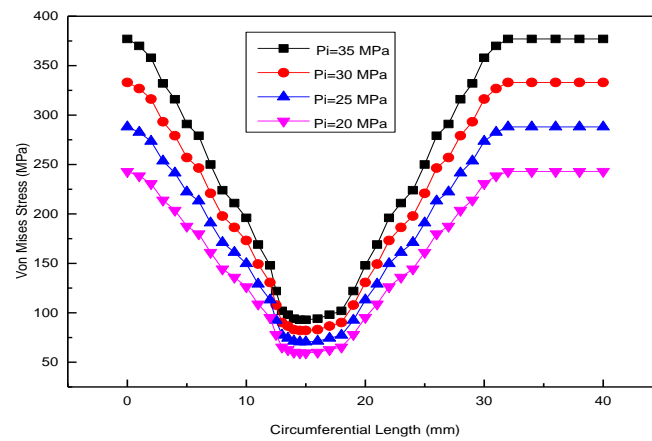


Figure 12. Effect of pressure on Von Mises stress distribution as a function of circumferential length of corrosion in the case ($a/t=0.5$; $a/c=0.5$)

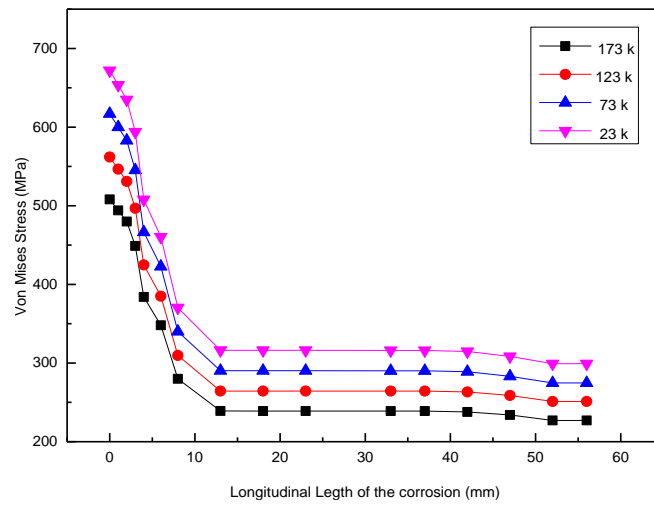


Figure 13. Variation of Von Mises stresses compared to longitudinal length of the corrosion for different temperatures in the case ($a/t=0.5, a/c=0.7$)

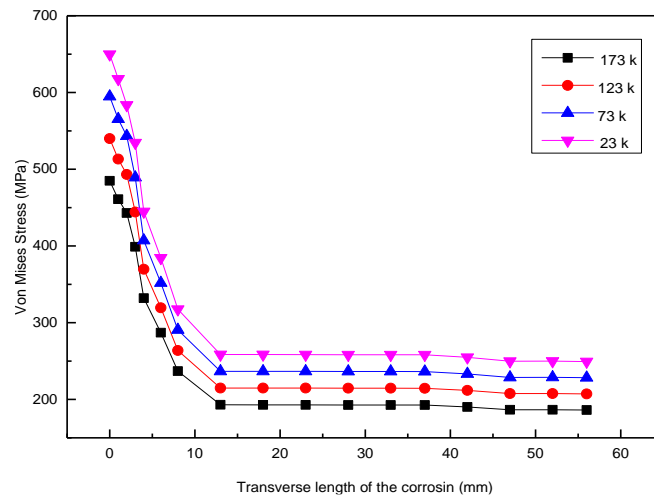


Figure 14. Variation of VonMises stresses compared to transverse length of the corrosion for different temperatures in the case ($a/t=0.5, a/c=0.7$)

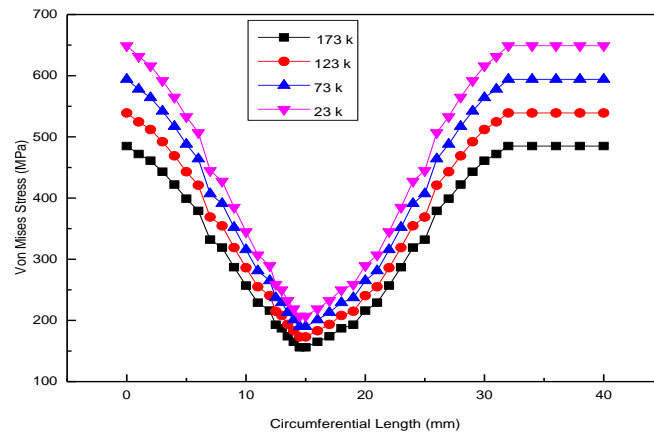


Figure 15. Effect of temperature on the Von Mises stress distribution as a function of the circumferential length of the corrosion in the case ($a/t=0.5; a/c=0.5$).

5.3. Variation of the Von stress as a function of pressure and temperature for the three Paths

The graphs in Figure 16 represent the evolution of the maximum Von Mises stresses as a function of the pressure for the different Paths. Von Mises stresses increases with the increase in internal pressure. The Path 3 shows high values of Von Mises stresses compared to other Paths. The

increase in internal pressure causes a decrease in the concentration of Von Mises stress.

Figure 17 shows the variation of stress as a function of temperature in the various paths. We note that the constraint decreases much more in path2 compared to the other two Path. Also, it can be seen that when the temperature increases, the stress decreases. Thus, the effect of repair is reduced in the transverse direction in relation to the longitudinal and circumferential direction.

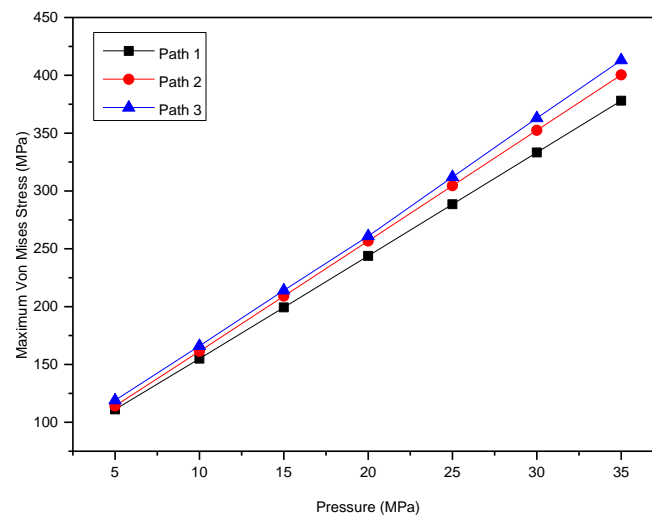


Figure 16. The evolution of the maximum Von Mises stresses as a function of pressure in the case ($a/t=0.5$; $a/c=0.5$).

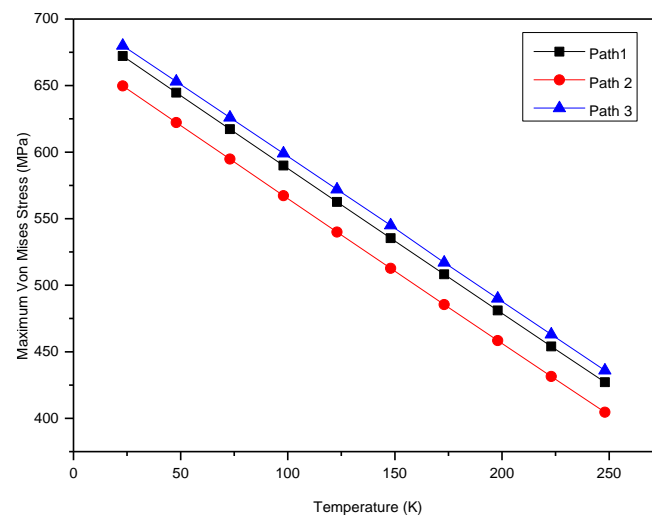


Figure 17. The evolution of the maximum Von Mises stresses as a function of temperature in the case ($a/t=0.5$; $a/c=0.5$)

5.4. The effect of fiber orientation on Von Mises stress repair as a function of corrosion length

Figure 18 shows the effect of the orientation of the fibers on the repair of the VonMises stresses as a function of the longitudinal length of the corrosion. It can be seen that the distribution of Von Mises stresses at the bottom of the defect always has a maximum. This figure also shows that the Von stress decreases when the length increases in the longitudinal direction, beyond the point of corrosion, the variation of the stress will remain constant. It is constant that the carbon/epoxy composite gives a higher value of stress 633 MPa which orients to 0° and 90°, while the values decrease from 600 MPa to 567 MPa for the orientation of the plies is of the form [0/90]s and [0/45]s. Thus, the stacking sequence with the lowest Von Mises stress value is [45/90/0]s.

Figure 19 shows the effect of the orientation of the fibers on the repair of VonMises stresses as a function of the transverse length of the corrosion. In this figure, we observe that the Von Mises stress decreases by oscillation according to the transverse length, beyond the point of corrosion the variation of the stress will remain constant. This same behavior was observed for all the different orientations. As this figure shows, the increase in the Congruence of Von Mises is up to the point of 571MPa upon leaving the wrap of orientation 0° and 90°. While the stresses increase from 540MPa to 507MPa for the orientation of the fibers is of the form [0,45]s and [0,90]s. Among the results obtained, the stacking sequence [45/90/0] is the best since it gives the lowest value of the stresses.

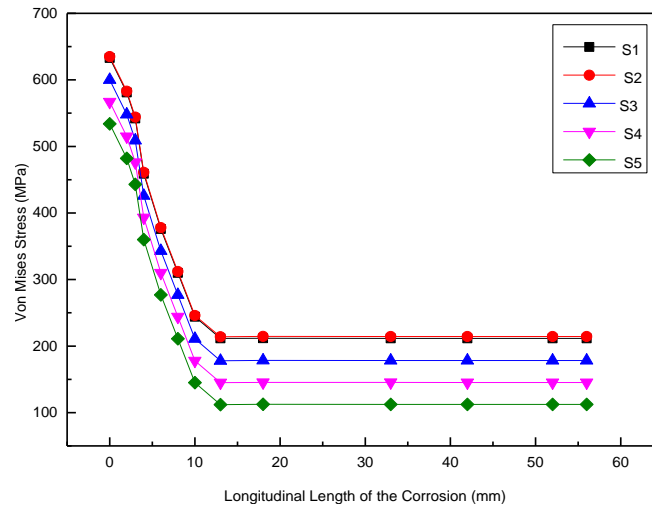


Figure 18. Variation of VonMises stresses compared to longitudinal length of the corrosion for different orientations in the case (a/t=0.5,a/c=0.7)

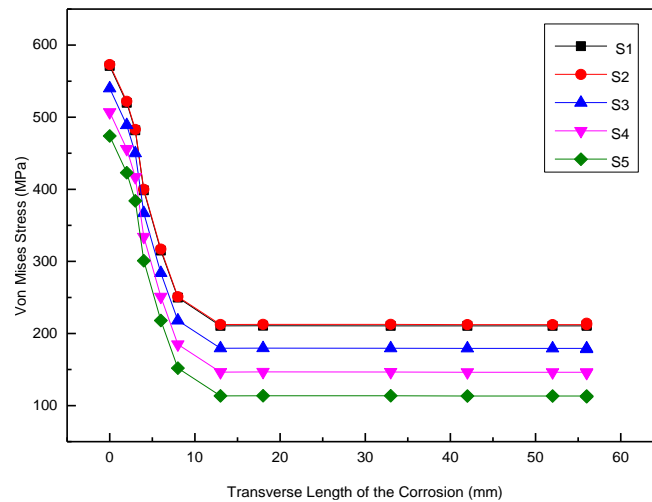


Figure 19. Variation of Von Mises stresses compared to transverse length of the corrosion for different pressure orientations in the case (a/t=0.5,a/c=0.7)

6. Conclusion

This research was part of a broader effort to better understand the corrosion behavior of 6061 aluminum alloy tanks. The results are obtained using the finite element method of a corroded tank repaired by a composite material. The effects of mechanical and thermal loading on the structural strength along with the impact of the length of the corrosion in the three directions, in addition to the influence of the composite wrap repair on the reinforcement of the reservoir, and the effect of the orientation of the fibers on the distribution of the Von stresses all led to the following conclusions:

- As the pressure increases, the Von Mises stress distribution at the bottom of the corrosion also increases.
- The lowering of the temperature of the fluid inside the structure significantly increases the evolution of Von Mises stresses at the level of the corrosion crater.
- Maximum stresses are reached at the lowest temperature, indicating a significant risk of structural failure.
- By increasing the circumferential length of the corrosion, a maximum increase of opening in the vicinity of the corrosion point can be observed.
- The stress increases considerably in the case of circumferential length (path3) compared to the corrosion length for the other Paths of a tank.
- The stress concentration at the corrosion edge is directly affected by the orientation of the wrap. This impact is amplified at the corrosion point.
- wrap repair using fiber-reinforced polymer composites extends the durability of cryogenic tanks, although the rate of improvement is highly dependent on operating conditions, such as pressure and temperature.

References

- [1] M. Abo-Elkhier, and K. Muhammad, "Failure analysis of an exploded large-capacity liquid storage tank using finite element analysis," *Engineering Failure Analysis*, vol. 110, 104401, 2020, doi.org/10.1016/j.engfailanal.2020.104401.
- [2] H. Kacem, and S. Hariri, "Comportement mécanique en statique et en fatigue des aciers à 9% Nickel dans des conditions cryogéniques," In *CFM 23ème Congrès Français de Mécanique*. AFM, Maison de la Mécanique, 39/41 rue Louis Blanc-92400 Courbevoie, 2017.
- [3] Z. Liu, Y. Yang, Y. Liu, and Y. Li, "Effect of gas injection mass flow rates on the thermal behavior in a cryogenic fuel storage tank," *International Journal of Hydrogen Energy*, vol. 47, no. 32, pp. 14703-14713, 2022, doi.org/10.1016/j.ijhydene.2022.02.205.
- [4] P. Cheng, X. J. Gong, S. Aivazzadeh, and X. Xiao, "Experimental observation of tensile behavior of patch repaired composites," *Polymer testing*, vol. 34, pp. 146-154, 2014, doi.org/10.1016/j.polymertesting.2014.01.007.
- [5] H. I. Beloufa, and D. Ouinas, "Renforcement des fissures tridimensionnelle émanant d'entaille circulaire par patch en composite (S06)," In *CFM 2015-22ème Congrès Français de Mécanique*. AFM, Maison de la Mécanique, 39/41 rue Louis Blanc-92400 Courbevoie, 2015.
- [6] W. Xugang, F. Xiaobo, C. Xianshuo, "Forming limit of 6061 aluminum alloy tube at cryogenic temperatures," *Journal of Materials Processing Technology*, vol. 36, pp. 117649, 2022, doi.org/10.1016/j.jmatprotec.2022.117649.
- [7] Weber, Matthew, P.D. Eason, H. Özdeş, and M. Tiryakioğlu, "The effect of surface corrosion damage on the fatigue life of 6061-T6 aluminum alloy extrusions," *Materials Science and Engineering*: vol. 690, pp. 427-432, 2017, doi.org/10.1016/j.msea.2017.03.026.
- [8] J. Wang, X. Chen, L. Yang, and G. Zhang, "Sequentially combined thermo-mechanical and mechanical simulation of double-pulse MIG welding of 6061-T6 aluminum alloy sheets," *Journal of Manufacturing Processes*, vol. 77, pp. 616-631, 2022, DOI:10.1016/j.jmapro.2022.03.046.
- [9] S. M. K. Mohammed, R. Mhamdia, A. Albedah, B. B. Bouiadjra, and F. Benyahia, "Fatigue crack growth in aluminum panels repaired with different shapes of single-sided composite patches," *International Journal of Adhesion and Adhesives*, vol. 105, 102781, 2021, doi.org/10.1016/j.ijadhadh.2020.102781.
- [10] J. J. Schubbbe, S. H. Bolstad, and S. Reyes, "Fatigue crack growth behavior of aerospace and ship-grade aluminum repaired with composite patches in a corrosive environment," *Composite Structures*, vol. 144, pp. 44-56, 2016, doi.org/10.1016/j.compstruct.2016.01.107.
- [11] A. K. Bakare, A. A. Shaikh, and S. S. Kale, "Comparison of SCC behaviour of crack in thin aluminium structure with and without single sided composite patch repair," *Engineering Failure Analysis*, vol. 118, 104781, 2020, DOI:10.1016/j.engfailanal.2020.104781.
- [12] M. Salem, M. Berrahou, B. Mechab, and B. B. Bouiadjra, "Analysis of the Adhesive Damage for Different Patch Shapes in Bonded Composite Repair of Corroded Aluminum Plate Under Thermo-Mechanical Loading," *Journal of Failure Analysis and Prevention*, vol. 21, no.4, pp. 1274-1282, 2021.
- [13] Berrahou, M., Mokadem, S., Mechab, B., & Bachir Bouiadjra, B. "Effect of the corrosion of plate with double cracks in bonded composite repair," *Struct. Eng. Mech*, vol. 64, no. 3, pp. 323-328, 2017, doi.org/10.1590/1516-1439.259613.
- [14] A. K. Bakare, A. A. Shaikh, and S. S. Kale. "Corrosion behaviour of stop-hole and notch instead of crack in thin aluminium alloy sheet repaired with bonded patch exposed to saline environment under constant load," *Engineering Failure Analysis*, vol. 120, 105067, 2021, doi.org/10.1016/j.engfailanal.2020.105067.
- [15] M. W. Junior, J. M. L. Reis, and C. Mattos, "Polymer-based composite repair system for severely corroded circumferential welds in steel pipes," *Engineering Failure Analysis*, vol. 81, pp. 135-144, 2017, doi.org/10.1016/j.engfailanal.2017.08.001.
- [16] D. M. Ryu, L. Wang, S. K. Kim, and J. M. Lee, "Comparative study on deformation and mechanical behavior of corroded pipe: Part I-Numerical simulation and experimental investigation under impact load," *International Journal of Naval Architecture and Ocean Engineering*, vol. 9, no. 5, pp. 509-524, 2017, doi.org/10.1016/j.ijnaoe.2017.01.005.
- [17] M. Perl, and T. Saley, "The detrimental effect of autofrettage on externally cracked modern tank gun barrels," *Defence Technology*, vol. 15, no. 2, pp. 146-153, 2019, doi.org/10.1016/j.dt.2018.10.001.
- [18] J. H. Hong, M. G. Han, and S. H. Chang, "Safety evaluation of 70 MPa-capacity type III hydrogen pressure vessel considering material degradation of composites due to temperature rise," *Composite Structures*, vol. 113, pp. 127-133, 2014, doi.org/10.1016/j.compstruct.2014.03.008.
- [19] Z. Hu, M. Chen, and B. Pan, "Simulation and burst validation of 70 MPa type IV hydrogen storage vessel with dome reinforcement," *International Journal of Hydrogen Energy*, vol. 46, no. 46, pp. 23779-23794, 2021, doi.org/10.1016/j.ijhydene.2021.04.186.

- [20] S. D. Manshadi, and M. R. Maheri, "The effects of long-term corrosion on the dynamic characteristics of ground based cylindrical liquid storage tanks," *Thin-Walled Structures*, vol. 48, no. 12, pp. 888-896, 2010, doi.org/10.1016/j.tws.2010.05.003.
- [21] X. Zhao, Y. Yan, J. Zhang, F. Zhang, Z. Wang, and Z. Ni, "Analysis of multilayered carbon fiber winding of cryo-compressed hydrogen storage vessel," *International Journal of Hydrogen Energy*, vol. 47, no. 20, pp. 10934-10946, 2022, doi.org/10.1016/j.ijhydene.2022.01.136.
- [22] D. Ouinas, B. B. Bouiadjra, and B. Serier, "The effects of disbands on the stress intensity factor of aluminium panels repaired using composite materials," *Composite structures*, vol. 78, no. 2, pp. 278-284, 2007, doi.org/10.1016/j.compstruct.2005.10.012.
- [23] F. Benyahia, A. Albedah, and B. B. Bouiadjra, "Elliptical and circular bonded composite repair under mechanical and thermal loading in aircraft structures," *Materials Research*, 17(5), 1219-1225, (2014).
- [24] M. Salem, M. Berrahou, B. Mechab, and B. B. Bouiadjra, "Effect of the angles of the cracks of corroded plate in bonded composite repair," *Frattura ed Integrità Strutturale*, vol. 12, no. 46, pp.113-123, 2018, doi:10.3221/IGF-ESIS.46.12.
- [25] H. Benzineb, M. Berrahou, and M. Serier, "Analysis of the adhesive damage for different shapes and types patch's in corroded plates with an inclined crack," *Frattura e Integrità Strutturale*, vol. 60, 2022, doi.org/10.3221/IGF-ESIS.60.23 .
- [26] M. Berrahou, and B. B. Bouiadjra, "Analysis of the adhesive damage for different patch shapes in bonded composite repair of corroded aluminum plate," *Structural engineering and mechanics: An international journal*, vol. 59, no.1, pp. 123-132, 2016, DOI:10.12989/sem.2016.59.1.123.
- [27] K. Amari, and M. Berrahou. "Experimental and Numerical Study of the Effect of Patch Shape for Notched Cracked Composite Structure Repaired by Composite Patching," *Journal of Failure Analysis and Prevention*, vol. 22, no. 3, pp.1040-1049, 2022, doi.org/10.1007/s11668-022-01391-z.
- [28] N. Beithou, M. Abu Hilal, " Experimental Energy Study for Domestic Hot Water Storage Tanks," *Jordan Journal of Mechanical and Industrial Engineering*, Vol. 5, no. 5, pp. 471 – 477, 2011.
- [29] N. Beithou, M. Abu Hilal, I. Abu-Alshaiikh, " Thermal Analysis of Discrete Water supply in Domestic Hot Water Storage Tank," *Jordan Journal of Mechanical and Industrial Engineering*, Vol. 5 , no. 1, pp. 29- 32, 2011.
- [30] N. Beithou , M. Abu Hilal, " Hot Water Management of DHW Storage Tank: Supply Features," *Jordan Journal of Mechanical and Industrial Engineering*, Vol. 4, no. 6, pp. 789- 796, 2010.
- [31] Ammar A. T. Alkhalidi, Patrick Bryar, Ryo S. Amano, "Improving Mixing in Water Aeration Tanks Using Innovative Self-Powered Mixer and Power Reclamation from Aeration Tank," *Jordan Journal of Mechanical and Industrial Engineering*, Vol. 10, no. 3, pp. 211-214, 2016.
- [32] H. Qiu, M. Enoki, Y. Kawaguchi, and T. Kishi, "A model for the static fracture toughness of ductile structural steel," *J. Engineering Fracture Mechanics*, vol. 70, pp. 599–609, 2003, doi.org/10.1016/S0013-7944(02)00079-6.
- [33] Y. Q. Qin, Y. Gong, Y. W. Yuan, and Z. G. Yang, "Failure analysis on leakage of hydrogen storage tank for vehicles occurring in oil circulation fatigue test," *Engineering Failure Analysis*, vol. 117, 104830, 2020, doi.org/10.1016/j.engfailanal.2020.104830.
- [34] S. Fintová, I. Kuběna, L. Trško, V. Horník, and L. Kunz, "Fatigue behavior of AW7075 aluminum alloy in ultra-high cycle fatigue region," *Mater. Sci. Eng.*, vol. 774, 138922, 2020, doi.org/10.1016/j.msea.2020.138922.
- [35] ABAQUS Standard/User's Manual, Version 6.11. Hibbit Karlsson & Sorensen, Inc., Pawtucket, RI, USA, 2007.
- [36] M. Bertin, F. Touchard, M.C. Lafarie-Frenot, "Experimental study of the stacking sequence effect on polymer/composite multi-layers submitted to thermomechanical cyclic loadings," *International Journal of Hydrogen Energy*, vol. 35, no. 20, pp.11397-11404, October 2010, doi:10.1016/j.ijhydene.2010.07.018.

Study the Effect of the Shape of the Laser's Path on the Mechanical Properties of Acrylic Layer

Raed Naeem Hwayyin^{a,*}, Azhar Sabah Ameen^b, Ahmed Salman Hamood^c

^a Electromechanical Engineering Department, University of Technology- Iraq.

^b Electromechanical Engineering Department, University of Technology- Iraq.

^c Factory and Training Center, University of Technology- Iraq.

Received 1 Jul 2022

Accepted 19 Oct 2022

Abstract

The study examined the reinforcement of the mechanical properties of acrylic by using a laser's path following three different functions without additives. The laser Paths are created by using a laser ray at different power and speed. The shapes of the path of laser Paths are designed according to different functions and investigate their effect on the acrylic micro-structure. The study investigated the influences of the crack shape caused by the laser, the laser's power, and speed on the mechanical characteristics of the acrylic layer. The study predicted mathematical equations of crack shape functions f_1 , f_2 , and f_3 while the equation $F(z)$ described the empirical results as a relationship of laser power and laser speed with tensile stress. The maximum increase of stress due to the crack shape functions f_1 , f_2 , and f_3 was 22.94 %, 19.08%, and 28.24 % at the different laser power and laser speed.

© 2022 Jordan Journal of Mechanical and Industrial Engineering. All rights reserved

Keywords: Mechanical properties, Laser ray, Crack functions, Laser power, Laser speed..

Nomenclature

e : Engineering strain

L : Is the initial measuring length (mm).

ΔL : The variation in length's gage ($L_f - L_o$), (mm).

L_f : The final length, (mm).

L_o : The initial length, (mm).

F : The tensile force (N)

A : is the initial crosssectional area (mm^2).

f_1 : The laser path's function has a slope (41°).

f_2 : The laser path's function has a slope (29°).

f_3 : The laser path's function has a slope (24°).

f_1 , f_2 and, f_3 : The equations describes the relationship of the empirical results at different laser speed and power.

CW : Clockwise motion.

O : Original acrylic samples of tensile test without crack.

A : is the samples with crack shape function (f_1) at various laser power of 40 watts, 50 watts, and 60 watts, and various laser speeds of 15 mm/sec, 30 mm/sec, and 45 mm/sec.

B : is the samples with crack shape function (f_2) at various laser power of 40 watts, 50 watts, and 60 watts, and various laser speeds of 15 mm/sec, 30 mm/sec, and 45 mm/sec.

C : is the samples with crack shape function (f_3) at various laser power of 40 watts, 50 watts, and 60 watts, and various laser speeds of 15 mm/sec, 30 mm/sec, and 45 mm/sec.

τ_{max} : Maximum shear stress (MPa).

σ : The stress (MPa).

1. Introduction

At present, Acrylic material is one of the essential materials that will be used in many future applications. On the other side, laser applications have taken a wide range

in industry, structures, and technology field processes, in addition to using of lasers for polymers and heat treatments. They showed the influence of the laser beam on NiTi at the midline that achieves better transmission in the microstructure, which leads to acceptable mechanical properties without introducing interlayers [1]. Cladding techniques are widely used to modify the surface microstructure and properties of alloys [2,3], including the cladding using the laser, which showed some useful future properties [4-6]. First, it is a simple, green, economical, and efficient process, which can improve the corrosion resistance of the surface coating [7, 8]. Second, it can improve the metallurgical bond between the coating and the substrate [5, 9, 10], so that the size of the heat-affected zone (HAZ) is usually small [5, 11, 12]. The study showed that increasing the laser scanning speed enhances the shift from planar crystals to dendrites and purifies the grains simultaneously [13]. They studied the optimal conditions for the desired microstructure on the surface of the H13-TiC composite at a scanning speed of 12 mm/sec, a pulse width of 9.96 ms, and an operating distance of 5.94 mm [14]. They examined the improvement of the mechanical properties of the coating by changing the composition of the alloy powders by studying the improved internal structure and mechanical properties of the nickel-based composite coatings [15]. Laser cutting of metal and non-metallic materials depends on the energy of the laser ray focused on a specific point in the material to be cut. The laser ray is 0.1 to 0.4 mm in diameter and the ray energy required for cutting depends on the thickness of

* Corresponding author e-mail: 10596@uotechnology.edu.iq.

the material, in which the material is heated to the melting or evaporation temperature. [16-18]. Examined to get better of the mechanical characteristics of acrylic through variation of the speed and power of the laser at one specific path. They investigated the influence of the laser's ray energy and speed on improving the mechanical features [19]. They studied mechanical features under high-pressure conditions and high-temperature conditions and needs to the reinforcement of the mechanical features through the laser[20]. The study used Taguchi's method for optimum cutting conditions for acrylic material, cutting speed, feed rate and cutting tool angle [21]. The study carried out a finite element analysis that was adopted to simulate penetrating welding using a polycarbonate laser ray to facilitate the selection of appropriate process parameters to obtain suitable welding [22]. The study analysis was based on building a digital model for the welding process using a type (CO₂) laser ray for the thermoplastic polymer material to determine the appropriate factors for practical testing [23]. They investigated the preparation of a mathematical model for selective laser sintering (SLS) for a polymer material that has good strength properties that can be achieved taking into account the processing factors (laser speed, density, and energy)[24]. The study analysis of crack initiation on plates is limited by variable hole dimensions. The researchers performed the analysis for the crack initiation of the panels involving variable perforations (circular, ellipsoid, and rectangular). The study concluded that the influence of the hole shape and its dimension that must be taken into account when calculating the fracture factors [25]. The study investigates the improvement of the impact energy of acrylic by a core of composite material reinforcement consisting of a metal mesh of different shapes with polyester resin of different diameters [26]. The investigation depends on composite material of natural fibers from agricultural waste with epoxy to improve mechanical properties such as tensile and flexural strength [27]. The study investigated the effect of fiber orientation reinforced by graphite and epoxy on improving mechanical properties such as dynamic transverse shear stress of the composite [28]. The study investigated the polyester composite material reinforced with fiberglass and the effect of temperature on the creep stress on the behavior of the viscoelastic of the composite material and the measurement of the Poisson ratio, which indicates the amount of improvement in the properties of the composite material [29]. Compared to the previous papers that focus on improving the properties, what characterizes the present study is adopting specific laser paths to work on the dispersion of the stress concentration in the material under stress as in the study of Raed N. and Ahmed S. [19], which saves time and cost instead of using the laser to harden the entire surface of the sample's material. Adopting specific laser paths opened the horizon to focus on designing laser paths to disperse internal forces and improve the failure resistance of these products without any additives. The aim of the present study is to upgrade the mechanical features of acrylic by depending on the influence of the laser's ray on its internal structure and without additives by depending on the design of three new lasers' paths and their influence on the dispersion of the internal concentration's forces at different laser speeds and powers.

2. Theoretical methodology

The uniform stress intensity exposed to the body leads to internal stress in it. To illustrate these internal stresses, we will take a hypothetical section of the body in which the stress changes according to the cutting angle of the body, the stress in perpendicular cutting as in Figure 1-a is equal to [30]:

$$\sigma_1 = A_1 \cdot F \quad (1)$$

while, when changing the angle to 45 degrees to cut off the body as in Figure 1-b, the stress will be redistributed again to be [30]:

$$\sigma_2 = A_2 \cdot F \quad (2)$$

$$\text{And since } A_2 = A_1 \cdot \sqrt{2}$$

The stress will decrease to be equal to [30]:

$$\sigma_2 = \frac{F}{A_2 \cdot \sqrt{2}} \quad (3)$$

The tensile force is recorded as an indicator of the increase in gauge length when drawing the relationship between the tensile strength and the tensile elongation, which has a small value, if they were not normalized with the dimensions of the sample. Engineering stress, or nominal stress, (σ), is defined as [31]:

$$\sigma = \frac{F}{A} \quad (4)$$

The engineering strain, is defined as,

$$e = \frac{\Delta L}{L} \quad (5)$$

The total elongation is, $\Delta L = L_f - L_o$. A stress-strain curve; an identical curve in the figure can be drawn with the force elongation curve. The dependence on the stress-strain curve is an alternative to the forces-elongation curve because the stress-strain curve is independent of the sample dimensions. With failure due to fracture, new surfaces are created (i.e. fracture surface) with the start creating of the crack at surfaces. The kinematics cannot be described simply, and therefore, depend on the empirical results to describe them [31]. According to the Tresca theory, it is now considered a different kind of failure. As the material deforms in a more complex manner with the development of the measurement

of slip deformation of visible bands. The bands are called Lüders (slip) bands which apply to ductile steels and other types of metals so that shear bands of more brittle materials. These bands or slips appeared in a material that is subjected to tensile stress at about 45° to the loading direction. The failure occurs in the type of failure to shear when the material is sheared along with those slips at those planes. The assumption is that failure occurs when the shear stress exerted at these slips at the plane is large enough for shear to occur along these planes. In the tensile test, let the applied tension be (σ) at the point when the elastic limit (or the yield stress) is reached. In Figure 2, the shear stress is applied to the samples to reach the maximum shear stress that occurs at

an angle of 45 degrees from the loading axis according to the equation below [31]:

$$\tau_{max} = \frac{\sigma}{2} \quad (6)$$

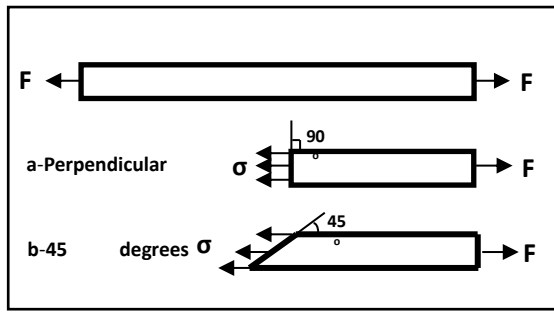


Figure 1-a and b. Illustrate the internal stresses Perpendicular angle and 45 degrees angle of a hypothetical section of the body

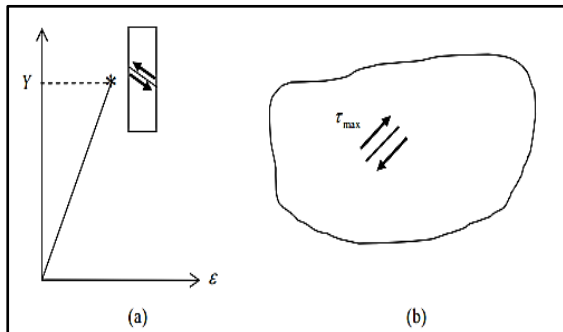


Figure 2. Failure through shear; (a) stress-strain curve in a tension test, (b) shear failure in a three-dimensional component [31]

In the present study, Figure 3 shows the stress concentration in the test sample and the influence of the curve of the laser path. The curve contributes to the analysis of the forces on it and its dispersion along the path of the laser ray. The dispersion of forces strengthened the material's resistance to breakage, which is in agreement with the behavior of the material described by Piaras Kelly [32].

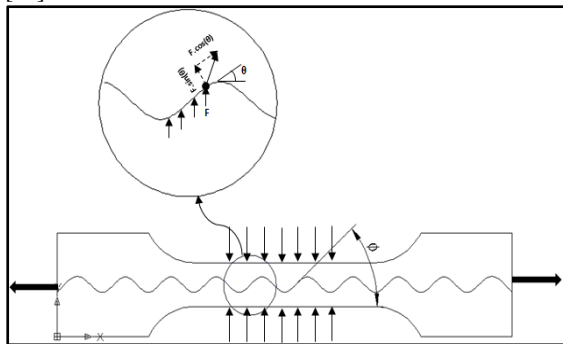


Figure 3. The stress concentration on the tensile sample and the dispersion of the forces on the curve of laser path

Figure 3 shows the idea of the study in dispersing the stress on the curved paths of the laser path, which affected the internal structure of the sample, which contributes to reducing the vertical stress that leads to failure and thus enhancing the sample's resistance to fracture. So, the study takes into account Tresca's theory assuming that the movement of a slide in the direction of a shear stress plane at an angle of 45o in the microstructure of the material., and investigates changing the direction of movement of slides by using different laser paths according to specific equations. The slope of the equations specified for the slit of the laser with the tensile stress axis at angles 24°, 29°, and 41°. Changing the direction of these slips increases the material's resistance to failure, which means increasing the material's resistance to failure without reinforcing it with

another material. The research has adopted three crack path functions f_1 , f_2 , and f_3 produced by a laser ray as follows:

$$f_1 = 3 * \text{Sin} \left(\frac{x}{1.7} + 6.3 \right) \tag{7}$$

Where the equation's wave of laser path (f_1) has a slope with an x-axis angle of about 41°

$$f_2 = 3 * \text{Sin} \left(\frac{x}{3.2} + 6.3 \right) \tag{8}$$

Where the equation's wave of laser path (f_2) has a slope with an x-axis angle of about 29°.

$$f_3 = 3 * \text{Sin} \left(\frac{x}{3.6} + 1.5 \right) \tag{9}$$

Where the equation's wave of laser path (f_3) has a slope with an x-axis angle of about 24°.

The length of the path of laser path is determined by the following equation [33]:

$$L = \int_a^b \sqrt{1 + \left(\frac{dy}{dx} \right)^2} . dx \tag{10}$$

The length of the path of the laser follows the laser's path shape functions f_1 , f_2 , and f_3 determined by the following equations:

$$L_{f_1} = 3.5 * \int_0^{2\pi} \sqrt{1 + (f_1'(x))^2} dx \tag{11}$$

$$L_{f_2} = 2 * \int_0^{2\pi} \sqrt{1 + (f_2'(x))^2} dx \tag{12}$$

$$L_{f_3} = 1.6 * \int_0^{2\pi} \sqrt{1 + (f_3'(x))^2} dx \tag{13}$$

Where, the laser's path lengths of f_1 , f_2 , and f_3 are approximately equal to 57mm, 47mm, and 42 mm respectively.

3. Material and Methods

The samples were made from acrylic layers used in the industrial field and cleaned with alcohol to prepare them for tests to measure mechanical properties at different parameters such as variation of the laser's path, the speed of the laser, and its power.

3.1. Materials

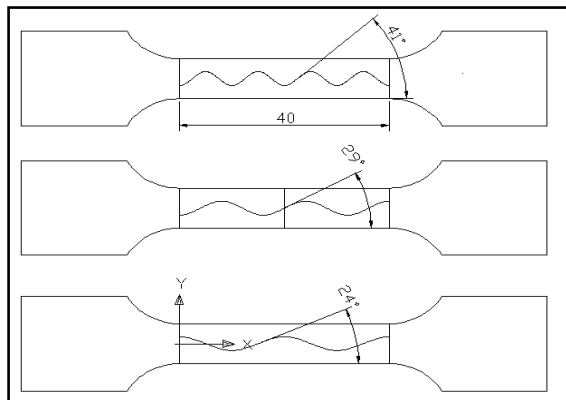
The empirical test used an acrylic layer with properties as shown in Table 1 to prepare tensile test samples for studying the influence of the functions of the laser's path on the mechanical properties. Acrylics are used widely in typical applications due to being lightweight, rigid, weather resistant, and more impact-resistant than glass, etc. [34] and tourist submarines [35] The shape functions of the laser ray have adopted three different functions for contributing to the re-distribution of the stresses in the samples through subjecting the tensile. The tensile test samples are prepared according to different laser path functions by using the (CNC) laser machine. The laser rays power is used to form different crack functions at different laser power with continuous ray type CO₂ at 40 watts, 50 watts, and 60 watts. The laser Machine properties consist of work dimensions (140 cm *190cm), maximum power of 80 watts, and a distance from the laser lens to the sample of 6.5mm. The laser speed of creating the crack functions by laser ray for tensile samples according to three different functions of the laser's path at different speeds 15 mm/sec, 30 mm/sec, and 45 mm/sec.

Table1.The characteristics of Acrylic layer [21].

Properties	Therm. Expan. μ°/K	Thermal. Conductivity W/m.K	Specific heat J/kg.K	Glass transition temp. $^{\circ}C$	Density kg/m^3	Shrinkage %	Friction coefficient	Refractive Index
Value	50-90	0.167- 0.25	1466	105	1170 - 1200	0.3 - 0.8	0.54	1.42

3.2. Methods

Tensile testing is important for many reasons, including the results of tensile tests of different materials used for engineering applications. The tensile test is the tool to determine the specifications of materials used for quality assurance of the material, in addition, measuring the tensile properties of different materials is used for developing different engineering materials and to predict the behavior of the material during a tensile test [36]. A laser ray is characterized by having photons of the same frequency, wavelength, and phase, as compared to a normal ray. Hence, the laser has higher energy density and better focusing properties. These unique features of laser rays are useful in the material processing of many industries, types of research, and other fields. The laser ray realizes the possibility of processing various materials and manufacturing processes such as creating cracks, engraving, cutting, heat treatment, and others. The current study depends on generating the crack's paths according to three specific functions which are equations 4, 5, and 6, in which the wave's inclination achieves a variable angle of 24, 29, and 41 degrees as shown in Figures.4-a,b, and c. The tensile samples are prepared from acrylic depending on the ASTM D412 standard. [36] standard of thermoplastic polymers which are commonly produced and distributed in the form of pellets and shaped into the final product form by melting, pressing, or injection molding. Figure 5 shows the drawing of the standard tensile samples by depending on Auto-cad software by transforming drawing files to the (CNC) laser machine for cutting the tensile samples according to their dimensions so that creating the laser's path on samples. Many microscopic images are obtained by microscopic type (Bel) at (X1600). The study used a laser machine to create three types of cracks according to three functions f_1, f_2 , and f_3 on one side of the acrylic samples.



Figures. 4 :a- Crack shape according to(f_1), b- Crack shape according to (f_2) and c-Crack shape according to (f_3)

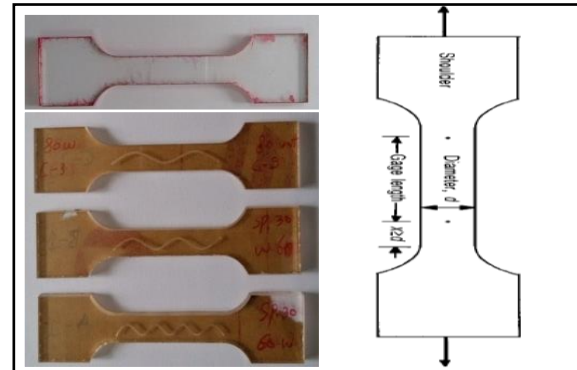


Figure 5. The standard sample type ASTM D412 [36].

4. Results and discussion

The heat generated from laser rays causing to create the crack's edge and its effect on the microstructure in the laser's path zone. The laser path zone works as a reinforcement region to prevent the occurred failure in the acrylic, which has affected the sample's resistance to failure compared to the samples that didn't have a laser path. The various functions of the laser's path shape have slopes at different angles with the loading axis to change the direction of growth of crack failure. The laser paths are achieve the following different functions that contribute to the redirection of the crack's failure for increased material resistance. The equations f_4, f_5 , and f_6 describe a relationship between the empirical results at different factors affecting the creation process of the crack's path achieved through the laser ray, such as the laser's power of 40 watts, 50 watts, and 60 watts, and laser speed at 15,30 and, 45 mm/sec respectively on the tensile stress.

$$f_4 = 42420.728 - 8882.325 \cdot z + 767.875 \cdot z^2 - 35.07 \cdot z^3 + 0.893 \cdot z^4 - 0.012 \cdot z^5 + 6.664E-5 \cdot z^6 \quad (14)$$

$$f_5 = 3325.661 - 724.486 \cdot z + 64.847 \cdot z^2 - 3.0387 \cdot z^3 + 0.0786 \cdot z^4 - 0.001 \cdot z^5 + 5.892E-6 \cdot z^6 \quad (15)$$

$$f_6 = 4875.614 - 789.812 \cdot z + 52.613 \cdot z^2 - 1.839 \cdot z^3 + 0.0356 \cdot z^4 - 0.00036 \cdot z^5 + 1.5E-006 \cdot z^6 \quad (16)$$

The empirical results are described in the general function :

$$F(z) = f_a + f_b \cdot z + f_c \cdot z^2 + f_d \cdot z^3 + f_e \cdot z^4 + f_g \cdot z^5 + f_h \cdot z^6 \quad (17)$$

4.1. Laser ray effect on crack zone

A topographic scan of the three-dimensional laser path zone is shown in Figures 6,7, and 8 which form an edge extending along the laser path. The images in Figures 6, 7, and, 8 of the topographic scan got by using the PHYWE Atomic Force Microscope device of different paths and conditions of the laser beam. Heating by the laser beam led

to a change in the internal structure of the acrylic material due to the effect of laser beam heat along the edge of the tensile samples in the laser path that appear in a microscopic as a form cantilever's shadow is an area that enhances resistance of the growth of the crack, which means an increase in the resistance to failure. Figures 6, 7, and 8 show the effect of the laser paths on the internal structure at different functions of the f_1 , f_2 and f_3 crack laser paths generated on acrylic samples, at conditions of power 50 W, speed of 15 mm/sec. The protrusions formed are differently shaped in the microstructure of the acrylic material by the effect of the laser beam in the region of different laser paths at the same conditions of power and speed of the laser beam. The images of the laser paths have zone dimensions ($49.5 \mu\text{m} * 50 \mu\text{m}$) and have variable depths due to the change in the laser path. The three dimensions images at a speed of 15 m/sec and laser power of 50 watts showed that the maximum protrusion relative to the neutral line was 54.2 nm and the lowest drop was 45,8 nm at f_1 so that at f_2 the maximum protrusion was 161 nm and the lowest drop 96.4 nm while the maximum protrusion is 110 nm and the lowest drop 162 nm at f_3 .

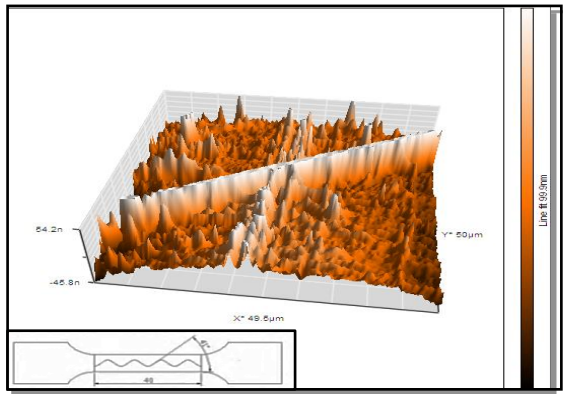


Figure 6. 3D topography scan of the laser's path according function (f_1) at 50 watts and 15 mm/sec.

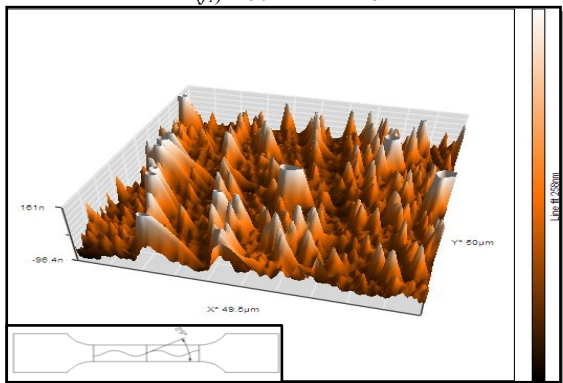


Figure 7. 3D topography scan of the laser's path according function (f_2) at 50 watts and 15 mm/sec.

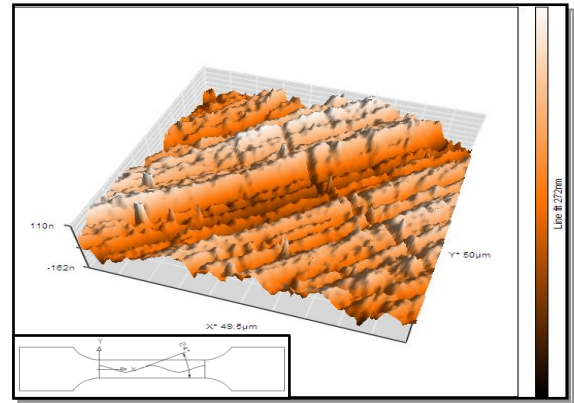


Figure 8. 3D topography scan of the laser's path according function (f_3) at 50 watts and 15 mm/sec.

4.2. Influence of laser's path functions (f_1 , f_2 , and f_3)

The empirical results in Figure9 showed an increase in the stress with a ratio of 14.66%, 14.45 %, and 14.01 % of samples type A, B, and C of the laser's path according to functions f_1 , f_2 , and f_3 at 40 watts and 15 mm/sec. The samples type A, B, and C of the laser's path according to functions f_1 , f_2 , and f_3 at 40 watts and 15mm/sec increased at ratios 15.01%, 12.33%, and 18.02% respectively compared to samples type (O) as shown in Figure10.

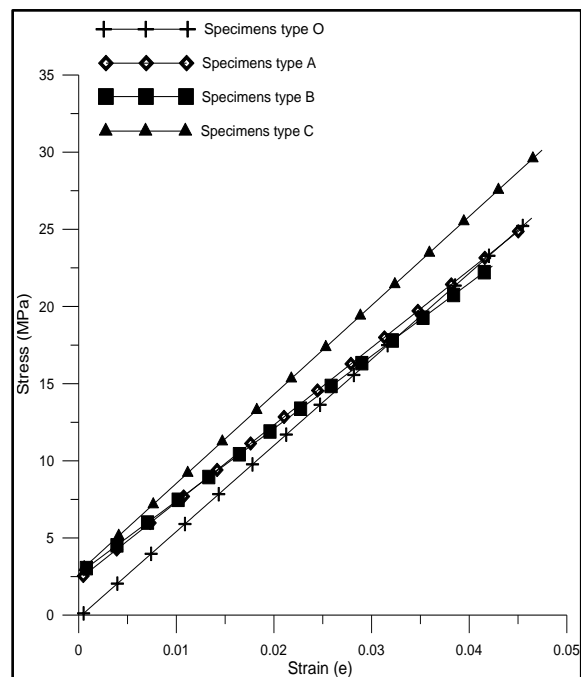


Figure 9. The effect of crack shape functions on the tensile test at 40 watts and 15 mm/sec

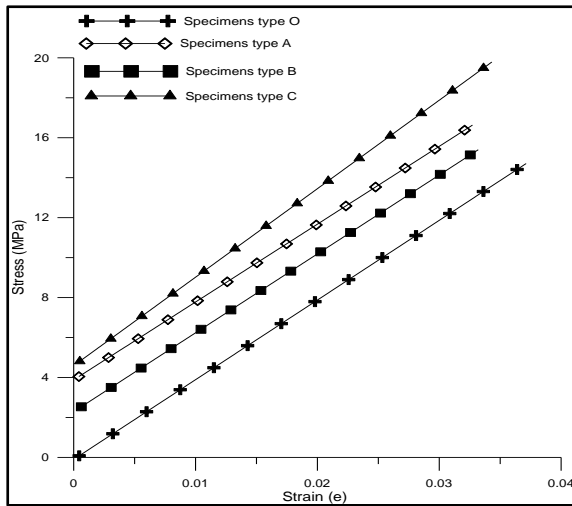


Figure 10. The effect of crack shape functions on the tensile test at 50 watts and 15 mm/sec

The variable influencing the increase in the stress value of Figures 11, 12, and 13 was the increase of the laser's power with the fixing of other factors such as the laser speed and the functions of the crack's path shape. The variation in the microstructure caused by heat-producing from the laser ray along the region of the crack's path formed a zone of resistance to stress concentration. The increase in the stress is a result of the influence of the crack's path function which was created on one surface in tensile samples due to tensile stress resistance by redistributing the stresses resulting from the tensile test along the edge side of the crack. Figure 11 shows the samples type A, B, and C of the laser crack's path shape according to functions f_1 , f_2 , and f_3 at 60 watts, and 15 mm/sec which increased the stress with ratios of 12.69%, 16.44%, and 18.91% respectively compared to samples type (O) while Figure 12 offers the samples type A, B, and C of the crack's path shape according to functions f_1 , f_2 , and f_3 at 40 watts and 30 mm/sec which increased the stress with ratios 12.91%, 14.8%, and 19.31% respectively. So, the tensile stress increased with ratios of 14.12%, 11.54%, and 21.91% due to increasing the laser's power by 50 watts as in Figure 13 while increasing at ratios of 14.18%, 19.08%, and 20.39% due to increasing the laser's power 60 watts as shown in Figure 14 which compared to the sample type (O).

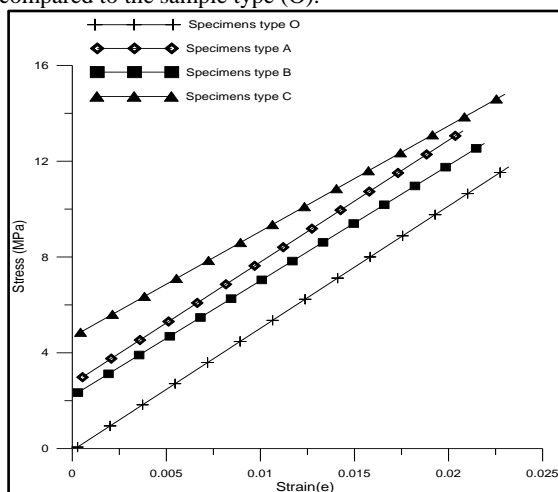


Figure 11. The effect of crack shape functions on the tensile test at 60 watts and 15 mm/sec

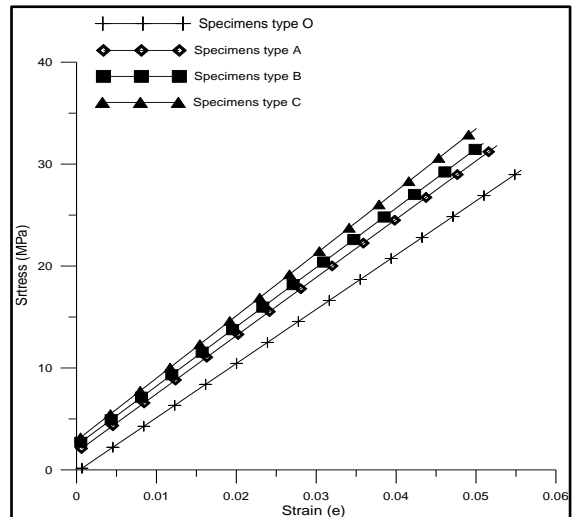


Figure 12. The effect of crack shape functions on the tensile test at 40 watts and 30 mm/sec

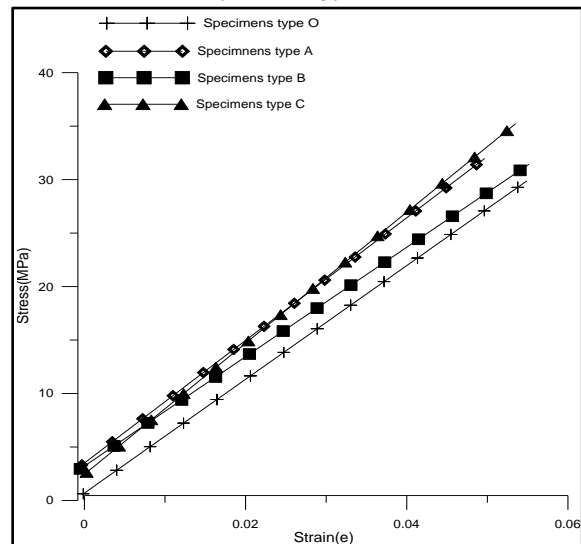


Figure 13. The effect of crack shape functions on the tensile test at 50 watts and 30 mm/sec

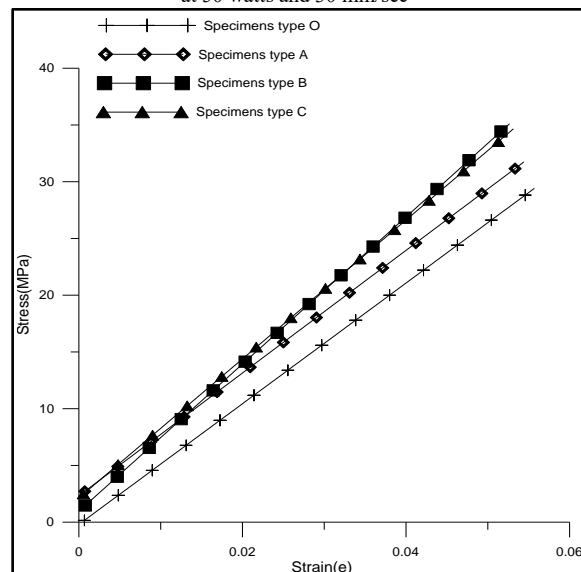


Figure 14. The effect of crack shape functions on the tensile test at 60 watts and 30 mm/sec.

Figures 15, 16, and 17. shows the influence of an increase in the laser's power at a laser speed of 45 mm/sec on the tensile stress which increases the stress with ratios of 17.14%, 20.97 %, and 21.16% due to increasing the laser's power at 40 watts, 50 watts, and 60 watts when compared to sample type (O). Figure 15 shows that at a laser speed of 45 mm/sec and laser power of 40 watts the kind of samples A, B, and C of the laser slit shape according to the functions f_1 , f_2 , and f_3 tensile stress increases by 6.94%, 16.26% and, 28.42% respectively compared to the type of sample (O) while increasing by 14.12%, 11.54% and, 21.91% respectively when the laser's power is increased to 50 watts as in Figure 16 In addition, the laser's power increased to 60 watts due to an increase the tensile stress by 22.94%, 16.23% and 24.33% as in Figure 17.

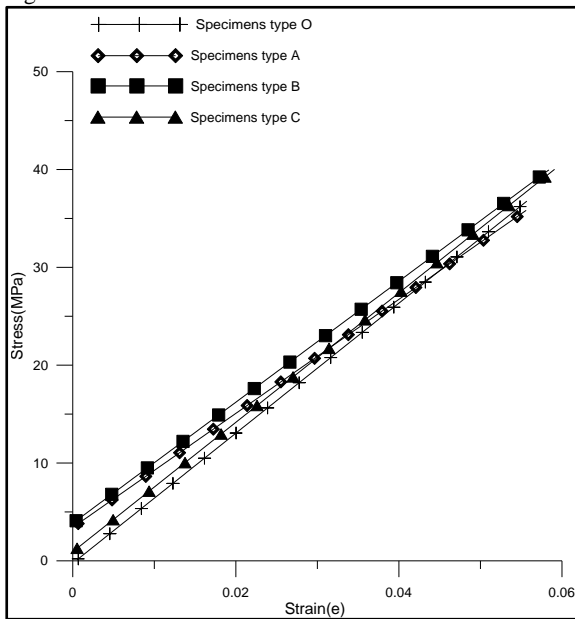


Figure 15. The effect of crack shape functions on the tensile test at 40 watt and 45 mm/sec.

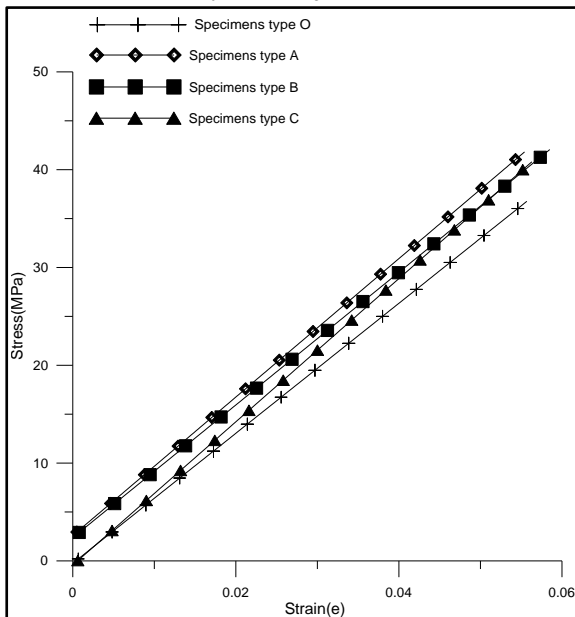


Figure 16. The effect of crack shape functions on the tensile test at 50 watt and 45 mm/sec

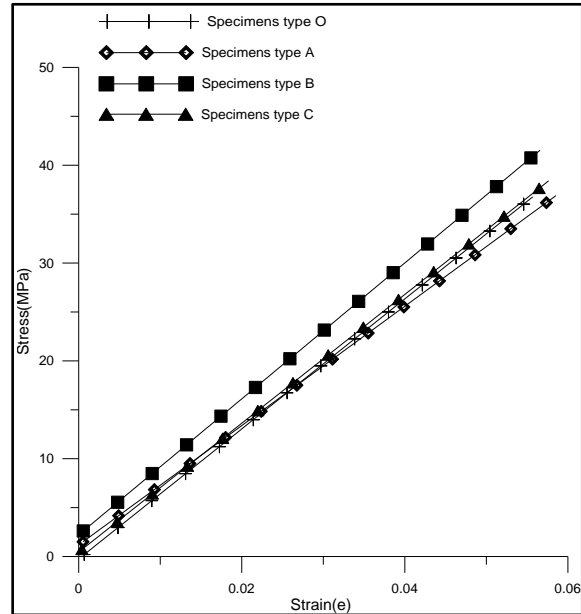


Figure 17. The effect of crack shape functions on the tensile test at 60 watt and 45 mm/sec

4.3. Effect of laser speed on the tensile stress

Increasing the laser speed from 15mm/s to 30mm/s indicates a decrease in the time of exposure of the samples to the laser ray that is focused on the crack zone at a ratio of 50%, which reduces its effect on the microstructure due to the heat produced by the laser ray. Also, the constant speed of the laser ray with the increase in the laser's power on the tensile samples for creating the crack according to specific functions indicates that an increase in the laser's power on the crack zone caused to generate more heating in it, which has a more effect on the micro-structure of the crack zone. Increasing the laser speed from 15 mm/sec to 45 mm/sec increases the stress at different crack's path functions f_1 , f_2 , and f_3 with an average ratio of 50.44%, 11.12 %, and 48.42% respectively at the power of 40 watts and increasing at a ratio of 13.62%, 30.8%, and 34.71% respectively, at power 50 watts, while the laser's power increases the tensile stress at average ratio 44.66%, 14.94%, and 22.29% respectively at power 60 watts compared to samples type (O). The empirical results offer the influence of the crack shape function through the angle of the path's slope with stress axis and the path's length, where the increase in the laser speed shows an increase in the stress ratio at a wave function f_1 has an angle of 24 degrees compared to a function of type f_2 and f_3 which have a wave that has a higher slope angle and greater length of the wave path. Figures 18, 19, and 20 produce the influence of the conditions of the laser speed at a laser power of 40 watts, 50 watts, and 60 watts on the micro-structure of the tensile samples of acrylic.

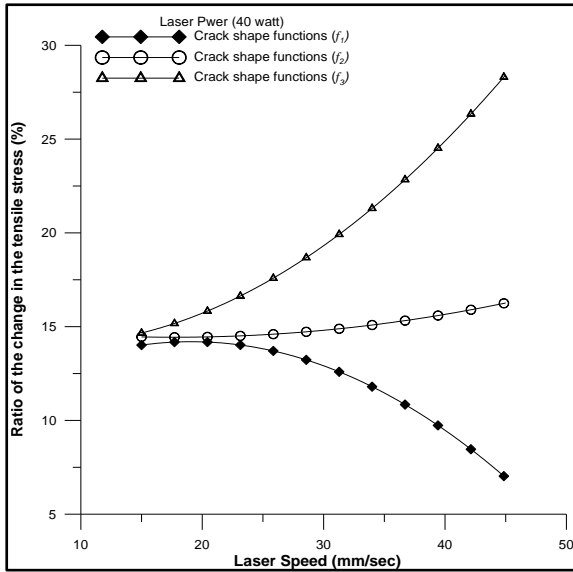


Figure 18. The laser speed and average change in tensile stress of crack shape functions (f_1 , f_2 , and f_3) at laser power (40 watt)

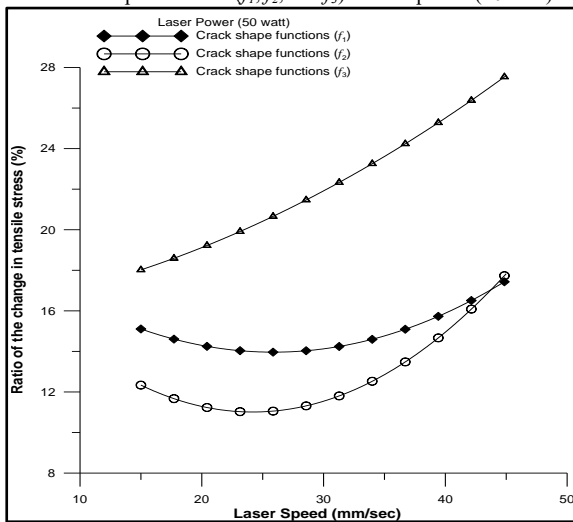


Figure 19. The laser speed and average change in tensile stress of crack shape functions (f_1 , f_2 , and f_3) at laser power 50 watt

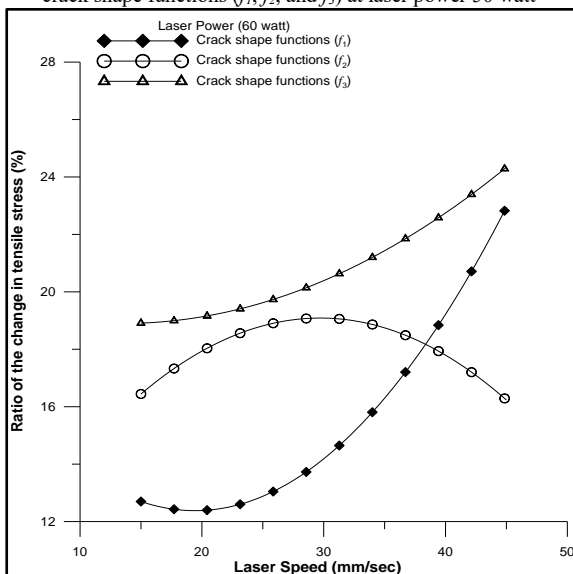


Figure 20. The laser speed and average change in tensile stress of crack shape functions (f_1 , f_2 , and f_3) at power 60 watts

4.4. Effect of laser power on the tensile stress

Increasing the laser's power from 40 watts to 60 watts indicates an increase in the heating of the crack zone at a ratio of 33.3%, causing to increase in its effect on the microstructure. Also, the specification of the influence of laser power on the tensile stress by taking other factors such as (laser speed and crack shape functions) be constant. The laser's power increases the stress of crack shape functions f_1 , f_2 , and f_3 with an average ratio of 9.39%, 12.1%, and 22.47% respectively at a laser speed of 15 mm/sec, and increasing at ratios of 8.97%, 22.42%, and 5.26% respectively, at laser speed 30 mm/sec, while the laser's power increasing the tensile stress at average ratio 69.73%, 8.97%, and 14.37% respectively at laser speed 45 mm/sec compared to samples type (O).

The empirical results in Figures 21, 22, and 23 clarify an increase in the ratio change in the stress of a function of type (f_1) with an increase in the laser energy, with a relative confirmation of the change in the stress ratio of the maximum effect in the microstructure composition of the tensile sample of acrylic at the lowest velocity of the laser ray and the type of function crack (f_1) that has the longest path. It increases in the ratio change in the stress until the laser's power 50 watts, then it decreases to high laser power 60 watts because it causes a weak point in the structure of the samples and then a structure to the tensile stress due to the high energy and the low velocity of the laser ray which has a longer wave path, While it decreases in the low energy ranges, it increased as there is an implicit factor which is the angle of inclination of the wave 29 degrees, and the path length of the wave is less.

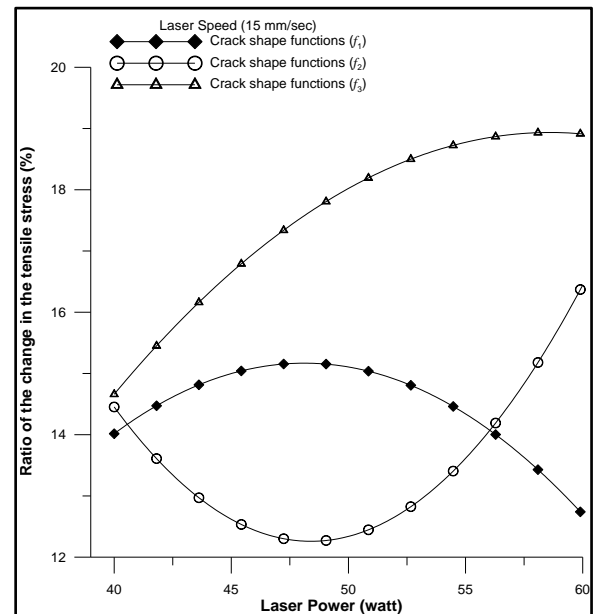


Figure 21. The laser's power and average change in tensile stress of crack shape functions (f_1 , f_2 , and f_3) at speed 15 (mm/sec)

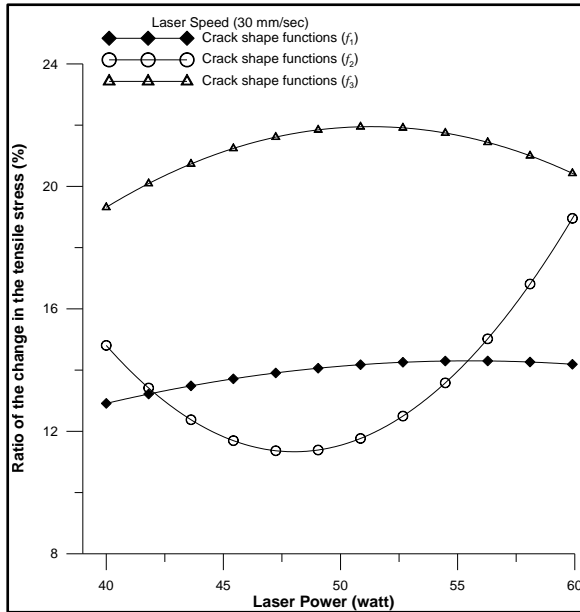


Figure 22. The laser's power and average change in tensile stress of crack shape functions (f_1, f_2 , and f_3) at speed 30 (mm/sec)

So, clarify decreasing the influence of rising the laser energy at high speed on the ratio change in tensile stress due to the decrease in the period exposure of the tensile samples at the crack zone to the laser ray power.

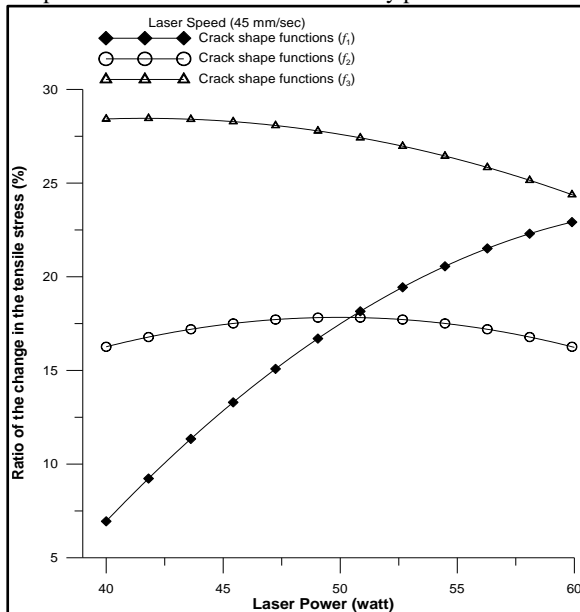


Figure 23. The laser's power and average change in tensile stress of crack shape functions (f_1, f_2 , and f_3) at laser speed 45 (mm/sec)

The maximum influence of the crack's path of function's type (f_1) at a laser speed of 45mm/sec and laser power of 60 watts leads to an increase in the tensile stress with a ratio of 22.94 %. The crack function's type (f_2) achieved a maximum increase in the stress at a laser speed of 30 mm/sec and 60 watts with a ratio of 19.08% while the maximum influence of the crack's path of function's type (f_3) at laser speed 45mm/sec at laser power 40 watts caused to increase the stress with ratio 28.24%. The increased stress caused by the influence of the laser's path function and created on the one surface in tensile samples is due to increasing the resistance by redistributing the stresses through tensile test along the edge side of the laser

crack's path. The disparity ratio in the stress of different types of the path of crack function f_1, f_2 , and f_3 at different boundary conditions of creating crack by using a laser ray. The average ratio of disparity of tensile stress at the different shapes of crack function in which type (f_3) gets maximum average disparity at a ratio of 32.31% and the average disparity of the function shape type (f_2) gets a ratio of 24.91%, while the average disparity ratio in increasing of tensile stress in the shape crack function type (f_1) get ratio 22.82%. The results confirmed the influence of the crack shape functions and have slope angles of 24°,29°, and 41°of f_1, f_2 , and f_3 respectively, the influence of the slope of the crack's path is to redirect the concentration of the stress produced through the tensile test far away from the slope of the shear plane.

5. Conclusions

The study found that the maximum stress affected by the laser path function type f_1 increased by 22.94% at 45mm/sec laser speed and 60W power, for f_2 it increased by 19.08% at 30mm/sec and 60W, while f_3 increased by 28.24% At a laser speed of 45 mm/sec and a power of 40 watts, therefore, these represent the ideal conditions for each type of laser path to optimize mechanical properties.

The study concluded that the effect of the speed of the laser beam on improving the mechanical properties varies by (0.7 - 1.41%) compared with the laser power effect at a variation of the sample's type, where increasing the laser speed of samples types A, B, and C increases the stress with a ratio of 15.99% and 17.16% and 18.35%, respectively, while the laser power increases the stress by 15.27%, 16.47%, and 19.76%, respectively. It is concluded that heat produced by the laser ray affected the microstructure of acrylic in the crack zone and enhanced the sample's resistance to tensile stress while the crack function (f_3) with a slope angle of 24° achieved maximum resistance to tensile stress with a ratio 28.24% due to the change direction of the crack's growth of failure far away from shear angle 45°. The mathematical equations for the crack path through the functions f_1, f_2 , and f_3 are described by fitting the empirical results equation $F(z)$ where the results are described as a relationship between laser power and laser speed with tensile stress to analyze their ability to disperse stresses away from the failure path. Finally, the study presents a new field for improving industrial product stress resistance by using laser power's influence on the microstructure according to paths designed to dissipate the concentration of internal forces in those products. The future scope of the study is to use high laser power at different paths to investigate its effect on the mechanical properties of metals and stress concentration regions in industrial products to enhance their resistance to failure.

Acknowledgement

We would like to thank the University of Technology, especially the Electromechanical Engineering Department and Center of Training, and Factory for their support in completing this work.

References

- [1] Shamsolhodaie A., Sun Q., Wang, X., Pantan B., Di H., Zhou Y. N., "Effect of Laser Positioning on the Microstructure and Properties of NiTi-Copper Dissimilar Laser Welds". *Journal of Materials Engineering and Performance*, Volume 29, Issue 2, pp.849-857,2020.
- [2] Z. P. Shi, Z. B. Wang, F. G. Chen, "Cavitation Erosion And Corrosion Behavior Of Niti Cladding With Cu And Nb Interlayers". *Journal of Materials Engineering and Performance*, Vol. 29, No. 6, pp. 3840-3851, 2020.
- [3] Z.-P. Shi, Z.-B. Wang, J. Q. Wang, "Effect Of Ni Interlayer On Cavitation Erosion Resistance Of NitiCladding By Tungsten Inert Gas (TIG) Surfacing Process". *Acta Metallurgica Sinica*, Vol. 33 No. 3, pp. 415-424, 2020.
- [4] J. L. Chen, J. Li, R. Song, L. L. Bai, J. Z. Shao, C. C. Qu, "Effect Of The Scanning Speed On Microstructural Evolution And Wear Behaviors Of Laser Cladding Nicrbsi Composite Coatings". *Optics & Laser Technology*, vol. 72, pp. 86-99, 2015.
- [5] C. T. Kwok, H. C. Man, F. T. Cheng, K. H. Lo, "Developments In Laser-Based Surface Engineering Processes: With Particular Reference To Protection Against Cavitation Erosion". *Surface and Coatings Technology*, vol. 291, pp. 189-204, 2016.
- [6] X. B. Liu, X. J. Meng, H. Q. Liu, "Development And Characterization Of Laser Clad High Temperature Self-Lubricating Wear Resistant Composite Coatings On Ti-6Al-4V Alloy". *Materials & Design*, Vol. 55, pp. 404-409, 2014.
- [7] Z. Chen, H. Yan, P. Zhang, Z. Yu, Q. Lu, J. Guo, "Microstructural Evolution And Wear Behaviors Of Laser-Clad Stellite 6/NbC/H-BN Self-Lubricating Coatings". *Surface and Coatings Technology*, Vol. 372, pp. 218-228, 2019.
- [8] Z. Zhang, R. Kovacevic, "Laser Cladding Of Iron-Based Erosion Resistant Metal Matrix Composites". *Journal of Manufacturing Processes*, Vol. 38, pp. 63-75, 2019.
- [9] X. Li, C. H. Zhang, S. Zhang, "Manufacturing Of Ti 3 Sic 2 Lubricated Co-Based Alloy Coatings Using Laser Cladding Technology". *Optics & Laser Technology*, vol. 114, pp. 209-215, 2019.
- [10] Q. Wu, W. Li, N. Zhong, W. Gang, W. Haishan, "Microstructure And Wear Behavior Of Laser Cladding VC-Cr₇ C₃ Ceramic Coating On Steel Substrate". *Materials & Design*, Vol. 49, pp. 10-18, 2013.
- [11] L. Meng, W. Zhao, K. Hou, "A Comparison Of Microstructure And Mechanical Properties Of Laser Cladding And Laser-Induction Hybrid Cladding Coatings On Full-Scale Rail". *Materials Science and Engineering: A*, Vol.748, 2019.
- [12] R. A. R. Rashid, S. Palanisamy, H. Attar, M. Bermingham, M. S. Dargusch, "Metallurgical Features Of Direct Laser-Deposited Ti₆Al₄V With Trace Boron". *Journal of Manufacturing Processes*, Vol. 35, pp. 651-656, 2018.
- [13] YanxinQiao, Jie Huang, Ding Huang, Jian Chen, Wen Liu, Zhengbin Wang, Zheng Zhibin, "Effects Of Laser Scanning Speed On Microstructure, Microhardness, And Corrosion Behavior Of Laser Cladding Ni45 Coatings". *Hindawi Journal of Chemistry*, Article ID 1438473, pp. 1-11, 2020.
- [14] Maryam Kazemi, Hassan Saghafan, Milad Hooshyar, "Evaluating The Impacts Of Laser Process Parameters On Microstructure And Microhardness Of H13-Tic Composite Using The Mathematical Modeling". *Springer Nature Switzerland AG, SN Applied Sciences* Vol. 2, Article number: 1942, pp.1-14, 2020.
- [15] Lin Yinghua, Ping Xuelong, KuangJiacai, Deng Yingjun, "Improving The Microstructure And Mechanical Properties Of Laser Cladded Ni-Based Alloy Coatings By Changing Their Composition: A Review". *Rev. Adv. Mater. Sci.*; 59: pp.340–351, 2020.
- [16] Silfvast, W. T. *Laser Fundamentals*. Cambridge University Press. Cambridge; 2004.
- [17] Caristan L. C. *Laser cutting guide for manufacturing*. Dearborn, Michigan: Society of Manufacturing Engineers; 2004.
- [18] Konar R., Mician M. Hlavaty I., "Defect detection in pipelines during operation using Magnetic Flux Leakage and Phased Array ultrasonic method". *Manufacturing Technology*, Vol. 14, No. 3, 337-341, 2014.
- [19] Raed N. Hwayyin, Ahmed S. Hammood, "Improving the Properties of Acrylic by Creating Crack Using Laser Beam". *1st International Conference on Petroleum Technology and Petrochemicals*, University of Technology Campus, Baghdad, Republic of Iraq, 1-10, 2019.
- [20] Abouda E, Dal M, Aubry P, Tarfa T N, Demirci I, Gomy C, Malot T., "Effect Of Laser Cladding Parameter On The Microstructure And Properties Of High Chromium Hard Facing Alloy". *9th International Conference on Photonic Technology*, physics Procedia 83, Germany, 684-696, 2016.
- [21] Irfan Khan, MukeshVerma, S. S. Mann, "Optimization of burr height in drilling of commercial Acrylic sheet using Taguchi method". *International Journal of Engineering Research and Applications (IJERA)*, Vol. 2, Issue 1, pp. 305-310, 2012.
- [22] Misra D., Acherjee B., Kuar A.S., Mitra S., "Transmission Laser Contour Welding Of Polycarbonates With A Moving Laser Beam. Process Simulation Via FEM". *Proceedings of the 24th International Congress on Applications of Lasers & Electro-Optics*, United States, 11-14, 2005.
- [23] Casalino G., Ghorbel E., "Numerical Model Of Co₂ Laser Welding Of Thermoplastic Polymers". *J. Materials Processing Technology*, 207, 63-71, 2008.
- [24] Ana Pilipovi'c, TomazBrajlih, Igor Drstvenšek, "Influence Of Processing Parameters On Tensile Properties Of SLS Polymer Product". *Polymers*, 1208; doi:10.3390/polym10111208, 2018.
- [25] Eluri, Vamsi, Parimi Vnskanardhan, "Stress Analysis Of Different Shaped Holes On A Packaging Material". *Master's Degree Thesis*. ISRN: BTH-AMT-EX--2016/D05—SE. Department of Mechanical Engineering, Blekinge Institute of Technology, Sweden, 2016.
- [26] D. Gross, T. Seelig. *Fracture Mechanics: With An Introduction To Micromechanics*. Mechanical Engineering Series. Springer-Verlag Berlin Heidelberg. DOI 10.1007/978-3-642-19240-1_2; 2011.
- [27] RaedNaemHwayyin, Ahmed Salman Hammood, Azhar Sabah Ameen, "Study The Effect Of Reinforcement The Acrylic With Different Types Of Composite Material On The Impact Energy". *Jordan Journal of Mechanical and Industrial Engineering*, Vol. 16, No. 3, 333–341, 2022.
- [28] FadiAlfaqs, "Dynamic Behavior of Thin Graphite/Epoxy FRP Simply Supported Beam Under Thermal Load Using 3-D Finite Element Modeling". *Jordan Journal of Mechanical and Industrial Engineering*, Vol. 15, No. 3, 301–308, 2021.
- [29] RaedNaemHwayyin, Azhar Sabah Ameen, "The Time Dependent Poisson's Ratio of NonlinearThermoviscoelastic Behavior of Glass/Polyester Composite". *Jordan Journal of Mechanical and Industrial Engineering*, Vol. 16, No. r 4, 515 – 528, 2022.
- [30] Sachin G. Ghalme, "Improving Mechanical Properties of Rice Husk and Straw Fiber Reinforced Polymer Composite through Reinforcement Optimization". *Jordan Journal of Mechanical and Industrial Engineering*, Vol.15, No. 5, 411 - 417, 2021.
- [31] George W. Housner, Thad Vreeland. *The Analysis Of Stress and Deformation*. Sixth printing; 1991.

- [32] Piaras Kelly. Solid Mechanics- Part I: An Introduction to Solid Mechanics. Department of Engineering Science by University of Auckland. New Zealand. 272-282; 2013.
- [33] George B., Thomas Maurice, D. Weir and Joel, R. Hass. Thomas Calculus (Twelfth Edition). publishing by Pearson education, United Kingdom. 1- 1152; 2010.
- [34] Rajib Kumar Mandal, AsishBandyopadhyay, Santanu Das". An Experimental Investigation on Laser Beam Welding of Acrylics", Indian Welding Journal Vol.47, No. 4,75-82 , 2014.
- [35] Selma Ergin, C. GuedesSoares,"Sustainable Development and Innovations in Marine Technologies". England- London, ISBN: 9781003358961 , 1 - 474, <https://doi.org/10.1201/9781003358961>,1st Edition, 2022.
- [36] Joseph R. Davis, "Tensile Testing (2nd ed.). ASM International.United States. ISBN: 978-0-87170-806-9. 283; 2004.

A New Trajectory Planning Method of 6-DOF Apple Picking Manipulator

Junying Li

College of Electromechanical Engineering, Qingdao University of Science & Technology, Qingdao, 266061, China

Received 13 Jul 2022

Accepted 20 Sep 2022

Abstract

In order to control the 6-DOF apple picking manipulator to complete the picking task accurately and safely, a new trajectory planning method of 6-DOF apple picking manipulator is studied. Based on the mathematical model of the 6-DOF apple picking manipulator, the pose information and arm shape information of the forward and reverse motion of the manipulator are analyzed. On the basis of the obstacle avoidance method for the apple picking manipulator based on the improved artificial potential field, the obstacle model is constructed to obtain the obstacle distribution information. Through the two-way planning algorithm of the manipulator obstacle avoidance based on the improved artificial potential field method, the pose information and arm shape of the forward and reverse motion of the manipulator are controlled. On this basis, the trajectory planning control method of 6-DOF apple picking manipulator based on sliding mode PID control is used to control the manipulator to pick apples accurately and safely. After testing, the 6-DOF apple picking manipulator can realize the safe picking of apples according to the set picking position and speed.

© 2022 Jordan Journal of Mechanical and Industrial Engineering. All rights reserved

Keywords: 6-DOF; Apple picking; Picking; Manipulator; Trajectory planning.

1. Introduction

As the representative of contemporary high-tech industry, robot industry began in the 1960s. The rapid development of robotics and robotics industry benefits from the emergence and rapid development of microcomputer technology. At present, millions of robots have been applied in various fields, especially in manufacturing systems [1].

Big data, cloud computing and mobile Internet technology, which are familiar to us, promote the development of robot technology. Their integration with robot technology makes the degree of artificial intelligence of robots higher and higher. Military UAVs, autonomous cars, home service robots and so on have been realized, and even common [2]. In the world, many media generally believe that it is no exaggeration to use "The Pearl at the top of the crown" to describe the position of robots in the manufacturing industry. Now an important sign to measure the level of a country's high-end manufacturing industry is the R & D, manufacturing and application of robots. With the wave after wave of industrial revolution, we have moved from automation to informatization and then to robotics. It has to be admitted that the emergence of robots has greatly improved the production efficiency of industrial production. In modern life, the situation that robots gradually replace people to take the post of physical labor or even mental labor has been slowly accepted by people [3].

With the high development of productivity, the accuracy and stability of motion put forward high requirements for robots. How to improve the working efficiency of the robot and minimize the error caused by the movement process is the key problem to be solved in its application, because the most important index to measure the performance of the robot is the working efficiency and quality of the robot. Therefore, more in-depth research on robot system is the basis of robot design and development [4]. The research on manipulator trajectory planning is the premise and foundation to solve the problem.

The so-called trajectory planning is to discuss the method of calculating trajectory. The trajectory can reflect the motion path of the manipulator in space. Those who know something about the robot system know that the smoothness and stability of the motion process of the manipulator (avoiding the sudden change of displacement, speed and acceleration as much as possible) is a principle that must be followed in the motion process of the robot system. In fact, abrupt motion requires a lot of power, which is difficult to provide due to the physical limitations of the motor[5,6]. Therefore, this reflects the importance of motion trajectory planning. Using simple technology to plan the motion of the robot can make its motion smooth and stable, and produce less impact and vibration, which basically ensures the long-term and stable operation of the system. However, the vibration of rigid body and the sudden change of motion are difficult to be guaranteed [7]. Therefore, we have to deeply study the trajectory planning

* Corresponding author e-mail: lijuny00@163.com.

of robot in order to meet the increasing performance requirements.

The technology of trajectory planning is also developing and improving with the improvement of productivity and tracking accuracy[8]. There are many performance optimization indexes of robot trajectory planning algorithm, such as optimal time and optimal impact. The most studied is the robot trajectory planning algorithm in the optimal time. This most studied trajectory algorithm is indeed a very active research field in the past ten years [9].

ZHENG C-E et al. proposed the trajectory planning method of the apple picking manipulator based on the deep deterministic policy gradient algorithm (DDPG) of stepwise migration strategy. The progressive space constraint of DDPG was used to train the strategy step by step, and the transfer learning idea was used to transfer the trained strategy to the promiscuous obstacle scene. Finally, the DOF apple picking manipulator was simulated. This method can improve the training efficiency in the process of trajectory planning training, but it is difficult to ensure that the apple picking robot arm can safely and accurately pick the target apple during the picking process [10]. LIU X-F et al. designed a stretchable, fixed torque, self-transporting efficient apple picking manipulator based on a variety of mechanical structures. This mechanical arm not only improves the picking efficiency, but also reduces the cost of picking apples, which can ensure personal safety to a certain extent. However, this mechanical arm is difficult to pick apples accurately according to the set apple picking position, and its accuracy needs to be improved [11]. FAN Z-Y et al. proposed a trajectory planning method for camellia fruit picking manipulator based on the improved Gray Wolf algorithm. The kinematics and working space of the manipulator were analyzed, and the trajectory fitting planning was carried out. The gray Wolf algorithm was improved based on the analysis of Wolf writing and hunting, and the improved gray Wolf algorithm was used to carry out the trajectory optimization simulation experiment of the manipulator picking operation. This method can obtain the trajectory planning results with optimal time, but ignores the security and accuracy of picking operations [12]. SI G-B et al. designed a path planning method for agricultural picking manipulator based on cloud platform and Q-learning algorithm. This paper analyzes the application of Q learning algorithm in the path planning of agricultural picking manipulator, introduces the working mode of cloud platform and calculates the path planning, designs the control system of agricultural picking manipulator, and realizes the path planning of picking manipulator. This method can better avoid the obstacles in the environment, and the path deviation of the overall motion curve is small, but its picking accuracy is difficult to be guaranteed [13].

There are many kinds of trajectory planning algorithms. Its development has experienced a process from low-level to high-level, simple to complex. Its interpolation accuracy is higher, and the interpolation speed is faster. Classical interpolation algorithms include straight line, arc, helix and so on. Straight line interpolation and arc interpolation are the two most basic interpolation algorithms. At present, the most studied algorithms are parametric curve algorithms, such as B-spline curve, NURBS curve and so on. Combined with the current research data, this paper puts forward a new trajectory planning method of 6-DOF apple picking manipulator. This method can not only

accurately realize apple picking according to the specified information, but also has good obstacle avoidance effect.

2. Methods

2.1. Mathematical model of 6-DOF apple picking manipulator

To study the motion of the manipulator, it must firstly establish the kinematic equation. When studying the 6-DOF apple picking manipulator, the corresponding coordinate system should be established on each corresponding manipulator link. In order to understand the motion of the manipulator, the relationship between the link coordinate systems must be established [14]. In order to determine the translation vector of the connection between the coordinate systems and the direction of each link coordinate system, this paper uses the D-H parameter method to reflect the relative position of the adjacent links for the multi degree of freedom manipulator.

2.1.1. Forward kinematics model

The forward motion pose ${}^0H'$ of the 6-DOF apple picking manipulator is constructed as follows:

$${}^0_1H' = \begin{bmatrix} YX\alpha_1 & -XX\alpha_1 & 0 & 0 \\ XX\alpha_1 & XY\alpha_1 & 0 & 50 \\ 0 & 0 & 1 & 0 \\ 0 & 0 & 0 & 1 \end{bmatrix} \quad (1)$$

$${}^0_2H' = \begin{bmatrix} YX\alpha_2 & -XX\alpha_2 & 0 & 0 \\ 0 & 0 & 1 & 0 \\ -XX\alpha_2 & -YX\alpha_2 & 1 & 425 \\ 0 & 0 & 0 & 1 \end{bmatrix} \quad (2)$$

$${}^0_3H' = \begin{bmatrix} YX\alpha_3 & -XX\alpha_3 & 0 & 0 \\ XX\alpha_3 & YX\alpha_3 & 1 & 0 \\ 0 & 0 & 1 & 50 \\ 0 & 0 & 0 & 1 \end{bmatrix} \quad (3)$$

$${}^0_4H' = \begin{bmatrix} YX\alpha_4 & -XX\alpha_4 & 0 & 0 \\ 0 & 0 & 1 & 425 \\ -XX\alpha_4 & -YX\alpha_4 & 1 & 0 \\ 0 & 0 & 0 & 1 \end{bmatrix} \quad (4)$$

$${}^0_5H' = \begin{bmatrix} YX\alpha_5 & -XX\alpha_5 & 0 & 0 \\ 0 & 0 & -1 & 0 \\ XX\alpha_5 & YX\alpha_5 & 0 & 0 \\ 0 & 0 & 0 & 1 \end{bmatrix} \quad (5)$$

$${}^0_6H' = \begin{bmatrix} YX\alpha_6 & -XX\alpha_6 & 0 & 0 \\ 0 & 0 & 1 & 0 \\ -XX\alpha_6 & YX\alpha_6 & 0 & 100 \\ 0 & 0 & 0 & 1 \end{bmatrix} \quad (6)$$

Where, YX and XX are cosine function and sine function in turn. The product of six transformation matrices between adjacent joints is the forward kinematics solution.

2.1.2. Reverse kinematics model

The reverse motion pose of the 6-DOF apple picking manipulator is:

$${}^0H = {}^0H(\alpha_1) {}^1H(\alpha_2) {}^2H(\alpha_3) {}^3H(\alpha_4) {}^4H(\alpha_5) {}^5H(\alpha_6) {}^6H(\alpha_6) \quad (7)$$

To solve each joint variable α_j , due to the particularity of the 6-DOF apple picking manipulator, the 6-DOF apple picking manipulator can have different postures at the same point, resulting in the multiplicity of joint variables of the 6-DOF apple picking manipulator, because α_1 and α_3 have two solutions, and their combination makes α_2 have four groups of solutions. And the wrist joint “flipping” will get another four solutions:

$$\alpha_4 = \alpha'_4 - 180^\circ \quad (8)$$

$$\alpha'_5 = -\alpha_5 \quad (9)$$

$$\alpha_6 = \alpha'_6 - 180^\circ \quad (10)$$

Where, α'_4 , α'_5 and α'_6 are the angles of joint connecting rod after the turnover of the 4th, 5th and 6th wrist joints respectively. Therefore, there are 8 sets of solutions for inverse kinematics. That is, there are 8 groups of joint angles, which can meet the same posture from the end of the 6-DOF apple picking manipulator. However, due to mechanical constraints, not all of these 8 sets of solutions can be achieved [15].

In the trajectory planning of 6-DOF manipulator, it is one of the important works to determine the unique inverse solution. Otherwise, the shape of the manipulator at the end of the manipulator is uncertain during the movement, which will be very dangerous [16]. Therefore, the arm shape parameters should be introduced here:

$$rr = \begin{cases} rr > 0 & \text{Left shoulder} \\ rr < 0 & \text{Right shoulder} \end{cases} \quad (11)$$

$$cr = \begin{cases} cr > 0 & \text{High elbow} \\ cr < 0 & \text{Low elbow} \end{cases} \quad (12)$$

$$vr = \begin{cases} vr > 0 & \text{High wrist} \\ vr < 0 & \text{Low wrist} \end{cases} \quad (13)$$

Where, rr , cr and vr are the shape parameters of the shoulder, elbow and wrist of the manipulator respectively.

2.2. Obstacle avoidance method of apple picking manipulator based on improved artificial potential field

Based on the posture information and arm shape information of the forward and reverse motion of the 6-DOF apple picking manipulator mastered in Section 2.1, through the obstacle avoidance method of the apple picking manipulator based on the improved artificial potential field, the obstacle model in the operating environment of the apple picking manipulator is constructed to obtain the obstacle distribution information, and the obstacle avoidance of the manipulator is realized through the two-way planning algorithm of the manipulator based on the improved artificial potential field method.

2.2.1. Obstacle model

Because the obstacles such as fruit trees and branches generally have irregular shapes, it is difficult to describe them accurately. In this paper, the spherical envelope of

the obstacles is used to approximate the modeling. Although this modeling method expands the obstacle region to a certain extent, it simplifies the description of the obstacle region and the calculation of the spherical envelope approximation method, effectively improves the planning efficiency and ensures the safety of path planning [17].

The spherical envelope of the obstacle can be described as $N(q_0, s_n)$, as shown in Figure 1, in which the maximum and minimum values of the vertex coordinates of the obstacle are (x_a, y_a, z_a) and (x_b, y_b, z_b) in turn, the coordinate of the ball center in the base coordinate system is $q_0(x_0, y_0, z_0)$, and the radius of the surrounding ball is s_n .

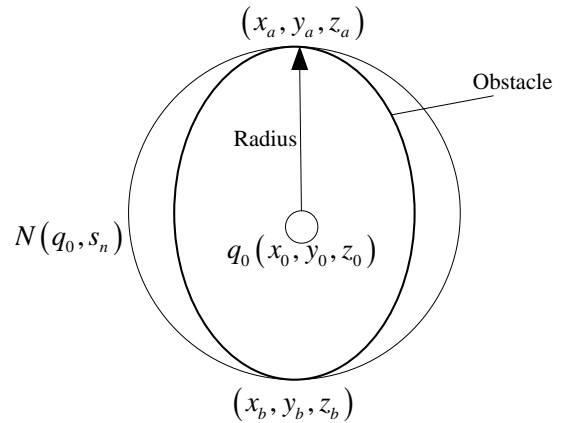


Figure 1. Model of obstacles spherical envelope

$$s_n = \frac{(x_a - x_b)^4 + (y_a - y_b)^4 + (z_a - z_b)^4}{2} \quad (14)$$

The bounding sphere is defined as:

$$S = \{(x, y, z)^T\} \quad (15)$$

Where x_a , y_a and z_a are the maximum values of x axis coordinates, y axis coordinates and z axis coordinates of obstacles; x_b , y_b and z_b are the minimum values of x axis coordinates, y axis coordinates and z axis coordinates of obstacles; T stands for transpose.

2.2.2. Bi-directional planning algorithm for obstacle avoidance of manipulator based on improved artificial potential field method

The 6-DOF apple picking manipulator belongs to the research category of picking robot. The artificial potential field method is widely used in the path planning of mobile robot. Its basic idea is to regard the 6-DOF apple picking manipulator as a particle and establish an artificial potential field composed of gravitational field $V_{att}(p)$ and repulsive field $V_{rep}(p)$ in its workspace. The gravity $G_{att}(p)$ and repulsive force $G_{rep}(p)$ generated by them act on the joint target point of the 6-DOF apple picking manipulator. The principle of artificial potential field method is shown in Figure 2.

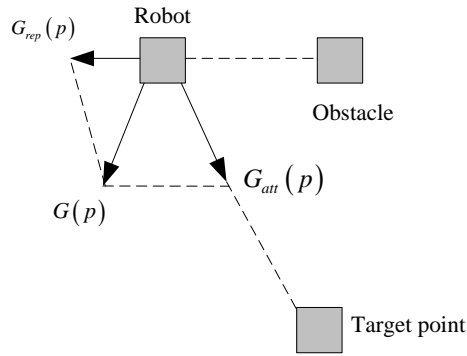


Figure 2. Principle of artificial potential field method

Assuming that the current pose of the 6-DOF apple picking manipulator is p , $p = {}^0H_j + {}^0H'_j$, and the sum of rr , cr and vr is referred to as the morphological parameter rcv , the resultant force exerted by the artificial potential field on the manipulator is:

$$G(p) = SG_{att}(p)rcv + SG_{rep}(p)rcv \quad (16)$$

When planning the path of the manipulator with the artificial potential field method, we should not only ensure that the end of the manipulator reaches the target point, but also consider the possible collision between the connecting rod of the manipulator and the obstacle [18]. In this paper, an appropriate artificial potential field is established in the workspace of the manipulator, and the artificial potential field method is improved from three aspects: oscillation problem, algorithm efficiency and local minimum point.

In order to better apply the artificial potential field method to the path planning of manipulator, the gravitational field and repulsive field are established in joint space and Cartesian space respectively. The gravitational field exists between the manipulator and the target position. The farther away from the target position, the greater the gravity, and the generated gravity pulls the manipulator to the target position [19].

When planning the path of multi degree of freedom manipulator in Cartesian space, the inverse kinematics solution needs to be carried out continuously, which often leads to the emergence of singular solutions [20]. In order to avoid this problem, the gravitational field $V_{att}(p)$ is established in the joint space of the manipulator.

$$V_{att}(p) = \begin{cases} rcv \left\| \frac{p\theta}{2} - \frac{p_{goal}\theta}{2} \right\| & \|p - p_{goal}\| \leq e \\ rcv \left\| \theta ep - \theta ep_{goal} \right\| - \frac{1}{2} \theta e^2 & \|p - p_{goal}\| > e \end{cases} \quad (17)$$

Where, p_{goal} is the pose of the apple, which belongs to the desired pose of the manipulator; θ is the gravitational gain. The distance threshold e is set to prevent the robot arm from obstacle avoidance failure due to excessive gravity.

It can calculate the negative gradient of the gravitational field $V_{att}(p)$ to obtain the gravitational force:

$$G_{att}(p) = \begin{cases} rcv \left\| -\theta p + \theta p_{goal} \right\| & \|p - p_{goal}\| \leq e \\ -e \cdot rcv \frac{\theta(ep - ep_{goal})}{\|ep - ep_{goal}\|} & \|p - p_{goal}\| > e \end{cases} \quad (18)$$

The repulsion field exists between the manipulator and the obstacle. The generated repulsion force $G_{rep}(p)$ keeps the manipulator away from the obstacle, and its size is inversely proportional to the shortest distance $\gamma(p)$ between the manipulator and the obstacle.

It is very complex to establish the repulsive force field in the joint space, so it is necessary to calculate the minimum $\gamma(p)$ in all the manipulator attitudes P_{obs} in the collision. Therefore, it is easier to calculate $\gamma(p)$ and establish the repulsion field of the manipulator in Cartesian space.

Since the manipulator cannot be regarded as a particle, several control points are defined on the manipulator as the force points of the manipulator in the repulsion field. Select the coordinate origin O_1 , O_2 and O_3 of the 3th, 5th and 6th joints of the manipulator as the control points, as shown in Figure 3.

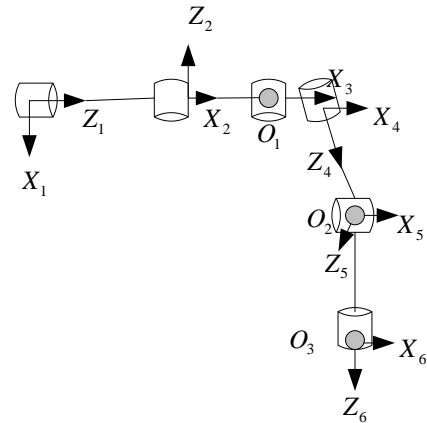


Figure 3. Manipulator control points

Let $b_j(p)$ as the coordinate of the control point O_j when the manipulator is in position and attitude p , and there is repulsive potential energy for the control point O_j :

$$V_{rep}^j(p) = \begin{cases} \frac{\partial_j}{2} \left(\frac{rcv}{\gamma(b_j(p))} - \frac{rcv}{\gamma_0} \right)^2 & \gamma(b_j(p)) \leq \gamma_0 \\ 0 & \gamma(b_j(p)) > \gamma_0 \end{cases} \quad (19)$$

Where ∂_j is the repulsion gain of control point O_j ; $\gamma(b_j(p))$ is the shortest distance from O_j to the obstacle; γ_0 is the maximum distance of the repulsion of the obstacle to O_j .

The further repulsive force O_j can be applied on:

$$G_{rep}^j(p) = \begin{cases} rcv \left(\frac{\partial_j}{\gamma(b_j(p))} - \frac{\partial_j}{\gamma^2(b_j(p))} \right) \frac{\gamma(b_j(p))}{\gamma^2(b_j(p))} & \gamma(b_j(p)) \leq \gamma_0 \\ 0 & \gamma(b_j(p)) > \gamma_0 \end{cases} \quad (20)$$

Finally, the gravity $G_{rep}^j(p)$ in the operating environment of the manipulator in Cartesian space is converted into joint force $G_{rep}(p)$:

$$G_{rep}^j(p) = G_{rep}(p) / \sum_{j=1}^3 I_{v,j}(p)rcv \quad (21)$$

Where, $I_{v,j}(p)$ is the part of the central line velocity of the Jacobian matrix of the manipulator.

At some positions in the repulsion area, the manipulator will appear alternately with $G_{att}(p) > G_{rep}(p)$ and $G_{att}(p) < G_{rep}(p)$. Under the action of such potential field force, the manipulator will move back and forth, resulting in oscillation of obstacle avoidance path [21].

In this regard, the repulsive variable gain coefficient ε is introduced to make the repulsive gain decrease gradually in the oscillation stage, reduce the ratio of repulsive gain to gravitational gain, avoid the sudden change of resultant force direction, and realize a relatively smooth track, as follows:

$$\partial_j = \varepsilon \cdot \partial_0 \tag{22}$$

Where ∂_0 is the initial repulsion value.

In order to further improve the search efficiency of the algorithm, an adaptive step size strategy is introduced in the process of path search.

The next pose p_{next} of the manipulator is determined by the gradient descent direction. Set the current pose of the manipulator as p , including:

$$p_{next} = rcv \cdot \varepsilon \rho + \frac{\sigma G(p)}{\|G(p)\|} \tag{23}$$

$$\|p_{goal} - p\| > \rho \tag{24}$$

Where σ and ρ are the search step size and the maximum allowable error respectively.

The algorithm adaptively modifies the step size according to the distance between the control point of the manipulator and the obstacle. When the obstacles are far away, large step size is adopted to improve the search efficiency of obstacle avoidance path [22]; When the obstacle is close, reduce the step size to ensure the accuracy of the algorithm, as follows:

$$\sigma = \sigma_0 + rcv \cdot \sum_{j=1}^3 \varepsilon \mu_j \gamma(b_j(p)) / 3 \tag{25}$$

Where σ_0 is the initial step size; μ_j is the weight coefficient of the manipulator control point O_j .

Aiming at the problem that the path planning by artificial potential field method is easy to fall into local minima, a two-way planning algorithm based on artificial potential field method is proposed. The specific manifestation of the local minimum point is: when the manipulator is searching for the obstacle avoidance path, the resultant force of the gravity and repulsion received by the manipulator at a certain position is just at a minimum point. At this time, the change of any joint angle will lead to the increase of the resultant force, the manipulator will move repeatedly at this position, the manipulator will fall into the local minimum, and the algorithm will fail [23]. Bi directional planning is to use the artificial potential field method to plan two opposite paths from the initial point and the target point respectively. The target point of each search for the obstacle avoidance path will be updated, and the gravity of the manipulator will change accordingly, avoiding the emergence of local minimum points to a certain extent [24]. Finally, the two paths are spliced into the final path.

The specific steps of two-way planning are as follows:

1. From the initial point of the end of the 6-DOF apple picking manipulator in Cartesian space and the apple picking target point, the initial value and target value of the obstacle avoidance trajectory of the manipulator in joint space are obtained [25].
2. The initial value of the obstacle avoidance trajectory of the 6-DOF apple picking manipulator in the joint space is planned forward, and the initial target is p_{goal} . For p_{goal} , the initial target of the obstacle avoidance trajectory becomes p_{start} .
3. After the calculation of the improved artificial potential field method, the current position of the 6-DOF apple picking manipulator is updated to p_j^f and p_j^r by forward and reverse programming respectively. The position planning result includes the pose and arm shape of the 6-DOF apple picking manipulator. These two values will be set as the target point for the next search.
4. Repeat step (3) until after i times of search, when the 6-DOF apple picking manipulator moves forward and backward, the result of obstacle avoidance path planning meets the following conditions, and the algorithm ends.

$$\begin{cases} \|p_j^f - p_j^r\| < F \\ \|p_j^f - p_j^r\| < E \end{cases} \tag{26}$$

Where, F and E are the maximum allowable errors of joint quantity and space quantity.

2.3. Trajectory planning control method of 6-DOF apple picking manipulator based on sliding mode PID control

Based on the basic knowledge of the picking obstacle avoidance of the manipulator realized in Section 2.2, in order to ensure the stability and success of the 6-DOF apple picking manipulator, the error model of the 6-DOF apple picking manipulator is set as follows:

$$\psi_t = p_j^f \cdot p_j^r (\psi_{t+1} + h_1 + h_0) \tag{27}$$

Where h_1 and h_0 are the design parameters of sliding mode PID controller. When $\psi^2 + h_1\psi + h_0 = 0$, the 6-DOF apple picking manipulator is stable. ψ is the damping ratio, t is the picking time, and ψ_{t+1} is the damping ratio of the manipulator at time $t + 1$.

The design process of sliding mode PID controller is divided into two steps. Firstly, a sliding mode surface function is defined, and then an appropriate control law is designed to make the system reach and maintain the desired sliding mode surface $\lambda = 0$.

$$\lambda = p_j^f \cdot p_j^r (\psi_{t+1} - \psi_t) \tag{28}$$

If the desired sliding surface exists, $\lambda = 0$ can be made. Let $\psi_{t+1} = \psi_t$, introduce equation (28) into equation (27), then:

$$h_1\psi_{t+1} + h_0\psi_t = 0 \tag{29}$$

Equation (29) as time increases, the error of the 6-DOF apple picking manipulator when picking apples will eventually converge to 0.

The control input vc of the 6-DOF apple picking manipulator is designed as follows:

$$vc = P_j^f \psi_{PID} \cdot P_j^r \psi_{PID} \tag{30}$$

Where, ψ_{PID} is the control parameter output value of sliding mode PID control of 6-DOF apple picking manipulator.

The gain of traditional PID controller is generally fixed, which can not meet the control quality requirements of manipulator under forward and reverse changing conditions [26]. Therefore, the three control gains ψ_P (proportional), ψ_I (integral) and ψ_D (differential) designed in this paper can be obtained by online learning of the following adaptive law, where $\zeta_j > 0$ represents the adaptive learning rate.

$$\psi_{PID} = -\zeta_j \mathbf{1} \cdot \psi_i \tag{31}$$

Where $\mathbf{1}$ is a symbolic function. Using this formula, three control gains ψ_P , ψ_I and ψ_D can be obtained through online learning, and the mechanical arm can be dynamically controlled to complete apple picking accurately and safely under forward and reverse changing working conditions [27].

3. Experimental analysis

In order to verify the feasibility of this method, simulation experiments are carried out in MATLAB 7.0 environment. The experimental environment information is shown in Table 1.

Table 1. Experimental environment information

Name	Working space
Spatial range	[-200,200]mm×[-200,200]mm
Unit size	20mm×20mm
Number of obstacle units / piece	5

In the experimental environment shown in Table 1, the obstacle avoidance effect of the 6-DOF apple picking manipulator when performing the picking task under the use of the method in this paper is tested. The effect diagram is shown in Figure 4.

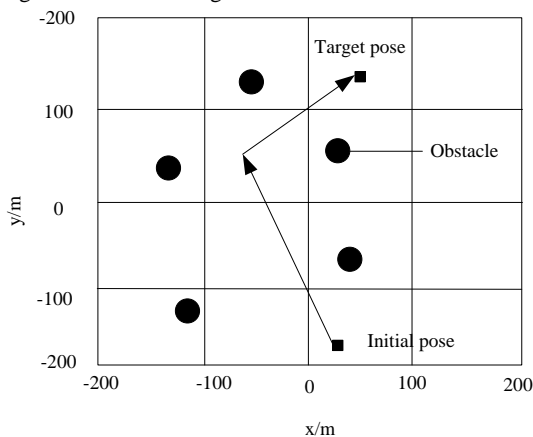
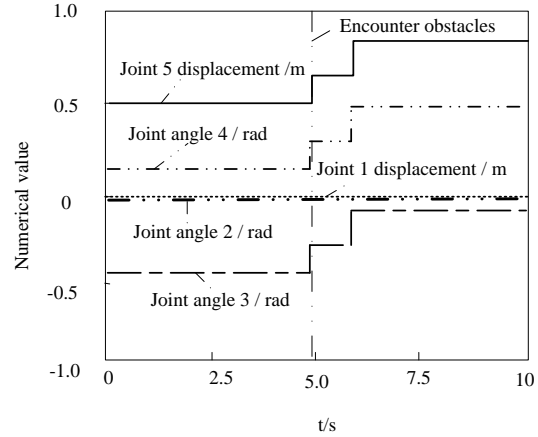


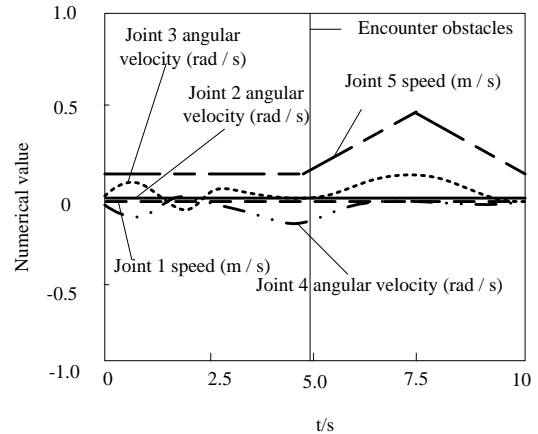
Figure 4. Obstacle avoidance effect of 6-DOF apple picking manipulator during picking task

As shown in Figure 4, the manipulator moves from the initial pose to the target pose, and there is no collision with the obstacles in the workspace in this process, and the obstacle avoidance effect passes the test.

During the obstacle avoidance movement of the manipulator, the variation curves of the motion angle and angular velocity parameters of each joint are shown in Figure 5.



(a) Movement change state of each joint angle



(b) Angular velocity motion change state of each joint

Fig 5. Motion parameters of manipulator joints

Because the joint 1 and rotating joint 2 of the 6-DOF apple picking manipulator are set on the motion carrier where the manipulator is located, the two joints did not act in the experiment, so the motion parameter curves of joints 1 and 2 coincide. It can be seen from the analysis of Figure 5 that the movement of joint 3, joint 4, joint 5 and joint 6 is stable. When approaching the obstacle each time, the angular velocity of the joint decreases. After completing obstacle avoidance, the speed increases rapidly, so as to shorten the time of the whole movement process. The control time of the whole obstacle avoidance process of the manipulator is less than 10s, the movement process of the manipulator is stable and the speed is continuous, which shows the effectiveness of this method.

Under the use of the method in this paper, the picking effect of 6-DOF apple picking manipulator is shown in Figure 6.

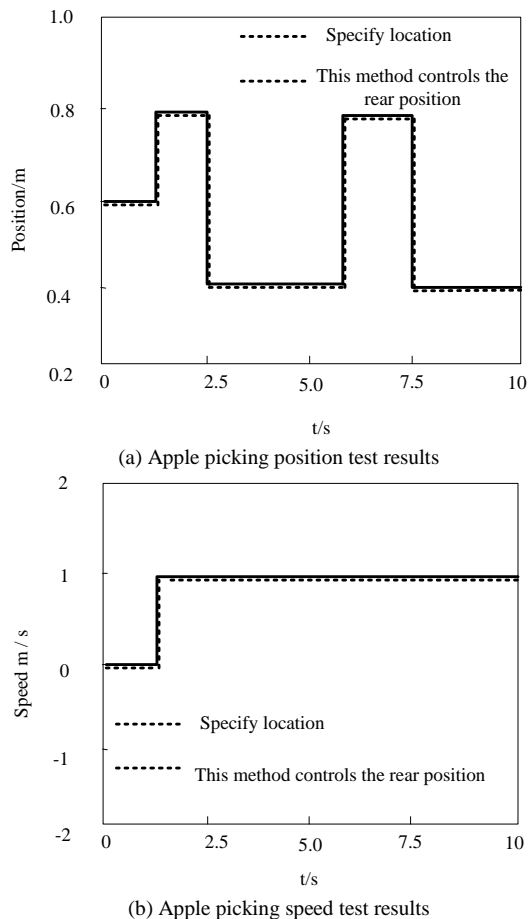


Figure 6. Picking effect of 6-DOF apple picking manipulator

As shown in Figure 6, under the control of the method in this paper, the 6-DOF apple picking manipulator can pick according to the set value of the apple picking target position, and the picking speed also meets the set value, indicating that this method is effective.

4. Discussion

The 6-DOF apple picking manipulator belongs to the research category of fruit tree picking robot. Combined with the research content of this paper, the existing problems of fruit tree picking robot are discussed, and the control suggestions are given.

4.1. Problems of fruit and vegetable picking robot

At present, the picking robot has achieved remarkable results in strawberries, cucumbers, oranges and other fruits and vegetables, but it has not really met the requirements of replacing human beings to complete the picking task. In the development process of the picking robot, there are still some key factors restricting its development. The author believes that the existing problems are as follows.

1. The identification and positioning efficiency of fruit and vegetable robot is not high

In order to complete the picking operation, the picking robot must first have the function of accurately identifying the types of fruits and vegetables, and be able to distinguish the differences between mature and immature fruits and vegetables. At present, gray threshold method, shape feature method and color chroma method are mainly

used. Gray threshold method and color chroma method judge fruits and vegetables based on spectral reflection characteristics. The image obtained in this way is easy to be affected by light and produce image noise, which affects the recognition accuracy; Shape feature method is a positioning method based on the condition that the shape of fruits and vegetables can form a complete boundary. In the process of operation, affected by the growth environment of fruits and vegetables, fruits and stems and leaves often coincide together. Therefore, it is very difficult to capture the complete boundary and cannot effectively distinguish the specific shape features of fruits and vegetables. It can be seen that the identification and positioning of fruits and vegetables by the picking robot is the key factor affecting the grasping efficiency.

2. The obstacle avoidance and picking rate of fruit and vegetable robot is not high

In the process of grasping fruits and vegetables, the picking robot is in an unstructured picking environment. The fruits not only overlap each other, but also are covered by branches and leaves. The degree of freedom and flexibility of the picking manipulator and manipulator are the key factors to determine whether they can successfully avoid obstacles. In addition, affected by the motion control program, image processing algorithm, mechanical structure and other aspects, the picking efficiency of most fruit and vegetable robots is low. For example, the picking robot can harvest 5 strawberries, 6 oranges, 3 cucumbers, 8 tomatoes and 6 apples in one minute. How to improve the working efficiency is one of the key problems in the development of picking robot.

3. The manufacturing and maintenance cost of fruit and vegetable robot is high

Compared with industrial robots, the working environment of fruit and vegetable robots is more complex and diverse. Affected by the weather and crop growth environment, its mechanical structure, control system and walking device are more complex, the manufacturing cost is higher, and the research and development cycle is also very long. As a kind of intelligent agricultural equipment with high precision, high intelligence and high technology, the technical level and cost of equipment maintenance are very expensive. How to reduce the development cycle and maintenance cost is one of the key problems in the development of picking robot.

4.2. Control countermeasures of fruit and vegetable picking robot

1. The motion control and path planning methods of the apple picking manipulator were studied to improve the obstacle avoidance ability and harvesting efficiency of the fruit and vegetable picking robot. The motion control and path planning of the picking manipulator should be determined according to the characteristics of the manipulator, the position of the apple and the picking requirements. Firstly, the kinematics and dynamics of the apple picking manipulator should be modeled. Through the forward motion model, the forward motion posture of the manipulator should be constructed, and the reverse motion posture of the manipulator should be constructed by the reverse motion model, so as to determine the manipulation scheme of the picking manipulator for apple under the six degrees of freedom. In the actual apple picking

process, environmental factors will have a great impact on the operation of the manipulator, so it is necessary to establish an obstacle model. According to the improved artificial potential field method, this paper proposes a bidirectional obstacle avoidance planning algorithm for the manipulator. The optimization of model parameters was verified by motion simulation analysis, and the path tracking control algorithm was studied to timely compensate the problem of target position offset in the process of robot motion, ensure the position tracking error in a reasonable range, and finally improve the success rate of obstacle avoidance and fruit harvest rate of fruit and vegetable picking robot.

2. Research and develop modular open control system to improve the expansion flexibility of fruit and vegetable picking robot and reduce the development cost. At present, the picking robot adopts special mechanical structure, control system and program language. This closed way is not conducive to the expansion and extension of robot function. Therefore, the functions of the picking robot can be subdivided, and the control device with module as the sub unit can be constructed according to the unified norms and standards, so as to adapt to different types of fruits and vegetables by replacing the mechanical parts or control devices with different degrees of freedom. It can be seen that this method with good universality and expansibility can not only quickly build a new robot picking control system, but also greatly reduce the development cost and maintenance cost, and greatly improve the flexibility and flexibility of the picking robot. The device is suitable for different types of fruits and vegetables. It can be seen that this method with good universality and expansibility can not only quickly build a new robot picking control system, but also greatly reduce the development cost and maintenance cost, and greatly improve the flexibility and flexibility of the picking robot.

The trajectory planning method of 6-DOF manipulator studied in this paper can be used as a reference for the research of fruit and vegetable picking robot, which has reference value.

5. Conclusions

Nowadays, as the agricultural production in the process of picking manipulator of the application of common equipment has been heavily promoted, but because in the present agricultural picking, picking manipulator's high cost, low accuracy picking, picking low efficiency, poor security were picking process problems, in this paper, the trajectory planning method of six degrees of freedom mechanical arm were studied. The mathematical model of the 6-DOF apple picking manipulator was established. Based on the forward and reverse motion models of the manipulator, the pose information and arm shape information of the manipulator were analyzed. On the basis of the improved artificial potential field method, the obstacle model is constructed, which is convenient for the manipulator to obtain the obstacle information more accurately in the process of picking and avoid the obstacle according to the planned path. Through the obstacle avoidance bidirectional planning algorithm, the control

and trajectory planning of the manipulator are completed in the process of apple picking. The application effect of the method proposed in this paper is tested by experiments, and the following conclusions are drawn:

1. Under the application of this method, in the process of the manipulator moving from the initial pose to the target pose, there is no collision with obstacles in the workspace, indicating that the manipulator has a good effect of obstacle avoidance under the method in this paper;
2. In the process of apple picking, the joint motion of the manipulator is stable. When the manipulator is close to the obstacle, the joint angular velocity will become smaller. After the obstacle avoidance is completed, the speed can be rapidly improved and the time consumed in the whole movement process of the manipulator is shortened. And the control time of the manipulator in the whole obstacle avoidance process is less than 10s, indicating that the manipulator motion process is stable and the speed is continuous, which proves that this method is effective;
3. Under the control of the method, the 6-DOF apple picking manipulator can accurately pick apples according to the set target position, and the picking speed also meets the set requirements, indicating that the method in this paper can accurately pick apples and meet the safety requirements.

Reference

- [1] C.Sun, L. Cao, "Research on trajectory tracking control of 7-DOF picking manipulator". Science Progress, Vol.104, No. 1, 2021, 467-475.
- [2] B. Li, S. Gu & Q. Chu, "Development of transplanting manipulator for hydroponic leafy vegetables". International Journal of Agricultural and Biological Engineering, Vol. 12, No. 6, 2019, 38-44.
- [3] D.J.Lee, G.P. Jung, "Snatcher: A Highly Mobile Chameleon-Inspired Shooting and Rapidly Retracting Manipulator". IEEE Robotics and Automation Letters, Vol. 5, No. 4, 2020, 6097-6104.
- [4] A.Yx, B. Xw & C. Ti, "Compensation of base disturbance using optimal trajectory planning of dual-manipulators in a space robot". Advances in Space Research, Vol. 63, No. 3, 2019, 1147-1160.
- [5] J.W. Guo, Y.B. Lv, H.Zhang, "Coordinated Gait Control of Snake Like Robot Based on Electromechanical Tracking". Jordan Journal of Mechanical and Industrial Engineering, Vol. 16, No. 1, 2022, 87-95.
- [6] Z.H. Meng, "Trajectory Tracking Control Algorithm of Six Degrees of Freedom Industrial Robot". Jordan Journal of Mechanical and Industrial Engineering, Vol. 16, No. 1, 2022, 97-104.
- [7] L.Biagiotti, L. Moriello & C. Melchiorri, "Improving the Accuracy of Industrial Robots via Iterative Reference Trajectory Modification". IEEE Transactions on Control Systems Technology, Vol. 28, No. 3, 2020, 831-843.
- [8] Y.G. Cui, "Parallel Computing-Based Dynamics Model for Tracking Moving Targets". Jordan Journal of Mechanical and Industrial Engineering, Vol. 16, No. 1, 2021, 79-86.
- [9] F.Li, H. Peng & H. Yang, "A symplectic kinodynamic planning method for cable-driven tensegrity manipulators in a dynamic environment". Nonlinear Dynamics, Vol. 106, No. 4, 2021, 2919-2941.
- [10] C.E.Zheng, P. Gao, H. Gan, et al. "Trajectory Planning Method for Apple Picking Manipulator Based on Stepwise

- Migration Strategy". Transactions of the Chinese Society for Agricultural Machinery, Vol. 51, No. 12, 2020, 15-23.
- [11] X.F.Liu, S. Wang, W.H. Sha, "Design of stretchable, constant torque, self-transporting apple picking manipulator". South Agricultural Machinery, Vol. 50, No. 18, 2019, 32-59.
- [12] Z.Y.Fan, L.J. Li, Y.H. Li, et al. "Trajectory Planning of Camellia Fruit Picking Manipulator Based on Improved Grey Wolf Optimization". Machine Design & Research, Vol. 38, No. 1, 2022, 195-201.
- [13] G.B.Si, C.X. Wang, "Path Planning of Agricultural Picking Manipulator —Based on Cloud Platform and Q-learning Algorithm". Journal of Agricultural Mechanization Research, Vol. 43, No. 10, 2021, 23-27.
- [14] W.Jiang, G. Wu & L. Yu, "Manipulator multi-objective motion optimization control for high voltage power cable mobile operation robot". Journal of ambient intelligence and humanized computing, Vol. 10, No. 3, 2019, 893-905.
- [15] T.T. Yoshiaki, "Joint Trajectory Planning Based on Minimum Euclidean Distance of Joint Angles of a Seven-Degrees-of-Freedom Manipulator for a Sequential Reaching Task". Journal of Advanced Computational Intelligence and Intelligent Informatics, Vol. 23, No. 6, 2019, 997-1003.
- [16] A.A.Zelenskii, V.A. Frants & E.A. Semenishchev, "Trajectory-Planning Algorithm Based on Engineering Vision in Manipulator Management". Russian Engineering Research, Vol. 40, No. 1, 2020, 1-5.
- [17] C. Kacprzak, G. Pajk, "Trajectory Planning of the Humanoid Manipulator". International Journal of Applied Mechanics and Engineering, Vol. 24, No. 3, 2019, 591-602.
- [18] L.Zhang, Y. Wang & X. Zhao, "Time-optimal trajectory planning of serial manipulator based on adaptive cuckoo search algorithm". Journal of Mechanical Science and Technology, Vol. 35, No. 7, 2021, 3171-3181.
- [19] A. Gonaves, E. Guerrero-pea & A. AFR, "Evolutionary Trajectory Planning with Obstacles for a Mobile Manipulator". IFAC-PapersOnLine, Vol. 53, No. 2, 2020, 7921-7926.
- [20] C.Luo, Y. He & S. Abubakar, "Solving Inverse Kinematics of the Shotcrete Manipulator Based on the Plane Two-Link Model and Trajectory Planning". Journal of Robotics, No. 16, 2020, 1-12.
- [21] Z.Huang, X. Lai & Y. Wang, "Position control for planar 3R underactuated manipulator with second-order non-holonomic constraints". Dongnan Daxue Xuebao (Ziran Kexue Ban)/Journal of Southeast University (Natural Science Edition), Vol. 49, No. 2, 2019, 245-250.
- [22] S.Yi, K. Watanabe & I. Nagai, "Anti-disturbance control of a quadrotor manipulator with tiltable rotors based on integral sliding mode control". Artificial Life and Robotics, Vol. 26, No. 4, 2021, 513-522.
- [23] J. Shi, Y. Mao & P. Li, "Hybrid Mutation Fruit Fly Optimization Algorithm for Solving the Inverse Kinematics of a Redundant Robot Manipulator". Mathematical Problems in Engineering, No. 1, 2020, 1-13.
- [24] Y.Qian, J. Yuan & W. Wan, "Improved Trajectory Planning Method for Space Robot-System with Collision Prediction". Journal of Intelligent & Robotic Systems, Vol. 99, No. 2, 2020, 289-302.
- [25] J.Batista, D. Souza & J. Silva, "Trajectory Planning Using Artificial Potential Fields with Metaheuristics". IEEE Latin America Transactions, Vol. 18, No. 5, 2020, 914-922.
- [26] M. Badrikouhi, M. Bamdad, "Novel Manipulability for Parallel Mechanisms with Prismatic-Revolute Actuators, GA-DP Trajectory Planning Application". Mechanics of Solids, Vol. 56, No. 2, 2021, 278-291.
- [27] H.Y. You, S. He & H.W. Liu, "The Mechanical Arm of 9-Dof Path Planning Based on bi RRT Algorithm". Computer Simulation, Vol. 36, No.7, 2019, 308-313.

Experimental Research and Mathematical Modeling of Parameters Affecting Cutting Tool Wear in Turning Process of Inconel 625

Fitim Zeqiri ^a, Burim Fejzaj ^{b*}

^a Department of Mechanical Engineering, University "Isa Boletini" Mitrovica, Kosovo.

^b Department of Mechanical Engineering, University of Montenegro, Podgorica.

Received 13 Jul 2022

Accepted 20 Sep 2022

Abstract

This study aims to present the effects of cutting parameters on cutting tool wear during turning process of material Inconel 625 using Taguchi experimental design. Taguchi L9 orthogonal array was used to investigate the effects of machining parameters. Optimal cutting conditions are determined using the signal/noise (S/N) ratio which is calculated by average cutting tool wear. Using results of analysis, effects of parameters on both average of cutting tool wear calculated on Minitab 18 using ANOVA method. It was clear from the ANOVA that the regression model is capable to predict the tool wear with high accuracy. Numerical simulation of orthogonal cutting operation is presented using FEM modeling with Deform 3D v.11.0. The results of tool wear during the turning of Inconel 625 material are obtained by changing the cutting regimes (v, f, d), without cooling means. After using the three cutting regimes levels, we found that the optimal parameters go to the numerical level so that the cutting speed remains the same used in the experiment (v=65m/min), while the other optimal parameters come out the depth of cut (d=0.733mm) and feed (f=0.06mm/rev) so it can be seen in the two forms of research, the theoretical one with FEM and the experimental one. During the research, numerical methods and FEM simulations analysis were used for turning process. Confirmation test of results showed that the Taguchi method was very successful in the optimization of machining parameters for minimum cutting tool wear during CNC turning process.

© 2022 Jordan Journal of Mechanical and Industrial Engineering. All rights reserved

Keywords: Inconel 625, Taguchi design, Deform 3D, tool wear, FEM modeling.

1. Introduction

The machining industry always intends to be perfect. Cutting process also requires a high degree of machined surfaces. As the quality of machined materials is growing, there is a growing need for cutting tools to be of high quality. One of the factors that are affecting the processing accuracy is the cutting tool wear. The use of different methods in this case Taguchi and ANOVA have greatly facilitated the research of cutting tool wear. The turning of Inconel 625 and tracking tool wear is the primary task in this paper. Many authors have dealt with tool wear using different methods and achieving results in their own forms [1 – 3].

The Finite element simulation and experimental validation of tool wear effect on cutting forces in turning operation was investigated by authors, which obtain results that the finite element results correlates with the experimental results for no wear condition with less than 10% error. Tool wear is mostly affected by different parameters like feed rate, cutting speed, and depth of cut [4 – 6].

Taguchi method is a powerful tool for the design of high quality systems. It provides simple, efficient and

systematic approach to optimize designs for performance, quality and cost. Taguchi method is efficient method for designing process that operates consistently and optimally over a variety of conditions [7 – 10]. One of the most important and effective factors of the manufacturing standards is tool wear [11, 12].

With Wear estimation of ceramic and coated carbide tools in turning of Inconel 625 3D FE analysis deal authors, which develop an accurate 3D finite element model to predict the tool wear of PVD-TiAlN coated carbide and ceramic inserts in turning of Inconel 625 [13 – 15].

The present work will be helpful to predict the influence of cutting speed, feed, depth of cutting, amplitude and temperature in used tool (CNMG 120408 NN) without cooling means [14 – 22].

Tool wear design of experiments (DOE) and statistical techniques Design of Experiments (DOE) method is regarded by several researchers, in the reported literature, as a inconvenient method for monitoring of influence of different parameters on tool wear during turning process [23 – 25].

* Corresponding author e-mail: burimfejzaj@hotmail.com.

2. Design of The Experiment

Taguchi's technique makes use of a special design of orthogonal array (OA) to examine the quality characteristics through a minimum number of experiments. The experimental results based on the orthogonal array are then transformed into S/N ratios to evaluate the performance characteristics. Taguchi's Design of experiments is used to design the orthogonal array for three parameters varied through three levels. The control parameters and their levels chosen are shown in Table 2.1.

Table 2.1. Experimental results using L_9 orthogonal array.

Exp.	Process parameters and its level			Experimental results		
	Speed	Feed	Depth of cutting	T °C	Amplitude	VB [μm]
1	50	0.04	0.4	329.05	0.493	215.33
2	50	0.06	0.7	361.21	0.400	232.21
3	50	0.08	1.0	374.29	0.108	348.24
4	65	0.04	0.7	333.22	0.311	253.22
5	65	0.06	1.0	286.44	0.428	356.13
6	65	0.08	0.4	299.44	0.462	253.34
7	80	0.04	1.0	443.66	0.432	361.36
8	80	0.06	0.4	333.75	0.522	265.57
9	80	0.08	1.0	372.71	0.654	371.02

3. Measurement of Tool Wear, Equipment and Measuring Process

Measurement of tool wear was conducted with equipment TOOL MASTER 10 which is digital apparatus and allows displacement according to three axes. Cutting blade was cleaned from micro particles by cloth with alcohol after each experiment and then the measurements were realized. The experiment was conducted with the clutch with new cutting edge without coolant tool. Circular cutting length of 0.5 km and increased cutting regimes until gaining an adopted wear value as the basic criterion $VB=221\mu\text{m}$ was taken for determining the wear.

4. Analysis of Variance (Anova)

ANOVA table is generally prepared to find the significant input parameters which will mostly affect the output responses. Analysis of variance table was prepared for each output response with a significant level of $\alpha = 0.05$ and confidence level of 95%. The sources present in the ANOVA table having P-Value less than 0.05 had been treated as the significant parameter for the respective output response. The following table shows the analysis with ANOVA, for cutting tool wear.

ANOVA results for means of tool wear are given in Table 4.1. It can be observed that the percentage contribution on tool wear was depth of cutting (59.49) followed by cutting speed (21.70%), feed (10.81%), temperature (0.08%), and amplitude (0.21%). From the present analysis, it is also observed that depth is the most influencing parameter in tool wear. Table 2.1 and 4.1, shows the influence of cutting speed, feed, depth of cutting; temperature and amplitude which are illustrated in Figure 4.1, 4.2 and 4.3.



Figure 3.1. Equipment for measurement wears TOOL MASTER 10.

Table 4.1. Analysis of Variance for cutting tool wear VB.

Source	DF	Seq SS	Adj SS	Adj MS	F-Value	P-Value	Contribution
Regression	5	28968.7	28968.7	5793.7	7.18	0.068	92.28%
v	1	6812.1	2528.7	2528.7	3.13	0.175	21.70%
f	1	3393.4	1089.7	1089.7	1.35	0.329	10.81%
d	1	18673.2	12422.3	12422.3	15.39	0.029	59.49%
t	1	23.8	35.6	35.6	0.04	0.847	0.08%
a	1	66.2	66.2	66.2	0.08	0.793	0.21%
Error	3	2422.3	2422.3	807.4			7.72%
Total	8	31391.0					100.00%

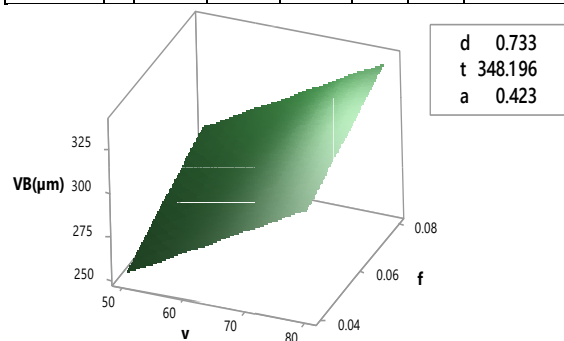


Figure 4.1. Effect of *speed cutting* and *feed* on the main V_B .

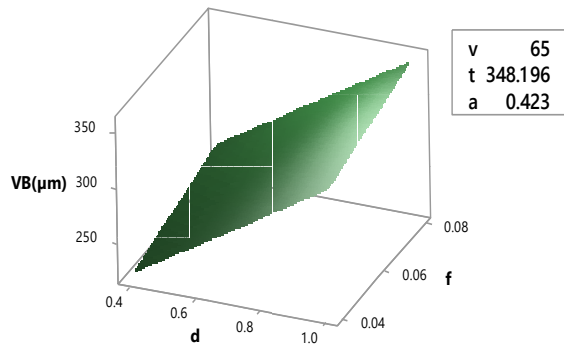


Figure 4.2. Effect of depth cutting and feed on the main VB.

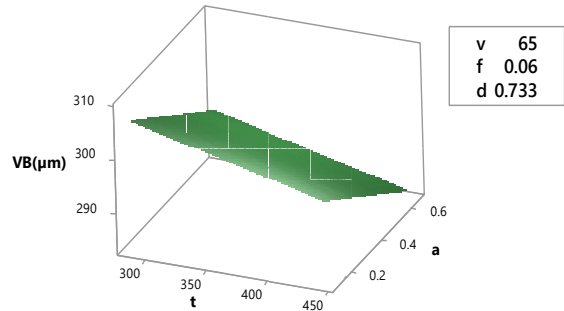


Figure 4.3. Effect of temperature and vibration on the main VB.

Table 4.2. Residual output and probability output.

Observation	Predicted VB	Residuals	Standard Residuals	Percentile	VB
1	192.68	22.64	1.30	5.555	215.33
2	260.86	-28.65	-1.64	16.666	232.21
3	335.32	12.91	0.74	27.777	253.22
4	278.70	-25.48	-1.46	38.888	253.34
5	345.79	10.33	0.59	50	265.57
6	252.00	1.33	0.07	61.111	348.24
7	350.90	10.45	0.60	72.222	356.13
8	262.48	3.08	0.17	83.333	361.36
9	377.65	-6.63	-0.38	94.444	371.02

Figure 4.4 shows the predicted values for calculated tool wear using: linear equation along with the experimental values. It can be observed that the predicted values are in good agreement with experimental results with average error of less than 6%.

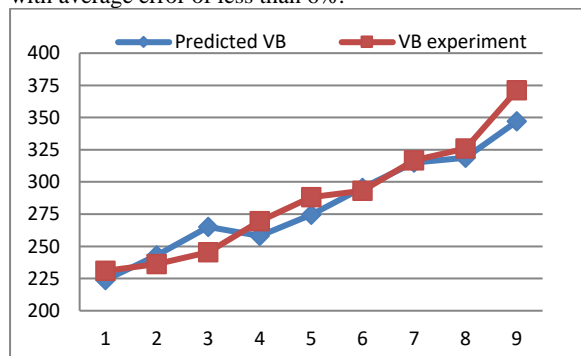


Figure 4.4. Comparison between experimental results and predicted values of cutting tool wear.

5. Fea and Simulation of Tool Wear with Deform 3d

Finite element method has been proved to be an effective technique for analysing chip formation process

and predicting machining performance characteristics such as temperatures, forces, stresses etc. (Fagan, 1992; Lorentzon and Jarvstrat, 2008; Lorentzon et al., 2009; Yue et al., 2009;). In this work, finite element method is used to simulate turning of Inconel 625 using PVD coated tungsten carbide tool. Johnson and Cook (1993) developed a material model based on torsion and dynamic Hopkinson bar test over a wide range of strain rates and temperatures. This constitutive equation was established as follows:

$$\bar{\sigma} = \left[A + B \cdot \bar{\epsilon}^n \right] \cdot \left[1 + C \cdot \ln \left(\frac{\dot{\epsilon}}{\dot{\epsilon}_0} \right) \right] \cdot \left[1 - \left(\frac{T - T_{room}}{T_{melt} - T_{room}} \right)^m \right] \quad (5.1)$$

Johnson-cook model is suitable for material modeling because of high strain, strain rate, strain hardening and non-linear material properties that are involved in turning process (Uhlmann et al., 2007; Ezilarasan et al., 2014). The material model given in 6.3 expression. It is defined in DEFORM 3D material library. The constant of Johnson-cook model is shown in table 5.1.

Table 5.1. Johnson-Cook model constants for Inconel 625.

A (MPa)	B (MPa)	n	C	m	$\dot{\epsilon}_0$ (1/s)	T_{room} ($^{\circ}C$)	T_{melt} ($^{\circ}C$)
559	22.01	0.8	0.00021	1.146	0.0016	20	1297

Work piece geometry and mesh generation In the *Workpiece Shape* menu, specify the work piece details. Depending upon the work piece diameter user can specify either a flat model or a curved model. The template will prompt for the related data, and will generate the work piece setup in the display area. For the current lab we use a 'simplified model' with 5mm length.

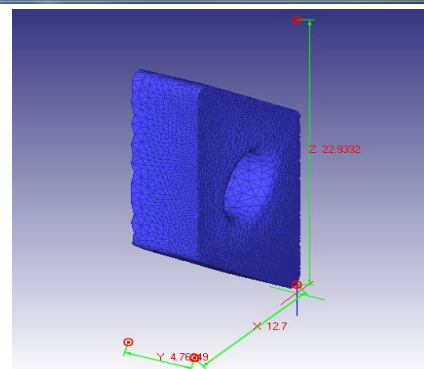
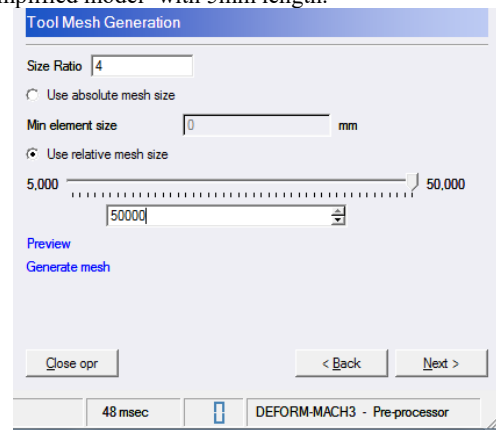


Figure 5.1. Modelling of CNMG 120408 NN tool insert.

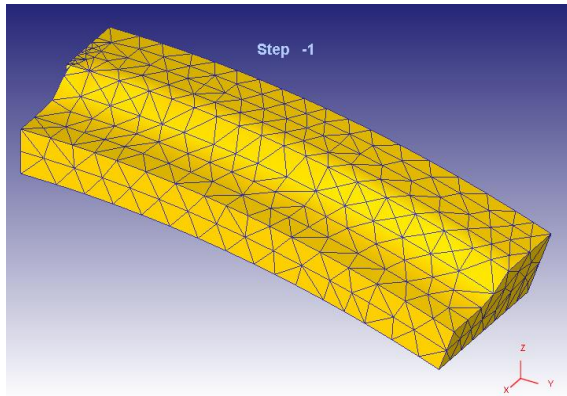


Figure 5.2. Modelling of Inconel 625 work piece.

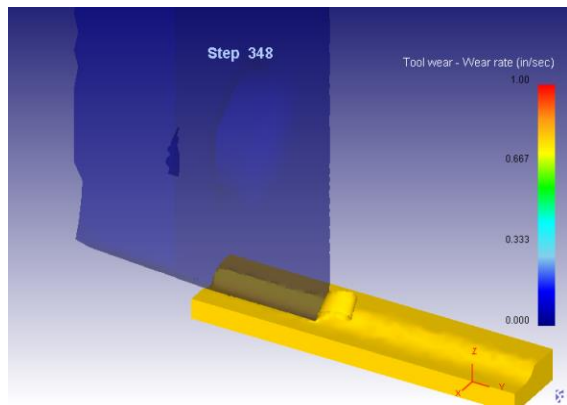


Figure 5.3. Simulation result of tool wear.

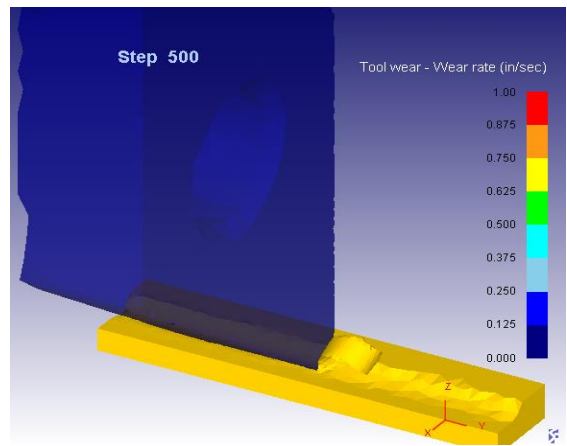


Figure 5.4. Simulation result of tool wear rate (solid).

Table 5.2. Analytical results using L_9 orthogonal array.

Exp.	Process parameters and its level			Analysing data using Deform 3d		
	Speed	Feed	Depth of cutting	T (°C)	Amplitude	VB _{FEA} [µm]
1	50	0.04	0.4	398.15	0.59653	232.863
2	50	0.06	0.7	437.06	0.484	251.431
3	50	0.08	1.0	452.89	0.13068	380.064
4	65	0.04	0.7	403.2	0.37631	278.542
5	65	0.06	1.0	346.59	0.51788	387.743
6	65	0.08	0.4	362.32	0.55902	272.674
7	80	0.04	1.0	536.83	0.52272	391.496
8	80	0.06	0.4	403.84	0.63162	291.127
9	80	0.08	1.0	450.98	0.79134	403.122

ANOVA results for means of tool wear are given in Table 5.3. It can be observed that the percentage contribution on tool wear was depth of cutting (59.80%) followed by cutting speed (21.90%), feed (10.46%), temperature (0.13%), and amplitude (0.38%). From the present analysis, it is also observed that depth of cutting is the most influencing parameter in tool wear.

Table 5.3. Analysis of Variance for cutting tool wear VB_{FEA}.

Source	DF	Seq SS	Adj SS	Adj MS	F-Value	P-Value	Contribution
Regression	5	34557.6	34557.6	6911.5	7.57	0.063	92.66%
v	1	8168.7	3282.3	3282.3	3.60	0.154	21.90%
f	1	3899.4	1191.9	1191.9	1.31	0.336	10.46%
d	1	22301.9	14779.2	14779.2	16.19	0.028	59.80
t	1	46.7	70.8	70.8	0.08	0.799	0.13%
a	1	140.8	140.8	140.8	0.15	0.721	0.38%
Error	3	2737.8	2737.8	912.6			7.34%
Total	8	37295.3					100.00%

From the table 5.2 and 5.3, can be seen the influence of cutting speed, feed, depth of cutting, temperature and amplitude that are illustrated in Figure 5.6, 5.7 and 5.8.

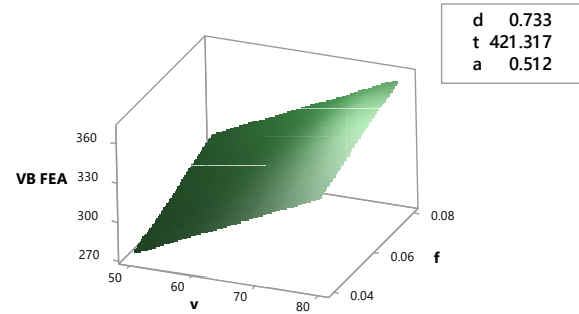


Figure 5.6. Effect of speed cutting and feed on the main VB_{FEA}.

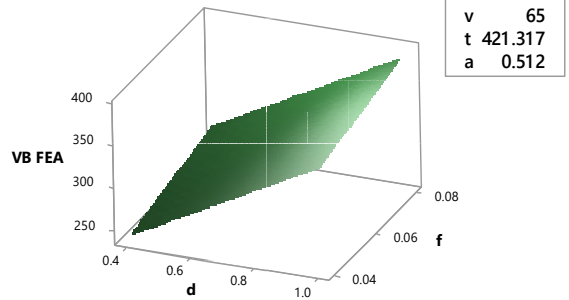


Figure 5.7. Effect of depth cutting and feed on the main VB_{FEA}.

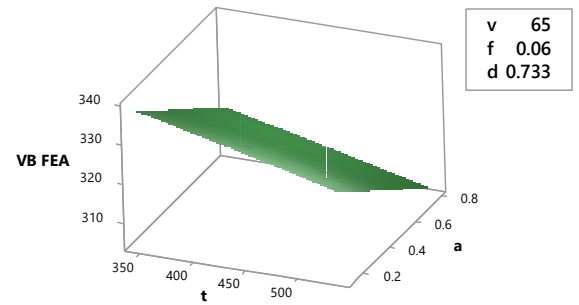


Figure 5.8. Effect of temperature and vibration on the main VB_{FEA}.

Table 5.4. Residual output and probability output.

Observation	Predicted VB	Residuals	Standard Residuals	Percentile	VB _{FEA}
1	229.179	1.754	0.155	5.556	232.863
2	228.469	2.002	0.177	16.667	251.431
3	234.018	5.476	0.485	27.778	380.064
4	279.604	6.849	0.606	38.889	278.542
5	251.037	-2.907	-0.257	50.000	387.743
6	275.673	-22.406	-1.983	61.111	272.674
7	289.854	-13.174	-1.166	72.222	391.496
8	335.907	10.048	0.889	83.333	291.127
9	323.862	12.358	1.094	94.444	403.122

Figure 5.9 shows the predicted values for tool wear calculated using: linear equation along with the experimental values. It can be observed that the predicted values are in good agreement with experimental results with average error of less than 7.8%.

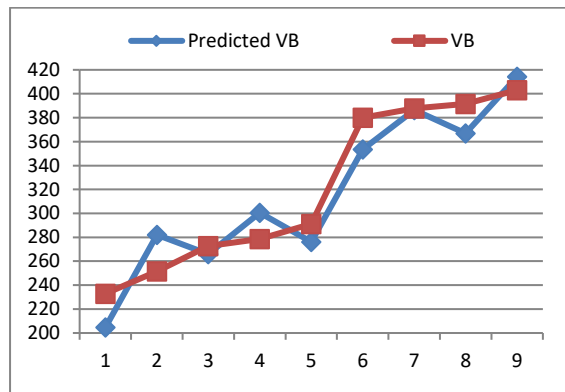


Figure 5.9. Comparison between analysis results and predicted values for cutting tool wear.

5.1. Regression Analysis Equations

Regression analysis is a statistical process used to estimate the relationships between variables. This analysis is focused on the relationship between a dependent variable and one or more independent variables; it includes many techniques for modelling and analysing various variables. Regression analysis was used to derive the predicted equations of the cutting tool forces and the roundness error in this study. In Minitab 17, equations for Cutting Tool Wear calculation have been formed by ANOVA analysis. Regression analysis equations for cutting tool wear are as follow:

$$VB = 30.1 + 1.88 \cdot v + 715 \cdot f + 177.5 \cdot d - 0.056 \cdot t - 26.1 \cdot a \quad (5.2)$$

Model Summary

S	R-sq	R-sq(adj)	R-sq(pred)
28.4153	92.28%	79.42%	14.45%

$$VB_{FEA} = 38 + 2.15 \cdot v + 748 \cdot f + 193.6 \cdot d - 0.065 \cdot t - 31.5 \cdot a \quad (5.3)$$

Model Summary

S	R-sq	R-sq(adj)	R-sq(pred)
30.2090	92.66%	80.42%	17.48%

5.2. Normal Probability Charts

The normal probability table was obtained to check the validity or accuracy of the above statistical model. In this way, the model will not be inadequate and unusual structure, and in the future better results will be estimated. The charts given Figure 5.10 and Figure 5.11 clearly show the conformity of our statistical model.

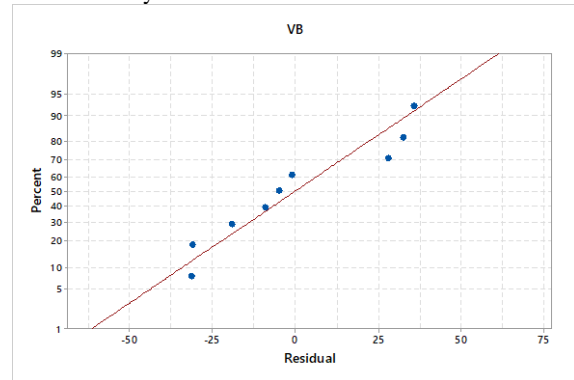


Figure 5.10. Normal probability charts for cutting tool wear V_B.

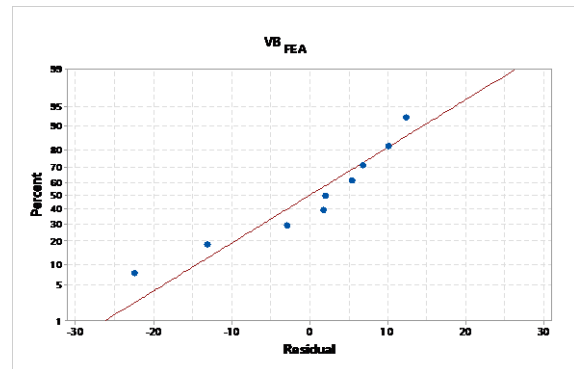


Figure 5.11. Normal probability charts for cutting tool wear VB_{FEA}.

6. CONCLUSIONS

Turning of the Inconel 625 is done with cutting tool CNMG 120408NN. Cutting tool wear is one of the most negative phenomenon in the cutting process, developed in difficult conditions, and differs from the various cutting parameters and the production technology. As we can see from obtained mathematical models presented in expression (5.2) and (5.3) and form the calculation realised with Minitab 2017 (DOE, Taguchi method, ANOVA), where as a point here, we can have discussions of the comparison and reliability of the results. The coefficients of tool wear (R-sq) achieved using the linear regression for VB and VB (FEA) were obtained to be 92.28% and 92.66%. From the calculated result presented above and figure, 4.1 and 5.6, it can be seen that with the increase of the cutting speed, the cutting tool wear increase. Results gained and illustrated in figure (4.2 and 5.7) show that with the increase of the cutting depth, the amount of the cutting tool wear also increases, and that the depth of cut has a greater impact in tool wear. Looking at figures (4.1, and 5.6), it can be seen that cutting feed has a lower impact in tool wear related to the cutting speed and the depth of cutting. Parameters, such as temperature and vibrations have a smaller impact on the consumption of the tool.

7. Acknowledgement

The authors express their unreserved thanks to the supporters of this research the University "Isa Boletini", Faculty of Mechanical and Computer Engineering - Kosovo and University of Montenegro, Faculty of Mechanical engineering - Montenegro.

References

- [1] Muammer N, Hasan G, Ihsan T, Gokhan S, The experimental investigation of the effects of uncoated, PVD- and CVD-coated cemented carbide inserts and cutting parameters on surface roughness in CNC turning and its prediction using artificial neural networks, *Robotics and CIM* 25 (2009) 211–223.
- [2] Bulent K, Cuneyt O, Huseyin M. E, Force-torque based on-line tool wear estimation system for CNC milling of Inconel 718 using neural networks, *advances in Engineering Software* 42 (2011) 76–84.
- [3] Murat S, Abdulkadir G, Taguchi design and response surface methodology based analysis of machining parameters in CNC turning under MQL, *Journal of Cleaner Production* 65 (2014) 604e616.
- [4] C. J. Rao, D. Nageswara R, P. Srihari, Influence of cutting parameters on cutting force and surface finish in turning operation, *Procedia Engineering* 64 (2013) 1405 – 1415.
- [5] Hemant J, Jaya T, Ravindra B, Sanjay J, Avinash K, Optimization and evaluation of machining parameters for turning operation of Inconel-625, *Materials Today: Proceedings* 2-2015, 2306 – 2313.
- [6] R. Ramanujam, K. Venkatesan, Vimal S, Nilendukar C, Vikash C, Influence of cutting parameters on machinability of inconel 718 alloy with coated carbide insert-a taguchi based fuzzy logic approach (tfla), *ARNP Journal of Engineering and Applied Sciences*.
- [7] Duong Xuan-T, Tran Minh-D, Effect of cutting condition on tool wear and surface roughness during machining of inconel 718, *International Journal of Advanced Engineering Technology* E-ISSN 0976-3945.
- [8] Dong-Hyeon Kim, Choon-Man Lee, A study of cutting force and preheating-temperature prediction for laser-assisted milling of Inconel 718 and AISI 1045 steel, *International Journal of Heat and Mass Transfer* 71 (2014) 264–274.
- [9] Krupal P, R. D. Palhade, Multi-objective Optimization of CNC Turning Process Parameters for High Speed Steel (M2) Using Taguchi and ANOVA Method, *International Journal of Hybrid Information Technology*, Vol.8, No.4 (2015), pp.67-80
- [10] Mohd. Suhail A, Deepak Sh, Sagar N, Study of Cutting Forces and Surface Roughness in Turning of Bronze Filled Polytetrafluoroethylene, *IJAME*. ISSN 2250-3234, Number 2 (2014).
- [11] Kompan Ch, Somkiat J, Optimization Parameters of tool life Model Using the Taguchi Approach and Response Surface Methodology, *IJCSI International Journal of Computer Science Issues*, Vol. 9, Issue 1, No 3, January 2012.
- [12] Dinesh K, Vishal P, Jasveer S, M.K.Gour, Taguchi Method and ANOVA: An Approach for Selection of Process Parameters of EDM of EN-353 Steel, *International Journal of Emerging Technology and Advanced Engineering*, Volume 4, Issue 6, June 2014.
- [13] S.A. Khan, S.L. Soo, D.K. Aspinwall, Tool wear/life evaluation when finish turning Inconel 718 using PCBN tooling, *5th CIRP Conference on High Performance Cutting* 2012.
- [14] Zeqiri F, M Alkan, B Kaya, S Toros. "Experimental Research and Mathematical Modeling of Parameters Effecting on Cutting Force and Surface Roughness in CNC Turning Process", *IOP Conference Series: Materials Science and Engineering*, 2018.
- [15] Yong Liu, Lin He, Sen Yuan, "Wear Properties of Aluminum Alloy 211z.1 Drilling Tool", *Jordan Journal of Mechanical and Industrial Engineering*, Volume 15, Number 1, March. 2021.
- [16] M. N. Abijitha, Adithya Rajeev Naira, M. Aadharsha, R. Vaira Vignesh, R. Padmanaban, M. Arivarasub, "Investigations on the Mechanical, Wear and Corrosion Properties of Cold Metal Transfer Welded and Friction Stir Welded Aluminium Alloy AA2219", *Jordan Journal of Mechanical and Industrial Engineering*, Volume 12, Number 4, December. 2018.
- [17] V. Ramakoteswara Rao, N.Ramanaiah b, M.M.M.Sarcar, "Optimization of volumetric wear rate of aa7075-tic metal matrix composite by using taguchi technique", *Jordan Journal of Mechanical and Industrial Engineering*, Volume 10 Number 3, September.2016
- [18] Behnam Davoodi, Behzad Eskandari. "Tool wear mechanisms and multi-response optimization of tool life and volume of material removed in turning of N-155 iron–nickel-base superalloy using RSM", *Measurement*, 2015.
- [19] Lorentzon, J., Jarvstrat, N., "Modelling tool wear in cemented-carbide machining alloy 718", *Int. J. Machine Tools and Manuf.*, 48 ,2008.
- [20] Fagan, M.J. (1992) *Finite Element Analysis: Theory and Practice*. Longman, New York, ISBN 0-582-02247-9.
- [21] Lorentzon, J. and Jarvstrat, N. (2008) Modelling tool wear in cemented-carbide machining alloy 718. *International Journal of Machine Tools and Manufacture*. 48 (10) p. 1072-1080.
- [22] Lorentzon, J., Jarvstrat, N. and Josefson, B. L. (2009) Modelling chip formation of alloy 718. *Journal of Materials Processing Technology*. 209 (10) p. 4645-4653.
- [23] Botsaris, Pantelis & Tsanakas, Ioannis (John) & Vogiatzi, Maria. (2011). *Tool Wear Monitoring by Design of Experiments (DOE) for Drilling*.
- [24] Zeqiri Fitim, *Experimental Research and Mathematical Modelling of Parameters Affecting Cutting Force, Cutting Tool Wear and Surface Roughness in Turning Process of Inconel 625*, Doktora thesis, Nigde OmerHalisdemir University 2018.
- [25] B. D. Bachchhav, K. N. Hendre, "Wear Performance of Asbestos-Free Brake Pad Materials" *Jordan Journal of Mechanical and Industrial Engineering*, Volume 16, Number 4, September. 2022.

An Optimization Approach for Predictive-Reactive Job Shop Scheduling of Reconfigurable Manufacturing Systems

A.A. Abdul Rahman^{a*}, O.J. Adeboye^a, J.Y. Tan^a, M.R. Salleh^a, M.A. A.Rahman^b

^aFaculty of Manufacturing Engineering, Universiti Teknikal Malaysia Melaka, Hang Tuah Jaya, 76100 Durian Tunggal, Melaka, Malaysia.

^bSchool of Mechanical and Aerospace Engineering, Queen's University Belfast, 123 Stranmillis Road, Ashby Building, BT9 5AH Belfast, United Kingdom

Received 1 Aug 2022

Accepted 31 Oct 2022

Abstract

The manufacturing industry is now moving forward rapidly towards reconfigurability and reliability to meet the hard-to-predict global business market, especially job-shop production. However, even if there is a properly planned schedule for production, and there is also a technique for scheduling in Reconfigurable Manufacturing System (RMS) but job-shop production will always come out with errors and disruption due to complex and uncertainty happening during the production process, hence fail to fulfil the due-date requirements. This study proposes a generic control strategy for piloting the implementation of a complex scheduling challenge in an RMS. This study is aimed to formulate an optimization-based algorithm with a simulation tool to reduce the throughput time of complex RMS, which can comply with complex product allocations and flexible routings of the system. The predictive-reactive strategy was investigated, in which Genetic Algorithm (GA) and dispatching rules were used for predictive scheduling and reactivity controls. The results showed that the proposed optimization-based algorithm had successfully reduced the throughput time of the system. In this case, the effectiveness and reliability of RMS are increased by combining the simulation with the optimization algorithm.

© 2022 Jordan Journal of Mechanical and Industrial Engineering. All rights reserved

Keywords: Scheduling; Simulation; Optimization; Genetic Algorithm; Predictive-Reactive; Reconfigurable Manufacturing System.

1. Introduction

The contemporary market continues to drive all kinds of companies and businesses, particularly manufacturers, towards flexibility. The control of today's production systems is becoming more complex due to an increasing number of product variants, short-time delivery requirements and non-standardized production processes. [1], [2], [3]. The complexity and limitations of production processes cause the products throughput time has greatly increased and unable to achieve due date requirements [4]. Manufacturing sectors are forced to handle demand fluctuations, rapidly adopt new products and order changes to make sure that the products are finished within a specific time [5].

Reconfigurable Manufacturing Systems (RMS) are primarily designed for rapid change in their structure [6], to quickly adjust their production capacity and functionality, within a part family, in response to market changes [7]. Cost, product quality, and market reactivity are the three primary aims of any production system. Designing manufacturing systems with upgradable capacity and adaptable functionality enables responsiveness. The benefits of RMS are highlighted when compared to Dedicated Manufacturing Systems (DMS) &

Flexible Manufacturing Systems (FMS) [8] from the standpoint of these objectives [6].

Reconfigurable Manufacturing Systems (RMS) has been quite common in recent research works, and most algorithms, dispatching rules, and strategies have already been developed. However, there is no clear framework or specific strategy developed to get these systems reliable and easy to control [9], [5]. The majority of studies in job scheduling concentrate on static scheduling constraints and do not consider dynamic factors [10]. Conventional approaches suggest a high approximation of real systems and are complex in the formulation; indeed, due to the complexity of a large number of variables and restrictions, most of the current algorithms do not give good results in a reasonable time [11], [12], [13], [14], [15].

The predictive-reactive approach can adapt to rapid changes in the shop floor's execution and provide a flexible schedule [16]. It is very difficult to perform optimization processes analytically during such complicated processes, hence simulation-based optimization is useful [17]. On the other hand, scheduling and controlling with simulation-based optimization can increase the performance and efficiency of the manufacturing systems, and provide an easy and fast evaluation of new layouts and schedules with direct production control [18], [19], [20], [21].

* Corresponding author e-mail: azrulazwan@utem.edu.my.

Due to dynamic job shop scheduling problems being Non-deterministic Polynomial-time – hard (NP-hard) combinatorial optimization problems, heuristic methods are useful for solving these types of problems [10]. Hence, this research focused on modelling the simulation model for RMS that can provide versatility in system layout and product mix with flexible routing and production sequence. The optimization framework was developed based on the model schedule [22], [23]. In this research, the combination of simulation and optimization-based algorithms for scheduling the RMS under various optimization restrictions was studied. For the predictive part, the feasible schedule for the RMS flow shop was predicted and decided. Rule-based simulation and optimization are then implemented into the schedule: first, a rough schedule was determined using an optimization algorithm, and then rule-based simulation systems were used to refine the schedule to obtain the most optimal results. For the reactive phase, the schedule obtained was adjusted and validated by the real-life system.

The application of GA with the dispatching rules can effectively optimize a manufacturing system providing engineers with the needed flexibility and control in the industry 4.0 context. The result obtained can be considered an important contribution to the research community in the field of industrial Engineering and smart manufacturing systems.

2. Literature review

Literature reviews for several papers regarding the different topics which are related to this study are summarized into two categories, which are state-of-the-art research and state-of-the-art implementation. All the summarized papers are research articles for the most recent five years from now (2016 – 2020) and are applied in the field of manufacturing.

Among all these papers related to the simulation field, including the objectives, application of the simulation process and research results, it can be summarized that majority of the simulation process is carried out for experiments purposes in a simple production system without considering the dynamic aspects of the manufacturing systems. However, time becoming one of the most common objectives in research and simulations also proved to obtain satisfactory results in those experiments.

Besides, some papers were studied on several methods to solve related manufacturing problems with evolutionary algorithms, together with the technique chosen, objectives functions, application, and future study. The majority of the study had shown that the genetic algorithm is the most popular technique used in the study, but not the basic Genetic Algorithm (GA). The GA is integrated with other heuristics or methods for experiment purposes. Moreover, the objectives functions are majority based on time, and suggestions for future studies are more to adapting the proposed algorithm or strategy in different situations or on different objectives. However, there is still a lack of research on the parameters for GA used in experiments on simulation optimization problems, and also a lack of studies focusing on RMS which included dynamic aspects and focus on complex routings and product mix.

Besides, according to Doh et al. [19], previous research on the topic of flexible job shop scheduling can be divided into two categories: single process plans with only alternative machines and multiple process plans with both alternative operations and machines. The reconfigurable job-shop scheduling problem consider in this study has a significant difference compared to previous studies in terms of the system's operational characteristics. Part of the difference includes, the number of transportation equipment is limited, the component input sequencing considered, and the material flow in the system is considered based on the flexible routing and the machines for a specific operation.

2.1. State-of-the-art Research

The papers that emphasized proposal, investigation, analysis and study of specific processes in manufacturing systems to establish facts and reach new conclusions are classified into this section. The papers are divided into different fields based on the research.

2.1.1. Simulation and Optimization

In the simulation research area, Mourtzis [24] had done a review focused on scholarly peer-reviewed journals that use modelling in manufacturing-related fields over 58 years. The exponential growth in publications on the subject reveals the ever-increasing importance of simulation in manufacturing. To estimate the total amount of relevant work, a search in the Scopus database using the keywords (a) simulation in manufacturing and (b) simulation in the design and operation of manufacturing systems was conducted to get the exact quantity of the total related work. The first search yielded more than 23,000 publications, while the second yielded more than 10,000. As a result, simulation is an ever-increasing part of manufacturing that can help with a variety of issues.

Figure 1 depicts the progression of research on this subject over time, with research findings classified from 1970 until today. More precisely, the results of this study show that there has been a significant rise in simulation-related publications over the last decade. Hence, there is still space for further research and development in this area.

In recent 5 years from 2016 - 2021, several publications mentioned and emphasized the simulation tool analysis. Siderska [25] analysed a single nail production line by introducing the construction of a simulation model for production and logistic processes conditions using Tecnomatix Plant Simulation and successfully proved that Tecnomatix Plant Simulation is an effective IT tool for increasing the efficiency of the existing system, optimizing resource consumption, limiting stocks and shortening the production time. Yann et al. [26] aimed to optimize the production control system in product customization manufacturing environments by generating and tested on four models with different generic routings with a sample of data from an industrial case using the software Work in Progress Simulation (WIPSIM). The author concluded that the proposed models generated worthwhile generic routings and help manufacturers to make decisions based on their product customization-specific context.

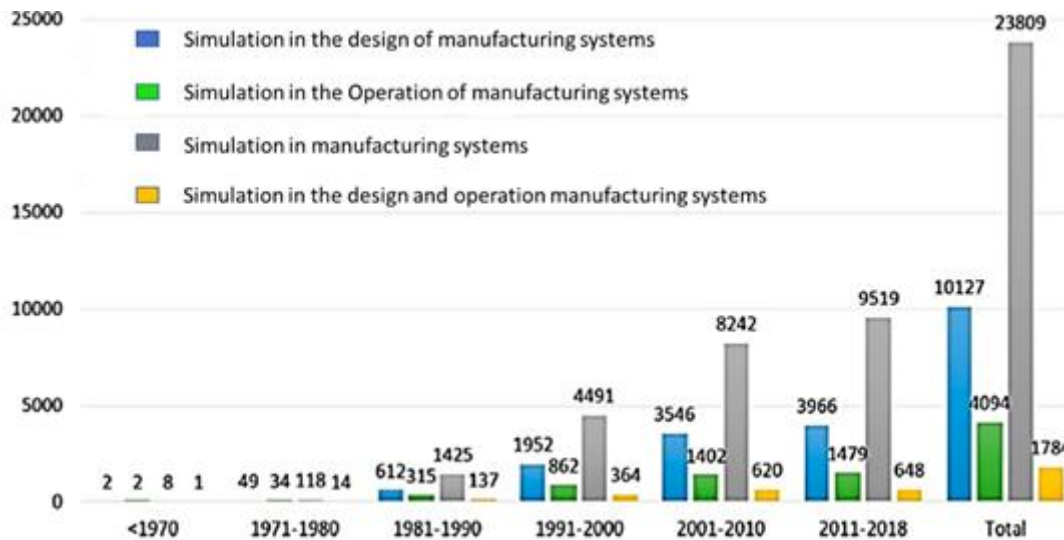


Figure 1. Number of publications based on Scopus database score [19].

For using simulation for solving scheduling problems, Doh et al. [19] researched simulating the scheduling problem in a flexible job shop. The flexible job shop is equipped with a conventional job shop and a reconfigurable manufacturing cell, with the objectives, fixed on minimizing makespan, mean flow time and mean tardiness, and the best rule combinations were identified for each of the three performance measures. Nasiri et al. [15] developed a simulation-based real-time scheduling composite dispatching rule approach in open job shop scheduling to minimize the mean waiting time of jobs, resulting in the optimal composite dispatching rule dominating the known dispatching rules. Xiong et al. [27] had done a simulation-based analysis of dispatching rules for scheduling in a dynamic job shop with batch release to minimize the total tardiness and the percentage of tardy jobs. The four new proposed dispatching rules effectively minimise the tardiness of jobs and the relative performance of dispatching rules can be affected by some model parameters. Lin et al. [28] carried out experiments and comparisons of statistical tests for several search methods for Automated Guided Vehicle (AGV) and machines in Flexible Manufacturing Systems (FMS) to evaluate the performance of scheduling decisions by proposing a simulation-based optimization to address the simultaneous scheduling of vehicles and machines. The proposed method successfully enhanced solution quality and search efficiency.

2.1.2. Algorithms and Heuristics

The research involving the development of algorithm or heuristics were popular in these 5 years from 2016 – 2021, and most of them used simulation to validate the algorithms. Few papers use the GA approach together with other techniques for investigation. Kundakci and Kulak [10] proposed a GA, a new Karmarkar-Karp (KK) heuristic and dispatching rules to approach solving job-shop scheduling problems with dynamic events to minimize the makespan. The authors wish to apply to different environments and use different performance measures for further study. Deng et al. [29] conducted experiments and compared the proposed Bee Evolutionary

Guiding Nondominated Sorting Genetic Algorithm II (BEG-NSGA-II) with benchmark problems to minimize the maximal completion time, the workload of the most loaded machine, and the total workload of all machines. However, this study did not concentrate on dynamic and real-time scheduling problems. Piroozfard et al. [30] had proposes an improved multi-objective evolutionary algorithm with GA for solving the newly extended bi-objective problem with considerations of environmental objectives, which is to minimize the total carbon footprint and total late work criterion. In future, the author would like to consider other scheduling criteria, objectives and heuristics approach. Lin et al. [28] proposed a Local search Genetic Algorithm Optimal computing budget allocation (L-GAOCBA) algorithm to address the simultaneous scheduling of vehicles and machines in FMS to evaluate the performance of scheduling decisions including stochastic elements, such as vehicle congestion, deadlock, and uncertain processing time, and decided to consider multi-objectives in future. Zan et al. [31] proposed a new Pareto-based GA for solving the multi-objective scheduling problem of deadlock-prone Automated Manufacturing Systems (AMSs) with limited resource capacity, aimed to optimize makespan, mean of earliness and tardiness, and mean completion time. Sivarat and Apichat [32] develop the simulation-optimization approach using artificial neural networks and GA to support observational data-driven manufacturing capacity planning for Small and Medium-sized Enterprises (SMEs) by reducing the amount of work involved in the exploitation of the data.

There were also some papers which used techniques other than GA, and the majority of the research was focused on time as an objective. Valledor et al. [33] proposed a rescheduling architecture for solving the problem based on a predictive-reactive strategy and a new method to calculate the reactive schedule in each rescheduling period to evaluate the dispatching rules for analysis of makespan, total weighted tardiness and stability. The result proved that the random rule provides better behaviour compared to other evaluated rules and a lower ratio of non-dominated solutions compared to Apparent Tardiness Cost (ATC) and First-in-first-out

(FIFO) rules, however, this approach could be tested in a dynamic system in future. Touzout and Benyoucef [34] aimed to reduce the total production cost, total completion time and maximum exploitation time by proposing and comparing three hybrid heuristics which are the Repetitive Single-Unit Process Plan (RSUPP) heuristic, Iterated Local Search on Single-Unit Process Plans heuristic (LSSUPP) and Archive-Based Iterated Local Search heuristic (ABILS) using the generated numerical results in RMS. The author would like to compare and analyse other local search-based metaheuristics with RMS. Zheng and Jin [35] proposed an improved Back and Forth Nudging algorithm (IBFN) to use in single-machine lot scheduling problems of indivisible jobs for minimizing the total completion time of jobs. However, the proposed algorithm required enhancements in future. Amir et al. [36] created a metamodel to replace the simulation experiments aimed at reducing the computation and test the proposed method on Stochastic Job Shop Scheduling Problem (SJSSP) by presenting a new Evolutionary Learning Based Simulation Optimization (ELBSO) method embedded within the Ordinal Optimization using Genetic Programming (GP). The author wanted to apply this improved method in solving existing production planning and scheduling problem. Gheisariha et al. [32] proposed an enhanced multi-objective algorithm which is the Enhanced Multi-Objective Harmony Search (EMOHS) algorithm and a Gaussian mutation. [32] also designed a simulation-optimization framework for implementing the rework process and compare the algorithm with the well-known 5 types of algorithms for minimizing both maximum completion time and mean tardiness.

2.2. State-of-the-art Implementation

The papers that emphasized the realization of an application, execution of algorithms and model, are classified into this section. The papers are divided into different fields based on the papers.

2.2.1. Simulation and Optimization

The studies that were mainly based on the implementation of the simulation process into real industry cases were included by experimenting and analysing the results generated. Niehues et al. [14] proposed a WIP regulating method for production control for job-shop productions in the automotive industry to reduce the impacts of control activities on orders by experimenting with the production system. The results shown in the simulation model demonstrated the suitability and effectiveness of production control in manual job-shop production systems. Kuck et al. [38] proposed an adaptive simulation-based optimization approach for individual selection of dispatching rules in production control by conducting experiments on a scenario from the semiconductor industry which resulted in improved solution quality at the beginning of the optimization process (local optimum), but not very good in global optimum. Wang et al. [39] analysed a semiconductor packaging facility for enhancement of the sustainability of a factory simulation model by proposing five strategies, while the result proved that the three strategies proposed

successfully reduced the requirement of money, time, and effort in building the factory simulation model. However, the sustainability of a simulation model is still uncertain for several years after it is built. Grabowik et al. [40] analysed a single-car manufacturing line to examine production efficiency based on a few proposed changes in system organization. The author declared that simulation is useful in checking different models of organizational solutions and following the long-term behaviour of the system simply and effectively.

2.2.2. Algorithms and Heuristics

There are only several papers that implemented the algorithms, especially GA into the real situation system. Niehues et al. [21] proposed a new approach in sequence scheduling for a job shop control system and verify its effectiveness through simulation with Tecnomatix Plant Simulation and MATLAB using GA. The author aimed to improve the adherence to delivery dates was fulfilled by improving due date compliance. Sobottka et al. [41] developed a hybrid simulation optimization module for use in a novel production optimization tool using GA in a food processing facility by considering the material flow and thermal-physical behaviour for the improvement of the energy efficiency of the production system. Wang et al. [42] proposed a two-stage energy-saving optimization method for Flexible Job Shop Scheduling Problem (FJSSP) in the metal-production industry using GA and Particle Swarm Optimization (PSO) to reduce energy consumption and production cost. The author would like to integrate the proposed method with big data technology in future studies.

All these studies concluded that in the literature, there is still a gap between the flexibility of the system and the complexity of the product mix and intelligence decision-making in optimized results, considering the design complexity of the manufacturing system which can be implemented into the dynamic condition. Besides, the majority of the research is taking makespan or completion time as objectives. Hence, makespan become the most common performance measure to be studied among the others. This lead gave proper direction to the experimentation part of this research paper.

3. Method

To close the gap, an integration approach is proposed. The combination of simulation and optimization-based algorithms with the predictive-reactive approach for scheduling the RMS under various optimization restrictions was studied through experiments. For the predictive part, the feasible schedule for the RMS job shop is predicted and decided. Rule-based simulation and optimization are then implemented into the schedule: first, a rough schedule was determined using an optimization algorithm, and then rule-based simulation systems were used to refine the schedule to obtain the most optimal results. For the reactive phase, the schedule obtained is adjusted and validated by the MONTRAC monorail system. The results obtained from the experiments are compared and analysed to find out the effectiveness of the proposed method structure, algorithms and architecture.

3.1. Real System

This research is using MONTRAC, manufactured by the company MONTRACTEC GmbH, Germany as an example. This system is a modular monorail system that allows the interlink of production processes between robots and workplaces more flexibly. Pioneering medical institutions and manufacturing firms in automobile, chemicals, household products, optics, food, medicinal and pharmaceutical markets using this system to increase their product throughput and reduce cycle times. In conjunction with this system, the MONTRAC shuttles are the main components of the MONTRAC system, which are intelligent single or twin-axle conveyors mounted with an onboard power supply. The shuttles are moving self-centred on the monorail, fitted with state-of-the-art sensors that avoid possible collisions with barriers or other shuttles. Each shuttle is operated by an axle-located, maintenance-free, low-voltage engine. Shuttle velocity and stopping positions are defined by cams on the T-grooves along the track [43].

Figure 2 shows the schematic illustration of the MONTRAC system. The real system's structure is modelled using Tecnomatix Plant Simulation V12 and consists of rails, buffers and workstations. Firstly, parts will be loaded into the system, transported by rail-guided vehicles and unloaded in buffers near workstations for further processing. After the specific process had been done at the workstation, the product will be loaded in another buffer and waiting for pick up by the rail-guided vehicles again to transport further. After the product had finished all the operations, the product will be unloaded at the final buffer for further processing.

3.2. Computer Simulation Software

The real system is modelled using computer simulation software which is Tecnomatix Plant Simulation V12 by Siemens. Tecnomatix Plant Simulation is an object-oriented 3D program founded by German company Siemens PLM Software, the leading global supplier of software for Product Lifecycle Management (PLM) and

Manufacturing Operations Management (MOM), which specifically designed for discrete production simulation process and modelling into a digital model. The models built in the Plant Simulation can be run by experiments and scenarios for analysis of causes and effects in the current production systems or the newly designed systems without disturbing the working process of production systems. Plant simulation is provided with well-developed analytical tools that promote the analysis of a system's bottlenecks, together with the illustration of diagrams and statistic configurations, and even can import 3D geometrical models from CAD systems, visualise the entire manufacturing system including workstations and transportations [25], [40].

Job Shop Scheduling Problem

In this study, the job shop scheduling problem is described as a set of n jobs, J_i where $i = 1, 2, \dots, n$ which are going to operate on a set of m machines, M_k where $k = 1, 2, \dots, m$. Every single job contains a set of operations, each of which needs to be processed during an uninterrupted period of a given length on a given machine. Operation of the i th job on the k th machine will be denoted by O_{ik} . There are several constraints and assumptions set on jobs and machines as follows [44], [45], [1].

1. The job release dates are time $T = 0$.
2. All the machines are available at time $T = 0$.
3. The number of machines and jobs is finite and constant in time (with respect to their characteristics).
4. The machine breakdowns and the setup times are statistically included in the processing times.
5. Each machine can process only one operation at a time and each job can be processed by only one machine at a time.
6. Once a job begins processing, it cannot be interrupted until it is completed, and no precedence constraints exist among jobs.
7. The due dates are specified.
8. The time to put the parts on or to take them off the material handling vehicles is negligible.

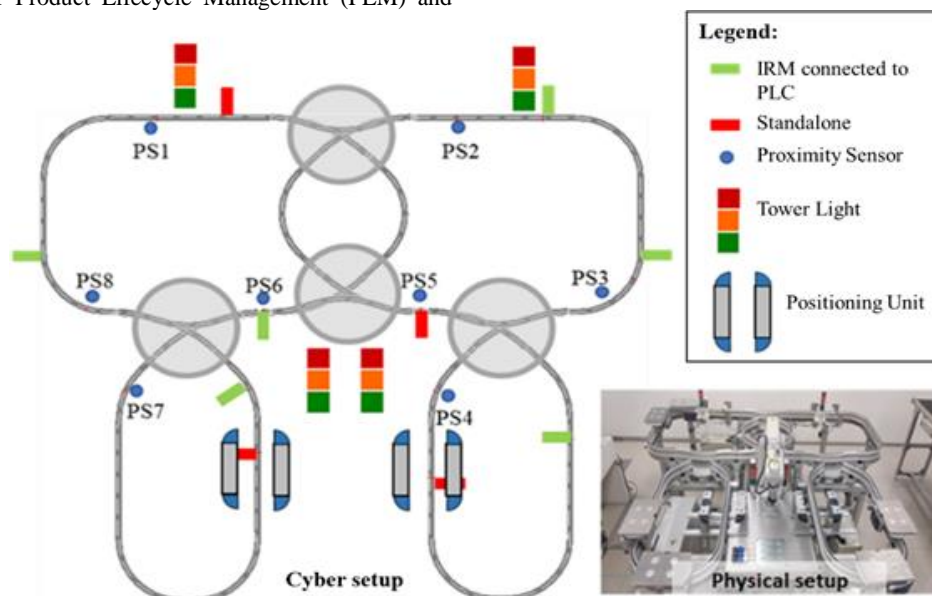


Figure 2. Schematic MONTRAC monorail material handling system

3.2.1. Scheduling Procedure

Before the scheduling process starts, there are some parameters required to be decided, such as the objective functions. The selection of objective function is decided by the industry itself, while in this study, the results will be reported for the objectives of minimizing the makespan denoted by C_{max} which is defined as the time when the last job leaves the system:

$$C_{max} = \max (C_1, C_2, \dots, C_{max}) \quad (1)$$

where C_i is the completion time of the job, J_i .

Besides objective functions, the initial data and some related settings are required to be provided in the model, including the schedules of the workstations, speed of transporters, the number of parts to be entered into the system etc. The schedules provided then undergo process simulation, together with the application of optimization methods including priority dispatching rules and GA to obtain an optimized solution.

The reconfigurable job shop considered in this study has both operations and routing flexibilities, which can be interpreted in the form of a multiple-process plan, for example, each component can be processed through alternative machines, and each component can be transported through alternative routes. The scheduling problem contained three decision variables: (a) selection of operation machines for each part; (b) sequencing of parts to be entered into the RMS, and (c) routing of the parts transported to each machine. These three decisions are made at the same time by combining operation machine selection rules, input sequencing rules and part sequencing rules with genetic algorithm. The rules combination performances will be tested through simulation experiments, where the dispatching rules that are considered in this study as recommended by Zeestraten [46] are shown in Table 1.

After achieving a suitable schedule, the simulation is run with the logging option activated to obtain logs that are used to control the real system. The logs obtained contains information including the start and stop of processing time at every station, all transportation activities, and the sequence of products and paths for every part. During the control stage of the real system, rescheduling requests might be triggered due to disturbances such as station failure, planned maintenance or sudden changes in order. Therefore, the reactive loop represents the transfer of system status information to the model and the reactivation of the scheduling procedure with new inputs. The scheduling procedure is illustrated in Figure 3.

Table 1. The dispatching rules that have been considered for optimization purposes in the model.

Dispatching rule	Explanation
Earliest Due Date (EDD)	Select the job that has the earliest due date first.
First Come First Served (FCFS)	Select the operation that is available first.
Shortest Processing Time (SPT)	Select the job that has the shortest processing time of the first process.
Longest Processing Time (LPT)	Select the job that has the longest processing time of the first process.
Fewest Operations Remaining (FOPR)	Select the job that has the smallest number of successive operations.
Most Operations Remaining (MOPR)	Select the job that has the largest number of successive operations.
Shortest Remaining Processing Time (SRPT)	Select the job that has the shortest sum of processing times
Longest Remaining Processing Time (LRPT)	Select the operation that has the longest sum of processing times.

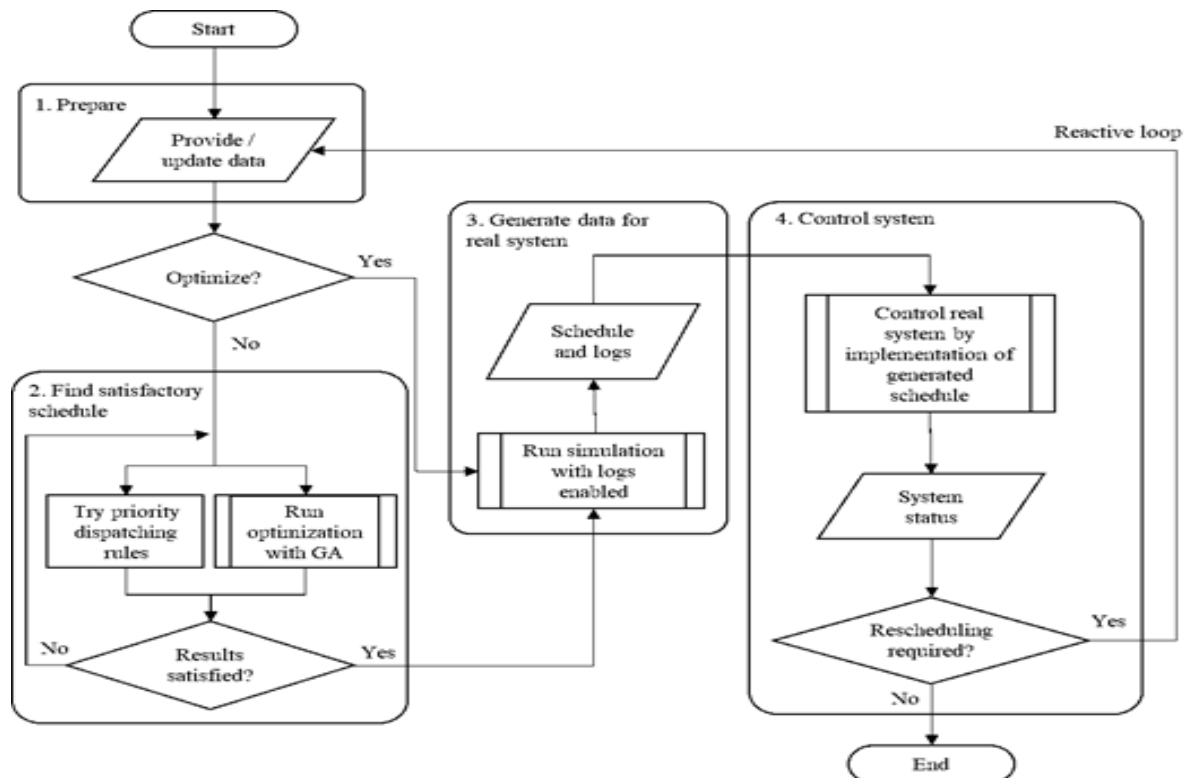


Figure 3: Algorithm of scheduling procedure.

3.3. Construction of Feasible Schedule

A schedule defines the execution sequence of all operations for all jobs on machines [47]. Before the simulation process begins, several feasible schedules are required as primary input data for the construction of the simulation model. In this study, these feasible schedules are built with a predictive approach, which included the process plan for every type of product, the time schedule that specified the durations of every operation, the workstation’s plan that indicated which type of process to be operated and also the due date schedule together with the quantity required for the customers.

3.3.1. Process Plan

A process schedule is constructed for the process sequence required to be done for each product type as illustrated in Table 2.

There is a total of 10 types of product types and each of the product types has different process sequences. In this study, a maximum of 5 processes for each product type will be considered, but the simulation model is built to fit a maximum of 9 processes for each product type to reach the dynamic aspects of market requirements.

The sequence of each product type can also be decided whether or not to follow the sequences during the operations. In this case, the schedule had been set to follow the partial order, where the product that set to keep the process sequence for all product types except product Type_6, Type_7 and Type_8, which means that these product types can proceed to any operations first depends on the system.

Table 2. The process plan for every product type.

Name	Keep Sequence	1st Process	2nd Process	3rd Process	4th Process	5th Process
Type_1	true	Proc_1	Proc_3	Proc_4		
Type_2	true	Proc_2	Proc_5	Proc_1	Proc_4	
Type_3	true	Proc_5	Proc_2	Proc_4	Proc_3	
Type_4	true	Proc_3	Proc_4	Proc_5	Proc_1	Proc_2
Type_5	true	Proc_2	Proc_4	Proc_3	Proc_1	
Type_6	false	Proc_2	Proc_3	Proc_4		
Type_7	false	Proc_1	Proc_4	Proc_5		
Type_8	false	Proc_2	Proc_4			
Type_9	true	Proc_5	Proc_3	Proc_1		
Type_10	true	Proc_2	Proc_3	Proc_5		

3.3.2. Workplace Operation Time Schedule

There is a total of 4 workplaces or stations to be included in the system in this study, which are given the names H1, H2, H3 and H4. Each workstation has a specific operation time schedule that indicates different operations with different processing times. Each workstation is also fixed with a different type of process, and in this study, the maximum amount of operation to be done in a specific workstation is fixed with 2 types of operations. Table 3 shows the time needed for every operation (Proc_1, Proc_2, Proc_3, Proc_4) based on the product type (Type_1 to Type_10), and also the workstations that are eligible to carry out the specific process.

Table 3. The workplace operation time schedule for every product type.

	H1	H2		H3		H4	
	Proc_1 (s)	Proc_1 (s)	Proc_2 (s)	Proc_3 (s)	Proc_5 (s)	Proc_4 (s)	Proc_5 s)
Type_1	1200	1200	-	1800	-	420	-
Type_2	1500	1500	900	-	240	600	240
Type_3	-	-	660	510	420	735	420
Type_4	180	180	120	300	210	135	210
Type_5	1830	1830	1200	915	-	495	-
Type_6	-	-	600	720	-	1200	-
Type_7	600	600	-	-	600	900	600
Type_8	-	-	840	-	-	1500	-
Type_9	1080	1080	-	480	1200	-	1200
Type_10	-	-	2100	660	600	-	600

3.3.3. Due Date Schedule

Different product has different quantity and due date to meet customers' requirements, therefore due date schedule is constructed with the desired amount of product and the due date as well, as shown in Table 4.

Table 4: The due date schedule for every product type.

Product Name	Qty (unit)	Due Date (date, time)
Type_1	5	01.12.21, 13:10
Type_2	10	01.12.21, 11:35
Type_3	12	02.12.21, 10:55
Type_4	4	01.12.21, 14:55
Type_5	8	02.12.21, 16:15
Type_6	10	01.12.21, 11:40
Type_7	3	01.12.21, 09:40
Type_8	6	01.12.21, 20:40
Type_9	15	02.12.21, 11:40
Type_10	2	01.12.21, 18:40

The due date is written in the format of the date (dd.mm.yy), then followed by the time. All the products have to be finished before the due date with the specific amounts, for example, Type_1 product is required to produce 5 quantities before the 1st of December 2021, 1.10 pm.

3.4. Construction of Simulation Model

The simulation model is built to represent the real system, including the position of the buffers and workstations. There is a total of 11 buffers, 6 rail-guided vehicles and 4 workstations included. The model is built with high flexibility where the layout and the position of buffers and workstations can be modified or added easily. The construction of a simulation model is mainly divided into two categories, one is for controlling the simulation process of the model and the other one is for the preparation of necessary input data for the simulation process.

3.4.1. Path Generations

The most important methods in this model are the path generations method, which indicated the generations of the products' paths along the whole system. Every path generated consists of a sequence of objects including tracks, buffers and workstations, which implies the process plan and allocation. This method written aimed to obtain all the information regarding all the possible transportation routes for every single job and product type intelligently without needing to enter the information manually into the settings for the optimization process. This method also acted as preparation for the process of population initialization and evaluation required for the GA. All the output generated from this method is stored in a table named "PathsTable".

The path generations are started with product type by generating a sequence of processes with the permutation method. After that, for every sequence of processes, a sequence of workstations is created. The concept of generations of all these outputs is by checking every station table to ensure whether the specific stations provide

the process. After all possible station sequences are generated, then search for paths beings. The method follows the tracks from one station to the next station until all possible ways are discovered. The application of complexity level is also included in this method by eliminating long paths and keeping the shorter paths.

3.4.1.1. Permutation

Especially when a product is not necessary to strictly follow the process plan, possible sequences of processes are generated through this method. This method is programmed to receive a string of characters and return a list of permuted strings. The algorithm of this method is illustrated in Figure 4 by taking characters 1, 2, 3, and 4 as an example.

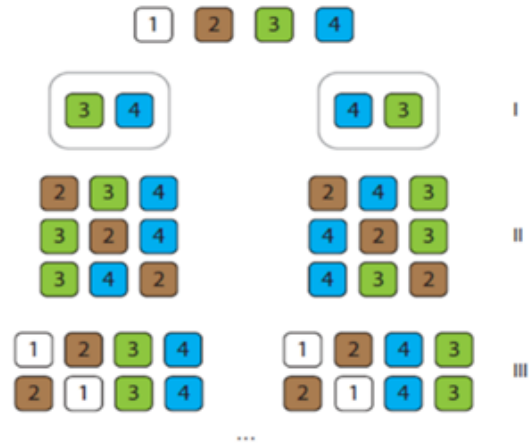


Figure 4. Permutation algorithm illustration.

The algorithm of permutation started with the last character selected which is 4. Then, the preceding character 3 is inserted into every available position, which is before and after 4. This resulted in two strings as shown in stages I, that is 34 and 43. After this stage, the same procedure continues with inserting the next character into every string. Taking the first string 34 as an example, character 2 is inserted before, between and after characters 3 and 4 respectively, thus the result obtained are 234, 324 and 342. The action is performed until the first character is inserted into all strings. The total number of obtained permuted strings is $N!$ where N is the number of characters. For this given example, the total number of obtained permuted strings is 24.

3.5. GA Setup and Control

In this study, GA is used to find the optimum solution by choosing one of the paths for each instance of a product, combining all products in different sequences and running simulations to assess their objective function values. The GA in this model is run by an object named "GAV12V" which is a frame that contains a lot of methods and other objects that are used to control the GA optimization process. GAWizard provided some settings or options related to the GA process for the user to choose and enter manually, and most of these settings are transferred with a method named "SetGA" between the user interface dialogue and the wizard.

The GA process run by GAWizard which is a user interface created by the author in the simulation software program and is divided into a few steps, which involved

the definition of chromosomes in the initial population, the selection of parent's chromosomes, and the generation of offspring chromosomes. The process of GA will be terminated when there is no improvement in the fitness value of the best individual during N generations. The termination of the GA process will also be triggered when the set time limit had reached.

3.5.1. Initialization of the Population of Chromosomes

The GA is started by defining chromosomes, each chromosome stands for one entity with its respective work order number. Every chromosome encodes with a sequence of operations. In the generation of the initial population, each chromosome is initialized by following the entity arrangement in "Release_List" where the entities are generated in random sequences. Table 5 shows the example of chromosome representation for a population of chromosomes generated at random.

There are a total of 75 entities to be processed, therefore the chromosomes generated for each generation and each individual will be a total of 75 chromosomes. The generation of chromosome populations are depending on the size of the generations and the number of generations. For example, if the generation size is set to 10, then 10 genes or 10 individuals will be generated with 75 chromosomes with random path variants and random entity sequences. If the number of generations is set to 5, then the 10 genes and individuals generated with the 75 chromosomes will be created until 5 generations. During a generation process, the genetic operator's processes will be performed on chromosomes to obtain better solutions.

Table 5: Example of a population of chromosome representation based on product type and work order number.

Chromosome	1	2	3	4	5	6	7	8	9	10
Work order number (Entity)	10	51	26	67	29	55	43	28	3	56
Part Type	2	7	3	9	4	8	6	4	1	8

3.5.2. Selection

Before the genetic operators are performed, GA will authorize a population composed of a large number of individuals to evolve under specified selection rules to a state that maximizes the fitness value. The fitness of an algorithm is a measure of how effectively it has learned to anticipate outputs from inputs. A fitness evaluation aims to provide information to the learning algorithm on which individuals should be allowed to multiply and reproduce and which should be eliminated from the population [48].

In this case, the process of selection is done by Roulette Wheel selection to select the parents. According to Kofjač and Kljajić [49], the Roulette Wheel selection method is the most common method used in GA selection. The Roulette Wheel selection is depending on the fitness values assigned to the chromosomes by fitness functions, while the fitness value is used to relate the possibility of selection with each chromosome. The probability of being selected is denoted as:

$$P_i = \frac{f_i}{\sum_{j=1}^n f_j} \tag{2}$$

where f_i is the fitness of an individual i in the population, n is the number of individuals in the population and j is the job.

In GAWizard, the parent selection settings can be chosen either deterministic or random. If the option "deterministic" is chosen, then the parents will be selected randomly according to their fitness values with roulette wheel selection, and individuals with good fitness values will be used more often as parents for creating the next generation. However, individuals with bad fitness values also have a chance to be used as parents. While for the "random" option, the fitness values are not used and all individuals are having the same likelihood to be used as parents.

In this model, the option deterministic is chosen and the fitness value is to be set as minimized since the objective function is to minimize the makespan. After a specific number of individuals had been generated based on the generation size, GA will calculate the fitness value for all the individuals, and the individuals with the best fitness value will be selected as parents for further processes.

3.5.3. Crossover

The crossover mechanism is a random process with a probability of crossover and is used to create a new generation of a pair of children's chromosomes from a pair of parent chromosomes via the crossover operation. The crossover operator's average probability ranged between 0.6 and 1.0 [50]. In this model, the crossover processes are done randomly between 75 entities in every generation. There are two types of crossover processes generated by GAWizard, which are order crossover (OX) and partially matched crossover (PMX). OX crossover preserves the relative position or neighbour relation of the items of the solution to each other, while PMX crossover stresses the absolute position of the objects. The crossover algorithm for OX crossover and PMX crossover is illustrated in Figures 5 and 6 respectively.

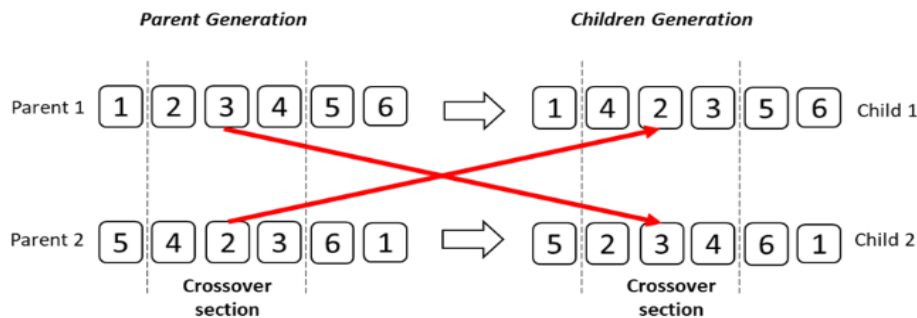


Figure 5. Example of OX crossover between two parents and two children.

For OX crossover, two parents and two offspring are considered as an example. Firstly, the genes (1 5 6) are copied from Parent 1 to Child 1 and located outside the crossover section following Parent 1's sequences, while genes (5 6 1) are duplicated from Parent 2 to Child 2 with the same order and location. The gene position inside the crossover section for both Child 1 and Child 2 will remain empty. The missing genes gap in both children is filled by duplicating the genes from the crossover section from both parents in opposite manner, which means that the genes (2 3 4) from Parent 1 will be duplicated to place in the crossover section in Child 2, while the genes (4 2 3) from Parent 2 will be duplicated to locate in crossover section in Child 1.

For PMX crossover, the first step is the same as in OX crossover where the genes outside the crossover section in both parents will be copied and placed in both children to the gene's original position and sequence. However, the genes in the crossover section in both parents will not be duplicated to the children in the opposite manner and followed the sequences during the process. To produce a feasible schedule, the gap in each child must be filled with the missing genes by taking in order each valid gene from the parent. For example, the genes (2 3 4) in Parent 1 are used to fill the crossover section gap in Child 1 while the genes (4 2 3) in Parent 2 are used to fill the crossover section gap in Child 2 but the sequences are different from the original sequences of the genes in parent's generation.

3.5.4. Mutation

After the crossover process is done, the mutation process will follow. The mutation process is crucial to the GA's success because it diversifies the search directions and prevents convergence to local optima. This process has only involved some offspring randomly. The size is decided by the probability of mutation which the value is typically between 0.0015 and 0.03 [48]. The mutation rate is calculated as:

$$P_m = 1 - \frac{f_{best}}{f_{child}} \tag{3}$$

where f_{best} is the fitness function value of the chromosome that has yielded the best result, while f_{child} is the fitness function value of the child that requires mutation. The chromosome with the fitness value closer to the f_{best} would have a lower pm than the one with a fitness value closer to the worst value [49].

In this model, the mutation operations are done randomly between 75 entities in every generation. The mutation process is taking part in the allocation task by swapping the locations of genes that were chosen randomly to produce a feasible solution, or by determining a value from the allocation set or chosen from the defined interval randomly and then allocated to the selected gene in sequence task. The mutation algorithm for the mutation process is illustrated in Figure 7.

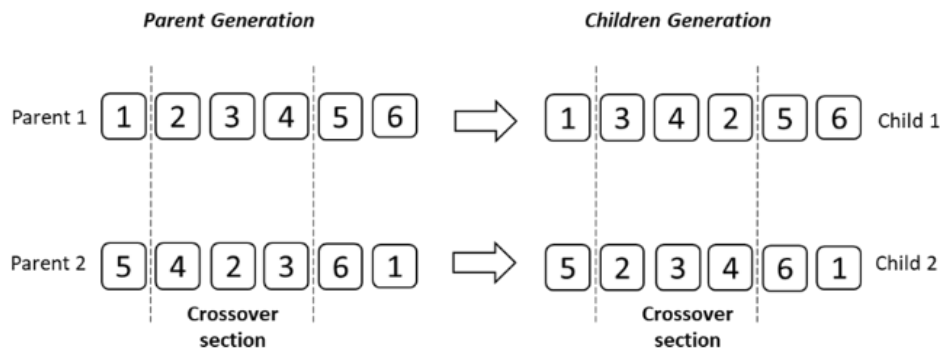


Figure 6: Example of PMX crossover for two parents and two children.



Figure 7: Example of EX mutation in a parent and a child.

4. Results and Discussion

The experiments were conducted with a 2.3 GHz Intel Core i3 processor and 6GB RAM and the heuristics were implemented together with GA using SimTalk which is the programming language used in Tecnomatix Plant Simulation. Due to the lack of benchmarks in the literature related to process plan generation in a reconfigurable manufacturing environment, the experiments are performed with randomly generated instances using GA for the reactive scheduling situation.

The parameters used for analysis and comparison purposes are the number of generations and the generation size, which refer to the parameters in the previous study of Gibbs et al. [50] as follows: generation size = 6, 10, 25 and number of generations = 5, 10. Besides, the makespan, release control with various path generator complexity levels and dispatching rules are being compared. The parameters and conditions included in the experiments are summarized as shown in Table 6.

Table 6: The parameters involved in the experiment.

Parameter / Condition	Values
Maximum number of MUs	18
Number of transporters	6
Transporter speed (m/s)	0.226
Intersection transfer time (s)	0.2
Transporter load/ unload time (s)	5
Keep process sequence	Selective
Use buffer after workplace	Yes
Pick up on the way to buffer	Yes
Pick up after unloading	Yes
Release control	Default, Option 1, Option 2, Option 3
Path generator complexity level	Level 1, Level 2, Level 3
Number of generations	5, 10
Generation size	6, 10, 25
Observations per individual	1

4.1. Makespan

The main objective of this study is to reduce the makespan of the overall process of a reconfigurable

manufacturing system, thus the system was run without using GA first to obtain the initial makespan for every type of dispatching rules, then with GA and for a different number of generations and different generation sizes. For both the default and first option (Op1) release control option during the generation of the initial makespan, the system resulted in block condition, while the second and third options (Op2 and Op3) with three levels of path generators generated the results.

4.1.1. Number of Generations

The experiment was run with fix generation size which is 6 with a different number of generations which is 5 and 10 respectively. Figure 8 shows the makespan for every type of dispatching rule to a different number of generations with a generation size of 6 for the reactive scheduling situation. The initial makespan for the situation resulted in the longest duration, while for both the number of generations of 5 and 10 it resulted in a shorter makespan. However, for the reactive scheduling situation, the difference between both generation numbers 5 and 10 is larger. The percentage of reduction in makespan is calculated and tabulated in Table 7.

The percentage of reduction in makespan for reactive scheduling cases is successfully reduced by more than 15% except for the reactive scheduling case of generation number 5. However, generation number 10 for the reactive scheduling case had successfully proven to have a percentage of reduction of more than 15%. It can be concluded that the highest percentage reduction of 38% for the reactive scheduling case. The combination of GA and dispatching rules in finding the optimized schedule of solutions for reconfigurable manufacturing systems is effective even in the small number of generations, also higher generation numbers denoted to better results.

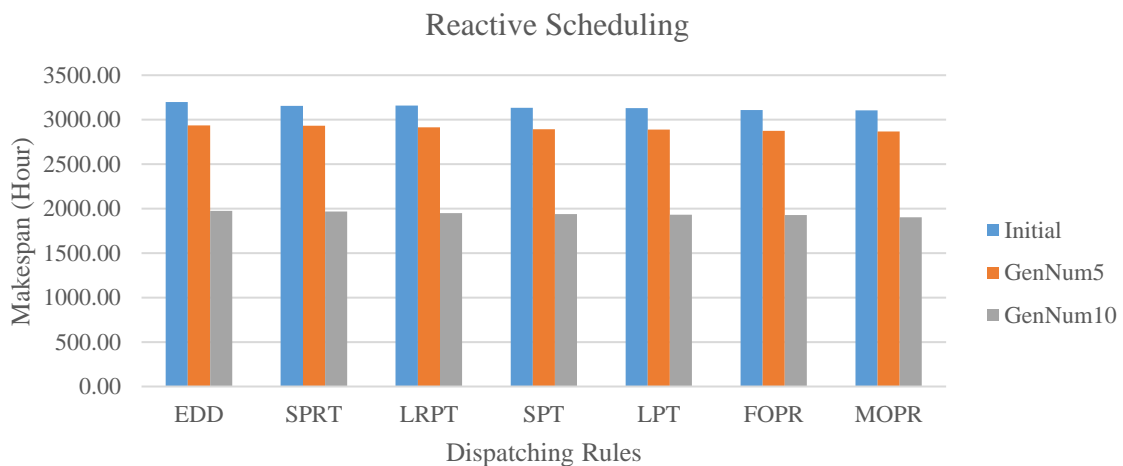


Figure 8. Makespan for rescheduling for the number of generations = 5 and 10 with generation size = 6.

4.1.2. Generation Size

The experiment was then run with a fixed number of generations which is 5 with different generation sizes which are 6, 10 and 25 respectively.

Figure 9 show the makespan for every type of dispatching rule regarding different generation sizes with a generation number of 5 for reactive scheduling situation. The initial makespan for this situation resulted in the

longest duration, while the other generation sizes resulted in a shorter makespan compared to the initial results. However, for the reactive scheduling situation, the difference between all three types of generation sizes is more consistent. The percentage of reduction in makespan based on these situations is calculated and tabulated in Table 8.

Table 7: The percentage reduction in makespan for reactive scheduling compared with initial makespan for the number of generations = 5 and 10 with generation size = 6.

Reactive Schedule	Makespan (Hour)						
	EDD	SPRT	LRPT	SPT	LPT	FOPR	MOPR
Initial	3199.043	3155.293	3159.888	3134.600	3128.705	3107.003	3104.078
GenNum5	2935.663	2931.593	2914.122	2894.285	2889.378	2873.448	2867.085
% Reduction	8.233	7.090	7.778	7.667	7.649	7.517	7.635
Initial	3199.043	3155.293	3159.888	3134.600	3128.705	3107.003	3104.078
GenNum10	1974.555	1969.215	1950.927	1937.278	1930.105	1928.515	1902.098
% Reduction	38.277	37.590	38.260	38.197	38.310	37.930	38.723

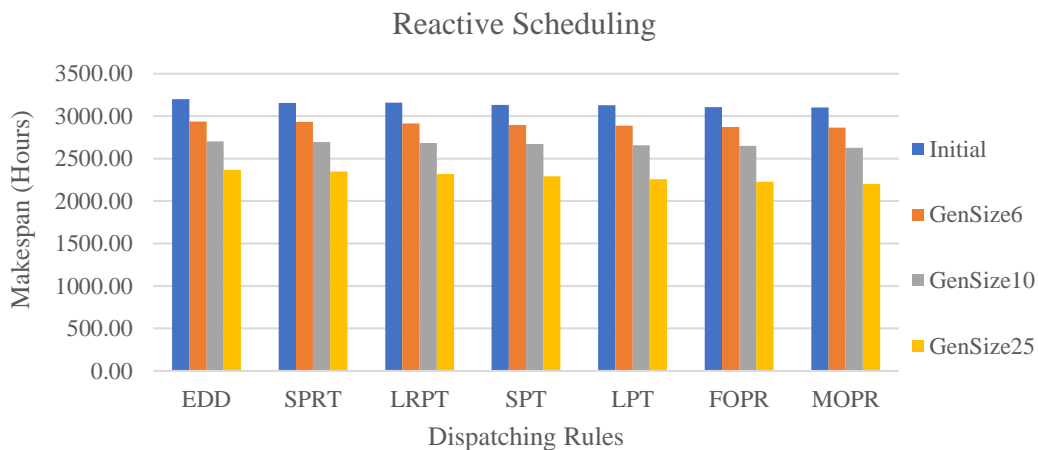


Figure 9. Makespan for reactive scheduling for generation size = 6, 20 and 25 with a number of generations = 5.

Table 8. The percentage reduction in makespan for reactive-scheduling compared with initial makespan for generation size = 6, 10 and 25 with generation number = 5.

Reactive Schedule	Makespan (Hour)						
	EDD	SPRT	LRPT	SPT	LPT	FOPR	MOPR
Initial	3199.043	3155.293	3159.888	3134.600	3128.705	3107.003	3104.078
GenSize6	2935.663	2931.593	2914.122	2894.285	2889.378	2873.448	2867.085
% Reduction	8.233	7.090	7.778	7.667	7.649	7.517	7.635
Initial	3199.043	3155.293	3159.888	3134.600	3128.705	3107.003	3104.078
GenSize10	2703.058	2694.205	2682.417	2671.153	2658.500	2650.988	2628.122
% Reduction	15.504	14.613	15.110	14.785	15.029	14.677	15.333
Initial	3199.043	3155.293	3159.888	3134.600	3128.705	3107.003	3104.078
GenSize25	2369.228	2347.748	2318.100	2291.793	2259.630	2227.118	2201.882
% Reduction	25.939	25.593	26.640	26.887	27.777	28.319	29.065

Based on Table 8, the percentage of reduction in makespan reactive scheduling cases is successfully reduced by more than 15% except for rescheduling cases of generation size = 6. However, other generation sizes = 10 and 25 for reactive scheduling cases had successfully proven to have a percentage of reduction of more than 15%. Again, it can be concluded that, with the highest percentage reduction of 29% for reactive scheduling cases, the combination of GA and dispatching rules in finding the optimized schedule of solutions for reconfigurable manufacturing systems is effective even in small generation size, while higher generation size contributed to better results.

4.2. Dispatching Rules

Bajpai and Kumar [51] stated that combining other approaches with GA can improve effectiveness and efficiency. Hence, the dispatching rules were experimented with GA to identify the results and comparisons of the performances. The performance of the dispatching rules was compared by using the fitness values obtained after each GA run. The fitness value is derived from Rastrigin’s function which is defined by Bajpai and Kumar [51] as:

$$Ras(x) = 20 + x_1^2 + x_2^2 - 10(\cos 2\pi x_1 + \cos 2\pi x_2) \quad (4)$$

Where x_1 & x_2 represent the values of independent variables

Since the objective function is set to be a shorter makespan, hence the direction of optimization is set to be

minimum. Therefore, for this study, the smaller the fitness value indicated the better result. The fitness function value for all dispatching rules was tested with a different number of generations and different generation sizes as well.

4.2.1. Number of Generations

The experiment was run with fix generation size which is 6 with a different number of generations which is 5 and 10 respectively for the reactive scheduling conditions. The results are illustrated in Figure 10. As a result, for the reactive scheduling, the generation number = 10 resulted in a lower value of fitness compared to the generation number = 5 for all dispatching rules. The dispatching rules LRPT with the number of generations = 10 resulted in the smallest value of fitness function, which is 6906506.463 while dispatching rules SRPT resulted in the highest value of fitness function in generation number = 5.

Conclusively, higher generations number resulted in better results, however, there are no great differences in a better result for any dispatching rules to be selected.

4.2.2. Generation Size

The experiment was then run with a fixed number of generations which is 5 with different generation size which is 6, 10 and 25 respectively. Based on Figure 11, there is an obvious difference between each generation size, while the dispatching rules MOPR indicated the lowest fitness value with generation size = 25.

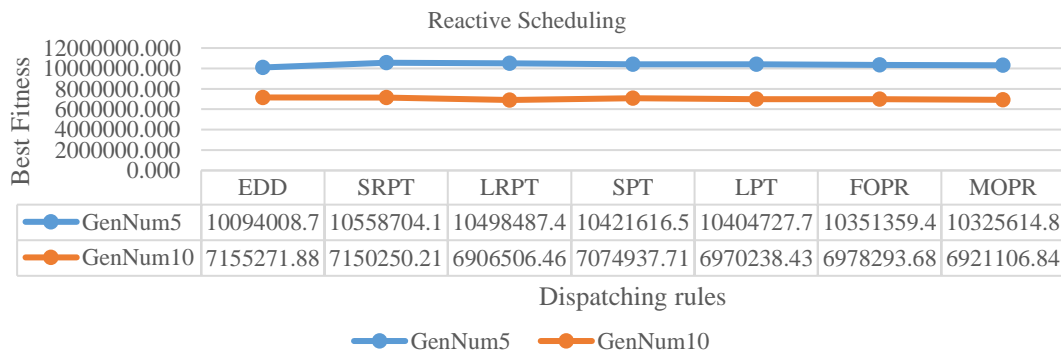


Figure 10: The best fitness value in terms of dispatching rules of the reactive scheduling for the number of generations = 5 and 10 with generation size = 6.

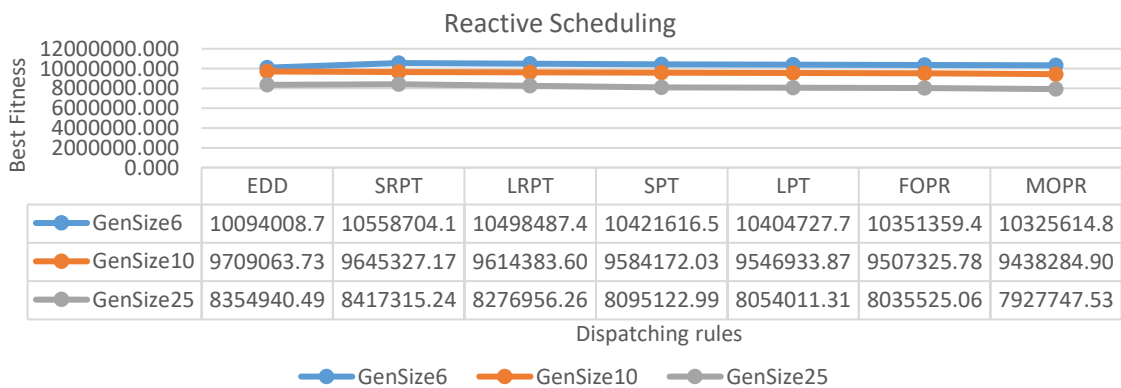


Figure 11: The best fitness value in terms of dispatching rules of the reactive scheduling for generation sizes = 6, 10 and 25 with the number of generations = 5.

For the experiments in terms of dispatching rules regarding different generation sizes and numbers, the results indicated that the dispatching rules to be selected are mainly depending on the objective functions. For the objective function makespan, there are no big differences.

4.3. Improvement Rate

There are durations when the experiments are running, and those readings are classified as optimization time, which indicated how long a specific experiment needs to run until the result was obtained. For stochastic simulation, the individuals should be evaluated by several simulation runs. However, due to limited time issues, the observation per individual is set to only 1. In Tecnomatix Plant Simulation, when the GA Wizard executes, it will calculate the number of simulations to be run based on the formula below and run the simulation:

Number of simulation runs

$$= O_i \times (GS + 2 \times GS \times (GN - 1))$$
 (5)

where O_i = Observations per individual, GS = Generation Size, GN = Number of Generations.

Hence, the larger the number of generations or generation size, the larger the number of simulations runs, therefore resulting in longer optimization time.

4.3.1. Number of Generations

To analyse the relationship of improvement rate with the generation size, a formula is used to calculate the rate from the data generated from the experiment as follows:

$$Rate = \frac{Best\ fitness\ value}{Optimization\ time} \tag{6}$$

The experiment was run with the fixed number of generations = 5 and varied generation sizes = 6, 10 and 25. Table 9 shows the results from the calculation of the formula (6) for the reactive scheduling conditions with different dispatching rules.

Table 9. The improvement rate for the reactive scheduling of dispatching rules with the number of generations = 5 and generation sizes = 6,10 and 25.

	Gen Size 6	Gen Size 10	Gen Size 25
	Reactive Scheduling	Reactive Scheduling	Reactive Scheduling
EDD	17830.482	10755.993	3444.372
SRPT	19668.227	10477.326	3518.048
LRPT	19115.259	9735.380	3378.730
SPT	20799.089	10367.003	3344.148
LPT	17140.189	10125.550	3306.326
FOPR	18432.581	10539.054	3378.890
MOP			
R	17802.480	14580.917	3488.352

The data from Table 9 were generated into Figure 12 for analysis. From Figure 12, firstly the improvement rate for generation size = 6 is the highest for the situation, and when the generation sizes increase, then the improvement rate decrease linearly for the reactive scheduling case. Results show that the performances are getting better when the generation size is larger.

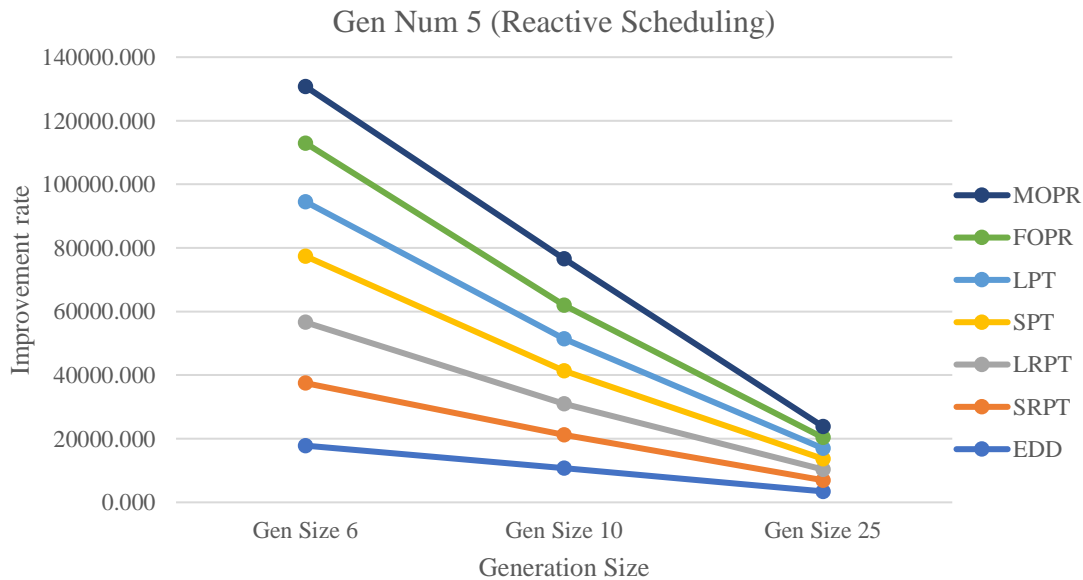


Figure 12. The improvement rate for reactive scheduling with the generation number = 5 and varied generation sizes.

5. Conclusion

This study is to analyze several aspects of combining simulation and optimization-based algorithms for job-shop scheduling of reconfigurable manufacturing systems with a predictive-reactive approach using priority dispatching rules and GA. A predicted feasible schedule will be first determined and tested from a developed model where the reconfigurable production system in real-life is taken as a reference and case study. The simulations were run with GA together with dispatching rules, together with different conditions and settings of the reconfigurable manufacturing system to identify the results in a different environment.

The parameters such as the number of generations and generation size have also been analyzed to identify the effect towards the results, however, due to limited time, only some parameters were tested based on the previous study in the literature. The result showed that the model built had demonstrated good efficiency and the ability to find an effective schedule in a specified period and the algorithm can tackle the complicated scheduling issue successfully and in lesser time.

The results obtained from this simulation run with GA using Tecnomatix Plant Simulation included the makespan, the best fitness value, the optimization running time, the best parameter of the allocation of the products, the best sequences of the products, the evolution and performance of the fitness value during the generations, the details included the children and parents' genetics data and so on. However, the performance and schedule optimization degree cannot be compared to other scheduling methods, because this model only provided the optimization possibility using GA and dispatching rules. The series of optimization runs do not provide an adequate collection of data to conclude the recommendations for the best selection of GA options and dispatching rules of the reconfigurable manufacturing system. Overall, the model proved the efficacy of integrating simulation and optimization with a genetic algorithm, providing engineers with the needed flexibility and control.

Conclusively, although various methods and algorithms have been created in the literature, only a few comparisons have been made. Other research suggests that the proposed approaches perform well under certain assumptions, but not so well or even poorly under others. Part of future works to be carried out will involve benchmark problems of a certain type of production system operation must be established with specific test objective functions. Reasonable comparisons between different approaches may also be made to validate the effectiveness of the suggested solutions more precisely.

Acknowledgement

The authors would like to thank Universiti Teknikal Malaysia Melaka (UTeM) and UTeM Zamalah Scholarship Scheme 2.0, for the support and opportunity to conduct this research study.

References

- [1] L. Asadzadeh, "A local search genetic algorithm for the job shop scheduling problem with intelligent agents". *Computers and Industrial Engineering*, Vol. 85, 2015, 376–383.
- [2] M. Niehues, F. Buschle, G. Reinhart, "Adaptive job-shop control based on permanent order sequencing". *Procedia CIRP*, Vol. 33, 2015, 127–132.
- [3] A. Allahverdi, E. Pesch, M. Pinedo, F. Werner, "Scheduling in manufacturing systems: new trends and perspectives". *International Journal of Production Research*, Vol. 56, No. 19, 2018, 6333–6335.
- [4] B. Scholz-Reiter, D. Lappe, S. Grundstein, "Capacity adjustment based on reconfigurable machine tools – Harmonising throughput time in job-shop manufacturing". *CIRP Annals*, Vol. 64, No. 1, 2015, 403–406.
- [5] R. Angkiriwang, Pujawan, I. Nyoman, B. Santosa, "Managing uncertainty through supply chain flexibility: reactive vs. proactive approaches. *Production & Manufacturing Research*". Vol. 2, No. 1, 2014, 50–70.
- [6] Y. Koren, X. Gu, W. Guo, "Reconfigurable Manufacturing Systems: Principles, design, and future trends," *Frontiers of Mechanical Engineering*, Vol. 13, No. 2, 2017, 121–136.
- [7] R. Pansare, G. Yadav, M. R. Nagare, "Reconfigurable Manufacturing System: A systematic review, meta-analysis and future research directions,". *Journal of Engineering, Design and Technology*, Vol. 33, 2021, 543-574.
- [8] P.L. Mareddy, S.R. Narapureddy, V.R. Dwivedula, S.V. Prayagi, "Simultaneous Scheduling of Machines, Tool Transporter and Tools in a Multi-Machine Flexible Manufacturing System Without Tool Delay Using Crow Search Algorithm". *Jordan Journal of Mechanical and Industrial Engineering*, Vol. 16, No. 3, 2022, 403-419.
- [9] D.Y. Lee, F. DiCesare, "Integrated Scheduling of Flexible Manufacturing Systems Employing Automated Guided Vehicles". *IEEE Transactions on Industrial Electronics*, Vol. 41, No. 6, 1994, 602–610.
- [10] N. Kundakci, and O. Kulak, "Hybrid genetic algorithms for minimizing makespan in dynamic job shop scheduling problem". *Computers and Industrial Engineering*, Vol. 96, 2016, 31–51.
- [11] T. Nehzati, "Research Outline on Reconfigurable Manufacturing System Production Scheduling Employing Fuzzy Logic". *International Journal of Information and Electronics Engineering*, Vol. 2, No. 5, 2012, 812–816.
- [12] Y.C. Choi, P. Xirouchakis, "A holistic production planning approach in a reconfigurable manufacturing system with energy consumption and environmental effects". *International Journal of Computer Integrated Manufacturing*, Vol. 28, No. 4, 2015, 379–394.
- [13] X.-Q. Wan, H.-S. Yan, "Integrated scheduling and self-reconfiguration for assembly job shop in knowledgeable manufacturing". *International Journal of Production Research*, Vol. 53, No. 6, 2015, 1746–1760.
- [14] M. Niehues, P. Sellmaier, T. Steinhäusser, G. Reinhart, "Adaptive Job-Shop Control Using Resource Accounts". *Procedia CIRP*, Vol. 57, 2016, 351–356.
- [15] M.M. Nasiri, R. Yazdanparast., F. Jolai, "A simulation optimisation approach for real-time scheduling in an open shop environment using a composite dispatching rule". *International Journal of Computer Integrated Manufacturing*, Vol. 30, No. 12, 2017, 1239–1252.
- [16] L. Tang, X. Wang, "A predictive reactive scheduling method for color-coating production in steel industry". *International Journal of Advanced Manufacturing Technology*, Vol. 35, No. 7–8, 2008, 633–645.
- [17] P. Korytkowski, T. Wiśniewski, S. Rymaszewski, "An evolutionary simulation-based optimization approach for

- dispatching scheduling.” *Simulation Modelling Practice and Theory*, Vol. 35, 2013, 69–85.
- [18] M. Fera, F. Fruggiero, A. Lambiase, G. Martino, M. Elena, “Production Scheduling Approaches for Operations Management. In: Massimiliano Schiraldi, editor. In *Operations Management*, United Kingdom: InTech; 2013, p. 113-139.
- [19] H.H. Doh, J.M. Yu, Y.J. Kwon, D.H. Lee, M.S. Suh, “Priority scheduling for a flexible job shop with a reconfigurable manufacturing cell”. *Industrial Engineering and Management Systems*, Vol. 15, No. 1, 2016, 11–18.
- [20] M. Leusin, E. Frazzon, M.U. Maldonado, M. Kück, M. Freitag, “Solving the Job-Shop Scheduling Problem in the Industry 4.0 Era”. *Technologies*, Vol. 6, No. 4, 2018, 107.
- [21] M. Niehues, M. Blum, U. Teschemacher, G. Reinhart, “Adaptive job shop control based on permanent order sequencing: Balancing between knowledge-based control and complete rescheduling”. *Production Engineering*, Vol. 12, No. 1, 2018, 65–71.
- [22] O. Bataineh, R.A. Aomar, A.A. Shakra, “Simulation-Based Optimization for Performance Enhancement of Public Departments”. *Jordan Journal of Mechanical and Industrial Engineering*, Vol. 4, No. 3, 2010, 346-351.
- [23] A. Azab, A. Ziout, W. Elmaraghy, “Modeling and Optimization for Disassembly Planning”. *Jordan Journal of Mechanical and Industrial Engineering*, Vol. 5, No. 1, 2011, 1-8.
- [24] D. Mourtzis, “Simulation in the design and operation of manufacturing systems: state of the art and new trends”. *International Journal of Production Research*, Vol. 58, No. 7, 2020, 1927–1949.
- [25] J. Siderska, “Application of Tecnomatix Plant Simulation for Modeling Production and Logistics Processes”. *Business, Management and Education*, Vol. 14, No. 1, 2016, 64–73.
- [26] J. Yann, J. Anicia, Z.M. Fatima, T. Damien, B. Patrick, “A new methodological support for control and optimization of manufacturing systems in the context of product customization”. *Journal of Industrial and Production Engineering*, Vol. 38, No. 5, 2021, 341-355.
- [27] H. Xiong, H. Fan, G. Jiang, G. Li, “A simulation-based study of dispatching rules in a dynamic job shop scheduling problem with batch release and extended technical precedence constraints”. *European Journal of Operational Research*, Vol. 257, No. 1, 2017, 13–24.
- [28] J.T. Lin, C.C. Chiu, Y.H. Chang, Simulation-based optimization approach for simultaneous scheduling of vehicles and machines with processing time uncertainty in FMS”. *Flexible Services and Manufacturing Journal*, Vol. 31, No. 1, 2019, 104–141.
- [29] Q. Deng, G. Gong, X. Gong, L. Zhang, W. Liu, Q. Ren, “A Bee Evolutionary Guiding Nondominated Sorting Genetic Algorithm II for Multiobjective Flexible Job-Shop Scheduling”. *Computational Intelligence and Neuroscience*, Vol. 2017, 2017, 1-20.
- [30] H. Piroozfard, K.Y. Wong, W.P. Wong, “Minimizing total carbon footprint and total late work criterion in flexible job shop scheduling by using an improved multi-objective genetic algorithm” *Resources, Conservation and Recycling*, Vol. 128, 2018, 267–283.
- [31] X. Zan, Z. Wu, C. Guo, Z. Yu, “A Pareto-based genetic algorithm for multi-objective scheduling of automated manufacturing systems”. *Advances in Mechanical Engineering*, Vol. 12, No. 1, 2020, 1–15.
- [32] T. Sivarat, S. Apichat, “A simulation-optimization approach for adaptive manufacturing capacity planning in small and medium-sized enterprises”. *Expert Systems with Applications*, Vol. 168, No. 114451, 2021, 1-13.
- [33] P. Valledor, A. Gomez, P. Priore, J. Puente, “Solving multi-objective rescheduling problems in dynamic permutation flow shop environments with disruptions”. *International Journal of Production Research*, Vol. 56, No. 19, 2018, 6363–6377.
- [34] F.A. Touzout, L. Benyoucef, “Multi-objective multi-unit process plan generation in a reconfigurable manufacturing environment: a comparative study of three hybrid metaheuristics”. *International Journal of Production Research*, Vol. 57, No. 24, 2019, 7520–7535.
- [35] F. Zheng, K. Jin, “An improved heuristic for single machine lot scheduling problem”. *IFAC-PapersOnLine*, Vol. 52, No. 13, 2019, 217–222.
- [36] G. Amir, A. Amir, H. Cathal, “Evolutionary Learning Based Simulation Optimization for Stochastic Job Shop Scheduling Problems”. *Applied Soft Computing Journal*, Vol. 106, 2021, 1-19.
- [37] E. Gheisariha, M. Tavana, F. Jolai, M. Rabiee, “A simulation–optimization model for solving flexible flow shop scheduling problems with rework and transportation”. *Mathematics and Computers in Simulation*, Vol. 180, 2021, 152–177.
- [38] M. Kuck, B. Eike, M. Freitag, “Towards Adaptive Simulation - Based Optimization To Select Individual. Winter simulation conference, Las Vegas, Nevada, 2017.
- [39] Y.C. Wang, T.C.T. Chen, L.C. Wang, “Simulating a Semiconductor Packaging Facility: Sustainable Strategies and Short-time Evidences”. *Procedia Manufacturing*, Vol. 11, 2017, 787–795.
- [40] C. Grabowik, K. Kalinowski, G. Cwikla, K. Niemiec, I. Paprocka, “A computer simulation as a tool for a production system analysis and optimization”. *IOP Conference Series: Materials Science and Engineering*, Vol. 400, No. 2, 2018, 1-15.
- [41] T. Sobottka, F. Kamhuber, M. Rössler, W. Sihn, “Hybrid simulation-based optimization of discrete parts manufacturing to increase energy efficiency and productivity”. *Procedia Manufacturing*, Vol. 21, 2018, 413–420.
- [42] H. Wang, Z. Jiang, Wang, Yan, H. Zhang, Wang, Yanhong, “A two-stage optimization method for energy-saving flexible job-shop scheduling based on energy dynamic characterization”. *Journal of Cleaner Production*, Vol. 188, 2018, 575–588.
- [43] B. Wally, J. Vyskocil, P. Novak, C. Huemer, R. Sindelar, P. Kadera. “Flexible Production Systems: Automated Generation of Operations Plans Based on ISA-95 and PDDL”. *IEEE Robotics And Automation Letters*, Vol. 4, No. 4, 2019, 4062-4069.
- [44] Yang, B., and Geunes, J., 2008. Predictive-reactive scheduling on a single resource with uncertain future jobs. *European Journal of Operational Research*, Vol. 189, No. 3, 1267–1283.
- [45] E. S. Nicoară, F. G. Filip, N. Paraschiv, “Simulation-based optimization using genetic algorithms for multi-objective flexible JSSP”. *Studies in Informatics and Control*, Vol. 20, No. 4, 2011, 333–344.
- [46] MJ, Zeestraten, “Scheduling Flexible Manufacturing Systems. PhD Thesis, Technische Universiteit Delft (The Netherlands)”. 1991.
- [47] P. Ning, "An Adaptive Scheduling Method for Resources in Used Automobile Parts Recycling". *Jordan Journal of Mechanical and Industrial Engineering*, Vol. 14, No. 1, 2020, 53-60.
- [48] K. Mesghouni, “Evolutionary algorithms for job-shop scheduling” Vol. 14, No. 1, 2004, 91–103.
- [49] D. Kofjač, M. Kljajić, “Application of genetic algorithms and visual simulation in a real-case production optimization”. *WSEAS Transactions on Systems and Control*, Vol. 3, No. 12, 2008, 992–1001.

[50] M.S. Gibbs, H.R. Maier, G.C. Dandy, J.B. Nixon, "Minimum number of generations required for convergence of genetic algorithms". 2006 IEEE Congress on Evolutionary Computation, CEC, Vancouver, Canada, 2006.

[51] P. Bajpai, M. Kumar, "Genetic algorithm—an approach to solve global optimization problems". *Indian Journal of computer science and engineering*, Vol. 1, No. 3, 2010, 199–206.

An Integrated Systematic Approach for Reconfiguration of Facilities Layout in a Stochastic Product Demand

A.A. Abdul Rahman^{1,2*}, R.N.H. Leong¹, O.J. Adeboye¹, E. Mohamad², T.J. Yee¹, M.H. Md Saad²

¹Faculty of Manufacturing Engineering, Universiti Teknikal Malaysia Melaka, Melaka, Malaysia.

²Institute of IR4.0, Universiti Kebangsaan Malaysia, Bangi, Selangor, Malaysia.

Received 1 Aug 2022

Accepted 31 Oct 2022

Abstract

A factory layout is designed to obtain a physical arrangement of different entities of a facility that most economically meets the required output, in terms of both quantity and quality. An optimum and good arrangement can make the flow of the material free from any interruption and will increase the productivity. New challenges to the manufacturing layout will occur when there is an increase in demand for customer-specific products, and an increasingly shorter product life cycle. Manufacturing companies that undergo production expansion to their current facilities without careful facilities planning, would in most situations, encounter many issues which could retard their overall operations. Due to ever reducing space in the plant, when a transfer is done, this causes tremendous pressure on its current facilities, causing several production bottlenecks and affecting productivity. The aim of this study is to develop a systematic integrated approach to re-configure its current layout to an optimum layout under this stochastic product demand. The approach is to select three key production optimization methodologies based on their individual strengths for the specific task required in developing this integrated approach. The development of this integrated approach takes into consideration the combination of these three key methodologies of the production optimization into a process flowchart, which are the Systematic Layout Planning (SLP), the Theory of Constraint (TOC), and the Discrete Event Simulation (DES). The step of developing the alternative layout is an integration of SLP with the TOC. The translated layouts were then validated by comparing the layout as it is (AS-IS) or the existing layout with the alternative layouts and analysed with the DES for the optimum layout in terms of productivity. The results from the case study revealed that Option 2 which was developed through this integrated approach is the optimum layout. Via this integrated approach, the throughput per hour of Option 2 improved by 15% over the existing layout and by 23% over the Option 1 layout. Total distance covered for the forklift movement with Option 2 shows a much lower distance travelled than the other two layouts. This study reveals the effectiveness of the developed integrated approach in developing the optimized layout with a better material flow strategy.

© 2022 Jordan Journal of Mechanical and Industrial Engineering. All rights reserved

Keywords: Material Flow Analysis; Manufacturing System; Plant Simulation; Factory Layout; Production Optimization.

1. Introduction

Factory can be referred to as an industrial site, usually containing buildings and machineries where workers operate machines to manufacture and process goods from one product into another. The re-layout of a factory or facility design is aimed at improving the productivity of machines, designing an effective workflow, workers, and material flow [1].

Re-layout for a factory is important to improving and expanding the efficient production process and addressing the requirements of workers [2]. It is also important because it affects the flow of material and processes, labour efficiency, supervision and control, use of space and expansion possibilities, etc. [3]. A well-designed and structured manufacturing layout plan can reduce up to 50%

of the operating cost and improve productivity [4]. A poor layout results in wasted time and energy and creates confusion [5].

The most used techniques or methods that can be utilized to design and redesign a facility layout is the Systematic Layout Planning (SLP) by Muther, 1961 [6]. This is a phase in preparation to manage and control the layout of the factory Systematic Planning System (SLP) aims at achieving the quickest material flow at the lowest cost and least amount of material handling during the manufacturing process [7][8][9]. This study is conducted in collaboration with ABC Company. The factory is located in Melaka, Malaysia. A company established in Malaysia for over 44years specialized in manufacturing and supply of diverse, quality and innovative soft and hard haberdashery products and knitting accessories.

* Corresponding author e-mail: azrulazwan@utem.edu.my.

ABC company over the years has gone through several expansion of relocation from other group overseas production sites, production machineries to its current site here in Malaysia plant. Most of these production expansions did not take into consideration proper facilities planning as it was done in a haste, just to allow the production of these new products to commence production in a short time.

The SLP approach is initiated by Muther (1961). This is an undertaking in the preparation and in the control of the layout of the factory SLP aimed at achieving the fastest material flow at the lowest cost and the least movement of material handling during the manufacturing process [10]. There was also a study showcasing the use of SLP in the food industry and in hospitals [11][12][13].

Table 1: Charts in SLP

Chart	Purpose
From-To chart	Quantitative measuring of movements between departments in terms of the amount transported.
Activity relationship chart	Find the most dependent department based on sequential activity.
Relationship diagram	Positioning activities or operations in which they are situated in a two-dimensional space.
Space relationship diagram	Present the space of each related departments.

According to Tompkins [14], the mechanism involved in the execution of the SLP is uncomplicated. However, this does not rule out that there will be no complications in the application of the SLP. This process requires several different charts and diagrams to be developed by the facility planner. The advantage of this process is that it leaves room for imagination which allows for easy grasping of concept adaption. The charts and diagrams created in this process are illustrated in Table 1.

Theory of Constraint (TOC) is a production management system to pinpoint and to eliminate the impact of bottlenecks in a company [15]. The TOC is a technique in identifying the most important limiting factor (i.e., constraint) that obstructs goal reaching and thereafter, systematically addressing the constraint issue till it ceases to be a limiting factor. In manufacturing, the constraint is often referred to as a bottleneck.

Material flow analysis is a systematic assessment of the flows and stocks of materials within a system defined in space and time. It connects the sources, the pathways, and the intermediate and final sinks of a material [11]. Material flow analysis and improvement of a manufacturing system due to factory re-layout can be carried out using several modelling software that provides analysis of its operations in dynamic environment. The process of imitation of the various operation involved in a real-world process or system [4] over time is called simulation.

In simulating a process or a system, it first requires an already established model. The model represents the system itself, whereas the simulation represents the operation of the system over time [16]. Based on the facts above, material flow analysis and layout optimization of a manufacturing system under stochastic demand [5] play a vital role in any facility planning and layout study [17].

Discrete Event Simulation (DES) is a common tool for production throughput analysis and manufacturing system performance optimization [18].

This study aim is to develop a methodological approach in assisting manufacturing companies which has undergone expansion in manufacturing facilities, to reconfigure or re-layout its current layout to an optimum layout.

The first objective is to study the state-of-the-art approach to re-configure facilities layout under stochastic demands [19]. The second objective is formulating a systematic approach based on the SLP, the TOC [20] and to develop a simulation-based approach for re-configuration of facilities layout. Another objective (3) is to validate this formulated algorithm and integrated approaches on ABC company. The final objective (4) is to evaluate the effectiveness of this approach with the state-of-the-art approaches. Two alternative layouts are developed using this approach and to determine its effectiveness, they are analysed using the DES of Tecnomatix Plant Simulation Software v14 to obtain key productivity data and to compare with the AS-IS layout data. Upon obtaining the results, the best of the two alternative layouts based on the optimum productivity data for the manufacturing production of ABC Company is selected.

2. Methodology

With the aim to develop a novel approach for layout reconfiguration, several steps were used in planning, development, validation, and analysis phases. Each step is designed to demonstrate the relationships and the interaction of the development. Figure 1 presents the methodology utilized in performing this study.

The study starts with analysing available state of the art approaches and methods, under development in research and implementation at the industries. After evaluation of all these methods, a selection will be made on which of these methodologies would be best suited for this study. The selected methodologies are then integrated together to formulate a novel approach that supports layout design and re-layout design process. The capability and effectiveness of this formulated systematic approach will then be validated by a real industrial case study from the ABC company.

In the context of this study, the combination of SLP, TOC and DES were selected and integrated. During the validation process, SLP procedures i.e., Form-To chart, Activity relationship chart, Relationship diagram and Space relationship diagram are created and analysed. Necessary data that relevant for the SLP is collected. This requires numerous visits to the site (ABC company).

Information gained from the SLP procedure is used to develop an AS-IS model. Modelling process follows the simulation project procedure proposed by the Association of German Engineers (Verein Duestcher Ingenieure -VDI). Based on the analysis of the AS-IS planned layout model the two alternatives layout models will be analysed and compared to the AS-IS layout model. Incorporating TOC to the development of the alternative layout is another key factor. Simulation evaluation will be done, and the best

alternatives in terms of optimum material flow and higher throughput will be proposed for implementation.

2.1. Data Collection

This sub-session describes about the investigation method that is used to achieve the necessary information. The data collection method is the typically determining for the data analysis [21]. Through observations and interviews with engineering personnel was the data for the factory layout collected starting from raw material to packaging even to dispatch. The principal data collected spans from the type and nature of the product, their respective production process flow, factory layout and setup relative to the product discussed and need to recognize for all the process which incorporate into the production line.

The data demonstrate the present creation line and their material flow system for each product per production. Other than that, is the time for each number of

workstations, working shift, processing time, frequency of forklift movement and the number of batched per demand. Besides, data is gathered, so that, the cycle time for each workstation in the production lines, and also the number of batches is transporting from a process to another process can be accounted for. With the data collected, the layout alternatives can be developed both on paper and then simulated.

2.2. Material Flow and Production Process

To further create the experimental model relative to the real-time model, all five products were studied thoroughly from the raw material stage to the level as it comes as a finished product. These products included (i) Safety Pins; (ii) Straight Pin; (iii) Snap fastener; (iv) Aluminium Imra hook; (v) Aluminium Susan bates. Table 2 shows the production process and data collection of the safety pins product as an example. Similar data has been collected for other four products.

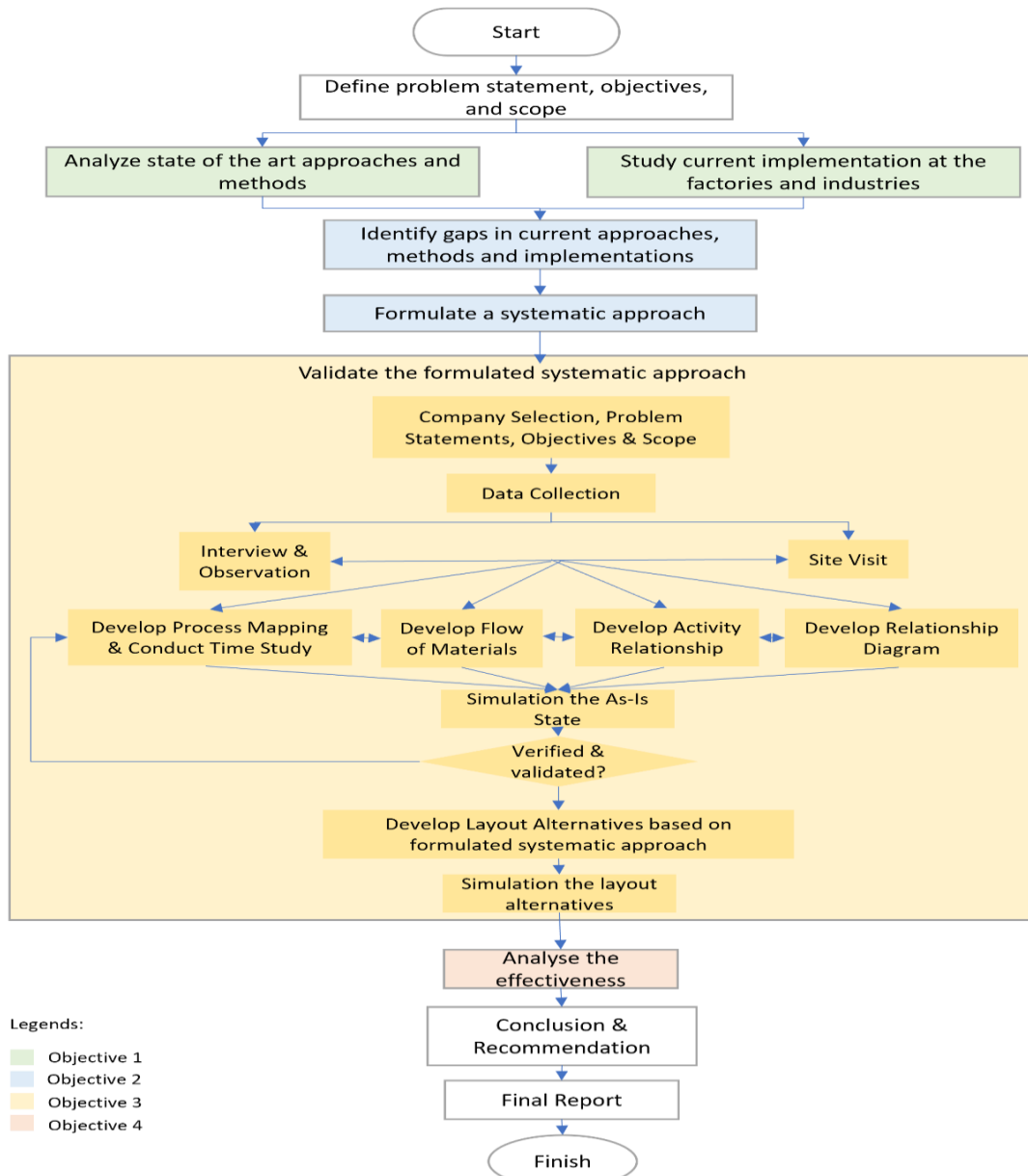


Figure 1. Methodology of the study

Table 2: Example of data collection for safety pins product

Process	Processing time	No. of machine	Batch size
Demand = 120kg			
Raw material	-	-	Pin – 24kg per batch x 5
Pointing	5hrs	5	120kg
Assembly	3hrs/batch	1	24kg per batch
Nikel plating	8hrs	1 shift	120kg
Buffer Storage Area	-		
Quality Control	5hrs		120kg
WIP and kitting area	2hrs	5	24kg per batch
Packaging	2hrs	5	24kg per batch

The manufacturing of all these products is subdivided into three factories, located within the same premises of the company. These three factories will be simulated using the Tecnomatix Plant Simulation software. The production process of each product differs, so every product has to be simulated based on their own production line respectively. This will allow the simulated or experimental model of the real-time model to be created of which later alternatives layout created utilizing the new integrated approach will be generated for final simulation analysis.

2.3. Develop Layout Alternatives

With the integration SLP and TOC into a single approach of layout re-configuration, several layout alternatives will be developed. The alternatives highlighting all the desired options that will go with the desired objectives; improve the overall throughput and material flow [22]. These alternative layout options are later compared with the existing or AS-IS layout by the simulation process with its differing factory arrangement, however, the process flow for production remains unchanged.

2.4. Simulation and Data Analysis

Upon the completion of data collection, the simulation model for all alternatives is then created. The simulation can be configured and reconfigured to match the desired objectives with the availability of a completed data. Simulation software uses a dedicated library or custom-designed computer support CAD data and allows flexibility of the appropriate visualization approach to demonstrate the project in a 2D virtual environment.

Experimentation with the model and applying the design of experiments techniques are happening at this step [23]. Further in this step, investigating decisions about other alternative models and the return to the initial steps

of the process for each major model may change. Having the operation of the model studied and the properties associated with the workings of the actual system or sub-system, it can then be deduced accurately through the simulation.

Wide statistics and chart boards are used and shown to support a dynamic analysis of the performance parameters, including line workloads, crashes, idle time and fixes and the proprietary key performance factors. As an example, with the advantage of having a data analysis, bottlenecks can be pinpointed fast and various secondary channels can then be explored by comparing the working time, the waiting time, the processing time and the cycle time of the workstation.

3. Results and Discussion

3.1. Integrated Approach

The methodology for reconfiguring a plant or manufacturing layout, is crucial by first developing an integrated approach which is suitable and best suited for the application under this Stochastic Product Demand. As shown in Figure. 2, the integrated approach for layout re-configuration.

The development of this integrated approach takes into consideration of combining 3 key methodology of production optimization process. The first is to select the best layout procedure and, in this case, SLP was selected of the 5 layout procedures due to it's easy to understand and methodological steps. Although, the procedure to developed a good layout had been developed, the ever-changing stochastic product demand in the company will create potential bottlenecks in the production flow and this will create constraint which eventually retard productivity and throughput. In order to encounter these challenges, TOC was incorporated in this process flow as to ensure any bottleneck in the production flow is taken into consideration at this early stage of planning. The final key process to complete this integrated approach is to verify among the alternative layout, developed in the earlier steps was to select the best among them. And by including computer simulation in the last stage of the flow chart, would eventually lead to the most optimised selection of the layout, by means of generating key specific productivity data in this simulation process.

3.2. From-To Chart

A review is required in minimizing the material handling cost of flow among departments. In our layout design, the priority is to focus on the need to minimize the movements of materials; raw materials, semi-finished and/or finished goods from one process department to another and to reduce the bottleneck material flows.

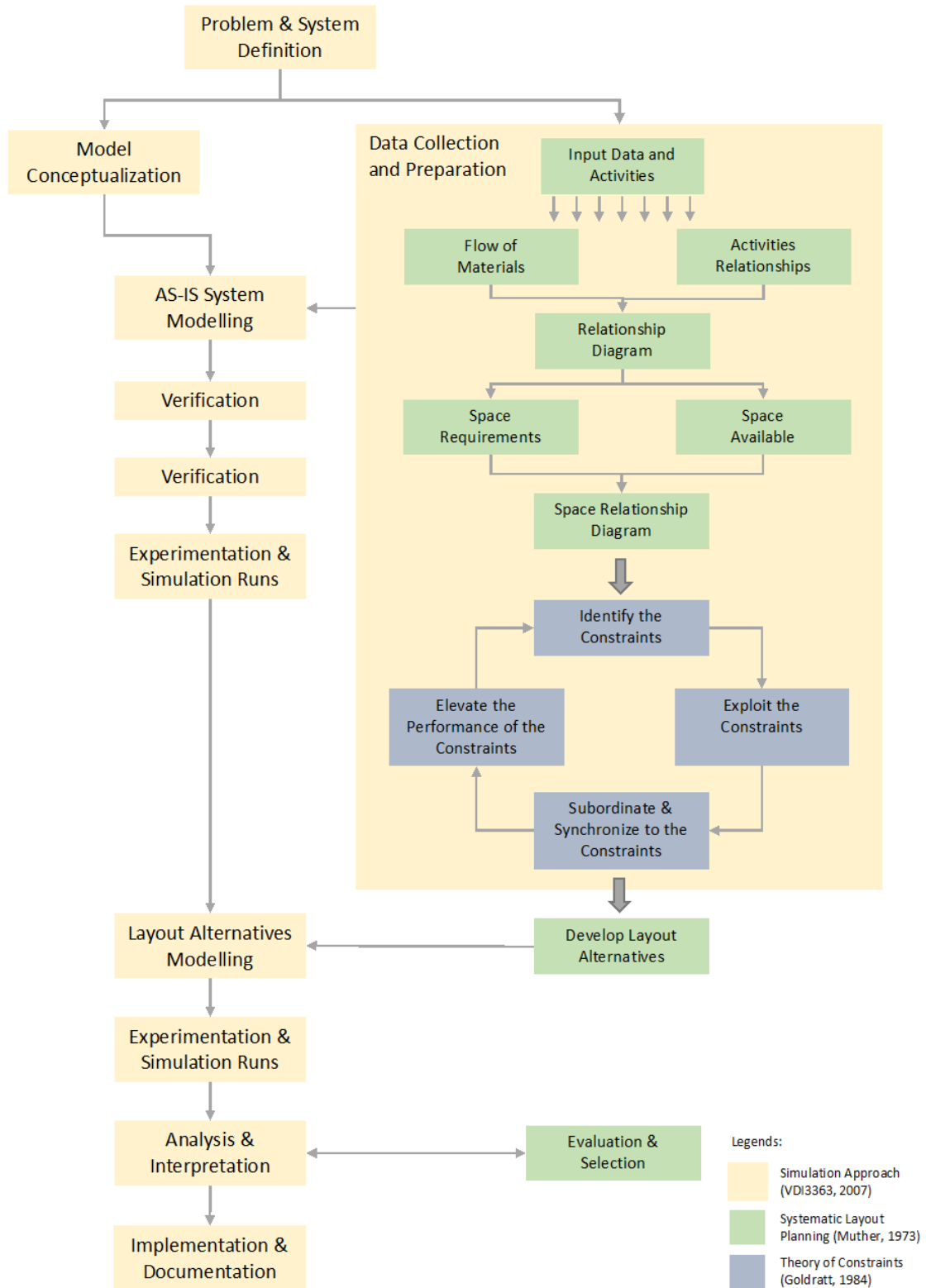


Figure. 2. Integrated Approach for Layout Re-Configuration

From	To	Store	Pointing	Wire Forming	Assembly	Nickel plating	QC	BSA	Kitting	Packing	Warehouse / dispatch	
		Frequency										
Stores		5	5									
Pointing					5							
Wire Forming					5							
Assembly						1						
Nickel Plating							5					
QC								1				
BSA									1			
Kitting										1		
Packing											1	

Figure 3. Example of From-To chart for safety pins product

From figure 3 shows the sample from-to chart data for safety pin, using this data as a sample data to represent same procedure and data taken for other products. By the figure, it is clearly noted that the higher the numbers between the departments and to the departments intended, there is also a corresponding high frequency of the material travels. As such, considerable effort and care must be taken to locate them either closer together or to minimize the travel distances between these two departments in order to achieve the best possible optimized.

3.3. Activity Relationship Chart

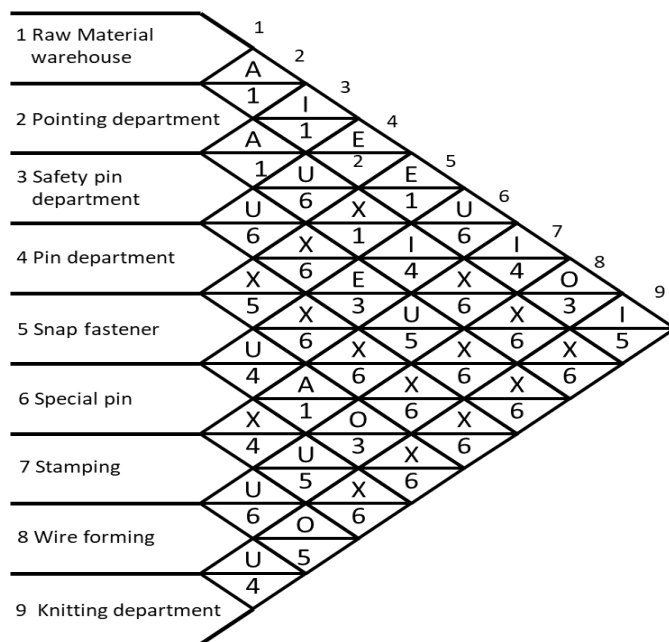
In Figure 4 for factory 1 represents the sample figure for the activity relation diagram for ABC company and this procedure is replicated for factory 2 and 3 respectively. The values may be recorded, with the reasons for the closeness value using the relationship chart because the Activity relationship chart, measures in quality definition, using the closeness relationship values. The aim is to maximize the closeness rating scores between departments based on a closeness function.

In figure 4, the location and position of every department depend highly on the rating of importance of the specific department and the high frequency of usages between them. This information must be taken into consideration when developing the alternative layouts as it will affect the material flows of the individual products.

3.4. Theory of Constraints

Upon completing the above From-To Chart, ARC, and Space Requirements, the next step is to determine if there will be any constraints of material flows if the TOC is applied. By applying the five focusing steps mentioned by [24] (identify the constraint, exploit the constraint, subordinate the constraint, elevate the constraint, and repeat the process) to each of the production process and by eliminating any possible constraints along the material process flow, this ensures the reduction of any potential bottlenecks. From the current layout, it is discovered that the bottleneck or constraint is evident at the WIP build-up due to inefficient handling of materials at the pointing and safety pins sections. By relocating the pointing and safety pins closer in the alternative layout, next to the raw materials store, this can potentially reduce this constraint.

This exercise is repeated for the other processes and departments throughout the factory for the elimination of all the constraints.



Value	Closeness
A	Absolutely necessary
E	Especially Important
I	Important
O	Ordinary closeness okay
U	Unimportant
X	Not desirable

Figure 4. Sample ARC Chart of Factory 1

3.5. Simulation Result and Analysis

Table 3 shows the total summary of all the results generated for all layout simulated using Tecnomatix Plant Simulation Software according to the fourfold analysis discussed.

Table 3. Summary of all the Simulation Results Obtained

Results	Existing Layout	Option 1	Option 2
Total Simulation Time (HH:MM: SS)	14:07:02	15:02:01	11:51.17
Working Percentage (%)	62.60%	62.22%	56.78%
Waiting Percentage (%)	37.40%	37.75%	43.32%
Total throughput (unit)	16	16	16
Throughput per minute	0.02	0.02	0.02
Throughput per hour	1.14	1.03	1.34
Throughput per day	26.47	24.68	32.19
No. of forklift used for production	3	3	2
Factory 1 forklift (Total distance traveled)	3920m	2396m	2396m
Factory 2 forklift (Total distance traveled)	1827m	2605m	2920m
Factory 3 forklift (Total distance traveled)	481m	832m	-
Total distribution time for Factory 1 (minutes)	48.39	28.58	28.58

After simulation on the existing layout and option 1 layout, certain results were acquired apart from the observed result that can be used to buttress our analysis to the subject matter in meeting the desired objectives. The analysis of the result is carried out in threefold namely;

1. Working, waiting and total simulation time.
2. Total throughput per minute, per hour, per day.
3. The number of forklifts used, and its distance travelled.

3.5.1. Working, Waiting, and Total Simulation Time

The total simulation time signifies the Summation of time required for the simulation all process for each layout to be completed. As the materials of each five product go in through the source and out through the drain then the total time is obtained. In analysing the result in table 3, it is seen that option 1 has higher total simulation time compared to the other layout, followed by the existing layout then option 2. The option 2 layout is seen to have possessed a lower total simulation time which therefore means that production will finish faster than the existing layout and the option 1 layout due to certain advantages the layout has over the option 1 and existing layout. The lower total simulation time option 2 possesses tends to take a step closer to validating the intended objective of this project. The improvement of the total simulation time of option 2 over the existing layout and option 1 is approximately 23% as illustrated in Figure 5.



Figure 5. Total simulation time of the three layouts

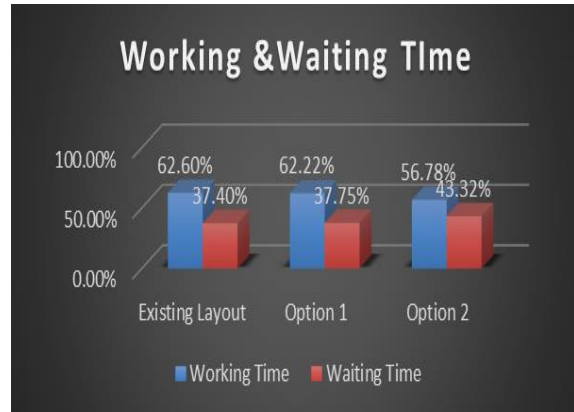


Figure 6. Working and waiting time of the three layouts

This is also validated through the working and waiting time of each option and the existing layout through the simulated results as shown in figure 6. Option 2 has a lower working time of about 10% reduction compared to the existing layout and the Option 1. Whether this will be a qualification for selection as the best-improved layout will be determined by the result of the other analysis.

3.5.2. Throughput of the Layout

The difference should be in the time it takes for it to exit which will help us define which layout will favour a system of stochastic demands. High throughput rate will be more productive thereby meeting the objective of this project. Option 2 has the highest number of throughput rate per hour and per day compared to the existing layout and option 1 layout as illustrated in Figure 7.



Figure 7. Throughput of the three layouts

The throughput per hour of option 2 is improved 15% over the existing layout and 23% over the option 1 layout while the throughput per day of option 2 seems to be improved 18% over the existing layout and 23% over option 1 layout. The throughput of each option reveals that option 2 possesses the highest throughput per hour and day which will show that option 2 will produce more output of products followed by the existing layout than the option 1. This validates the fact that it will be more preferable over the other layout as it produces the best result that meets the objectives of the study.

3.5.3. Total Distance Travelled & Number of Forklifts

Total distance covered for the forklift movement, option 2 shows a minimum total distance travelled even with 2 forklifts than existing and option 1 layout that utilized 3 forklifts for the full operation and option 2 was still able to meet the desired objective. From factory 2 and 3 of the option 1 shows the inefficiency of the developed option, intending to improve the production time and movement thereby increasing profitability. Factory 2 and 3 of option 2 shows a great measure of improvement compared to the existing layout alternative layout of option 1. With this improvement, there was improved forklift movement and total processing time as illustrated in Figure 8.



Figure 8. The distance travelled by the forklifts in the three layouts

4. CONCLUSION

From the above analysis and results obtained from the simulation, clearly reveals the best layout option of the 2 developed using SLP and TOC methodology, was layout Option 2. The case study conducted in this thesis on ABC Company was to develop the best optimum layout using the proposed integrated systematic approach, resulting in terms of highest productivity by means of throughput, shortest travelling distance, and shortest working and waiting time in a stochastic demand environment.

The first objective was achieved with the selection of SLP after the study the state-of-the-art approaches of layout re-configuration in a stochastic demand.

The next objective was achieved with the development of the integrated systematic approach by combination of SLP with TOC methodology to generate alternative layouts. By simulating the alternative layouts, we are able to determine which of the alternative layouts would be the best choice for the re-layout process in terms of overall plant productivity. This formulated approach was validated

in the case study conducted in a manufacturing company which was undergoing an expansion program.

Finally, the effectiveness of this formulated approach was confirmed through the result given by the case study. The best of the alternative layouts, with the highest throughput, least forklift utilization, least working and waiting time and shortest travelled distances was proposed for implementation. Option 2 layout was able to record an average of 50% improvement for factory 1 total distribution, 23% improvement to the overall total simulation time, 19% improvement to the average throughput per hour and 21% improvement to the throughput per day and 14% improvement of the total forklift distance travelled over the existing layout and option 1.

Acknowledgement

The authors would like to thank Universiti Teknikal Malaysia Melaka, ABC company and UTeM Zamalah Scholarship Scheme 2.0, for supporting this study.

References

- [1] G. Kovács, S. Kot, "Facility layout redesign for efficiency improvement and cost reduction", *Journal of Applied Mathematics and Computational Mechanics*, Vol. 16, No. 1, 2017, 63-74.
- [2] M. Iqbal, M. Hashmi, "Design and analysis of a virtual factory layout", *Journal of Materials Processing Technology*, Vol. 118, No. 1-3, 2001, 403-410.
- [3] S. Ali Naqvi, M. Fahad, M. Atir, M. Zubair, M. Shehzad, "Productivity improvement of a manufacturing facility using systematic layout planning", *Cogent Engineering*, Vol. 3, No. 1, 2016.
- [4] Y.H. Lee, M.K. Cho, S.J. Kim, B.Y. Kim, "Supply chain simulation with discrete-continuous combined modeling", *Computers and Industrial Engineering*, Vol. 43, 2002, 375-392.
- [5] Smith J., Tan B., *Handbook of Stochastic Models and Analysis of Manufacturing System Operations*. New York, NY: Springer, 2013.
- [6] Muther R., *Systematic Layout Planning*. 2nd ed. CBI Pub., 1973.
- [7] Sule D.R. *Manufacturing Facilities: Location, Planning, and Design*, 3rd ed. CRC Press, 2008.
- [8] Okpala, C., Chikwendu, Chukwumanya, E. 'Plant Layouts' Analysis And Design', *International Journal of Advanced Engineering Technology*, Vol. 7, Issue III, 2016, 0976-3945.
- [9] J. Kolińska, R. Domański, "The Analysis of Production Lines Bottlenecks–Identification and Ways of Management", 17th International Scientific Conference Business Logistics in Modern Management, Osijek, Croatia, 2017.
- [10] Buchari, U. Tarigan, M. Ambarita, "Production layout improvement by using line balancing and Systematic Layout Planning (SLP) at PT. XYZ", *IOP Conference Series: Materials Science and Engineering*, Sumatera Utara, Indonesia, 2018.
- [11] Lin, Qing-Lian, "Integrating systematic layout planning with fuzzy constraint theory to design and optimize the facility layout for operating theatre in hospitals", *Journal of Intelligent Manufacturing* Vol. 26, 2015, 87–95.
- [12] Y. Ojaghi, "Production layout optimization for small and medium scale food industry", *Procedia CIRP*. Elsevier B.V., Vol. 26, 2015, 247–251.

- [13] S. Helber, "A hierarchical facility layout planning approach for large and complex hospitals", *Flexible Services and Manufacturing Journal*, Vol. 28, No. 1, 2016, 5–29.
- [14] Tompkins J.A., White J.A., Bozer Y.A., Tanchoco J.M.A., *Facilities Planning*, 4th ed. John Wiley & Sons, 2010
- [15] Goldratt E., Cox J. *The Goal*. New York: North River Press; 1984.
- [16] Tulumis. What is simulation | Simulation Software Explained. [online] Available at: <https://www.tulumis.com/what-is-simulation/> [Accessed 26 Nov. 2019].
- [17] E. Grajo, "Strategic layout planning and simulation for lean manufacturing a LayOPT tutorial", *Proceedings of the 27th conference on Winter simulation*, Arlington, Virginia, USA, 1995.
- [18] O. Bataineh, R.A. Aomar, A.A. Shakra, "Simulation-based optimization for performance enhancement of public departments". *Jordan Journal of Mechanical and Industrial Engineering*, Vol. 4, No. 3, 2010, 1995-6665.
- [19] A. Azab, A. Ziout, W. ElMaraghy, "Modeling and optimization for disassembly planning". *Jordan Journal of Mechanical and Industrial Engineering*, Vol. 5, No. 1, 2011, 1995-6665.
- [20] S.A. Altarazi, N. Mandahawai, K. Gharaibah, "In-Production Product Value: A New Method for Part Type Prioritization". *Jordan Journal of Mechanical and Industrial Engineering*, Vol. 4, No. 2, 2010, 1995-6665.
- [21] Jupp V., Sapsford R., *Data collection and analysis*. London: SAGE, 1996.
- [22] W. Wan Mahmood, M. Rahman, M. Baba, J. Ghani, "Improving Production Line Performance: A Case Study", *Applied Mechanics and Materials*, Vol. 44-47, 2010, 4136-4140.
- [23] T. Abebe, 2020. *Introduction Of Simulation Process*. [online] Academia.edu. Available at: https://www.academia.edu/4991660/Introduction_of_Simulation_Process [Accessed 22 June 2020].
- [24] Z. T. Şimşit, N. S. Günay, and Ö. Vayvay, "Theory of constraints: A literature review," *Procedia - Social and Behavioral Sciences*, Vol. 150, 2014, 930–936.

A Conceptual Framework for Cyber-Physical Quality Monitoring System using Machine Learning

Mathew Chacko^{1,*}, Atul², Satish Babu Boddapati³

^{1,2} Mechanical Department, Alliance University, India

³ Department of Petroleum Engineering, RGIPT, Amethi, India

Received 1 Aug 2022

Accepted 5 Nov 2022

Abstract

In this paper, we propose a Cyber-Physical Quality System (CPQS) integrated framework that can predict, analyze, and validate the quality monitoring system in manufacturing with 95% accuracy in real-time using machine learning techniques. CPQS framework analyses real-time sensor networks and configures the importance of artificial intelligence-driven big data analytics for predicting the quality of cyber-physical production networks. Cyber-physical data like speed, feed, depth of cut, coolant temperature, vibrations, tangential cutting forces, and tool life for 400 parts were collected from the various sensors placed on Computerized Numerical Control (CNC) machines after doing modal analysis. Various machine learning techniques were used to predict the quality of the part wherein the inputs affecting it were predominately dominated by vibration and temperature.

Extreme Gradient Boosting (XGB) machine learning techniques out of many could predict the quality of the part with 96.2% accuracy. The caveat for the present results is that it has been tried out only for Titanium Alloy parts and the tool wear has been approximated using Taylor's equation which can be enhanced by using image processing. The model deployed in real-time could produce defect-free parts quickly. This could reduce the cost of quality by 80%, thereby increasing the production line's productivity, quality, and efficiency.

© 2022 Jordan Journal of Mechanical and Industrial Engineering. All rights reserved

Keywords: Cyber-Physical Systems, Machine Learning, Modal Analysis, Tangential Cutting Forces.

1. Introduction

The prediction of the quality of a machined part, while it is being manufactured, saves unnecessary time and money spent on inspection in the Cyber-Physical Quality System (CPQS) [1-2]. The accurate prediction of the quality of a machined part, while it is being manufactured, prevents quality failures in real-time and maintains compliance. It optimizes material usage, quickly isolates defects, and increases contribution margins [3-4]. This will help manufacturing companies stay competitive because the part can be manufactured quickly, at low cost, and with high quality. This study deals with the implementation of CPQS in a real factory setting to produce maximum parts and predict the quality of manufacturing of a flange in a CNC milling machine using different machine learning techniques. [5]. Industry 4.0 envisions new technologies [6], like the Internet of Things (IoT), Cyber-Physical-Systems (CPS), Big Data, High-Performance Computing (HPC), Edge Computing, and Cloud Computing for setting up a Digital Twin Shop-Floor that encompass an effective way to create the physical-virtual convergence of the real, virtual world and their connections. With the digital twin [7] serving as a digital controller of the real-world

manufacturing system we can use applications powered by Artificial Intelligence (AI) [9] to understand the manufacturing parameters that affect quality. With AI technology becoming more mature and affordable, new applications have been introduced into production systems to support manufacturers in complex decision-making and business processes [10]. Machine Learning (ML), a subset of AI, focuses on extracting useful knowledge [11] into the bottleneck of the problem through the learning and training process with a large volume of both structured and unstructured data [12-14]. Some of the machine learning applications used in manufacturing process diagnosis involve Logistic Regression, K Nearest Neighbor's (KNN), Support vector machine classifier (SVC), Gaussian Naïve Bayes (GNB), Decision Tree, Random Forest, Extreme Gradient Boosting (XGB), and Multi-Layer Perceptron (MLP) techniques [15-16]. These help in optimizing the manufacturing process for better quality and cheaper costs. Cyber-physical systems are also widely used in the manufacturing and processing industry to monitor product quality in real time. Computer vision systems are used to control robots, CNC machines, conveyors, and other equipment in the autonomous production line to automatically detect anomalies during machining [17]. The various modeling techniques that

* Corresponding author e-mail: chacko1959@yahoo.com.

have been used include Petri Nets (PNs) which simulate various types of asynchronous and concurrent processes in an industrial production system [18]. Smart Partial Least Squares/ Statistical Package for Social Sciences (PLS/SPSS) techniques are used to identify the correlation functions between the input and output parameters and machine-learning techniques are used to identify the anomalies.

1.1. Literature Survey

Manufacturing quality control is the ability to measure parts and provide assurance that parts have been produced according to their specifications. This is achieved by inspecting all incoming raw materials and establishing inspection points along the manufacturing process, to ensure part quality and spot any quality variations before they have an impact on the dimensional accuracy and surface finish. Broadly all research papers written so far can be classified as either Theoretical, Practical, or Simulation type based on the parameters of dimensional quality, surface finish, or both.

Table 1. Classification of papers

Focus Area		
Type of Research	Dimensional Quality	Surface finish
Theoretical	[19], [29], [23], [24], [25],[27],[28]	[21], [22], [26]
Experimental	[31],[33], [34], [35], [36]	[29] [32], [35]
Simulation	[37], [38], [39], [40],[41],[43],[43],[44],	

[] Reference papers

1.1.1. Theoretical:

Some of the theoretical studies done on this topic include

1. Developed a methodology for the development of an intelligent quality function deployment (IQFD) application for the Manufacturing Process. [19]
2. Review the challenges and limitations of the optimization techniques used in optimizing machining parameters in milling operations. [20]
3. Studied the correlation between primary waviness and roughness during hard turning through mathematical modeling. [21]
4. A paper that talks of various surface quality improvement techniques, including how to reduce surface defects, surface roughness, and dimensional inaccuracy [22]
5. b) Study on dimensional quality and distortion analysis of thin-walled alloy parts [23]
6. c) Study on combining online testing, sensor, network, and database technologies and quality control methods to realize the online process quality control system. [24]
7. Quality control methods for product reliability and safety using optimization techniques [25]
8. In this study, mathematical models were developed that established the correlation between input variables and quality characteristics in the plasma Computer Aided Manufacturing (CAM) process using Response Surface Methodology (RSM). [26]

9. Review paper on studies conducted on the interoperability between Internet of Things-based real-time production logistics and cyber-physical process monitoring systems. [27]
10. This paper reviews the current research on the Internet of Things-based real-time production logistics, sustainable industrial value creation, and artificial intelligence-driven big data analytics in cyber-physical smart manufacturing systems. [28]

1.1.2. Experimental:

Some of the experimental studies conducted include

1. A detailed study of the effects of machining parameters on the surface roughness in the end-milling process. [29]
2. Optimization of surface roughness in end milling using the Response Surface Method and Radian Basis Function Network. [30]
3. Setting up a web-based automated inspection of manufactured parts wherein they developed a platform to study the quality parameters. [31]
4. Select process parameters based on the Taguchi orthogonal array technique and use the analysis of variance (ANOVA) to establish a relationship between input parameters and surface roughness as output characteristics. [32]
5. Tool wears monitoring using in-process machine vision for Cyber-Physical Production Systems (CPPS): The author of this study [33] proposes a four-phased approach based on the CPS for in-process tool wear monitoring using machine vision.
6. Using a machine vision system to measure
7. tool wear parameters: In this study, they captured tool wear photographs with digital cameras and used image processing techniques to determine the tool wear zone to take necessary action. [34].
8. Data from a spindle probe, a coordinate measuring machine, and surface roughness data are used to characterize machine quality features, namely dimensional accuracy, and surface roughness. [35].
9. The impact of variables cutting speed, feed rate, depth of cut cooling method, blank size, and work material on the dimensional accuracy and surface quality of turned parts were investigated in this study. [36].

1.1.3. Simulation:

Some of the studies done about simulation are to do with understanding the relationship between deep learning-assisted smart process planning and Internet of Things-based real-time production logistics as regards cyber-physical smart manufacturing systems. This include

1. Design of a model for turning involving a neural network controller to track the desired vibration level of the turning machine. [37]
2. The Service-Oriented Cross-layer infRAstructure for Distributed smart Embedded devices (SOCRADES) is an initiative to achieve predetermined automation goals in which networked systems made up of smart embedded devices, collected data from a service-oriented ecosystem. [38]
3. Integration of process and quality control using multi-agent technology (MAT) (Ref: GRACE European Project). Using multi-agent system (MAS) principles,

performed real-time data analysis to dynamically modify production factors wherein concepts like Product Type Agents (PTA), Product Agents (PA), Resource Agents (RA), Independent Meta Agents (IMA), and other dynamic self-adaptation techniques along with feedback control loops were implemented. [39]

4. Adaptive Production Management (see: ARUM European Project). The project developed production planning, scheduling, and optimization strategies using agent technology to respond to anomalies according to Service-Oriented Architecture (SOA) principles. [40]
5. Deterministic models also have traditionally tested extraordinarily beneficial during the current industrial revolution involving digital data. Key deterministic models for distributed cyber-bodily systems have sensible faithful realizations through Cyber-physical structures. [41].
6. 5C architecture for the implementation of a CPS involves (i) Smart Connection (ii) Data-to-information conversion (iii) Cyber level (iv) Cognition (v) Configuration [42].
7. Empirical studies on the IoT- based real-time production logistics, cyber-physical process monitoring systems, and industrial artificial intelligence in sustainable smart manufacturing. [43]
8. Simulation studies and analyses on how data-driven supervision, predictive analytics, and optimization systems integrate product traceability, maintenance, and process performance in smart manufacturing. [44]

As per the literature survey done above, there is a need to analyze real-time sensor networks and configure the importance of artificial intelligence-driven big data analytics for use in cyber-physical production networks which is what this paper intends to do.

The rest of the paper is organized as follows. In section 2, the machining process parameters and their responses are discussed. Section 3 describes the proposed approach to developing a cyber-physical quality system. Section 4 gives a sneak preview of the experimental setup. Section 5 is all about data extraction and analysis. Results are explained in section 6. Conclusions are shown in section 7.

2. Machining process parameters and responses

The behavior of the product is depicted in Figure 1. below

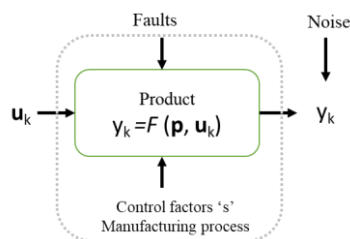


Figure 1. The general scheme of the product

can be described by the following relation

$$y_k = F(p, u_k) + \epsilon_k \tag{1}$$

where u_k and y_k are product inputs and outputs, respectively. p are parameters representing the physical characteristics of product components. Control factor s influence these values, in the production process. $F(\cdot)$ is the

relation between inputs, output, and parameters describing the behavior or properties of the product and ϵ_k represents the noise

The control factors 's' involved in CNC manufacturing are:

- Feed rate: The feed rate CNC parameter is the speed at which the cutter moves across the face of the material. It is measured in distance units per minute (e.g. millimeters per minute, or inches per minute).
- Plunge rate: Plunge rate is the speed at which the bit enters the material, meaning that this CNC parameter affects only pure vertical movement. It is measured in distance units per minute (e.g. millimeters per minute, or inches per minute).
- Depth per pass: Usually, a non-industrial CNC machine doesn't have enough power to cut through all the material thickness in a single attempt, unless you are cutting a soft and thin piece of material with a large bit. That's why your project will likely require multiple passes to get the desired depth. The CNC parameter – depth per pass dictates how deeply your machine carves down into your material on each pass.
- Spindle speed: Spindle speed is the speed at which your cutting tool rotates. It is measured in RPM (revolutions per minute).

2.1. Surface roughness

The theoretical one-dimensional expression of surface roughness R for a surface of profile length d is

$$R = \frac{1}{d} \int_0^d |f(x)| dx \tag{2}$$

where $f(x)$ is the difference between the local surface height at position x and the mean height over the profile based on the assumption that the overall profile is even. If the height f_n is measured at N locations along with the profile length d , the expression of the roughness is:

$$R \approx \frac{1}{N} \sum_{i=1}^N |f_n| \tag{3}$$

Converting the expression of surface roughness to a two-dimensional surface profile area A . The surface roughness of area A with $N \times M$ tested differences f_{ij} can be approximated as:

$$R \approx \frac{1}{NM} \sum_{i=1}^N \sum_{j=1}^M |f_{ij}| \tag{4}$$

2.2. Dimensional accuracy

Though CNC machining has the ability of manufacturing parts with complicated shapes, the dimensional accuracy is a limitation of the machining parameters like speed, feed, depth of cut, coolant temperature, material properties, and tool condition.

Dimensional accuracy is the deviation between the nominal size and the measured size of an as-built part. In this work, the lengths (L), widths (W), and heights (H) of the Computer-Aided Design (CAD) model of the part and the built part is used to define the dimensional accuracy [18]. The expressions of dimensional accuracy are

$$DL = |L_d - L_e| \tag{4}$$

$$DW = |W_d - W_e| \tag{5}$$

$$DH = |H_d - H_e| \tag{6}$$

where DL, DW, and DH denote the deviations, and the subscripts 'd' and 'e' denote the nominal size from the CAD model and the measured size from the as-built part, respectively.

3. Proposed Approach

A Cyber-Physical Quality System (CPQS) is an integration of computation, networking, and physical processes for measuring the quality of manufactured parts. It involves embedded computers and sensory networks that monitor and control the physical processes, with feedback loops, wherein physical processes affect computations and vice versa. The first step involves designing a CPQS architecture framework based on the collaboration among, manufacturing execution systems, the internet of things (IoT), simulations using artificial intelligence, advanced need quality systems for quality prediction, and operation control as in Figure 2.

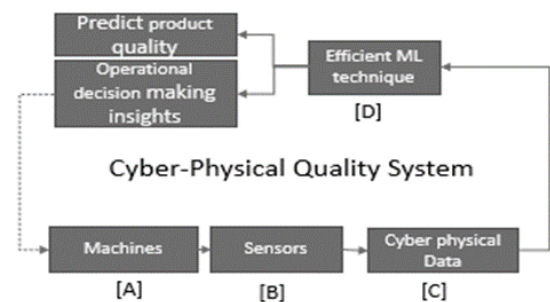


Figure. 2 The cyber-physical quality system framework

Based on this framework we can create a reconfigurable quality system as shown below in Figure.3.

which can predict the quality of the component being manufactured and appropriately take actions to ensure a defect-free production. This reconfigurable quality management system involves collecting the data from the CNC controllers, multi-sensory systems, and the local terminal which monitors the machining processes and transmits it to the database server. The features from these data and the signals are its time /frequency are then

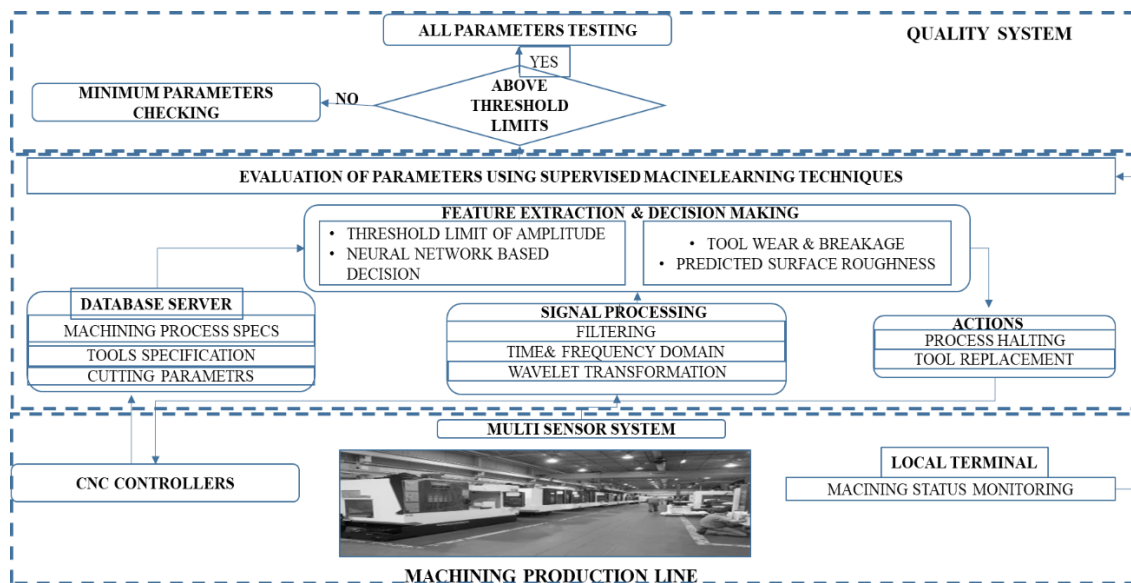


Figure 3. Reconfigurable quality management system

extracted and using different machine learning techniques are used to predict the tool wear, and surface finish and thereby accurately predicting the quality of the part being manufactured. This leads to producing quality parts and in case of anomalies taking actions to change the tool or stop the process thereby ensuring quality output at all times. The various environments involved in such a setup are described in detail.

3.1. Machining Environment

The manufacturing environment consists of the process, machine, tools, coolant, the part to be machined, and inspection gadgets.

3.1.1. Part

The part to be manufactured is the Hinge as shown in Figure 4

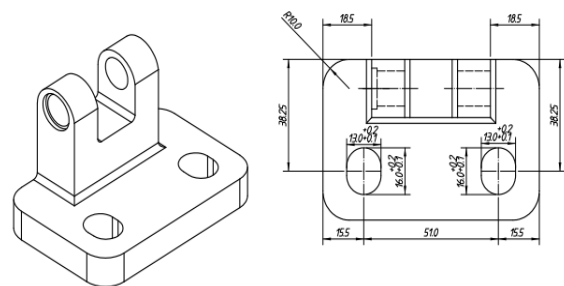


Figure 4. Hinge Type A

This is used to support the doors of any vehicle. It consists of two numbers per door and is different for the left vs right side of the vehicle. Its dimensions are crucial and they have to be within the tolerance limits to ensure that the doors close properly. 25 crucial parameters need to be checked for dimensions and the surface quality has to be within the permissible limits for the part to be adjudged as having passed the quality test

3.1.2. Machine

The machine used for manufacturing this part is the most versatile OKADA VM500 milling machine fitted with all the sensors and cameras as shown in Figure 5.



Figure 5. OKADA VM500 machine with sensors and cameras

3.1.3. Tools

To manufacture the part, we use mainly 3 tools. We use the milling cutter having carbide inserts (T1) for all the milling operations. This tool has Taylor's tool life exponent $n = 0.143$ and the constant $C=48.1$ for a cutting speed of 30m/sec. and is changed typically, after producing 50 components. The second tool (T2) is HSS used for all drilling operations. This tool has Taylor's tool life exponent $n = 0.2$ and the constant $C=63.53$ for a cutting speed of 30m/sec. This tool is changed after every 40 components are produced. The last tool (T3) is a forming/chamfering tool with Taylor's tool life exponent $n = 0.143$ and the constant $C=48.1$ for a cutting speed of 30m/second is used for making 80 components before it is re-sharpened or a new tool is replaced.

3.2. Sensor Environment

The various sensors used are for temperature, displacements, and vibration. Three types of vibrations are generated throughout the turning process: free, forced, and self-excited. These vibrations are caused by the machine tool system's lack of dynamic stiffness/rigidity, work material, machine, tool, and holder. Free vibrations are caused by shock, while forced vibrations are caused by machine tool imbalance, misalignment, mechanical rigidity, and gear faults. Frictional chatter is caused by rubbing on the clearance face, which causes vibration in the cutting force (F_c) and thrust force (F_t) directions. Temperature and strain rate in the plastic cause thermo-mechanical chatter. The presence of chatter has the following negative consequences: Poor surface quality, tool wear and damage, lower rate of material removal, waste of time, effort, energy, and higher costs in terms of production time. Hence the vibration sensors must be placed rightly in the right places for the experiments to be meaningful accordingly we need to do the vibration analysis of the spindle shown in Figure 6.

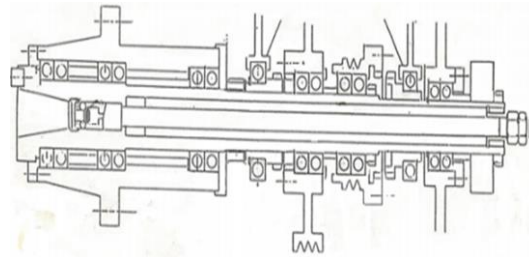


Figure 6. Schematic diagram of the spindle

3.2.1. 3D Model of the spindle

To carry out the modal analysis we need to first model the spindle, bearing, tool holder, and tool using the Computer-Aided Three dimensional Interactive Application (CATIA) software. A model of the same is shown in Figure 7.

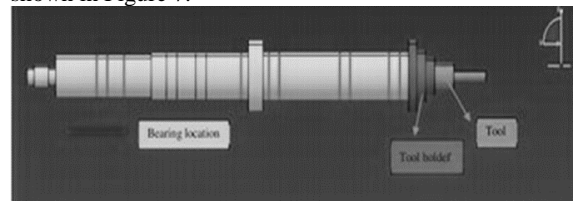


Figure 7. Model in CATIA

3.2.2. Modal analysis of the spindle

The spindle system model was imported into ANSYS® software and we used BEAM188 and SOLID187 elements. COMBIN14 elements for the bearings. The material property was that of tool steel with young's modulus, $E = 210 \text{ GPa}$, and density $= 7850 \text{ Kg/m}^3$ applied. four spring-damper elements replaced each bearing location as shown in Figure 4. At $k = 2.25 \times 10^8 \text{ N/m}$ is the natural frequency. The first natural frequency was zero as the spindle was not constrained along the longitudinal translational direction, the second/third, fourth/fifth, and sixth/seventh natural frequencies represent the bending of the spindle in Z/Y directions respectively, and the eighth natural frequency represents the torsional vibration of the spindle, as shown in Figure 8.

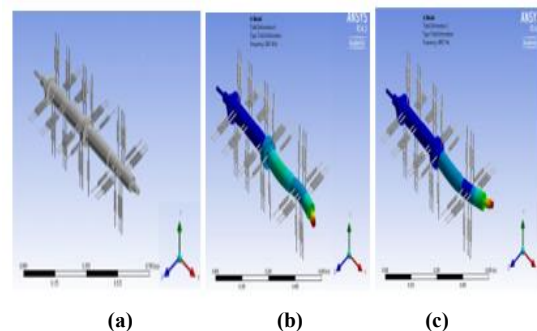


Figure 8. a) Solid with spring-damper b)8th c) 2nd -5th natural frequencies

Based on the above analysis the location to fix the vibration sensor was finalized which would give us the best output.

3.3. Digital Environment

The digital environment consists of two phases namely the development of a prediction model and quality performance prediction using machine learning techniques as shown in Figure 9

The steps involved in the prediction model development involve determining the Critical To Quality (CTQ) of the component to be manufactured and identifying the significant parameters that impact CTQ. The next step would be to determine the location of the sensors and build the model with the appropriate transfer functions determined through machine learning techniques

The performance metrics in the classification problem are different from regression problems. In classification, accuracy is a basic metric and more robust metrics are F1 score, Precision, and Recall [45]. The proper metric is selected based on the problem that is dealt with. In this scenario, the target is to predict the occurrence of output 0, so that we can make the required changes in the input features so that the overall cost of production is lowest.

Thus, Recall and Precision of classification 0 are more important than accuracy. Recall gives the fraction of 0's that the model can identify. Precision gives the fraction of relevant instances to retrieved instances [19]. We need high recall to identify all the Not ok quality manufactured pieces and the max possible precision.

Models with accuracy > 79% for Dimension prediction and models with accuracy > 86.25% for surface finish are reported in the Results section because any lesser accuracy means that any model giving 1's to all input can achieve the cut-off accuracy levels.

4. Experimental Set-Up

The overall experimental setup consists of the physical resources namely machines, tools, and sensors. Along with that, we have the local and database servers where the data of the processes and pre-processing of the sensor signals are done. We use cloud services for advanced signal processing and cognitive decisions making as shown in Figure 10.

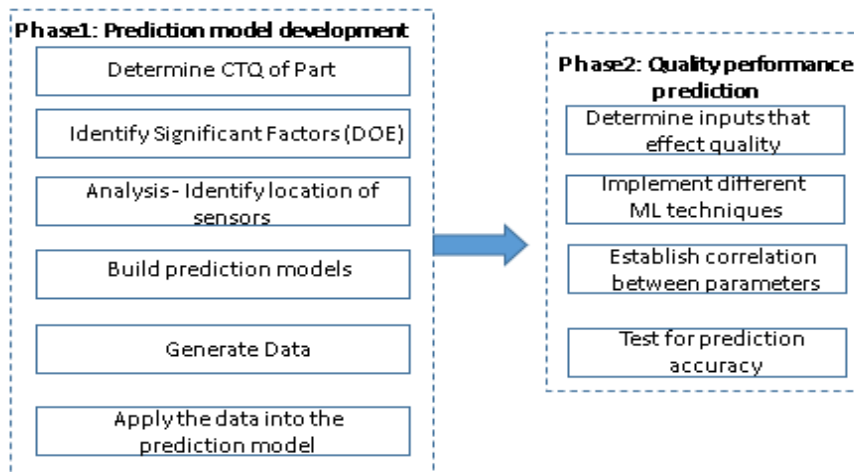


Figure 9. Stages of prediction model development and quality

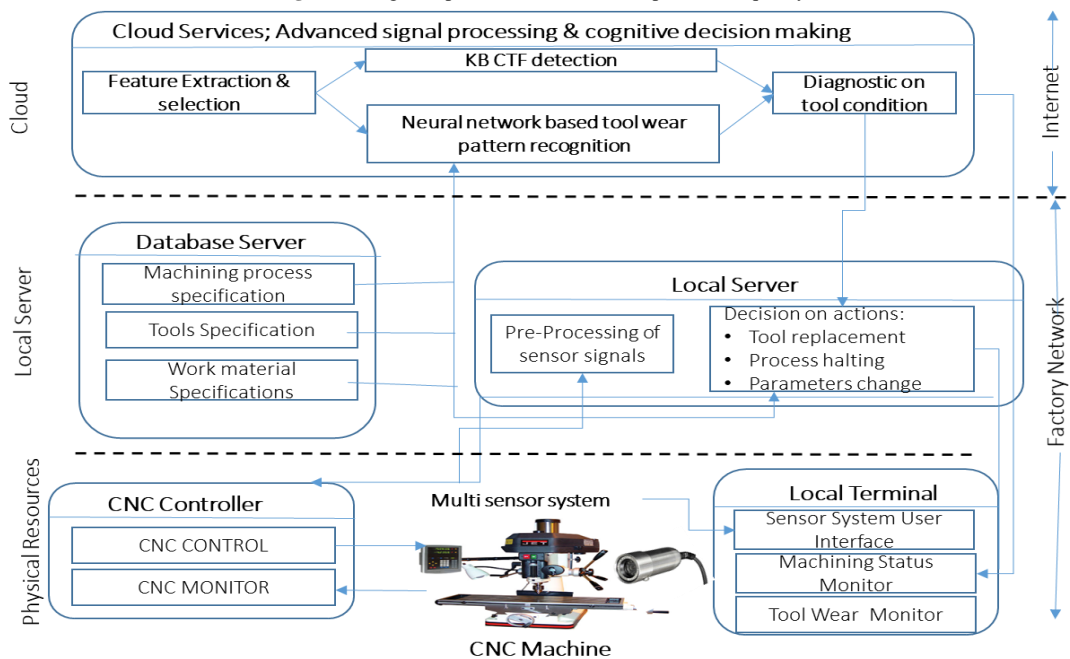


Figure 10. Experimental set-up

5. Feature Extraction and Analysis

5.1. Understanding Data

The data is collected for 400 flanges manufactured by varying different input parameters and values of target variables are decided after physical observation. Data is of dimension 400*11. 400 rows with 11 columns that contain 8 input features and 3 target variables.

Input features are speed (m/min), Feed (mm), depth (mm), coolant temperature (Celsius), Vibration (mm/sec), and the tool life of T1, T2, and T3 tools measured in min. Target variables include dimension quality, quality of surface finish, and final quality all taking the values 1 or 0, interpreted as Quality is ok, and Quality is not Ok respectively. The final quality is 1 if both the dimensional quality and quality of the surface finish are 1, else 0. In this paper, we try to predict the independent target variables, since the final quality can be calculated based on these 2 target variables. Statistical analysis of the results was done, to ensure that the differences in performance are statistically significant or not by using Friedman Aligned Rank Test using IBM SPSS gave the following results as in Table 2.

Table 2. Friedman Test statistics

Test Statistics ^a	
N	400
Chi-Square	9851.329
df	27
Asymp. Sig.	<.001

a. Friedman Test

wherein it was observed that the p-value < 0.05.

5.2. Data Preparation

The data is clean devoid of any null values and there are no irregular data types. The next step is to check for outliers. Box plot is constructed for the input parameters and observed for any outlier values based on [46]. Only the Coolant temperature is found to have 16 points as outliers where the temperature is less than 28.5 C as shown in Figure 11.

5.2.1. Coolant temperature distribution

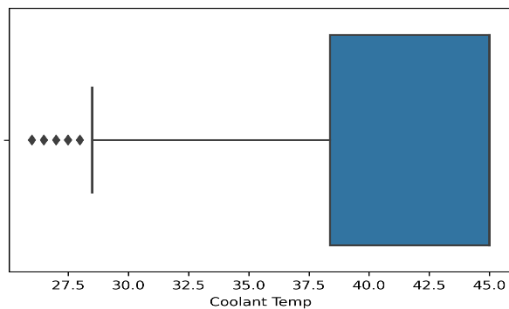


Figure 11. Box plot for Outlier detection

These 16 points correspond to 4% of the data and their effect on the result is negligible. Hence no manipulation is made of the data. The reason is that this temperature

reflects the starting point of the CNC machine and as the machine's working time progresses, the temperature increases [47].

5.3. Data Visualization

Pair plots and correlation heat maps [48] are made for the data to identify dependencies and pattern recognition. The correlation heat map is shown in Figure 12.

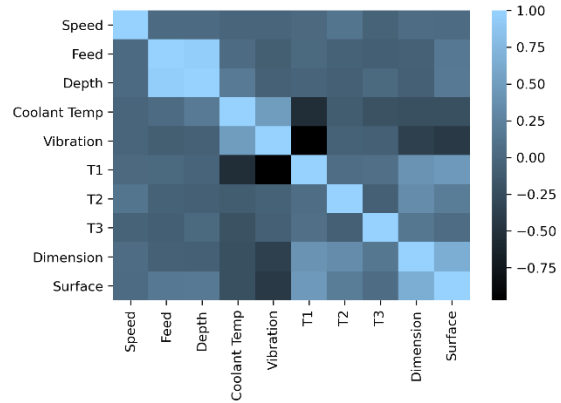


Figure 12. Correlation heat map

From the heat map, it is observed that dimensional quality is highly correlated to T1, and T2 tool life & vibration, and weakly correlated to coolant temperature. Surface finish quality is highly correlated to T1 & vibration and weakly correlated to coolant temperature and T2. Distribution plots for the input features are prepared. To understand the data better and check for the usefulness of features in predicting the target variables, kde (kernel density estimation) of the parameters T1, T2, and Vibration are shown in Figure.13 and Figure.14 using target variables as hue. As predicted high density of target variable 0 is observed at a high level of vibration and low tool life.

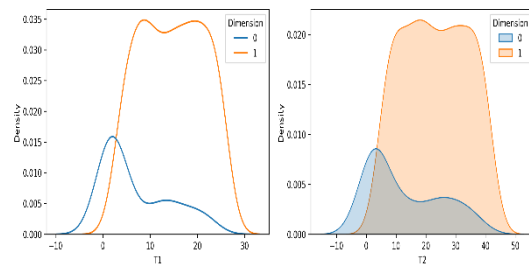


Figure 13. Kde Plots of T1 and T2 using dimension as hue.

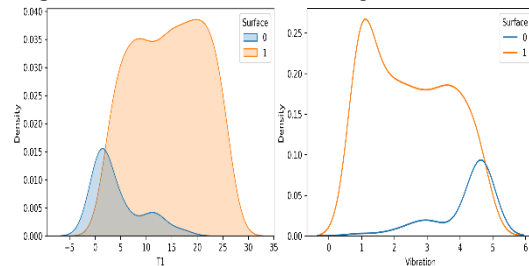


Figure 14. Kde Plots of T1 and Vibration using surface quality as hue

5.4. Data Modeling

This is a case of multi-label classification supervised learning. For optimal performance and high control of the process, the target variables are modeled independently and in two ways in each case. The results are compared to finalize the best model and the final quality is predicted by combining the predicted targets from the selected best models. The summary is shown in Table 3.

Table 3. Input features and target predicted for each method

Method	Input features used	Target predicted
1	T1, T2, and Vibration	Dimension quality
2	All 8 parameters	Dimension quality
3	T1 and vibration	Surface finish
4	All 8 parameters	Surface finish

The first step of modeling is to check if the data set is balanced or not. The count plot for Dimension and surface finish is shown in Figure 15. Category 0 implies the quality is not ok, while 1 implies ok. There is an imbalance in the data set but the modeling performed with stratified training and test data gave good results. Thus, no special techniques are used for further data processing.

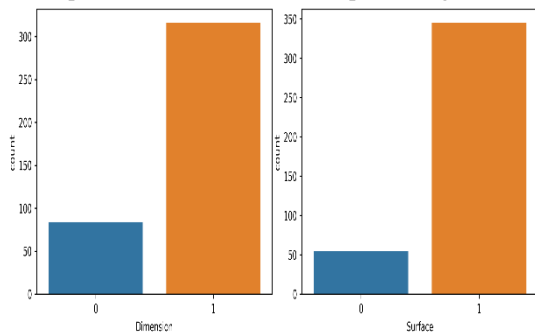


Figure 15. Count plot for Dimension and Surface finish

Dimension has 84-0's and 316-1's resulting in 21% minority class, while the Surface finish has 55-0's and 345-1's giving 13.75% as a minority class.

5.5. Data Analysis

The data is split using sklearn [49] test train split, test size =0.3, random state=42, and stratified using output variable considered in each method and then different models are applied to training data and the results are validated on the test set. The machine learning techniques evaluated are Logistic Regression, K Nearest Neighbors (KNN), Support Vector Machine Classifier (SVC), Gaussian Naïve Bayes (GNB), Decision Tree, Random Forest, Extreme Gradient Boosting (XGB), Multi-Layer Perceptron (MLP) classifiers and Artificial Neural Networks (ANN).

5.5.1. Dimensional accuracy

Dimensional accuracy is measured using method 1 and method 2 mentioned above with a cut-off of 79%.

1. Method-1: The performance of these models for Recall, F1 score, and Accuracy are shown in Figure 16. concerning input parameters T1, T2, and Vibration. To see that the models are not overfitted, Grid search CV

is used to find optimized hyperparameters of the model and are validated on test data. In some cases, there are already available techniques in the model used instead of Grid search CV.

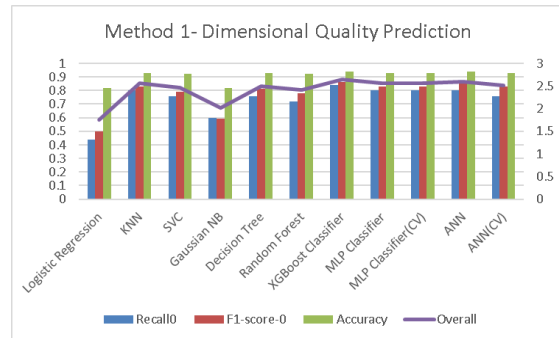


Figure 16. Plot for Dimensional accuracy using different ML techniques

It can be seen that Logistic regression and Gaussian Naïve Bayes have accuracies higher than cut-off accuracies, however, the Recall and F1 scores are poor. K Nearest Neighbours (KNN),

SVC, Decision tree, Random Forest, MLP, and ANN produced similar results but the best was given by XG Boost with values of 0.84for Recall,0.86 for F1 score and 0.96 for accuracy.

2. Method- 2: The performance of these models concerning Recall, F1 score, and Accuracy are shown in Figure 17. for all 8 input parameters.

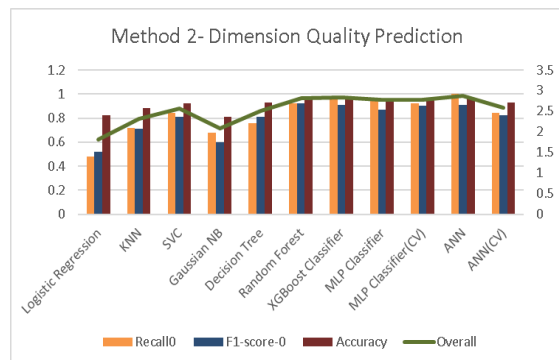


Figure 17. Plot for Dimensional accuracy using different ML techniques- method2

Here also we see that Logistic regression and Gaussian Naïve Bayes have accuracies higher than cut-off accuracies, however, the Recall and F1 scores are poor. K Nearest Neighbours (KNN), SVC, and Decision tree produced similar results, and Random Forest and MLP gave better results but again XG Boost and ANN gave marginally better results of 0.96for Recall,0.91 for F1 score, and 0.96 for accuracy.

5.5.2. Surface Finish

Surface Finish is measured using method 3 and method 4 mentioned above with a cut-off at 86.25%.

1. Method-3: The performance of these models for Recall, F1 score, and Accuracy are shown in Figure 18. for input parameters T1and Vibration. To see that the models are not overfitted, Grid search CV is used to find optimized hyperparameters of the model and are

validated on test data. In some cases, there are already available techniques in the model used instead of Grid search CV

It can be seen that Logistic regression, K Nearest Neighbours (KNN), Decision tree and Random Forest have accuracies higher than cut-off accuracies, however, the Recall and F1 scores are poor, SVC, MLP, XG Boost, and ANN produced similar results of 0.59 for Recall, 0.71 for F1 score and 0.93 for accuracy. All of them are equally good at predicting.

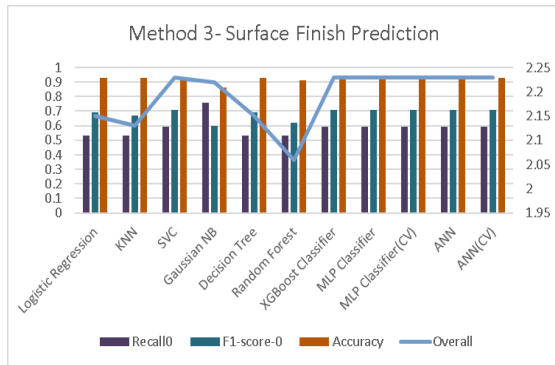


Figure 18. Plot for Surface finish prediction using different ML techniques- method 3

2. Method- 4: The performance of ML models for Recall, F1 score, and Accuracy are shown in Figure 19. for all 8 input parameters.

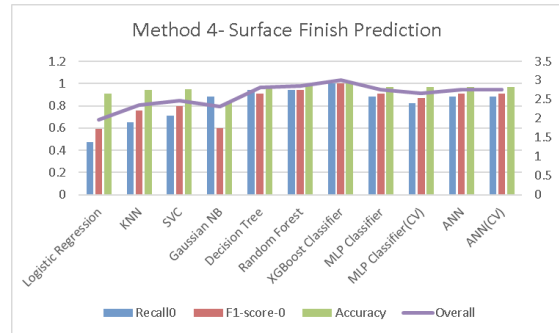


Figure 19. Plot for Surface finish prediction using different ML techniques- method 4

It can be seen that Logistic regression, K Nearest Neighbours (KNN), SVC, and Gaussian NB have accuracies higher than cut-off accuracies, however, the Recall and F1 scores are poor, Decision tree, Random Forest, MLP, and ANN produced similar results, but the best was given by XG Boost with values of 1.0 for Recall, 1.0 for F1 score and 1.0 for accuracy.

It can be concluded from the above that Extreme Gradient Boosting as shown in Figure 20. is a supervised learning algorithm that is similar to RF, that tries to accurately predict a target variable by combining the estimates of a set of simpler, weaker models. is the best for predicting both the dimensional accuracy and surface finish.

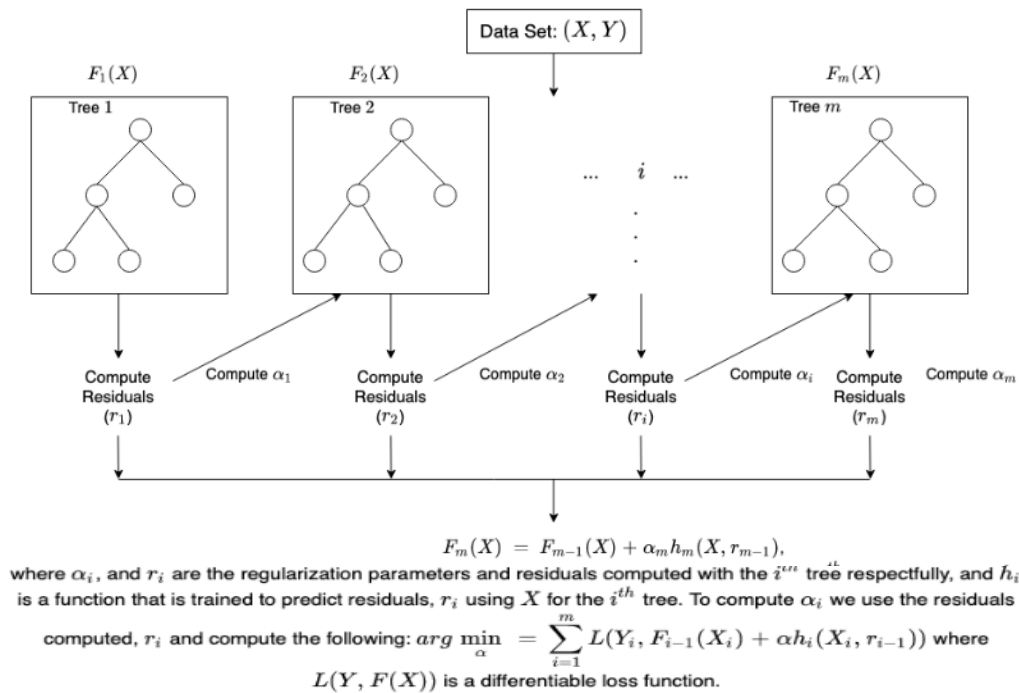


Figure 20. XG Boost illustration

To look at the overfitting issue, the classification error on both training data and test data is observed and early stopping is used. Training loss and testing loss of different methods are shown in Figure 21.

6. Results and Discussions

6.1. Quality Performance Prediction

This integrated framework wherein all the input parameters are captured in real-time with the sensors placed at the appropriate positions based on modal analysis and using the appropriate models can predict up to 25 output parameters with 96.2% accuracy. The results of all the models are shown in Table 4 below of which the top 4 models that are tuned with the best hyperparameters decided using Grid search CV are SVC, Random Forest, XG Boost Classifier, and MLP Classifier (CV).

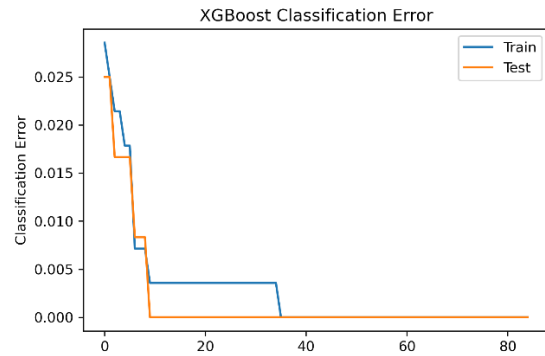


Figure 21. Classification error

The parameters used in modeling the above are given in Table 5 below:

Table 4. Recall-0, F1 score -0, and accuracy of all models

Model	cutoff= 79%						cutoff= 86.25%					
	Dimension Quality prediction						Quality of Surface finish prediction					
	Method1			Method2			Method3			Method4		
	Recall0	F1-score-0	Accuracy	Recall0	F1-score-0	Accuracy	Recall0	F1-score-0	Accuracy	Recall0	F1-score-0	Accuracy
Logistic Regression	0.44	0.5	0.82	0.48	0.52	0.82	0.53	0.69	0.93	0.47	0.59	0.91
KNN	0.8	0.83	0.93	0.72	0.71	0.88	0.53	0.67	0.93	0.65	0.76	0.94
SVC	0.76	0.79	0.92	0.84	0.81	0.92	0.59	0.71	0.93	0.71	0.8	0.95
Gaussian NB	0.6	0.59	0.82	0.68	0.6	0.81	0.76	0.6	0.86	0.88	0.6	0.83
Decision Tree	0.76	0.81	0.93	0.76	0.81	0.93	0.53	0.69	0.93	0.94	0.91	0.97
Random Forest	0.72	0.78	0.92	0.92	0.92	0.97	0.53	0.62	0.91	0.94	0.94	0.98
XGBoost Classifier	0.84	0.86	0.94	0.96	0.91	0.96	0.59	0.71	0.93	1	1	1
MLP Classifier	0.8	0.83	0.93	0.96	0.87	0.94	0.59	0.71	0.93	0.88	0.91	0.97
MLP Classifier(CV)	0.8	0.83	0.93	0.92	0.9	0.96	0.59	0.71	0.93	0.82	0.87	0.97
ANN	0.8	0.85	0.94	1	0.91	0.96	0.59	0.71	0.93	0.88	0.91	0.97
ANN(CV)	0.76	0.83	0.93	0.84	0.82	0.93	0.59	0.71	0.93	0.88	0.91	0.97

Table 5. Parameters used in modeling

Parameters used in modelling					
Model	Data	Method1	Method2	Method3	Method4
Logistic Regression	Actual	Default Parameters	Default Parameters	Default Parameters	Default Parameters
KNN	normalize	n_neighbors=3	n_neighbors=4	n_neighbors=6	n_neighbors=4
SVC	normalize	C=100,gamma=1,Kernel=rbf	C=10,gamma=1,Kernel=poly	C=100,gamma=1,Kernel=rbf	C=100,gamma=0.1,Kernel=rbf
Gaussian NB	Actual	Default Parameters	Default Parameters	Default Parameters	Default Parameters
Decision Tree	Actual	max_depth =3	max_depth =5	max_depth =1	max_depth =5
Random Forest	Actual	max_depth =3, estimators=9	max_depth =5, estimators=9	max_depth =1, estimators=15	max_depth =5, estimators=6
XGBoost Classifier	Actual	early stopping	early stopping	early stopping	early stopping
MLP Classifier	Actual	Default Parameters	Default Parameters	Default Parameters	Default Parameters
MLP Classifier(CV)	Actual	hidden_layer_size =40	hidden_layer_size =50	hidden_layer_size =25	hidden_layer_size =100
ANN	Actual	neurons=100, ann_default	neurons=100, ann_default	neurons=100, ann_default	neurons=100, ann_default
ANN(CV)	Actual	neurons=45, ann_default	neurons=50, ann_default	neurons=25, ann_default	neurons=60, ann_default
ann_default = Dense, 1 hidden layer, Relu activation, drop out = 0.3, adam optimizer					

All the models improved when the number of input features increased. Method 2 and method 4 have higher performance metrics than method 1 and method 3 respectively. It is observed that tree models have performed better than other models. XGB being a robust algorithm was able to predict the surface finish quality very perfectly using all features. RF and MLP gave very close results in method 2. Overall XGB is the best method for predicting both dimension quality and surface quality. RF and MLP are based on random generators and hence the results are not the same for each run, but similar results are achieved.

6.2. Decision-Making Insights:

The insights that we get into the live conditions of the manufacturing parameters and their effect on the dimensional and surface quality assist the operator in taking decisions like changing the tools or machine parameters resulting in error-free manufacture of components. It also helps in extracting maximum usage of the tool before it is worn out and brings in a paradigm shift in the process of changing tools after a specific number of operations. It would reduce the time spend on quality inspections as we are able to predict the quality accurately by up to 96.2%. This can be further increased if we can bring in image processing to determine tool wear and train the system over a larger sample size. In the long run, these could be automated and would help in reducing the cost of operation and make defect free parts

7. Conclusion

Contrary to individual post facto studies on quality this integrated real-time CPQS framework analyses real-time sensor networks together with artificial intelligence-driven big data analytics for predicting the quality of cyber-physical production networks can be a game changer. A detailed characterization of the manufacturing parameters responsible for the quality of a component manufactured on a 5-axis milling CNC machine showed the importance of vibration and the coolant temperature. Predicting the quality (dimensional and surface finish) of the part manufactured by using various machine learning techniques showed that the XG Boost

algorithm with 96.2% accuracy was the best. The major observations can be summarized as follows:

1. Placing the sensors at the right position using modal analysis to capture vibration is important.
2. The correlation heat map showed that dimensional quality is highly correlated to T1, T2 tool life & vibration, and weakly correlated to coolant temperature while the surface finish quality is highly correlated to T1 & vibration, and weakly correlated to coolant temperature and T2.
3. This is a case of multi-label classification supervised learning hence for optimal performance and high control of the process, the target variables are modeled independently and in two ways in each case
4. The performance metrics giving the best results were accuracy, F1 score, Precision, and Recall
5. It is observed that tree models have performed better than other models. XGB being a robust algorithm was

able to predict the surface finish quality very perfectly using all features. RF and MLP gave very close results.

In continuation to the present work, the author believes that the framework can be further enhanced by introducing image processing techniques to determine the tool life rather than using Taylor's equation and increasing the sample size to improve the accuracy further and automate the production to produce defect-free parts under the auspicious Industry 4.0 paradigm.

Acknowledgments

Authors acknowledge the use of various open-source software [50-52] and thank the developer communities, Alliance university faculties, the CEO, and staff of FerAux Engineering, Bangalore India. Raw data that was generated at FerAux Engineering is available at DOI: <https://doi.org/10.6084/m9.figshare.19367234>

References

- [1] M. Chacko & Atul. "Cyber-Physical Quality Systems in Manufacturing." Turkish Journal of Computer and Mathematics Education (TURCOMAT). Vol. 12 No. 2 (2021).
- [2] T. Wang, X. Wang, R. Ma, X. Li, X. Hu, F.T.S Chan & J. Ruan. Random Forest-Bayesian Optimization for Product Quality Prediction with Large-Scale Dimensions in Process Industrial Cyber-Physical Systems. IEEE Internet of Things Journal, 7(9), 8641–8653.
- [3] Y. Chen. Integrated and Intelligent Manufacturing: Perspectives and Enablers. *Engineering*, 3(5), 588–595.
- [4] T.B. Tseng, Y. J. Kwon. "Characterization of machining quality attributes based on spindle probe, coordinate measuring machine, and surface roughness data", Journal of Computational Design and Engineering, Vol. 1, No. 2 (2014) pp 128-135
- [5] T.T. Ademujimi, M.P. Brundage & V.V. Prabhu, "A Review of Current Machine Learning Techniques Used in Manufacturing Diagnosis." Advances in Production Management Systems. The Path to Intelligent, Collaborative and Sustainable Manufacturing, 2017, Volume 513
- [6] J. Lee, B. Bagheri and H. Kao." A Cyber-Physical systems architecture for Industry 4.0-based manufacturing systems" Science Direct Manufacturing Letters 3 (2015) 18–23.
- [7] K. Alexopoulos, N. Nikolakis, & G. Chryssolouris. "Digital twin-driven supervised machine learning for the development of artificial intelligence applications in manufacturing." International Journal of Computer Integrated Manufacturing, 33(5), 429–439.
- [8] K.S. Aggour, et al (2019). "Artificial intelligence/machine learning in manufacturing and inspection." A GE perspective. MRS Bulletin, 44(7), 545–558.
- [9] L. Monostori. "AI and machine learning techniques for managing complexity, changes, and uncertainties in manufacturing." Engineering Applications of Artificial Intelligence, 16(4), 277–291.
- [10] U.M.R. Paturi & S. Cheruku. "Application and performance of machine learning techniques in the manufacturing sector from the past two decades: A review." Materials Today: Proceedings, 38, 2392–2401.
- [11] M. Sharp, R. Ak & T. Hedberg. "A survey of the advancing use and development of machine learning in smart manufacturing." Journal of Manufacturing Systems, 48, 170–179.
- [12] T. Wuest, D. Weimer, C. Irgens & K.D. Thoben. "Machine learning in manufacturing: advantages, challenges, and

- applications.” *Production & Manufacturing Research*, 4(1), 23–45.
- [13] A. Dogan & D. Birant. “Machine learning and data mining in manufacturing.” *Expert Systems with Applications*, 166, 114060.
- [14] M. Hossin, & M.N Sulaiman. “A Review of Evaluation Metrics for Data Classification Evaluations.” *International Journal of Data Mining & Knowledge Management Process*, 5(2), 01–11.
- [15] T. El-Midany, M. El-Baz & M. Abd-ElWahed.” A Proposed Performance Prediction Approach for Manufacturing Process Using Artificial Neural Networks.” (Dept.M). *MEJ. Mansoura Engineering Journal*, 36(4), 39–49.
- [16] A. Essien & C. Giannetti. “A Deep Learning Model for Smart Manufacturing Using Convolutional LSTM Neural Network Autoencoders.” *IEEE Transactions on Industrial Informatics*, 16(9), 6069–6078.
- [17] H. Yetiş and M. Karaköse, “Adaptive vision-based condition monitoring and fault detection method for multi robots at production lines in industrial systems”. *International Journal of Applied Mathematics, Electronics and Computers* 4 (Special Issue-1) pp.271–276
- [18] T. Murata. “Petri nets: properties, analysis, and applications”, *Proc. IEEE* 77 (4) (1989) pp.541–580
- [19] Z. Ahmed and A. Moosa. “An Intelligent Quality Function Deployment (IQFD) for Manufacturing Process Environment.” *Jordan Journal of Mechanical and Industrial Engineering* (3) (2009) pp 23-30.
- [20] S. Mohsen and A. Mohammed. “A Review of the Recent Development in Machining Parameter Optimization.” *Jordan Journal of Mechanical and Industrial Engineering* (16)(2) (2022) pp 205-223.
- [21] T. Mite, B. Prangoski and K. Paweł. “Mathematical Modelling and Correlation Between the Primary Waviness and Roughness Profiles During Hard Turning.” *Jordan Journal of Mechanical and Industrial Engineering*. 15. 243-249.
- [22] A.W. Hashmi, H.S. Mali, and A.Meena. "A comprehensive review on surface quality improvement methods for additively manufactured parts", *Rapid Prototyping Journal*, Vol. ahead-of-print No. ahead-of-print.
- [23] A. Ahmed, A. Majeed, Z. Atta, and G. Jia. “Dimensional Quality and Distortion Analysis of Thin-Walled Alloy Parts of AlSi10Mg Manufactured by Selective Laser Melting.” *Journal of Manufacturing and Material. Processing*. Vol 3, Issue 2, 2019, 51
- [24] T. Yu and G. Wang, "Research of online process quality control system," *IEEE International Conference on Automation and Logistics*, 2008, pp. 351-356,
- [25] B. Mrugalska and E. Tytyk, "Quality Control Methods for Product Reliability and Safety", *Procedia Manufacturing*, Volume 3, 2015, Pages 2730-2737, ISSN 2351-9789.
- [26] A. Bahram, V. Durga, N. Clara, J. Jesus and R. Fischer. “Optimizing the quality of parts manufactured by the automated plasma cutting process using response surface methodology.” *20th Annual International Solid Freeform Fabrication Symposium, SFF 2009*.
- [27] M. Andronie, G. Lăzăroiu, M. Iatagan, C. Uță, R. Ștefănescu and M. Cocoșatu. “Artificial Intelligence-Based Decision-Making Algorithms, Internet of Things Sensing Networks, and Deep Learning Assisted Smart Process Management in Cyber-Physical Production Systems,” *Electronics* 10,(20), 2497.
- [28] E. Nica, C.I. Stan, P.A.G. Luțan and R.S. Oașa (Geambazi). “Internet of Things-based Real Time Production Logistics, Sustainable Industrial Value Creation, and Artificial Intelligence-driven Big Data Analytics in Cyber-Physical Smart Manufacturing Systems,” *Economics, Management, and Financial Markets* 16(1): 52–62.
- [29] M.T. Hayajneh, M.S. Tahat, and J. Bluhm. “A study of the Effects of Machining Parameters on the Surface Roughness in the End-Milling Process”. *Jordan Journal of Mechanical and Industrial Engineering* (1) (2007) pp1-5
- [30] K. Kadrigama, M.M. Noor, N.M.Zuki.N.M, M.M. Rahman, M.R.M. Rejaba, R.Dauda, K. A. Abou-El-Hossein. “Optimization of Surface Roughness in End Milling on Mould Aluminium Alloys (AA6061-T6) Using Response Surface Method and Radian Basis Function Network.” *Jordan Journal of Mechanical and Industrial Engineering*. Vol 2, No 4, 2008 pp 209- 214.
- [31] K. Soundararajan, S.M. Ramkumar, and I. Edinborough. “A Web-Based Approach To Automated Inspection And Quality Control Of Manufactured Parts Paper” *American Society for Engineering Education Annual Conference & Exposition (ASEE)*, Montreal, CA, 2002
- [32] M.N. Islam. “Effect of additional factors on dimensional accuracy and surface finish of turned parts”, *Journal Machining Science and Technology*, Volume 17, (2013) - Issue 1 pp145-162
- [33] A.A. Thakre, V.L. Aniruddha and K. Mala, “Measurements of Tool Wear Parameters Using Machine Vision System”. *Hindawi Modelling and Simulation in Engineering*, Volume 1 (2019), Article id 1876489.
- [34] R.G. Linsa, P.R.M. Araujo, M, Corazzim “In-process machine vision monitoring of tool wear for Cyber-Physical Production Systems”. *Robotics and Computer Integrated Manufacturing* 61 (2020) pp.85-101
- [35] T.B. Tseng, Y. J. Kwon. “Characterization of machining quality attributes based on spindle probe, coordinate measuring machine, and surface roughness data”, *Journal of Computational Design and Engineering*, Vol. 1, No. 2 (2014) pp 128-135
- [36] M.N. Islam. “Effect of additional factors on dimensional accuracy and surface finish of turned parts”, *Journal Machining Science and Technology*, Volume 17, (2013) - Issue 1 pp145-162
- [37] B. I. Kazem and N. F. H. Zangana. “A Neural Network-Based Real-Time Controller for Turning Process.” *Jordan Journal of Mechanical and Industrial Engineering*, Vol 1, No 1, 2007 pp 43-55
- [38] J.L. Berg et al. “Self-Optimization and self-ConfigurATIion in wirelEss networkS (SOCRATES).” *COST 2100TD (08)422*, Wroclaw, Poland, Feb 2008.
- [39] Universita Politecnica Delle Marche “Integration of process and quality control using multi-agent technology (GRACE)” report Cordis. European Union project id:246203
- [40] A. Schirrmann.” *Adaptive Production Planning and Scheduling: The ARUM approach based on MAS and SOA technologies*” Springer International Publishing, 2019 - Technology & Engineering
- [41] E.A. Lee.” *The Past, Present, and Future of Cyber-Physical Systems: A Focus on Models*”. *Sensors* 2015, 15(3), 4837-4869.
- [42] J. Lee, B. Bagheri and H. Kao.” *A Cyber-Physical Systems architecture for Industry 4.0-based manufacturing systems*” *Science Direct Manufacturing Letters* 3 (2015) 18–23.
- [43] U.M.R. Paturi & S. Cheruku. “Application and performance of machine learning techniques in the manufacturing sector from the past two decades: A review.” *Materials Today: Proceedings*, 38, 2392–2401.
- [44] L. Monostori, B.Kadar, Z.J. Viharosy, L. Mezgar, & P.Stefan. “Combined Use of Simulation and AI/Machine Learning Techniques in Designing and Manufacturing Processes and Systems.” *Journal for Manufacturing Science and Production*, 3(2–4), 2000, pp111–118.

- [45] T. Zeugmann, et al. "Precision and Recall." *Encyclopedia of Machine Learning*, 781.
- [46] Y. Fathy, M. Jaber, and A. Brintrup. "Learning with Imbalanced Data in Smart Manufacturing: A Comparative Analysis." *IEEE Access*, 9, 2734–2757.
- [47] Z. Ge, Z. Song, S.X. Ding, and B. Huang. "Data Mining and Analytics in the Process Industry: The Role of Machine Learning." *IEEE Access*, 5, 20590–20616.
- [48] A. Kusiak. "Smart manufacturing must embrace big data." *Nature*, 544(7648), 23–25.
- [49] Pedregosa, et al., Scikit-learn: Machine Learning in Python, *JMLR* 12, pp. 2825-2830, 2011.
- [50] G. van Rossum. "Python tutorial, Technical Report CS-R952." Centrum voor Wiskunde en Informatica (CWI), Amsterdam, May 1995.
- [51] J. D. Hunter. "Matplotlib: A 2D Graphics Environment." *Computing in Science & Engineering*, vol. 9, no. 3, pp. 90-95, 2007.
- [52] M. Waskom et al. mwaskom/seaborn: *Zenodo* v0.8.1 (September 2017),

Design Optimization of Selected Mechanical Engineering Components using Variants of Rao Algorithms

Ravipudi Venkata Rao*, Niket Zinzuvadia

Department of Mechanical Engineering, Sardar Vallabhbhai National Institute of Technology, Surat-395007, Gujarat, India.

Received 9 Aug 2022

Accepted 21 Aug 2022

Abstract

The present paper proposes self-adaptive multi-population elitist (SAMPE) Rao algorithms and chaotic Rao algorithms for design optimization of selected mechanical engineering components. The proposed algorithms are applied to 25 benchmark problems and 15 mechanical engineering design optimization problems to examine their performance. The Friedman rank test is utilized to demonstrate the significance of the proposed algorithms and the algorithms are ranked according to their performance. The results obtained using the proposed algorithms are compared with the results obtained using other advanced optimization algorithms to demonstrate the effectiveness of the proposed algorithms. It is observed that the performance of the proposed algorithms is either better or competitive to the basic Rao algorithms and the other advanced optimization algorithms.

© 2022 Jordan Journal of Mechanical and Industrial Engineering. All rights reserved

Keywords: Design optimization, Rao algorithms, Self-adaptive multi-population elitist Rao algorithms, Chaotic Rao algorithms.

1. Introduction

Engineering design is a process of decision-making to achieve certain goals while satisfying the constraints and human needs[1]. The optimum engineering design topic is very important to achieve the best product in terms of performance parameters related to the product. In the field of Mechanical engineering design optimization problems, the designers consider specific objectives, such as deflection, wear, strength, weight, corrosion, etc. A complete mechanical system design optimization leads to a complex mathematical formulation with many design variables. Thus, the optimization techniques are applied to individual components than a complete mechanical system[2]. The mathematical model formulation in engineering design optimization is a complex task for researchers and designers. The design optimization problems include design variables (continuous, integer and discrete variables) and design constraints. For the good performance of engineering elements, design constraints must be satisfied.

In the present study, the proposed algorithms are applied to 25 benchmark problems and 15 standard design optimization problems. The design optimization problems are difficult to solve as they depend on many design variables and must satisfy certain design constraints. The design optimization problems solved in the present work are from mechanical engineering. To solve any design optimization problems, first the mathematical model of that problem is formulated. The mathematical model

consists of the design objective, design variables and design constraints associated with the problem. In the present work, the mathematical models of design optimization problems are taken from the literature and the proposed algorithms are applied to those problems.

The researchers have developed different metaheuristic algorithms to solve design optimization problems. However, any single optimization algorithm cannot solve all the problems efficiently. So, researchers try to develop new algorithms or modify the existing algorithms to get more efficient results. They have proposed multi-population optimization algorithms based on different advanced optimization algorithms. The sub-population-based algorithms divide the population into the number of sub-population and thus increase the diversity of the search process. The number of sub-populations changes adaptively according to the improvement in solution after each iteration. The diversity of the search process can further be improved by the inclusion of elitism approach in multi-population based Rao algorithms[3]. So, in the present study the concept of elitism is integrated with multi-population based Rao algorithms.

In recent times, researchers have found that the solution's quality can be improved by combining optimization algorithms. Chaos is one of the techniques that can be combined with different optimization algorithms to solve optimization problems of various engineering fields. Chaotic systems are nonlinear dynamical systems that are very sensitive to their initial conditions. Chaos search is a powerful technique for hybridization because of its dynamic characteristics. Chaos

* Corresponding author e-mail: ravipudirao@gmail.com.

can be included in advanced optimization algorithms in three ways (1) by substituting the random numbers of the algorithm with chaotic numbers generated using chaotic maps, (2) by using the chaotic map function for the local search approaches, (3) by chaotically generating the control parameters of algorithms. In the present work, chaos is incorporated in Rao algorithms by replacing the random numbers with the chaotic sequence that is produced by the Chebyshev chaotic map.

The rest of the paper has the following structure: section 2 presents the previously proposed advanced optimization algorithm with the concept of multi-population and hybridization to solve optimization problems. Section 3 describes the Rao, SAMPE Rao and Chaotic Rao algorithms. Section 4 describes the application of the proposed algorithms to solve benchmark problems and design optimization problems. Section 5 discusses the results obtained after applying the proposed algorithms to different problems. Section 6 presents the conclusions of the present study.

2. Literature Review

Rao and Saroj [3] presented self-adaptive multi-population elitist (SAMPE) Jaya algorithm to solve engineering optimization problems. The elitism concept was used to improve the search mechanism of the proposed algorithm. SAMPE Jaya algorithm was applied to benchmark problems, mechanical design optimization problems and micro-channel heat sink design optimization problem to evaluate its performance. Alatas [4] proposed Harmony Search (HS) algorithm that uses chaotic maps for parameter adaptation. The classical HS algorithm was integrated with seven chaotic maps and they were applied to benchmark function to test their performance. The results demonstrated that the quality of the solution was improved for some optimization problems and in some cases global searching capability of the algorithm was enhanced. Zhang and Ding [5] presented a Multi-Swarm Self-Adaptive and Cooperative Particle Swarm Optimization (MSCPSO) algorithm. MSCPSO divides PSO into four sub-swarms. All sub-swarms update the records adaptively and cooperatively. It enhances the diversity of the search method and prevents the premature convergence of the algorithm. Gandomi et al. [6] presented a firefly algorithm (FA) with chaos. FA with 12 chaotic maps was employed to find the optimum results for benchmark functions. FA mimics the social behavior of fireflies based on flashing and attraction characteristics of fireflies. FA with chaos increases the effectiveness of the search process to find the global optimum.

Rao and Patel [7] presented a modified teaching learning based optimization (TLBO) algorithm. They applied it to solve the multi-objective optimization of shell and tube heat exchanger and plate-fin heat exchanger. The cost minimization of the exchanger and maximization of heat exchanger effectiveness are two objectives. The results proved the effectiveness and accuracy of the proposed algorithm are better than other algorithms. Rao and Saroj [8] presented a self-adaptive multi-population based Jaya (SAMP-Jaya) algorithm to solve optimization problems. The exploration and exploitation rates were controlled by dividing the population into sub-populations.

The proposed algorithm was applied to benchmark problems and plate-fin heat exchanger optimization problem. The results indicated the effectiveness of the SAMP Jaya algorithm. Farah and Belazi [9] presented chaotic Jaya algorithm by implementing three new mutation strategies. The chaotic sequence generated using the proposed 2D chaotic map was integrated with Jaya algorithm. The performance of the proposed algorithm was evaluated using sixteen benchmark functions. The Comparisons of results with other algorithms showed the enhancement in results by using proposed algorithm.

Yu et al. [10] proposed multi-population chaotic Jaya algorithm (MP-CJAYA) to solve the economic load dispatch. In the proposed algorithm, the method of multi-population and chaotic optimization algorithm were applied on the original Jaya algorithm. The comparisons of results with other algorithms indicated that MP-CJAYA performs better than all the other algorithms. Arora et al. [11] presented a modified butterfly optimization algorithm to solve mechanical design optimization problems and validated the algorithm for three engineering design problems. Chakraborty et al. [12] proposed an enhanced whale optimization algorithm and solved six engineering optimization problems.

Rao and Pawar [13] proposed Self-adaptive multi population Rao algorithms and investigated the algorithms on 14 design optimization problems. Rao and Pawar [14] solved the chosen mechanical system components design optimization problems using Rao algorithms. Talatahari et al. [15] developed a material generation algorithm and implemented it for the optimum design of engineering problems. Azizi et al. [16] proposed an atomic orbital search metaheuristic optimization algorithm. The performance of the proposed algorithm was tested on constrained design problems from different engineering fields.

The metaheuristic algorithms have been used since last few decades to solve various engineering optimization problems and these algorithms have been found successful [17-19]. The metaheuristic algorithms have their benefits, but most of them rely on algorithm-specific parameters besides the general controlling parameters like the population size and the number of iterations. These algorithm-specific parameters must be tuned correctly to get better results, otherwise it adversely affects the algorithm's performance. The perfect tuning of the algorithm-specific control parameters is tiresome process, and it increases the computational efforts. So, considering the above points, Rao [20] introduced three simple, algorithm-specific parameter less and metaphor-less optimization algorithms, known as Rao algorithms.

From the above literature, it is observed that by using subpopulation-based elitist optimization algorithms and by using chaos in metaheuristic algorithms, the performance of an optimization algorithm can be improved. So, the objectives of the present study are:

- To propose SAMPE Rao and Chaotic Rao algorithms.
- To examine the performance of the proposed algorithms on benchmark problems.
- To examine the performance of the proposed algorithms on 22 engineering optimization problems.

3. Rao, SAMPE Rao and Chaotic Rao algorithms

3.1. Rao algorithms

Rao algorithms are recently developed advanced optimization algorithms[20]. There are three versions of Rao algorithms, Rao1, Rao2 and Rao3 algorithm. They utilize the best and the worst candidate solutions from the whole population to get an optimal solution during the search process. In Rao2 and Rao3 algorithms, the candidate solutions interact randomly during the search process. Let $f(x)$ is the objective function, the number of design variables is 'm' and the number of candidate solutions (population size) is 'n'. Let us assume, for any iteration number 'q', the variable 'p' corresponding to the best and worst solutions are $x_{p,best,q}$ and $x_{p,worst,q}$ respectively. The value of the variable 'p' for the candidate 'r' during the iteration 'q' is $x_{p,r,q}$. Then the following equation are used to modify the value of $x_{p,r,q}$,

$$x'_{p,r,q} = x_{p,r,q} + r_{1,p,q} (x_{p,best,q} - x_{p,worst,q}) \quad (1)$$

$$x'_{p,r,q} = x_{p,r,q} + r_{1,p,q} (x_{p,best,q} - x_{p,worst,q}) + r_{2,p,q} (|x_{p,t,q} \text{ or } x_{p,s,q}| - |x_{p,s,q} \text{ or } x_{p,t,q}|) \quad (2)$$

$$x'_{p,r,q} = x_{p,r,q} + r_{1,p,q} (x_{p,best,q} - |x_{p,worst,q}|) + r_{2,p,q} (|x_{p,t,q} \text{ or } x_{p,s,q}| - (x_{p,s,q} \text{ or } x_{p,t,q})) \quad (3)$$

where, $x'_{p,r,q}$ is the updated value of $x_{p,r,q}$. $r_{1,p,q}$ and $r_{2,p,q}$ are random numbers in the range [0, 1] for the variable 'p' during the iteration 'q'.

$$x_{new} = x_{old} + r_1 (x_{best} - x_{worst}) \quad (4)$$

$$x_{new} = x_{old} + r_1 (x_{best} - x_{worst}) + r_2 (|x_{old} \text{ or } x_{random}| - |x_{random} \text{ or } x_{old}|) \quad (5)$$

$$x_{new} = x_{old} + r_1 (x_{best} - |x_{worst}|) + r_2 (|x_{old} \text{ or } x_{random}| - (x_{random} \text{ or } x_{old})) \quad (6)$$

3.2. Self-Adaptive Multi Population Elitist (SAMPE) Rao algorithms

In SAMPERao algorithms, the whole population is divided into the number of sub-populations based on the fitness function value. Each sub-population takes charge for the exploration or exploitation of the search space. Then the concept of elitism is used to further enhance the diversity of the search process. The number of sub-populations is changed based on the improvement of the fitness value after every iteration. The flowchart of SAMPE Rao algorithms is shown in Fig. 1.

The steps of the SAMPERao algorithms are as follows:

1. Decide the number of design variables (m), population size (n), elite size (ES) and termination criterion. The maximum number of function evaluations or the number of iterations or required accuracy may be considered as a termination criterion.
2. Generate the random initial candidate solutions.
3. Divide the population into the number of sub-populations according to the fitness function value of candidate solutions (initially number of sub-populations = 2). Then substitute the 'ES' number of the worst solutions of the inferior group by the best solutions of the superior group.
4. Modify the solutions in each sub-population using equations of Rao algorithms independently. The modified solutions are kept if there is an improvement from the old solutions.
5. Combine all sub-populations. If there is an improvement in the current best solution compared to the previous best solution, then increase the number of sub-population by 1 for exploration, otherwise decrease the number of sub-population by 1 for exploitation.
6. Check the termination criterion. If it is fulfilled, then report the best optimum solution. Otherwise, repeat steps 2 to 6 again.

3.3. Chaotic Rao algorithms

The working of the Chaotic Rao algorithms is like that of the Rao algorithms. In the present study, the initial population is generated randomly and then the chaotic sequence generated using the mathematical equation of a chaotic map is used to update the candidate solutions in each iteration by replacing random numbers with chaotic numbers. For example, if Chebyshev map chaotic function is used, then Eq. (7) is used for the chaotic random number generation.

$$x_{i+1} = |\cos(k \cos^{-1}(x_i))|, x_i \in [0,1], k > 1 \quad (7)$$

where, x_{i+1} and x_i are $(i+1)^{\text{th}}$ and i^{th} term of a chaotic sequence, respectively.

Many chaotic maps are available for chaotic number generation like logistic map, Bernoulli shift map, sine map, Chebyshev map, etc. The performance of chaotic Rao algorithms is observed using the above-mentioned maps for benchmark functions and design optimization problems. Chaotic Rao algorithms using Chebyshev chaotic map give better results than those using other maps. So, in the present study Chebyshev chaotic map is used for benchmark functions and design optimization problems in chaotic Rao algorithms. The flowchart of chaotic Rao algorithms is shown in Fig. 2.

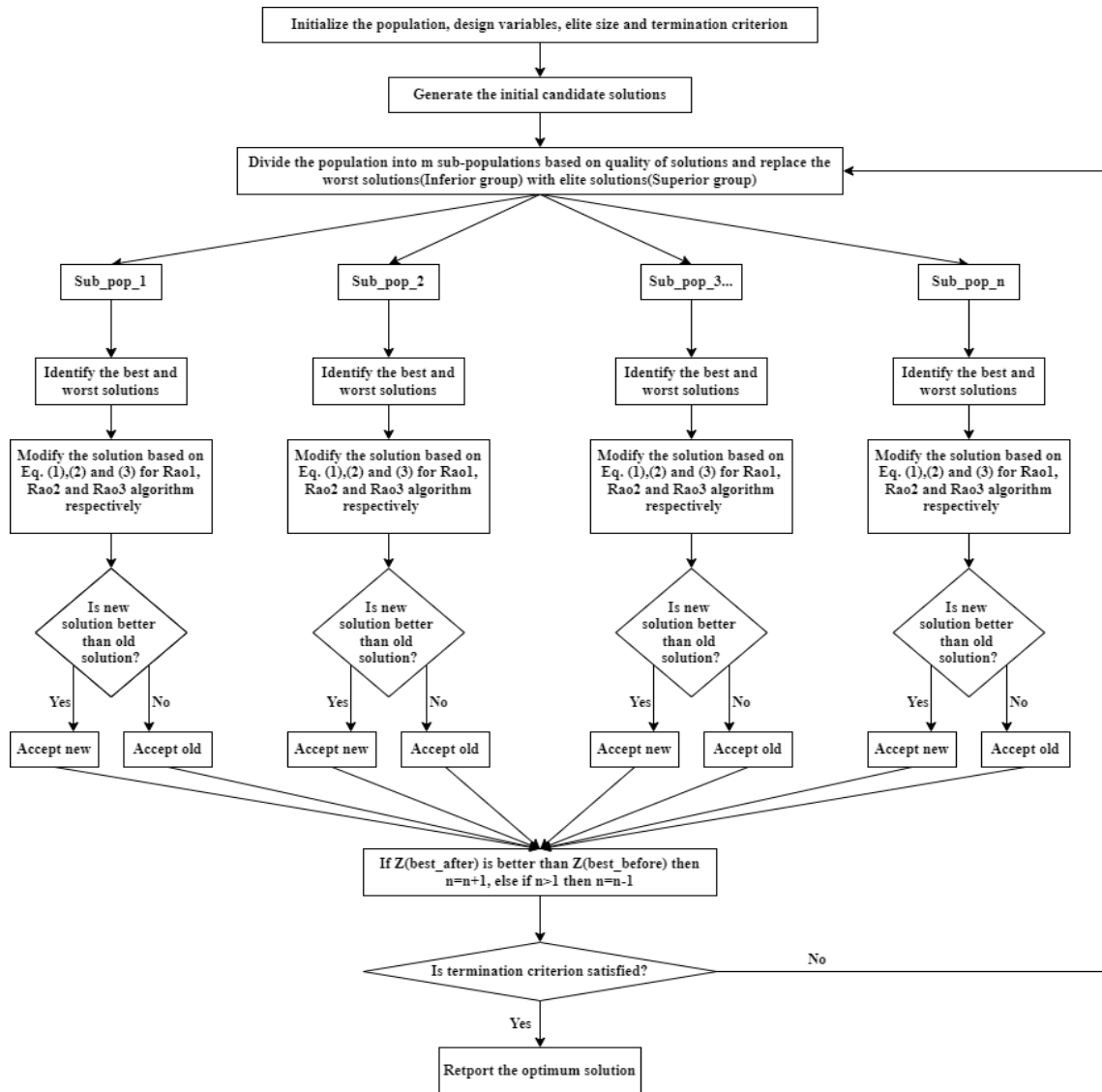


Figure 1. Flowchart of the SAMPE Rao algorithms

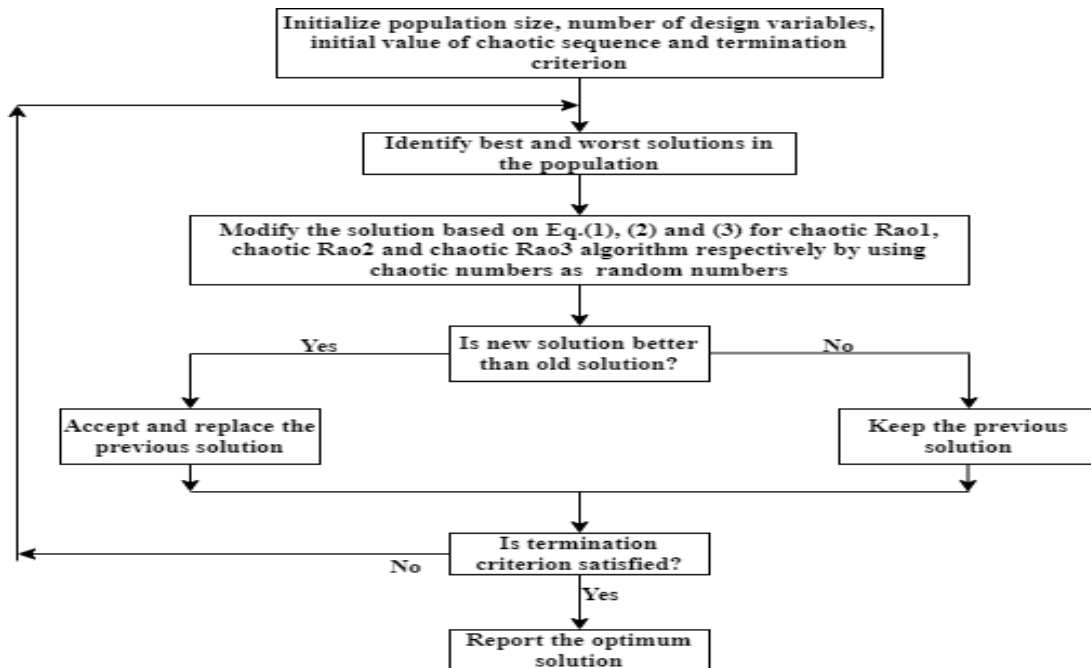


Figure 2. Flowchart of chaotic Rao algorithms

4. Application of the proposed algorithms

4.1. Benchmark problems

The mathematical formulations of benchmark problems are given in appendix A [20].The performance results for 25 unconstrained benchmark problems are obtained using the proposed modified Rao algorithms. The proposed algorithms are run for 30 times with 500000 function evaluations for each benchmark function and the statistical results are presented in Table 1. The optimization results for the same benchmark functions using Rao algorithms

presented in[20] are compared with the results attained using the proposed algorithms.The improvement in the results using the proposed Rao algorithms is highlighted in bold for each benchmark function. In terms of best (B) and mean (M) results of the benchmark problems, the proposed algorithms have obtained either the same or better results compared to the corresponding Rao algorithms. In terms of the mean function evaluations (MFE), it is observed that the performance of the proposed algorithms is better except the performance of SAMPE Rao1 algorithm for functions f_8 , f_{10} and f_{11} , SAMPE Rao 2 algorithm for functions f_7 and f_{11} , SAMPE Rao3 algorithm for function f_7 and Chaotic Rao2 algorithm for functions f_7 and f_{22} .

Table 1. Statistical results of proposed algorithms for 25 benchmark problems

Function		Rao1[20]	Rao2[20]	Rao3[20]	SAMPE Rao1	SAMPE Rao2	SAMPE Rao3	Chaotic Rao1	Chaotic Rao2	Chaotic Rao3
f_1	B	0.00E+00	0.00E+00	0.00E+00	0.00E+00	0.00E+00	0.00E+00	0.00E+00	0.00E+00	0.00E+00
	M	0.00E+00	0.00E+00	0.00E+00	0.00E+00	0.00E+00	0.00E+00	0.00E+00	0.00E+00	0.00E+00
	W	0.00E+00	0.00E+00	0.00E+00	0.00E+00	0.00E+00	0.00E+00	0.00E+00	0.00E+00	0.00E+00
	SD	0.00E+00	0.00E+00	0.00E+00	0.00E+00	0.00E+00	0.00E+00	0.00E+00	0.00E+00	0.00E+00
	MFE	499976	499791	277522	499968	499631	264202	499913	499435	277174
	NP,ES/CS₁	NA	NA	NA	30,2	30,2	20,1	30,0.2	30,0.2	12,0.2
f_2	B	0.00E+00	0.00E+00	0.00E+00	0.00E+00	0.00E+00	0.00E+00	0.00E+00	0.00E+00	0.00E+00
	M	0.00E+00	0.00E+00	0.00E+00	0.00E+00	0.00E+00	0.00E+00	0.00E+00	0.00E+00	0.00E+00
	W	0.00E+00	0.00E+00	0.00E+00	0.00E+00	0.00E+00	0.00E+00	0.00E+00	0.00E+00	0.00E+00
	SD	0.00E+00	0.00E+00	0.00E+00	0.00E+00	0.00E+00	0.00E+00	0.00E+00	0.00E+00	0.00E+00
	MFE	499975	499851	276556	499968	499674	242812	499895	499538	273111
	NP,ES/CS₁	NA	NA	NA	60,2	60,2	20,2	30,0.2	30,0.2	12,0.2
f_3	B	0.00E+00	0.00E+00	0.00E+00	0.00E+00	0.00E+00	0.00E+00	0.00E+00	0.00E+00	0.00E+00
	M	0.00E+00	0.00E+00	0.00E+00	0.00E+00	0.00E+00	0.00E+00	0.00E+00	0.00E+00	0.00E+00
	W	0.00E+00	0.00E+00	0.00E+00	0.00E+00	0.00E+00	0.00E+00	0.00E+00	0.00E+00	0.00E+00
	SD	0.00E+00	0.00E+00	0.00E+00	0.00E+00	0.00E+00	0.00E+00	0.00E+00	0.00E+00	0.00E+00
	MFE	9805	7612	7325	2998	2472	2218	7927	3729	5275
	NP,ES/CS₁	NA	NA	NA	10,2	10,2	10,2	20,0.8	10,0.6	15,0.6
f_4	B	-1.00E+00	-1.00E+00	-1.00E+00	-1.00E+00	-1.00E+00	-1.00E+00	-1.00E+00	-1.00E+00	-1.00E+00
	M	-5.67E-01	-1.00E+00	-1.00E+00	-1.00E+00	-1.00E+00	-1.00E+00	-7.00E-01	-1.00E+00	-1.00E+00
	W	0.00E+00	-1.00E+00	-1.00E+00	-1.00E+00	-1.00E+00	-1.00E+00	0.00E+00	-1.00E+00	-1.00E+00
	SD	5.04E-01	0.00E+00	0.00E+00	0.00E+00	0.00E+00	0.00E+00	4.66E-01	0.00E+00	0.00E+00
	MFE	3010	11187	14025	992	919	842	2607	3222	2860
	NP,ES/CS₁	NA	NA	NA	10,2	10,2	10,2	20,0.8	10,0.2	10,0.2
f_5	B	0.00E+00	0.00E+00	0.00E+00	0.00E+00	0.00E+00	0.00E+00	0.00E+00	0.00E+00	0.00E+00
	M	0.00E+00	0.00E+00	0.00E+00	0.00E+00	0.00E+00	0.00E+00	0.00E+00	0.00E+00	0.00E+00
	W	0.00E+00	0.00E+00	0.00E+00	0.00E+00	0.00E+00	0.00E+00	0.00E+00	0.00E+00	0.00E+00
	SD	0.00E+00	0.00E+00	0.00E+00	0.00E+00	0.00E+00	0.00E+00	0.00E+00	0.00E+00	0.00E+00
	MFE	77023	110544	143088	19863	76908	99996	26514	43283	49149
	NP,ES/CS₁	NA	NA	NA	10,2	20,2	20,2	10,0.2	10,0.2	10,0.2
f_6	B	0.00E+00	0.00E+00	0.00E+00	0.00E+00	0.00E+00	0.00E+00	0.00E+00	0.00E+00	0.00E+00
	M	0.00E+00	1.80E-24	7.87E-27	0.00E+00	0.00E+00	0.00E+00	0.00E+00	0.00E+00	0.00E+00
	W	0.00E+00	5.35E-23	1.32E-25	0.00E+00	0.00E+00	0.00E+00	0.00E+00	0.00E+00	0.00E+00
	SD	0.00E+00	9.76E-24	2.61E-26	0.00E+00	0.00E+00	0.00E+00	0.00E+00	0.00E+00	0.00E+00
	MFE	385066	477753	488127	164446	238352	239369	59000	80542	78871

	NP,ES/CS ₁	NA	NA	NA	15,2	15,2	15,2	15,0,2	15,0,2	15,0,2
f ₇	B	-5.00E+01	-5.00E+01	-5.00E+01	-5.00E+01	-5.00E+01	-5.00E+01	-5.00E+01	-5.00E+01	-5.00E+01
	M	-5.00E+01	-5.00E+01	-5.00E+01	-5.00E+01	-5.00E+01	-5.00E+01	-5.00E+01	-5.00E+01	-5.00E+01
	W	-5.00E+01	-5.00E+01	-5.00E+01	-5.00E+01	-5.00E+01	-5.00E+01	-5.00E+01	-5.00E+01	-5.00E+01
	SD	0.00E+00	0.00E+00	0.00E+00	0.00E+00	0.00E+00	0.00E+00	0.00E+00	0.00E+00	0.00E+00
	MFE	17485	37209	34796	15535	50948	48648	11470	55908	31416
	NP,ES/CS ₁	NA	NA	NA	15,2	15,2	15,2	15,0,2	6,0,2	6,0,2
f ₈	B	-2.10E+02	-2.10E+02	-2.10E+02	-2.10E+02	-2.10E+02	-2.10E+02	-2.10E+02	-2.10E+02	-2.10E+02
	M	-2.10E+02	-3.09E+01	-2.10E+02	-2.10E+02	-2.10E+02	-2.10E+02	-2.10E+02	-1.38E+02	-2.10E+02
	W	-2.10E+02	1.17E+03	-2.10E+02	-2.10E+02	-2.10E+02	-2.10E+02	-2.10E+02	9.30E+02	-2.10E+02
	SD	0.00E+00	4.13E+02	0.00E+00	0.00E+00	0.00E+00	0.00E+00	0.00E+00	2.74E+02	0.00E+00
	MFE	48231	144156	142253	89054	194142	130167	15966	92515	138122
	NP,ES/CS ₁	NA	NA	NA	20,2	20,2	20,2	10,0,2	10,0,7	15,0,2
f ₉	B	0.00E+00	0.00E+00	0.00E+00	0.00E+00	0.00E+00	0.00E+00	0.00E+00	0.00E+00	0.00E+00
	M	0.00E+00	0.00E+00	0.00E+00	0.00E+00	0.00E+00	0.00E+00	0.00E+00	0.00E+00	0.00E+00
	W	0.00E+00	0.00E+00	0.00E+00	0.00E+00	0.00E+00	0.00E+00	0.00E+00	0.00E+00	0.00E+00
	SD	0.00E+00	0.00E+00	0.00E+00	0.00E+00	0.00E+00	0.00E+00	0.00E+00	0.00E+00	0.00E+00
	MFE	345615	499767	258451	304884	347959	153980	318355	35444	242684
	NP,ES/CS ₁	NA	NA	NA	25,2	15,2	15,2	20,0,2	10,0,3	12,0,2
f ₁₀	B	0.00E+00	0.00E+00	0.00E+00	0.00E+00	0.00E+00	0.00E+00	0.00E+00	0.00E+00	0.00E+00
	M	0.00E+00	0.00E+00	0.00E+00	0.00E+00	0.00E+00	0.00E+00	0.00E+00	0.00E+00	0.00E+00
	W	0.00E+00	0.00E+00	0.00E+00	0.00E+00	0.00E+00	0.00E+00	0.00E+00	0.00E+00	0.00E+00
	SD	0.00E+00	0.00E+00	0.00E+00	0.00E+00	0.00E+00	0.00E+00	0.00E+00	0.00E+00	0.00E+00
	MFE	301513	499849	144367	499996	499724	127782	232622	499469	144354
	NP,ES/CS ₁	NA	NA	NA	20,1	30,2	20,2	15,0,2	30,0,2	12,0,4
f ₁₁	B	8.95E-26	1.86E-16	1.40E-14	2.17E-10	5.93E-12	3.87E-15	1.66E-28	3.60E-18	1.97E-18
	M	6.64E-01	7.40E-01	7.40E-01	4.07E+00	3.99E-01	6.82E-03	1.33E+00	1.33E-01	4.64E-08
	W	3.99E+00	2.22E+01	2.22E+01	6.98E+01	4.01E+00	1.78E-01	3.99E+00	3.99E+00	1.39E-06
	SD	1.51E+00	4.05E+00	4.05E+00	1.26E+01	1.22E+00	3.25E-02	1.91E+00	7.28E-01	2.54E-07
	MFE	489811	478410	478420	491910	492311	491894	462326	496479	498527
	NP,ES/CS ₁	NA	NA	NA	20,1	20,1	20,1	20,0,2	30,0,2	30,0,2
f ₁₂	B	6.67E-01	2.81E-30	6.67E-01	1.86E-26	1.82E-30	2.42E-30	4.38E-30	1.90E-30	6.67E-01
	M	6.67E-01	2.89E-01	6.67E-01	5.78E-01	3.56E-01	6.00E-01	6.44E-01	4.89E-01	6.67E-01
	W	6.67E-01	6.67E-01	6.67E-01	6.67E-01	6.67E-01	6.67E-01	6.67E-01	6.67E-01	6.67E-01
	SD	0.00E+00	3.36E-01	7.39E-05	2.30E-01	3.38E-01	2.03E-01	1.22E-01	3.00E-01	0.00E+00
	MFE	75427	113638	159231	208609	294330	139129	92647	274361	344089
	NP,ES/CS ₁	NA	NA	NA	20,2	30,2	30,2	30,0,2	30,0,2	30,0,2
f ₁₃	B	3.98E-01	3.98E-01	3.98E-01	3.98E-01	3.98E-01	3.98E-01	3.98E-01	3.98E-01	3.98E-01
	M	3.98E-01	3.98E-01	3.98E-01	3.98E-01	3.98E-01	3.98E-01	3.98E-01	3.98E-01	3.98E-01
	W	3.98E-01	3.98E-01	3.98E-01	3.98E-01	3.98E-01	3.98E-01	3.98E-01	3.98E-01	3.98E-01
	SD	1.05E-05	1.03E-05	1.44E-07	0.00E+00	0.00E+00	0.00E+00	0.00E+00	0.00E+00	0.00E+00
	MFE	102785	41263	80683	2059	4673	71397	1188	2456	46560
	NP,ES/CS ₁	NA	NA	NA	10,2	10,2	15,2	10,0,2	10,0,2	10,0,2
f ₁₄	B	0.00E+00	0.00E+00	0.00E+00	0.00E+00	0.00E+00	0.00E+00	0.00E+00	0.00E+00	0.00E+00
	M	0.00E+00	0.00E+00	0.00E+00	0.00E+00	0.00E+00	0.00E+00	0.00E+00	0.00E+00	0.00E+00
	W	0.00E+00	0.00E+00	0.00E+00	0.00E+00	0.00E+00	0.00E+00	0.00E+00	0.00E+00	0.00E+00
	SD	0.00E+00	0.00E+00	0.00E+00	0.00E+00	0.00E+00	0.00E+00	0.00E+00	0.00E+00	0.00E+00
	MFE	3129	4751	3425	1166	3573	1289	1127	1849	1512

	NP,ES/CS ₁	NA	NA	NA	15,2	15,2	15,2	10,0,2	10,0,2	10,0,2
f ₁₅	B	0.00E+00	0.00E+00	0.00E+00	0.00E+00	0.00E+00	0.00E+00	0.00E+00	0.00E+00	0.00E+00
	M	0.00E+00	0.00E+00	0.00E+00	0.00E+00	0.00E+00	0.00E+00	0.00E+00	0.00E+00	0.00E+00
	W	0.00E+00	0.00E+00	0.00E+00	0.00E+00	0.00E+00	0.00E+00	0.00E+00	0.00E+00	0.00E+00
	SD	0.00E+00	0.00E+00	0.00E+00	0.00E+00	0.00E+00	0.00E+00	0.00E+00	0.00E+00	0.00E+00
	MFE	2963	4272	3191	1096	1457	1126	1082	1673	1254
	NP,ES/CS ₁	NA	NA	NA	15,2	15,2	15,2	10,0,2	10,0,2	10,0,2
f ₁₆	B	0.00E+00	0.00E+00	0.00E+00	0.00E+00	0.00E+00	0.00E+00	0.00E+00	0.00E+00	0.00E+00
	M	0.00E+00	0.00E+00	0.00E+00	0.00E+00	0.00E+00	0.00E+00	0.00E+00	0.00E+00	0.00E+00
	W	0.00E+00	0.00E+00	0.00E+00	0.00E+00	0.00E+00	0.00E+00	0.00E+00	0.00E+00	0.00E+00
	SD	0.00E+00	0.00E+00	0.00E+00	0.00E+00	0.00E+00	0.00E+00	0.00E+00	0.00E+00	0.00E+00
	MFE	4725	12337	6821	1886	3658	2843	1572	4422	2352
	NP,ES/CS ₁	NA	NA	NA	15,2	15,2	15,2	10,0,2	10,0,2	10,0,2
f ₁₇	B	0.00E+00	0.00E+00	0.00E+00	0.00E+00	0.00E+00	0.00E+00	0.00E+00	0.00E+00	0.00E+00
	M	0.00E+00	0.00E+00	0.00E+00	0.00E+00	0.00E+00	0.00E+00	0.00E+00	0.00E+00	0.00E+00
	W	0.00E+00	0.00E+00	0.00E+00	0.00E+00	0.00E+00	0.00E+00	0.00E+00	0.00E+00	0.00E+00
	SD	0.00E+00	0.00E+00	0.00E+00	0.00E+00	0.00E+00	0.00E+00	0.00E+00	0.00E+00	0.00E+00
	MFE	5583	4485	4312	1348	1207	1168	2031	2362	2289
	NP,ES/CS ₁	NA	NA	NA	10,2	10,2	10,2	10,0,2	10,0,2	10,0,2
f ₁₈	B	-1.80E+00	-1.80E+00	-1.80E+00	-1.80E+00	-1.80E+00	-1.80E+00	-1.80E+00	-1.80E+00	-1.80E+00
	M	-1.80E+00	-1.80E+00	-1.80E+00	-1.80E+00	-1.80E+00	-1.80E+00	-1.80E+00	-1.80E+00	-1.80E+00
	W	-1.80E+00	-1.80E+00	-1.80E+00	-1.80E+00	-1.80E+00	-1.80E+00	-1.80E+00	-1.80E+00	-1.80E+00
	SD	0.00E+00	0.00E+00	0.00E+00	0.00E+00	0.00E+00	0.00E+00	0.00E+00	0.00E+00	0.00E+00
	MFE	3863	2694	2751	1091	1037	1239	1397	2704	2587
	NP,ES/CS ₁	NA	NA	NA	10,2	10,2	10,2	10,0,2	10,0,2	10,0,2
f ₁₉	B	-4.69E+00	-4.69E+00	-4.69E+00	-4.69E+00	-4.69E+00	-4.69E+00	-4.69E+00	-4.69E+00	-4.69E+00
	M	-4.67E+00	-4.43E+00	-4.49E+00	-4.68E+00	-4.54E+00	-4.57E+00	-4.68E+00	-4.63E+00	-4.64E+00
	W	-4.54E+00	-3.12E+00	-3.50E+00	-4.65E+00	-3.91E+00	-3.66E+00	-4.54E+00	-4.48E+00	-4.50E+00
	SD	3.09E-02	3.60E-01	2.79E-01	1.27E-02	1.63E-01	1.89E-01	3.05E-02	6.01E-02	5.14E-02
	MFE	39710	67252	58401	158680	109073	91618	23677	131485	99287
	NP,ES/CS ₁	NA	NA	NA	20,2	20,2	30,2	30,0,2	30,0,2	30,0,2
f ₂₀	B	3.00E+00	3.00E+00	3.00E+00	3.00E+00	3.00E+00	3.00E+00	3.00E+00	3.00E+00	3.00E+00
	M	3.00E+00	5.70E+00	3.00E+00	3.00E+00	3.00E+00	3.00E+00	3.00E+00	3.00E+00	3.00E+00
	W	3.00E+00	8.40E+01	3.00E+00	3.00E+00	3.00E+00	3.00E+00	3.00E+00	3.00E+00	3.00E+00
	SD	0.00E+00	1.48E+01	0.00E+00	0.00E+00	0.00E+00	0.00E+00	0.00E+00	0.00E+00	0.00E+00
	MFE	180121	180121	353893	91753	87284	326782	55361	103526	333562
	NP,ES/CS ₁	NA	NA	NA	10,2	10,2	10,2	10,0,2	15,0,2	15,0,2
f ₂₁	B	0.00E+00	0.00E+00	0.00E+00	0.00E+00	0.00E+00	0.00E+00	0.00E+00	0.00E+00	0.00E+00
	M	1.45E-10	0.00E+00	0.00E+00	0.00E+00	0.00E+00	0.00E+00	0.00E+00	0.00E+00	0.00E+00
	W	3.71E-09	0.00E+00	0.00E+00	0.00E+00	0.00E+00	0.00E+00	0.00E+00	0.00E+00	0.00E+00
	SD	6.78E-10	0.00E+00	0.00E+00	0.00E+00	0.00E+00	0.00E+00	0.00E+00	0.00E+00	0.00E+00
	MFE	82792	3139	4453	2065	2047	1809	2349	1671	2947
	NP,ES/CS ₁	NA	NA	NA	10,2	10,2	10,2	10,0,2	10,0,2	15,0,2
f ₂₂	B	1.51E-14	7.99E-15	4.44E-15	7.99E-15	7.99E-15	4.44E-15	7.99E-15	7.99E-15	4.44E-15
	M	5.67E-01	1.04E-14	6.69E-15	1.20E-01	1.02E-14	6.34E-15	7.04E-01	1.33E+01	5.63E-15
	W	2.22E+00	1.51E-14	1.51E-14	2.66E+00	2.22E-14	1.51E-14	2.00E+01	2.00E+01	7.99E-15
	SD	7.41E-01	3.14E-15	2.38E-15	5.09E-01	3.79E-15	2.42E-15	3.64E+00	9.57E+00	1.70E-15
	MFE	129392	417741	76352	410787	358564	161576	443238	325673	173332

	NP,ES/CS ₁	NA	NA	NA	90,2	40,2	120,2	80,0,2	25,0,2	60,0,2
f ₂₃	B	9.98E-01	9.98E-01	9.98E-01	9.98E-01	9.98E-01	9.98E-01	9.98E-01	9.98E-01	9.98E-01
	M	9.98E-01	9.98E-01	9.98E-01	9.98E-01	9.98E-01	9.98E-01	9.98E-01	9.98E-01	9.98E-01
	W	9.98E-01	9.98E-01	9.98E-01	9.98E-01	9.98E-01	9.98E-01	9.98E-01	9.98E-01	9.98E-01
	SD	0.00E+00	0.00E+00	0.00E+00	0.00E+00	0.00E+00	0.00E+00	0.00E+00	0.00E+00	0.00E+00
	MFE	18839	95983	243748	3812	58484	236463	3711	63048	239722
	NP,ES/CS ₁	NA	NA	NA	10,2	10,2	8,2	15,0,2	15,0,2	40,0,2
f ₂₄	B	-3.86E+00	-3.86E+00	-3.86E+00	-3.86E+00	-3.86E+00	-3.86E+00	-3.86E+00	-3.86E+00	-3.86E+00
	M	-3.86E+00	-3.86E+00	-3.86E+00	-3.86E+00	-3.86E+00	-3.86E+00	-3.86E+00	-3.86E+00	-3.86E+00
	W	-3.86E+00	-3.86E+00	-3.86E+00	-3.86E+00	-3.86E+00	-3.86E+00	-3.86E+00	-3.86E+00	-3.86E+00
	SD	0.00E+00	0.00E+00	0.00E+00	0.00E+00	0.00E+00	0.00E+00	0.00E+00	0.00E+00	0.00E+00
	MFE	4459	3022	3271	3077	2811	2280	2303	2198	3185
	NP,ES/CS ₁	NA	NA	NA	15,2	20,2	15,2	15,0,2	10,0,6	15,0,2
f ₂₅	B	1.35E-32	1.35E-32	1.35E-32	1.35E-32	1.35E-32	1.35E-32	1.35E-32	1.35E-32	1.35E-32
	M	1.47E-03	5.79E-02	1.60E-02	7.32E-04	4.71E-03	9.42E-03	1.10E-03	1.35E-32	2.17E-03
	W	1.10E-02	1.60E+00	1.41E-01	1.10E-02	9.74E-02	9.74E-02	1.10E-02	1.35E-32	2.10E-02
	SD	3.80E-03	2.91E-01	3.50E-02	2.79E-03	1.79E-02	2.44E-02	3.35E-03	0.00E+00	5.20E-03
	MFE	173661	115593	55637	422550	363520	195872	308780	390500	214620
	NP,ES/CS ₁	NA	NA	NA	80,2	80,2	80,2	60,0,2	60,0,2	60,0,2

B-Best solution, M-Mean solution, W-Worst solution, SD-Standard deviation, MFE-Mean function evaluations, NP-Population size, ES-Elite size, CS₁-Initial value of chaotic sequence, NA- Not available

The results attained by applying the proposed algorithms to the benchmark functions are used to perform the Friedman rank test [21]. The Friedman rank test examines the statistical performance of one algorithm against other algorithms. The statistical results achieved using different algorithms for a function are compared and the algorithm which gives the best result gets rank 1 and then other algorithms are ranked in ascending order according to their performance. Similarly, the ranks are given to algorithms for every function and then the mean rank of each algorithm is computed. Table 2 shows the results of the Friedman rank test. From the average ranking, it is seen that the Chaotic Rao1 algorithm performs better than the other algorithms. The rank of each algorithm according to its performance is also presented in Table 2. From the χ^2 score value of 56.128, the p value is obtained, and it is much less than 0.05, which validates the better performance of the proposed algorithms.

4.2. Mechanical engineering design optimization problems

The proposed algorithms are applied to 15 mechanical engineering design optimization problems to test their performance. The mathematical models of these problems

are described in the Appendix B. The detailed description of these problems is given in [16] and [22].

4.2.1. Four stage gear box:

This problem is designed to minimize the total weight of gear box. The material of gears is aluminum-bronze, so the aim is considered as the minimization of the total gear volume. 22 design variables (eight integer and other discrete variables) consist of the blank thickness, the number of teeth and the gear and pinion position. The 86 design constraints are related to the contact ratio, strength of the gears, size of gears, pitch, assembly of gears, and kinematics.

4.2.2. Rolling element bearing:

Fig. 3 shows schematic diagram of rolling element bearing. This problem is designed to maximize the load carrying capacity of a rolling element bearing. The ball diameter (D_b), pitch diameter (D_m), total number of balls (Z), the raceway curvature coefficient (f_i and f_o) are five design variables and the design parameters of the rolling element bearing problem (β , ϵ , e , K_{Dmin} , K_{Dmax} ,) are other five design variables. All design variables excluding Z are continuous variables. The design constraints are related to kinematic and manufacturing considerations.

Table 2. Friedman rank test results

Algorithm	Rao1	Rao2	Rao3	SAMPE Rao1	SAMPE Rao2	SAMPE Rao3	Chaotic Rao1	Chaotic Rao2	Chaotic Rao3
Friedman average rank	6.52	7.32	6.68	3.92	4.72	3.68	3.4	4.44	4.32
Rank for algorithm	7	9	8	3	6	2	1	5	4

4.2.3. Gas transmission compressor:

This problem is designed to minimize the cost of gas pipeline transmission system to deliver 100 million cubic feet of gas per day. The distance between the compressor stations (x_1 , in miles) and the compressor ratio (x_2 , division of discharge pressure and flow rate), the pipe diameter (x_3 , in inches) and flow rate (x_4 , in ft^3/sec) are four design variables. This problem has one inequality constraint.

4.2.4. Speed reducer:

Fig. 4 shows schematic diagram of speed reducer. This problem is designed to minimize the total weight of the speed reducer. The face width (b), the number of teeth on pinion (Z , integer variable), the gear module (m), shaft 1 diameter (d_1), and the shaft 2 diameter (d_2), the length of shaft 1 (l_1), the length of shaft 2 (l_2) are seven design variables. Except Z , all other design variables are

continuous variables. This problem has eleven constraints associated with the surface stress, the bending stress in the gear teeth, the stresses in the shafts, and transverse deflections of the shafts.

4.2.5. Pressure vessel:

Fig. 5 shows schematic diagram of pressure vessel. This problem is designed to minimize the total cost of Material, welding and forming. The design variables are the shell thickness as T_s (x_1), head thickness as T_h (x_2), shell inner radius as R (x_3), and cylindrical section length of the vessel without considering the head as L (x_4). Due to the constraint in the availability of rolled steel plates, T_s and T_h must be multiple of 0.0625 in. The remaining two variables are continuous. This problem has four design constraints.

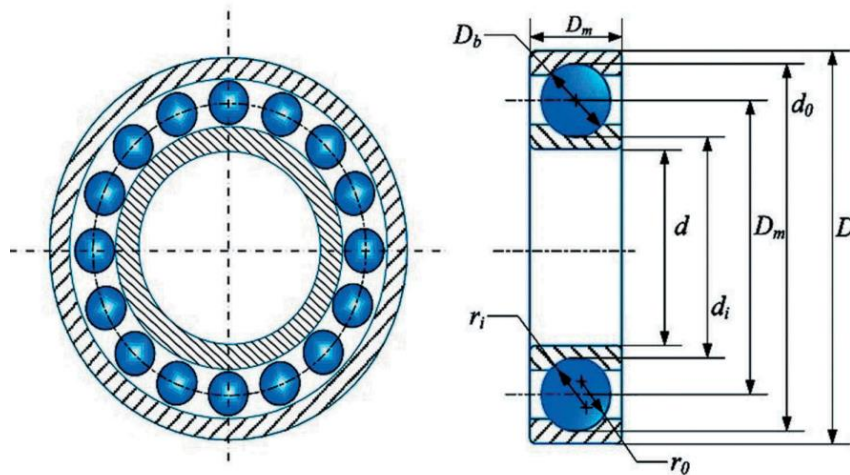


Figure 3. Rolling element bearing[13]

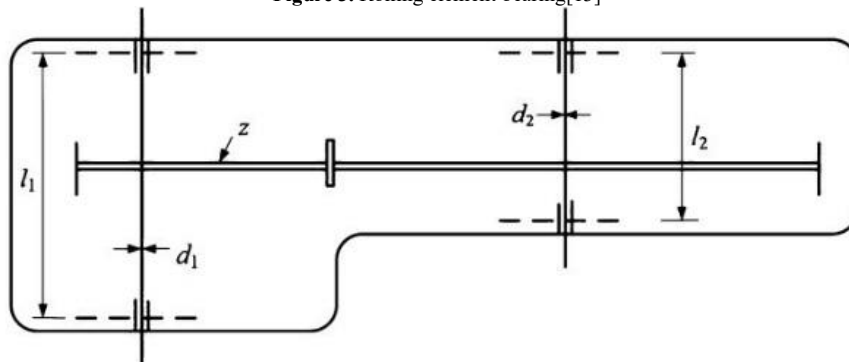


Figure 4. Speed reducer [25]

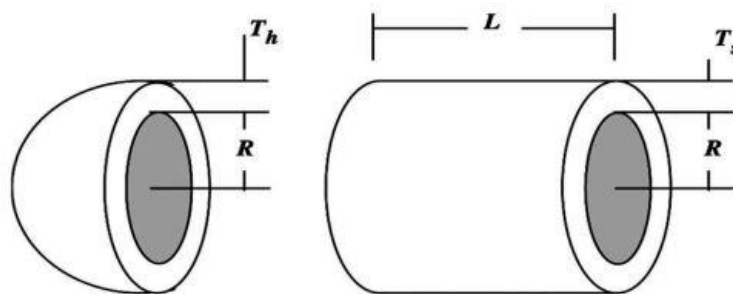


Figure 5. Pressure vessel [13]

4.2.6. Tension/compression spring – case 1:

Fig. 6 shows schematic diagram of tension/compression spring. This problem is designed to minimize the weight of a tension/compression spring. The wire diameter d (x_1), mean coil diameter D (x_2) and the number of active coils N (x_3) are three continuous design variables. Four design constraints are associated with the shear stress, minimum deflection, surge frequency and limits on outside diameter and design variables.

4.2.7. Tension/Compression spring – case 2:

This problem is designed to minimize the volume of a compression spring under static loading. The mean coil diameter D (x_2 , continuous), the wire diameter d (x_1 , discrete), and the number of active coils N (x_3 , integer) are three design variables. The value of variable d is taken from Table 3.

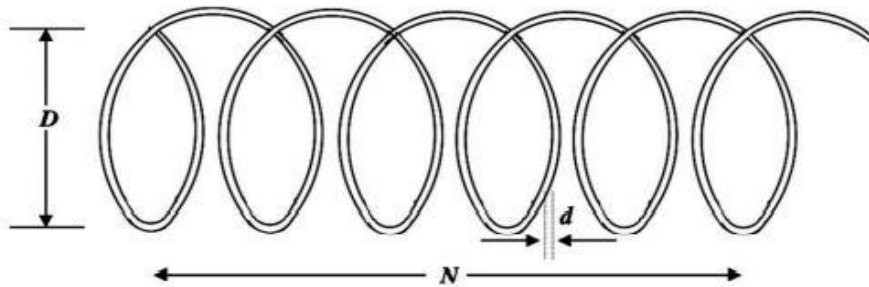


Figure 6. Compression spring [13]

Table 3. Wire diameter [24]

Wire diameters (in)							
0.009	0.0095	0.0104	0.0118	0.0128	0.0132	0.014	0.015
0.015	0.0162	0.0173	0.018	0.020	0.023	0.025	0.028
0.028	0.032	0.035	0.041	0.047	0.054	0.063	0.072
0.072	0.080	0.092	0.105	0.120	0.135	0.148	0.162
0.162	0.177	0.192	0.207	0.225	0.244	0.263	0.283
0.283	0.307	0.331	0.362	0.394	0.4375	0.500	

4.2.8. Piston lever:

Fig. 7 shows schematic diagram of piston lever. This problem is designed to minimize the oil volume by locating the piston components' position (H , D , B , and X) when the piston lever is raised from 0° to 45° . The inequality constraints imposed are related to equilibrium of forces, maximum bending moment of the lever, minimum piston stroke and geometrical conditions.

4.2.9. Gear train:

Fig. 8 shows schematic diagram of gear train. This problem is designed to minimize the gear ratio in the gear train. The number of teeth on the gears are four design variables. The given range for the number of teeth on each gear is considered as the constraints.

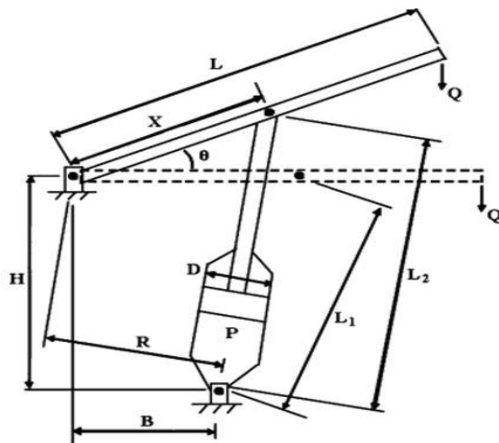


Figure 7. Piston lever [25]

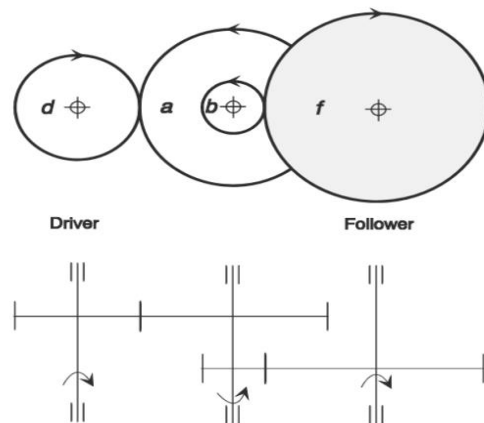


Figure 8. Gear train[16]

4.2.10. Corrugated bulkhead:

This problem is designed to minimize the weight of a corrugated bulkhead used in tankers. The length (l), width (w), depth (h) and thickness (t) of the bulkhead are four design variables considered with six inequality constraints.

4.2.11. Planetary gear train:

Fig. 9 shows schematic diagram of planetary gear train. This problem is designed to minimize the maximum errors in the gear ratio of a planetary gear train. The number of teeth in the gears (Z_1, Z_2, Z_3, Z_4, Z_5 and Z_6 - integer variables), the number of planet gears (Z_p), module of the first gear (m_1) and module of the second gear (m_2) are nine design variables. P, m_1 , and m_2 are discrete design variables. The design constraints (ten inequality constraints and one equality constraint) are related to various assembly and geometric restrictions.

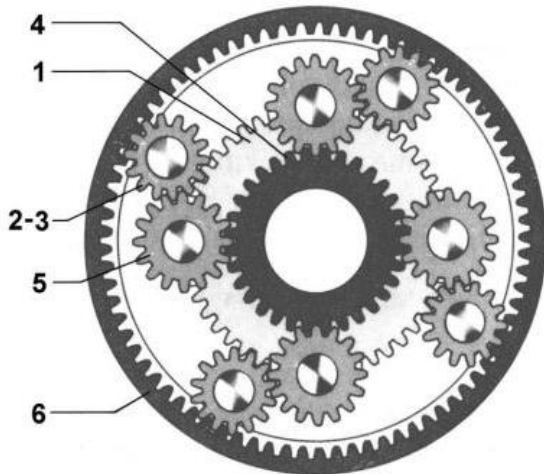


Figure 9. Planetary gear train [23]

1: Small sun gear, 2,3: Broad planet gear, 4: Large sun gear, 5: Narrow planet gear, 6: Ring gear

4.2.12. Step cone pulley:

Fig. 10 shows schematic diagram of step cone pulley. This problem is designed to minimize the weight of the step cone pulley. The pulley diameter in each step (d_1, d_2, d_3, d_4) and width of the pulley (w) are five design variables. Eight inequality constraints and three equality constraints ensure that the belts have the same tension ratios, same belt length for every step and transmit same power. The step pulley transmits minimum 0.75 hp.

4.2.13. Hydrostatic thrust bearing:

Fig.11 shows schematic diagram of hydrostatic thrust bearing. This problem is designed to minimize the power loss related to bearing. Oil viscosity (μ), flow rate (Q), Bearing step radius (R) and recess radius (R_0) are four design variables. Total seven constraints are related to oil film thickness, load-carrying capacity, rise in oil temperature, inlet oil pressure and some physical requirements.

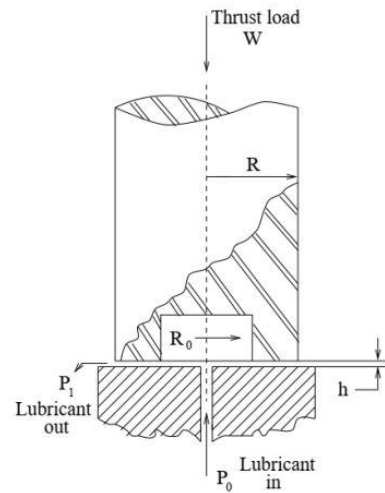


Figure 11. Hydrostatic thrust bearing[16]

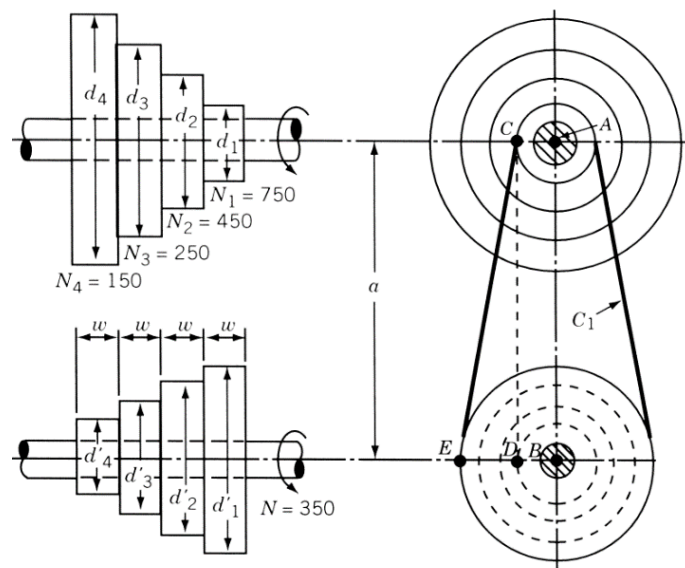


Figure 10. Step cone pulley [16]

4.2.14. Welded beam:

Fig. 12 shows schematic diagram of welded beam. This problem is designed to minimize the fabrication cost of the welded beam. The weld thickness as $h(x_1)$, weld length as $l(x_2)$, the bar height as $t(x_3)$ and bar thickness as $b(x_4)$ are four design variables. This design problem has seven constraints associated with the shear stress (τ), the bending stress in the beam (σ), the buckling load on the beam (P_c), the end deflection of the beam (δ), and the side constraints.

4.2.15. Multiple disk clutch brake:

Fig. 13 shows schematic diagram of multiple disk clutch brake. This problem is designed to minimize the total mass of the clutch brake. The actuating force (F), outer radius (r_o), inner radius (r_i), disc thickness (t) and the number of contact surfaces (Z) are five discrete design variables. This problem has eight non-linear design constraints.

5. Results and discussion

In the present work, the results are obtained with the R2019a version of the MATLAB tool. The laptop with the 1.80-GHz Intel Core i7-8550U processor and 8GB RAM is used for computation. Each design optimization problem is solved using Rao, SAMPE Rao and Chaotic Rao algorithms for 25 times. The statistical results achieved using Rao, SAMPE Rao, Chaotic Rao algorithms and other advanced optimization algorithms presented in [16] and [22] are compared for each design optimization problem. [16] and [22] considered maximum functions evaluations as 200000 and 60000, respectively for design optimization problems presented in their respective papers. The best fitness function values and the statistical results achieved using the proposed algorithms are compared with those achieved using other advanced optimization algorithms in the previous studies. Different combinations of population size and elite sizes for SAMPE Rao algorithms and different combinations of population size and initial value of chaotic sequence are tested for all the problems, the combination which gives the best result for different algorithms is mentioned in the statistical results comparison tables.

5.1. Four stage gear box:

The maximum FEs in this problem is considered as 50000. Table 4 compares the statistical results of this problem over 25 runs. The best fitness value obtained is $f(\bar{x}) = 36.26590769 \text{ cm}^3$ at $\bar{x} = (19, 41, 19, 39, 18, 38, 18, 38, 3.175, 3.175, 3.175, 3.175, 101.6, 63.5, 63.5, 88.9, 88.9, 88.9, 76.2, 76.2, 50.8, 50.8)$ using SAMPE Rao1 algorithm. Table 5 compares the best fitness value obtained in the present study and the same obtained by ABC-GA (Artificial Bee Colony-Genetic Algorithm), ABC-DE (Artificial Bee Colony-Differential Evolution), ABC-BBO (Artificial Bee Colony-Biogeography-based optimization), TLBO, ABC, and AOS. The best fitness value is obtained by SAMPE Rao1 algorithm.

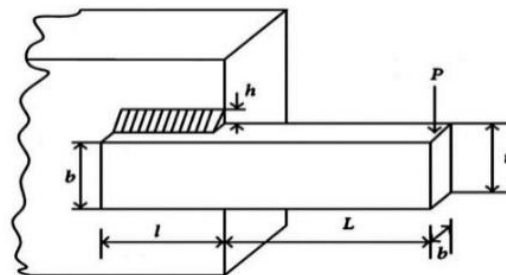


Figure 12. Welded beam [13]

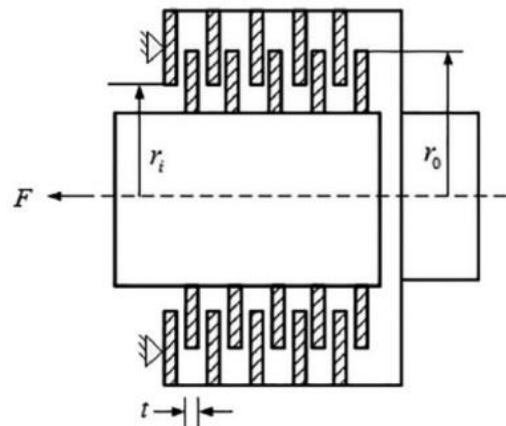


Figure 13. Multiple disk clutch brake [14]

Table 4. Statistical results comparison for a four stage gear box design problem

Algorithm	B	M	W	SD	MFE	NP, ES/CS ₁
AOS ^a	37.4042245	52.83708891	90.81422082	1.190E+01	NA	NA
Rao1	37.35797821	72.20780915	156.2196704	3.320E+01	41396	25
Rao2	36.5289327	103.3275184	240.5116744	4.620E+01	26237	25
Rao3	37.28608556	68.17318794	151.9493665	3.100E+01	35015	25
SAMPE Rao1	36.26590769	56.27290804	85.24647758	1.340E+01	40910	25.2
SAMPE Rao2	36.443023	60.79267004	113.2822656	2.260E+01	42548	50.6
SAMPE Rao3	36.29036038	54.07181791	106.5927524	1.750E+01	44856	50.6
Chaotic Rao1	36.47490382	74.97541999	130.3131561	2.890E+01	38794	25,0.7
Chaotic Rao2	36.48867434	168.5684829	618.2785095	1.350E+02	30084	29,0.6
Chaotic Rao3	36.46666447	138.4370045	275.2995689	6.550E+01	30737	30,0.6

^a Results are taken from [16]

Table 5. Comparison of best fitness value for a four stage gear box design problem

Algorithm	ABC-GA ^a	ABC-DE ^a	ABC-BBO ^a	TLBO ^a	ABC ^a	AOS ^b	Present study
Best result	55.494494	59.763563	46.623205	43.792433	49.836165	37.4042245	36.26590769

^a Results are taken from [2]; ^b Results are taken from [16]

5.2. Rolling element bearing:

The maximum FEs in this problem is considered as 25000. Table 6 compares the statistical results of this problem over 25 runs for TLBO, AOS, and the proposed algorithms. The best fitness value obtained is $f(\bar{x}) = 81859.741597$ N at $\bar{x} = (125.719056, 21.42559, 0.515, 0.515, 11, 0.462578, 0.7, 0.809635, 0.3, 0.064782)$ by all the proposed algorithms and TLBO. The result given by AOS algorithm is inferior and it is an infeasible solution because the number of rolling elements was considered by [16] as a continuous variable.

5.3. Gas transmission compressor:

The maximum FEs in this problem is considered as 200000. Table 7 compares the statistical results of this problem over 25 runs. The best fitness value obtained is

$f(\bar{x}) = 2964895.417$ at $\bar{x} = (50, 1.178281, 24.592121, 0.388346)$ using all the proposed algorithms and the AOS algorithm.

5.4. Speed reducer:

The maximum FEs in this problem is considered as 25000. Table 8 compares the statistical results of this problem over 25 runs obtained by CGO, SEA (Simple Evolutionary Algorithm), OASBS (Optimization Algorithm based on Socio Behavioural Simulation Model), CSA, and DSS-MDE (Dynamic Stochastic Selection-Multimember Differential Evolution). The best fitness value obtained is $f(\bar{x}) = 2994.424466$ kg at $\bar{x} = (3.5, 0.7, 17, 7.3, 7.715320, 3.350541, 5.286655)$ by all the proposed algorithms. The SEA, OASBS, and CSA have obtained inferior values. The Chaotic Rao1 algorithm requires the minimum FEs to reach an optimal solution.

Table 6. Statistical results comparison for a rolling element bearing design problem

Algorithm	B	M	W	SD	MFE	NP, ES/CS ₁
TLBO ^a	81859.74	81438.987	80807.8551	6.600E-01	NA	50
AOS ^{a*}	83918.49253	82175.21266	83826.38337	2.338E+01	NA	NA
Rao1	81859.741597	81564.87429	80807.82664	3.603E+02	10997	30
Rao2	81859.741597	81817.666137	80807.855077	2.104E+02	11306	30
Rao3	81859.741597	81817.66614	80807.85508	2.104E+02	11045	30
SAMPE Rao1	81859.741597	81790.21112	80807.85508	2.090E+02	9909	40,2
SAMPE Rao2	81859.741597	81859.741597	81859.741597	0.000E+00	9515	35,2
SAMPE Rao3	81859.741597	81859.741597	81859.741597	0.000E+00	9588	35,2
Chaotic Rao1	81859.741597	81859.741597	81859.741597	0.000E+00	8726	20,0.2
Chaotic Rao2	81859.741597	81859.741597	81859.741597	0.000E+00	16201	30,0.3
Chaotic Rao3	81859.741597	81859.741597	81859.741597	0.000E+00	15760	30,0.3

^a Results are taken from [16]; ^{*} Infeasible solution because the number of rolling elements was considered as a continuous variable

Table 7. Statistical results comparison for a gas transmission compressor design problem

Algorithm	B	M	W	SD	MFE	NP, ES/CS ₁
AOS ^a	2964895.417	2965102.327	2966483.832	2.518E+02	NA	NA
Rao1	2964895.419	2964895.444	2964895.52	2.667E-02	162163	10
Rao2	2964895.419	2999784.479	3626159.761	1.356E+05	153950	10
Rao3	2964895.419	2995303.489	3147941.927	6.822E+04	127464	10
SAMPE Rao1	2964895.417	2994126.234	3147941.927	6.340E+04	148446	10,2
SAMPE Rao2	2964895.417	3026809.386	3358534.842	1.044E+05	121613	10,2
SAMPE Rao3	2964895.417	3005984.840	3147941.927	7.315E+04	135558	10,2
Chaotic Rao1	2964895.417	2964895.424	2964895.517	1.954E-02	151003	10,0.4
Chaotic Rao2	2964895.417	4012200.787	12061229.75	2.653E+06	113224	10,0.3
Chaotic Rao3	2964895.417	3119110.378	3771891.386	2.296E+05	110822	10,0.9

^a Results are taken from [16]

Table 8. Statistical results comparison for a speed reducer design problem

Algorithm	B	M	W	SD	MFE	NP, ES/CS ₁
SEA ^a	3025.005	3088.7778	3078.5918	NA	NA	100
OASBS ^a	3008.08	3012.12	3028.28	NA	NA	100
CSA ^a	3000.981	3007.1997	3009	4.963E+00	NA	50
DSS-MDE ^a	2994.471066	2994.471066	2994.471066	3.580E-12	NA	20
CGO ^a	2994.443649	2994.465397	2995.504933	1.102E-01	NA	NA
Rao1	2994.424466	2994.424466	2994.424466	0.000E+00	6373.2	15
Rao2	2994.424466	2994.424466	2994.424466	0.000E+00	12848	30
Rao3	2994.424466	2994.424466	2994.424466	0.000E+00	12897	30
SAMPE Rao1	2994.424466	2994.424466	2994.424466	0.000E+00	6270	15,2
SAMPE Rao2	2994.424466	2994.424466	2994.424466	0.000E+00	9108	25,2
SAMPE Rao3	2994.424466	2994.424466	2994.424466	0.000E+00	9540	25,2
Chaotic Rao1	2994.424466	2994.424466	2994.424466	0.000E+00	3958	10,0.2
Chaotic Rao2	2994.424466	2994.424466	2994.424466	0.000E+00	12621	25,0.8
Chaotic Rao3	2994.424466	2994.424466	2994.424466	0.000E+00	12409	25,0.8

^aResults are taken from[22]

5.5. Pressure vessel:

The maximum FEs in this problem is considered as 10000. Table 9 compares the statistical results of this problem over 25 runs obtained by CPSO (Coevolutionary Particle Swarm Optimization), QPSO (Quantum behaved PSO), NM-PSO (Nelder–Mead PSO), MBA (Mine Blast Algorithm), and CGO (Chaos Game Optimization) algorithm. The best fitness value obtained is $f(\bar{x}) = 6059.714335$ \$ at $\bar{x} = (0.8125, 0.4375, 42.098446, 176.636596)$ by all the proposed algorithms. The results obtained by CPSO, QPSO, NM-PSO, and MBA algorithms violate the requirement that the variables $T_s(x_1)$ and $T_h(x_2)$ are to be integer multiples of 0.0625 inch. The best mean fitness value is attained using the Chaotic Rao1 algorithm.

5.6. Tension/compression spring – case 1:

The maximum FEs in this problem is considered as 60000. Table 10 compares the statistical results of this problem over 25 runsfor CGA (Co-evolutionary Genetic

Algorithm), OASBS, STA (State Transition Algorithm), BA (Bat Algorithm) and CGO (Chaos Game Optimization). The best fitness value obtained is $f(\bar{x}) = 0.01266525$ in³at $\bar{x} = (0.0516173, 0.3549922, 11.3910097)$ using Chaotic Rao1 algorithm. Even though the best fitness value obtained by BA and CGO seem to be slightly better, but these are to be considered infeasible due to violation of a constraint.

5.7. Tension/Compression spring – case 2:

The maximum FEs in this problem is considered as 10000. Table 11 compares the statistical results of this problem over 25 runsfor AOS and the proposed algorithms. The best fitness value obtained is $f(\bar{x}) = 2.625281953$ in³at $\bar{x} = (0.263, 0.9048483122, 15)$ by all the proposed algorithms. Even though the best fitness value obtained by AOS algorithm seems to be slightly better, but this is to be considered infeasible due to violation of a constraint. The best mean fitness value is attained using Chaotic Rao3 algorithm.

Table 9. Statistical results comparison for a pressure vessel design problem

Algorithm	B	M	W	SD	MFE	NP, ES/CS1
CPSO ^{a*}	6061.0777	6147.1332	6363.8041	8.645E+01	NA	NA
QPSO ^{a*}	6059.7208	6440.3786	7544.4925	4.484E+02	NA	20
NM-PSO ^{a*}	5930.3137	5946.7901	5960.0557	9.161E+00	NA	NA
MBA ^{a*}	5889.3216	6200.6477	6392.5062	1.603E+02	NA	50
CGO ^a	6247.672819	6250.957354	6330.958685	1.075E+01	NA	NA
Rao1	6059.714335	6088.684774	6128.630739	2.020E+01	6413.0	30
Rao2	6059.714335	6065.997125	6103.736305	1.240E+01	8943.0	30
Rao3	6059.714335	6062.390819	6090.579595	6.600E+00	9142.0	30
SAMPE Rao1	6059.714335	6073.607190	6097.912054	1.220E+01	5579.0	25,2
SAMPE Rao2	6059.714335	6064.985476	6093.022428	1.030E+01	8850.0	30,2
SAMPE Rao3	6059.714335	6061.806949	6090.526208	6.500E+00	9422.0	30,2
Chaotic Rao1	6059.714335	6061.583912	6072.623805	3.810E+00	8345.0	20,0.3
Chaotic Rao2	6059.714335	6063.910489	6095.724076	1.080E+01	9454.0	30,0.8
Chaotic Rao3	6059.714335	6061.721305	6090.526309	6.290E+00	9435.6	30,0.8

^a Results are taken from [22]; ^{*} Infeasible solution because the variables $T_s(x_1)$ and $T_h(x_2)$ are not integer multiples of 0.0625 inch.

Table 10. Statistical results comparison for a tension/compression spring case-1 design problem

Algorithm	B	M	W	SD	MFE	NP, ES/CS ₁
CGA ^a	0.01270478	0.0127692	0.01282208	3.939E-05	NA	NA
OASBS ^a	0.0126692	0.0129227	0.0167172	5.198E-05	NA	30
STA ^a	0.01266534	0.01266534	0.01272968	2.167E-05	NA	30
BA ^{a*}	0.01266522	0.01266522	0.0168954	1.420E-03	NA	10
CGO ^{a*}	0.01266524	0.012670085	0.012719055	1.090E-05	NA	NA
Rao1	0.012665712	0.012677199	0.012718743	1.168E-05	44440	10
Rao2	0.012665495	0.012986421	0.017773158	1.014E-03	17214	10
Rao3	0.012666085	0.012838545	0.01319258	2.262E-04	12070	10
SAMPE Rao1	0.012665361	0.012682374	0.012719054	2.044E-05	45396	10,2
SAMPE Rao2	0.012665459	0.012710172	0.012719054	1.879E-05	21958	10,2
SAMPE Rao3	0.012665564	0.012702301	0.012721539	2.346E-05	15390	10,2
Chaotic Rao1	0.01266525	0.012665568	0.012666418	3.000E-07	46446	10,0.2
Chaotic Rao2	0.01266527	0.012803096	0.01319258	1.999E-04	10463	10,0.2
Chaotic Rao3	0.012665349	0.012862042	0.01319258	2.322E-04	6939	10,0.2

^a Results are taken from [22]; ^{*} Infeasible solution due to violation of a constraint.

Table 11. Statistical results comparison for a tension/compression spring case-2 design problem

Algorithm	B	M	W	SD	MFE	NP, ES/CS ₁
AOS ^{a*}	2.615360373	2.64371161	2.863796184	4.285E-02	NA	NA
Rao1	2.625281953	2.626052428	2.63408739	1.93E-03	5788	10
Rao2	2.625281953	2.983025419	5.39453905	7.62E-01	1669	10
Rao3	2.625281953	2.88088446	6.720428845	8.54E-01	1554	10
SAMPE Rao1	2.625281953	2.62577663	2.631345549	1.39E-03	5573	15,2
SAMPE Rao2	2.625281953	2.648636546	3.142985801	1.04E-01	2160	15,2
SAMPE Rao3	2.625281953	2.648636546	3.142985801	1.04E-01	3195	15,2
Chaotic Rao1	2.625281953	2.625282751	2.625282751	1.64E-07	4649	15,0.2
Chaotic Rao2	2.625281953	2.785515745	5.104522609	5.64E-01	4648	15,0.7
Chaotic Rao3	2.625281953	2.625281953	2.625281953	0.00E+00	4759	15,0.7

^a Results are taken from [16]; ^{*} Infeasible solution because number of active coils in a spring is considered as continuous variable.

5.8. Piston lever:

The maximum FEs in this problem is considered as 20000. Table 12 compares the statistical results of this problem over 25 runs obtained by HPSO (Hierarchy Particle Swarm Optimization), GA (Genetic Algorithm), DE, CS, MGA, and AOS algorithm. The best fitness value obtained is $f(\bar{x}) = 8.412698 \text{ in}^3$ at $\bar{x} = (0.05, 2.04151359, 4.08302718, 120)$ by all the proposed algorithms. The best mean fitness value is attained using SAMPE Rao1 algorithm.

5.9. Gear train:

The maximum FEs in this problem is considered as 500. Table 13 compares the statistical results of this problem over 25 runs. The best fitness value obtained is $f(\bar{x}) = 2.70086\text{E-}12$ at $\bar{x} = (49, 19, 16, 43)$ by all the proposed algorithms. The best mean fitness value is attained using SAMPE Rao3 algorithm. Table 14

compares the best fitness value obtained in the present study and the same obtained by CS (Cuckoo Search), ALO, MFO (Moth Flame Optimization), MVO (Multi Verse Optimizer), and AOS algorithms. Even though the best fitness value obtained by AOS algorithm seems to be slightly better, but this is to be considered infeasible because the number of gear teeth was considered as a continuous variable in [16].

5.10. Corrugated bulkhead:

The maximum FEs in this problem is considered as 15000. Table 15 compares statistical results of this problem over 25 runs. The best fitness value obtained is $f(\bar{x}) = 6.84295801$ at $\bar{x} = (57.69230769, 34.14762035, 57.69230769, 1.05)$ by all the proposed algorithms except CSA. The best fitness value obtained by CSA is infeasible as the corresponding values of \bar{x} violates a constraint. The Chaotic Rao1 algorithm requires the minimum FEs to reach an optimal solution.

Table 12. Statistical results comparison for a piston lever design problem

Algorithm	B	M	W	SD	MFE	NP, ES/CS ₁
HPSO ^a	162	187	197	1.340E+01	NA	NA
GA ^a	161	185	216	1.820E+01	NA	NA
DE ^a	159	187	199	1.420E+01	NA	NA
CSA ^a	8.4271	40.2319	168.592	5.906E+01	NA	50
AOS ^b	8.419142742	33.7412759	60.66498628	9.347E+01	NA	NA
Rao1	8.412698	84.76151	167.4727	8.111E+01	6944	10
Rao2	8.412698	103.8487	167.4727	7.953E+01	11207	15
Rao3	8.412698	97.48632	167.4727	8.058E+01	9935	20
SAMPE Rao1	8.412698	73.0191	167.4727	7.884E+01	8184	20,2
SAMPE Rao2	8.412698	84.76151	167.4727	8.111E+01	7778	15,2
SAMPE Rao3	8.412698	84.76151	167.4727	8.111E+01	7578	15,2
Chaotic Rao1	8.412698	78.39911	167.4727	8.058E+01	5113	20,0,3
Chaotic Rao2	8.412698	91.12391	167.4727	8.111E+01	11543	15,0,3
Chaotic Rao3	8.412698	91.12391	167.4727	8.111E+01	9575	11,0,2

^aResults are taken from [15]; ^bResults are taken from [16]

Table 13. Statistical results comparison for a gear train design problem

Algorithm	B	M	W	SD	MFE	NP, ES/CS ₁
AOS ^{a*}	2.29E-19	6.25E-15	9.06E-14	1.260E-14	NA	NA
Rao1	2.70086E-12	2.44995E-08	2.38608E-07	4.734E-08	225	10
Rao2	2.70086E-12	5.74147E-08	8.949E-07	1.781E-07	220	10
Rao3	2.70086E-12	8.81838E-08	8.949E-07	2.437E-07	212	10
SAMPE Rao1	2.70086E-12	1.36555E-08	8.92118E-08	2.005E-08	256	10,2
SAMPE Rao2	2.70086E-12	1.68745E-08	1.76128E-07	3.482E-08	267	15,2
SAMPE Rao3	2.70086E-12	1.14852E-08	7.80223E-08	1.732E-08	199	10,2
Chaotic Rao1	2.70086E-12	2.08542E-08	1.5244E-07	3.778E-08	238	10,0,2
Chaotic Rao2	2.70086E-12	5.30282E-08	5.04146E-07	1.223E-07	251	10,0,6
Chaotic Rao3	2.70086E-12	6.0809E-08	8.949E-07	1.773E-07	244	15,0,4

^aResults are taken from [16];

Table 14. Best fitness value comparison for a gear train design problem

Algorithm	CS ^a	ALO ^a	MFO ^a	MVO ^a	AOS ^{b*}	Present study
Best result	2.701e-12	2.7009e-12	2.7009e-12	2.7009e-12	2.29e-19	2.70086e-12

^aResults are taken from [13]; ^bResults are taken from [16]; *Infeasible solution because number of gear teeth was considered as a continuous variable.

Table 15. Statistical results comparison for a corrugated bulkhead design problem

Algorithm	B	M	W	SD	MFE	NP, ES/CS ₁
CSA ^{a*}	5.894331	5.988257	6.126749	6.436E-02	NA	NA
AOS ^a	6.84295801	7.060808377	7.066936186	6.491E-04	NA	NA
Rao1	6.84295801	6.84295801	6.84295801	0.000E+00	4290	10
Rao2	6.84295801	6.84295801	6.84295801	0.000E+00	4573	10
Rao3	6.84295801	6.84295801	6.84295801	0.000E+00	4260	10
SAMPE Rao1	6.84295801	6.84295801	6.84295801	0.000E+00	4231	14,2
SAMPE Rao2	6.84295801	6.84295801	6.84295801	0.000E+00	4326	10,2
SAMPE Rao3	6.84295801	6.84295801	6.84295801	0.000E+00	4066	10,2
Chaotic Rao1	6.84295801	6.84295801	6.84295801	0.000E+00	3442	10,0,2
Chaotic Rao2	6.84295801	6.84295801	6.84295801	0.000E+00	4277	10,0,9
Chaotic Rao3	6.84295801	6.84295801	6.84295801	0.000E+00	4132	8,0,6

^a Results are taken from [16]; * Infeasible solution due to violation of a constraint

5.11. Planetary gear train:

The maximum FEs in this problem is considered as 200000. Table 16 compares the statistical results of this problem over 25 runs using the proposed algorithms, PSO (Particle Swarm Optimization), ABC (Artificial Bee Colony), PVS (Passing Vehicle Search), AOS, and QSA (Queueing Search Algorithm). The best fitness value obtained is $f(\bar{x}) = 0.52325$ at $\bar{x} = (40, 21, 14, 19, 14, 69, 5, 1.75, 2)$ using all the proposed algorithms and AOS algorithm. The mean fitness values attained using the proposed algorithms are slightly higher than the same obtained using AOS algorithm.

5.12. Step cone pulley:

The maximum FEs in this problem, is considered as 15000. Table 17 compares the statistical results of this problem over 25 runs for TLBO (Teaching Learning Based Optimization), WOA (Whale Optimization Algorithm), WCA (Water Cycle Algorithm), MBA (Mine Blast Algorithm), and AOS. The best fitness value obtained is $f(\bar{x}) = 16.63450485$ kg at $\bar{x} = (85.98624253, 40,$

$54.76430076, 73.01317694, 88.42841982)$ by all the proposed algorithms. Even though the result obtained by AOS appears to be better, but it is to be considered as an infeasible solution because the value of one design variable is out of the given range. The best mean fitness value is attained using the Chaotic Rao2 algorithm.

5.13. Hydrostatic thrust bearing:

The maximum FEs in this problem is considered as 25000. Table 18 compares the statistical results of this problem over 25 runs for TLBO, AOS, and the proposed algorithms. Table 19 compares the best fitness value obtained in present study and those obtained by PSO, GASO (Genetic Algorithm aided Stochastic Optimization), GeneAS (Genetic Adaptive Search), ABC, TLBO, and AOS algorithm. Even though the result obtained by AOS appears to be better, but it is to be considered as an infeasible solution because of the violation of a constraint. The best fitness value is obtained by SAMPE Rao1 algorithm, and the value is $f(\bar{x}) = 1625.031214$ btu/s at $\bar{x} = (5.955330, 5.388607, 2.269248, 0.000005358845)$.

Table 16. Statistical results comparison for a planetary gear train design problem

Algorithm	B	M	W	SD	MFE	NP,ES/CS ₁
PSO ^a	0.53	0.5361934	NA	NA	NA	50
ABC ^a	0.525769	0.5272922	NA	NA	NA	50
QSA ^a	0.525589	0.525589	NA	NA	NA	30
PVS ^a	0.525588	0.53063	NA	NA	NA	NA
AOS ^b	0.52325	0.529848233	0.537058824	3.894E-03	NA	NA
Rao1	0.52325	0.534683372	0.553181818	6.143E-03	12459	30
Rao2	0.52325	0.588581422	1.87875	2.689E-01	9880.8	30
Rao3	0.52325	0.545598896	0.805652174	5.460E-02	14033	35
SAMPE Rao1	0.52325	0.531301937	0.549705882	6.245E-03	10611	20,2
SAMPE Rao2	0.52325	0.53330837	0.549849108	5.618E-03	9283	20,2
SAMPE Rao3	0.52325	0.532603237	0.545064935	5.561E-03	11022	40,2
Chaotic Rao1	0.52325	0.53293644	0.549705882	5.719E-03	11623	25,0.6
Chaotic Rao2	0.52325	0.54700953	0.805652174	5.436E-02	9379.2	40,0.2
Chaotic Rao3	0.52325	0.536461805	0.549311686	5.899E-03	14137.6	40,0.4

^aResults are taken from [15]; ^bResults are taken from [16]

Table 17. Statistical results comparison for a step cone pulley design problem

Algorithm	B	M	W	SD	MFE	NP,ES/CS ₁
TLBO ^a	16.63451	24.0113577	74.022951	3.400E-01	NA	50
WOA ^a	16.6345213	20.93829477	24.8488259	3.349E+00	NA	20
WCA ^a	16.63450849	17.53037682	18.83302997	9.229E-01	NA	20
MBA ^a	16.6345078	16.702535	18.3237145	2.627E-01	NA	20
AOS ^{a*}	16.08558875	16.29548945	16.80334816	1.772E-01	NA	NA
Rao1	16.63450485	16.72640748	17.59405649	2.198E-01	12845	20
Rao2	16.63450485	16.74252202	17.51387727	2.471E-01	12888	20
Rao3	16.63450485	16.78532149	18.01364527	3.673E-01	13249	20
SAMPE Rao1	16.63450485	16.69646353	17.25819841	1.400E-01	12812	30,2
SAMPE Rao2	16.63450485	16.70155067	17.30303274	1.598E-01	13647	25,2
SAMPE Rao3	16.63450485	16.7270869	17.4362292	2.204E-01	12669	30,2
Chaotic Rao1	16.63450485	16.67806324	16.88845818	8.562E-02	10208	15,0.3
Chaotic Rao2	16.63450485	16.64720778	16.95205707	6.351E-02	14751	20,0.2
Chaotic Rao3	16.63450485	16.74985978	19.24078858	5.204E-01	14552	20,0.2

^aResults are taken from [16]; ^{*}Infeasible solution because the value of one design variable is out of the given range

5.14. Welded beam:

The maximum FEs in this problem is considered as 15000. Table 20 compares the statistical results of this problem over 25 runs obtained by CDE (Co-evolutionary Differential Evolution), WCA (Water Cycle Algorithm), IAPSO (Improved accelerated PSO), STA (State Transition Algorithm), and CGO. The best fitness value obtained is $f(\bar{x}) = 1.724852309$ \$ at $\bar{x} = (0.20573, 3.470489, 9.036624, 0.20573)$ by all the algorithms. The best fitness values given by algorithms STA and CGO algorithms are not feasible as the corresponding values of the design variables violate a constraint. The Chaotic Rao1 algorithm requires the minimum FEs to reach an optimal solution.

5.15. Multiple disk clutch brake:

The maximum FEs in this problem is considered as 500. Table 21 compares the statistical results of this problem over 25 runs obtained by CGO, WCA, TLBO, and C-ITGO (constrained Iterative Topographical Global Optimization) and the proposed algorithms. The best fitness value obtained is $f(\bar{x}) = 0.235242458$ kgat $\bar{x} = (70, 90, 1, 1000, 2)$ by all the proposed algorithms. The results obtained by WCA, TLBO, and C-ITGO are inferior. The Chaotic Rao2 algorithm requires the minimum FEs to reach an optimal solution.

Table 18. Statistical results comparison for a hydrostatic thrust bearing design problem

Algorithm	B	M	W	SD	MFE	NP,ES/CS ₁
TLBO ^a	1625.44276	1797.70798	2096.8012	1.900E-01	NA	50
AOS ^{b*}	1621.926212	1752.413561	1831.449755	2.362E+01	NA	NA
Rao1	1625.143383	1643.604394	1808.117508	3.670E+01	23984	10
Rao2	1625.346729	1815.285715	3386.590418	4.763E+02	21576	10
Rao3	1625.221851	1730.441329	3388.349231	3.491E+02	21469	10
SAMPE Rao1	1625.031214	1840.052283	3385.845191	4.331E+02	22935	10,2
SAMPE Rao2	1625.089866	1744.303738	3386.979117	3.741E+02	22990	10,2
SAMPE Rao3	1625.084662	1744.362308	3385.814478	3.502E+02	22386	10,2
Chaotic Rao1	1625.10655	1637.083563	1692.563375	1.974E+01	23530	10,0,3
Chaotic Rao2	1625.087311	1836.948829	3386.439864	5.049E+02	22797	10,0,3
Chaotic Rao3	1625.171166	1949.270479	3385.588751	6.433E+02	22051	10,0,4

* Infeasible solution due to violation of a constraint; ^a Results are taken from [13]; ^b Results are taken from [16]

Table 19. Comparison of best fitness value for a hydrostatic thrust bearing design problem

Algorithm	GASO ^a	GeneAS ^a	ABC ^a	TLBO ^a	AOS ^{b*}	Present study
Best result	1950.286	2161.4215	1625.44276	1625.44276	1621.9262	1625.031214

^a Results are taken from [13]; ^b Results are taken from [16]; * Infeasible solution due to violation of a constraint

Table 20. Statistical results comparison for a welded beam design problem

Algorithm	B	M	W	SD	MFE	NP,ES/CS ₁
CDE ^a	1.733461	1.768158	1.824105	2.219E-02	NA	NA
WCA ^a	1.724856	1.726427	1.744697	4.290e-03	NA	NA
IAPSO ^a	1.724852	1.724853	1.724862	2.020e-06	NA	50
STA ^{a*}	1.6956397	1.6956397	1.7530472	1.830E-02	NA	30
CGO ^{a*}	1.670335792	1.670378098	1.670902785	9.300E-05	NA	NA
Rao1	1.724852309	1.724852309	1.724852309	0.000E+00	14631	10
Rao2	1.724852309	1.724852309	1.724852309	0.000E+00	14888	20
Rao3	1.724852309	1.724852309	1.724852309	0.000E+00	14844	20
SAMPE Rao1	1.724852309	1.724852309	1.724852309	0.000E+00	10260	15,2
SAMPE Rao2	1.724852309	1.724852309	1.724852309	0.000E+00	14171	20,2
SAMPE Rao3	1.724852309	1.724852309	1.724852309	0.000E+00	14477	20,2
Chaotic Rao1	1.724852309	1.724852309	1.724852309	0.000E+00	6650	10,0,2
Chaotic Rao2	1.724852309	1.724852309	1.724852309	0.000E+00	14881	20,0,6
Chaotic Rao3	1.724852309	1.724852309	1.724852309	0.000E+00	14821	20,0,6

^a Results are taken from [22]; * Infeasible solution due to violation of constraints.

Table 21. Statistical results comparison for a multiple disk clutch brake design problem

Algorithm	B	M	W	SD	MFE	NP,ES/CS ₁
WCA ^a	0.313656	0.313656	0.313656	1.690E-16	NA	NA
TLBO ^a	0.313657	0.3271662	0.392071	6.700E-01	NA	20
C-ITGO ^a	0.313656	0.313656	0.313656	1.130E-16	NA	20
CGO ^a	0.235242458	0.235242458	0.23524246	1.950E-10	NA	NA
Rao1	0.235242458	0.235242458	0.235242458	0.000E+00	132.0	10
Rao2	0.235242458	0.235242458	0.235242458	0.000E+00	119.0	20
Rao3	0.235242458	0.235242458	0.235242458	0.000E+00	123.0	20
SAMPE Rao1	0.235242458	0.235242458	0.235242458	0.000E+00	128.0	15,4
SAMPE Rao2	0.235242458	0.235242458	0.235242458	0.000E+00	113.0	15,2
SAMPE Rao3	0.235242458	0.235242458	0.235242458	0.000E+00	99.0	10,2
Chaotic Rao1	0.235242458	0.235242458	0.235242458	0.000E+00	113.0	10,0,2
Chaotic Rao2	0.235242458	0.235242458	0.235242458	0.000E+00	93.0	15,0,2
Chaotic Rao3	0.235242458	0.235242458	0.235242458	0.000E+00	98.0	15,0,2

^a Results are taken from [22]

6. Conclusions

The Self-adaptive Multi-population Elitist (SAMPE) Rao algorithms and Chaotic Rao algorithms are proposed in the present work. These algorithms are based on the recently developed Rao algorithms. The SAMPE Rao algorithms increase the exploration and exploitation rate of the search process in finding the optimal solution. The Chaotic Rao algorithms help to find the optimal solution without getting stuck at the local optimum. 25 unconstrained benchmark functions and 15 constrained mechanical engineering design optimization problems are solved using the proposed algorithms to test their performance. The Friedman rank test is used to validate the proposed algorithms' superior performance. The proposed algorithms are ranked according to their performance in the Friedman rank test; the chaotic Rao1 algorithm is ranked first. The best fitness value and the statistical results achieved by the proposed algorithms and previously reported results using other advanced optimization algorithms for engineering optimization problems are compared. This comparison shows that the proposed algorithms effectively solve most of the benchmark problems and the constrained engineering design problems. In this paper, design optimization problems of mechanical engineering components are considered but the proposed algorithms can also be applied to more complex design optimization problems. The proposed algorithms can also be used to solve multi-objective optimization problems.

References

- [1] R. V. Rao, V. J. Savsani, D. P. Vakharia, 2011. Teaching-learning-based optimization: A novel method for constrained mechanical design optimization problems, *CAD Computer Aided Design*, vol. 43, no. 3, pp. 303–315.
- [2] R. V. Rao, V. J. Savsani, 2012. *Mechanical design optimization using advanced optimization techniques*, Springer Verlag London.
- [3] R. V. Rao, A. Saroj, 2019. An elitism-based self-adaptive multi-population Jaya algorithm and its applications, *Soft Computing*, vol. 23, no. 12, pp. 4383–4406.
- [4] B. Alatas, 2010. Chaotic harmony search algorithms, *Applied Mathematics and Computation*, vol. 216, no. 9, pp. 2687–2699.
- [5] J. Zhang, X. Ding, 2011. A multi-swarm self-adaptive and cooperative particle swarm optimization, *Engineering Applications of Artificial Intelligence*, vol. 24, no. 6, pp. 958–967.
- [6] A. H. Gandomi, X. S. Yang, S. Talatahari, A. H. Alavi, 2013. Firefly algorithm with chaos, *Communications in Nonlinear Science and Numerical Simulation*, vol. 18, no. 1, pp. 89–98.
- [7] R. V. Rao, V. Patel, 2013. Multi-objective optimization of heat exchangers using a modified teaching-learning-based optimization algorithm, *Applied Mathematical Modelling*, vol. 37, no. 3, pp. 1147–1162.
- [8] R. V. Rao, A. Saroj, 2017. A self-adaptive multi-population based Jaya algorithm for engineering optimization, *Swarm and Evolutionary Computation*, vol. 37, pp. 1–26.
- [9] A. Farah, A. Belazi, 2018. A novel chaotic Jaya algorithm for unconstrained numerical optimization, *Nonlinear Dynamics*, vol. 93, no. 3, pp. 1451–1480.
- [10] Z. Yu, T. Xu, P. Cheng, W. Zuo, X. Liu, T. Yoshino, 2014. Optimal design of truss structures with frequency constraints using interior point trust region method, *Proceedings of Romanian Academy Series A - Mathematics, Physics, Technical Sciences and Information Sciences*, vol. 15, no. 2, pp. 165–173.
- [11] S. Arora, S. Singh, K. Yetilmezsoy, 2018. A modified butterfly optimization algorithm for mechanical design optimization problems, *Journal of the Brazilian Society of Mechanical Science and Engineering*, vol. 40, no. 1, pp. 1–17.
- [12] S. Chakraborty, A. K. Saha, S. Sharma, S. Mirjalili, R. Chakraborty, 2021. A novel enhanced whale optimization algorithm for global optimization, *Computers and Industrial Engineering*, vol. 153, pp. 28–44.
- [13] R. V. Rao, R. B. Pawar, 2020. Self-adaptive Multi-population Rao Algorithms for Engineering Design Optimization, *Applied Artificial Intelligence*, vol. 34, no. 3, pp. 187–250.
- [14] R. V. Rao, R. B. Pawar, 2020. Constrained design optimization of selected mechanical system components using Rao algorithms, *Applied Soft Computing*, vol. 89, 106141.
- [15] S. Talatahari, M. Azizi, A. H. Gandomi, 2021. Material generation algorithm: A novel metaheuristic algorithm for optimization of engineering problems, *Processes*, vol. 9, no. 5, pp. 1–35.
- [16] M. Azizi, S. Talatahari, A. Giaralis, 2021. Optimization of engineering design problems using atomic orbital search algorithm, *IEEE Access*, vol. 9, pp. 102497–102519.
- [17] S. H. Aghdeab, L. A. Mohammed, A. M. Ubaid, 2015. Optimization of CNC turning for aluminum alloy using simulated annealing method, *Jordan Journal of Mechanical and Industrial Engineering*, vol. 9, no. 1, pp. 39–44.
- [18] A. H. Q. Ayun, J. Triyono, E. Pujiyanto, 2022. Optimization of injection molding simulation of bioabsorbable bone screw using Taguchi method and particle swarm optimization, *Jordan Journal of Mechanical and Industrial Engineering*, vol. 16, no. 2, pp. 319–325.
- [19] M. Soori, M. Asmael, 2022. A review of the recent development in machining parameter optimization, *Jordan Journal of Mechanical and Industrial Engineering*, vol. 16, no. 2, pp. 205–223.
- [20] R. V. Rao, 2020. Rao algorithms: Three metaphor-less simple algorithms for solving optimization problems, *International Journal of Industrial Engineering Computations*, vol. 11, no. 1, pp. 107–130.
- [21] J. Derrac, S. García, D. Molina, F. Herrera, 2011. A practical tutorial on the use of nonparametric statistical tests as a methodology for comparing evolutionary and swarm intelligence algorithms, *Swarm and Evolutionary Computation*, vol. 1, no. 1, pp. 3–18.
- [22] S. Talatahari, M. Azizi, 2020. Optimization of constrained mathematical and engineering design problems using chaos game optimization, *Computers and Industrial Engineering*, vol. 145, p. 106560, 2020.
- [23] P. A. Simionescu, D. Beale, G. V. Dozier, 2006. Teeth-number synthesis of a multispeed planetary transmission using an estimation of distribution algorithm, *Journal of Mechanical Design*, vol. 128, no. 1, pp. 108–115.
- [24] S. He, E. Prempan, Q. H. Wu, 2004. An improved particle swarm optimizer for mechanical design optimization problems, *Engineering Optimization*, vol. 36, no. 5, pp. 585–605.
- [25] A. H. Gandomi, X. S. Yang, A. H. Alavi, 2013. Cuckoo search algorithm: A metaheuristic approach to solve structural optimization problems, *Engineering with Computers*, vol. 29, no. 1, pp. 17–35.

Appendix A:

Table A.1 Unconstrained benchmark functions considered[20]

No.	Function	Formulation	D	Search range	C
f ₁	Sphere	$f_1(x) = \sum_{i=1}^D x_i^2$	30	[-100, 100]	US
f ₂	SumSquares	$f_2(x) = \sum_{i=1}^D ix_i^2$	30	[-10, 10]	US
f ₃	Beale	$f_3(x) = (2.25 - x_1 - x_1x_2^2)^2 + (1.5 - x_1 + x_1x_2)^2 + (2.625 - x_1 + x_1x_2^3)^2$	5	[-4.5, 4.5]	UN
f ₄	Easom	$f_4(x) = -\cos(x_1)\cos(x_2)\exp(-(x_1 - \pi)^2 - (x_2 - \pi)^2)$	2	[-100, 100]	UN
f ₅	Matyas	$f_5(x) = 0.26(x_1^2 + x_2^2) - 0.48x_1x_2$	2	[-10, 10]	UN
f ₆	Colville	$f_6(x) = 100(x_1^2 - x_2)^2 + (x_3 - 1)^2 + (x_1 - 1)^2 + 90(x_3^2 - x_4)^2 + 19.8(x_2 - 1)(x_4 - 1) + 10.1((x_2 - 1)^2 + (x_4 - 1)^2)$	4	[-10, 10]	UN
f ₇	Trid 6	$f_7(x) = \sum_{i=1}^D (x_i - 1)^2 - \sum_{i=2}^D x_i x_{i-1}$	6	[-D ² , D ²]	UN
f ₈	Trid 10	$f_8(x) = \sum_{i=1}^D (x_i - 1)^2 - \sum_{i=2}^D x_i x_{i-1}$	10	[-D ² , D ²]	UN
f ₉	Zakharov	$f_9(x) = \sum_{i=1}^D x_i^2 + \left(\sum_{i=1}^D 0.5ix_1 \right)^2 + \left(\sum_{i=1}^D 0.5ix_1 \right)^4$	10	[-5, 10]	UN
f ₁₀	Schwefel 1.2	$f_{10}(x) = \sum_{i=1}^D \left(\sum_{j=1}^i x_j^2 \right)^2$	30	[-100, 100]	UN
f ₁₁	Rosenbrock	$f_{11}(x) = \sum_{i=1}^D [100(x_{i+1} - x_i^2)^2 + (x_i - 1)^2]$	30	[-30, 30]	UN
f ₁₂	Dixon-Price	$f_{12}(x) = (1 - x_1)^2 + \sum_{i=2}^D i(x_{i-1} - 2x_i^2)^2$	30	[-10, 10]	UN
f ₁₃	Branin	$f_{13}(x) = \left(x_2 - \frac{5.1x_1^2}{4\pi^2} + \frac{5x_1}{\pi - 6} \right)^2 + 10 \left(1 - \frac{1}{8\pi} \right) \cos(x_1) + 10$	2	[-5, 10] [0, 15]	MS
f ₁₄	Bohachevsky 1	$f_{14}(x) = x_1^2 + x_2^2 - 0.3\cos(3\pi x_1) - 0.4\cos(4\pi x_2) + 0.7$	2	[-100, 100]	MS
f ₁₅	Bohachevsky 2	$f_{15}(x) = x_1^2 + 2x_2^2 - 0.3\cos((3\pi x_1)(4\pi x_2)) + 0.3$	2	[-100, 100]	MN
f ₁₆	Bohachevsky 3	$f_{16}(x) = x_1^2 + 2x_2^2 - 0.3\cos(3\pi x_1 + 4\pi x_2) + 0.3$	2	[-100, 100]	MN
f ₁₇	Booth	$f_{17}(x) = (x_1 - 2x_2 - 7)^2 + (2x_1 + x_2 - 5)^2$	2	[-10, 10]	MS

f ₁₈	Michalewicz 2	$f_{18}(x) = - \sum_{i=1}^D \sin x_i \left(\sin \left(\frac{ix_i^2}{\pi} \right) \right)^{20}$	2	[0, π]	MS
f ₁₉	Michalewicz 5	$f_{19}(x) = - \sum_{i=1}^D \sin x_i \left(\sin \left(\frac{ix_i^2}{\pi} \right) \right)^{20}$	5	[0, π]	MS
f ₂₀	Goldstein-Price	$f_{20}(x) = [1 + (19 - 14x_1 + 3x_1^2 - 14x_2 + 6x_1x_2 + 3x_2^2)(x_1 + x_2 + 1)^2] [30 + (2x_1 - 3x_2)^2(18 - 32x_1 + 12x_1^2 + 48x_2 - 36x_1x_2 + 27x_2^2)]$	2	[-2, 2]	MN
f ₂₁	Perm	$f_{21}(x) = \sum_{k=1}^D \left[\sum_{i=1}^D (i_k + \beta) \left(\left(\frac{x_i}{i} \right)^k - 1 \right) \right]^2$	4	[-D, D]	MN
f ₂₂	Ackley	$f_{22}(x) = -20 \exp \left(-0.2 \sqrt{\frac{1}{D} \sum_{i=1}^D x_i^2} \right) - \exp \left(\frac{1}{D} \sum_{i=1}^D \cos 2\pi x_i \right) + 20 + e$	30	[-32, 32]	MN
f ₂₃	Foxholes	$f_{23}(x) = \left[\frac{1}{500} + \sum_{j=1}^{25} \frac{1}{j + \sum_{i=1}^2 (x_i - a_{ij})^6} \right]^{-1}$	2	[-65.536, 65.536]	MS
f ₂₄	Hartman 3	$f_{24}(x) = - \sum_{i=1}^4 c_i \exp \left[- \sum_{j=1}^3 a_{ij} (x_j - p_{ij})^2 \right]$	3	[0, 1]	MN
f ₂₅	Penalized 2	$f_{25}(x) = 0.1 \left[\sin^2(\pi x_1) + \sum_{i=1}^{D-1} (x_i - 1)^2 \{1 + \sin^2(3\pi x_{i+1})\} + (x_D - 1)^2 + (1 + \sin^2(2\pi x_D)) \right] + \sum_{i=1}^D u(x_i, 5, 100, 4)$	30	[-50, 50]	MN
		$u(x_i, a, k, m) = \begin{cases} k(x_i - a)^m, & x_i > a \\ 0, & -a \leq x_i \leq a \\ k(-x_i - a)^m, & x_i < -a \end{cases}$			

D: Dimension, C: Characteristics, U: Unimodal, M: Multimodal, S: Separable, N: Non-separable.

Appendix B: Mathematical formulations of the design optimization problems considered [16]**Problem 1: Planetary gear train:**

Design variables:

$$\bar{x} = [Z_1, Z_2, Z_3, Z_4, Z_5, Z_6, Z_p, m_1, m_2] \quad \text{B.1}$$

Objective function:

Minimize,

$$f(\bar{x}) = \max |i_k - i_{0k}|, k = \{1, 2, R\} \quad \text{B.2}$$

$$i_1 = \frac{Z_6}{Z_4}, i_{01} = 3.11, i_2 = \frac{Z_6(Z_1Z_3 + Z_2Z_4)}{Z_1Z_3(Z_6 - Z_4)}, i_{02} = 1.84, i_R = -\frac{Z_2Z_6}{Z_1Z_3}, i_{0R} = -3.11 \quad \text{B.3}$$

Design constraints:

$$C_1(\bar{x}) = D_{\max} - m_3(Z_6 + 2.5) \geq 0 \quad \text{B.4}$$

$$C_2(\bar{x}) = D_{\max} - m_1(Z_1 + Z_2) - m_1(Z_2 + 2) \geq 0 \quad \text{B.5}$$

$$C_3(\bar{x}) = D_{\max} - m_2(Z_4 + Z_5) - m_2(Z_5 + 2) \geq 0 \quad \text{B.6}$$

$$C_4(\bar{x}) = m_1 + m_2 - |m_1(Z_1 + Z_2) - m_2(Z_6 - Z_3)| \geq 0 \quad \text{B.7}$$

$$C_5(\bar{x}) = 2 + \delta_{22} + Z_2 - (Z_1 + Z_2)\sin(\pi/Z_p) \geq 0 \quad \text{B.8}$$

$$C_6(\bar{x}) = Z_3 + 2 + \delta_{33} - (Z_6 - Z_3)\sin(\pi/Z_p) \geq 0 \quad \text{B.9}$$

$$C_8(\bar{x}) = (Z_3 + Z_5 + 2 + \delta_{35})^2 - (Z_6 - Z_3)^2 - (Z_4 + Z_5)^2 + 2(Z_6 - Z_3)(Z_4 + Z_5)\cos(2\pi/Z_p - \beta) \geq 0 \quad \text{B.10}$$

Where,

$$\beta = \frac{\cos^{-1}((Z_6 - Z_3)^2 + (Z_4 + Z_5)^2 - (Z_3 + Z_5)^2)}{2(Z_6 - Z_3)(Z_4 + Z_5)} \quad \text{B.11}$$

$$C_9(\bar{x}) = 4 + 2\delta_{34} - Z_6 + 2Z_3 + Z_4 \geq 0 \quad \text{B.12}$$

$$C_{10}(\bar{x}) = 4 + 2\delta_{56} - Z_6 + Z_4 + 2Z_5 \geq 0 \quad \text{B.13}$$

$$h(\bar{x}) = \frac{Z_6 - Z_4}{Z_p} = \text{integer} \quad \text{B.14}$$

Where,

$$Z_p = (3, 4, 5), m_1, m_2 = (1.75, 2, 2.25, 2.5, 2.75, 3) \text{ mm} \quad \text{B.15}$$

$$17 \leq Z_1 \leq 96, 14 \leq Z_2 \leq 54, 14 \leq Z_3 \leq 51, 17 \leq Z_4 \leq 46, 14 \leq Z_5 \leq 51, 48 \leq Z_6 \leq 124, \quad \text{B.16}$$

$$Z_i = \text{integer}, i = 1, 2, \dots, 6$$

$$D_{\max} = 220 \text{ mm}, \delta_{22} = 0.5, \delta_{33} = 0.5, \delta_{55} = 0.5, \delta_{35} = 0.5, \delta_{56} = 0.5, \delta_{34} = 0.5$$

Problem 2: Step-cone pulley

Design variables:

$$\bar{x} = [d_1, d_2, d_3, d_4, w] \quad \text{B.17}$$

Objective function:

$$\text{Minimize, } f(x) = \frac{\pi}{4} \rho w \left\{ d_1^2 \left[1 + \left(\frac{N_1}{N} \right)^2 \right] + d_2^2 \left[1 + \left(\frac{N_2}{N} \right)^2 \right] + d_3^2 \left[1 + \left(\frac{N_3}{N} \right)^2 \right] + d_4^2 \left[1 + \left(\frac{N_4}{N} \right)^2 \right] \right\} \quad \text{B.18}$$

Design constraints:

$$C_1(x) = c_2 - c_1 = 0 \quad \text{B.19}$$

$$C_2(x) = c_3 - c_1 = 0 \quad \text{B.20}$$

$$C_3(x) = c_4 - c_1 = 0 \quad \text{B.21}$$

$$C_{4,5,6,7}(x) = 2 - R_i \leq 0 \quad \text{B.22}$$

$$C_{8,9,10,11}(x) = (0.75 \times 745.6998) - P_i \leq 0 \quad \text{B.23}$$

Where: c_i : belt length, N_i : Speed to be achieved

$$c_i = \frac{\pi d_i}{2} \left(\frac{N_i}{N} + 1 \right) + \frac{\left(\frac{N_i - 1}{N} \right)^2 d_i^2}{4a} + 2a \quad \text{B.24}$$

R_i : tension ratio

$$R_i = \exp \left\{ \mu \left[\pi - 2 \sin^{-1} \left\{ \frac{d_i}{2a} \left(\frac{N_i}{N} - 1 \right) \right\} \right] \right\} \quad \text{B.25}$$

P_i : power transmitted at each step

$$P_i = stw \left[1 - \exp \left\{ -\mu \left[\pi - 2 \sin^{-1} \left\{ \frac{d_i}{2a} \left(\frac{N_i}{N} - 1 \right) \right\} \right] \right\} \right] \times \left(\frac{\pi d_i N_i}{60} \right) \quad \text{B.26}$$

$$\rho = 7200 \text{ kg/m}^3, \mu = 0.35, a = 3 \text{ m}, t = 8 \text{ mm}, s = 1.75 \text{ MPa},$$

$$16 \leq w(\text{mm}) \leq 100, 40 \leq d_i(\text{mm}) \leq 100, i=1, 2, 3, 4 \quad \text{B.27}$$

$$N = 350 \text{ rpm}, N_1 = 750 \text{ rpm}, N_2 = 450 \text{ rpm}, N_3 = 250 \text{ rpm}, N_4 = 150 \text{ rpm}$$

Problem 3: Hydrostatic thrust bearing:

Design variables:

$$\bar{x} = [R, R_0, Q, \mu] \quad \text{B.28}$$

$$\text{Minimize, } f(\bar{x}) = \frac{1}{12} \left(\frac{QP_o}{0.7} + E_f \right) \quad \text{B.29}$$

Design constraints:

$$C_1(\bar{x}) = W_s - W \leq 0 \quad \text{B.30}$$

$$C_2(\bar{x}) = P_o - P_{max} \leq 0 \quad \text{B.31}$$

$$C_3(\bar{x}) = \Delta T_{max} - \Delta T \leq 0 \quad \text{B.32}$$

$$C_4(\bar{x}) = h_{min} - h \leq 0 \quad \text{B.33}$$

$$C_5(\bar{x}) = R_0 - R \leq 0 \quad \text{B.34}$$

$$C_6(\bar{x}) = \left(\frac{\gamma}{gP_o} \right) \left(\frac{Q}{2\pi R h} \right)^2 - 0.001 \leq 0 \quad \text{B.35}$$

$$C_7(\bar{x}) = \left(\frac{W}{\pi(R^2 - R_0^2)} \right) - 5000 \leq 0 \quad \text{B.36}$$

Where,

$$\gamma = \text{weight density of oil} = 0.0307 \frac{\text{lb}}{\text{in}^3}, \quad \text{B.37}$$

$$C = \text{specific heat of oil} = 0.5 \text{ BTU/lb}^\circ\text{F}, n = -3.55; C_1 = 10.04, W_s = 100982.74 \text{ lb}$$

$$P_{max} = 1000 \text{ psi}, \Delta T_{max} = 50^\circ\text{F}, h_{min} = 0.001 \text{ in}, g = 386.4 \text{ in/s}^2, N = 750 \text{ rpm} \quad \text{B.38}$$

$$P = \frac{(\log_{10}(\log_{10}(8.122 \times 10^6 \mu + 0.8))) - c_1}{n} \quad \text{B.39}$$

$$\Delta T = 2((10^P) - 560) \quad \text{B.40}$$

$$E_f = 9336 Q \gamma C \Delta T \quad \text{B.41}$$

$$h = \left(\frac{2\pi N}{60} \right)^2 \left(\frac{2\pi \mu}{E_f} \right) \left(\frac{R^4 - R_0^4}{4} \right) \quad \text{B.42}$$

$$P_o = \left(\frac{6\mu Q}{\pi h^3} \right) \ln \left(\frac{R}{R_0} \right) \quad \text{B.43}$$

$$W = \left(\frac{\pi P_o}{2} \right) \left(\frac{R^2 - R_0^2}{\ln(R/R_0)} \right) \quad \text{B.44}$$

$$1 \leq R, R_0(\text{in}), Q(\text{in}^3/\text{s}) \leq 16, 10^{-1} \leq \mu \leq 16 \times 10^{-6} \quad \text{B.45}$$

Problem 4: Four stage gearbox

Design variables:

$$\bar{x} = [N_{p1}, N_{g1}, N_{p2}, N_{g2}, N_{p3}, N_{g3}, N_{p4}, N_{g4}, b_1, b_2, b_3, b_4, x_{p1}, x_{g1}, x_{g2}, x_{g3}, x_{g4}, y_{p1}, y_{g1}, y_{g2}, y_{g3}, y_{g4}] \quad \text{B.46}$$

Objective function:

$$\text{Minimize, } f(\bar{x}) = \frac{\pi}{1000} \left[\frac{b_1 c_1^2 (N_{p1}^2 + N_{g1}^2)}{(N_{p1} + N_{g1})^2} + \frac{b_2 c_2^2 (N_{p2}^2 + N_{g2}^2)}{(N_{p2} + N_{g2})^2} + \frac{b_3 c_3^2 (N_{p3}^2 + N_{g3}^2)}{(N_{p3} + N_{g3})^2} + \frac{b_4 c_4^2 (N_{p4}^2 + N_{g4}^2)}{(N_{p4} + N_{g4})^2} \right] \quad \text{B.47}$$

Design constraints:

$$C_1(\bar{x}) = \left(\frac{366000}{\pi \omega_1} + \frac{2c_1 N_{p1}}{N_{g1} + N_{p1}} \right) \left(\frac{(N_{p1} + N_{g1})^2}{4b_1 c_1^2 N_{p1}} \right) \leq \frac{\sigma_N J_R}{0.0167 W K_o K_m} \quad \text{B.48}$$

$$C_2(\bar{x}) = \left(\frac{366000 N_{g1}}{\pi \omega_1 N_{p1}} + \frac{2c_2 N_{p2}}{N_{g2} + N_{p2}} \right) \left(\frac{(N_{p2} + N_{g2})^2}{4b_2 c_2^2 N_{p2}} \right) \leq \frac{\sigma_N J_R}{0.0167 W K_o K_m} \quad \text{B.49}$$

$$C_3(\bar{x}) = \left(\frac{366000 N_{g1} N_{g2}}{\pi \omega_1 N_{p1} N_{p2}} + \frac{2c_3 N_{p3}}{N_{g3} + N_{p3}} \right) \left(\frac{(N_{p3} + N_{g3})^2}{4b_3 c_3^2 N_{p3}} \right) \leq \frac{\sigma_N J_R}{0.0167 W K_o K_m} \quad \text{B.50}$$

$$C_4(\bar{x}) = \left(\frac{366000 N_{g1} N_{g2} N_{g3}}{\pi \omega_1 N_{p1} N_{p2} N_{p3}} + \frac{2c_4 N_{p4}}{N_{g4} + N_{p4}} \right) \left(\frac{(N_{p4} + N_{g4})^2}{4b_4 c_4^2 N_{p4}} \right) \leq \frac{\sigma_N J_R}{0.0167 W K_o K_m} \quad \text{B.51}$$

$$C_5(\bar{x}) = \left(\frac{366000}{\pi \omega_1} + \frac{2c_1 N_{p1}}{N_{p1} + N_{g1}} \right) \left(\frac{(N_{p1} + N_{g1})^3}{4b_1 c_1 N_{g1} N_{p1}^2} \right) \leq \left(\frac{\sigma_H}{C_p} \right)^2 \left(\frac{\sin \phi \cos \phi}{0.0334 W K_o K_m} \right) \quad \text{B.52}$$

$$C_6(\bar{x}) = \left(\frac{366000 N_{g1}}{\pi \omega_1 N_{p1}} + \frac{2c_2 N_{p2}}{N_{p2} + N_{g2}} \right) \left(\frac{(N_{p2} + N_{g2})^3}{4b_2 c_2 N_{g2} N_{p2}^2} \right) \leq \left(\frac{\sigma_H}{C_p} \right)^2 \left(\frac{\sin \phi \cos \phi}{0.0334 W K_o K_m} \right) \quad \text{B.53}$$

$$C_7(\bar{x}) = \left(\frac{366000 N_{g1} N_{g2}}{\pi \omega_1 N_{p1} N_{p2}} + \frac{2c_3 N_{p3}}{N_{p3} + N_{g3}} \right) \left(\frac{(N_{p3} + N_{g3})^3}{4b_3 c_3 N_{g3} N_{p3}^2} \right) \leq \left(\frac{\sigma_H}{C_p} \right)^2 \left(\frac{\sin \phi \cos \phi}{0.0334 W K_o K_m} \right) \quad \text{B.54}$$

$$C_8(\bar{x}) = \left(\frac{366000 N_{g1} N_{g2} N_{g3}}{\pi \omega_1 N_{p1} N_{p2} N_{p3}} + \frac{2c_4 N_{p4}}{N_{p4} + N_{g4}} \right) \left(\frac{(N_{p4} + N_{g4})^3}{4b_4 c_4 N_{g4} N_{p4}^2} \right) \leq \left(\frac{\sigma_H}{C_p} \right)^2 \left(\frac{\sin \phi \cos \phi}{0.0334 W K_o K_m} \right) \quad \text{B.55}$$

$$C_{9-12}(\bar{x}) = N_{pi} \sqrt{\frac{\sin^2 \phi}{4} + \frac{1}{N_{pi}} + \left(\frac{1}{N_{pi}} \right)^2} + N_{gi} \sqrt{\frac{\sin^2 \phi}{4} + \frac{1}{N_{gi}} + \left(\frac{1}{N_{gi}} \right)^2} - \frac{\sin \phi (N_{pi} + N_{gi})}{2} \geq CR \cos \phi_{min} \quad \text{B.56}$$

$$C_{13-16}(\bar{x}) = d_{min} \leq \frac{2c_i N_{pi}}{N_{pi} + N_{gi}} \quad \text{B.57}$$

$$C_{17-20}(\bar{x}) = d_{min} \leq \frac{2c_i N_{gi}}{N_{pi} + N_{gi}} \quad \text{B.58}$$

$$C_{21}(\bar{x}) = x_{p1} + \left(\frac{(N_{p1} + 2)c_1}{N_{p1} + N_{g1}} \right) \leq L_{max} \quad \text{B.59}$$

$$C_{22-24}(\bar{x}) = \left[x_{g(i-1)} + \left(\frac{(N_{pi} + 2)c_i}{N_{pi} + N_{gi}} \right) \right]_{i=2,3,4} \leq L_{max} \quad \text{B.60}$$

$$C_{25}(\bar{x}) = -x_{p1} + \left(\frac{(N_{p1} + 2)c_1}{N_{p1} + N_{g1}} \right) \leq 0 \quad \text{B.61}$$

$$C_{26-28}(\bar{x}) = \left[-x_{g(i-1)} + \left(\frac{(N_{pi} + 2)c_i}{N_{pi} + N_{gi}} \right) \right]_{i=2,3,4} \leq 0 \quad \text{B.62}$$

$$C_{29}(\bar{x}) = y_{p1} + \left(\frac{(N_{p1} + 2)c_1}{N_{p1} + N_{g1}} \right) \leq L_{max} \quad \text{B.63}$$

$$C_{30-32}(\bar{x}) = \left[y_{g(i-1)} + \left(\frac{(N_{pi} + 2)c_i}{N_{pi} + N_{gi}} \right) \right]_{i=2,3,4} \leq L_{max} \quad \text{B.64}$$

$$C_{33}(\bar{x}) = -y_{p1} + \left(\frac{(N_{p1} + 2)c_1}{N_{p1} + N_{g1}} \right) \leq 0 \quad \text{B.65}$$

$$C_{34-36}(\bar{x}) = \left[-y_{g(i-1)} + \left(\frac{(N_{pi} + 2)c_i}{N_{pi} + N_{gi}} \right) \right]_{i=2,3,4} \leq 0 \quad \text{B.66}$$

$$C_{37-40}(\bar{x}) = \left[x_{gi} + \left(\frac{(N_{gi} + 2)c_i}{N_{pi} + N_{gi}} \right) \right]_{i=1,2,3,4} \leq L_{max} \quad \text{B.67}$$

$$C_{41-44}(\bar{x}) = -x_{g_i} + \left(\frac{(N_{gi} + 2)c_i}{N_{pi} + N_{gi}} \right) \leq 0 \quad \text{B.68}$$

$$C_{45-48}(\bar{x}) = y_{g_i} + \left(\frac{(N_{gi} + 2)c_i}{N_{pi} + N_{gi}} \right) \leq L_{max} \quad \text{B.69}$$

$$C_{49-52}(\bar{x}) = -y_{g_i} + \left(\frac{(N_{gi} + 2)c_i}{N_{pi} + N_{gi}} \right) \leq 0 \quad \text{B.70}$$

$$C_{53-56}(\bar{x}) = (0.945c_i - N_{pi} - N_{gi})(b_i - 5.715)(b_i - 8.255)(b_i - 12.70)(-1) \leq 0 \quad \text{B.71}$$

$$C_{57-60}(\bar{x}) = (0.646c_i - N_{pi} - N_{gi})(b_i - 3.175)(b_i - 8.255)(b_i - 12.70)(+1) \leq 0 \quad \text{B.72}$$

$$C_{61-64}(\bar{x}) = (0.504c_i - N_{pi} - N_{gi})(b_i - 3.175)(b_i - 5.715)(b_i - 12.70)(-1) \leq 0 \quad \text{B.73}$$

$$C_{65-68}(\bar{x}) = (c_i - N_{pi} - N_{gi})(b_i - 3.175)(b_i - 5.715)(b_i - 8.255)(+1) \leq 0 \quad \text{B.74}$$

$$C_{69-72}(\bar{x}) = (N_{pi} + N_{gi} - 1.812c_i)(b_i - 5.715)(b_i - 8.255)(b_i - 12.70)(-1) \leq 0 \quad \text{B.75}$$

$$C_{73-76}(\bar{x}) = (N_{pi} + N_{gi} - 0.945c_i)(b_i - 3.175)(b_i - 8.255)(b_i - 12.70)(+1) \leq 0 \quad \text{B.76}$$

$$C_{77-80}(\bar{x}) = (N_{pi} + N_{gi} - 0.646c_i)(b_i - 3.175)(b_i - 5.715)(b_i - 12.70)(-1) \leq 0 \quad \text{B.77}$$

$$C_{81-84}(\bar{x}) = (N_{pi} + N_{gi} - 0.504c_i)(b_i - 3.175)(b_i - 5.715)(b_i - 8.255)(+1) \leq 0 \quad \text{B.78}$$

$$C_{85}(\bar{x}) = \omega_{min} \leq \frac{\omega_1(N_{p1}N_{p2}N_{p3}N_{p4})}{N_{g1}N_{g2}N_{g3}N_{g4}} \quad \text{B.79}$$

$$C_{86}(\bar{x}) = \frac{\omega_1(N_{p1}N_{p2}N_{p3}N_{p4})}{N_{g1}N_{g2}N_{g3}N_{g4}} \leq \omega_{max} \quad \text{B.80}$$

where,

$$CR_{min} = 1.4, d_{min} = 25.4 \text{ mm}, \phi = 20^\circ, W = 55.9, J_R = 0.2, \quad \text{B.81}$$

$$K_M = 1.6, K_o = 1.5, L_{max} = 127 \text{ mm},$$

$$\sigma_H = 3290 \frac{kg}{cm^2}, \sigma_N = 2090 \frac{kg}{cm^2}, \omega_1 = 5000 \text{ rom}, \quad \text{B.82}$$

$$\omega_{min} = 245 \text{ rpm}, \omega_{max} = 255 \text{ rpm}, C_p = 464$$

$$x_{p1}, y_{p1}, x_{gi}, y_{gi} = (12.7, 25.4, 38.1, 50.8, 63.5, 76.2, 88.9, 101.6, 114.3) \text{ mm} \quad \text{B.83}$$

$$b_i = (3.175, 5.715, 8.255, 12.7) \text{ mm} \quad \text{B.84}$$

$$7 \leq N_{pi}, N_{gi} \leq 76, N_{pi}, N_{gi} = \text{integer} \quad \text{B.85}$$

Problem 5: Rolling element bearing

Design variables:

$$\{x\} = [D_m, D_b, f_i, f_o, Z, K_{Dmax}, K_{Dmin}] \quad \text{B.86}$$

Objective function:

Maximize,

$$f(\bar{x}) = \begin{cases} f_c Z^{2/3} D_b^{1.8} & , \text{if } D_b \leq 25.4 \text{ mm} \\ 3.647 f_c Z^{2/3} D_b^{1.4} & , \text{if } D_b > 25.4 \text{ mm} \end{cases} \quad \text{B.87}$$

where

$$f_c = 37.91 \left[1 + \left\{ 1.04 \left(\frac{1-\gamma}{1+\gamma} \right)^{1.72} \left(\frac{f_i(2f_o-1)}{f_o(2f_i-1)} \right)^{0.41} \right\}^{10/3} \right]^{-0.3} \left[\frac{\gamma^{0.3}(1-\gamma)^{1.39}}{(1+\gamma)^{1/3}} \right] \left[\frac{2f_i}{2f_i-1} \right]^{0.41} \quad \text{B.88}$$

$$\gamma = \frac{D_b \cos \alpha}{D_m} \quad (\text{Here } \alpha = 0) \quad \text{B.89}$$

Design constraints:

$$C_1(x) = \frac{\varphi_0}{2 \sin^{-1}(D_b/D_m)} + 1 \geq Z \quad \text{B.90}$$

$$C_2(x) = 2D_b - (D - d)K_{Dmin} \geq 0 \quad \text{B.91}$$

$$C_3(x) = (D - d)K_{Dmax} - 2D_b \geq 0 \quad \text{B.92}$$

$$C_4(x) = \beta w - D_b \geq 0 \quad \text{B.93}$$

$$C_5(x) = D_m - (D + d)(0.5 - e) \geq 0 \quad \text{B.94}$$

$$C_6(x) = (D + d)(0.5 + e) - D_m \geq 0 \quad \text{B.95}$$

$$C_7(x) = 0.5(D - D_b - D_m) - (\varepsilon \times D_b) \geq 0 \quad \text{B.96}$$

$$C_8(x) = f_i - 0.515 \geq 0 \quad \text{B.97}$$

$$C_9(x) = f_o - 0.515 \geq 0 \quad \text{B.98}$$

where

$$\varphi_0 = 2\pi - 2 \cos^{-1} \left[\frac{\left(\frac{D}{2} - T - D_b\right)^2 - \left(\frac{d}{2} + T\right)^2 + U^2}{2\left(\frac{D}{2} - T - D_b\right)U} \right] \quad \text{B.99}$$

$$T = \frac{D-d-2D_b}{4}, \quad U = \frac{D-d}{2} - 3T \quad \text{B.100}$$

$$D = 160 \text{ mm}, d = 90 \text{ mm}, w = 30 \text{ mm}, \quad \text{B.101}$$

$$0.15(D - d) \leq D_b(\text{mm}) \leq 0.45(D - d), \quad 0.5(D + d) \leq D_m(\text{mm}) \leq 0.6(D + d), \quad \text{B.102}$$

$$0.515 \leq f_o \leq 0.6, \quad 0.515 \leq f_i \leq 0.6, \quad 4 \leq Z \leq 50, \quad \text{B.103}$$

$$0.4 \leq K_{Dmin} \leq 0.5, 0.6 \leq K_{Dmax} \leq 0.7, 0.3 \leq \varepsilon \leq 0.4, \quad \text{B.104}$$

$$0.02 \leq e \leq 0.1, 0.6 \leq \beta \leq 0.85 \quad \text{B.105}$$

Problem 6: Gas transmission compressor:

Design variables:

$$\bar{x} = [x_1, x_2, x_3, x_4] \quad \text{B.106}$$

Objective function:

$$\text{Minimize } f(\bar{x}) = 8.61 \times 10^5 \times x_1^{1/2} x_2 x_3^{-2/3} x_4^{-1/2} + 3.69 \times 10^4 \times x_3 + 7.72 \times 10^8 \times x_1^{-1} x_2^{0.219} - 765.43 \times 10^6 \times x_1 \quad \text{B.107}$$

Design constraints:

$$C_1(\bar{x}) = x_4 x_2^{-2} + x_2^{-2} - 1 \leq 0 \quad \text{B.108}$$

$$20 \leq x_1 \text{ (miles)} \leq 50, 1 \leq x_2 \leq 10, 20 \leq x_3 \text{ (in)} \leq 50, 0.1 \leq x_4 \text{ (ft}^3/\text{s)} \leq 60 \quad \text{B.109}$$

Problem 7: Tension/Compression spring Case-1

Design variables:

$$\bar{x} = [x_1, x_2, x_3] = [d, D, N] \quad \text{B.110}$$

Objective function:

$$\text{Minimize } f(\bar{x}) = (x_3 + 2)x_2 x_1^2 \quad \text{B.111}$$

Design constraints:

$$C_1(\bar{x}) = 71785x_1^4 - x_2^3 x_3 \leq 0 \quad \text{B.112}$$

$$C_2(\bar{x}) = -\frac{4x_2^2 - x_1 x_2}{12566(x_2 x_1^3 - x_1^4)} - \frac{1}{5108x_1^2 - 1} \geq 0 \quad \text{B.113}$$

$$C_3(\bar{x}) = 140.45x_1 - x_2^3 x_3 \geq 0 \quad \text{B.114}$$

$$C_4(\bar{x}) = x_1 + x_2 - 1.5 \leq 0 \quad \text{B.115}$$

$$0.05 \leq x_1(\text{in}) \leq 2, 0.25 \leq x_2(\text{in}) \leq 1.3, 2 \leq x_3 \leq 15 \quad \text{B.116}$$

Problem 8: Tension/Compression spring Case-2

Design variables:

$$\bar{x} = [x_1, x_2, x_3] = [d, D, N] \quad \text{B.117}$$

Objective function:

$$\text{Minimize } f(\bar{x}) = \frac{\pi^2 x_2 x_1^2 (x_3 + 2)}{4} \quad \text{B.118}$$

Design constraints:

$$C_1(\bar{x}) = \frac{8c_f F_{max} x_2}{(\pi x_1^3) - S} \leq 0 \quad \text{B.119}$$

$$C_2(\bar{x}) = l_f - l_{max} \leq 0 \quad \text{B.120}$$

$$C_3(\bar{x}) = d_{min} - x_1 \leq 0 \quad \text{B.121}$$

$$C_4(\bar{x}) = x_2 - D_{max} \leq 0 \quad \text{B.122}$$

$$C_5(\bar{x}) = 3 - \frac{x_2}{x_1} \leq 0 \quad \text{B.123}$$

$$C_6(\bar{x}) = \sigma_p - \sigma_{pm} \leq 0 \quad \text{B.124}$$

$$C_7(\bar{x}) = \sigma_p + \frac{F_{max} - F_p}{k} + 1.05(x_3 + 2)x_1 - l_f \leq 0 \quad \text{B.125}$$

$$C_8(\bar{x}) = \sigma_w - \frac{F_{max} - F_p}{k} \leq 0 \quad \text{B.126}$$

Where,

$$F_{max} = 1000 \text{ lb}, l_{max} = 14 \text{ in}, d_{min} = 0.2 \text{ in}, S = 189000 \text{ psi}, D_{max} = 3 \text{ in}, F_p = 300 \text{ lb}, \sigma_{pm} = 6 \text{ in}, \quad \text{B.127}$$

$$\sigma_w = 1.25 \text{ in}, G = 11.5 \times 10^6 \text{ psi}$$

$$c_f = \frac{4(x_2/x_1) - 1}{4(x_2/x_1) - 4} + \frac{(0.615x_1)}{x_2} \quad \text{B.128}$$

$$k = \frac{Gx_1^4}{8x_3x_2^2}, \sigma_p = \frac{F_p}{k} \quad \text{B.129}$$

$$l_f = \frac{F_{max}}{k} + 1.05(x_3 + 2)x_1 \quad \text{B.130}$$

$$0.009 \leq x_1(\text{in}) \leq 0.5, 0.6 \leq x_2(\text{in}) \leq 3, 1 \leq x_3 \leq 70 \quad \text{B.131}$$

Problem 9: Gear train

Design variables:

$$\bar{x} = [x_1, x_2, x_3, x_4] = [n_A, n_B, n_C, n_D] \quad \text{B.132}$$

Objective function:

$$\text{Minimize } f(\bar{x}) = \left(\frac{1}{6.931} - \frac{x_3 x_2}{x_1 x_4} \right)^2 \quad \text{B.133}$$

$$12 \leq x_1, x_2, x_3, x_4 \leq 60 \quad \text{B.134}$$

Problem 10: Piston lever:

Design variables:

$$\bar{x} = [H, B, D, X] \quad \text{B.135}$$

Objective function:

Minimize,

$$f(\bar{x}) = \frac{\pi D^2(L_2 - L_1)}{4} \quad \text{B.136}$$

Design constraints:

$$C_1(\bar{x}) = QL\cos(45) - RF \leq 0 \quad \text{B.137}$$

$$C_2(\bar{x}) = Q(L-X) - M_{\max} \leq 0 \quad \text{B.138}$$

$$C_3(\bar{x}) = 1.2(L_2 - L_1) - L_1 \leq 0 \quad \text{B.139}$$

$$C_4(\bar{x}) = \frac{D}{2} - B \leq 0 \quad \text{B.140}$$

Where,

$$R = \frac{|-X(X\sin(45) + H) + H(B - X\cos(45))|}{\sqrt{(X - B)^2 + H^2}} \quad \text{B.141}$$

$$P = 1500 \text{ psi}, F = \frac{\pi P D^2}{4}; L_1 = \sqrt{(X - B)^2 + H^2}; L_2 = \sqrt{(X * \sin(45) + H)^2 + (B - X * \cos(45))^2} \quad \text{B.142}$$

$$L = 240 \text{ in}, M_{\max} = 1.8 \times 10^6 \text{ lbs.in}, Q = 10000 \text{ lb} \quad \text{B.143}$$

$$0.05 \leq H, B, D \text{ (in)} \leq 500, 0.05 \leq X \text{ (in)} \leq 120 \quad \text{B.144}$$

Problem 11: Corrugated bulkhead

Design variables:

$$\bar{x} = [w, h, l, t] \quad \text{B.145}$$

Objective function:

Minimize,

$$f(\bar{x}) = \frac{5.885t(w + l)}{w + \sqrt{t^2 - h^2}} \quad \text{B.146}$$

Design constraints:

$$C_1(\bar{x}) = -th(0.4w + l/6) + 8.94(w + \sqrt{t^2 - h^2}) \leq 0 \quad \text{B.147}$$

$$C_2(\bar{x}) = -th^2(0.2w + l/12) + 2.2(8.94(w + \sqrt{t^2 - h^2}))^{4/3} \leq 0 \quad \text{B.148}$$

$$C_3(\bar{x}) = -t + 0.0156w + 0.15 \leq 0 \quad \text{B.149}$$

$$C_4(\bar{x}) = -t + 0.0156l + 0.15 \leq 0 \quad \text{B.150}$$

$$C_5(\bar{x}) = -t + 1.05 \leq 0 \quad \text{B.151}$$

$$C_6(\bar{x}) = -l + h \leq 0 \quad \text{B.152}$$

$$0 \leq w, h, l \text{ (cm)} \leq 100, 0 \leq t \text{ (cm)} \leq 5 \quad \text{B.153}$$

Problem 12: Speed reducer

Design variables:

$$\bar{x} = [b, m, Z, l_1, l_2, d_1, d_2] \quad \text{B.154}$$

Objective function:

Minimize,

$$f(x) = 0.7854bm^2(3.3333Z^2 + 14.9334Z - 43.0934) - 1.508b(d_1^2 + d_2^2) + 7.4777(d_1^3 + d_2^3) + 0.7854(l_1d_1^2 + l_2d_2^2) \quad \text{B.155}$$

Design constraints:

$$C_1(x) = 27 - bm^2Z \leq 0 \quad \text{B.156}$$

$$C_2(x) = 397.5 - bm^2Z^2 \leq 0 \quad \text{B.157}$$

$C_3(x) = 1.93l_1^3 - mZd_1^4 \leq 0$	B.158
$C_4(x) = 1.93l_2^3 - mZd_2^4 \leq 0$	B.159
$C_5(x) = \sqrt{(745l_1/mZ)^2 + (16.9 \times 10^6)} - 110d_1^3 \leq 0$	B.160
$C_6(x) = \sqrt{(745l_2/mZ)^2 + (157.5 \times 10^6)} - 85d_2^3 \leq 0$	B.161
$C_7(x) = mZ - 40 \leq 0$	B.162
$C_8(x) = 5m - b \leq 0$	B.163
$C_9(x) = b - 12m \leq 0$	B.164
$C_{10}(x) = 1.5d_1 - l_1 + 1.9 \leq 0$	B.165
$C_{11}(x) = 1.1d_2 - l_2 + 1.9 \leq 0$	B.166
$2.6 \leq b \leq 3.6, 0.7 \leq m \leq 0.8, 17 \leq Z \leq 28, 7.3 \leq l_1 \leq 8.3,$	B.167
$7.8 \leq l_2 \leq 8.3, 2.9 \leq d_1 \leq 3.9, 5 \leq d_2 \leq 5.5$	B.168

Problem13: Pressure vessel

Design variables:

$$\bar{x} = [x_1, x_2, x_3, x_4] = [T_s, T_h, R, L] \quad \text{B.169}$$

Objective function:

Minimize

$$f(\bar{x}) = 0.6224x_1x_3x_4 + 1.7781x_2x_3^2 + 3.1661x_1^2x_4 + 19.84x_1^2x_3 \quad \text{B.170}$$

Design constraints:

$$C_1(\bar{x}) = x_1 - 0.0193x_3 \geq 0 \quad \text{B.171}$$

$$C_2(\bar{x}) = x_2 - 0.00954x_3 \geq 0 \quad \text{B.172}$$

$$C_3(\bar{x}) = \pi x_3^2 x_4 + \frac{4}{3} \pi x_3^3 - 1296000 \geq 0 \quad \text{B.173}$$

$$C_4(\bar{x}) = 240 - x_4 \geq 0 \quad \text{B.174}$$

$$x_1, x_2 \in [0.0625, 0.125, \dots, 1.1875, 1.25] \text{ (in)}, \quad 10 \leq x_3, x_4 \text{ (in)} \leq 200 \quad \text{B.175}$$

Problem 14: Welded beam

Design variables:

$$\bar{x} = [x_1, x_2, x_3, x_4] = [h, l, t, b] \quad \text{B.176}$$

Objective function:

$$\text{Minimize } f(\bar{x}) = 1.10471x_1^2x_2 + 0.04811x_3x_4(14.0 + x_2) \quad \text{B.177}$$

Design constraints:

$$C_1(\bar{x}) = \tau(\bar{x})_{max} - \tau(\bar{x}) \geq 0 \quad \text{B.178}$$

$$C_2(\bar{x}) = \sigma(\bar{x})_{max} - \sigma(\bar{x}) \geq 0 \quad \text{B.179}$$

$$C_3(\bar{x}) = P_c(\bar{x}) - P \geq 0 \quad \text{B.180}$$

$$C_4(\bar{x}) = \delta(\bar{x})_{max} - \delta(\bar{x}) \geq 0 \quad \text{B.181}$$

$$C_5(\bar{x}) = x_4 - x_1 \geq 0 \quad \text{B.182}$$

$$C_6(\bar{x}) = x_1 - 0.125 \geq 0 \quad \text{B.183}$$

$$C_7(\bar{x}) = 5.0 - 0.10471x_1^2 - 0.04811x_3x_4(14.0 + x_2) \geq 0 \quad \text{B.184}$$

$$0.1 \leq x_1 \leq 2, 0.1 \leq x_2 \leq 10, 0.1 \leq x_3 \leq 10, 0.1 \leq x_4 \leq 2 \quad \text{B.185}$$

where,

$$\tau(\vec{x}) = \sqrt{(\tau')^2 + 2\tau'\tau''\frac{x_2}{2R} + (\tau'')^2}, \quad \tau' = \frac{P}{\sqrt{2x_1x_2}}, \quad \tau'' = \frac{MR}{J} \quad \text{B.186}$$

$$M = P\left(L + \frac{x_2}{2}\right) \quad \text{B.187}$$

$$R = \sqrt{\frac{x_2^2}{4} + \left(\frac{x_1+x_3}{2}\right)^2} \quad \text{B.188}$$

$$J = 2\left\{\sqrt{2}x_1x_2\left[\frac{x_2^2}{12} + \left(\frac{x_1+x_3}{2}\right)^2\right]\right\} \quad \text{B.189}$$

$$\sigma(\vec{x}) = \frac{6PL}{x_4x_3^2}, \quad \delta(\vec{x}) = \frac{4PL^3}{Ex_3^3x_4} \quad \text{B.190}$$

$$P_c(\vec{x}) = \frac{4.013E\sqrt{\frac{x_2^2x_4^2}{36}}}{L^2}\left(1 - \frac{x_3}{2L}\sqrt{\frac{E}{4G}}\right) \quad \text{B.191}$$

$$P = 6000 \text{ lb}, L = 14 \text{ in}, E = 30 \times 10^6 \text{ psi}, G = 12 \times 10^6 \text{ psi}, \quad \text{B.192}$$

$$\sigma_{\max} = 30000 \text{ psi}, \tau_{\max} = 13600 \text{ psi}, \delta_{\max} = 0.25 \text{ in} \quad \text{B.193}$$

Problem 15: Multiple disc clutch brake:

Design variables:

$$\bar{x} = [x_1, x_2, x_3, x_4, x_5] = [r_i, r_o, t, F, Z] \quad \text{B.194}$$

Objective function:

Minimize

$$f(\bar{x}) = \pi(x_2^2 - x_1^2)x_3(x_5 + 1)\rho \quad \text{B.195}$$

Design constraints:

$$C_1(\bar{x}) = \Delta r + x_1 - x_2 \leq 0 \quad \text{B.196}$$

$$C_2(\bar{x}) = -l_{\max} + (x_5 + 1)(x_3 + \delta) \leq 0 \quad \text{B.197}$$

$$C_3(\bar{x}) = P_{r_z} - P_{\max} \leq 0 \quad \text{B.198}$$

$$C_4(\bar{x}) = P_{r_z}v_{sr} - v_{sr\max}P_{\max} \leq 0 \quad \text{B.199}$$

$$C_5(\bar{x}) = v_{sr} - v_{sr\max} \leq 0 \quad \text{B.200}$$

$$C_6(\bar{x}) = T - T_{\max} \leq 0 \quad \text{B.201}$$

$$C_7(\bar{x}) = sM_s - M_h \leq 0 \quad \text{B.202}$$

$$C_7(\bar{x}) = -T \leq 0 \quad \text{B.203}$$

Where,

$$\Delta r = 20 \text{ mm}, l_{\max} = 30 \text{ mm}, \mu = 0.6, v_{sr\max} = 10000 \text{ mm/s}, \delta = 0.5 \text{ mm}, s = 1.5, \quad \text{B.204}$$

$$T_{\max} = 15 \text{ s}, N = 250 \text{ rpm}, I_z = 55 \text{ kg.m}^2, M_s = 40 \text{ Nm}, M_f = 3 \text{ Nm}, P_{\max} = 1 \text{ MPa}, \rho = 0.0000078 \text{ kg/mm}^3 \quad \text{B.205}$$

$$M_h = \frac{2}{3}\mu x_4 x_5 \frac{x_2^3 - x_1^3}{x_2^2 - x_1^2} \quad \text{B.206}$$

$$\omega = \frac{\pi N}{30}, \quad A = \pi(x_2^2 - x_1^2), \quad P_{r_z} = \frac{x_4}{A}, \quad R_{sr} = \frac{2x_2^3 - x_1^3}{3x_2^2 - x_1^2}, \quad \text{B.207}$$

$$v_{sr} = \frac{\pi R_{sr} N}{30}, \quad T = \frac{I_z \omega}{M_h + M_f} \quad \text{B.208}$$

$$x_1 = (60, 61, 62, \dots, 80) \text{ mm}, \quad x_2 = (90, 91, 92, \dots, 110) \text{ mm}, \quad x_3 = (1, 1.5, 2, 2.5, 3) \text{ N}, \quad \text{B.209}$$

$$x_4 = (600, 610, 620, \dots, 1000) \text{ N}, \quad x_5 = (2, 3, 4, 5, \dots, 9) \quad \text{B.210}$$

Study on the Impact of Sawtooth Roof Inclination Angles and Asymmetrical Opening Positions for An Isolated Building in Cross Ventilation

Osamah Hashem Al-Aghbari ^a, Lip Kean Moey ^{b, *}, Vin Cent Tai ^b, Tze Fong Go ^c,
Mohammad Hossein Yazdi ^d

^a Faculty of Engineering, Built Environment & Information Technology, SEGi University, Selangor, Malaysia

^b Centre for Modelling and Simulation, Faculty of Engineering, Built Environment & Information Technology, SEGi University, Selangor, Malaysia

^c Centre for Advance Materials and Intelligent Manufacturing, Faculty of Engineering, Built Environment & Information Technology, SEGi University, Selangor, Malaysia

^d New Materials Technology and Processing Research Center, Department of Mechanical Engineering, Neyshabur Branch, Islamic Azad University, Neyshabur, Iran

Received 9 Aug 2022

Accepted 21 Aug 2022

Abstract

The opening configurations and roof inclination angles are important to determine the effectiveness of wind driven cross ventilation within building. This study presents Computational Fluid Dynamics (CFD) simulations to analyse the natural ventilation flow in a generic isolated building with four opening configurations which are bottom-top, bottom-middle, middle-top and middle-middle. The sawtooth roof was considered with different inclination angle of 9°, 18° and 27°. The 3-D Steady Reynolds Averaged Navier Stokes (RANS) equations were solved with the shear stress transport k- ω turbulence model. Based on the simulation results, the roof configuration and roof inclination angles highly affect the airflow characteristics within the building. Additionally, the various opening positions strongly influence the indoor airflow. Whenever the roof inclination angle is increased, the indoor airflow velocity increases due to the pressure difference between the windward and leeward openings within the building. Meanwhile, the highest pressure coefficient is obtained for the middle-top opening position with the lower roof inclination angle of 9°. Furthermore, increasing in roof inclination angle up to 27° leads to reduce pressure coefficient due to the increasing of internal velocity. The highest volume flow rate (VFR) across all simulation cases is found to be the middle-top opening position with the roof inclined angle of 27°. This occurs because the roof inclination angle of 27° is the geometry with the largest leeward height, which increases the volume flow rate. Therefore, increasing the roof inclination angle with the leeward opening near the roof leads to increase in better volume flow rate for the building.

© 2022 Jordan Journal of Mechanical and Industrial Engineering. All rights reserved

Keywords: Computational Fluid Dynamics (CFD), Sawtooth Roof, Roof Inclination Angles (RIA), Opening Positions, Volume flow Rate (VFR).

1. Introduction

Natural ventilation is a passive design method for bringing cold air into a building that is typically warmer than the outside. It is possible to minimize power consumption for buildings by 10-30% with suitable building roof design and natural ventilation strategies [1]. The design of building openings can aid in ensuring a suitable ventilation circuit between incoming and exiting air flow [2]. However, the advent of air conditioners in the 1960s as well as the development of mechanical ventilation systems in buildings place a strain on the global energy consumption. According to Marina et al. the energy

utilized by commercial buildings amounts for a whopping 32% of overall energy consumption globally [3]. Additionally, Hassan et al. discovered that buildings in Malaysia consumed nearly half of the electricity produced in the country, with commercial buildings using up to 39 kGWh [4]. The majority of the energy provided to buildings is used for air conditioners, which cool down offices and provide thermal comfort to the occupants. Carbon dioxide emissions through conventional energy sources such as fossil fuels used to supply the ever-increasing demand for electricity contribute to global warming [5]. As a result, carbon dioxide emissions of buildings have increased over the years. Behari estimates that the world will become 1.5°C warmer between 2030

* Corresponding author e-mail: moeylipkean@segi.edu.my.

and 2052, which could lead to extreme weather conditions and stronger heat waves [6]. Renewable energy sources such as wind can offer important environmental, social and economic benefits [7, 8].

There are different types of roofs which include hip, venturi, gable and sawtooth configurations [9]. Lim et al. examined various design parameters such as tower height variations, tower shapes, rooftop tilt angles, and various roof shapes for a naturally ventilated wind tower to determine the extraction air flow rate and airflow pattern. The results showed that the biconcave shape tower helps to enhance the venturi effect with the constriction at its cross section, resulting in a low pressure zone with an increase in air velocity extracted. The effect of increasing the roof tilt angle showed a higher angle of attack on the airflow and helped increase the extraction rate whereby the 45° tilt angle was the best among all cases investigated [10]. Moey et al. performed a study on the effect of venturi shaped roof on the air change rate (ACH) for a stairwell. The study was carried out through a wind tunnel study and a numerical simulation. The simulation results showed that when the roof angle increased from 20°- 60°, an increase in ACH was obtained [11]. Furthermore, Moey et al. conducted a numerical study using CFD simulation to investigate the effect of saltbox roof and gable roof configurations on wind induced natural ventilation for an isolated building with various roof pitches of 15°, 25°, 35° and 45°. The results showed that the saltbox roof configuration exhibit better performance than gable roof based on the measured parameters [12]. On the other hand, Tominaga et al. performed CFD simulations and wind tunnel experiments to investigate the airflow patterns around an isolated gable roof building with varying inclination angles. The result indicated that the roof pitches influence the flow field along with the streamline, turbulent kinetic energy distribution and pressure coefficient spatial distribution around and over the building [13]. Liu et al. studied the exterior airflow surrounding buildings with various type of roofs, such as flat roof, gable roof and stepped roof. The large eddy simulations (LES) were applied in the current study. The simulation findings revealed that the roof design has a significant impact on velocity, flow pattern and streamline distribution near buildings particularly at the pedestrian level [14].

The sawtooth roof for buildings has the potential to improve sustainability and healthy indoor environment by allowing more natural ventilation compared to the basic flat roof. The sawtooth roof can produce consistent and higher intensity level of air by locating the opening near the roof rather than the opening at the center or bottom of the façade [15]. The sawtooth roof can be implemented in several types of buildings, such as hospitals, low rise residential and universities [16, 17]. Peren et al. performed CFD simulations to investigate the effect of the outlet opening positions and the sawtooth roof inclination angles on a natural ventilated building design. This study confirmed that sawtooth roof inclined angle effect the dimensionless velocity magnitude, pressure coefficient, and dimensionless streamwise wind speed ratio around the building. The numerical result showed an increase in roof inclination angle above 18° resulted in a significantly higher air flow rate. The roof including a 45° slant was the

best-case scenario. Similarly, positioning the outlet opening closer to the roof was proved to be preferable, as it boosted the flow rate about 25% [18]. Therefore, it is important to examine the impact of asymmetrical opening positions at both windward and leeward with roof inclination angle as this affects the volume flow rate and airflow pattern of a naturally ventilated building [18]. However, to the best of authors' knowledge, the study on the influence of sawtooth roof inclination angles in conjunction with asymmetric positions of windward and leeward openings for the building has not been thoroughly investigated in the literature. Hence, the focus of this study is to investigate the effect of sawtooth roof inclination angles (RIA) and asymmetrical opening positions at both windward and leeward for a generic isolated building in cross ventilation.

The model dimensions, computational setup, boundary condition, solver settings and grid sensitivity analysis are described in Section 2. The simulation cases of sawtooth roof with four opening positions and various roof inclination angle (RIA) are presented in Section 3. Section 4 presents the CFD simulation results of sawtooth roof building with the opening positions and the impact of roof inclination angles and opening positions on airflow pattern, pressure coefficient and volume flow rate. Lastly, Section 5 concludes the simulation findings of this paper.

2. CFD Simulation: Model and Computational Setup

2.1. Building Geometry Model

In the current study, the reference model used was based on the wind induced cross ventilation of a generic isolated building by Karava et al. [19]. This reference model has a reduced scale of 1:200 and with the dimensions of $0.1\text{ m} \times 0.1\text{ m} \times 0.08\text{ m}$ ($L \times W \times H$). The reference model has two asymmetric openings which the windward opening is at the lower end of the windward façade at $h = 0.02\text{ m}$ (from the ground to the window center) and the leeward opening at the upper end of the leeward façade $h = 0.06\text{ m}$. The windows opening dimensions were $0.046\text{ m} \times 0.018\text{ m}$ ($L \times H$). In addition, the reference building model's wall thickness remains uniform among all surfaces at 0.002 m [20]. Furthermore, the building model for simulation cases were constructed by determining a trapezoid height of sawtooth roof (increasing leeward height and reducing windward façade) along with different roof inclination angles (RIA), and different opening positions. More information on the simulation cases will be discussed in section 3. ANSYS 2021 R2 Space-Claim was used to generate the model's geometry. Figure 1 illustrates the roof inclination angle of 9° isometric view and side view.

2.2. Computational Flow domain and Grids

Based on the building geometry specified in the previous section, the computational flow domain can be generated. The isometric view of the flow domain is shown in Figure 2a while the front and side view of the domain are shown in Figure 2b and Figure 2c, respectively. The flow domain within the named selection zones such as symmetry, inlet, outlet, side wall, top wall

and ground is illustrated in Figure 2a. Additionally, the body of influence (BOI) around the building was created and named as near-field BOI. The near BOI was generated by an offset of $1H$ or 0.08 m from both sides, windward and leeward as illustrated in Figure 2b.

Next, in terms of the flow domain design specifications, the distance from the building to the sides of the flow domain was $5H$ whereby H is the building height of 0.08 m [21–23]. Adding up to that, the distance

from the leeward side of the building to the outlet plane of the flow domain is specified at $15H$ to ensure the flow is developed [24]. Meanwhile, the distance of windward façade of the building upstream to the inlet plane is set at $3H$ to control the occurrence of unintended streamwise gradients in the approach-flow profile. Overall, the flow domain design was set based on the CFD guidelines [20, 24, 25].

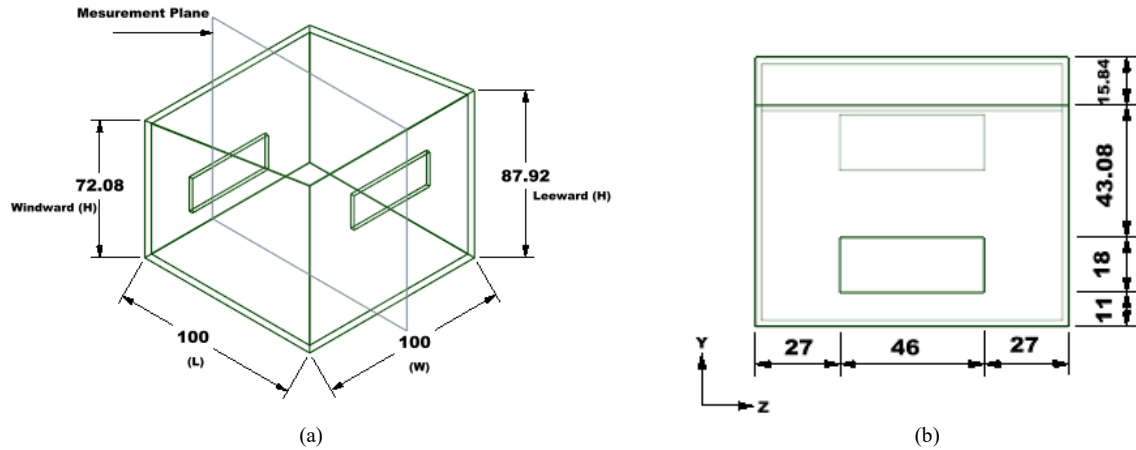


Figure 1. Reduced scale of sawtooth roof building model (a) RIA-9° isometric view and (b) RIA-9° side view of bottom-top opening position.

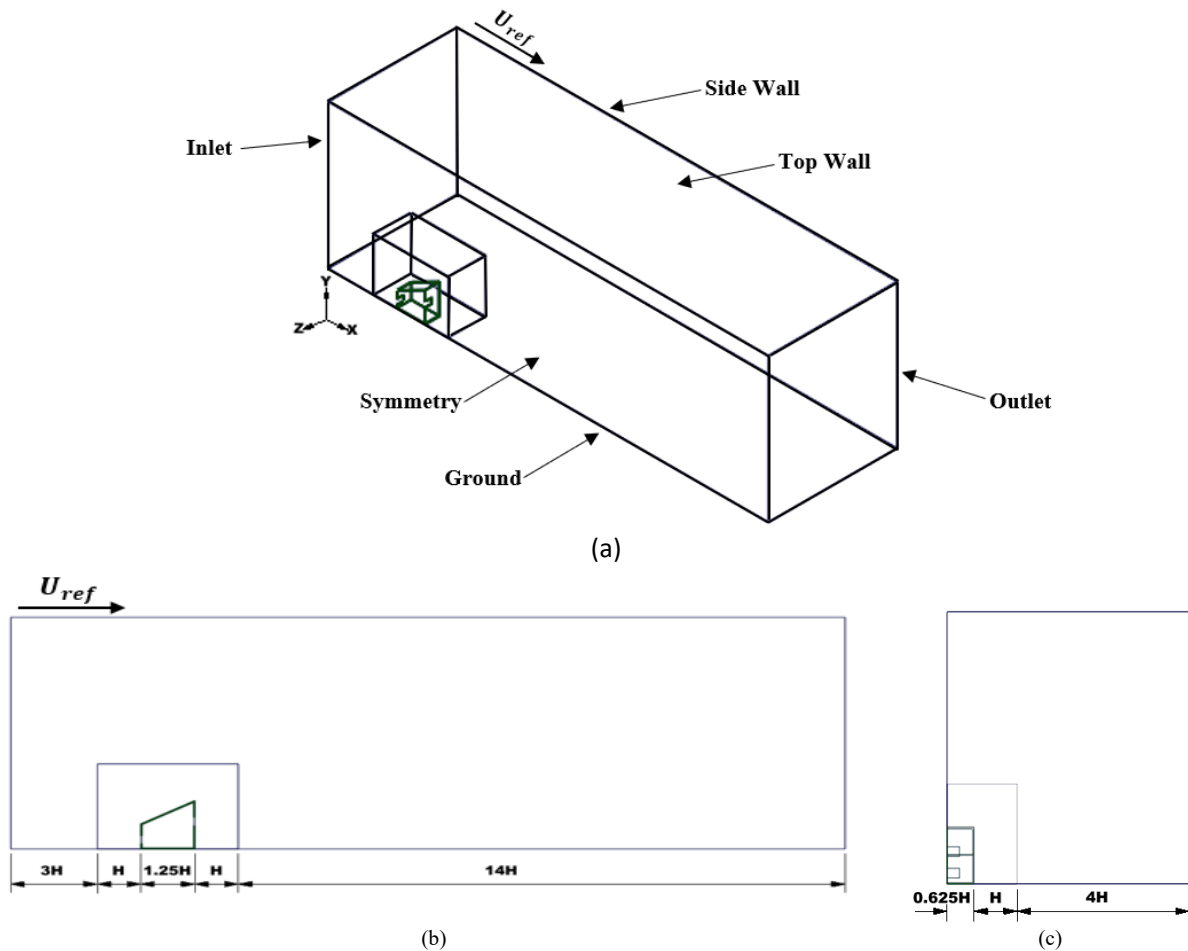


Figure 2. Computational flow domain (a) isometric view (b) front view and (c) side view.

Through using finite element approach, the meshing procedure describes the process of separating or splitting the geometry of the design across millions of uniformly dispersed parts defined as elements and nodes [26]. Fluent meshing from Ansys 2021 R2 [27] was used to produce the volume mesh as one of the pre-processing levels. After the design was constructed, the meshing procedure was carried out using the Watertight Meshing method. Furthermore, the building model was surrounded by a body of influence (BOI) with a size of $0.08\text{ m} \times 0.08\text{ m} \times 0.08\text{ m}$ ($L \times W \times H$) as 1H from the building sides as well as top and bottom, so that minimize computational time and enhancing precision of the findings by improving the mesh throughout this region, as recommended from the literature [12]. As a result, the body of influence and the building model were surrounded by the flow domain, and the mesh sizing has been accomplished by adjusting the global and local scoping size. Since the building under consideration is a generic design, a bluff body having sharp edges, flow separation at the rooftop of the building was unavoidable, particularly with such a high Reynolds number around 38K, which indicating a turbulent flow. The building was indeed subjected to proximity sizing in order to refine existing meshes around the building's edges. Whenever the local sizing was performed, the

global scope sizing was applied towards the surface mesh. The surface mesh growth rate was fixed to 1.2 to help ease the transition from the flow domain approaching the entire building [13]. Next, as depict in Figure 3, the volume mesh was implemented after the surface mesh. Figure 4 shows a poly-hexcore volume mesh containing 10 uniformly prismatic layers surrounding the building. According to Zore et al. [28], the benefit of implementing Poly-hexcore grid is it reduces simulation time about 10-40% while reducing cell count by 20-40%. Furthermore, the Poly-hexcore meshes contains polyhedral elements throughout the transition area, octree hexahedral elements mostly in bulk region, as well as layered premium quality iso poly-inflations inside the boundaries layer, as recommended from the literature [28]. The first cell height utilized was 0.0001 m , as indicated throughout the preliminary calculations based on the a y^+ of 3 and 10 inflation layers. A normal curvature angle of 12 degrees and two cells per gap have been established. Finally, the goal cell quality limit was set around 0.2-0.3, resulting in an inversely orthogonal quality (skewness) of 0.3, which is regarded as a good quality. Furthermore, the average skewness was 0.45, that belongs within an excellent range of cells quality [29].

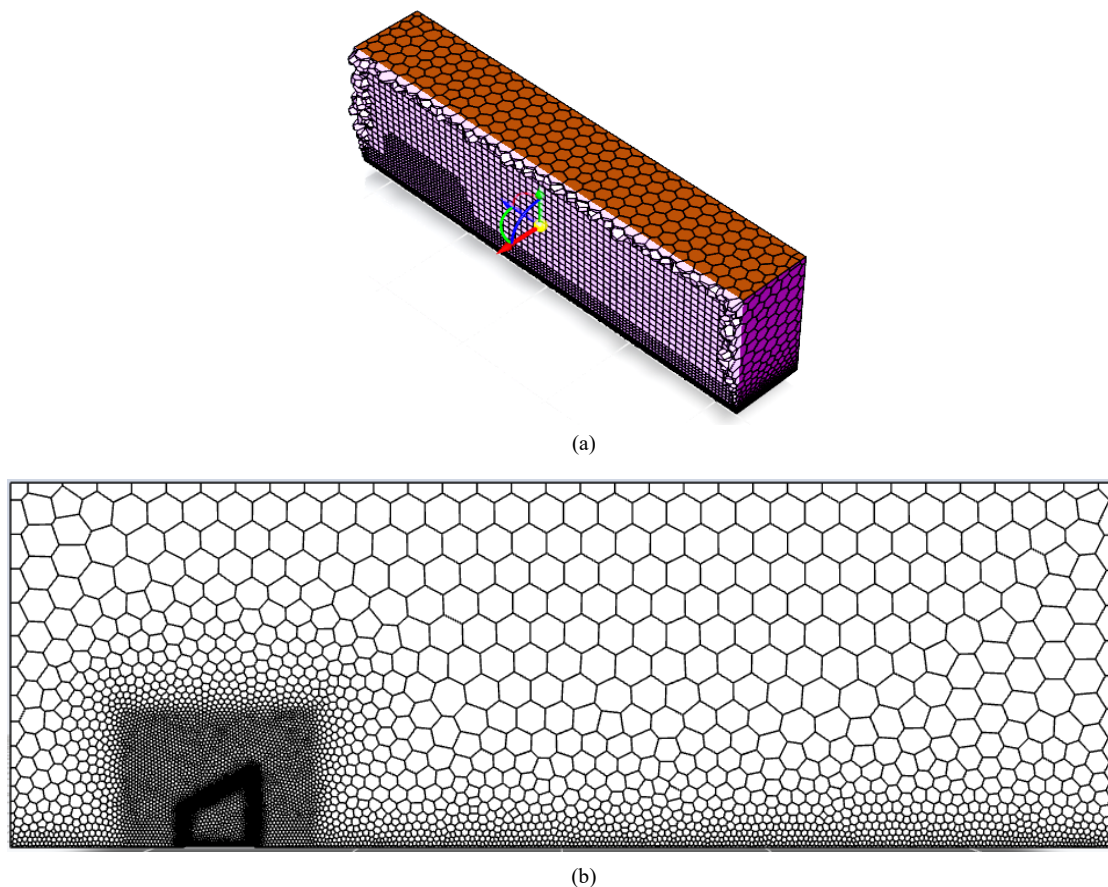


Figure 3. Poly-Hexcore of (a) volume meshing and (b) transition mesh at the building.

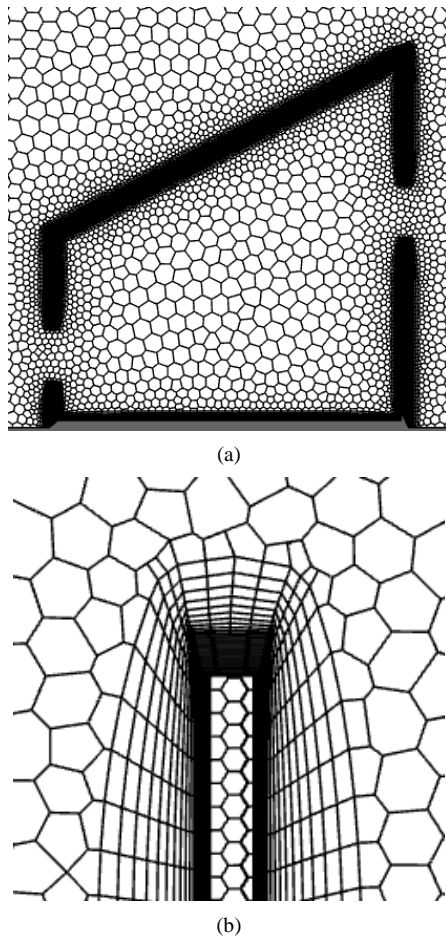


Figure 4. (a) Poly-Hexcore meshing around the building, (b) inflation layers throughout the building edges.

2.3. Boundary Conditions

Initially, throughout the wind tunnel experiment from the previous study [19], the mean wind speed and turbulence profiles were determined then it matched to a power law through a wind tunnel measurement of an amplitude of 0.25, as shown in Equation (1).

$$\left(\frac{U(z)}{U_H}\right) = \left(\frac{z}{H}\right)^{0.25} \quad (1)$$

The researchers in general believe that the logarithmic law is superior than the power law. Therefore, the logarithmic law has been employed for the velocity profile [20, 30]. Additionally, the logarithmic law was used to generate the requisite ABL frictional velocity at 0.35 m/s, that was needed for the turbulent dissipation rate, ε profile [31]. The aerodynamics roughness length, z_0 utilized was 0.000025 m, which is corresponding to 0.00005 m in full scale, and thus the Von Karmann's constant, κ becomes 0.42 and z is the height coordinate, which is the building height 0.08 m. The corresponding inlet wind velocity profile is represented in Equation (2).

$$U(z) = \frac{u^*_{ABL}}{\kappa} \ln\left(\frac{z+z_0}{z_0}\right) \quad (2)$$

Equation (3) was used to calculate the turbulent kinetic energy, k with the variability throughout the mean wind velocity and the computed turbulence intensity variations along the x , y , and z planes, whereas the I_u is the calculated streamwise turbulence intensity and 'a' is the

variable with a range of 0.5 to 1.5, [22, 32]. In the current study, the parameter of 'a' used was 0.5, which is recommended from the literature [18]. Equation (4) can then be used to compute the turbulent dissipation rate, ε [31]. The specific turbulent dissipation rate, ω , in Equation (5), can be computed through the turbulent dissipation rate with the connection of using k profile as well as the empirical constant value, C_μ , which is equal to 0.09.

$$k(z) = a(I_u(z)U(z))^2 \quad (3)$$

$$\varepsilon = \frac{(u^*)^3}{\kappa(z+z_0)} \quad (4)$$

$$\omega = \frac{\varepsilon}{C_\mu k} \quad (5)$$

$$k_S = \frac{9.793 z_0}{C_S} \quad (6)$$

The flow domain's outlet surface is identified as the pressure outlet, including zero static pressure and all standard gradients among all parameters set to zero to verify that the flow domain becomes completely generated [24, 25]. Aside from that, the domain's top and side walls were adjusted with symmetry conditions since it is normally done to ensure continuous flow. Finally, Equation (6) was used to calculate the corresponding sand-grain roughness, K_S , which employed for the surface of the flow domain's ground equal to 0.00028 m, and the roughness constant, C_S , was set to 0.874, which calculated depending on their relation with the aerodynamics roughness length, z_0 , as founded by Blocken et al. [24]. Regarding the building surface the sand-grain roughness, K_S , value was set to zero.

2.4. Solver Settings

In the current study, the commercial CFD code along with Ansys Fluent 2021 R2 [27] was used for CFD simulations. The 3-D steady Reynolds Averaged Navier Stokes (RANS) turbulence model was chosen for this study because it provides accurate results at a lesser computational time. The SST $k-\omega$ turbulence model contains considerable differences in indoor air speed and many other distinct models as illustrated by Perén et al. [18]. Therefore, the shear stress transport, SST, $k-\omega$ model was chosen.

The pressure-based solution has been employed as the pressure velocity couplings, combined with the Semi-Implicit Method using Pressure Related Algorithms (SIMPLE) scheme. The gradients were instead calculated using the Green-Gauss node approach and second-order discretization of pressure, momentum, turbulent kinetic energy, and specific dissipation rate [20, 33]. A standard initialization scope to all zones has been used to initialize the solutions. Moreover, the solution was considered to achieve convergence when the residuals stabilize and meet a minimum value of 10^{-6} for x and z velocities, 10^{-5} for y velocity, and eventually 10^{-4} for turbulent kinetic energy, k , continuity, as well as turbulent dissipation rate, ε and specific turbulent dissipation rate, ω .

2.5. Grid Sensitivity Analysis

The shear stress transport $k-\omega$ turbulence model was used to perform a grid sensitivity analysis for the

asymmetrical opening position case (Bottom-Top). Three different grids were created to evaluate the precision of the simulation solution. The basic or medium grid (Grid B) developed has a cell count of 937,976. The coarse grid (Grid A) was created through dividing the mesh's global and local scoping size by $\sqrt{2}$, whereas the fine grid (Grid C) was created through multiplying the mesh's global and local scoping size by $\sqrt{2}$. As a result, Grids A, B, and C contains 505,974, 937,976, and 1,125,188 cells, respectively. Moreover, all the grids with their various cell counts are illustrated in Figure 5. The three grids have a same amount of inflation layers which are 10 boundary layers.

Next, the grid convergence index (GCI) established by Roache [34] has been utilized in the current study to assess the differences of the dimensionless streamwise wind speed ratio, U/U_{ref} for the coarse grid versus the medium grid and medium grid versus the fine grid. The GCI calculation is illustrated below in Equation (7), with the safety of factor (FS) set to 1.25 once three or even more grids are evaluated. The grid refinement value, r , became 2 and the formal order of accuracy, p , became 2 because of the second order finite difference technique has been applied. Five horizontal lines were created inside the building at locations of $Y/H = 0.250$, $Y/H = 0.375$, $Y/H = 0.500$, $Y/H = 0.625$ and $Y/H = 0.750$ and the GCI values among all three grids at these locations were averaged to obtain the GCI among each grid as represented in Table 1. It should be noted that the letter 'H' represents the building height while the letter 'Y' represents the varying height within the building. Based on the coarse grid versus the medium grid, the GCI value along the horizontal lines of $Y/H = 0.250$, $Y/H = 0.375$, $Y/H = 0.500$, $Y/H = 0.625$ and $Y/H = 0.750$ were 7.76%, 2.22%, 1.35%, 2.00% and 3.46%, respectively. However, the basic or medium grid versus the fine grid has the GCI values of 3.75%, 2.08%,

1.47%, 1.29% and 1.66% across the horizontal lines of $Y/H = 0.250$, $Y/H = 0.375$, $Y/H = 0.500$, $Y/H = 0.625$ and $Y/H = 0.750$, respectively. The coarse grid has an average GCI of 3.36% whereas the medium grid has an average GCI of 2.05%. Therefore, the medium grid has been chosen for the remaining simulations because it delivers essentially grid independence outcomes and it has a lower GCI produced, which is in the acceptable range. Figure 6 shows the comparison of the U/U_{ref} values across the three grids at the locations measured which indicates that the data obtained is close to each other.

$$GCI = SF \left[\frac{r^p \frac{U_{coarse} - U_{fine}}{U_{ref}}}{r^p - 1} \right] \quad (7)$$

$$= 1.25 \left[\frac{\sqrt{2}^2 \left(\frac{U_{coarse} - U_{fine}}{U_{ref}} \right)}{1 - \sqrt{2}^2} \right]$$

$$= 2.5 \left[\left(\frac{U_{coarse}}{U_{ref}} - \frac{U_{fine}}{U_{ref}} \right) \right]$$

Table 1. Grid convergence index (GCI) along the horizontal line for coarse grid versus medium grid and medium grid versus fine grid

Location	Grid Convergence Index (GCI)	
	Coarse versus Medium	Medium versus Fine
$Y/H = 0.250$	7.76	3.75
$Y/H = 0.375$	2.22	2.08
$Y/H = 0.500$	1.35	1.47
$Y/H = 0.625$	2.00	1.29
$Y/H = 0.750$	3.46	1.66
Average	3.36	2.05

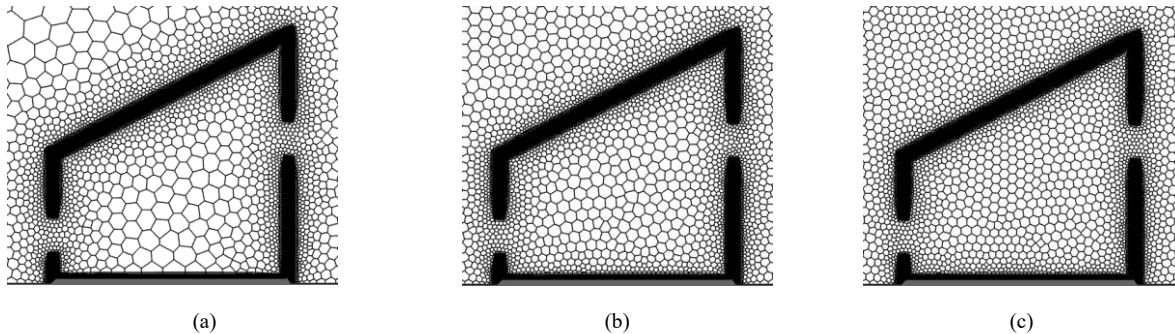


Figure 5. Grids in viewpoint for grid sensitivity analysis: (a) coarse grid with 505,974 cells (b) medium grid with 937,976 cells (c) fine grid with 1,125,188 cells.

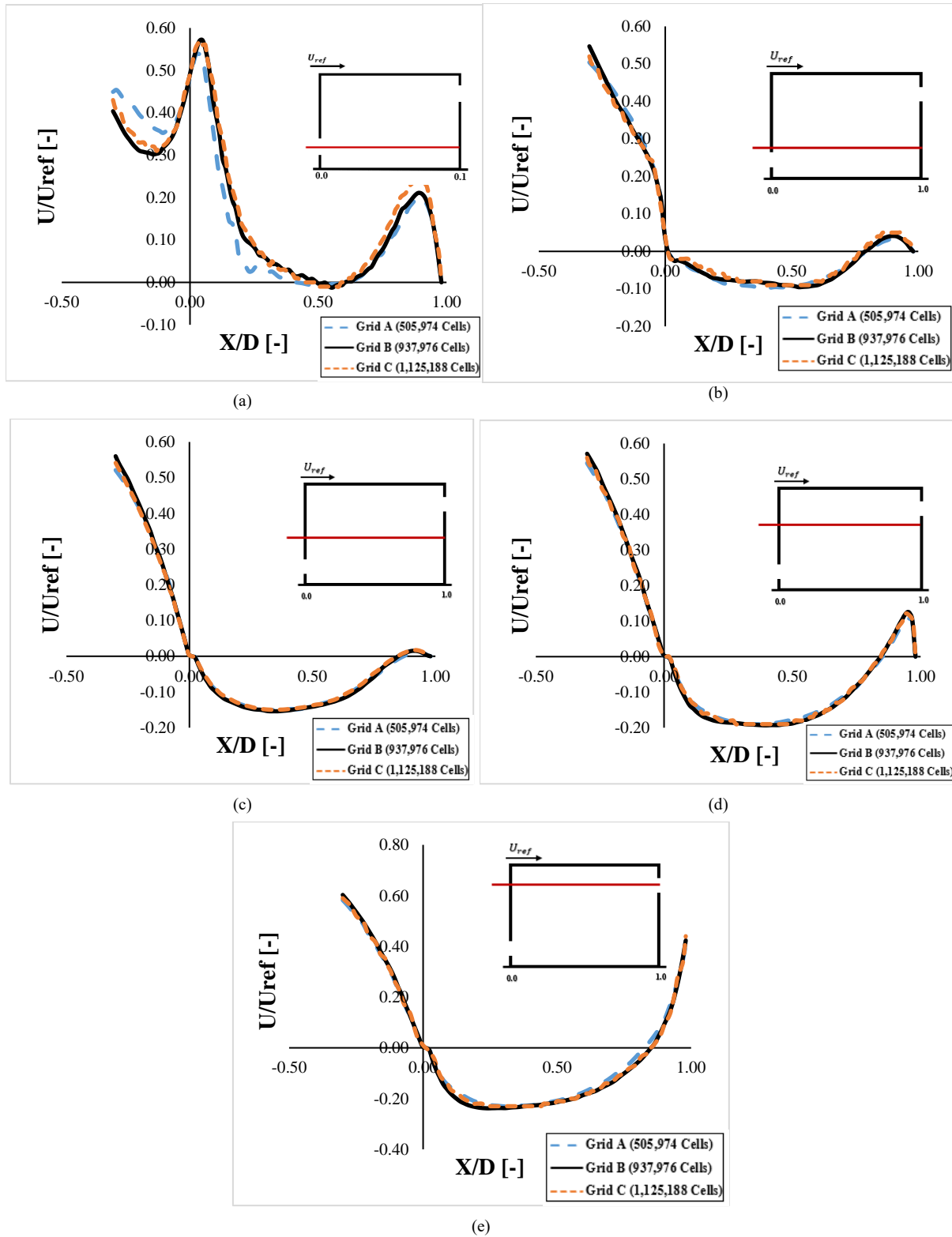


Figure 6. Grid sensitivity analysis of coarse grid (grid A), medium grid (grid B) and fine grid (grid C) for (a) $Y/H = 0.250$ (b) $Y/H = 0.375$ (c) $Y/H = 0.500$ (d) $Y/H = 0.625$ (e) $Y/H = 0.750$.

3. Simulation Cases

The sawtooth roof resembles a trapezoid design that is implemented in buildings and has a strong impact with the openings to improve the internal airflow through buildings. Table 2 shows the twelve simulation cases with sawtooth roof and various opening positions which are asymmetrical as Bottom-Top, Bottom-Middle, Middle-Top and symmetrical as Middle-Middle whereas each opening position with different roof inclination angle of 9° , 18° and 27° . The opening positions are termed based on the windward and leeward configuration. The center of the openings for the bottom, middle and top opening positions were located at 20 mm , 40 mm , and 60 mm from the ground as illustrated in Figure 7. Furthermore, all windward and leeward openings have the same size of $46\text{ mm} \times 18\text{ mm}$ ($L \times H$). The building model volume for all cases is 0.0008 m^3 . The building windward height at roof inclination angle 9° was reduced to 72.08 mm and the leeward height was increased to 87.92 mm by using a trapezoid method as illustrated in Figure 7e, which is similar to the previous study by Perén et al. [18]. The

building was split into half by the measurement plane to simulate the symmetry condition for the purpose of reduction in the computational time required for simulation.

Table 2. Summary of simulation cases for the sawtooth roof

Cases	Opening Position	Roof Inclination Angle	Roof Type
Case 1		9°	
Case 2	Bottom-Top	18°	
Case 3		27°	
Case 4		9°	
Case 5	Bottom-Middle	18°	
Case 6		27°	
Case 7		9°	Sawtooth Roof
Case 8	Middle-Top	18°	
Case 9		27°	
Case 10		9°	
Case 11	Middle-Middle	18°	
Case 12		27°	

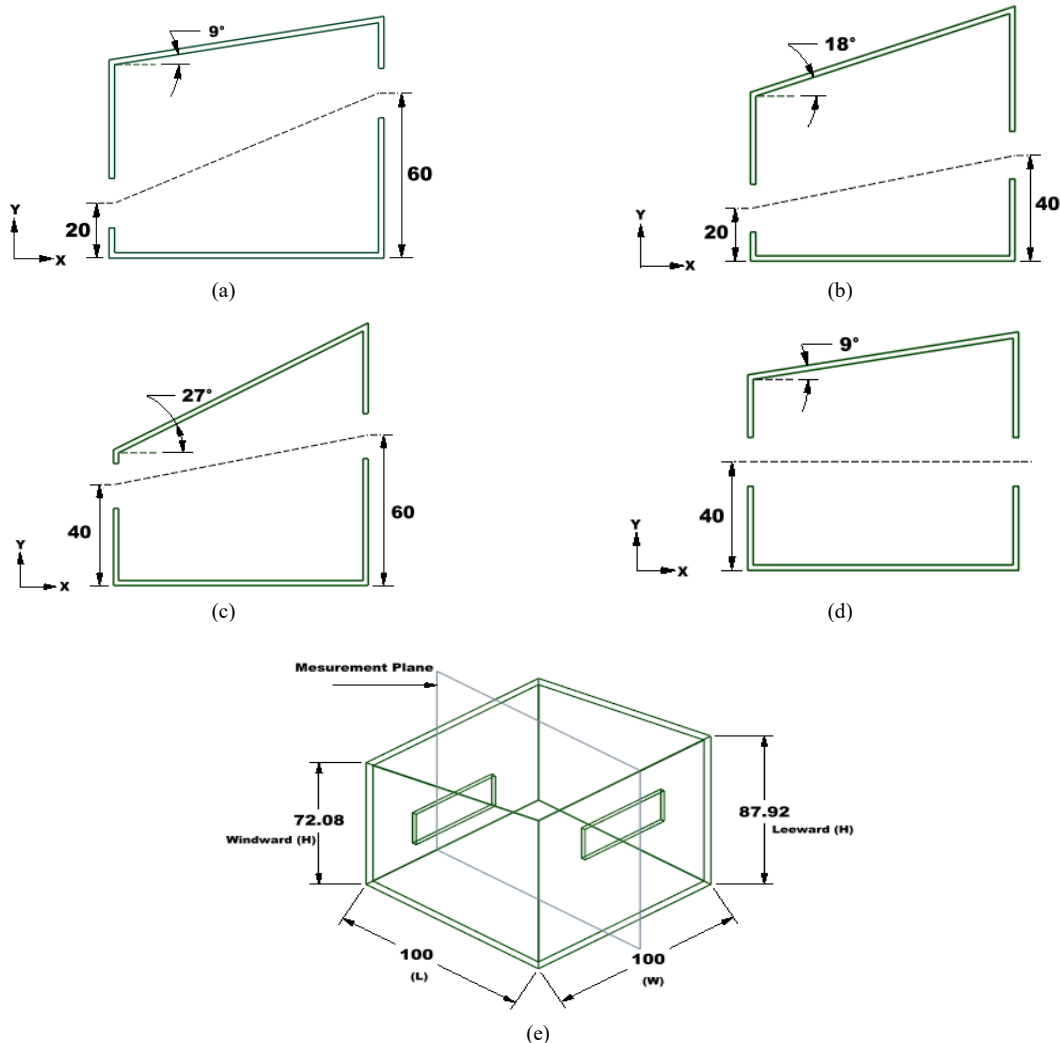


Figure 7. Opening positions with roof inclination angles (RIA) (a) bottom-top (b) bottom-middle (c) middle-top (d) middle-middle (e) RIA- 9° isometric view.

4. Results and Discussion

In this section, the dimensionless velocity magnitude ($|V|/U_{ref}$), dimensionless mean streamwise velocity ratio (U/U_{ref}), pressure coefficient (C_p), contours and volume flow rate (VFR) for sawtooth roof were discussed.

4.1. Dimensionless Velocity Magnitude ($|V|/U_{ref}$)

The dimensionless velocity magnitude contours for the sawtooth roof are illustrated in Figure 8. In terms of the airflow characteristics around and inside the building model, a large area of low-magnitude velocity gradient can be seen across all opening positions whereby it is above the incoming jet. For instance, at the bottom-top and bottom-middle opening positions, it can be seen that for low roof inclination angle, the jet flow is more directed downwards which resulting in high velocity magnitude after the windward opening at 9° , whereas the higher velocity magnitude observed at the windward opening for the roof inclination angle of 27° . Next, for the middle-middle opening configuration of sawtooth roof, the inlet jet is more downward compared to the middle-top opening position. Then it can be seen that the outlet jet for the opening configurations change in direction with the changing of opening positions and increasing of roof

inclination angles. Furthermore, the angle of the outlet velocity jet for bottom-top, bottom-middle and middle-middle opening positions can be seen to be angled upwards compared to middle-top opening position with roof inclination angles of 9° and 27° which are angled downward.

The peak region of the dimensionless velocity magnitude for sawtooth roof decreases and moves towards the ridge as the roof inclination angle increases to 18° . Similarly, the highest peak value of dimensionless velocity magnitude observed at roof inclination angle 9° for all opening configurations. The peak region reduces with the increases of roof inclination angles. The findings observed are in lined with the existing literature from Perén et al. [18].

The wind speed inside the building increases with the increased roof inclination angle, and the wind speed decreases when the air leaves the building. This is owing to the interdependence of air movement through the openings and the occurrence of recirculation region. The existence of the recirculation region at the bottom corner behind the building decreases gradually when the roof inclination angle increases. A significant recirculation region was noticed for the sawtooth roof, which could be attributed to the roof's sharp edge.

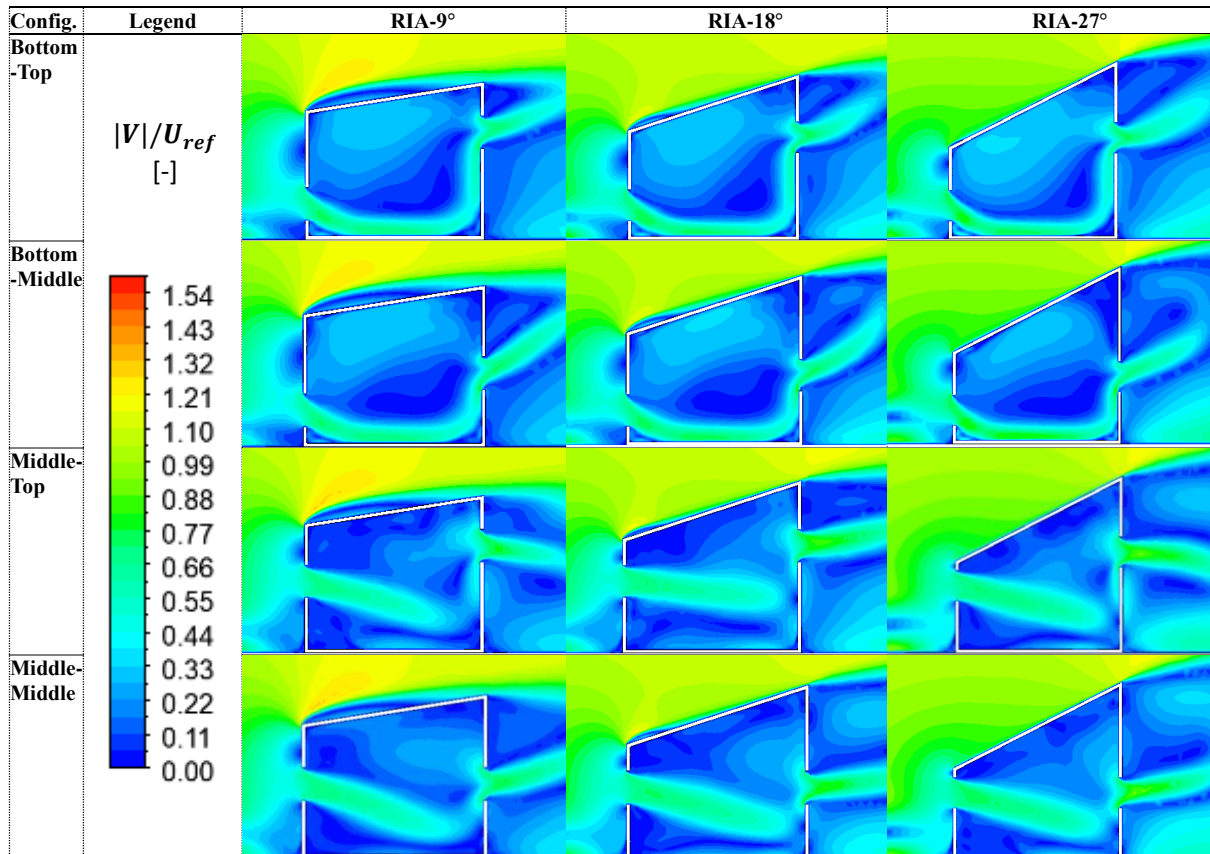


Figure 8. Contours of dimensionless velocity magnitude ($|V|/U_{ref}$) at vertical center plane.

4.2. Pressure Coefficient

The pressure coefficient, C_p , can be described as a non-dimensionless indication that identifies the differences between the static pressure beyond a specified fluid region and the freestream pressure as described in Equation (8). In the current study, the pressure coefficient between both the windward and leeward windows was determined. The average pressure coefficient through the windward and leeward façades was therefore subtracted to produce the difference in pressure coefficient, ΔC_p , which will be discussed in Section 4.4.

$$C_p = \frac{P - P_0}{0.5\rho U_{ref}^2} \quad (8)$$

The pressure coefficient contours for sawtooth roof are shown in Figure 9. The bottom-top and bottom-middle opening positions with the roof inclination angle 9° shows a high pressure gradient in the center of the building. However, it is observed that increasing the roof inclination angle up to 18° and 27° results in a low pressure within the building. In that note, the pressure increases with low inclination angles and reduced with the increased in roof inclination angles. Interestingly, the pressure coefficient contours for bottom-top opening position are in agreement with the results obtained by Perén et al. [18]. On the other hand, for the middle-top opening position, the high pressure gradient region is observed at the corner ground of leeward wall within the building for roof inclination angle of 9° . The internal high pressure gradient become

lower with the increases of roof inclination angle. Furthermore, the middle-top and middle-middle opening configuration shows a higher pressure gradient within the building compared to bottom-top and bottom-middle opening configurations.

Furthermore, from all the opening configuration contours recorded, the maximum pressure in front of the building of the windward opening drops uniformly with the increase of roof inclination angle. The maximum pressure observed on the windward façade due to the influence of air colliding to the windward wall. In other words, since the varying pressure distribution mostly on the windward side, the direction of the incoming jet fluctuates slightly for each case, resulting another more horizontally directed flow as the increases of the leeward wall height and roof inclination angle. It can say that the variance in low pressure behind the building across the various scenarios is greater than the variance within high pressure in front of the building.

In overall, the roof inclination angles and opening positions has a high influence on the internal pressure within the building. Sawtooth roof shows a significantly changes in internal pressure and external observed at the windward wall. From the contours below, it can be seen that the internal and external coefficient pressure decreases with the increased of roof inclination angle. This suggests that the roof inclination angle is indeed a critical geometrical component for increasing the wind-driven cross ventilation.

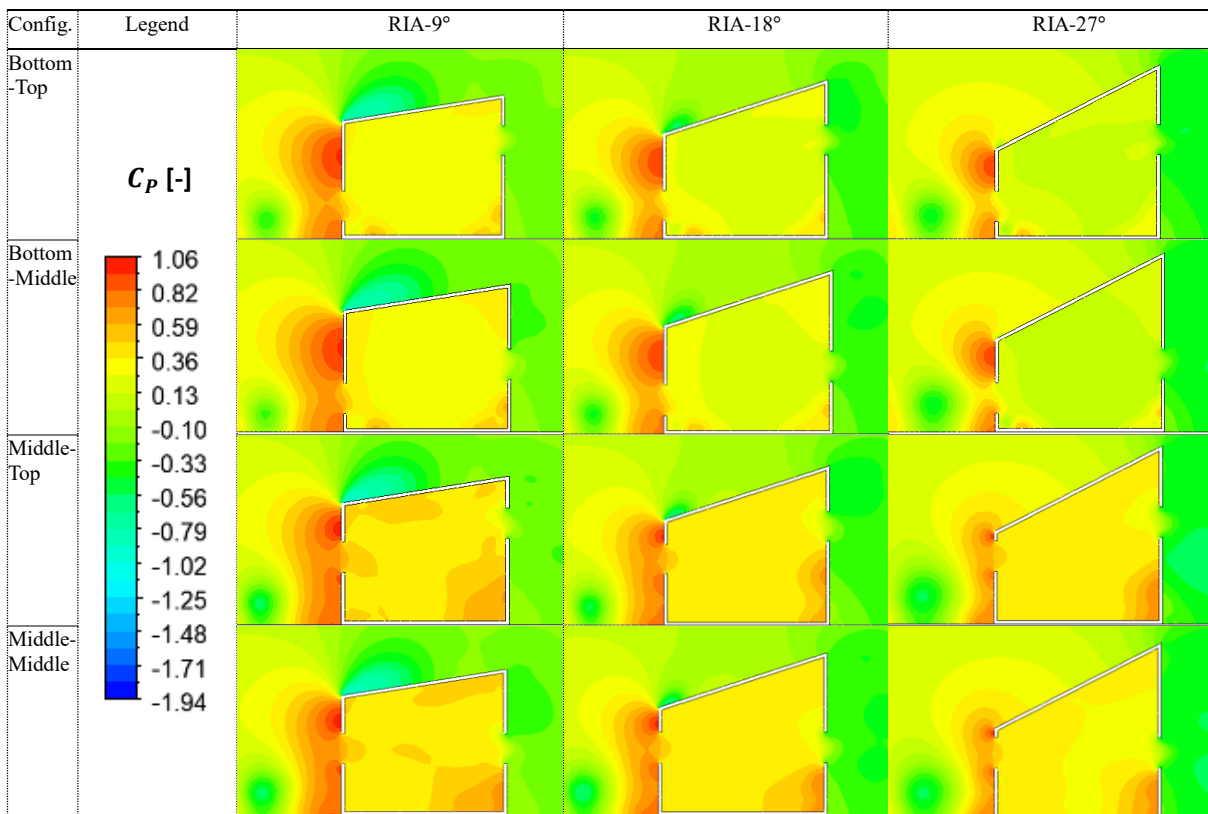


Figure 9. Contours of pressure coefficients (C_p) at vertical center plane.

4.3. Dimensionless Streamwise Wind Speed Ratio (U/U_{ref})

The velocity magnitude recorded within the building was divided by the reference velocity (U_{ref}) of 6.97 m/s at building height to make the variable obtained to be dimensionless. Thus, the resulting dimensionless streamwise wind speed ratio (U/U_{ref}) along the horizontal line were shown in Figure 10. The purpose of determine the dimensionless streamwise velocity along the horizontal line is to observe the influence of the roof inclination angles together with the impact of opening positions on the indoor airflow within the building.

For the bottom-top configuration, as the roof inclination angle increases, the streamwise wind velocity ratio increases along approximately the entire horizontal line. The indoor mean streamwise wind speed ratio along the horizontal line shows a difference in roof inclination angles, mostly between x/D of 0.1 and 0.9. Note that although the roof inclination angle of 9° has a lower streamwise wind speed ratio than the reference case (flat

roof), the indoor air velocity along the horizontal line was higher in some regions observed between $0.4 < x/D < 0.6$ compared to the reference case. Furthermore, for the bottom-middle configuration, it can be seen that the streamwise velocity ratio shows a small difference among the roof inclination angles, especially from $0.2 < x/D < 0.8$, whereas the streamwise wind speed ratio for roof inclination angle of 27° was shifted to the left from the other roof inclination angles, between $0.1 < x/D < 0.3$, despite the fact that a steeper decline of the indoor airflow compared to the bottom-top opening position. This is due to the leeward opening at the middle position that increase the resistance of the indoor air flow. On the other hand, middle-top opening position shows an increasing in streamwise wind speed ratio with increases of roof inclination angles between $0 < x/D < 0.1$. The same trend is shown for the middle-middle opening positions, which clearly indicate that the streamwise wind speed ratio increases with the increasing of roof inclination angle.

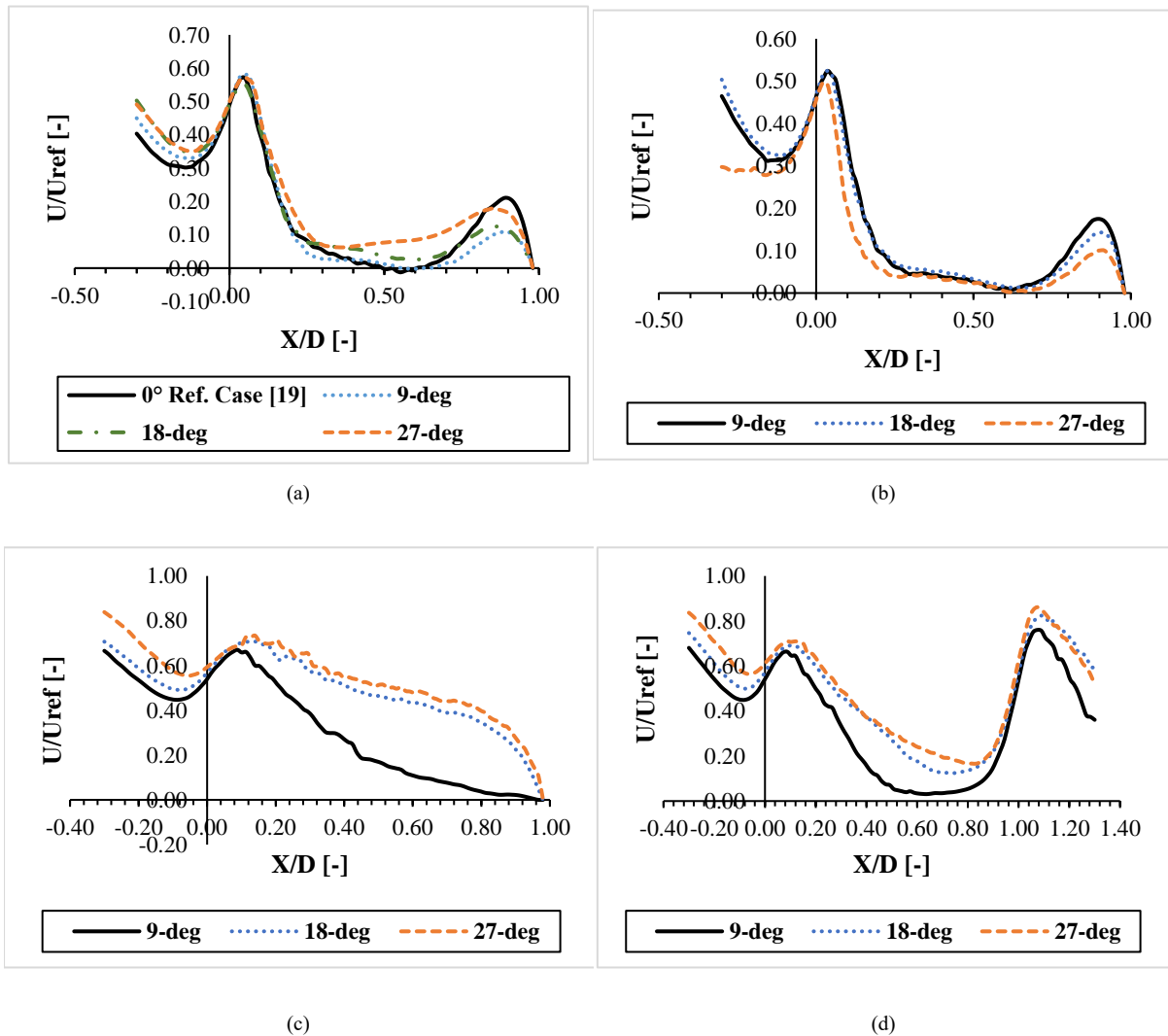


Figure 10. Dimensionless mean streamwise velocity ratio along the horizontal line for (a) bottom-top (b) bottom-middle (c) middle-top (d) middle-middle opening position.

4.4. Volume Flow Rate (VFR)

Overall volume flow rate was obtained using the following equations by Andy Walker [35]. The pressure difference, ΔC_p was calculated using the average pressure coefficients at both the windward and leeward façade, as shown in Equation (9).

$$\Delta C_p = C_{p.windward} - C_{p.leeward} \tag{9}$$

The flow coefficient, CQ was calculated using Equation (10) with the reference wind speed of 6.97 m/s and the discharge coefficient, C_D of 0.62 [36].

$$CQ = U_{ref} C_D \sqrt{\Delta C_p} \tag{10}$$

Furthermore, the flow coefficient, CQ was applied to Equation (11) to calculate the actual flow coefficient, C_a . The volume flow rate, Q was determined by using Equation (12) with the reference velocity, U_{ref} and the area of the openings, A_e of 0.000828 m^2 .

$$C_a = \frac{CQ}{1 + CQ} \tag{11}$$

$$Q = U_{ref} A_e C_a \tag{12}$$

To the best of authors' knowledge, the effect of sawtooth roof inclination angles of 9°, 18° and 27° together with symmetrical and asymmetrical opening configurations was not taken into account in the literature. Hence, in the current study, the volume flow rate was used to quantify the effects of increased roof angles and change in the position of openings on the volume flow rate.

The volume flow rate for all roof inclination angles of 9°, 18° and 27° along with the opening configurations were shown in Figure 11. It can be seen that the volume flow rate increases with the increase in roof inclination angle from all opening configurations. It can be seen that the roof inclination angle of 27° with middle-top opening position has the highest volume flow rate of 115% and then followed by the bottom-top, middle-middle and bottom-middle opening positions with the volume flow rate of 109%, 108% and 106%, respectively. This differences between the highest and the lowest volume

flow rate is due to the pressure differences across the windward and leeward openings. However, it should be mentioned that the roof angle of 27° is the geometry with the largest leeward height. The building height can be another factor that influences the volume flow rate. These findings are in line with the existing literature of the asymmetrical opening position by Perén which discovered that the increased of roof inclination angles more than 18° compared to the reference case (Flat roof) can increase the volume flow rate [18]. Furthermore, among all the three-inclination angles for the middle-top opening position can be seen only a slight difference in volume flow rate up to 0.68% which indicate in a better volume flow rate through the building for the middle-top opening position regardless of the roof inclination angles.

Next, the bottom-top opening position has a significant increase in volume flow rate of 5% from the roof inclination angle of 9° to 18° and 9% from the roof inclination angle of 18° to 27°. On the other hand, the bottom-middle opening configuration has the lowest volume flow rate from roof inclination angle of 27° at 106% while the roof inclination angles of 9° and 18° indicate a higher volume flow rate with 103% and 105% compared to bottom-top and middle-middle configurations. Additionally, the volume flow rate for middle-middle opening configuration increased by 3% from the roof inclination angle of 9° to 18° and 4% from the roof inclination angle of 18° to 27°. Increasing the roof inclination angle can increase the volume flow rate. The middle-middle opening position along with the roof inclination angles are in line with the previous study by Kindangen [37], which discovered that increasing of roof inclination angle has a significant impact on the volume flow rate inside the building.

In overall, higher volume flow rate was observed when the leeward opening located near the roof and the windward opening located at the middle. On the other hand, the building experienced weaker volume flow rate when the windward openings located near the ground. Nevertheless, changing the windward opening to a higher position near the roof can potentially increase the volume flow rate with the increases of roof inclination angles within the building [38].



Figure 11. Impact of roof inclination angle (RIA) and opening positions on volume flow rate (VFR)

5. Conclusion

The influence of sawtooth roof together with the opening positions and various roof inclination angles have been analysed. The roof inclination angles considered are 9°, 18° and 27° whereas the opening positions considered are bottom-top, bottom-middle, middle-top and middle-middle. These opening configurations mentioned were based on the windward and leeward positions. The computational domain was designed based on the recommendations and current practices for natural ventilation provided in the literature [20-23]. Grid convergence index (GCI) analysis was carried out and GCI average of less than 3% was achieved, which is within the acceptable range. The medium grid (Grid B) was chosen with the shear stress transport $k-\omega$ turbulence model for the subsequent simulation cases as it has a good agreement with a reference case from the literature [19]. The results from the simulations were analysed in terms of the dimensionless velocity magnitude, pressure coefficient, dimensionless streamwise wind speed ratio and volume flow rate collectively. The main findings from this study can be summarized as below:

- The speed of the airflow throughout the building is influenced by the recirculation region and internal stagnation point.
- Opening closer to the roof of the building generates a higher volume flow rate through the building regardless of the roof inclination angles used. Similarly, the highest volume flow rate obtained in the simulations was 115% from middle-top opening position with the roof inclination angle 27°. The findings were in lined with the findings from the existing literature [18].
- To enhance the volume flow rate (VFR) inside the low-rise building, the roof inclination angle should be greater than 18°, whereas lower roof inclination angle like 9°, results in a lower volume flow rate (VFR) compared to reference case building (flat roof).
- Pressure coefficient recorded was higher for the middle-top opening position and roof inclination angle 9° compared to middle-middle opening position across all roof configurations. This can be attributed to the added flow resistance by the difference in the position of the windward and leeward openings. Meanwhile, the bottom-top opening position recorded a lower pressure coefficient compared to the bottom-middle opening position.

Overall, it can be concluded that the current study has provided significant findings which can be considered novel in the field of natural ventilation as there are not many studies involving cross ventilation and roof inclination angle with opening positions concurrently and the implications of the volume flow rate, pressure coefficient and airflow pattern for the natural ventilated building. Nonetheless, further study can be done to assess the impact of roof configuration design parameters for the building ventilation performance.

6. Future Recommendation

The current study was an investigation on the natural ventilation of isolated building with limitations. However, some improvements can be included in future work for

better and broader research. Therefore, the future work can follow the below aspects:

- This research intends on the wind angle of 0°. The ventilation performance can be possibly changed for various wind angles.
- In the current research, all the simulations obtained for isothermal condition. Future work can focus on non-isothermal condition to analyse the impact of temperature gradients within the building, the balance across wind and buoyancy such as driving forces of the ventilation flow and better understanding the heat transfer within the building.
- In the current study, only the sawtooth roof with three roof inclination angles were considered which are 9°, 18°, and 27°. Future work different roof configurations and higher roof inclination angles can be considered to possibly increase the ventilation performance for the building.
- The impact of obstacles inside the building at different positions with the presence of roof configuration.

References

- [1] C.H. Lim, O. Saadatian, K. Sopian, M.Y. Sulaiman, S. Mat, E. Salleh, "Design configurations analysis of wind-induced natural ventilation tower in hot humid climate using computational fluid dynamics". *International Journal of Low-Carbon Technologies*, Vol. 10, No. 4, 2013, 332-346.
- [2] M.N. Khan, I. Janajreh, "Transevaporative cooling performance of a three-sided wind catcher". *Jordan Journal of Mechanical and Industrial Engineering*, Vol. 11, No. 4, 2017, 225-233.
- [3] Yong M, Lesjak M, Hor K, Rowse B, Tandon S. *Compendium of policy and financial instruments for accelerating building sector energy efficiency in Malaysia*. Kuala Lumpur: Building Sector Energy Efficiency Project (BSEEP); 2017.
- [4] N.A. Hassan, Z. Hashim, J.H. Hashim, "Impact of climate change on air quality and public health in urban areas". *Asia Pacific Journal of Public Health*, Vol. 28, No. 2, 2014, 38-48.
- [5] N.C. Kar, L.K. Moey, T.F. Go, P.L. Chong, and C.M. Chia, "Short review on renewable energy policy and energy consumption of buildings in Malaysia". *International Journal of Engineering and Advanced Technology*, Vol. 7, No. 1, 2022, 64-82.
- [6] R. Behari, "Special Report: Almost out of time | The Edge Markets," *The Edge Malaysia*, 2020. <https://www.theedgemarkets.com/article/special-report-almost-out-of-time> (Accessed 2 June 2022).
- [7] S.A. Ahmed, H.O. Mahammed, "A statistical analysis of wind power density based on the weibull and ralyeigh models of "Penjwen region" Sulaimani/Iraq". *Jordan Journal of Mechanical and Industrial Engineering*, Vol. 6, No. 2, 2012, 135-140.
- [8] N. Hussein, "Greenhouse gas emissions reduction potential of Jordan's utility scale wind and solar projects". *Jordan Journal of Mechanical and Industrial Engineering*, Vol. 10, No. 3, 2016, 199-203.
- [9] L.K. Moey, M.F. Kong, V.C. Tai, T.F. Go, N.M. Adam, "Effect of gable roof angle on natural ventilation for an isolated building". *Jordan Journal of Mechanical and Industrial Engineering*, Vol. 15, No. 3, 2021, 291-300.
- [10] C.H. Lim, O. Saadatian, M.Y. Sulaiman, S. Mat, K. Sopian, M.R. Mahyuddin, K.C. Ng, "Using computational fluid dynamics (CFD) method in analyzing different design configurations of Venturi-shaped wind-induced natural ventilation towers". *Latest trends in renewable energy and*

- environmental informatics : proceedings of the 4th international conference on renewable energy sources (RES '13), proceedings of the 1st international conference on environmental informatics (ENINF '13) : Kuala Lumpur, Malaysia, 2013.
- [11] L. K. Moey, N. M. Adam, K. A. Ahmad, "Effect of venturi-shaped roof angle on air change rate of a stairwell in tropical climate". *Journal of Mechanical Engineering.*, Vol. 4, No. 4, 2017, 135-150.
- [12] L.K. Moey, M.F. Kong, V.C. Tai, T.F. Go, N.M. Adam, "Effects of roof configuration on natural ventilation for an isolated building". *Journal of Mechanical Engineering Science*, Vol. 15, No. 3, 2021, 8379-8389.
- [13] Y. Tominaga, S.I. Akabayashi, T. Kitahara, Y. Arinami, "Air flow around isolated gable-roof buildings with different roof pitches: Wind tunnel experiments and CFD simulations". *Building and Environment*, Vol. 84, No. 1, 2015, pp. 204-213.
- [14] Z. Liu, Z. Yu, X. Chen, R. Cao, F. Zhu, "An investigation on external airflow around low-rise building with various roof types: PIV measurements and LES simulations". *Building and Environment*, Vol. 169, No. 2, 2020, 106-583.
- [15] J.I. Perén, T.V. Hooff, B.C.C. Leite, B. Blocken, "CFD simulation of wind-driven upward cross ventilation and its enhancement in long buildings: Impact of single-span versus double-span leeward sawtooth roof and opening ratio". *Building and Environment*, Vol. 96, No. 4, 2015, 142-156.
- [16] M.A. Lukiantchuki, R. Caram, E. Matsumoto, L.C. Labaki, "Natural Ventilation by Air Captors and Extractors Sheds in Hospitals in Brazil: Wind Tunnel Measurements". *Journal of Civil Engineering and Architecture*, Vol. 8, No. 10, 2014, 1293-1303.
- [17] N.S. Fouad, G.H. Mahmoud, N.E. Nasr, "Comparative study of international codes wind loads and CFD results for low rise buildings". *Alexandria Engineering Journal*, Vol. 57, No. 4, 2018, 3623-3639.
- [18] J.I. Perén, T.V. Hooff, B.C.C. Leite, B. Blocken, "CFD analysis of cross-ventilation of a generic isolated building with asymmetric opening positions: Impact of roof angle and opening location". *Building and Environment*, Vol. 85, No. 2, 2015, 263-276.
- [19] P. Karava, T. Stathopoulos, A.K. Athienitis, "Airflow assessment in cross-ventilated buildings with operable façade elements". *Building and Environment*, Vol. 46, No. 1, 2011, 266-279.
- [20] R. Ramponi, B. Blocken, "CFD Simulation of cross-ventilation for a generic isolated building: impact of computational parameters". *Building and Environment*, Vol. 53, 2012, 34-48.
- [21] J. Franke, A. Hellsten, H. Schlunzen, B. Carissimo, *Best practice guideline for the CFD simulation of flows in the urban environment*, 1st ed. Belgium: Cost Action; 2007.
- [22] Y. Tominaga, A. Mochida, R. Yoshie, H. Kataoka, T. Shirasawa, "AIJ guidelines for practical applications of CFD to pedestrian wind environment around buildings". *Journal of Wind Engineering and Industrial Aerodynamics*, Vol. 96, No. 10-11, 2008, 1749-1761.
- [23] R. Ramponi, B. Blocken, "CFD simulation of cross-ventilation flow for different isolated building configurations: Validation with wind tunnel measurements and analysis of physical and numerical diffusion effects". *Journal of Wind Engineering and Industrial Aerodynamics*, Vol. 104-106, 2012, 408-418.
- [24] B. Blocken, T. Stathopoulos, J. Carmeliet, "CFD simulation of the atmospheric boundary layer: wall function problems." *Atmospheric Environment*, Vol. 41, No. 2, 2007, 238-252.
- [25] B. Blocken, J. Carmeliet, T. Stathopoulos, "CFD evaluation of wind speed conditions in passages between parallel buildings - Effect of wall-function roughness modifications for the atmospheric boundary layer flow". *Journal of Wind Engineering and Industrial Aerodynamics*, Vol. 95, No. 9-11, 2007, 941-962.
- [26] T. Kolev, P. Fischer, M. Min, J. Dongarra, "Efficient exascale discretizations: High-order finite element methods". *International Journal of High Performance Computing Applications*, Vol. 35, No. 6, 2021, 527-552.
- [27] ANSYS, "Ansys Fluent 2021 R2 Theory Guide," 2021. [Online]. Available: <https://www.ansys.com/content/dam/campaigns/abm/technip/fluent-workflows.pdf> [Accessed 17 October 2021]
- [28] K. Zore, B. Sasanapuri, G. Parkhi, A. Varghese, "ANSYS mosaic Poly-Hexcore mesh for high-lift aircraft configurations". 21st AeSI Annual CFD Symposium, Bangalore, India, 2019.
- [29] Alawadhi EM. *Finite Element Simulations Using ANSYS*, Boca Raton: CRC Press; 2015
- [30] M. Shirzadi, P.A. Mirzaei, M. Naghashzadegan, Y. Tominaga, "Modelling enhancement of cross-ventilation in sheltered buildings using stochastic optimization". *International Journal of Heat and Mass Transfer*, Vol. 118, 2018, 758-772.
- [31] P.J. Richards R.P. Hoxey, "Appropriate boundary conditions for computational wind engineering models using the k-ε turbulence model". *Journal of Wind Engineering and Industrial Aerodynamics*, Vol. 46-47, No. 8, 1993, 145-153.
- [32] P. Karava, T. Stathopoulos, A.K. Athienitis, "Wind-induced natural ventilation analysis". *Solar Energy*, Vol. 81, No. 1, 2007, 20-30.
- [33] T. van Hooff, B. Blocken, Y. Tominaga, "On the accuracy of CFD simulations of cross-ventilation flows for a generic isolated building: Comparison of RANS, LES and experiments". *Building and Environment*, Vol. 114, 2017, 148-165.
- [34] P.J. Roache, "Quantification of uncertainty in computational fluid dynamics". *Annual Review of Fluid Mechanics*, Vol. 29, No. 1, 1997, 123-160.
- [35] A. Walker, "Natural Ventilation.," *Whole Building Design Guide* [Online], 2016. https://www.wbdg.org/resources/natural-ventilation?r=env_wall (Accessed 17 October 2021).
- [36] C.R. Chu, Y.H. Chiu, Y.J. Chen, Y.W. Wang, C.P. Chou, "Turbulence effects on the discharge coefficient and mean flow rate of wind-driven cross-ventilation". *Building and Environment*, Vol. 44, No. 10, 2009, 2064-2072.
- [37] J. Kindangen, G. Krauss, P. Depecker, "Effects of roof shapes on wind-induced air motion inside buildings". *Building and Environment*, Vol. 32, No. 1, 1997, 1-11.
- [38] N.F.M. Kasim, S.A. Zaki, M.S.M. Ali, N. Ikegaya, A.A. Razak, "Computational study on the influence of different opening position on wind-induced natural ventilation in urban building of cubical array". *Procedia Engineering*, Vol. 169, 2016, 256-263.



الجامعة الهاشمية



المملكة الأردنية الهاشمية

المجلة الأردنية
للهندسة الميكانيكية والصناعية

JJIMIE

مجلة علمية عالمية محكمة
تصدر بدعم من صندوق البحث العلمي

<http://jjmie.hu.edu.jo/>

ISSN 1995-6665

المجلة الأردنية للهندسة الميكانيكية والصناعية

المجلة الأردنية للهندسة الميكانيكية والصناعية: مجلة علمية عالمية محكمة تصدر عن الجامعة الهاشمية بالتعاون مع صندوق دعم البحث العلمي والابتكار- وزارة التعليم العالي والبحث العلمي في الأردن.

هيئة التحرير

رئيس التحرير

الاستاذ الدكتور علي جوارنه

مساعد رئيس التحرير

الدكتور احمد المقدادي

الدكتور مهند جريسات

الأعضاء

الاستاذ الدكتور طارق العزب

جامعة البلقاء التطبيقية

الاستاذ الدكتور طارق البشير

الجامعة الهاشمية

الاستاذ الدكتور ابراهيم ابو الشيخ

الجامعة الاردنية

الاستاذ الدكتور محمد المومني

جامعة العلوم والتكنولوجيا الاردنية

الاستاذ الدكتور نبيل بيظو

جامعة الطفيلة التقنية

الاستاذ الدكتور هيثم تيلان

الجامعة الهاشمية

فريق الدعم

المحرر اللغوي

الدكتور بكر محمد بني خير

تنفيذ واخراج

م. علي أبو سليمة

ترسل البحوث إلى العنوان التالي

الاستاذ الدكتور علي جوارنه

رئيس تحرير المجلة الأردنية للهندسة الميكانيكية والصناعية

الجامعة الهاشمية

كلية الهندسة

قسم الهندسة الميكانيكية

الزرقاء - الأردن

هاتف: 00962 5 3903333 فرعي 4147

Email: jjmie@hu.edu.jo

Website: www.jjmie.hu.edu.jo